264 High-Temperature Deformation

Pure Shear and Simple shear

Pure shear   +   Rigid body rotation   =   Simple shear
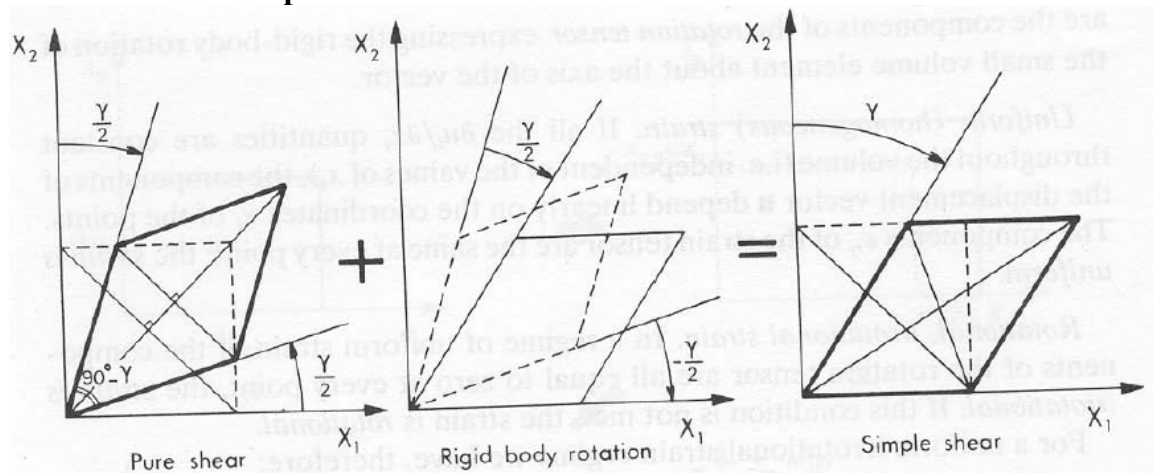
(Nicolas & Poirier, 1976)
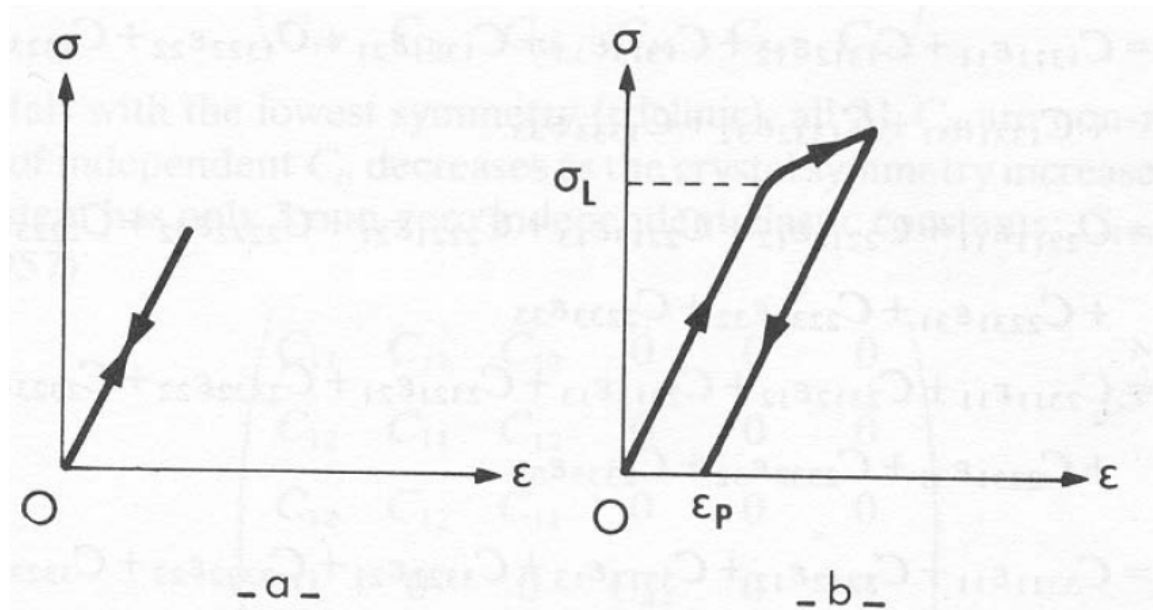
Elastic and Plastic Strain

Fig. 2.12. Stress strain diagram, stress: σ, strain: ε. (a) Elastic regime: stress is proportional to strain; when the stress is removed there is no residual deformation; (b) For $\sigma < \sigma_L$ (elastic limit), the deformation is elastic. For $\sigma > \sigma_L$: the deformation is plastic; when the stress is removed a residual plastic strain ε_p remains

(Nicolas & Poirier, 1976)

Elasticity and Moduli

bulk modulus or incompressibility

$$K = -V \frac{dP}{dV}$$

Young's modulus (relationship between longitudinal stress and strain)

$$E = \frac{\sigma}{\varepsilon}$$

shear modulus (relationship between shear stress and strain)

$$G, \mu = \frac{\sigma_{xy}}{2\varepsilon_{xy}}$$

Poisson's ratio (relationship between longitudinal extension and lateral contraction)

$$\nu = -\frac{\varepsilon_{zz}}{\varepsilon_{xx}}$$

Isochoric deformation

$$\varepsilon_{11} + \varepsilon_{22} + \varepsilon_{33} = 0$$

Point Defects
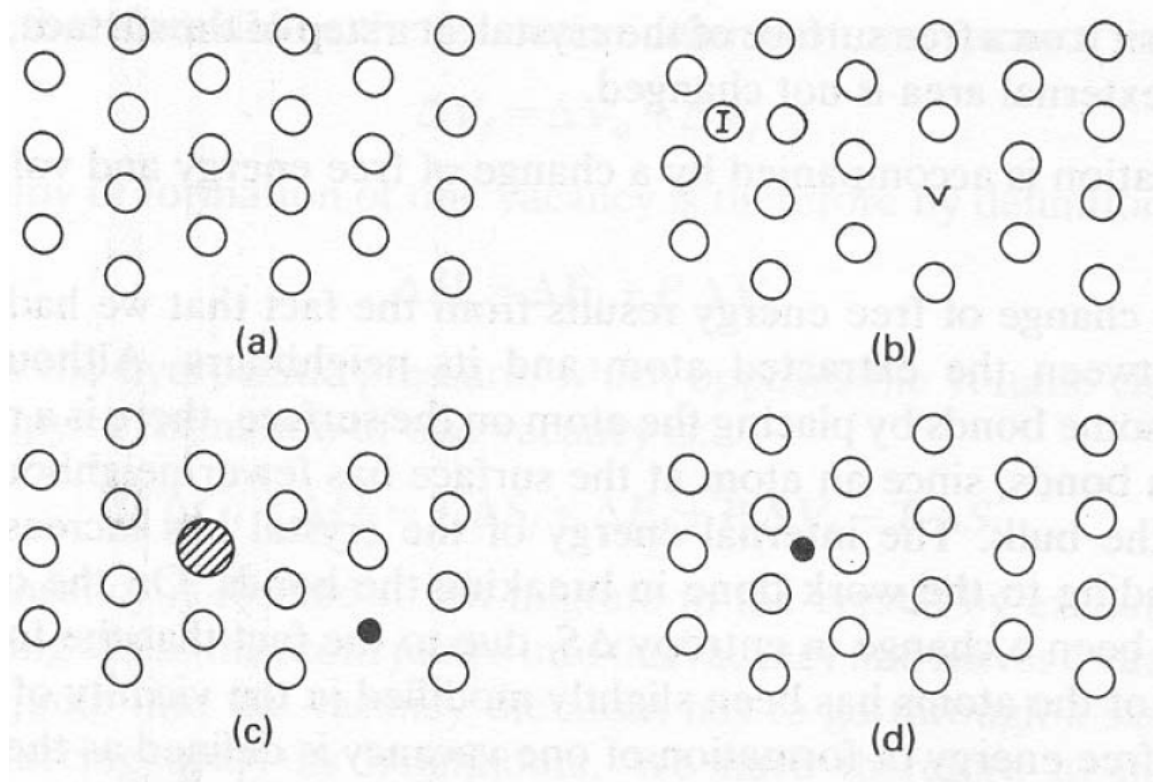are missing atoms (vacancies) or extra atoms in the crystal lattice.

Fig. 3. 1. Point defects: (a) perfect lattice; (b) I: self-interstitial, V: vacancy; (c) substitutional impurity atoms; (d) interstitial impurity atom

(Nicolas & Poirier, 1976)

Production of a vacancy has an energy cost associated with the breakage of some bonds, an energy cost associated with creating additional surface area, but a reduction in entropy and a relaxation around the vacancy.
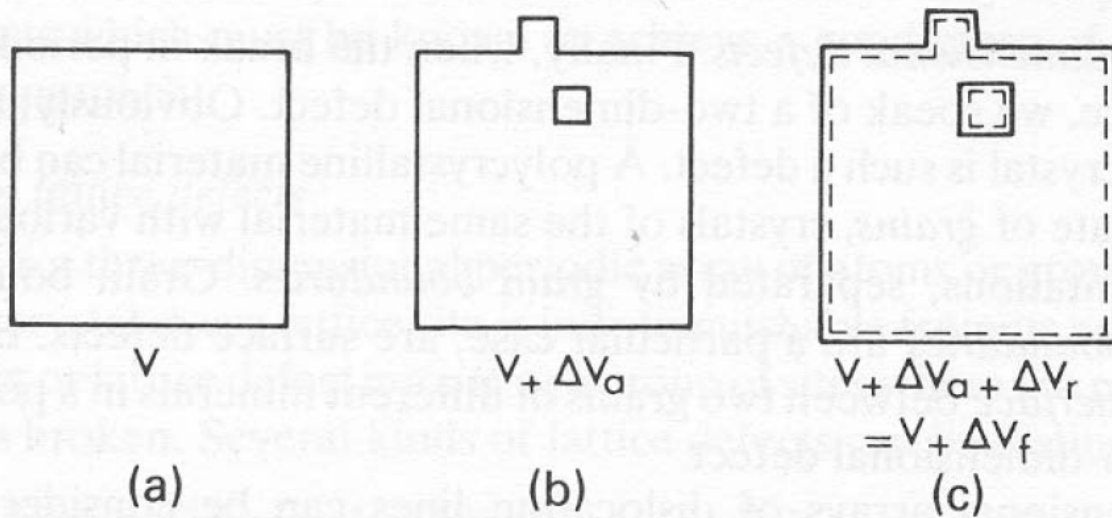

Fig. 3.2. Formation of a vacancy: (a) perfect crystal of volume V; (b) an atom is extracted from its site and deposited at the surface, the volume changes by an atomic volume ΔV_a; (c) the atoms relax around the vacancy. Here the relaxation volume ΔV_r is positive (the atoms relax outward). The total volume change is ΔV_f: formation volume of a vacancy

(Nicolas & Poirier, 1976)

This means that there is an equilibrium number of vacancies that allows the crystal to be in a lower free energy state than if it were perfect crystal:

$$\frac{n_v}{n} = \exp\left(-\Delta G_f / RT\right)$$

where n_v/n is the atomic fraction of vacancies and ΔG_f is the free energy of vacancy formation. For metals near melting, $n_v/n \sim 10^{-4}$–10^{-5}.
This means that crystals are always "ready to go" when it comes to diffusion.

Diffusion
Diffusive mass transfer takes place in response to chemical potential gradients. For the purposes of this class, we will simplify this, and consider diffusion to occur in response to concentration gradients.
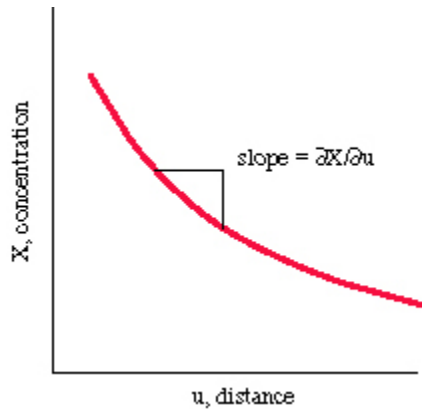
The partial differential $\partial X / \partial u$ is used to indicate that the concentration gradient can change as a function of time.

If a concentration gradient exists, diffusion will occur until the concentration is homogeneous. The flux (or rate at which material passes through a given area) is given by **Fick's first law**:

$$J = -D\, \partial X / \partial u$$

where D is the diffusivity. In terms of units, this equation is:

$$J \text{ [atoms m}^{-2}\text{ s}^{-1}] = -D \text{ [m}^2\text{ s}^{-1}]\, \partial X \text{ [atoms m}^{-3}]/ \partial u \text{ [m}^{-1}]$$

(instead of atoms, any other measure of mass can be used, such as moles).
The **diffusivity**, D, scales with temperature:

$$D \propto (kT/h)\, \exp(-Q^*/RT)$$

where k is Boltzmann's constant, h is Planck's constant, and Q^* is an activation energy. Often this is simplified to

$$D = D_o\, \exp(-Q^*/RT)$$

When diffusion is occurring, the concentration gradient changes in direct proportion to gradient in the diffusive flux:
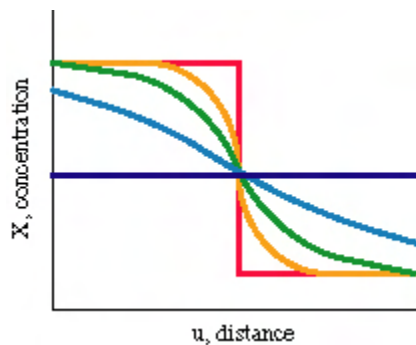
$$\partial X / \partial t = -\partial J / \partial u$$
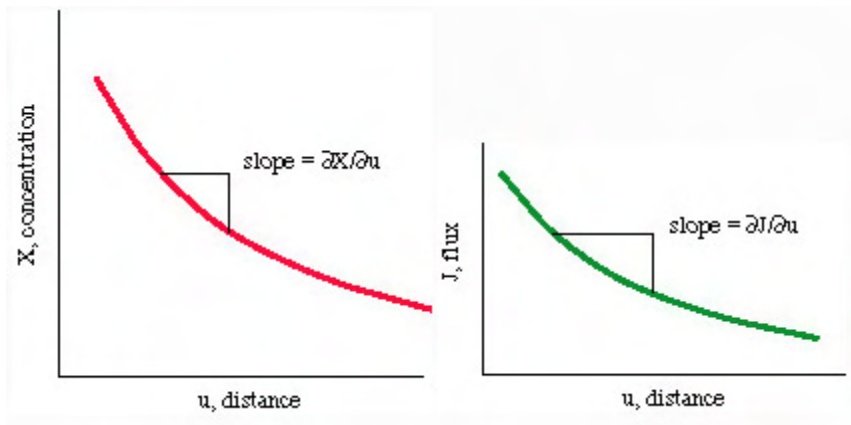
Substituting Fick's first law into this equation yields **Fick's second law**:

$$\partial X / \partial t = D \, \partial^2 X / \partial u^2$$

This equation tells us how fast the composition changes as a result of the diffusivity and the concentration gradient. For example, a concentration gradient that begins as a step function decays in the following manner:

$$X = X_o \, \mathrm{erf} \, [u / 2 \, (Dt)^{0.5}]$$

('erf' is a special indefinite integral). Note that this equation, describing how diffusion changes composition, contains the characteristic diffusion distance we looked at earlier when discussing how thermal diffusion changes temperature.

Slip System
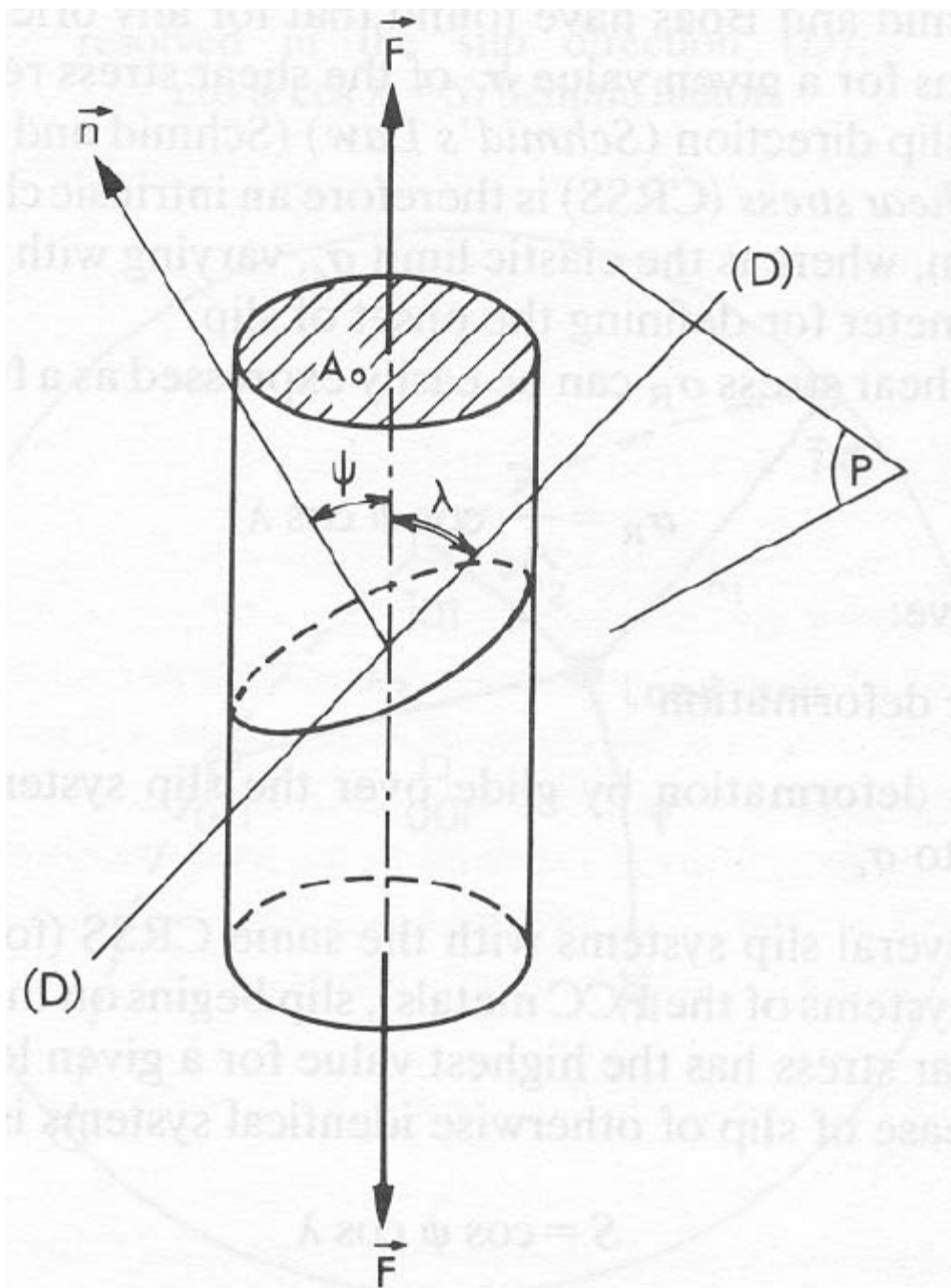
Fig. 2.17. Cylindrical single crystal under-
going plastic deformation under axial load
F. **n**: normal to slip plane (P); ψ: angle
between **n** and load axis: λ: angle between
slip direction (D) in plane (P) and load axis

(Nicolas & Poirier, 1976)

Resolved shear stress

$$\sigma_r = \frac{F}{A_o} \cos \psi \cos \lambda$$

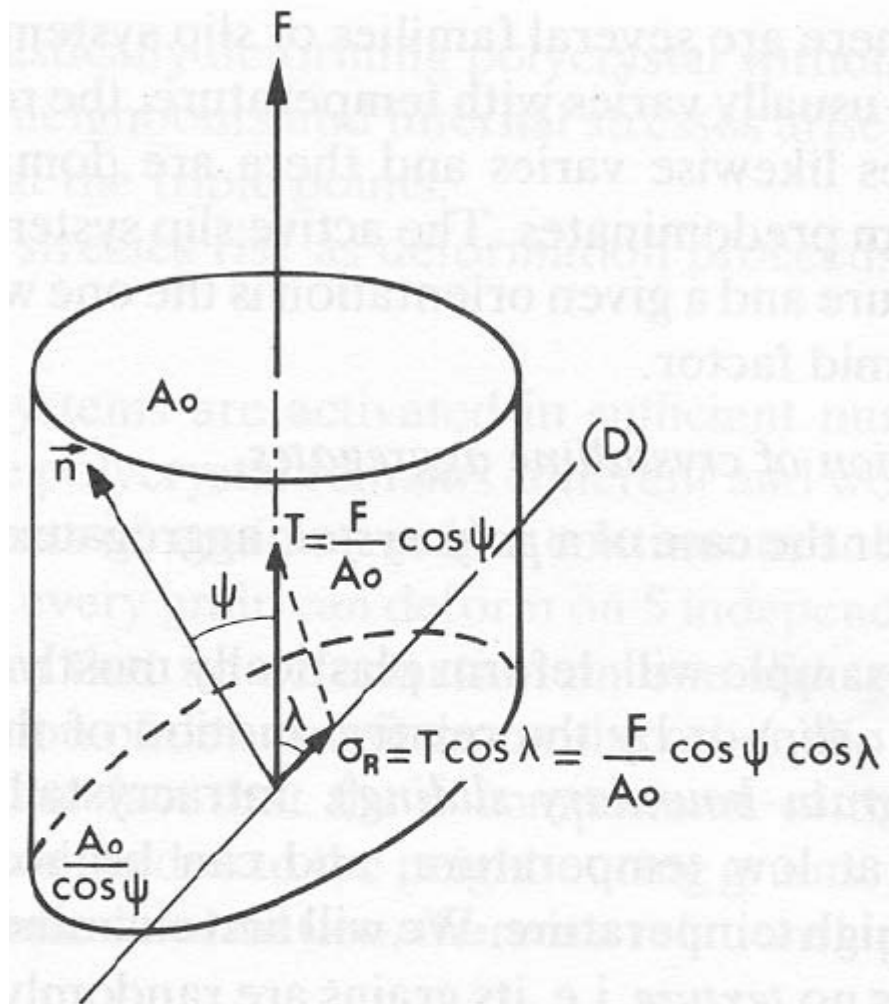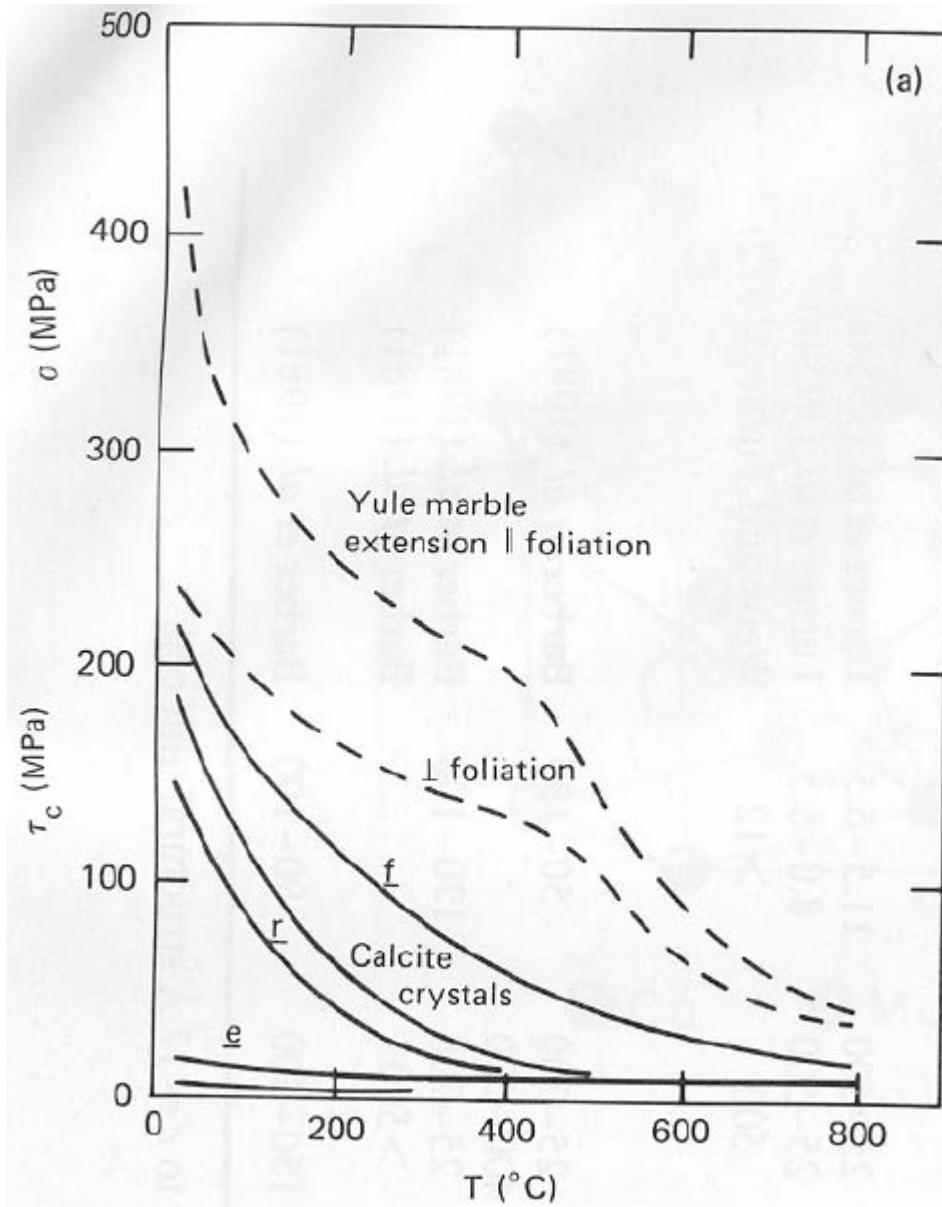critical resolved shear stress, CRSS, is that where slip begins

Fig. 2.18. Resolved shear stress. A_0: cross-section area of crystal; T: stress vector on slip plane normal to **n**, of area $A_0/\cos \psi$; σ_R: shear stress on slip plane, resolved in the slip direction (D); $\cos \psi \cos \lambda = S$: Schmid factor

(Nicolas & Poirier, 1976)

critical resolved shear stress for calcite (Wenk, 1985).

Schmid factor, S
$S = \cos\psi \cos\lambda$
slip system with highest Schmid factor is first to slip

Dislocations/Linear Defects
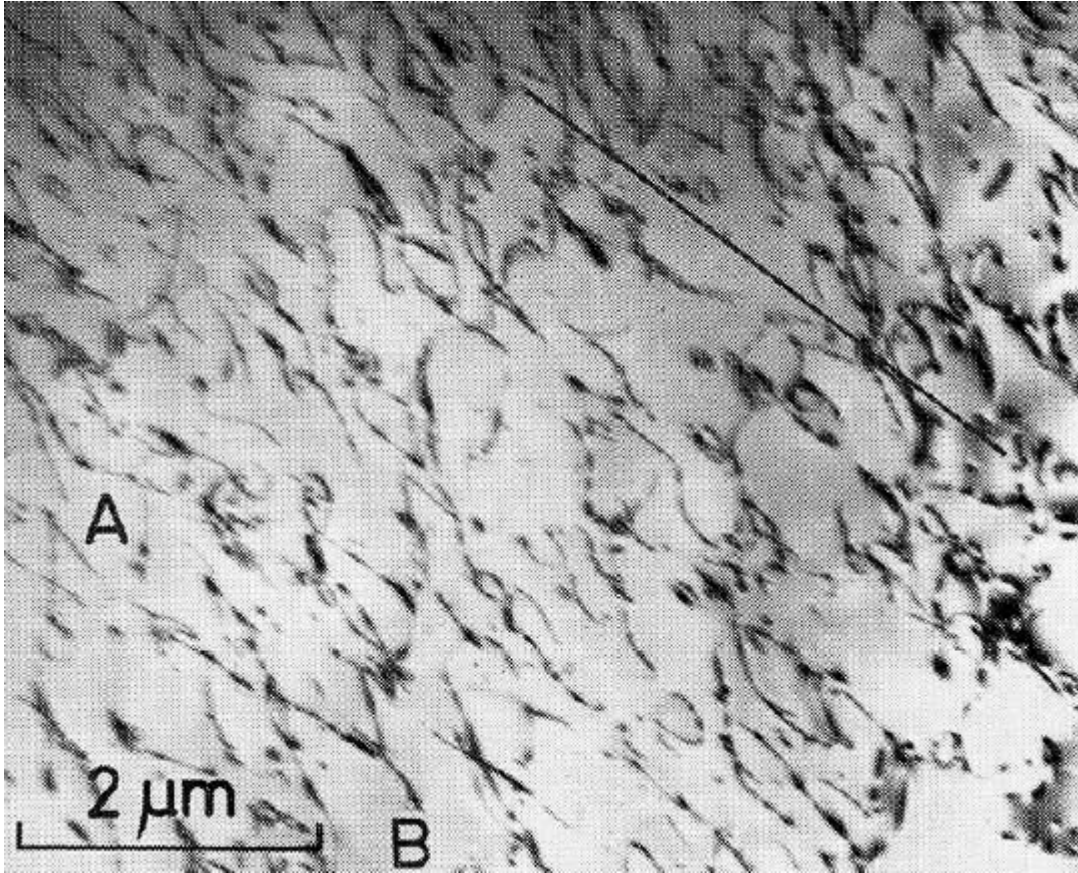
Dislocation in quartz. Predominant slip plane $(10\bar{1}0)$, marked by line, is perpendicular to section; note dislocations are subparallel to $(10\bar{1}0)$. (Hobbs et al., 1972)
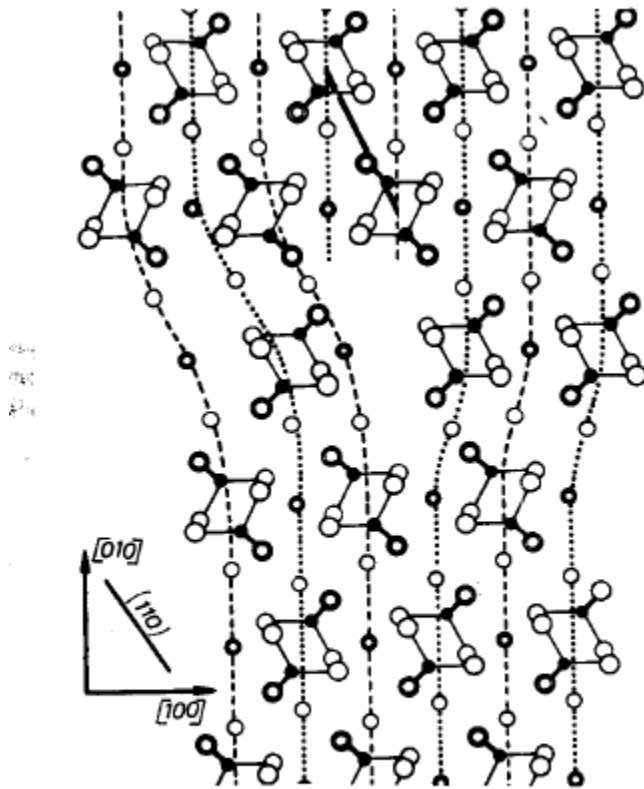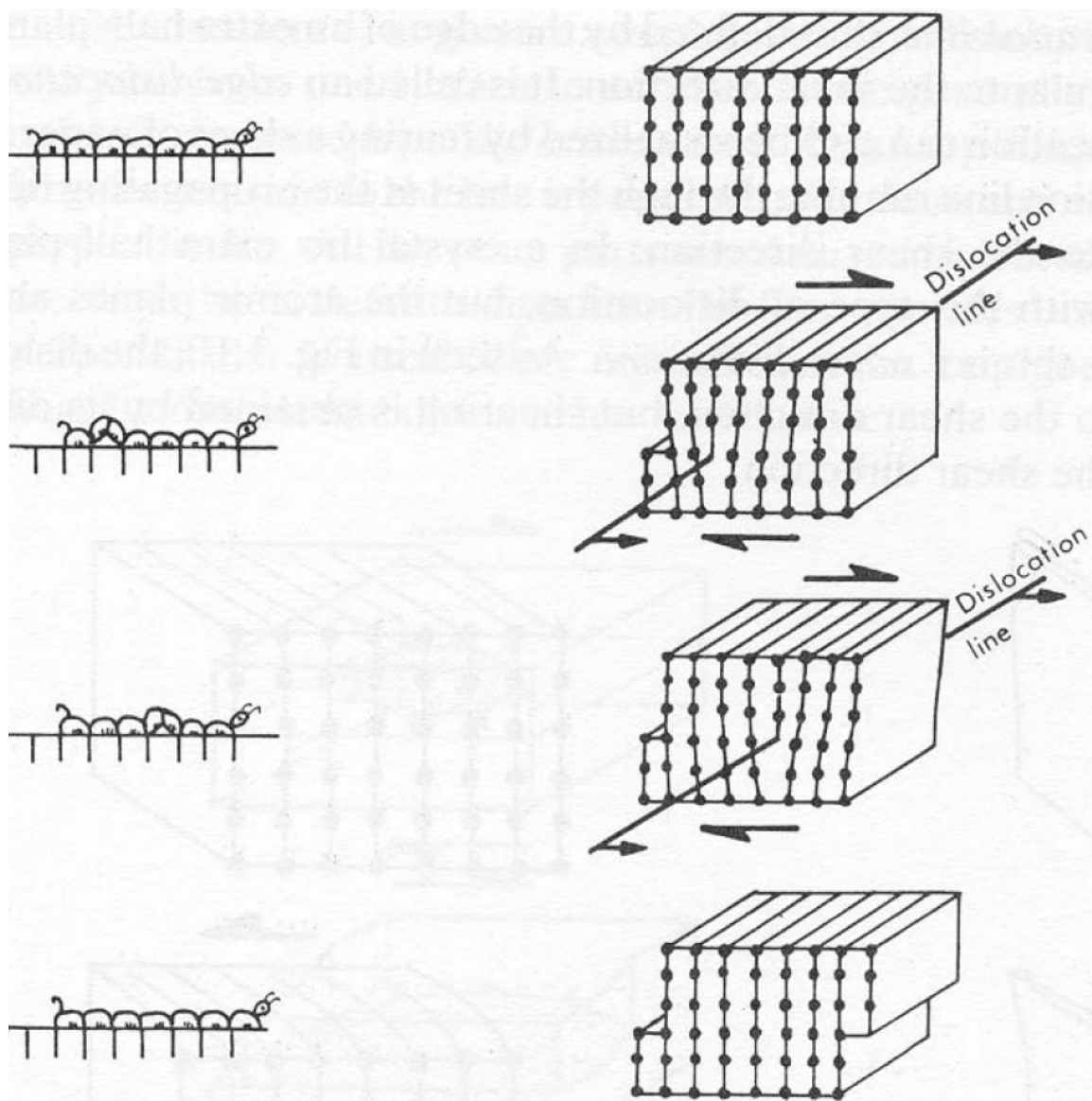
Fig. 5. Edge dislocation of line [00$\bar{1}$] , b = [100] glide plane (010). Dots represent Si atoms at the center of tetrahedra. One Si is linked to 4 Oxygen (circles). Isolated circles represent Mg atoms.

edge dislocation in olivine (Guéguen, 1979)
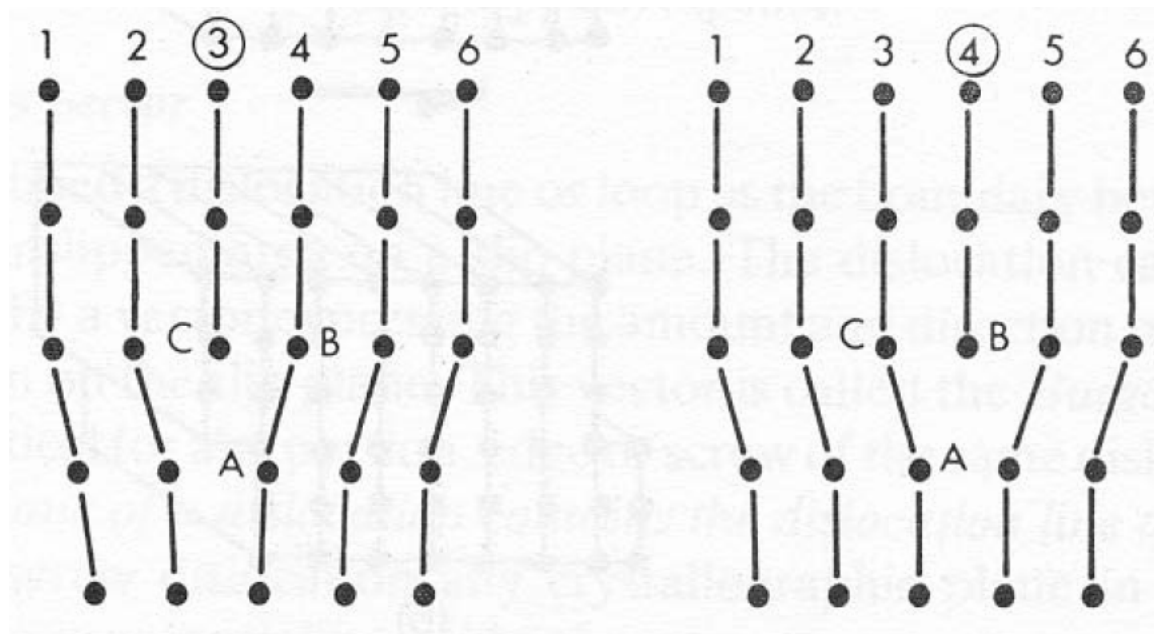
Propagation of edge dislocation (Nicolas & Poirier, 1976)

Propagation of edge dislocation (Nicolas & Poirier, 1976)
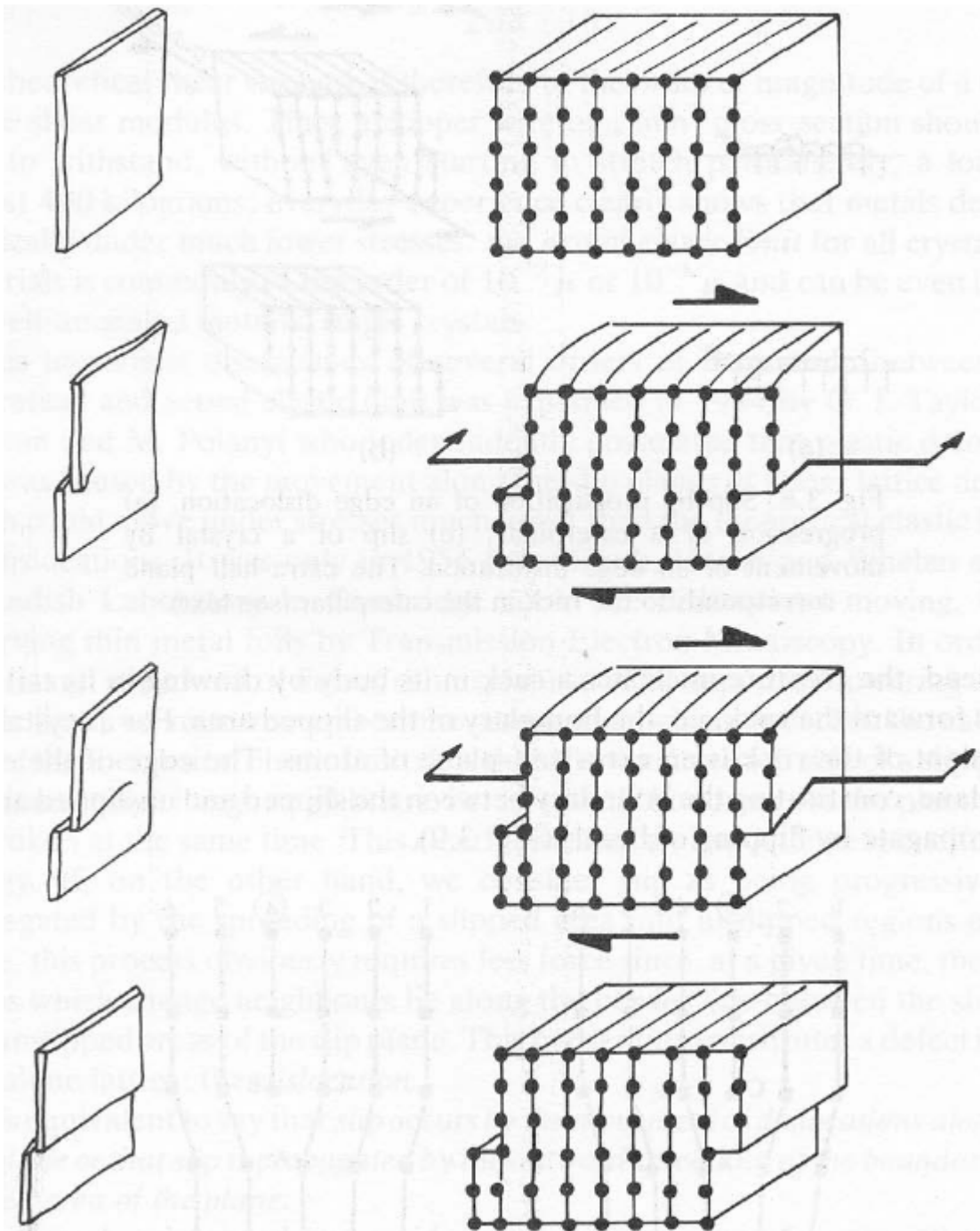
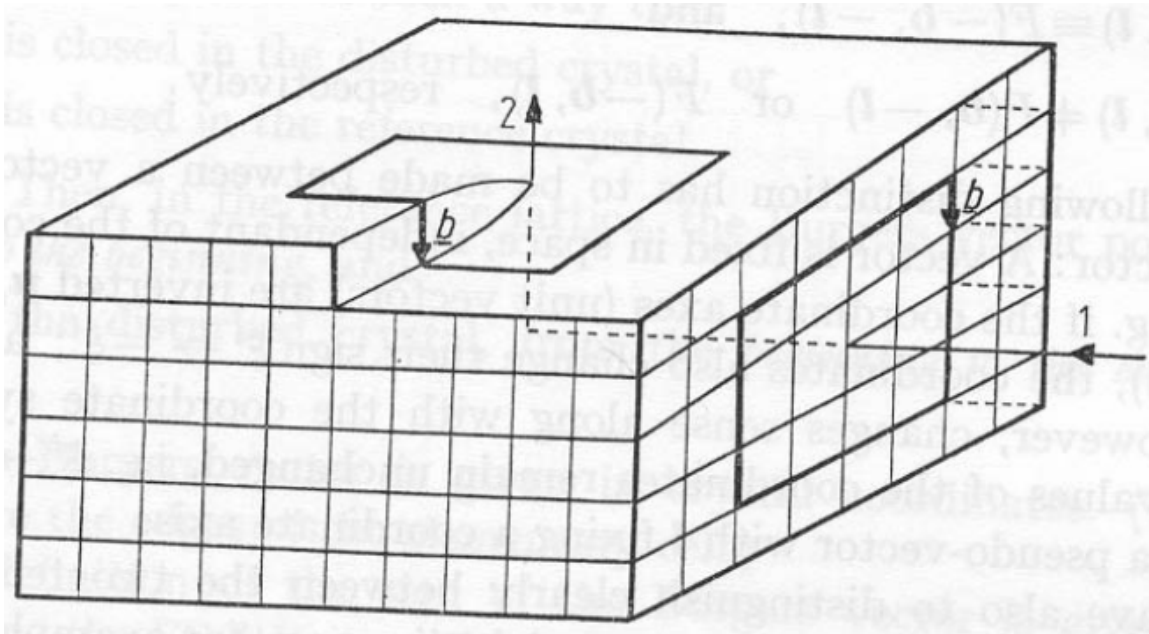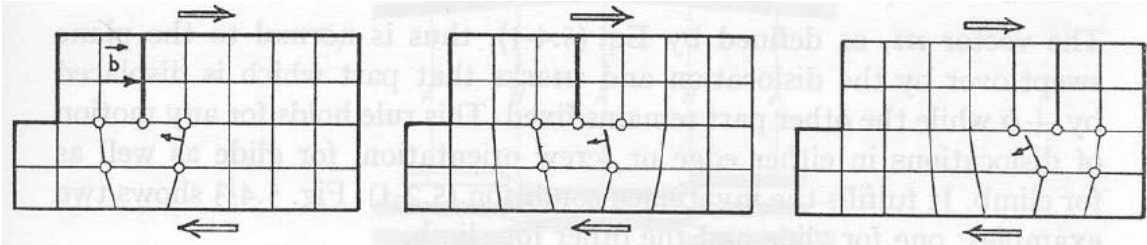Propagation of screw dislocation (Nicolas & Poirier, 1976)

Burgers vector
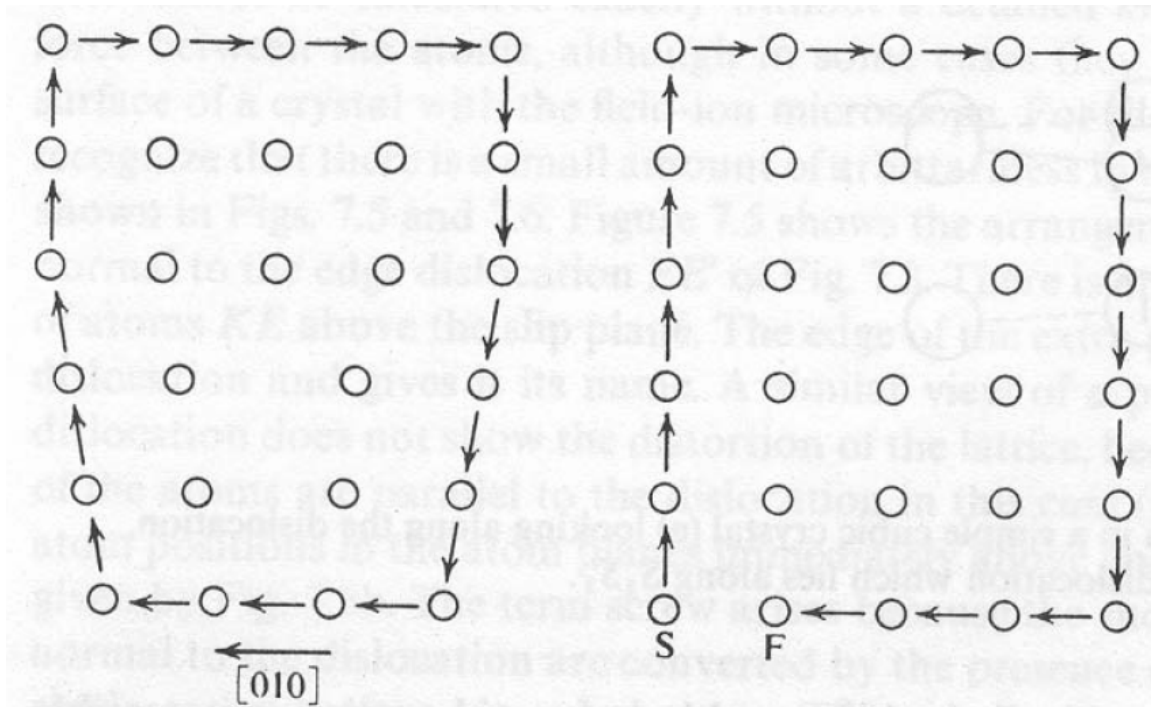
Fig. 7.7. **A Burgers circuit around an edge dislocation.**

(Kelly & Groves, 1970)

(Bollmann, 1970)
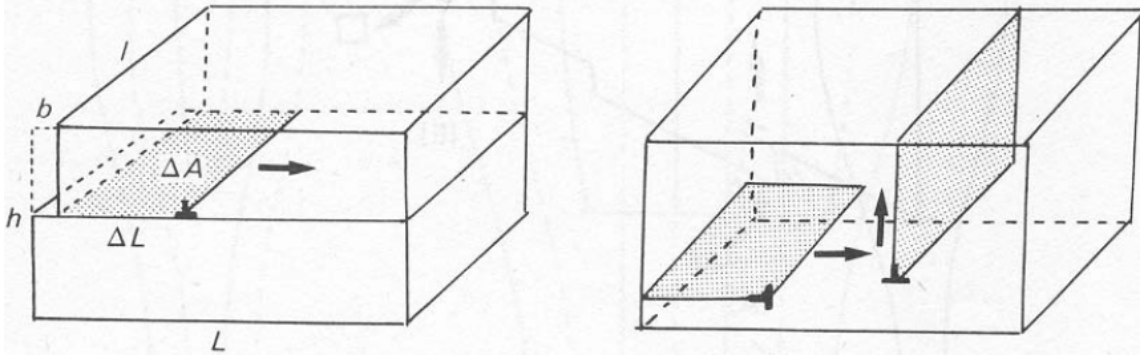
Dislocation Glide

(Bollmann, 1970)

Strain rate generated by dislocation glide:
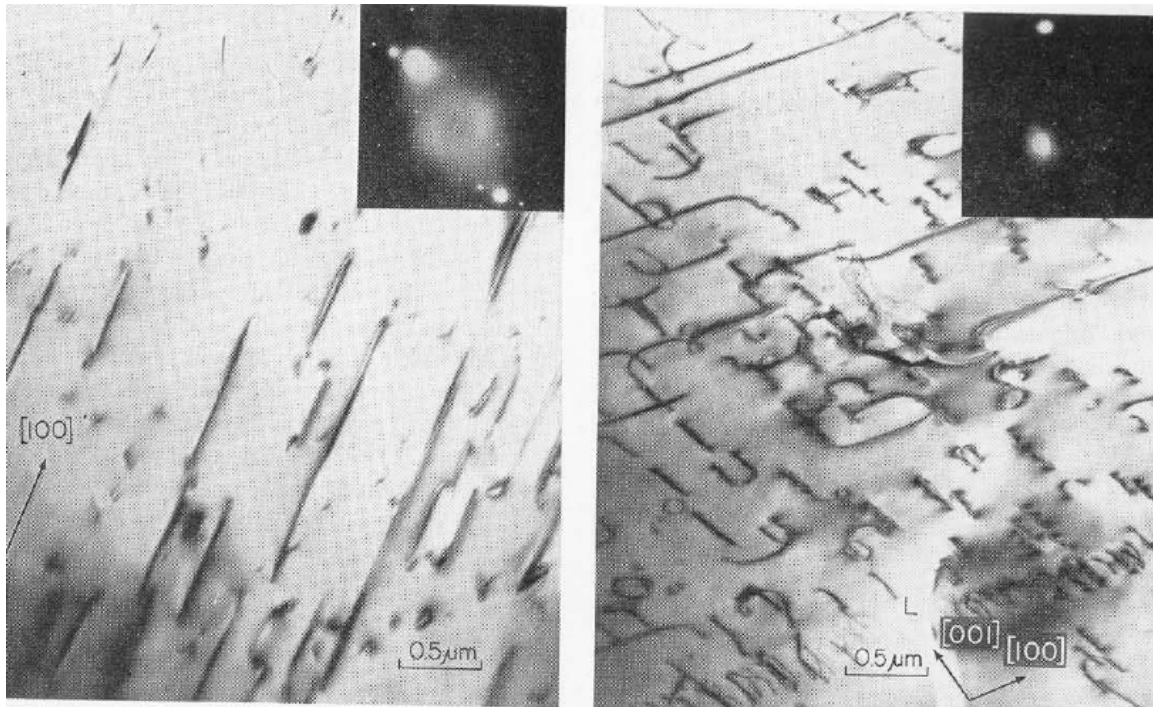$$\dot{\varepsilon} = \rho b v$$

where ρ is dislocation density and v is dislocation velocity.
Dislocations of opposite sign glide in opposite directions.

Fig. 2.15. Orowan's equation. (*a*) A straight edge dislocation, sweeping its glide plane over ΔL creates shear strain $\varepsilon = b\Delta L/hL$. (*b*) Two straight edge dislocations create a pure shear strain by climbing in opposite senses.
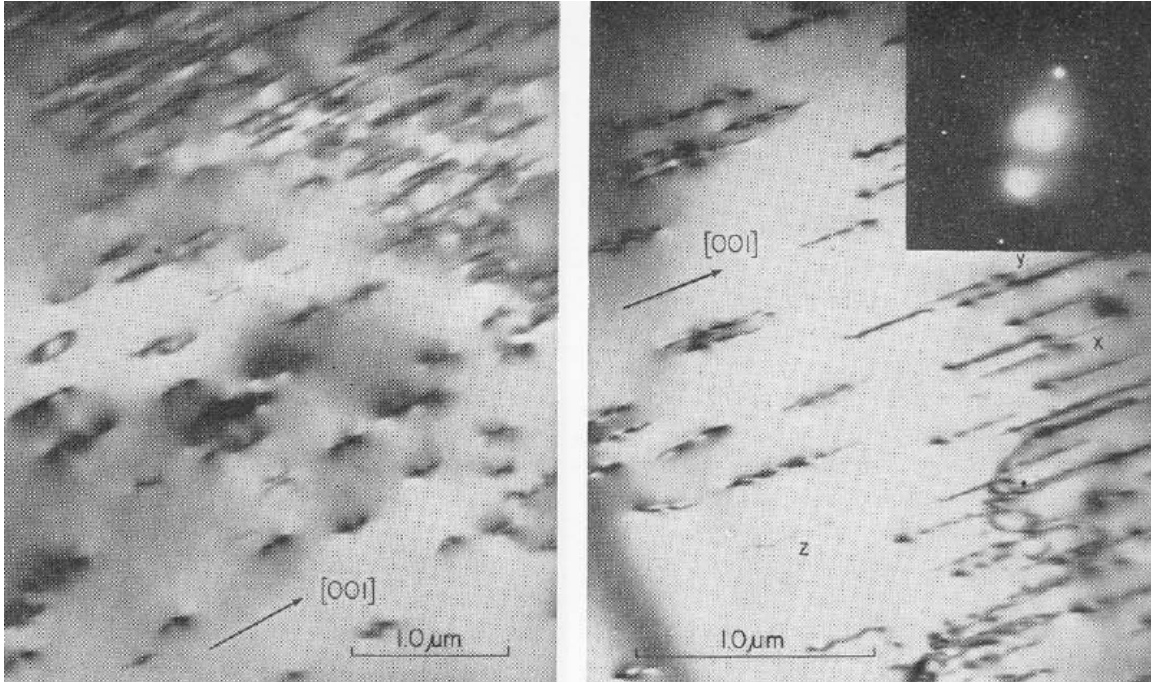
(Poirier, 1985)
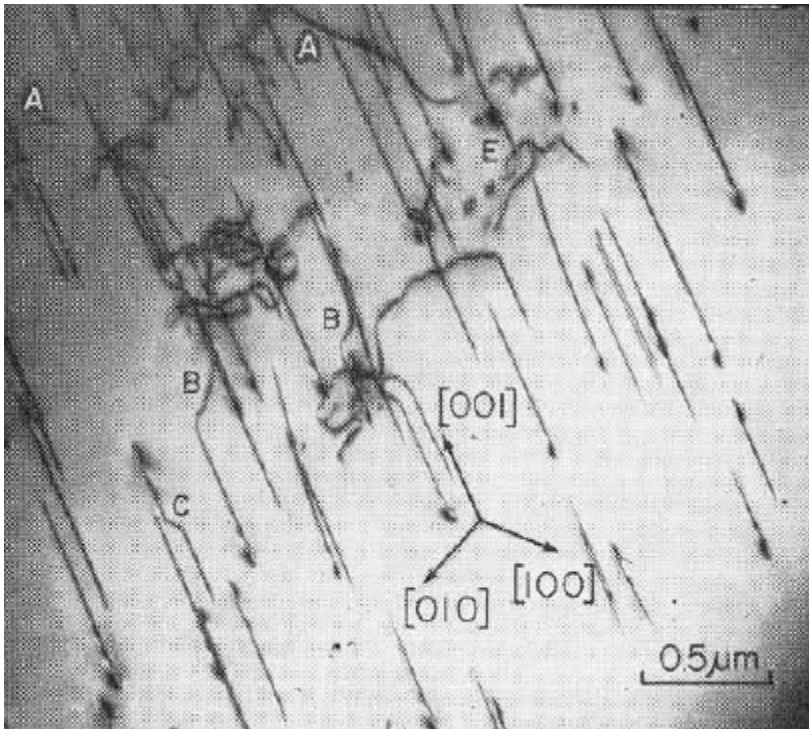
Dislocations in olivine. R, loops with [100] screw segments and [001] edge segments
(Phakey et al., 1972)
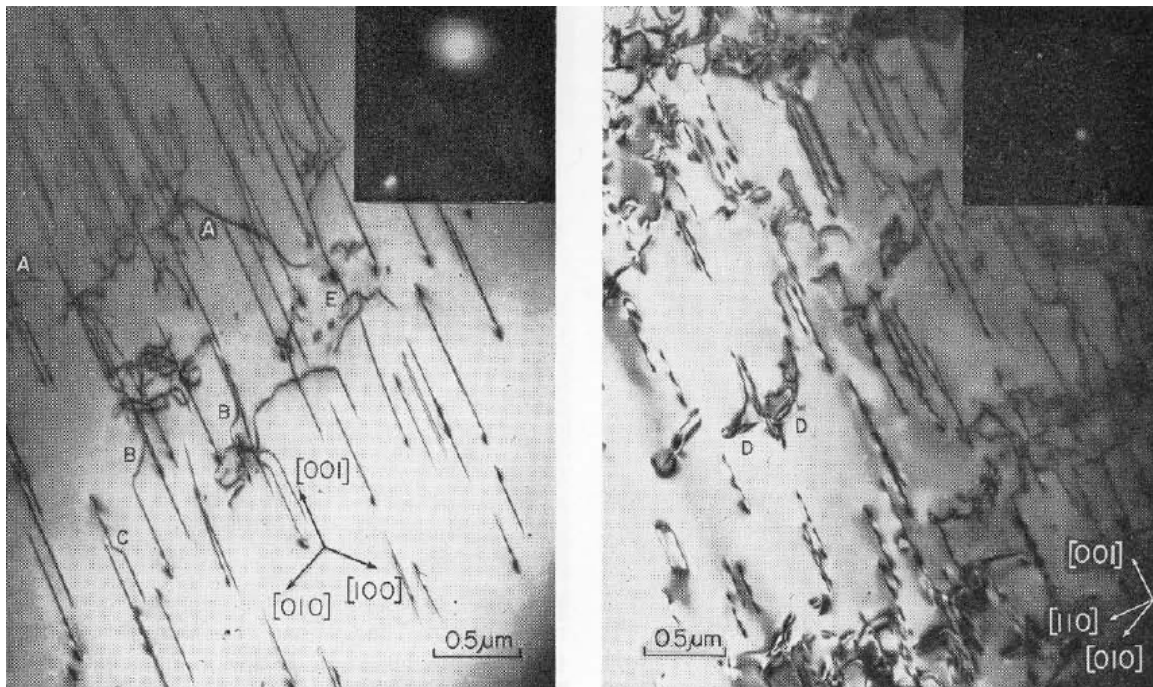
Dislocations in olivine. R, loops with [100] screw segments and [001] edge segments
(Phakey et al., 1972)

Straight, mostly unit dislocations parallel to [001] and with **b** = [001] in olivine.
Dislocation density is 7E8 cm^{-2} (Phakey et al., 1972)

Straight, mostly unit dislocations parallel to [001] and with **b** = [001] in olivine. Less
common 'A' dislocations are parallel to [100] and have **b** = [100]. 'B' and 'C' show jogs.
Dislocation density is 8E8 cm^{-2} (Phakey et al., 1972)
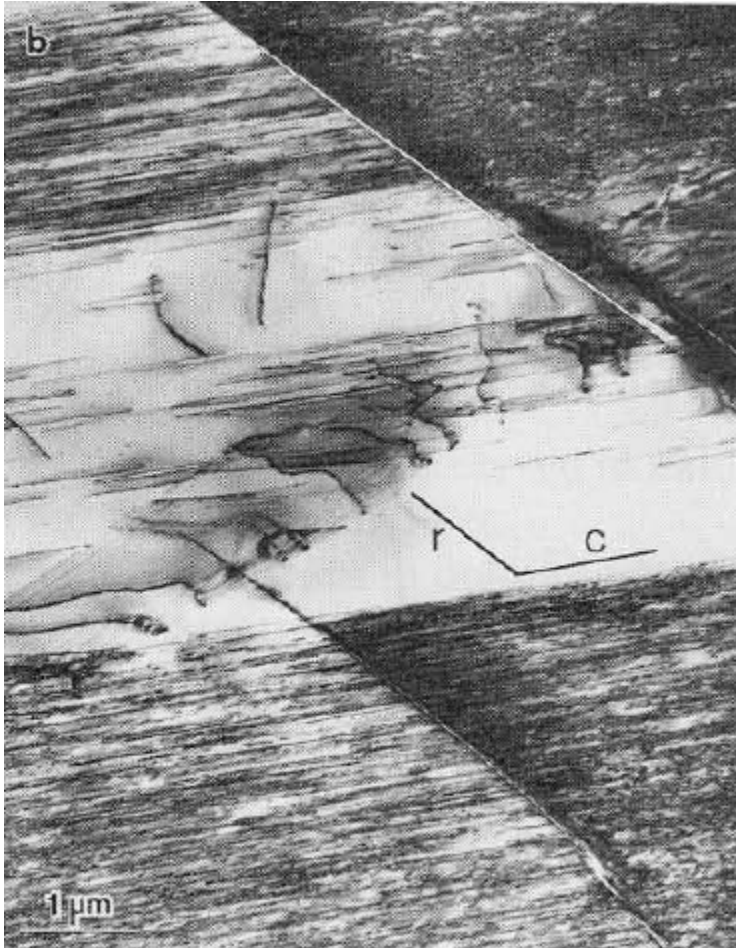
Screw dislocations in dolomite (Barber et al., 1981)
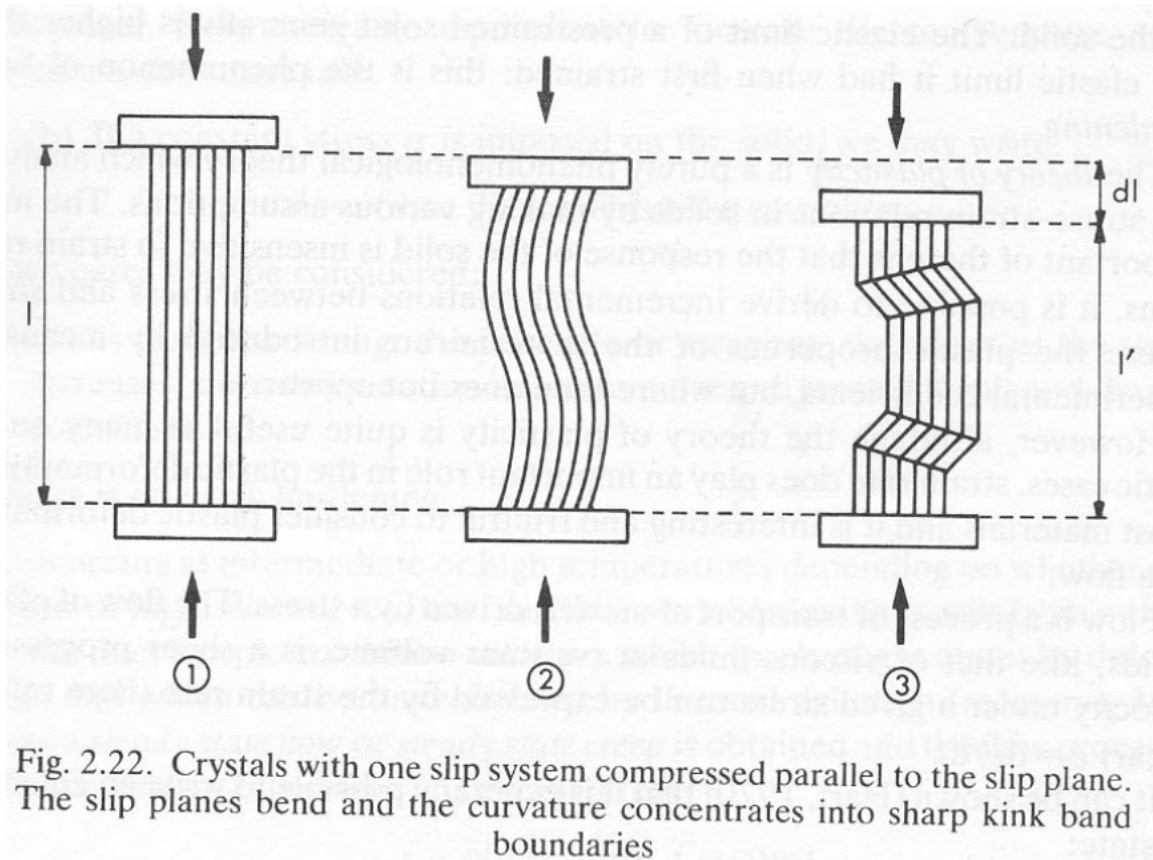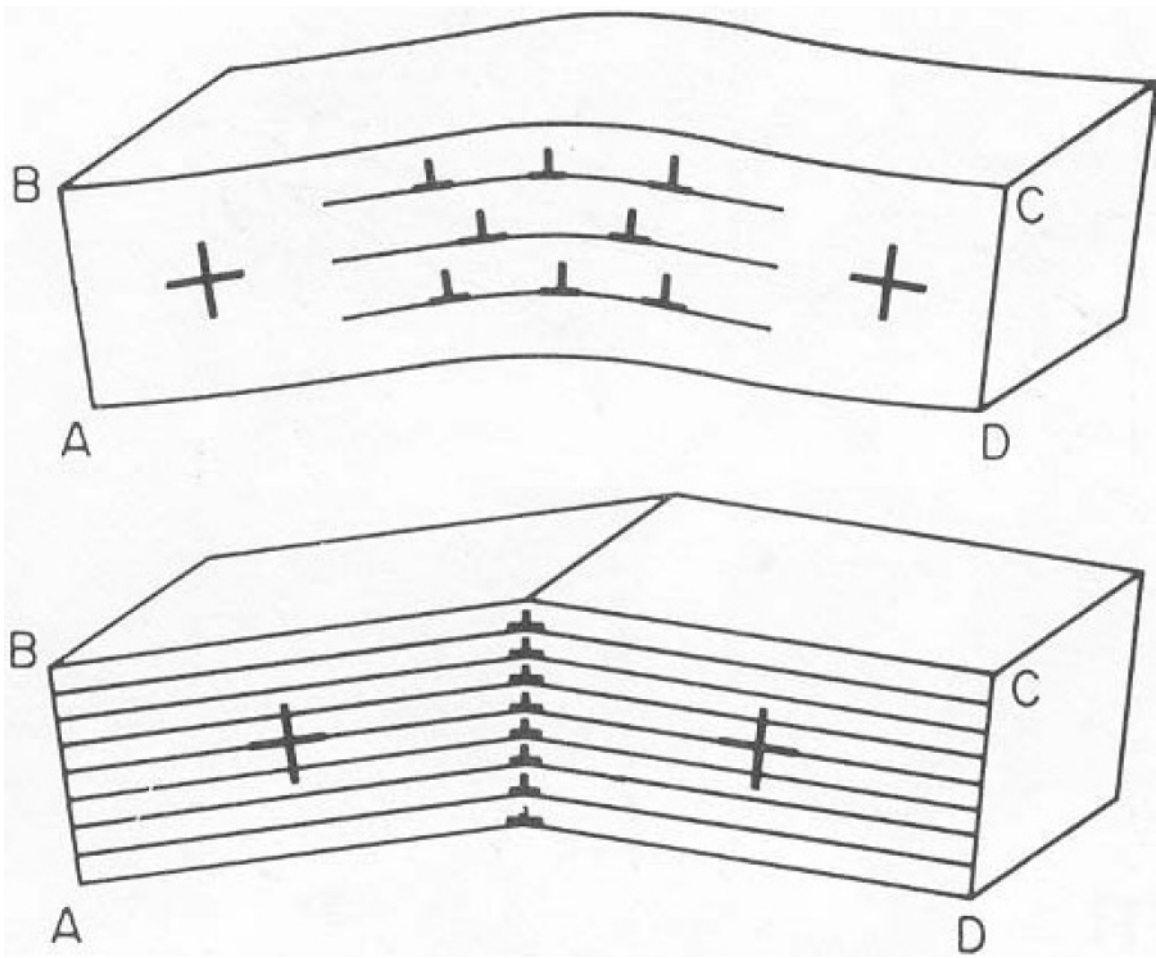
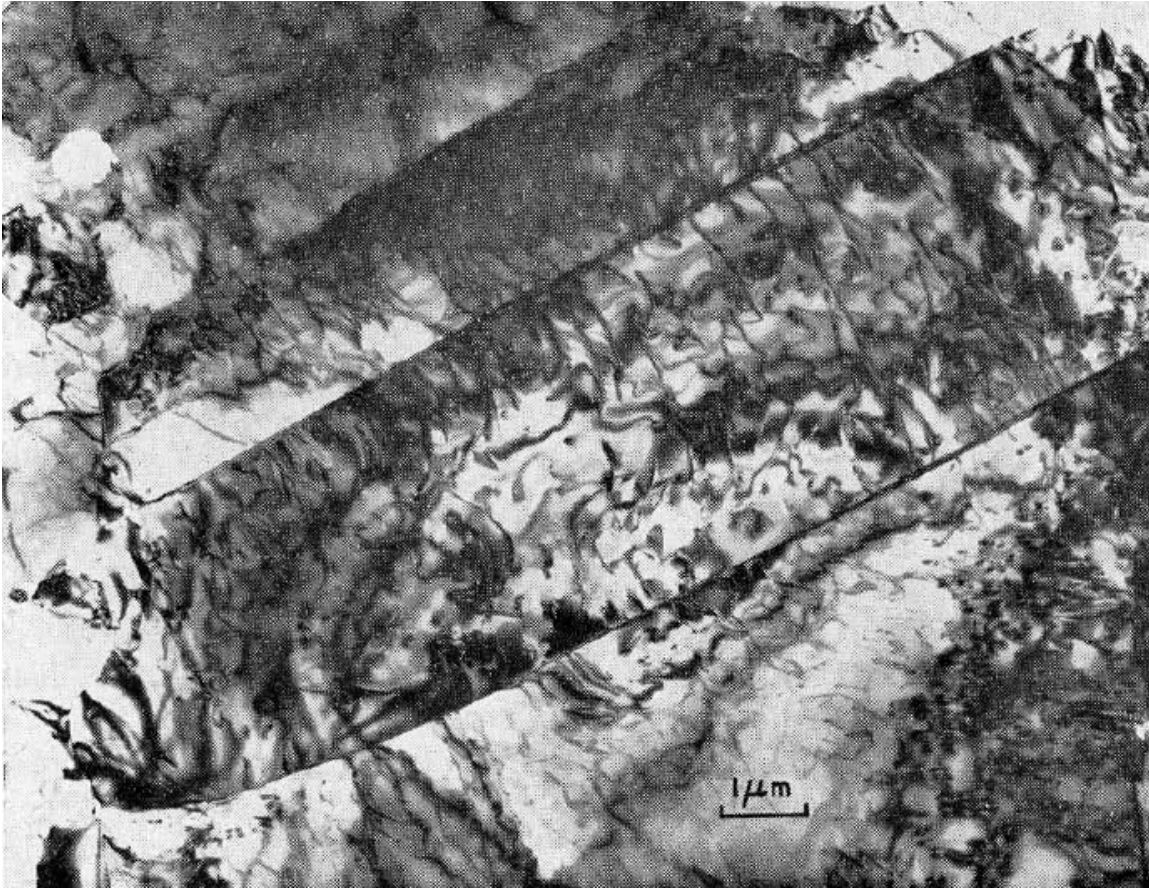**Kinking, kink bands, KBBs**
1 slip system

Fig. 2.22. Crystals with one slip system compressed parallel to the slip plane. The slip planes bend and the curvature concentrates into sharp kink band boundaries

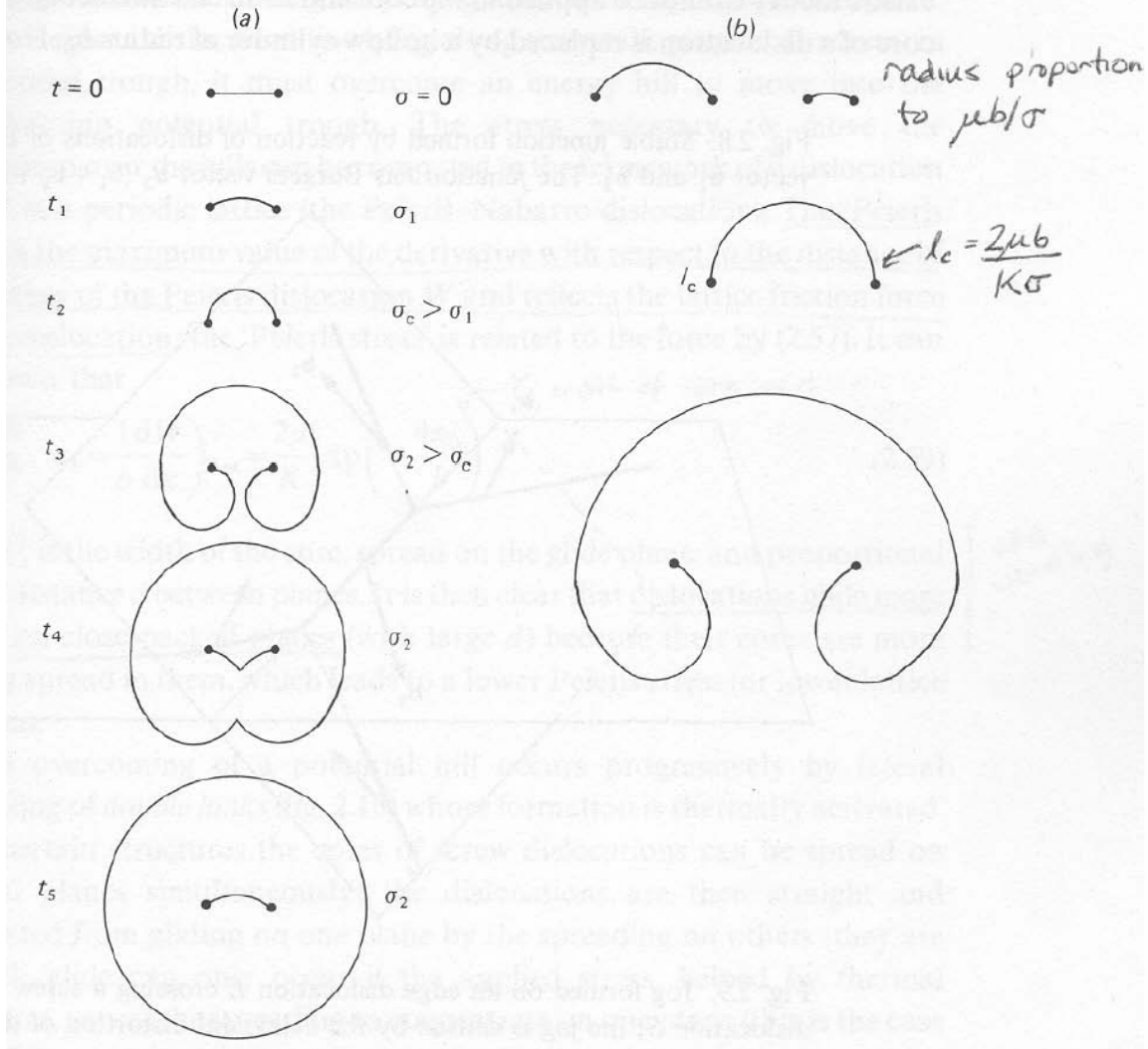(Nicolas & Poirier, 1976)

(Hull & Bacon, 1984)

Olivine kink bands. Band boundaries are (100) walls of edge dislocations perpendicular to $(01\bar{1})$ with **b** = [100]. Dislocations trending across the bands are [100] screws also with **b** = [100] (Green & Radcliffe, 1972)

Dislocation Generation
Frank-Read source

Fig. 2.6. Frank–Read source. (*a*) Dislocation segment of length *l*, stress σ increases with *t*, the source is activated for σ > σ_c. (*b*) Constant stress σ, distribution of segments of various lengths, the segments of length *l* > *l*_c are activated.

(*a*)   (*b*)

t = 0   σ = 0   radius proportion to μb/σ

*t*_1   σ_1   *l*_c = $\dfrac{2\mu b}{K\sigma}$

*t*_2   σ_c > σ_1
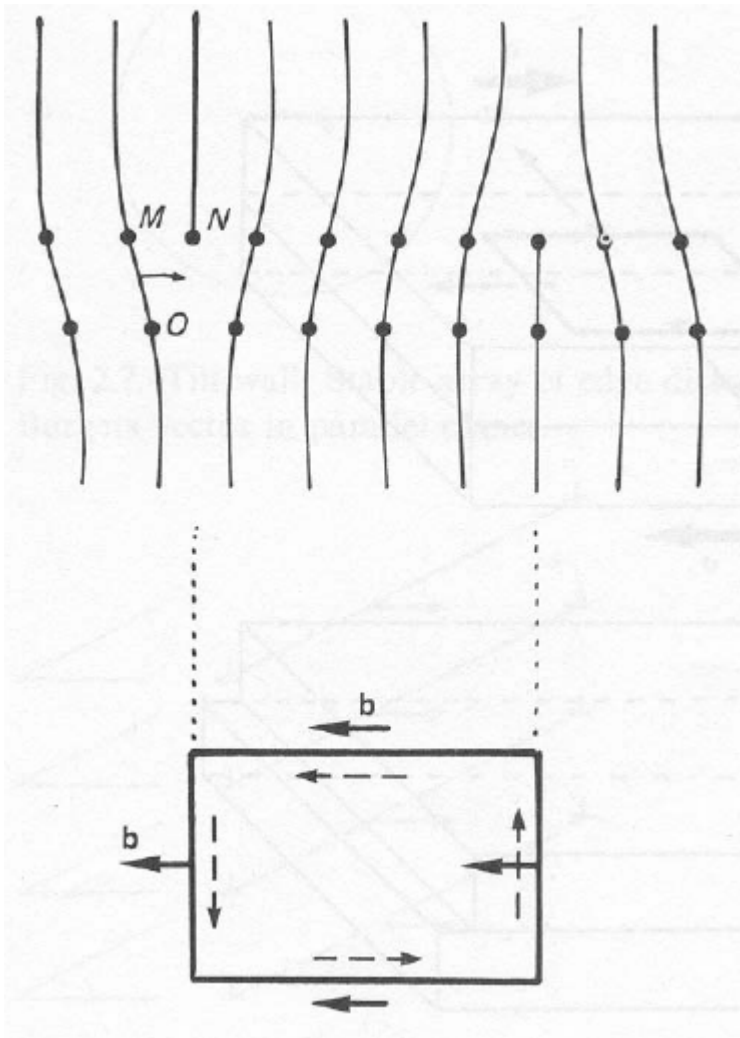
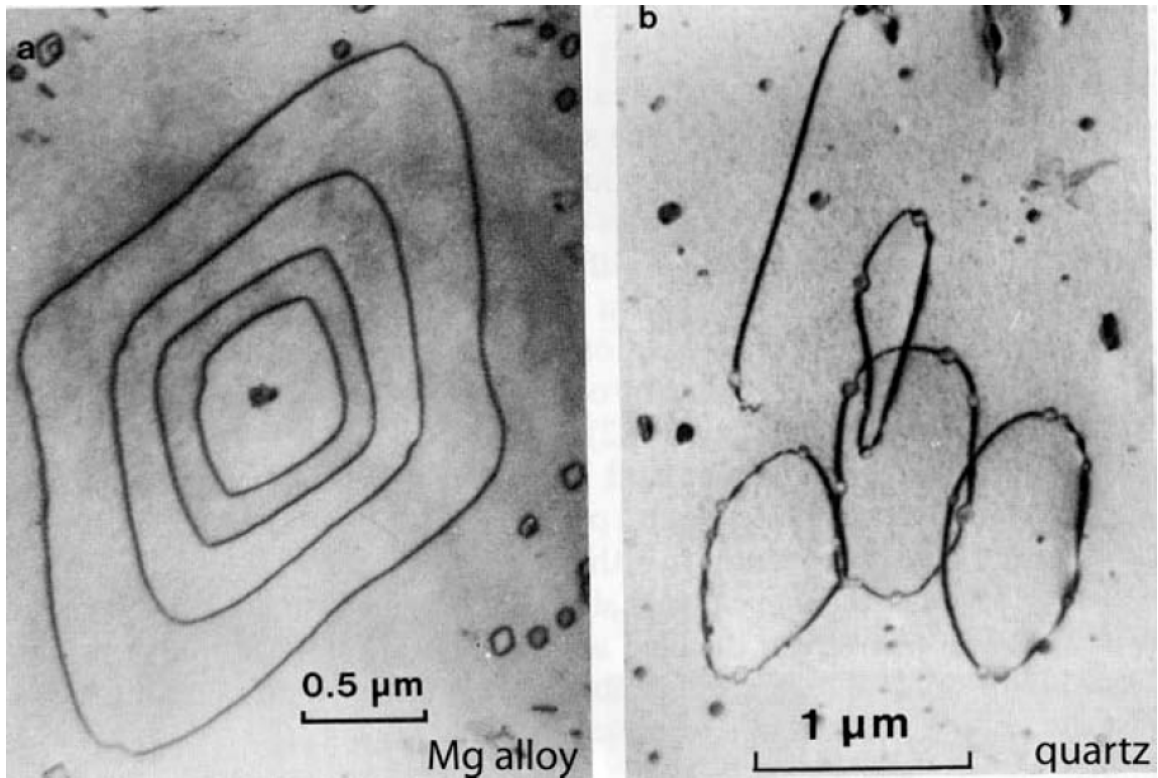*t*_3   σ_2 > σ_c

*t*_4   σ_2

*t*_5   σ_2

(Poirier, 1985)

The stress necessary to overcome lattice resistance is called the Peierls stress

$$\sigma_{Peierls} = \frac{\mu}{(1-\nu)} \exp\left(-\frac{2\pi\zeta}{b}\right)$$

where ζ is the dislocation half-width; this gives $\sigma = \mu/10^4$, comparable with experimental shear strength.

dislocation loop viewed from side and top (Poirier, 1985)

Dislocation loops in Mg and quartz.

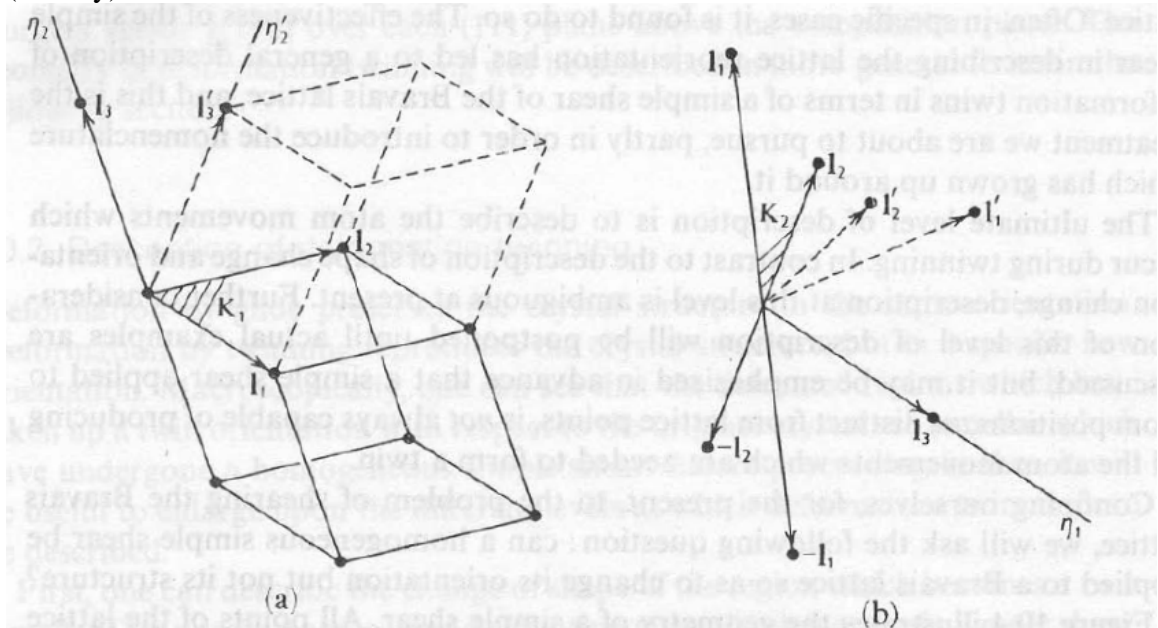## Twinning

(usually) rotation about an axis

Fig. 10.5. (a) Type 1 twin. (b) Type 2 twin. Lattice vector l_1 is sheared to l_1' and l_2 to l_2'. The vectors l_1' and l_2' are related to $-l_1$ and $-l_2$ by a rotation of 180° about η_1.
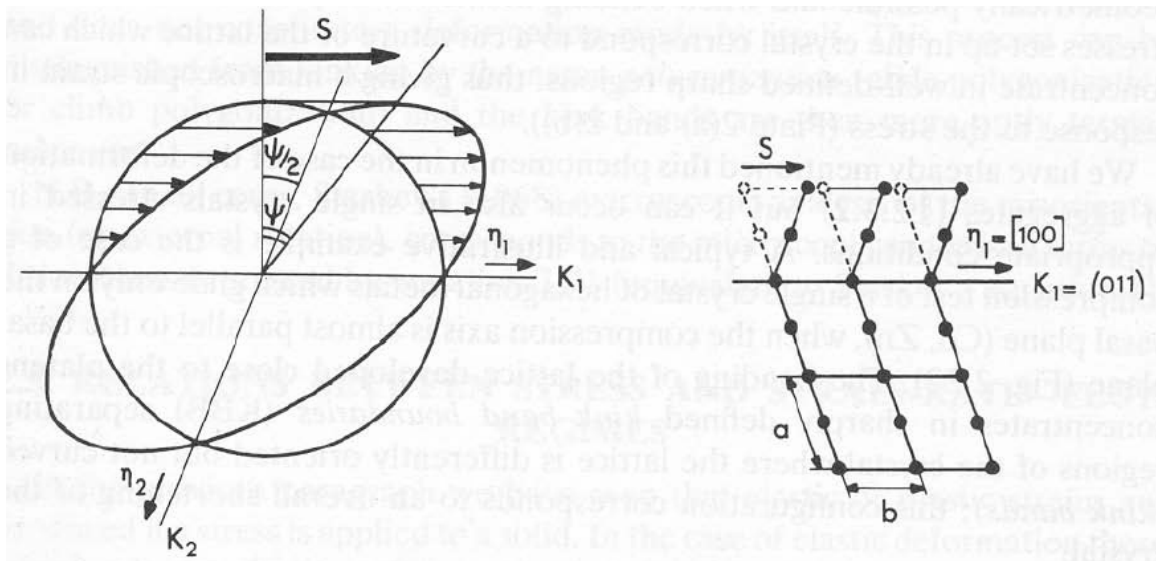
(Kelly & Groves, 1970)

Fig. 2.21. Twinning on the twin plane K_1 along the twin direction η_1. Twinning shear
$$S = \tan \psi' = 2 \tan \psi/2$$

(Nicolas & Poirier, 1976)

K_1 is twinning plane
n_1 is twinning direction
$S = 2\tan(\psi/2)$, shear
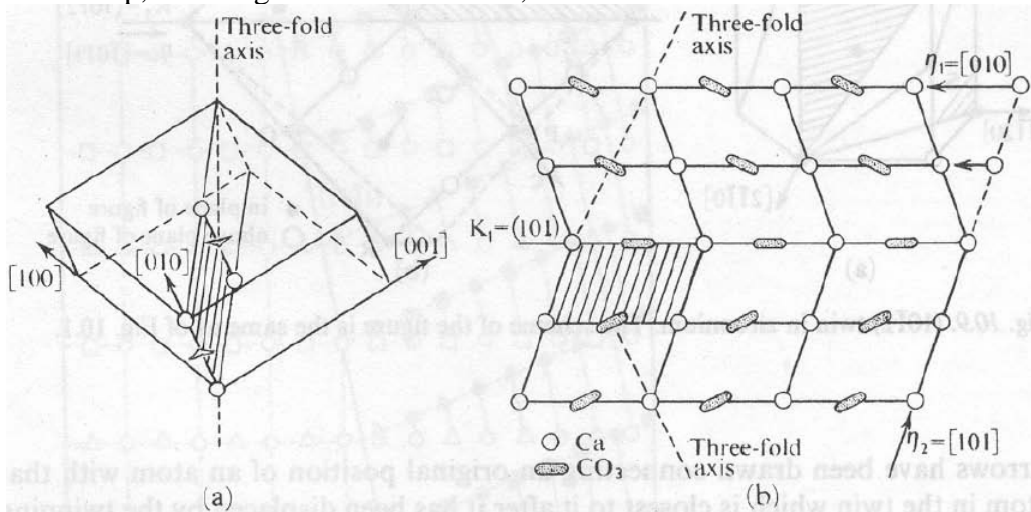unlike slip, twinning is an instantaneous, fixed strain

Fig. 10.8. Twin in calcite. The scheme of the figure is the same as of Fig. 10.1.
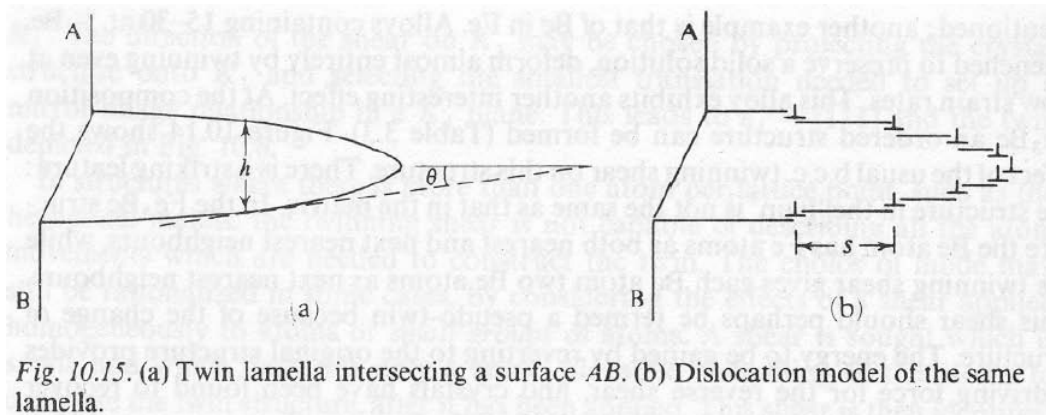
(Kelly & Groves, 1970)

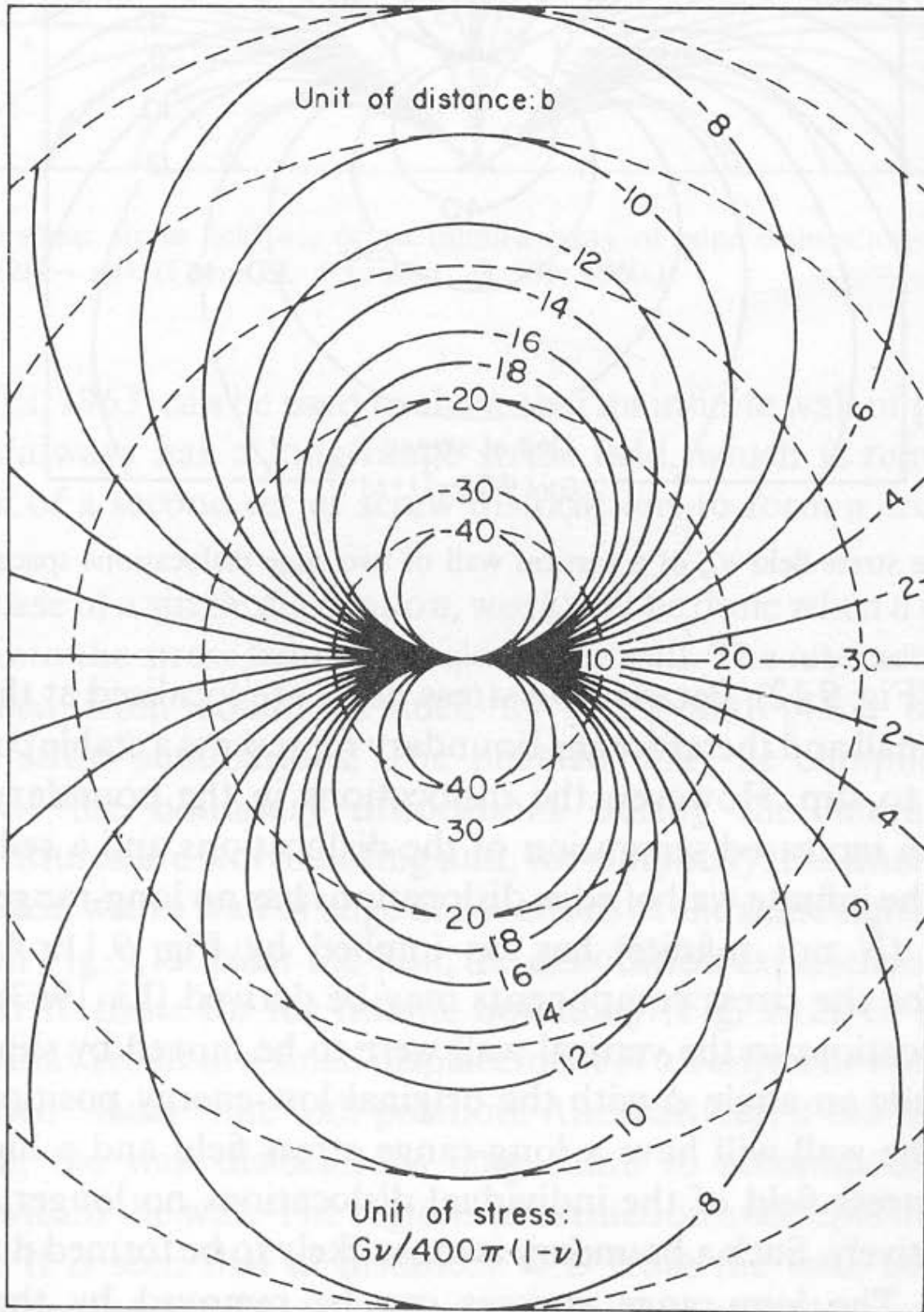*Fig. 10.15.* (a) Twin lamella intersecting a surface *AB*. (b) Dislocation model of the same lamella.
(Kelly & Groves, 1970)

Dislocation Stress Fields
The stress field around a screw dislocation has no radial component, only tangential:

$$\sigma_{\Theta z} = \frac{b\mu}{2\pi r}$$

Stress field around edge dislocation is more complicated.

Unit of distance: b

Unit of stress:
$G\nu/400\pi(1-\nu)$

(Li, 1963).

The mean internal stress field for a group of dislocations is proportional to the root of the dislocation density:

$$\sigma \propto \sqrt{\rho}$$
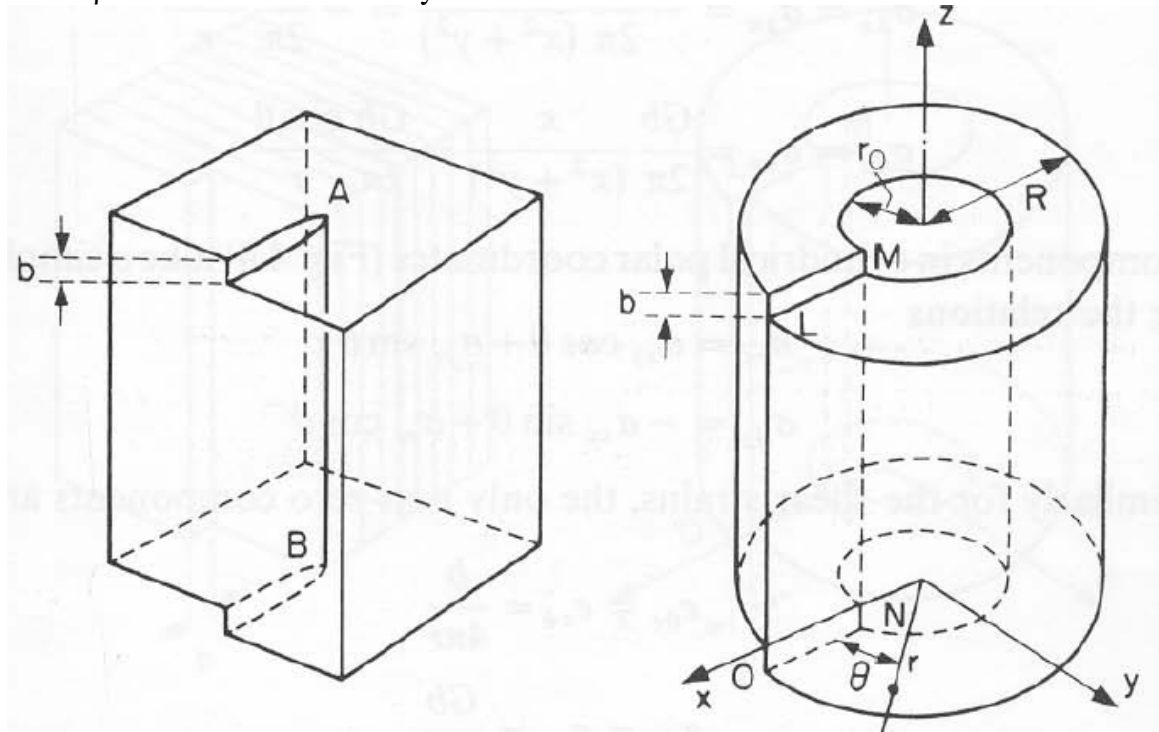
Dislocation Strain Energy
Elastic energy per unit length of a screw dislocation is

$$W_{screw} = \frac{\mu b^2}{4\pi} \ln\left(\frac{R}{b_o}\right)$$

where R is the spacing between dislocations and b_o is the radius of the dislocation core (a few times b). Most importance is the dependence on b *squared.* It is convenient to approximate the spacing between dislocations R as
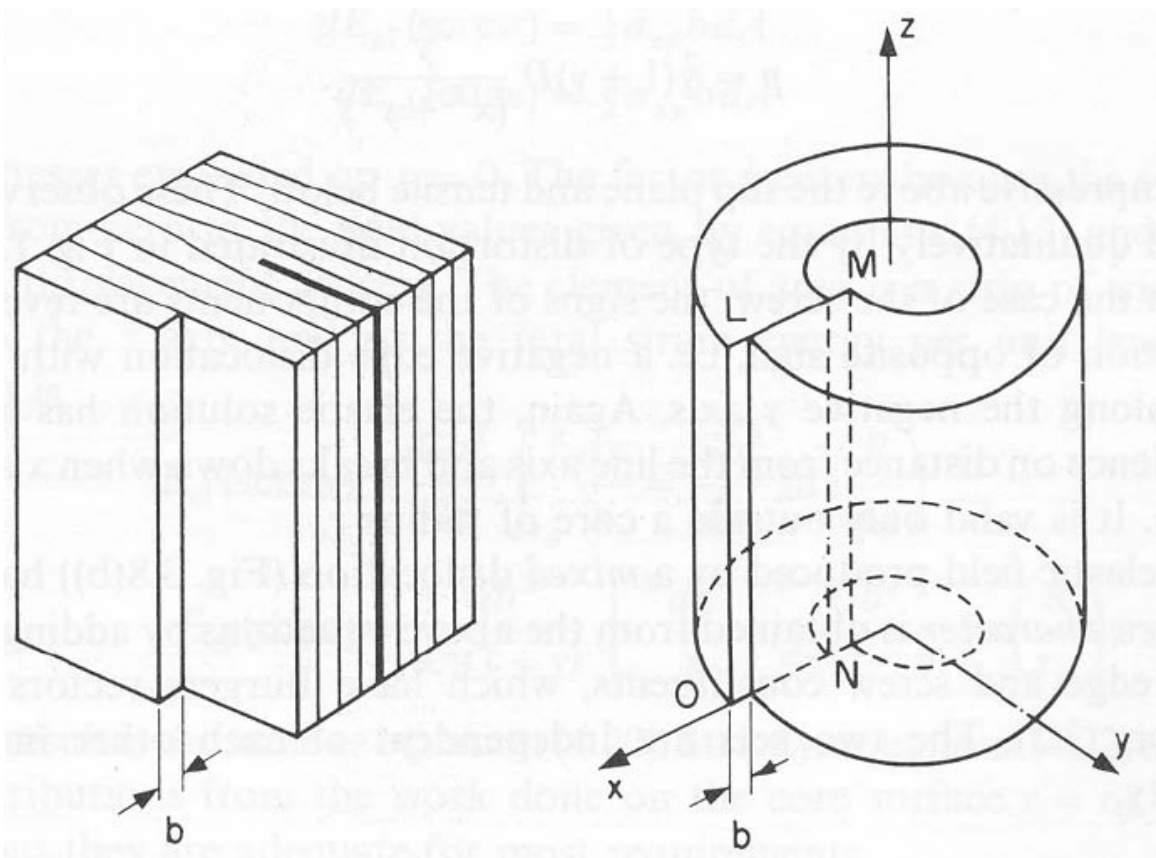
$$R^2 \cong \frac{1}{\rho}$$

where ρ is the dislocation density.
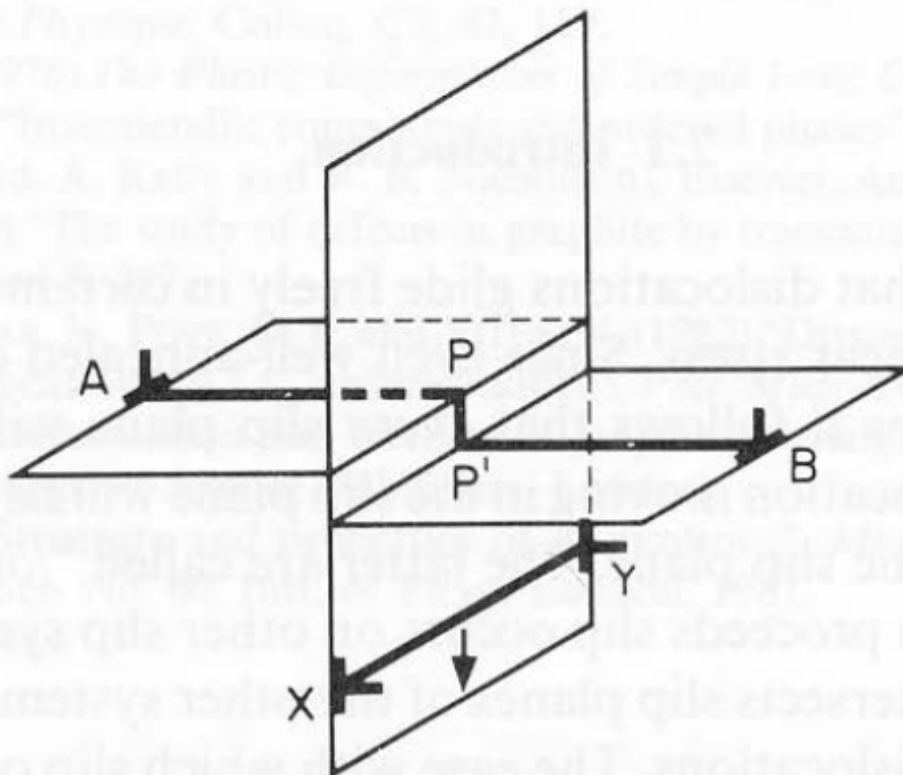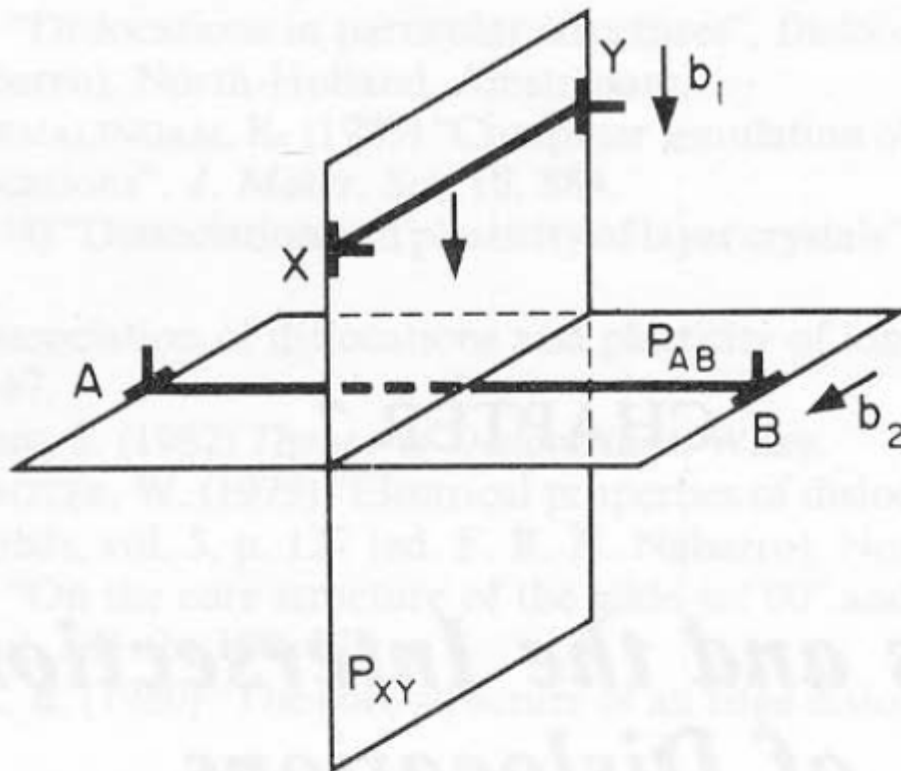

(Hull & Bacon, 1984)

For an edge dislocation,

$$W_{edge} = \frac{\mu b^2}{4\pi(1-v)} \ln\left(\frac{R}{b_o}\right)$$

(Hull & Bacon, 1984)

Dislocation Interaction and Work Hardening

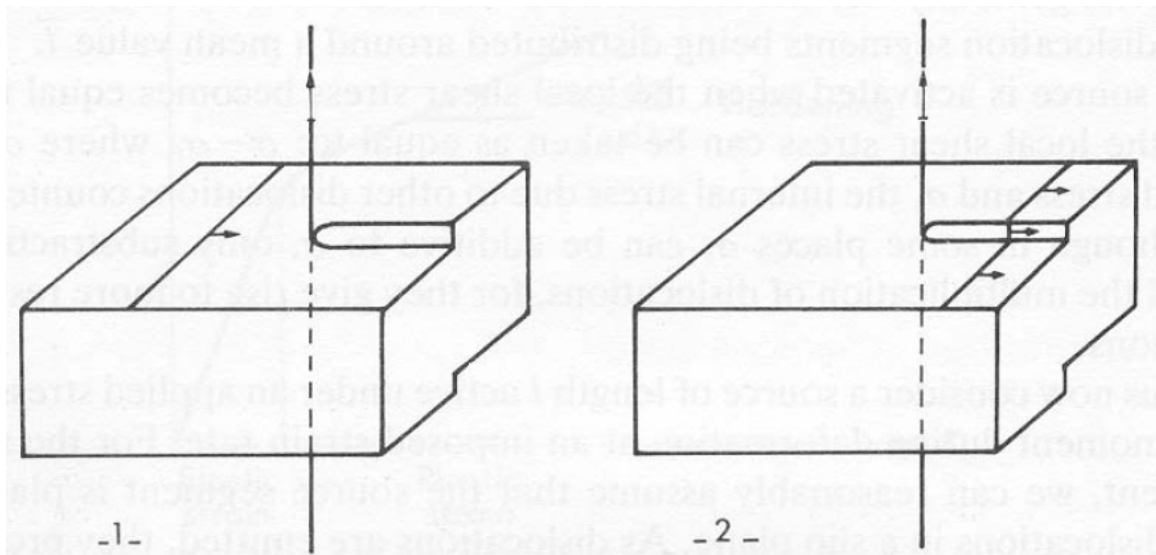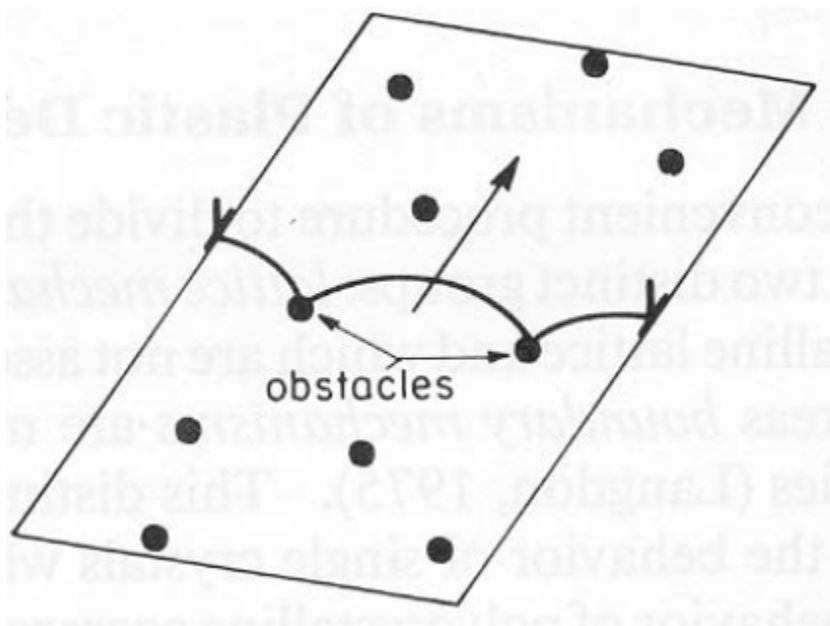dislocation interaction (Hull & Bacon, 1984)

Fig. 4.2. Edge dislocation in a horizontal glide plane threaded by a screw dislocation (tree). The edge dislocation acquires a jog when it cuts the tree

dislocation interaction (Nicolas & Poirier, 1976)

obstacles
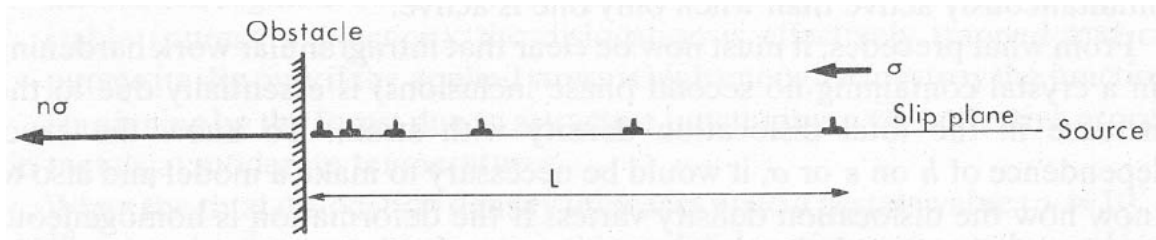
Obstacles to glide (Langdon, 1985).

Fig. 4.4. Edge dislocations piled up behind an obstacle under a stress σ. The stress ahead of the obstacle is multiplied by n (number of piled-up dislocations)

dislocation pile-up acts as a stress concentrator (Nicolas & Poirier, 1976). The shear stress at the head of a pile-up of n dislocations is just σn. Because a dislocation pile-up takes space, the number of dislocations that can pile-up is limited by grain size—bigger grains can have bigger pile-ups and thereby force their way through grain boundaries by generating bigger stresses:

$$\sigma \propto \frac{\sigma_{GB}}{\sqrt{d}}$$

where σ_{GB} is the intrinsic resistance of the grain boundary to shear and d is the grain size. This is the Hall–Petch relationship: fine-grained polycrystals are stiffer than coarse-grained polycrystals.
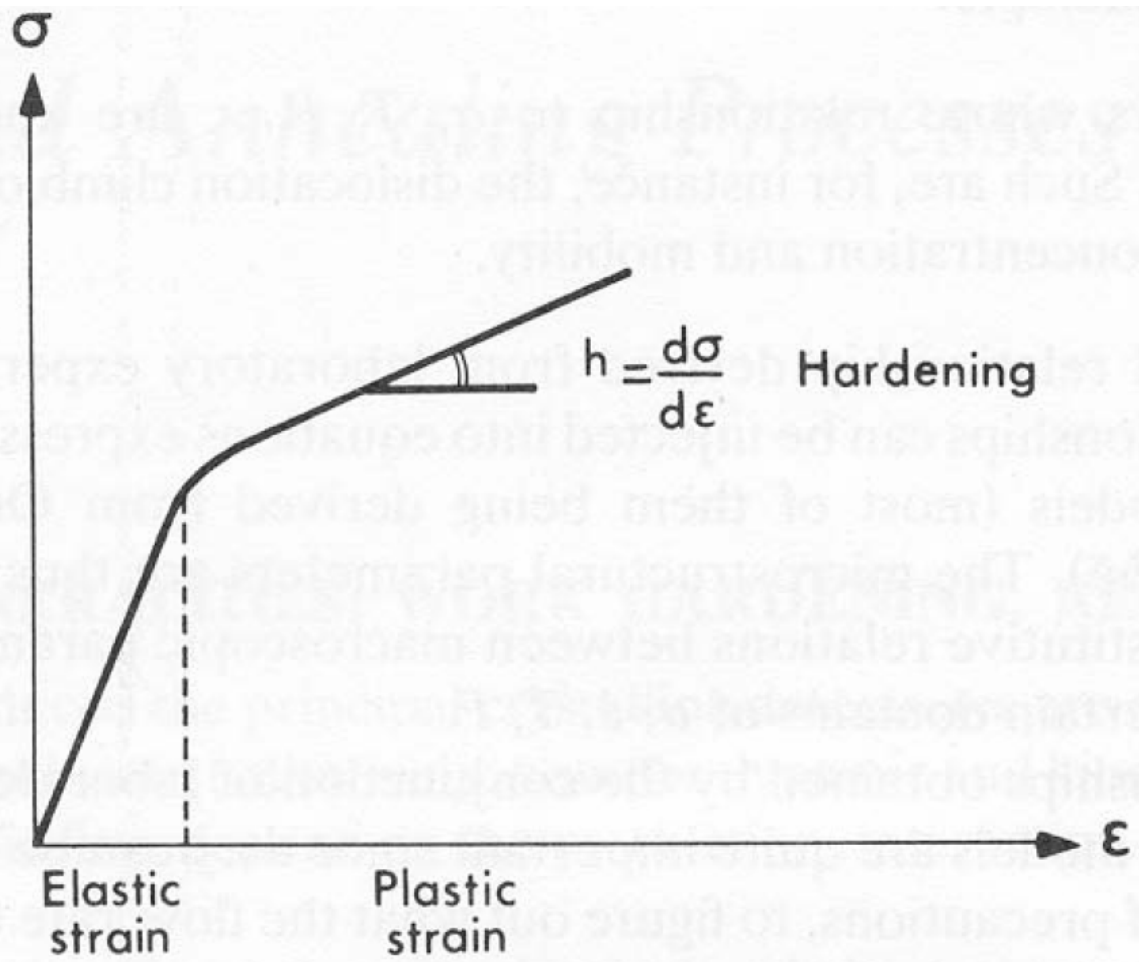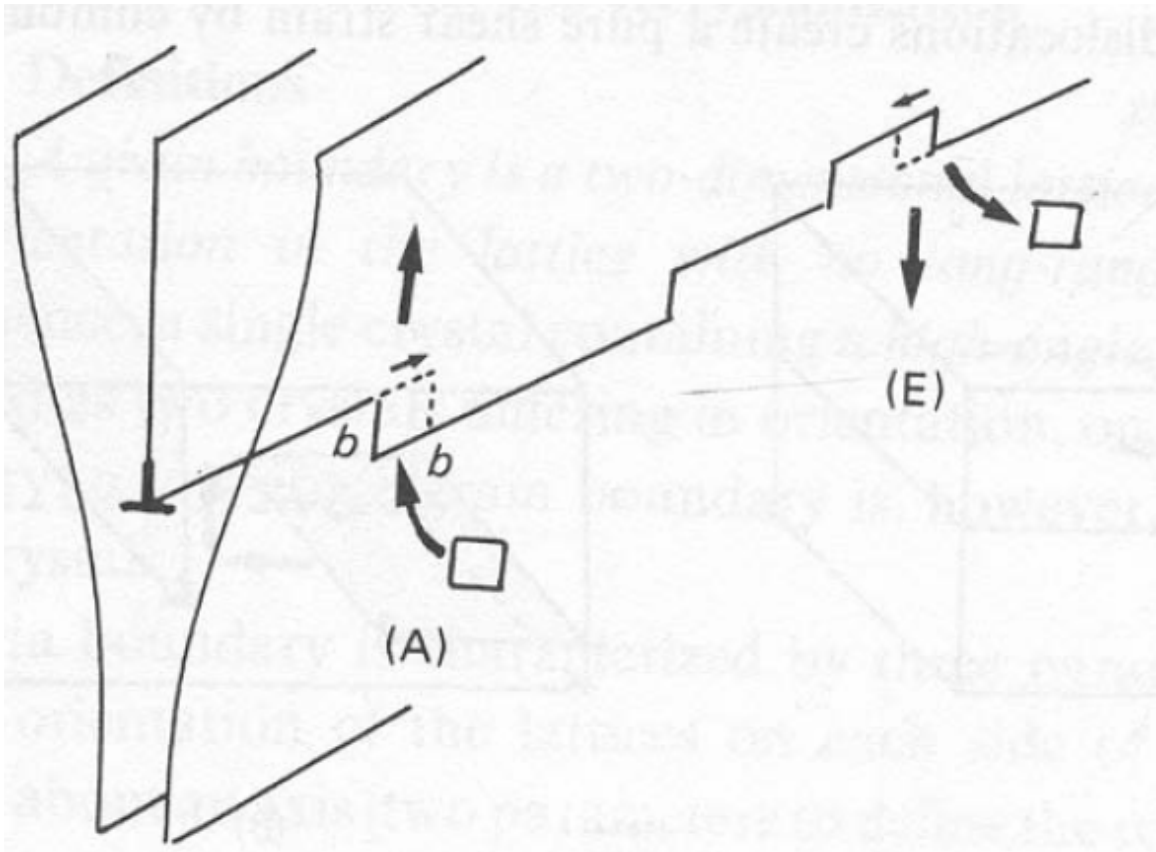
Fig. 4.1. Stress–strain curve at constant strain rate

(Nicolas & Poirier, 1976)

Dislocation Climb
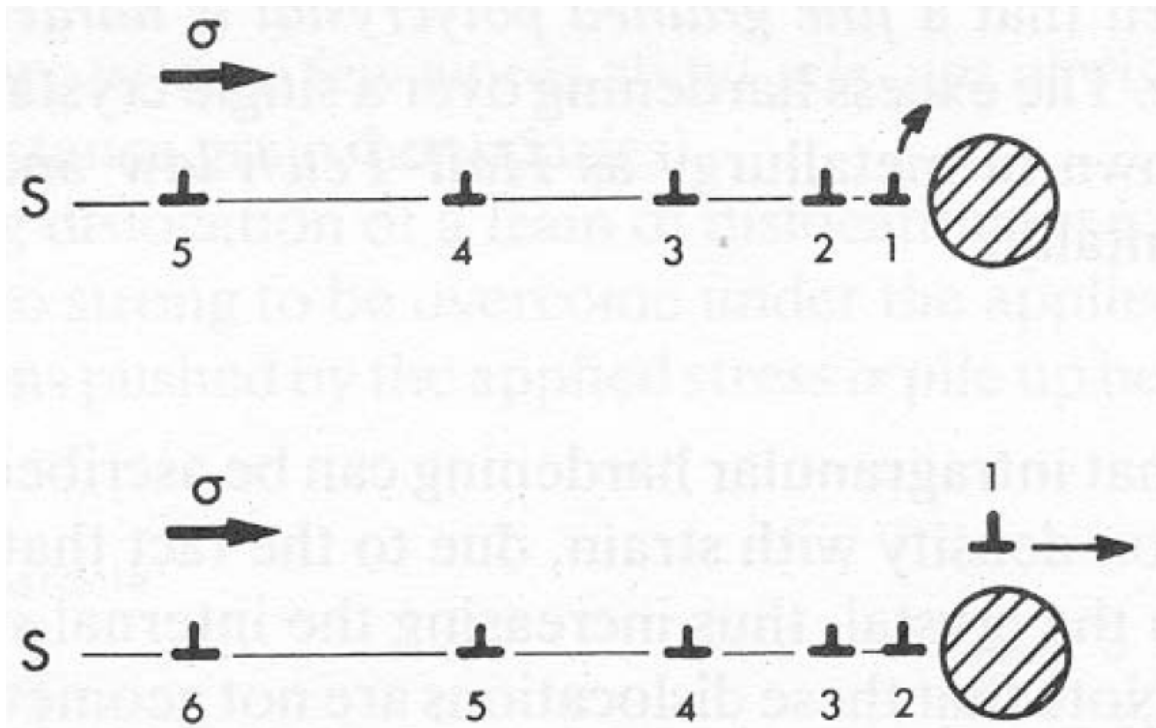
Climb of an edge dislocation (Poirier, 1985)

Fig. 4.6. Climb of the leading dislocation of a pile-up over an obstacle
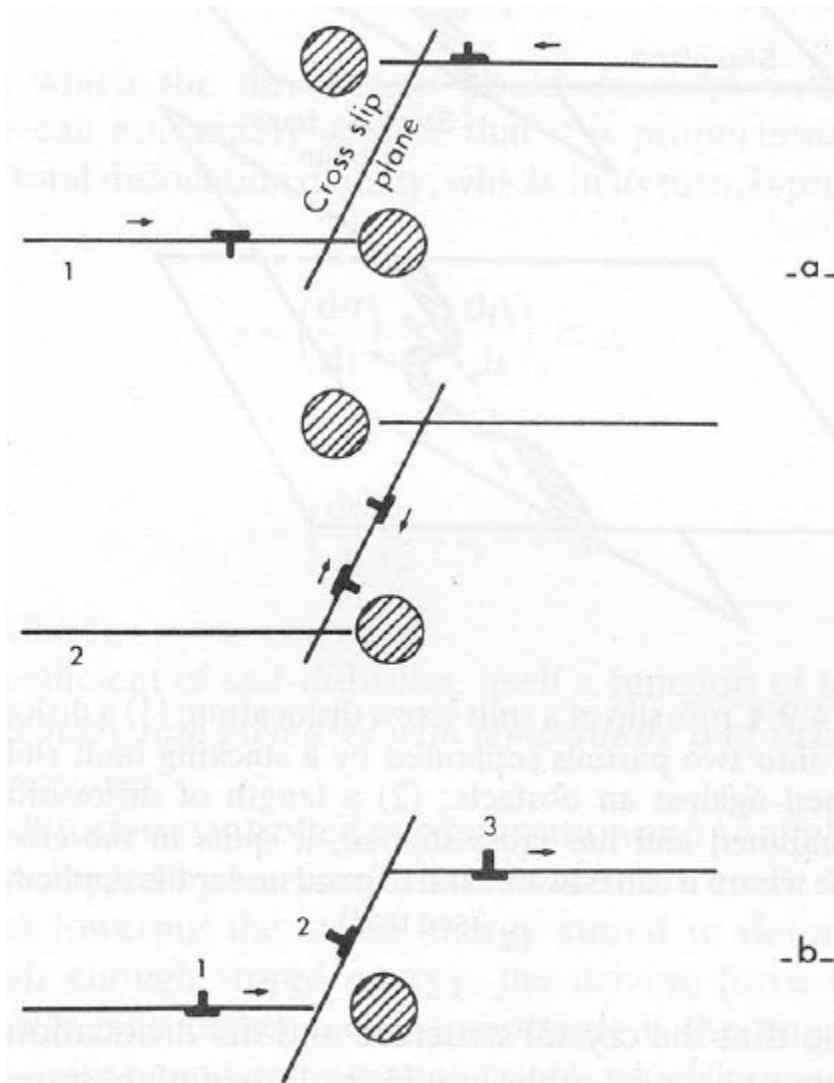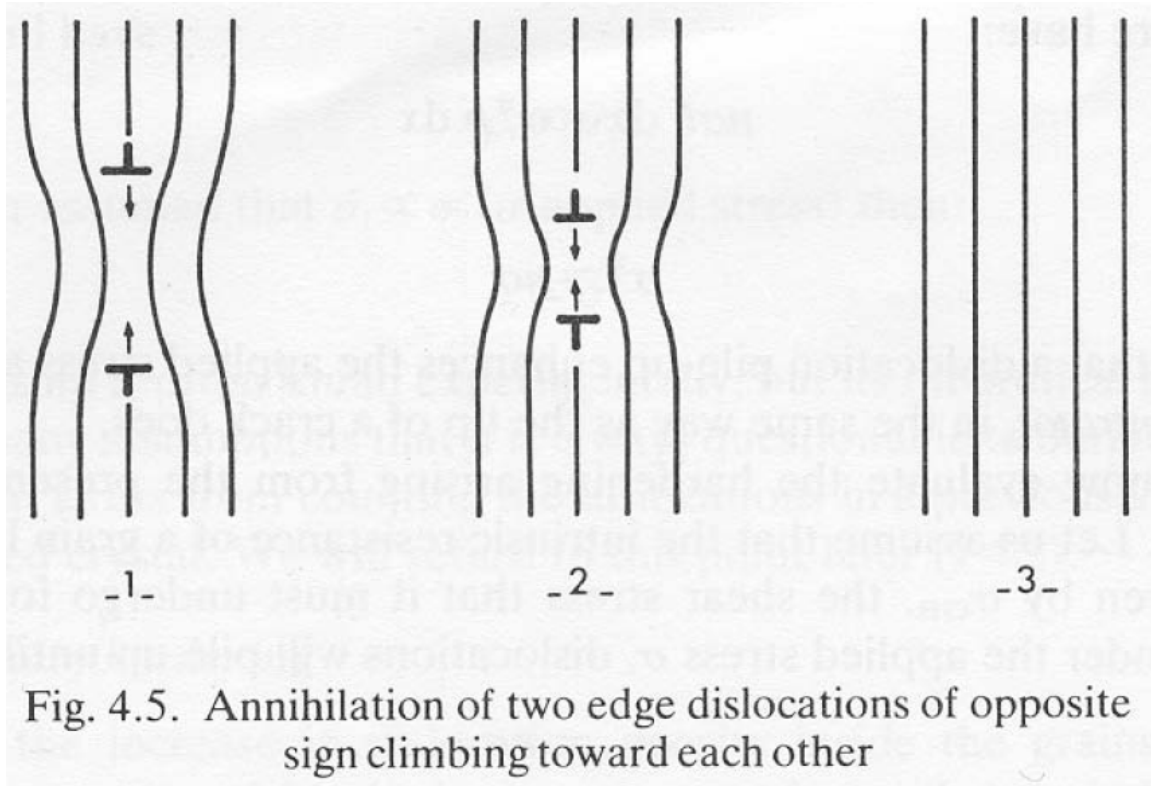
(Nicolas & Poirier, 1976)

Fig. 4.8. Cross slip of screw dislocations in front of an obstacle: (a) two screw dislocations of opposite sign annihilate by cross slip. (b) a screw dislocation cross-slips to avoid the obstacle and resumes gliding in a plane parallel to the former glide plane

(Nicolas & Poirier, 1976)

Fig. 4.5. Annihilation of two edge dislocations of opposite sign climbing toward each other
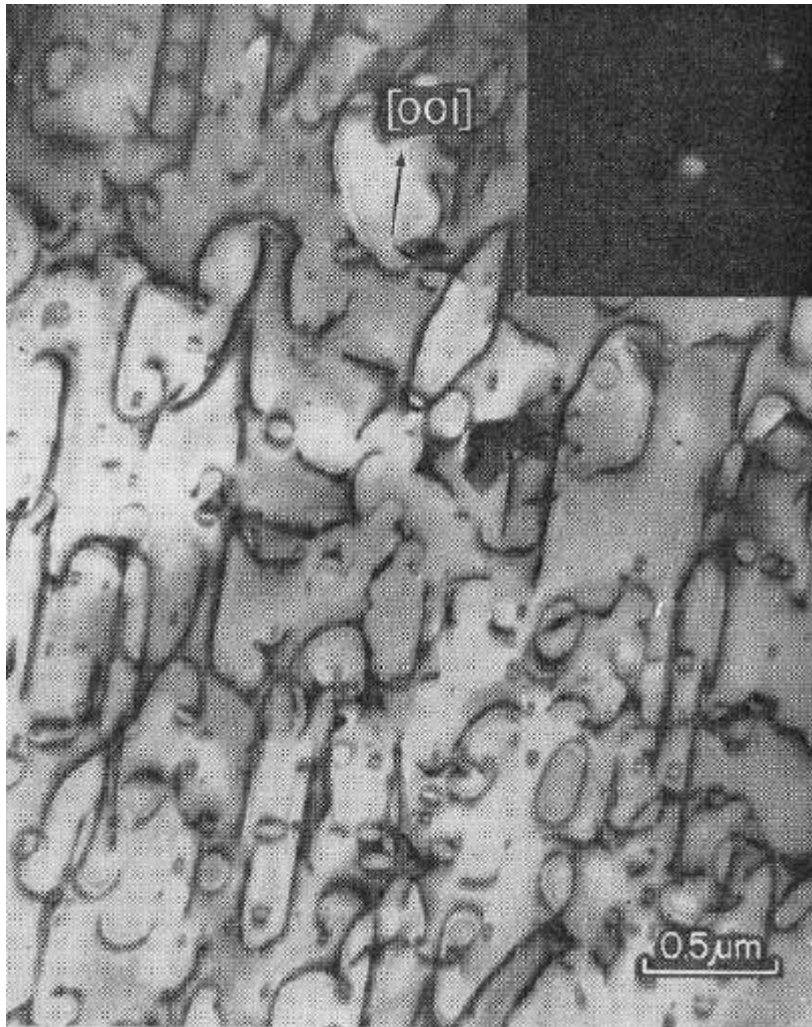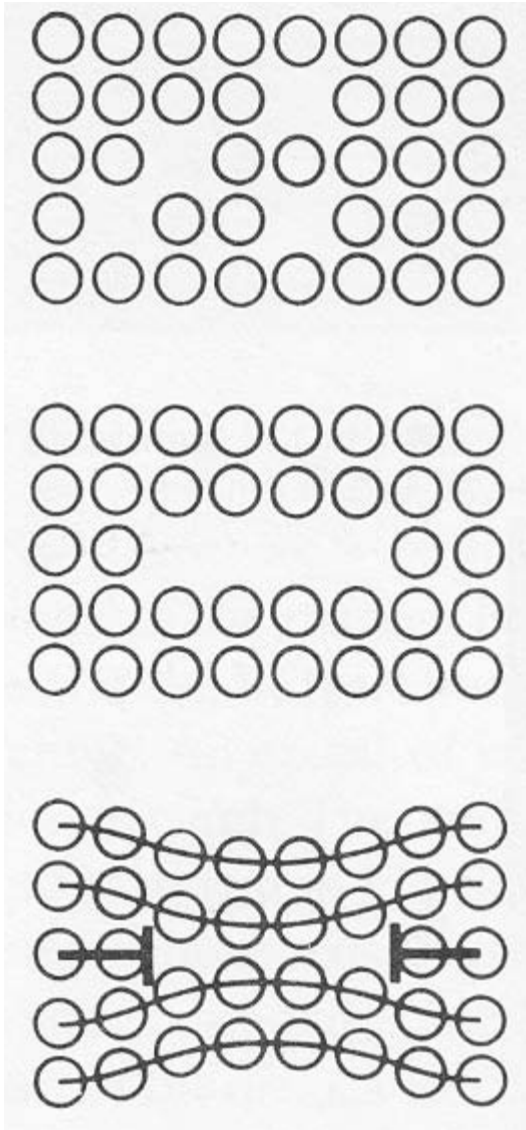
Curved dislocations and loops with **b** = [001] in olivine, indicating climb. The straight segments are aligned along [001]. Dislocation density is 3E9 cm^{-2} (Phakey et al., 1972)
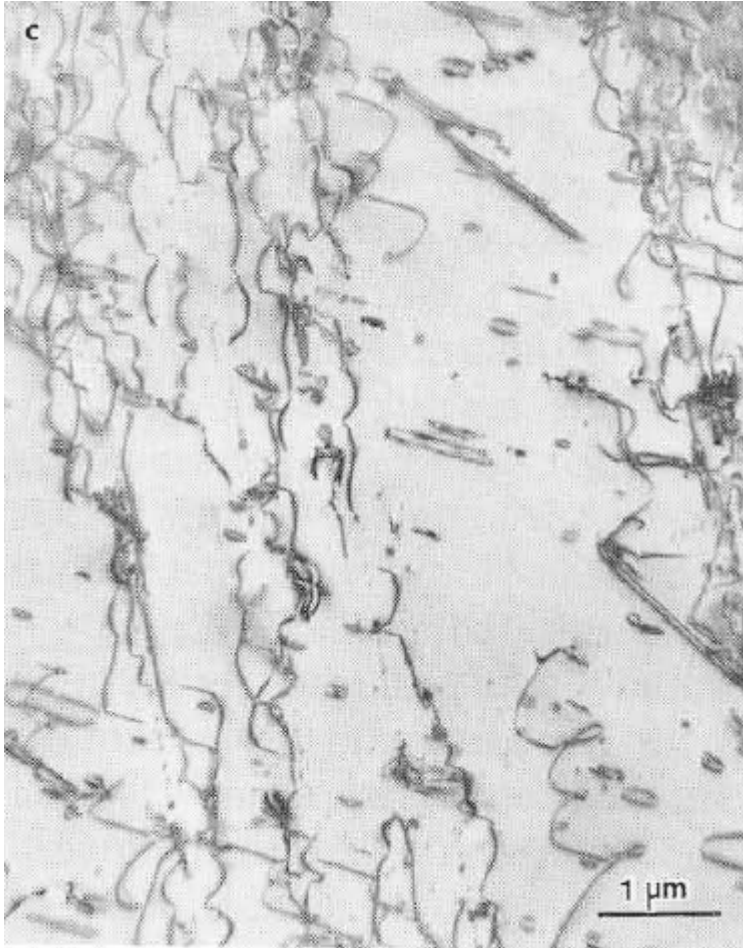
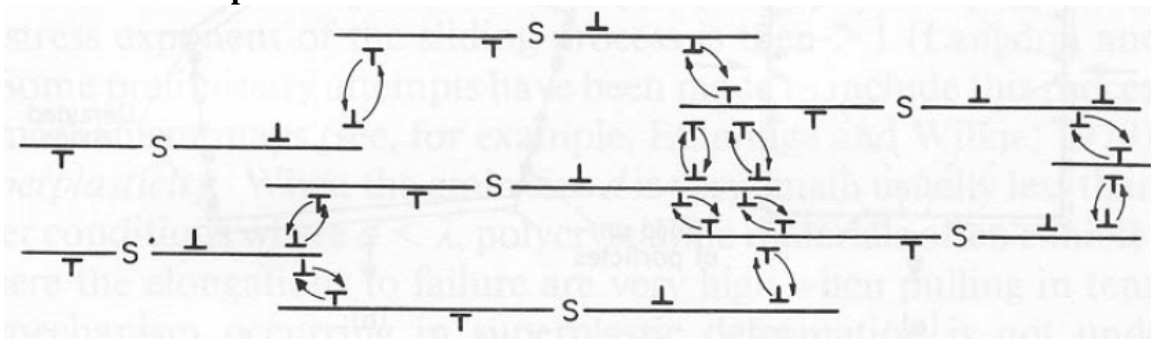Curved dislocations and loops in dolomite, indicating climb (Barber et al., 1981)

formation of a dislocation loop from the collapse of vacancies (Hull & Bacon, 1984)
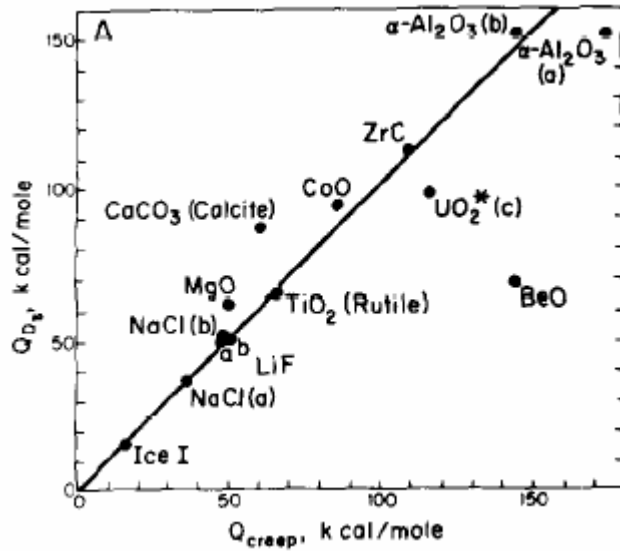
Dislocation Creep

Dislocation creep is the combination of dislocation glide and climb (Langdon, 1985). Slip is faster than climb, so this is often creep by climb-controlled glide of dislocations or Weertman creep. The creep rate is

$$\dot{\varepsilon} = \frac{D_{SD}}{b^2}\left(\frac{\sigma}{\mu}\right)^3 \frac{\mu b^3}{kT} \quad \text{or} \quad \dot{\varepsilon} = \dot{\varepsilon}_o\left(\frac{\sigma}{\mu}\right)^n \exp\left(-\frac{\Delta H_{SD}}{kT}\right)$$

note that the stress exponent is 3 and there is no dependence on grain size.
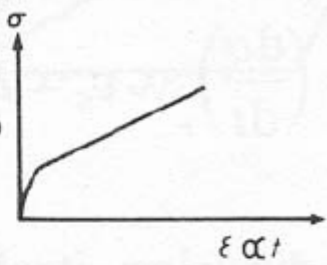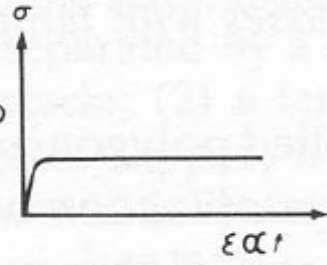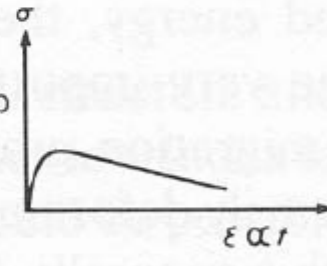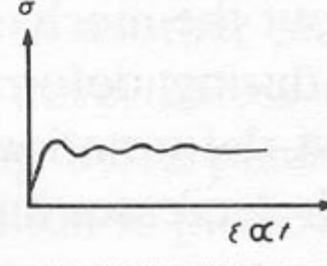
activation energy for self-diffusion of slowest-diffusing species compared to activation energy of creep (Kirby & Raleigh, 1973)

Recovery and Recrystallization

Recovery is the removal of line defects. If the recovery rate dσ/dt is proportional to the rate at which dislocations are removed, which is proportional to the climb rate, then the recovery rate is proportional to the rate of self diffusion,

$$\frac{d\sigma}{dt} \propto D_{SD}$$

		$\dot{\varepsilon}$ = Const.
COLD WORKING Low $\dfrac{T}{T_M}$ High $\dot{\varepsilon}$	$h\dot{\varepsilon} - r > 0$ Strain hardening, recovery	$\dfrac{\Delta\sigma}{\Delta t} > 0$
STEADY-STATE FLOW High $\dfrac{T}{T_M}$ Low $\dot{\varepsilon}$	$h\dot{\varepsilon} - r = 0$ Strain hardening, recovery	$\dfrac{\Delta\sigma}{\Delta t} = 0$
UNSTABLE FLOW High $\dfrac{T}{T_M}$ Low $\dot{\varepsilon}$	$h\dot{\varepsilon} - r < 0$ Strain hardening, recovery	$\dfrac{\Delta\sigma}{\Delta t} < 0$
HOT WORKING High $\dfrac{T}{T_M}$ High $\dot{\varepsilon}$	Strain hardening, recovery + Recrystallization	

deformation regimes (Nicolas & Poirier, 1976)

Cold-worked dislocation structures (low T/T_m)
high dislocation densities
little evidence of climb or recovery
long straight dislocations lying in their slip plane
self-locking pairs of dislocations called dipoles
if only 1 slip systems active
    dislocation tangles that form cell walls at high strain
    geometric constraints of other grains leads to strain inhomogeneities
    undulatory extinction, kinking and twinning

if multiple slip systems active
    similar, but 3-D networks and tangles
    dislocation tangles form cellular structure

Hot-worked dislocation structures (high T/T$_m$)
low free dislocation density
polygonized substructure consisting of misoriented, relatively dislocation-free subgrains
separated by dislocation tilt and twist walls
dislocation walls are formed by climb and relatively sharp compared to the tangles
formed at lower T
no bent planes and no undulatory extinction
dislocation loops
if only 1 slip systems active
    dislocation walls are subperpendicular to the slip plane
if multiple slip systems active
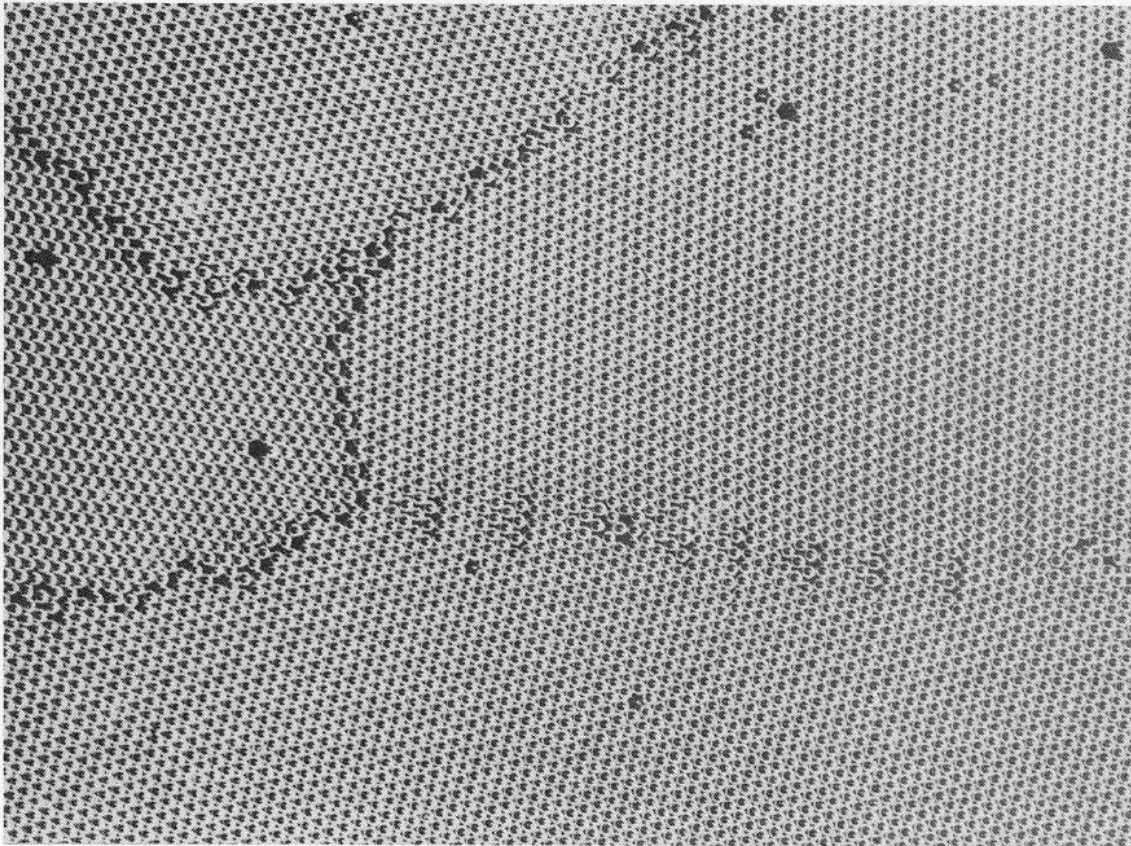   subgrains are more equiaxed

(Sub)Grain Boundaries

Fig. 3.11 Rafts of soap bubbles showing several grains of varying misorientation. Note that the boundary with the smallest misorientation is made up of a row of dislocations, whereas the high-angle boundaries have a disordered structure in which individual dislocations cannot be identified. (After P.G. Shewmon, *Transformations in Metals*, McGraw-Hill, New York, 1969, from C.S. Smith.)
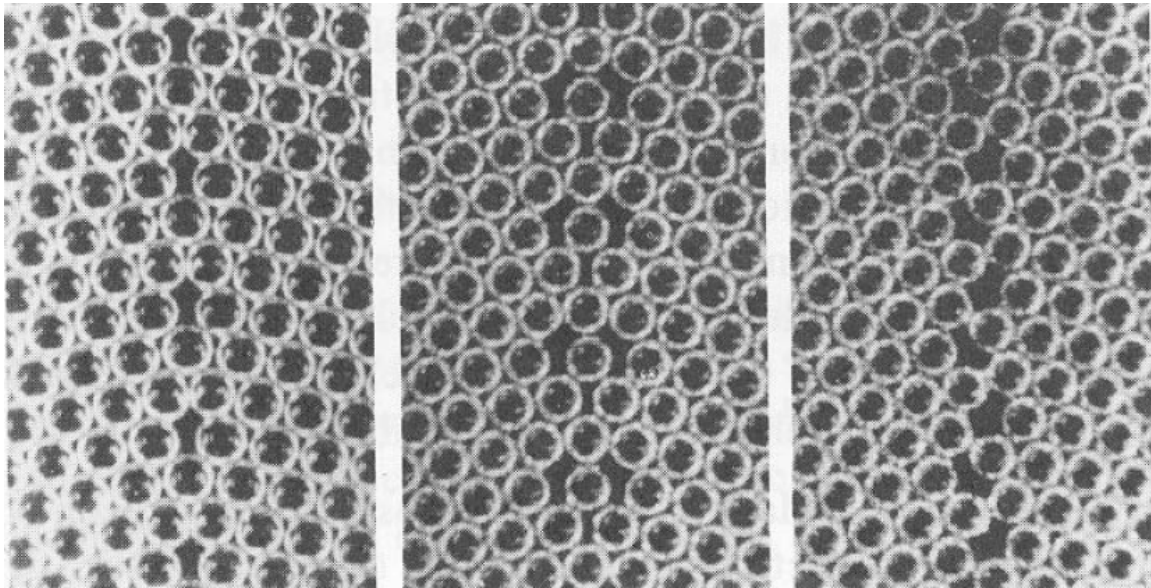
bubble-raft "grain boundaries" (Murr, 1975)

Table 3.3 Measured Boundary Free Energies for Crystals in Twin Relationships (Units mJ m^{-2})

Values selected from compilation given in *Interfacial Phenomena in Metals and Alloys*, by L.E. Murr, Addison-Wesley, London, 1975.

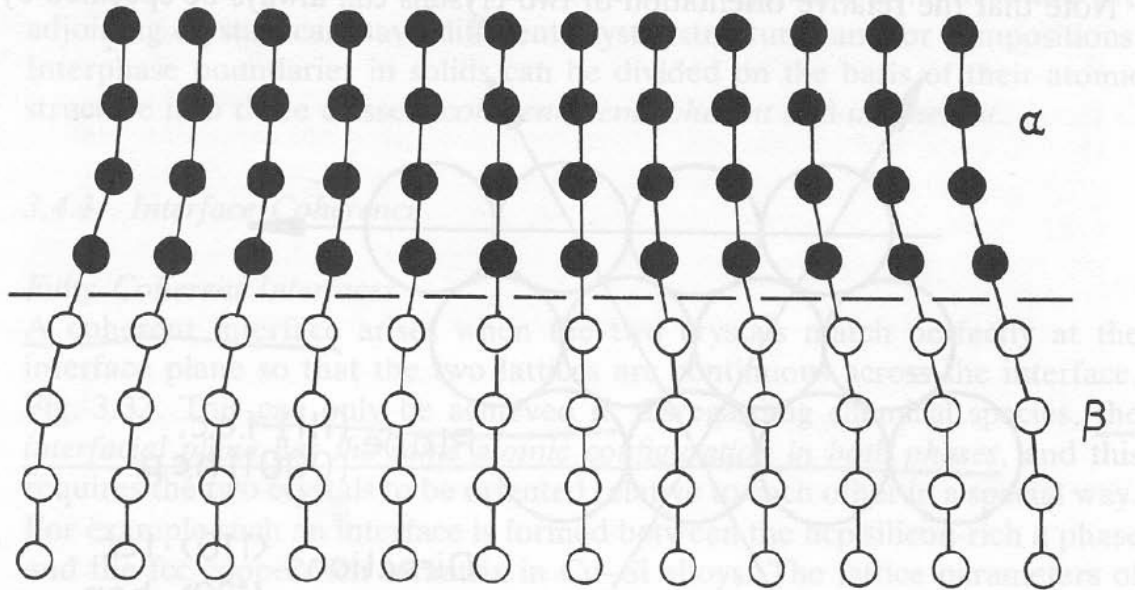| Crystal	Coherent twin boundary energy	Incoherent twin boundary energy	Grain boundary energy
Cu	21	498	623
Ag	8	126	377
Fe-Cr-Ni (stainless steel type 304)	19	209	835

Fig. 3.34   A coherent interface with slight mismatch leads to coherency strains in the adjoining lattices.
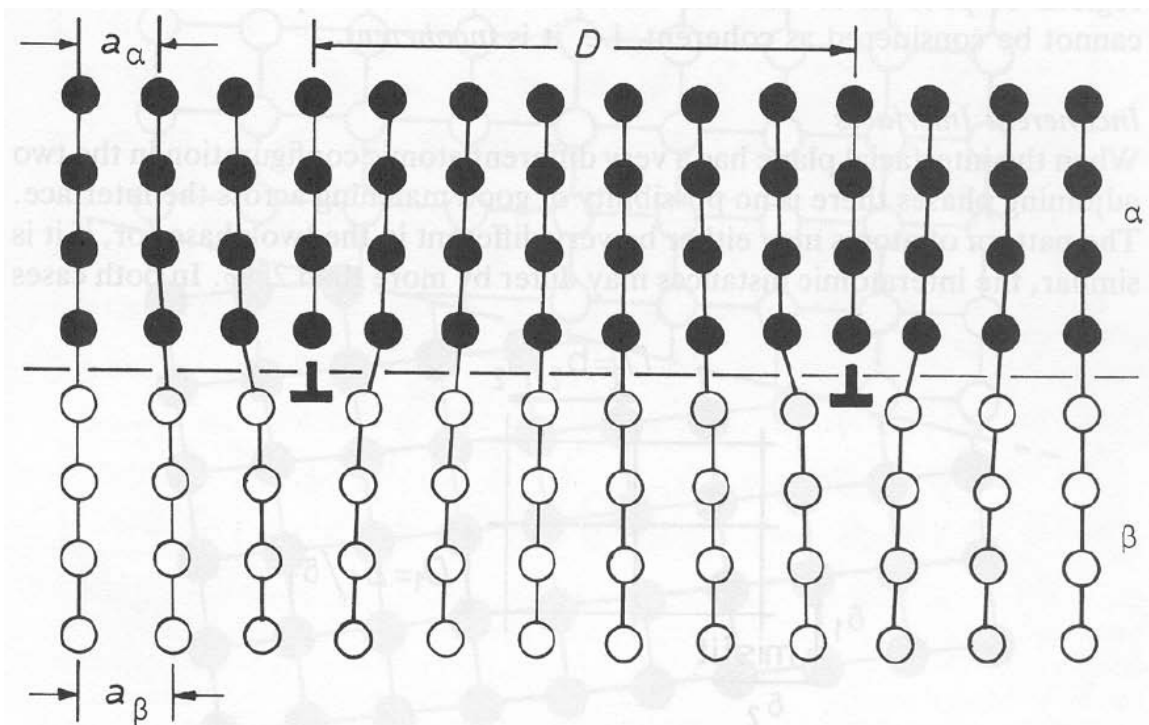
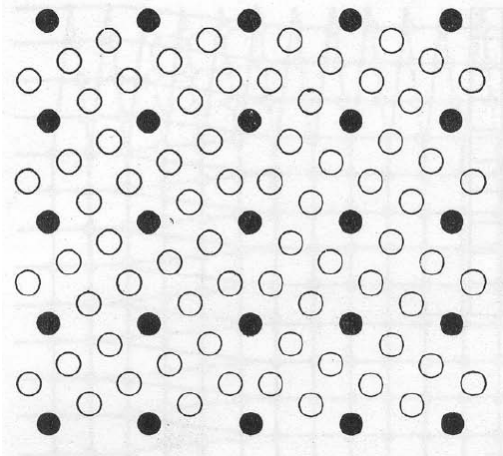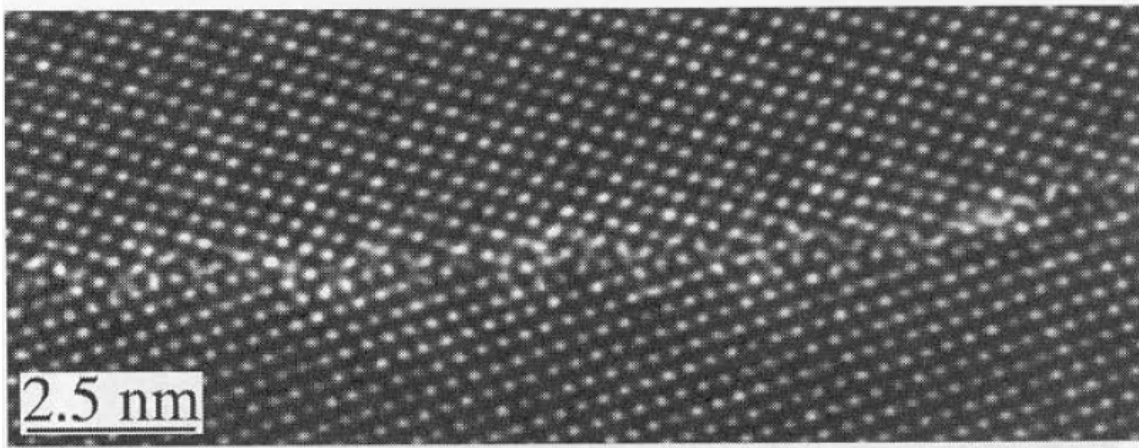(Porter & Easterling, 1981)

Fig. 3.35   A semicoherent interface. The misfit parallel to the interface is accommodated by a series of edge dislocations.
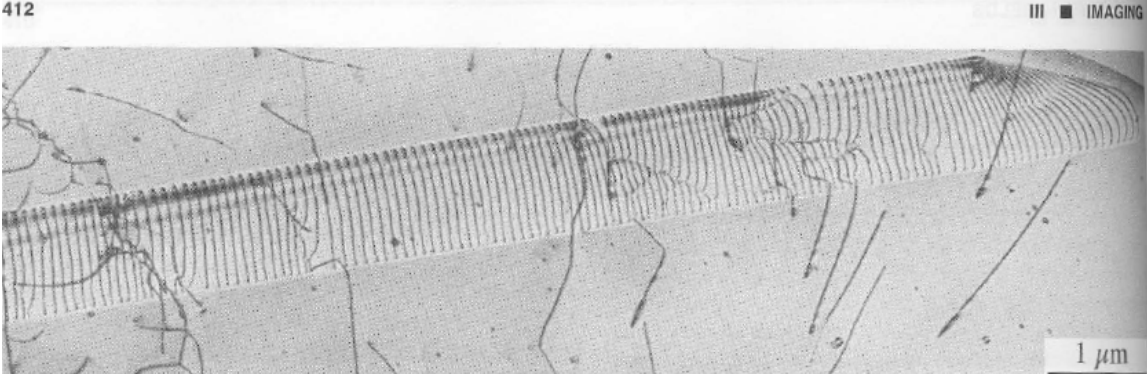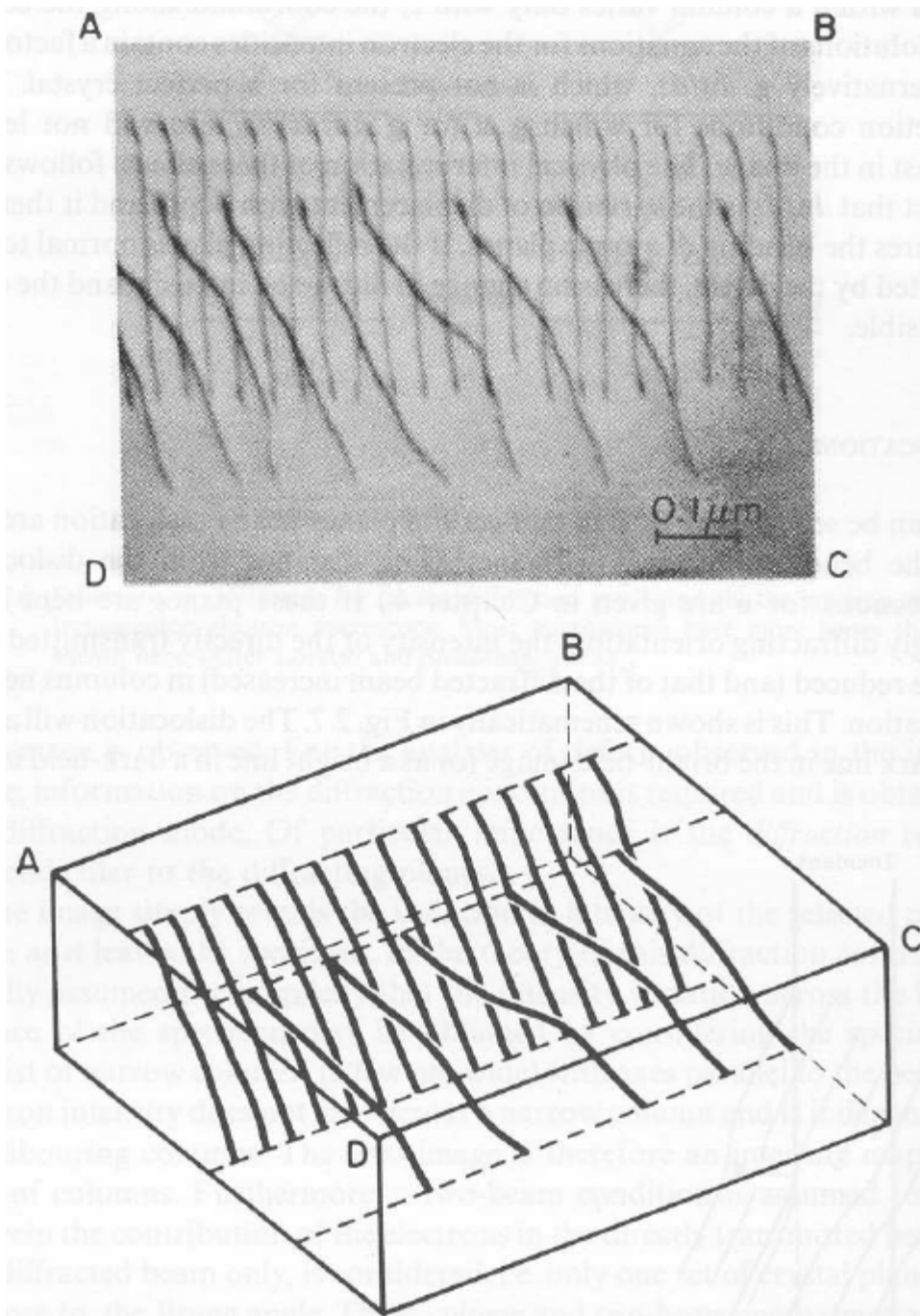
(Porter & Easterling, 1981)

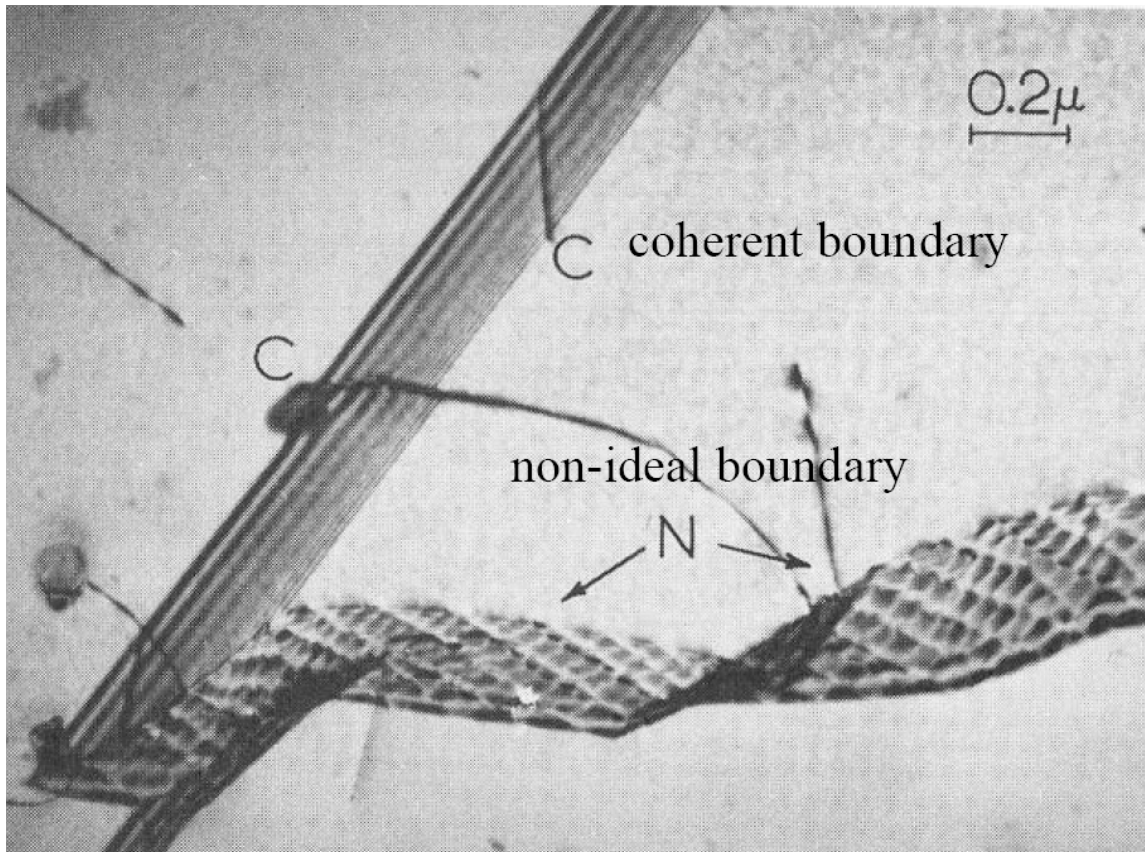symmetrical tilt boundary (Kelly & Groves, 1970)

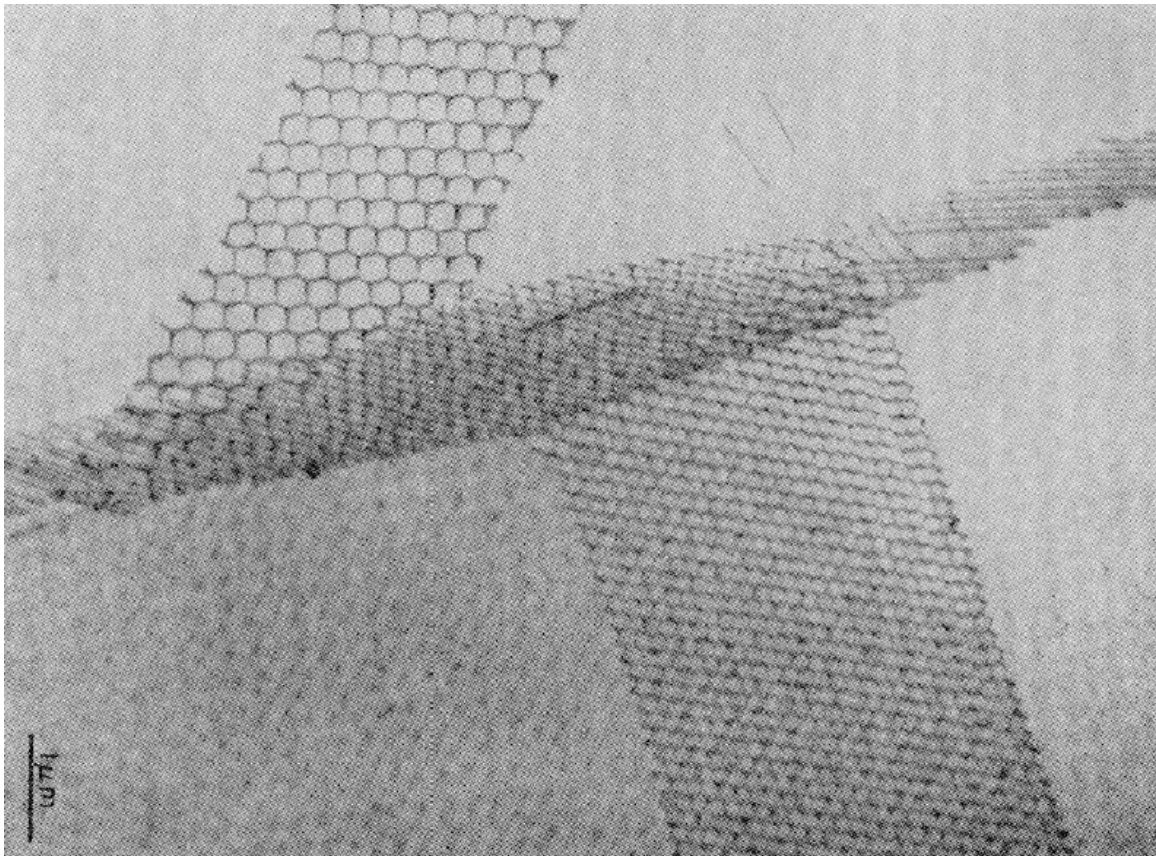HRTEM view of grain boundary (Williams & Carter, 1985).

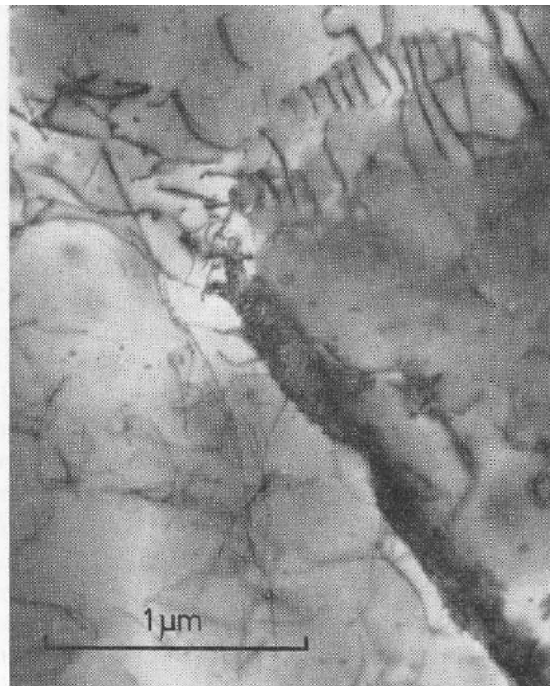HRTEM view of grain boundary (Williams & Carter, 1985).

what a dislocation array means (Hull & Bacon, 1984)

grain boundaries in steel (Murr, 1975)

Dislocation networks in BCC Fe. Each network consists of 3 sets of dislocations with **b** = ½<111>, ½$<11\bar{1}>$ and <100> (Hull & Bacon, 1984)
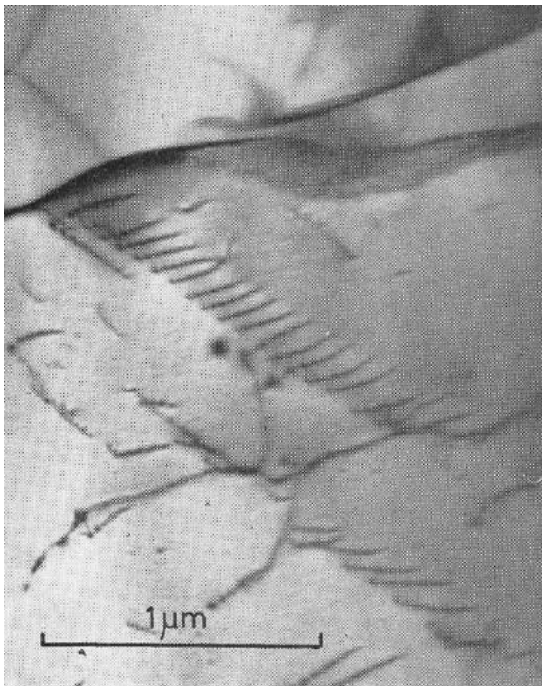
Chewings Range quartzite. L, low-angle subboundary parallel to <a>, producing tilt of [c] axis. R, simple array of dislocations parallel to <a> and subboundary subparallel to (0001) consisting of a dense tangle of dislocations (McLaren & Hobbs, 1972)
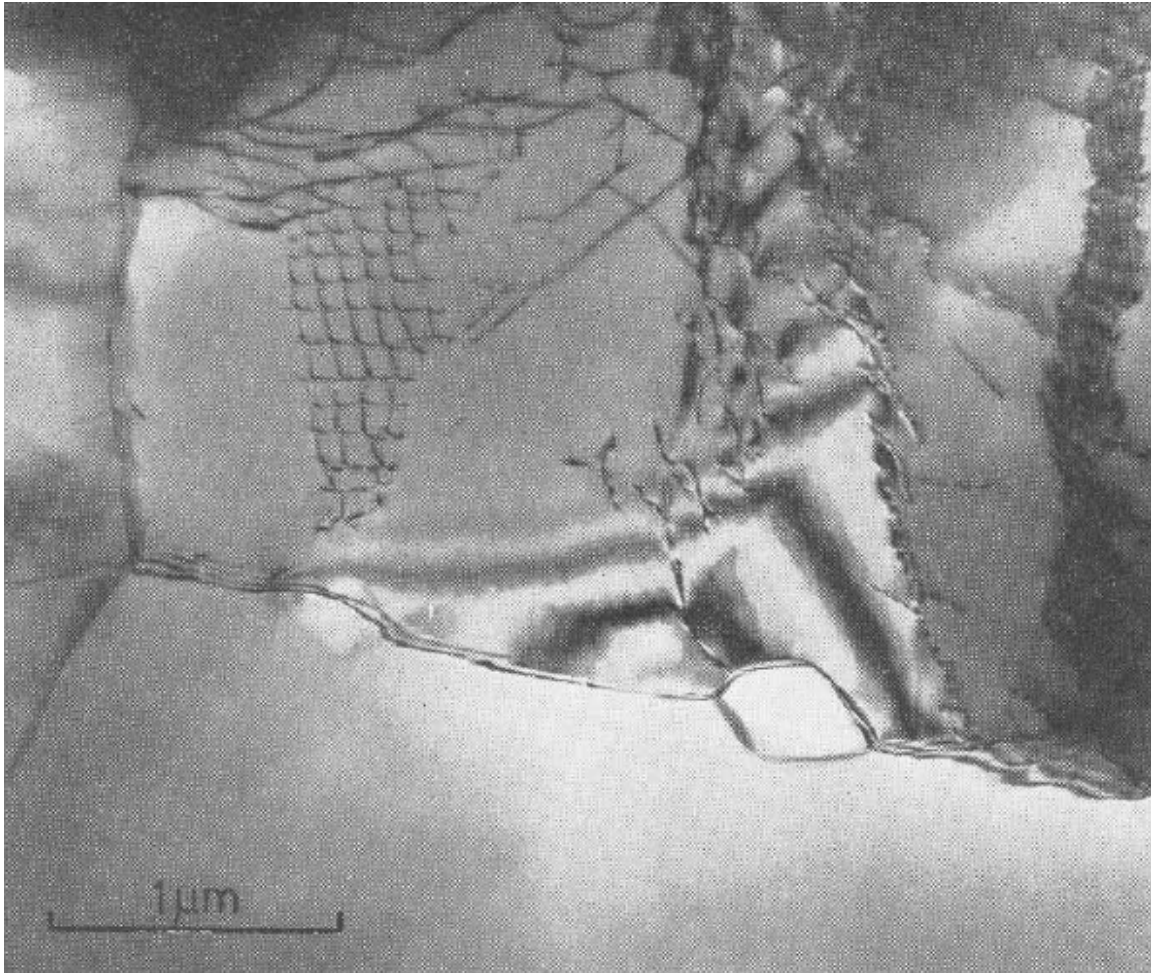
Chewings Range quartzite (McLaren & Hobbs, 1972)
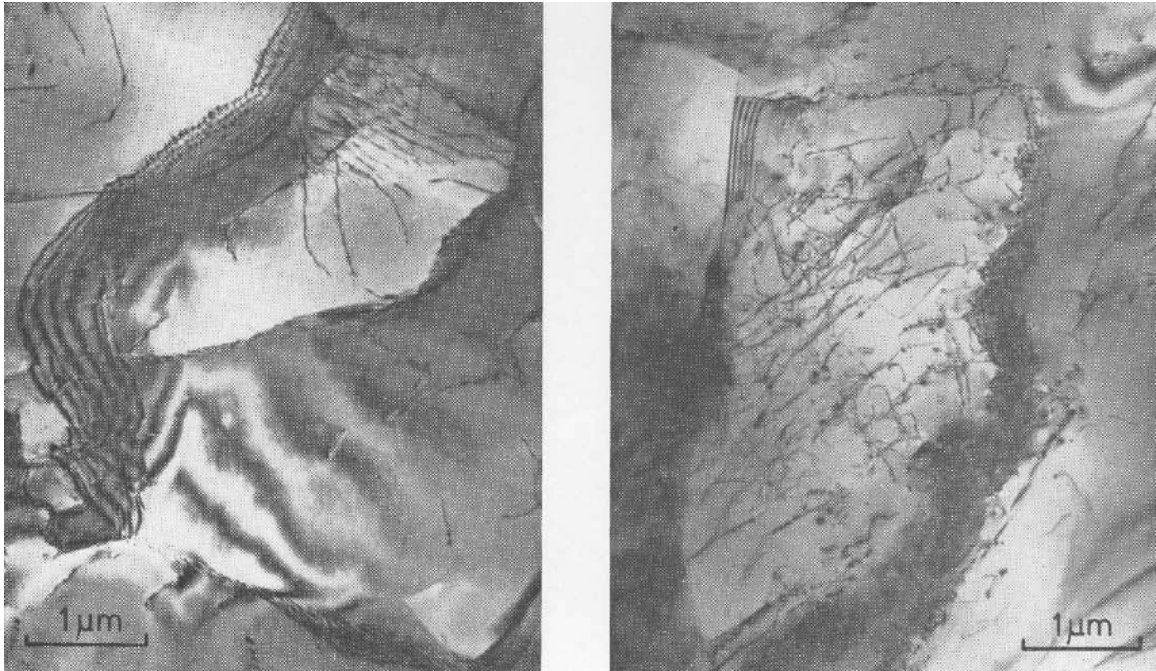
Chewings Range quartzite. In some parts of the subboundaries individual dislocations can be resolved, other parts are tangled an unresolvable. Note low density of dislocations in grains compared to subboundaries (McLaren & Hobbs, 1972)
\
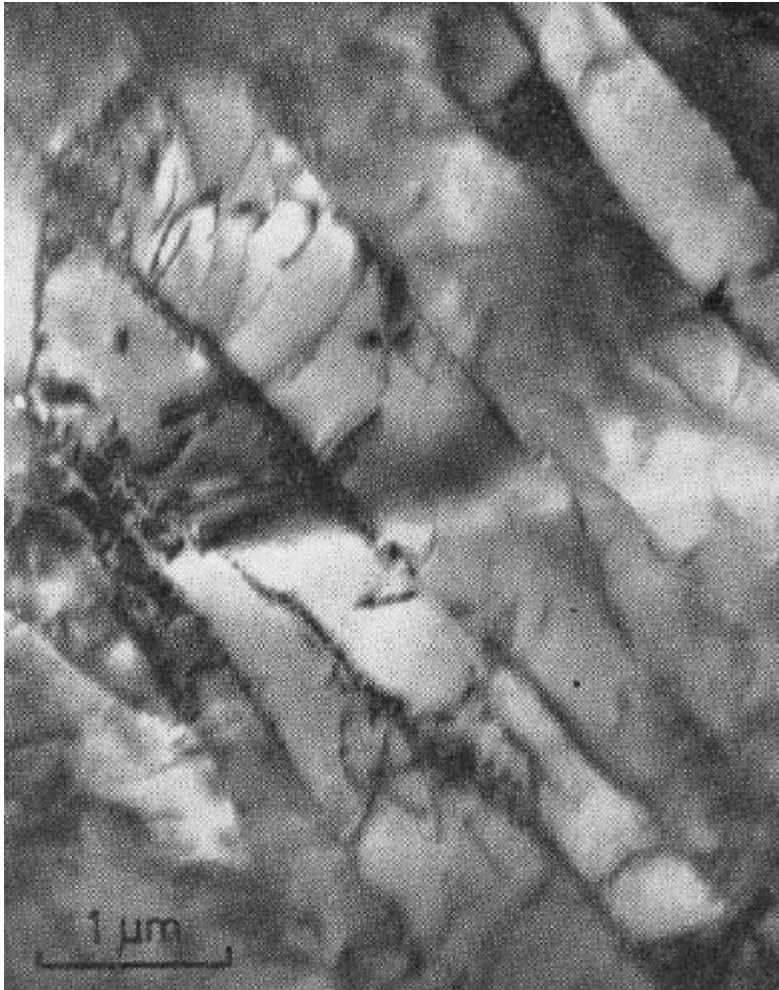
Elongate subgrains parallel to (0001) in Mt Isa quartzite (McLaren & Hobbs, 1972)
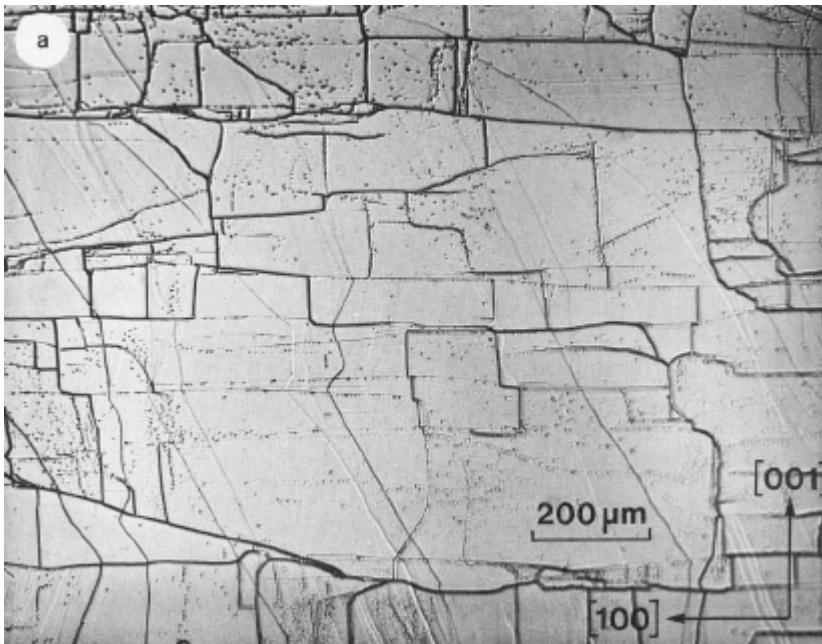
subgrain structure in San Carlos olivine (Kirby & Wegner, 1978)
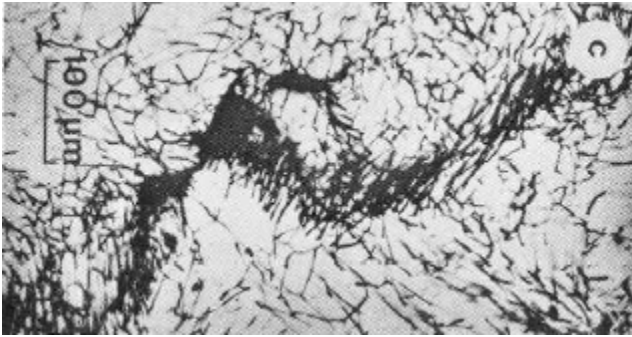
subgrain boundary in pyrope (Carstens, 1969)
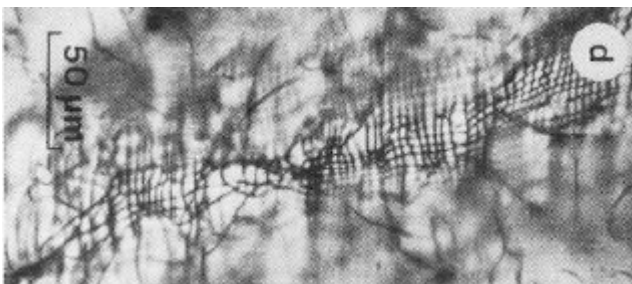
subgrain boundary in quartz (Carstens, 1968)
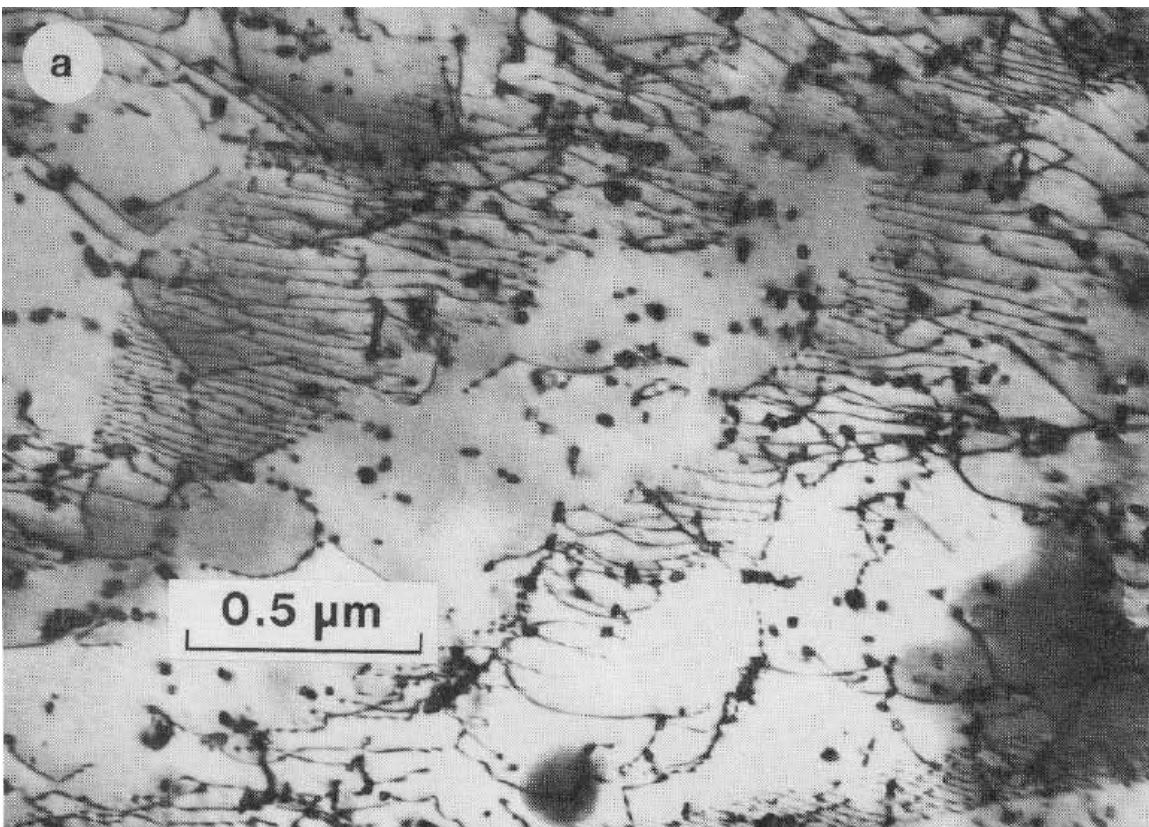
dislocation walls in steel (Nategh et al., 1981)

subgrain boundaries in Hualalai olivine (Green & Radcliffe, 1972)
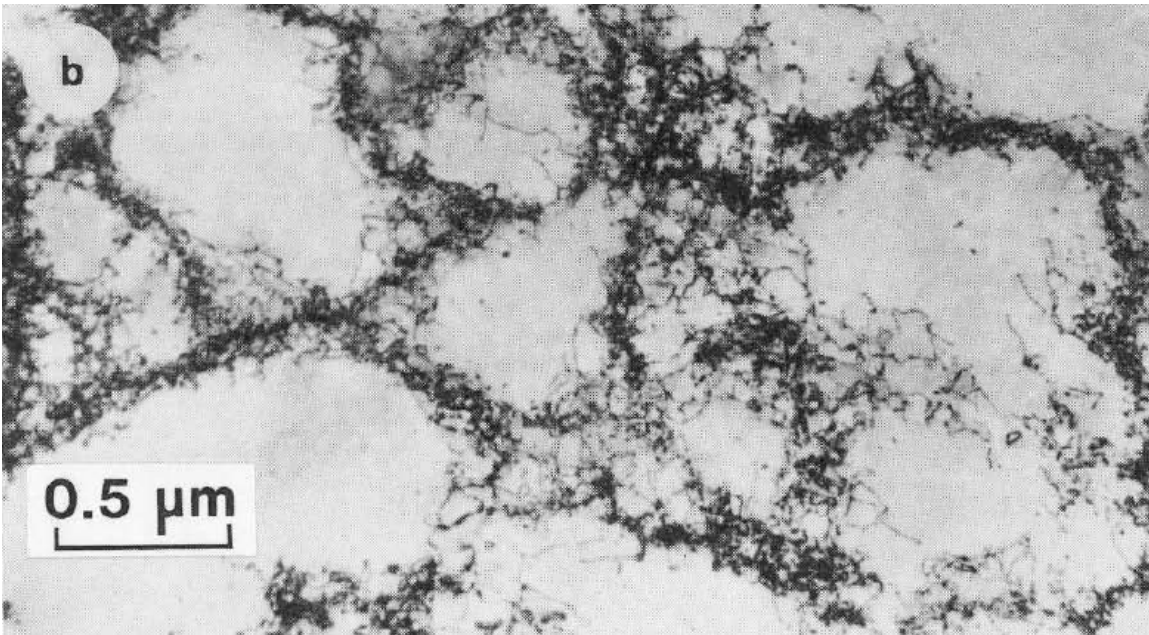
cell structure in Cu (Barber, 1985)

Fig. 12.8. Low angle symmetrical tilt boundary in a simple cubic lattice. The boundary is normal to the plane of the figure. From W. T. Read, Jr., *Dislocations in Crystals*, copyright 1953. Used with permission of McGraw-Hill Book Company.
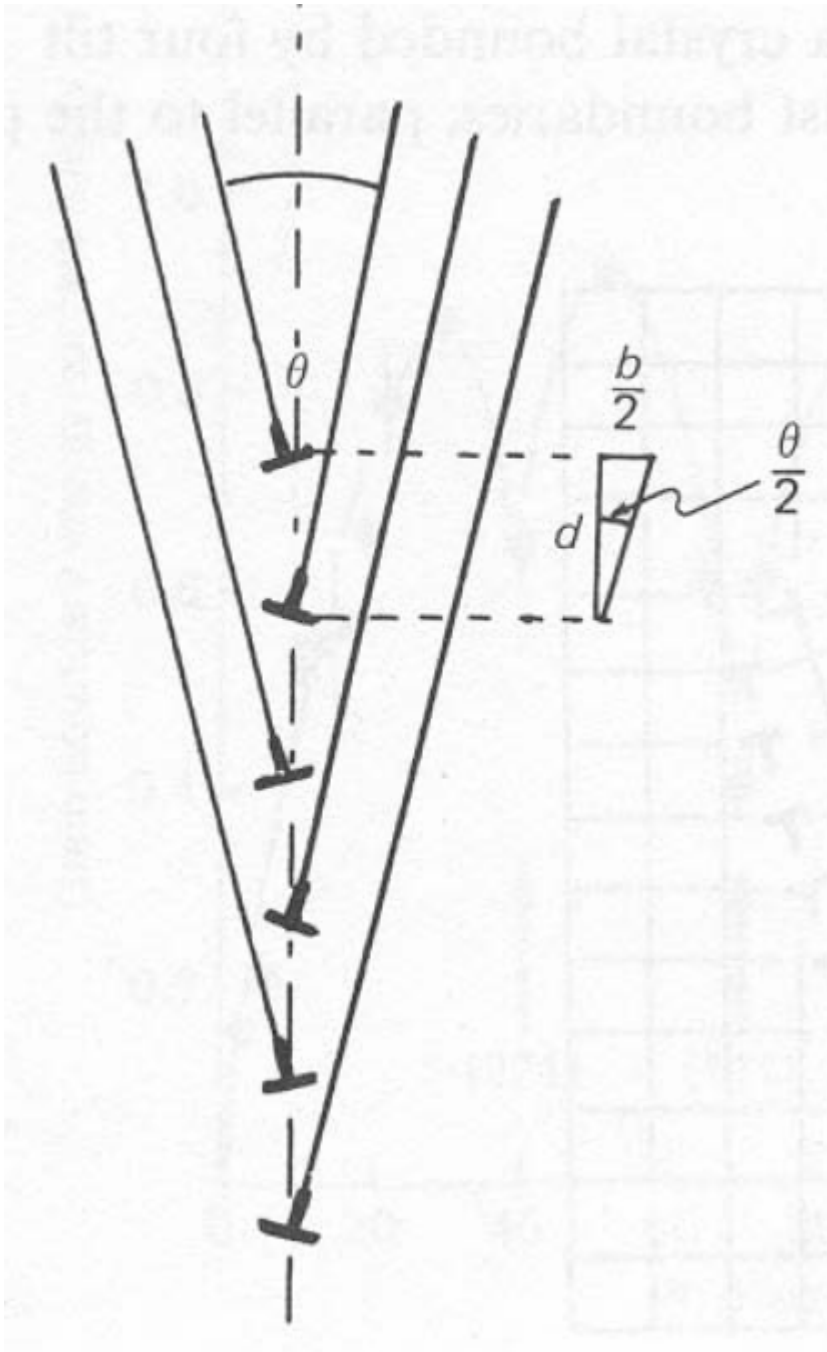
Low-angle tilt boundary (Poirier, 1985)
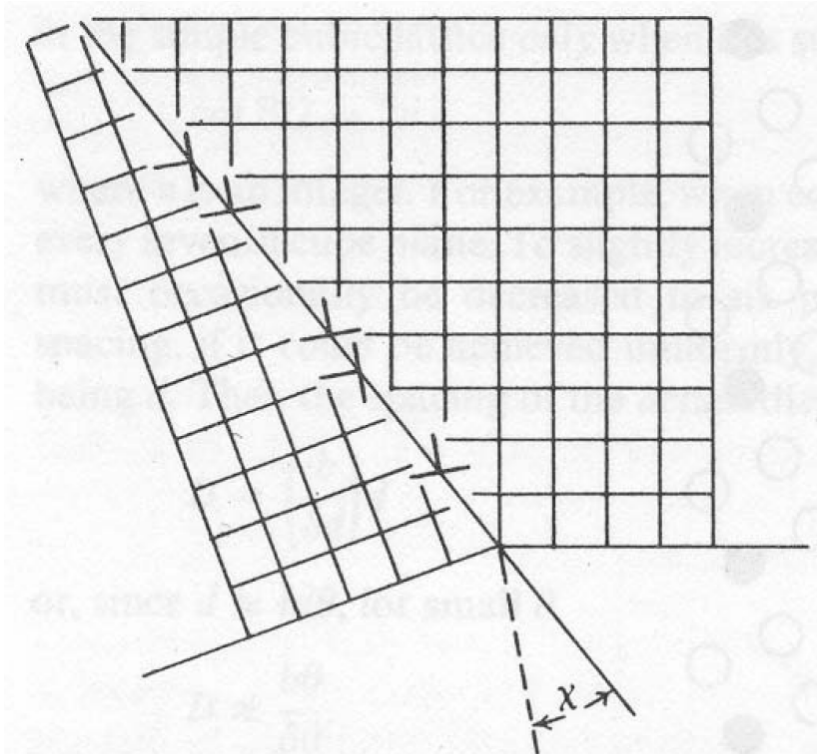
Fig. 12.11. **Unsymmetrical tilt boundary.**

(Kelly & Groves, 1970)
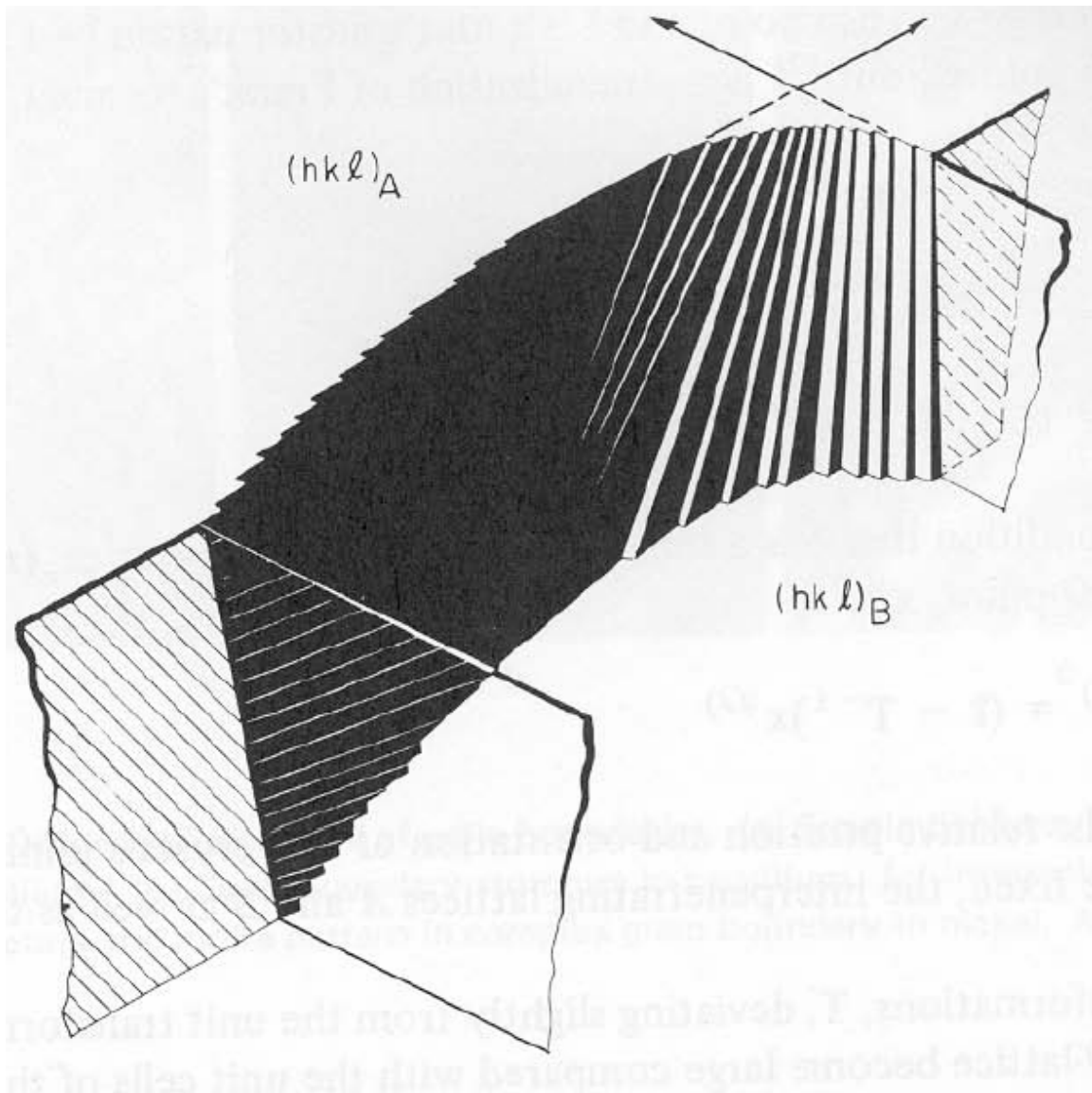
schematic dislocation structure of grain boundary (Murr, 1975)
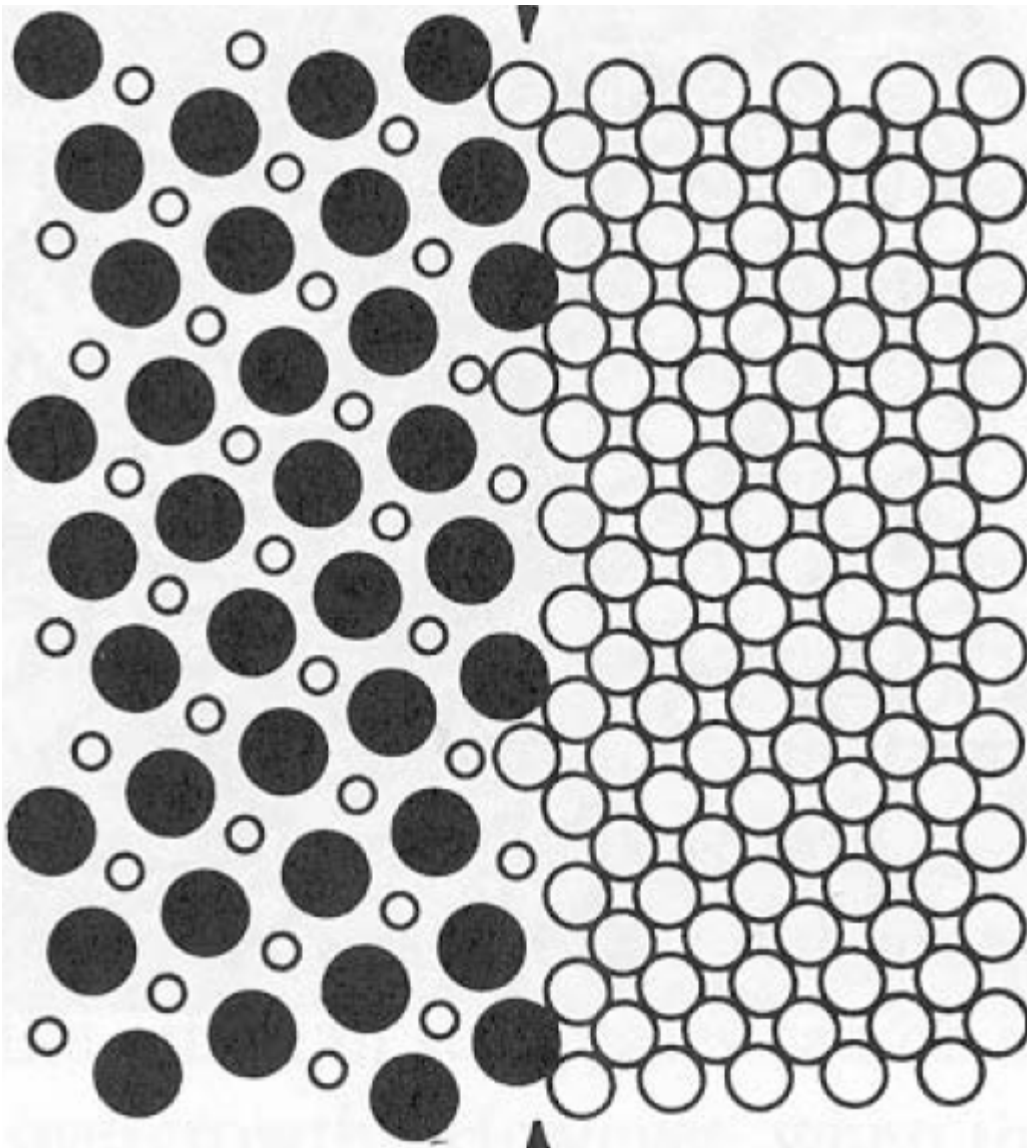
interphase boundary (Murr, 1975)
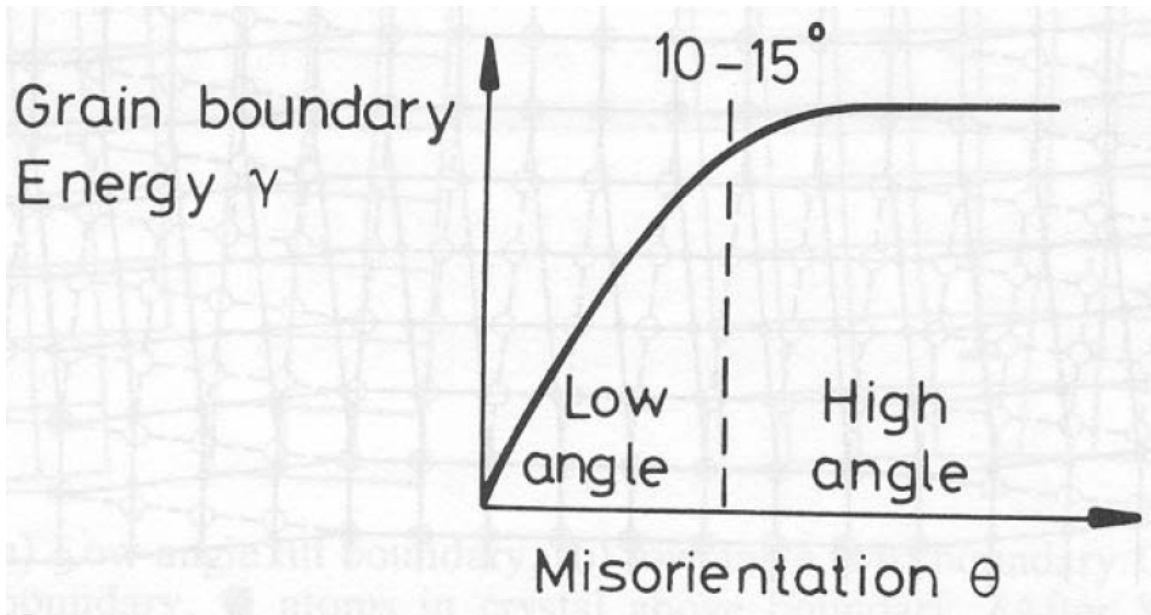
(Porter & Easterling, 1981)
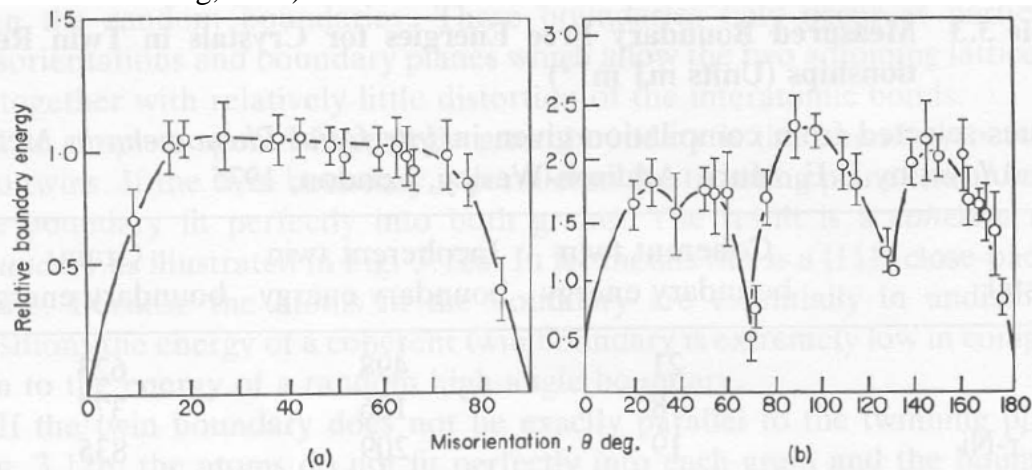
Fig. 3.13 Measured grain boundary energies for symmetric tilt boundaries in Al (a) when the rotation axis is parallel to ⟨100⟩, (b) when the rotation axis is parallel to ⟨110⟩. (After G. Hasson and C. Goux, *Scripta Metallurgica*, **5** (1971) 889.)
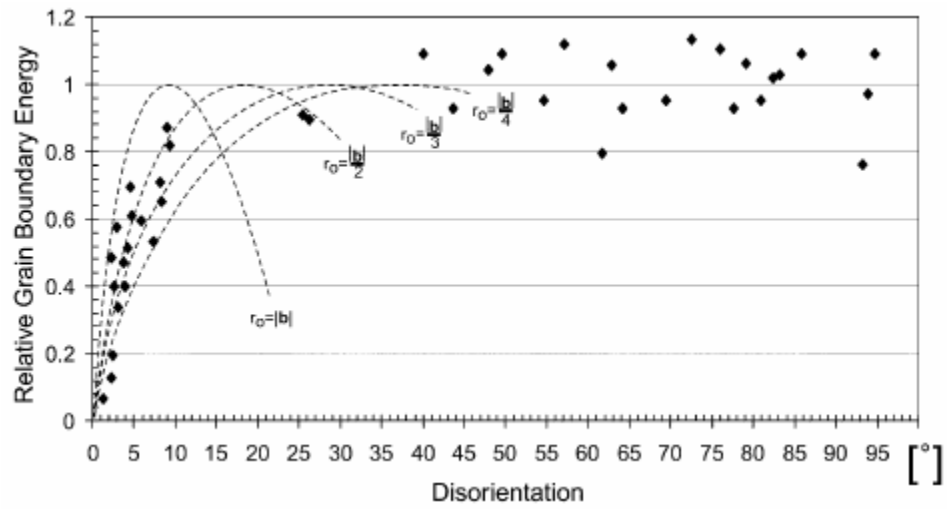
grain boundary energies in olivine (Duyster & Stöckhert, 2001)
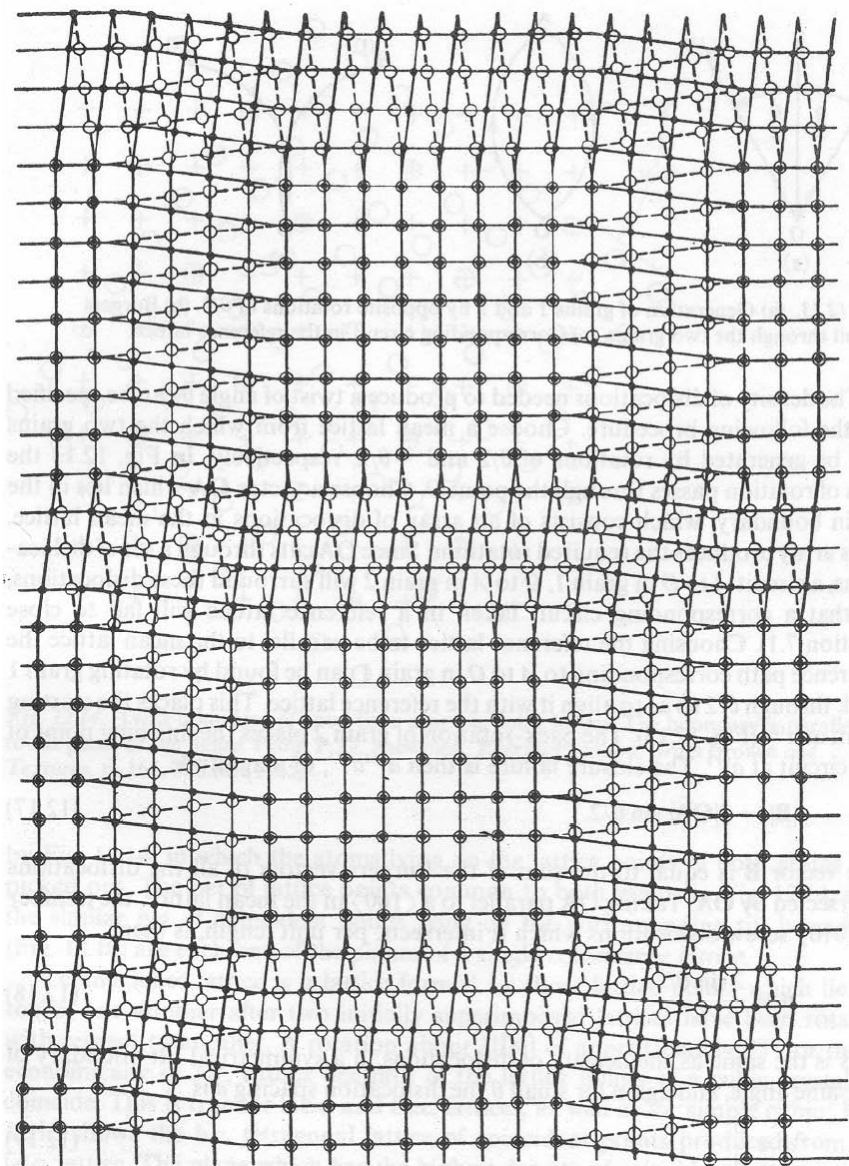
Fig. 12.12. Twist boundary in a simple cubic lattice. The boundary is parallel to the plane of the figure. From W. T. Read, Jr., *Dislocations in Crystals*, copyright 1953. Used with permission of McGraw-Hill Book Company.
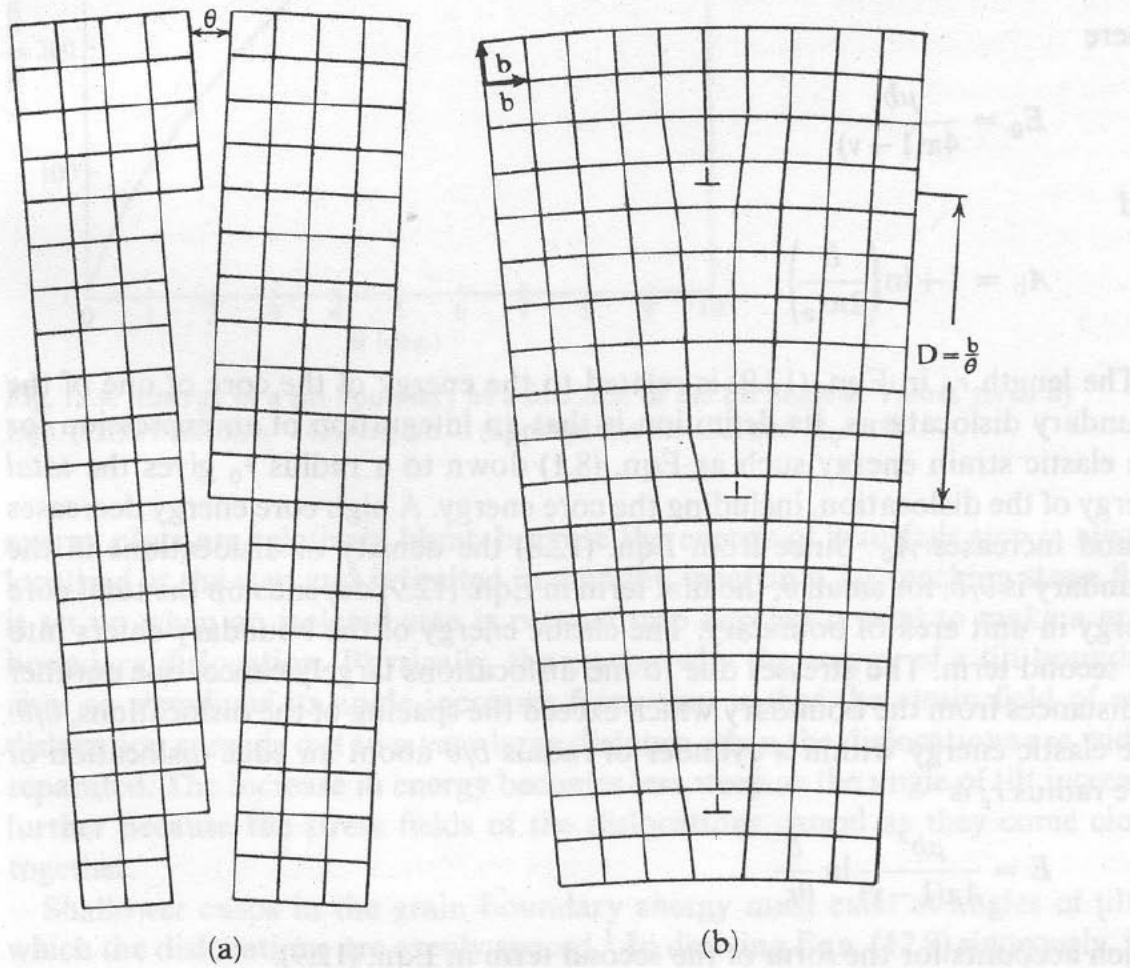
twist boundary

Inclusions
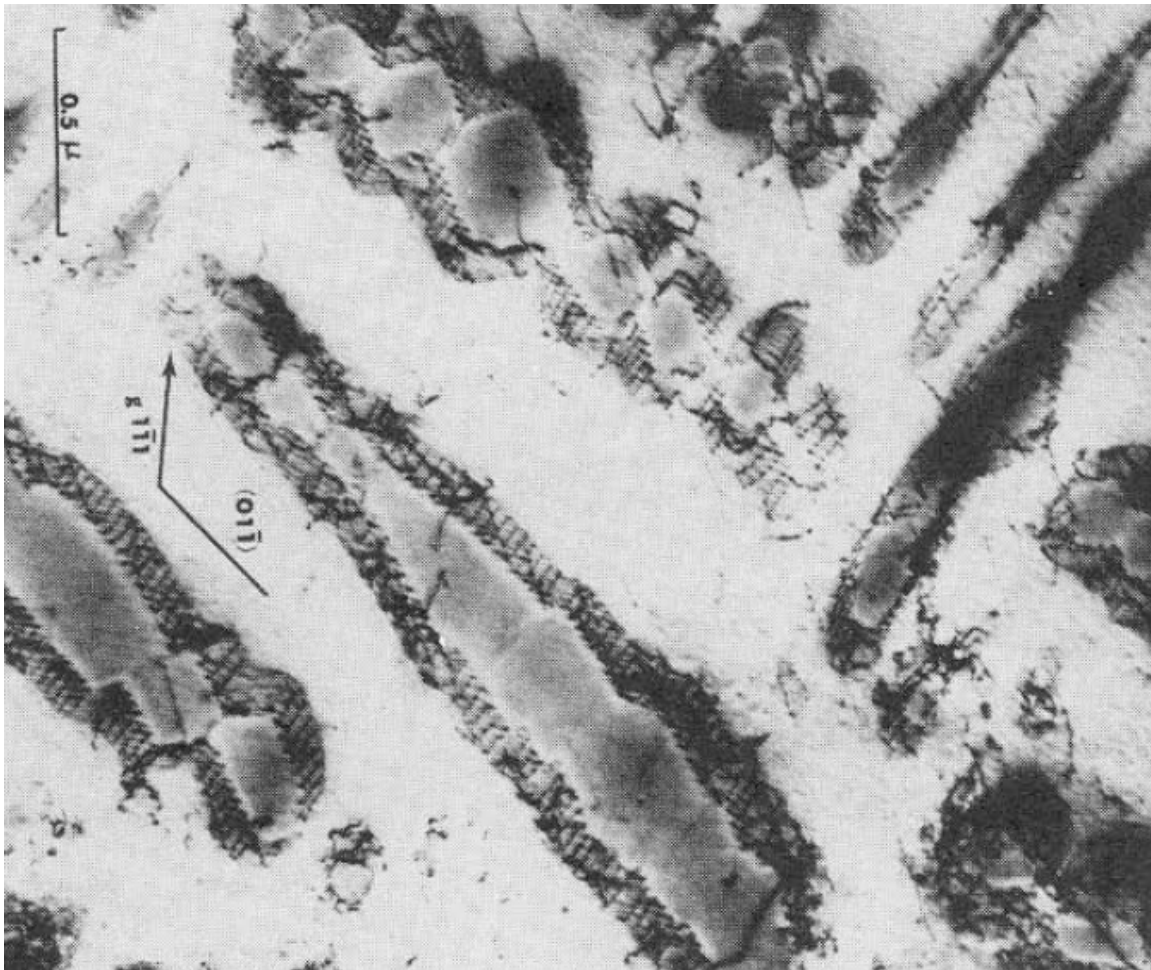
precipitates in Cu alloy (Murr, 1975)
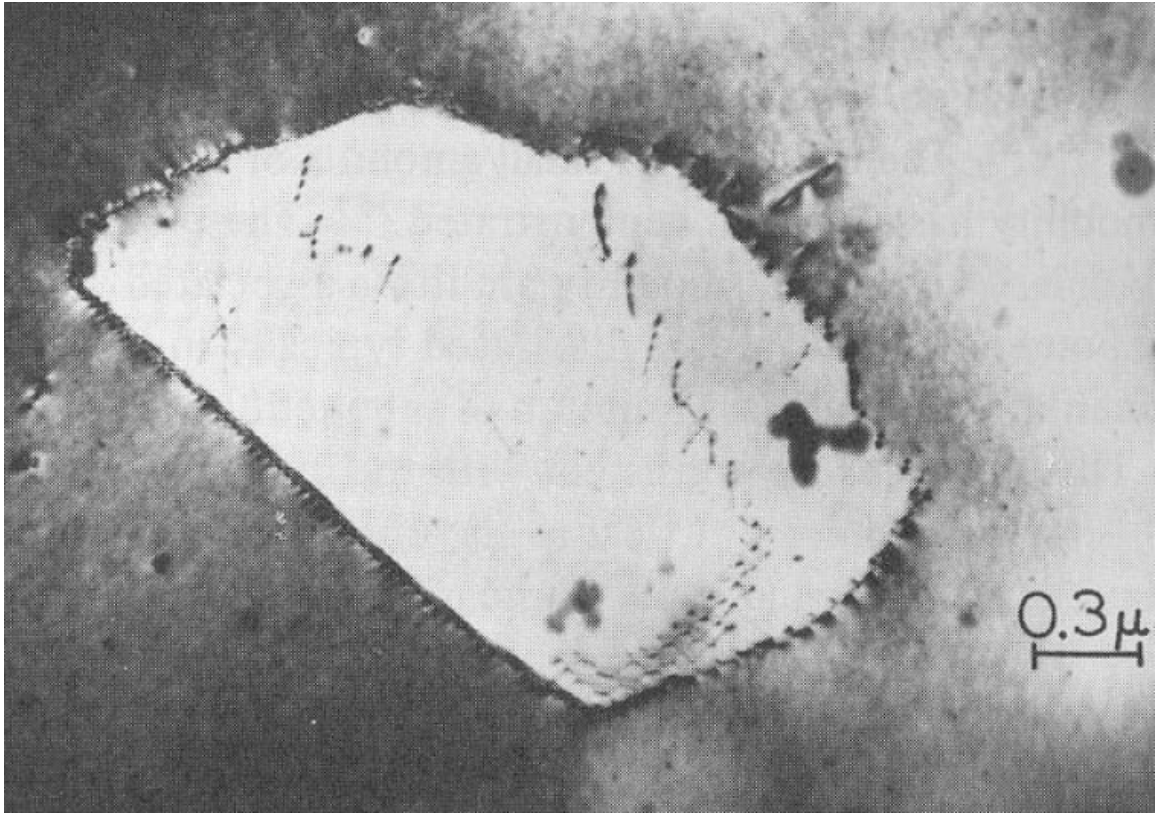
(Murr, 1975)
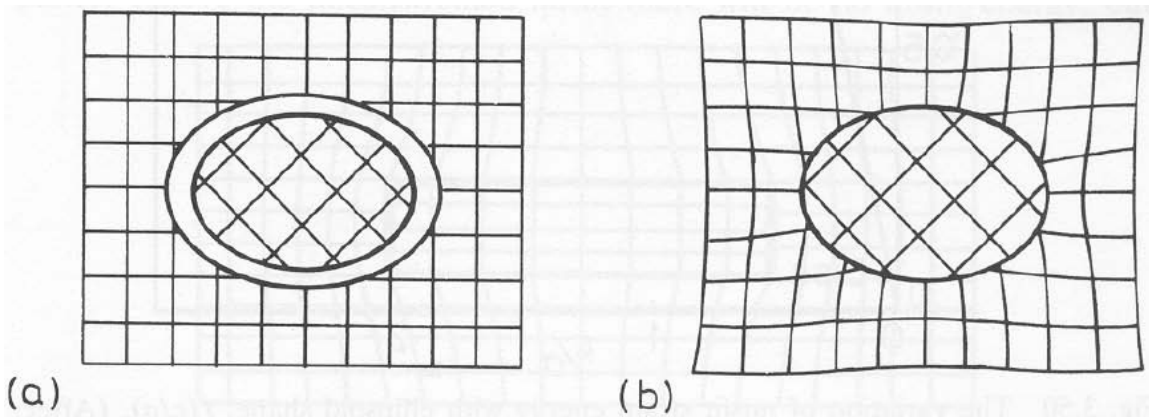
(a)　　　　　　　　　　(b)

Fig. 3.49　The origin of misfit strain for an incoherent inclusion (no lattice matching).

(Porter & Easterling, 1981)

(a)　　　　　　　　(b)　　　　　　　　(c)
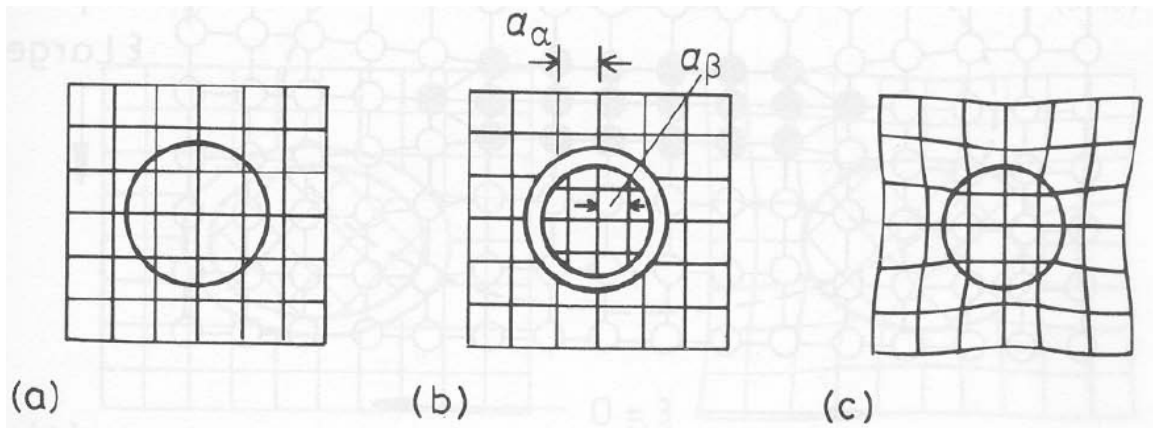
Fig. 3.47 The origin of coherency strains. The number of lattice points in the hole is conserved.

(Porter & Easterling, 1981)

The energy of a coherent precipitate is

$$\Delta G_{coherent} = 4\mu\delta^2 \frac{4}{3}\pi r^3 + 4\pi r^2 \gamma_{ch}$$

where δ is lattice misfit and γ_{ch} is chemical interfacial energy.

264 Lecture 2

Recrystallization
driving forces include
    intragranular defect energy (order of 10^3–10^7 J/m^3 for 10^8–10^{11} cm^{-2})
    grain-boundary energy
    chemical free energy (i.e., chemical potential gradients)
    external-load-supporting elastic strain energy

primary recrystallization driven by defect energy, secondary recrystallization driven by grain-boundary energy

Dislocation annihilation
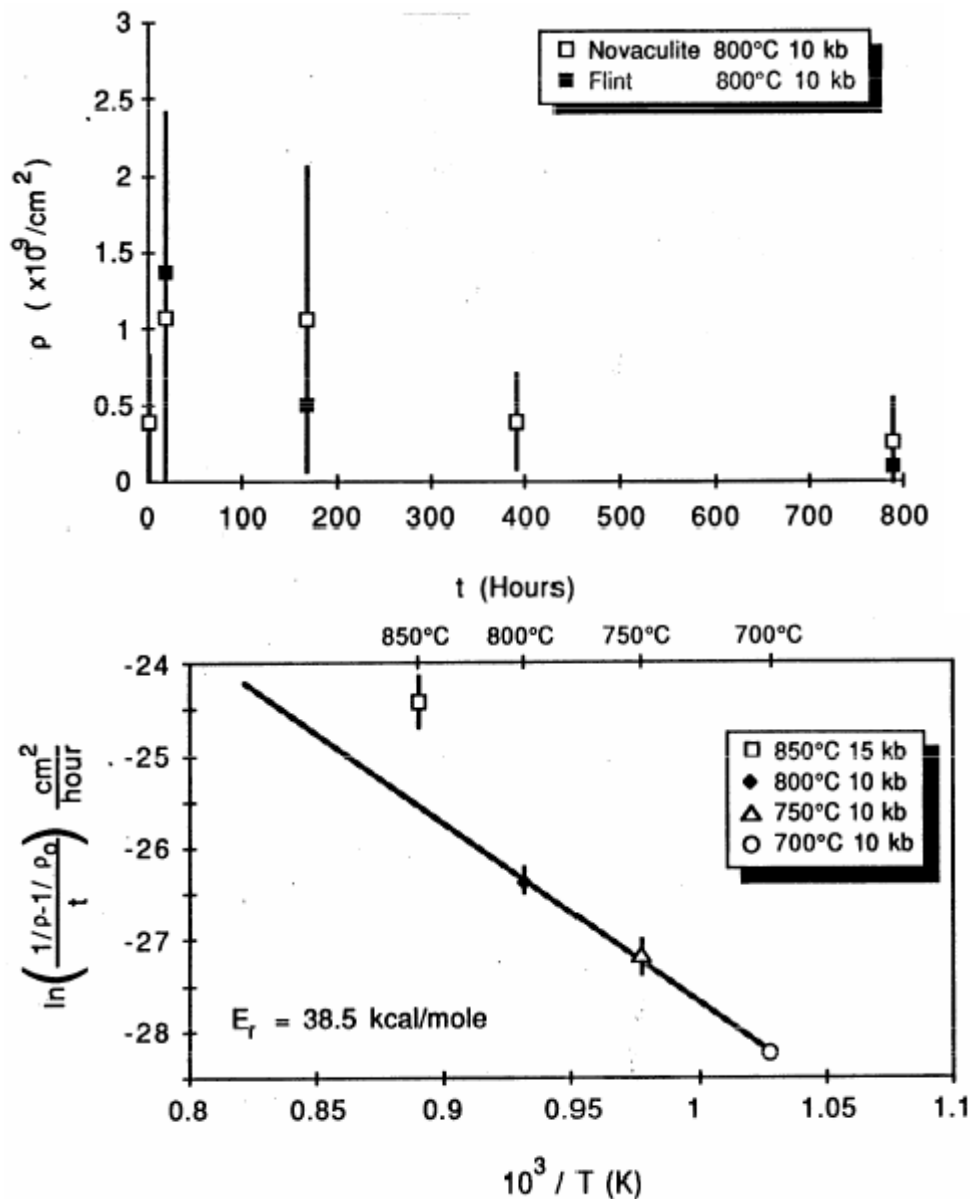
can be approximated as

$$\frac{d\rho}{dt} = -c_o \exp(-Q/RT)\rho^2 \ \text{(Li, 1966)},$$

which, integrated is

$$\frac{1}{\rho} - \frac{1}{\rho_o} = ct$$

where

$$c = c_o \exp(-Q/RT)$$

$c_o = 1.5E^{-8}$ cm^2/s and $Q = 146 \pm 12$ kJ/mol (Pierce, 1987)
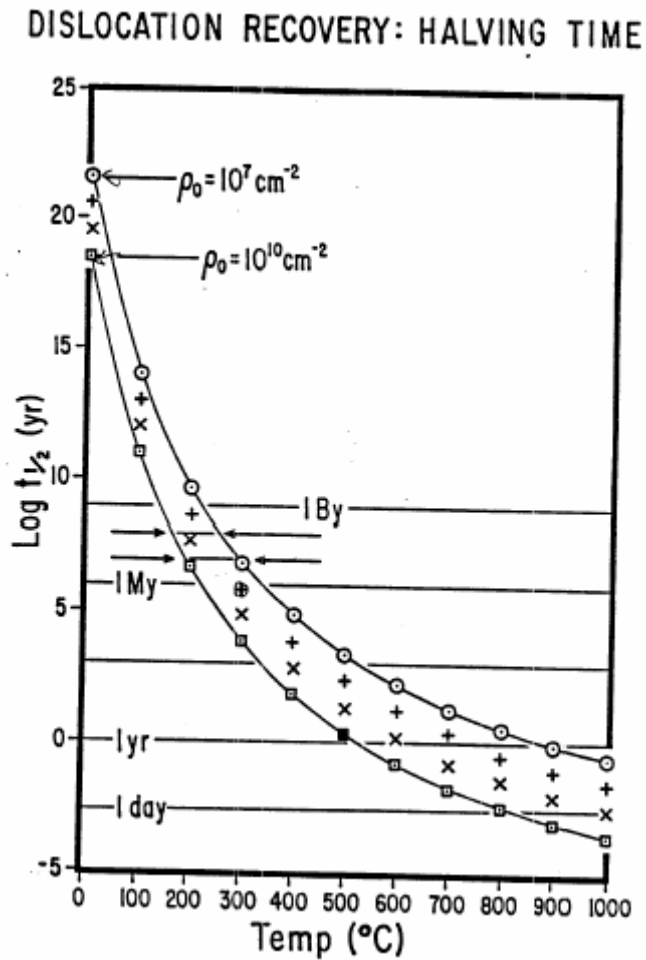
Rate of dislocation recovery extrapolated (Pierce, 1987).

Dynamic or Syntectonic Recrystallization
Grain boundaries often migrate away from their center of curvature during dynamic recrystallization.
A dynamically recrystallizing material can be subgrain free.
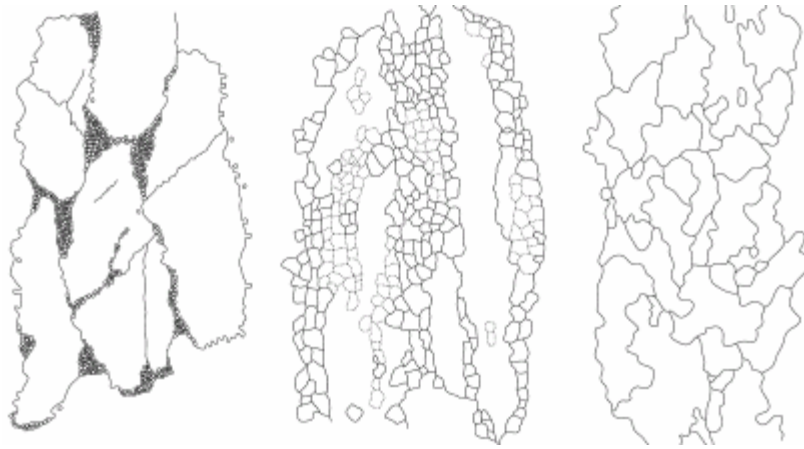
Types of recrystallization: bulging recrystallization, SGR, GBM recrystallization (Stipp et al., 2002).

Strain-Induced Grain-Boundary Bulging
Formation of a strain-free bulge along a high-angle grain boundary. Driving force is difference in defect density.
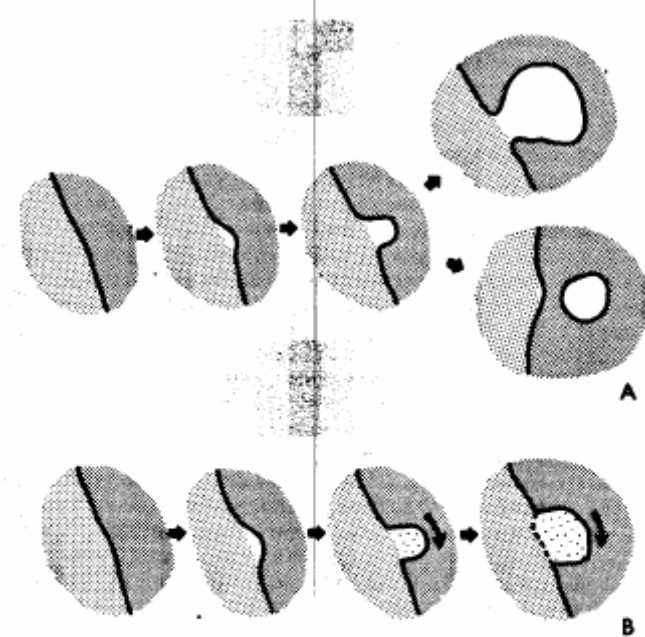
Fig. 3. Creation of new grains by grain boundary migration. (a) The bulge nucleation of Bailey and Hirsch (1962); note the appearence of "detached grains" due to sectioning at different levels in the sample. (b) The process is assisted by formation of a bridging subgrain boundary as proposed for dynamic recrystallization by Means (1981) and Etheridge and Kirby (in press).

(Urai et al., 1986)
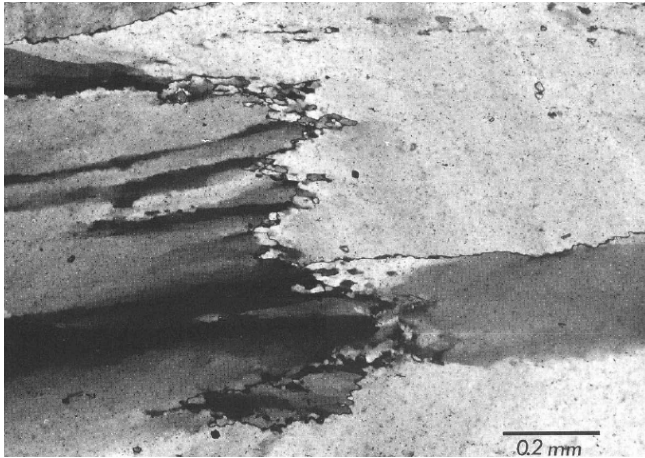
Grain-boundary bulging and migration at end of quartz ribbon from Chewings Range (Mawer, 1998)

Subgrain-rotation recrystallization
If the rate of hardening is balanced by the rate of recovery, subgrains progressively rotate until they have high-angle boundaries. Occurs without the development of strain-free grains and without significant boundary migration.
produces core-and-mantle textures
produces clusters of grains having similar orientations with smooth variation within a cluster and clusters of grains having similar sizes
recrystallized grain size should be similar to the optically visible subgrain size
Constant rate of recrystallization and zero energy flux.
not favored in minerals where there are few slip systems, because then strain is heterogeneous

A high-angle grain boundary is formed by this mechanism when a critical number of dislocations glide and climb into a low-energy subgrain boundary. Misorientation of subgrains occurs when dislocations of dominantly one sign glide and climb into the boundary, or when migrating subgrain boundaries incorporate dislocations of dominantly one sign (Urai *et al.* 1986). The amount of misorientation required to induce the transition from subgrain to high-angle grain boundary is still poorly understood, but it is clear that inhomogeneous deformation of individual grains is required (Drury & Urai 1990). Due to strain gradients which develop in the grain boundary regions, recrystallized grains initially form along the grain boundaries. This produces the distinctive core and mantle structure (White 1976)(Hirth & Tullis, 1992)
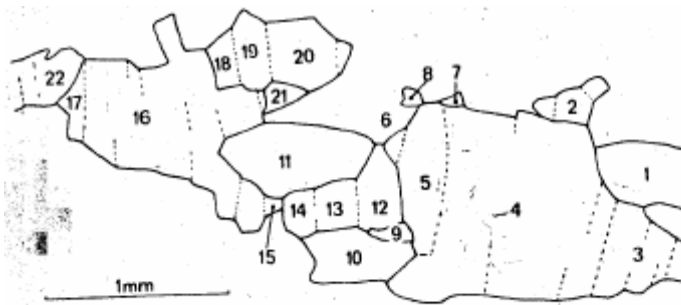
FIG. 5.—Drawings of olivine porphyroclasts and adjacent neoblasts. The angular relations are tailed on fig. 6.
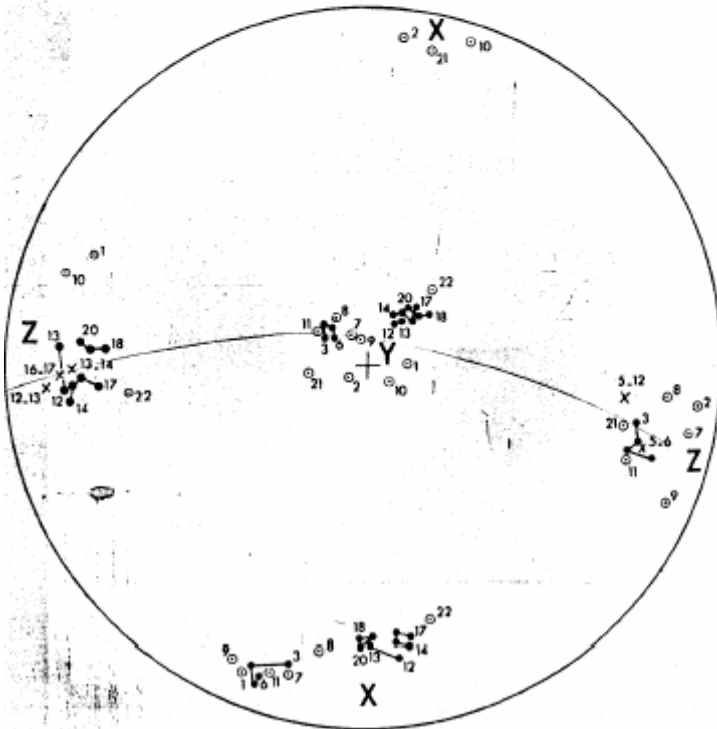
Misorientation relationships between olivine subgrains (Poirier & Nicolas, 1975)
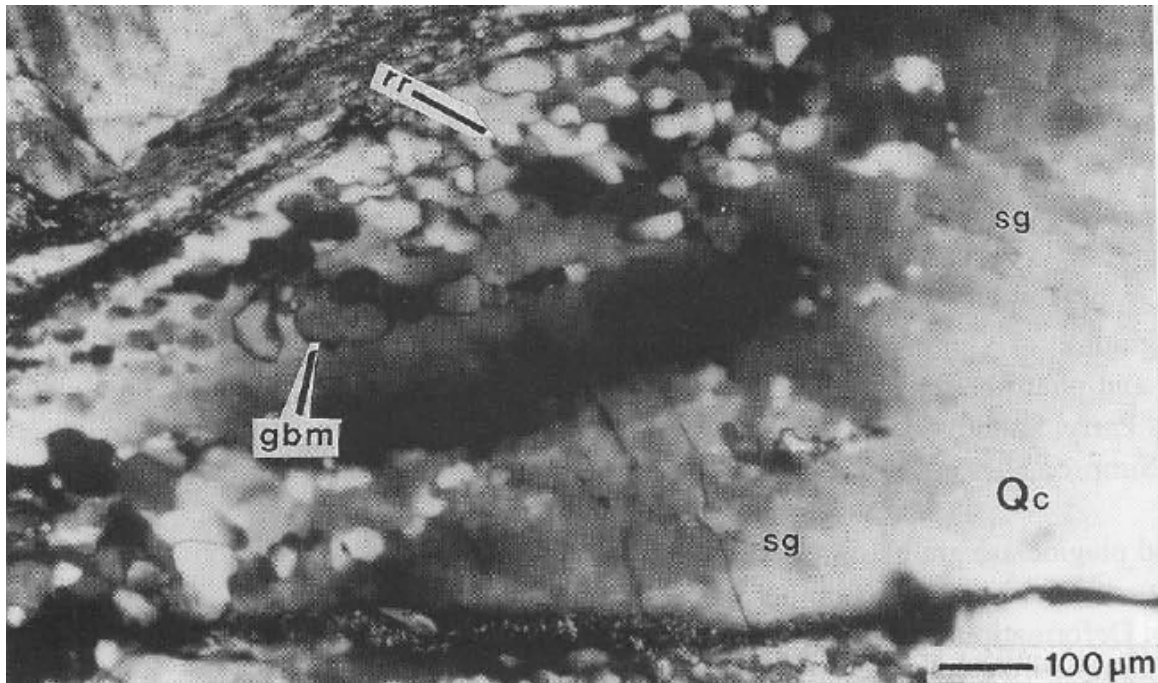
SGR in quartz ribbons from Borrego Springs greenschist-facies mylonite. Relatively undeformed quartz core (Qc) has a mantle of subgrains (sg) surrounded by mantle of rotation-recrystallized new grains (rr) (Simpson, 1998).
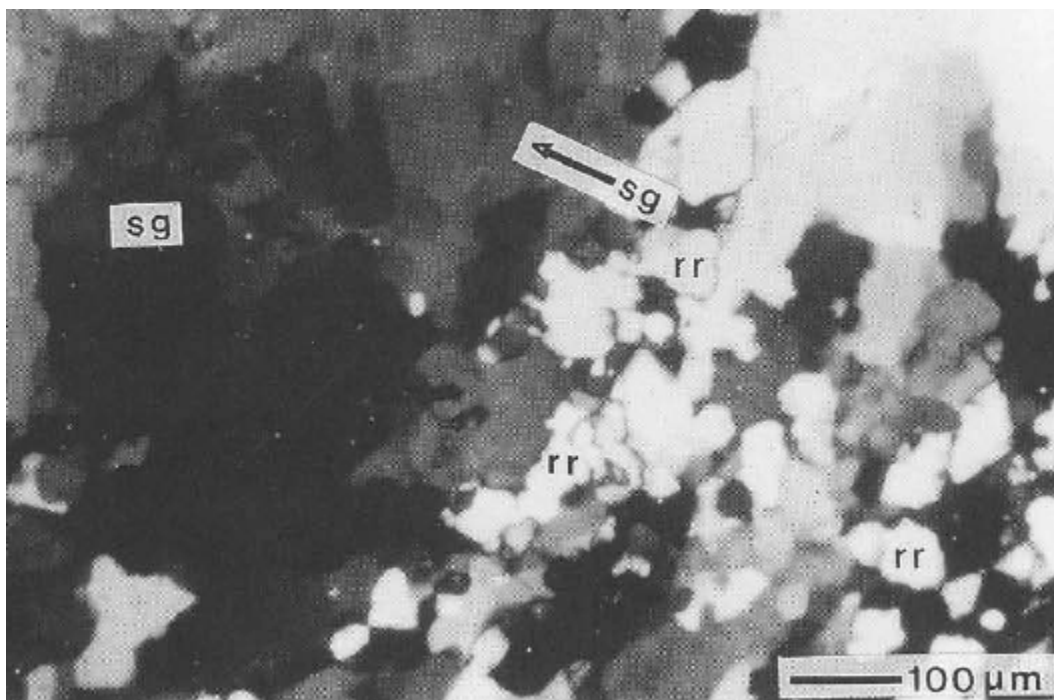
detail of above
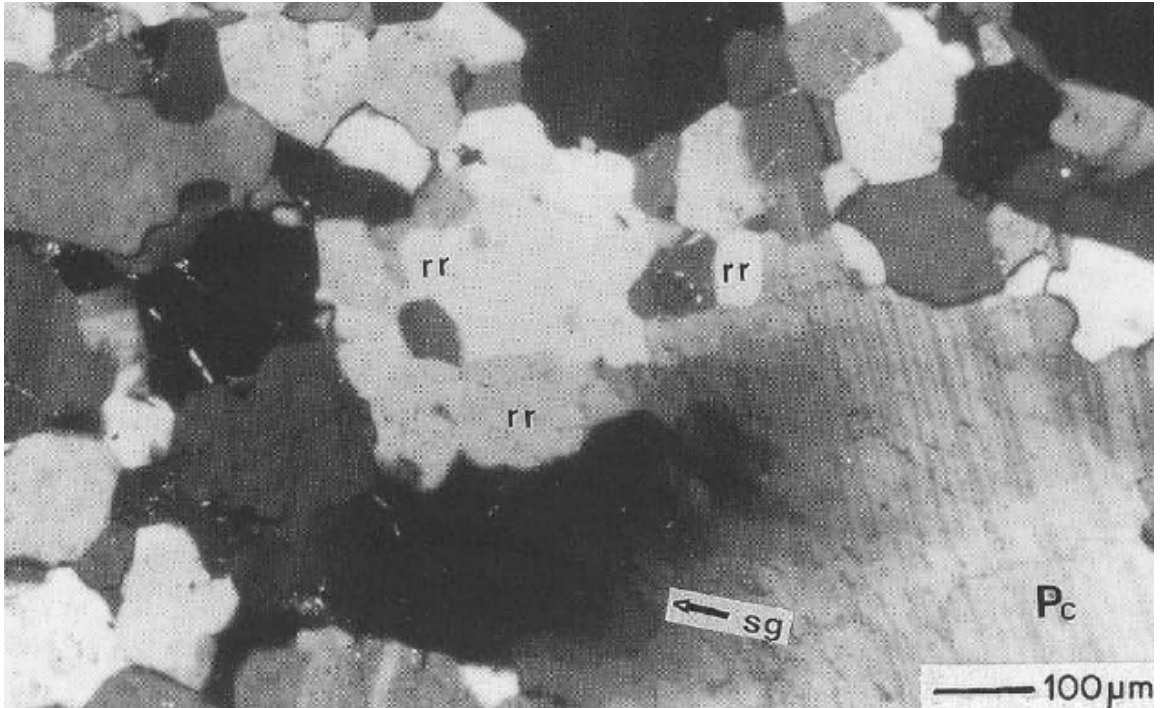
SGR in amphibolite-facies plagioclase pegmatite. Slight undulatory extinction in grain core (Pc). Zone of subgrains (sg) passes outward into rotation-recrystallized new grains (rr) (Simpson, 1998).

Static or Annealing Recrystallization
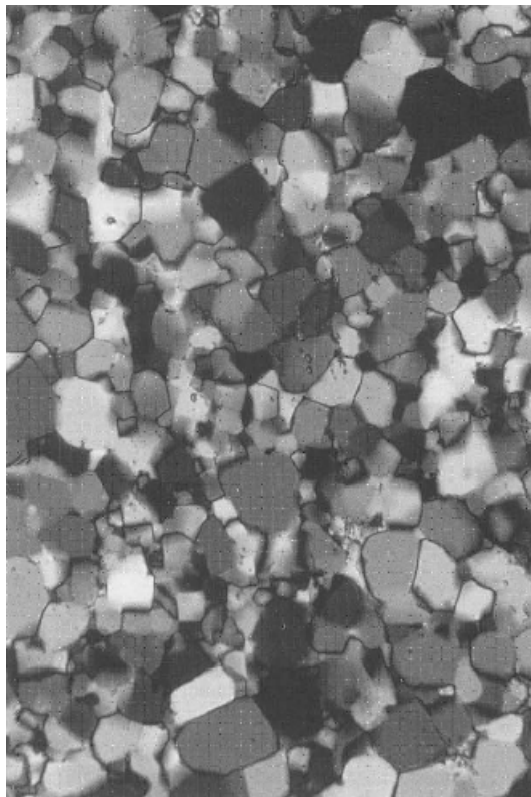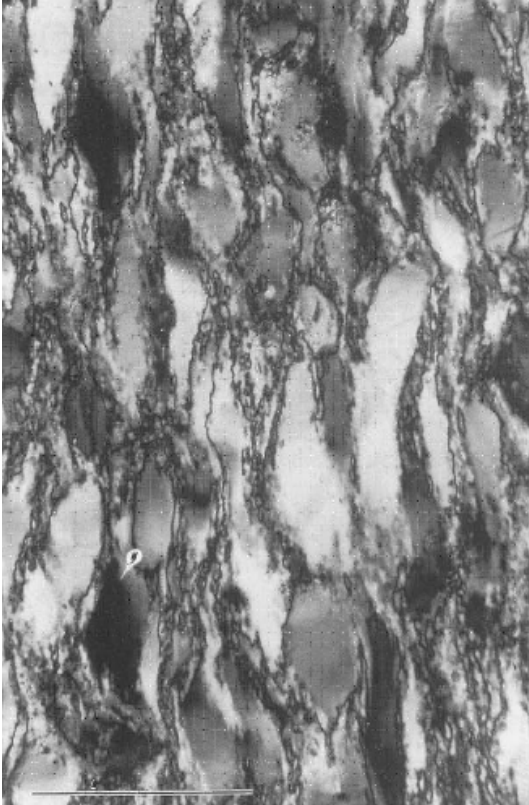
Quartzite shortened 60% at 800°C and 10^{-6} s^{-1} (regime 2) then annealed at 900°C for 120 hours (Tullis & Gleason, 1998)
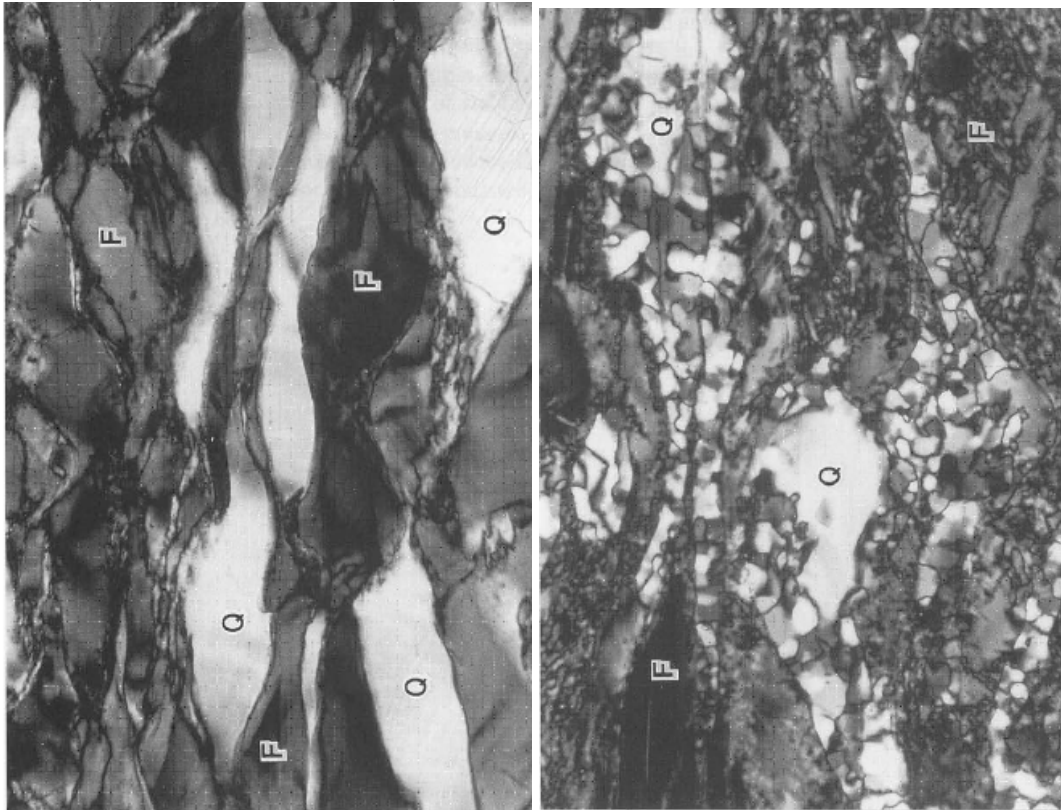
Aplite shortened 60% at 800°C and 10^{-6} s^{-1} (regime 2) then annealed at 900°C for 120 hours (Tullis & Gleason, 1998)
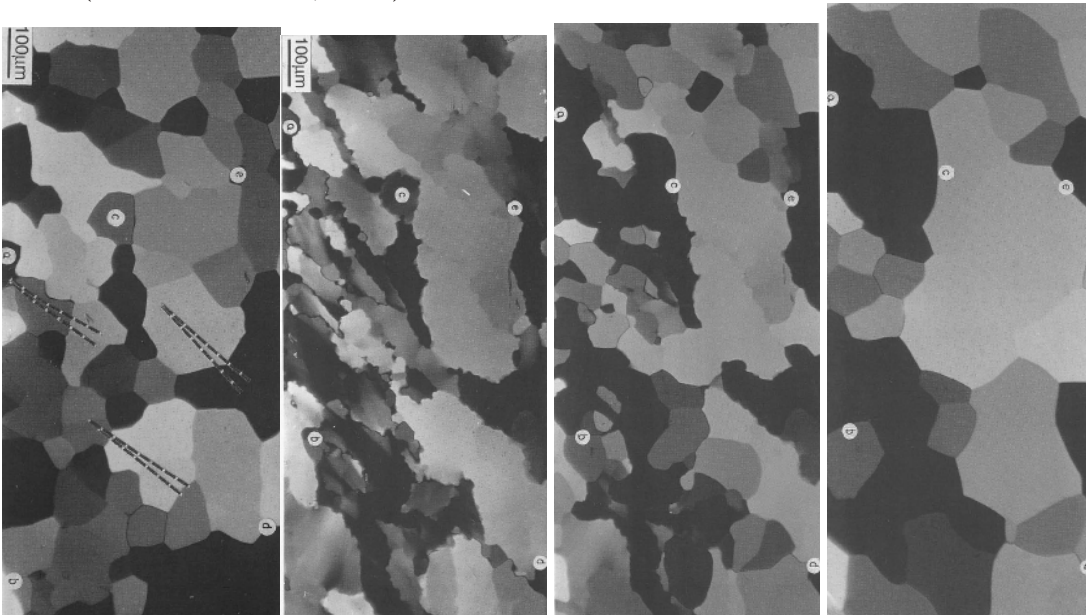
Annealing sequence in octachloropropane. (1) starting material; (2) deformed material; (3) beginning to lose SPO; (4) At end, some grains are old, some are new (Means & Dong, 1998)
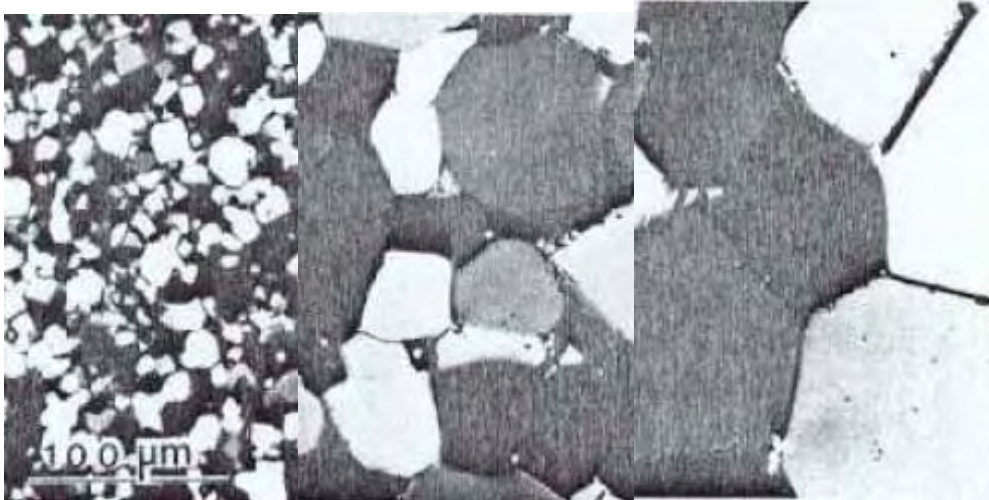
Grain growth in novaculite at 1000°C and 0, 172, and 800 hr (Tullis & Yund, 1982). 11 kcal/mole

The driving force for grain growth is

$$F = \frac{2\gamma}{r}$$

where γ is the grain-boundary energy per unit area of boundary and r is the radius of curvature. ($1E^{-5}$–$4E^{-5}$ J/cm^2 or 10^2–10^5 J/m^3 for gently (r = 1 mm) and tightly curved boundaries (r = 1 μm))

Grain boundaries migrate toward their center of curvature during static recrystallization so as to reduce curvature (Evans, 2001):
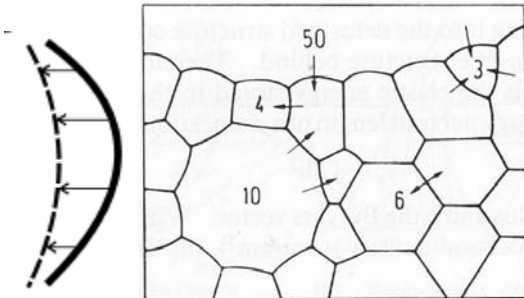
(Gottstein & Mecking, 1985)
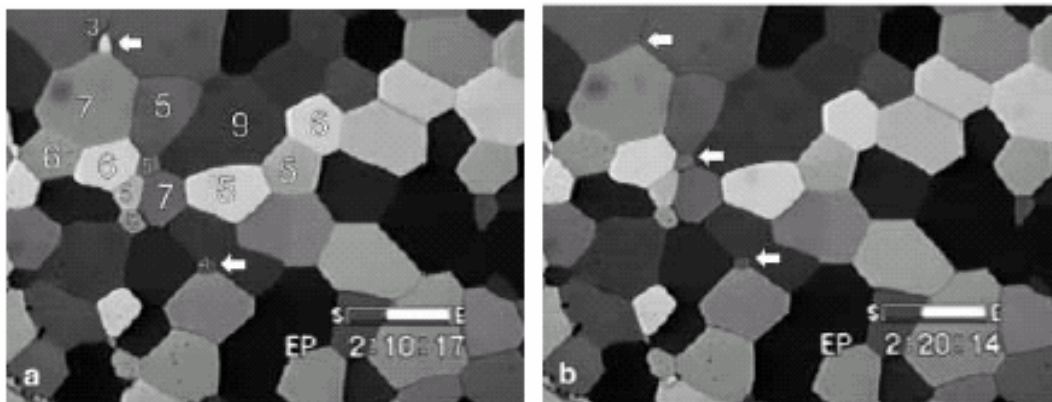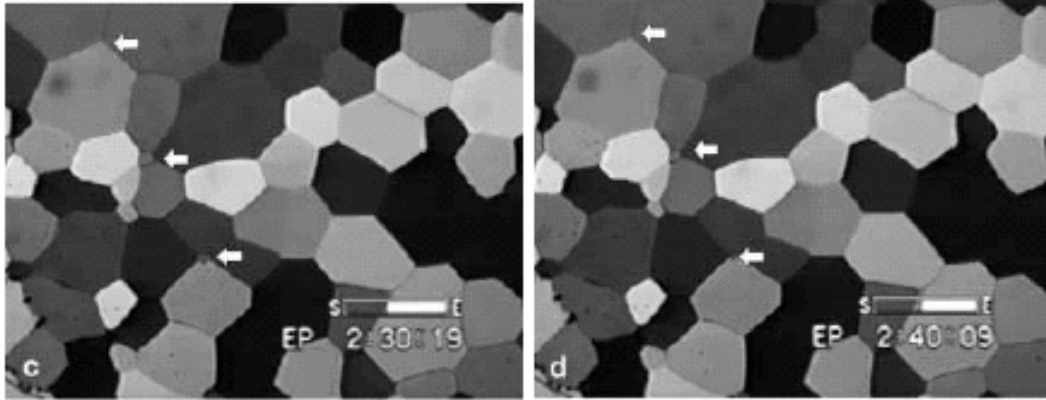
Grain growth in octachloropropane (Park et al., 1997). Grains with ≤5 sides get smaller and those with ≥7 sides get bigger. Several 3-sided grains (arrowed) disappear (Evans, 2001).

Grain size increases as:

$$\frac{dD}{dt} = \frac{M\gamma}{D} = \frac{c}{D}$$

where M is 'grain-boundary mobility' and

$$c = c_o \exp(-Q/RT)$$

Integration of the above

$$DdD = cdT$$

gives

$$\frac{D^2}{2} = ct + const$$

or

$$D^2 - D_o^2 = ct$$

where $c = 1$ cm^2/s and $Q = 243 \pm 33$ kJ/mol (Pierce, 1987)
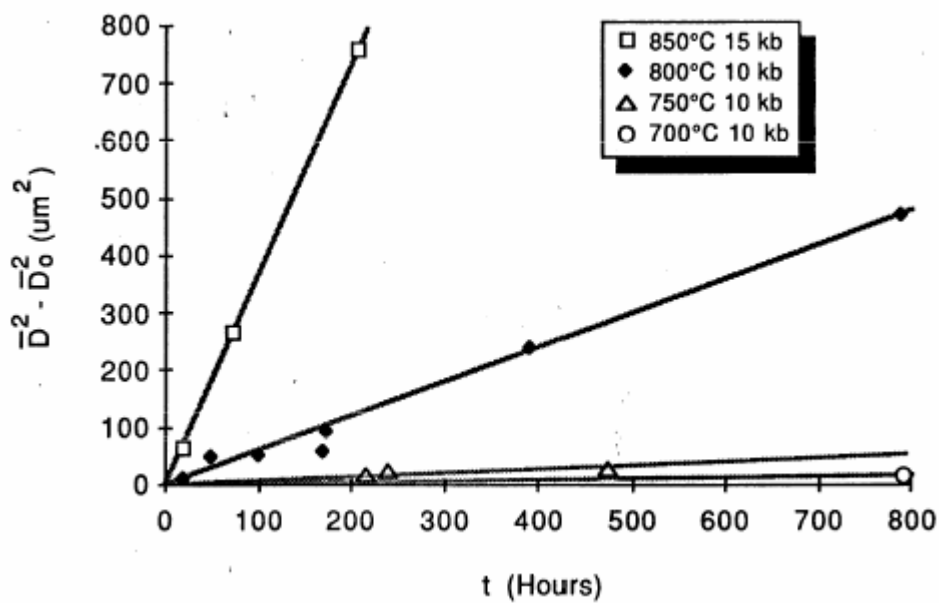
Grain growth in novaculite shown as change in grain area vs. time (Pierce, 1987)
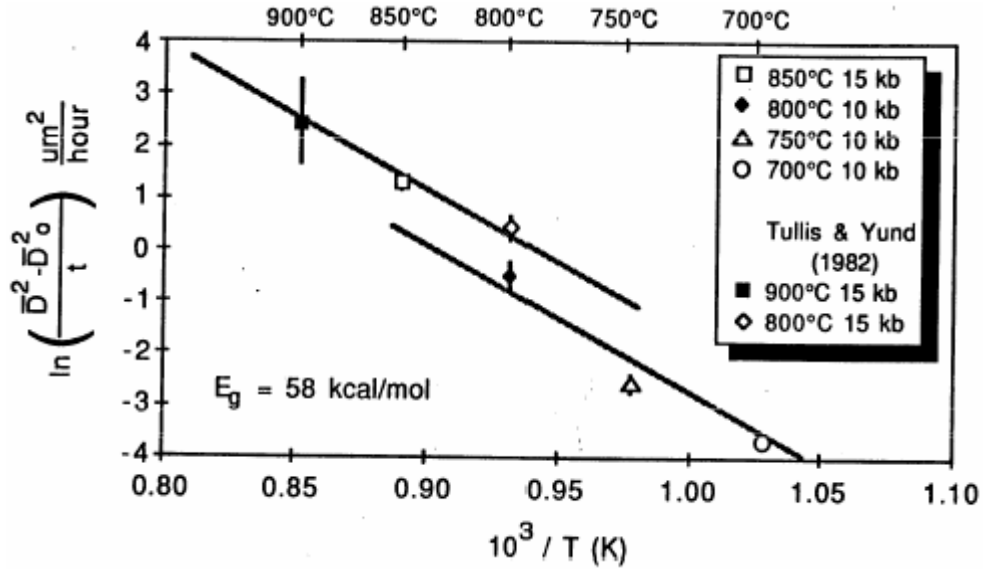
Activation enthalpy for grain growth in novaculite (Pierce, 1987)
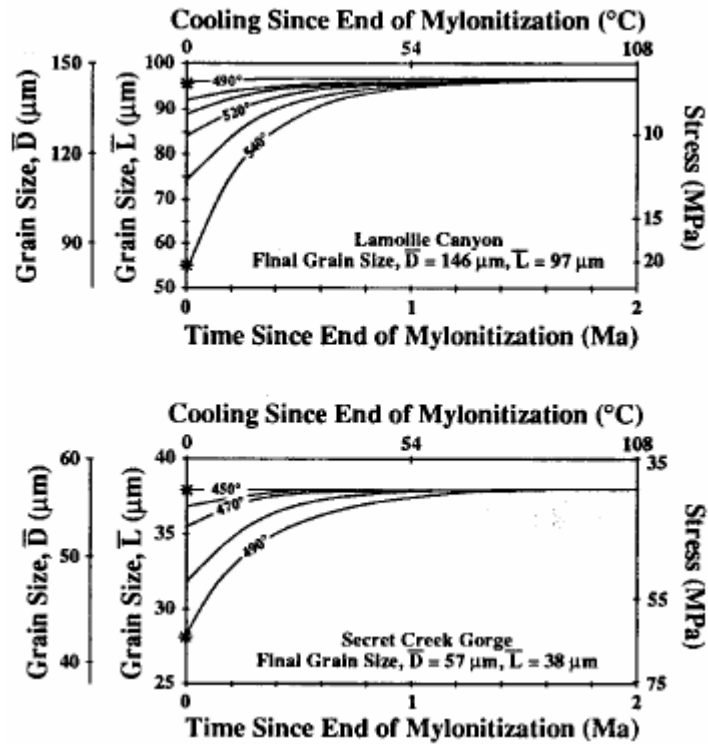
Calculated grain growth rates for Ruby Mtns core complex (Hacker et al., 1990)
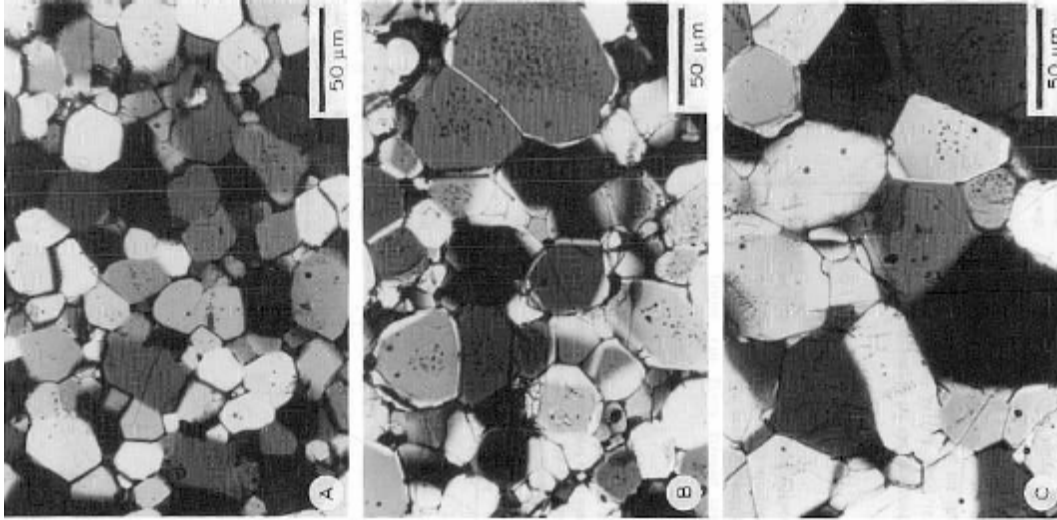
annealing sequence in olivine at 1200°C and 2, 4 and 8 hr (Karato, 1989). For

$$D^2 - D_o^2 = ct$$

$$c = c_o \exp(-Q/RT)$$

$c_o = 1.6E–6$ m^2/s and $Q = 160$ kJ/mol.

grain growth in marble (Walker et al., 1990)

Table 1 Some laboratory determination of grain growth kinetics in calcite and peridotite aggregates

Material	T (K)	n	Q (kJ/mol)	K_o (m^n/s)	Remarks	Reference
Calcite (Solnhofen)	650	3			Ostwald ripening in fluid	Chai (1974) Chai (1974)
	600–1000	2.5–7	190		Oven dried	Schmid et al. (1977)
	650–1000	2.5–5	200		Dry and wet	Tullis and Yund (1982)
	700–800	2.2	131		Water added	Rutter (1984)
	700–800	>5			Water added	Olgaard and Evans (1988)
Carrara (Synthetic)	1200	5.6			Oven dried	Olgaard (1990)
	650–800	3	174	2.5×10^{-9a}	Water added; melt present	Covey-Crump (1986)
	700–800	2.6–4	180±50		Dry and wet	Olgaard and Evans (1988)
	500–1200	3	172±60		Oven dried	Olgaard (1990)
	700–800	3	232	1×10^{-7a}	Pure samples with/with out fluids	Covey-Crump (1997)
	550–700	3	162	6×10^{-11a}	Fluid-added; pressure dependence of Q	
	550–700	4–9			Dry	
	973–1173	2	99	3×10^{-10a}	10 ppm Mn; P_c=300 MPa; dry	D. Freund and G. Dresen (personal communication, 2000)
		2.4	160	5×10^{-8a}	350 ppm Mn; P_c=300 MPa; dry	
		2.2	147	5×10^{-8a}	660 ppm Mn; P_c=300 MPa; dry	
Peridotite (Syn.)	1473–1673	4	290±20	8.1×10^{-16}	$K_{og} = 7.4 \cdot 10^{-16} \cdot f_{O_2}^{0.13}$	Nichols and Mackwell (1991)
		5	345±25	7.4×10^{-19}	$K_{og} = 7.4 \cdot 10^{-16} \cdot f_{O_2}^{0.13}$ P_c=0.1 MPa, swelling $\log f_{O_2} = -4$ to -11 (atmosphere)	
	1473–1673	2	520	5×10^{-8a}	P_c=0.1 MPa, swelling	Karato (1989a)
		3	600		$\log f_{O_2} = -10$ (atmosphere)	
	1473–1573	2	160	1.6×10^{-8a}	P_c=300 MPa, wet	
		(2)	(160)	5×10^{-8a}		Hirth and Kohlstedt (1995)

(Evans, 2001)
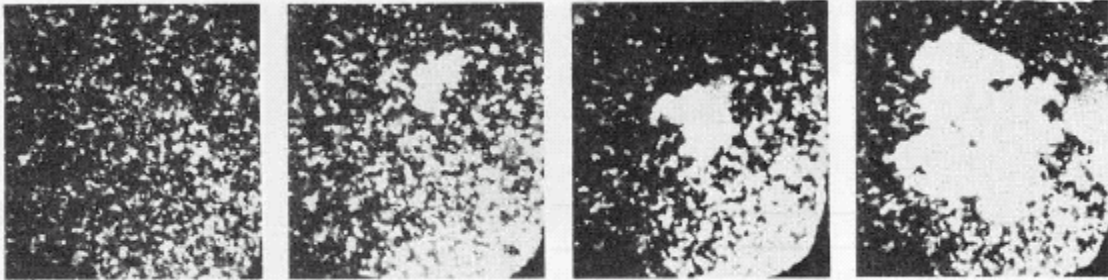
abnormal grain growth (Gottstein & Mecking, 19xx)

Quartz Deformation
Deformation Experiments
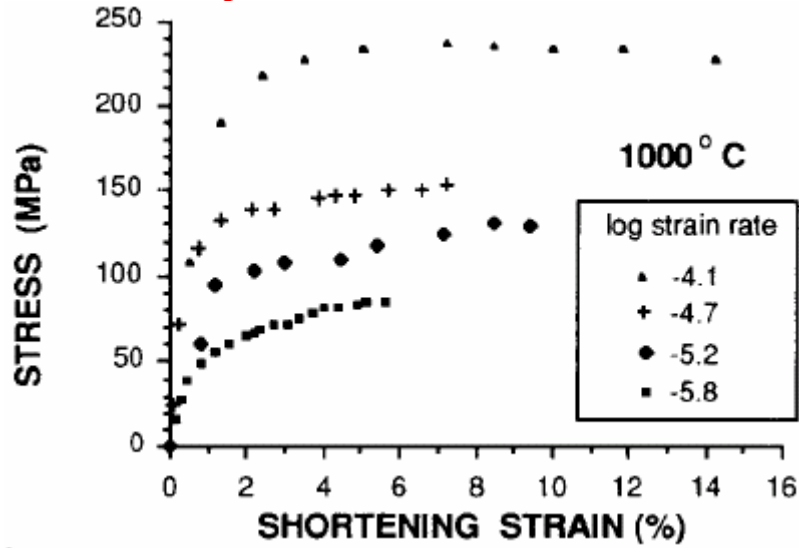
Experiments involving climb-accommodated creep (Regimes 2 and 3) (Gleason & Tullis, 1995)
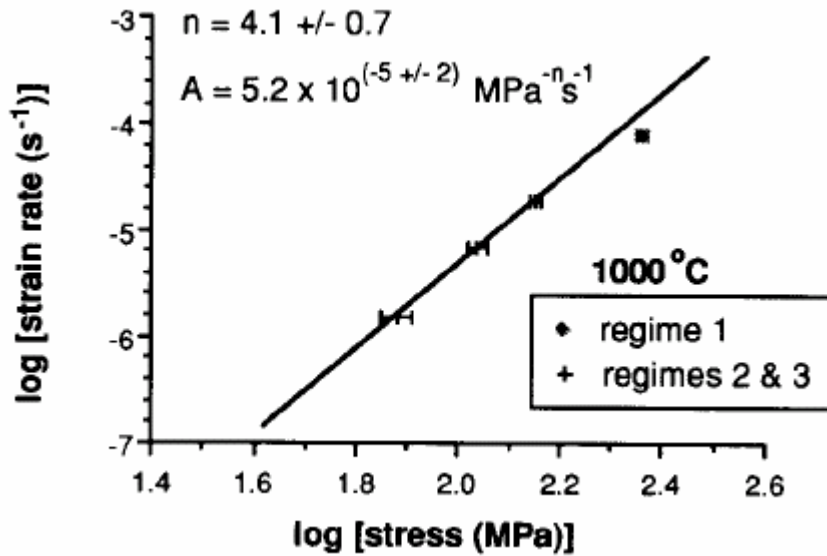
(Gleason & Tullis, 1995)

c)

Strain rate = $10^{-5.8} s^{-1}$

$Q = 220 +/- 55$ kJmol^{-1}

$A = 1.7 \times 10^{(-4 +/- 2)}$ MPa$^{-n} s^{-1}$
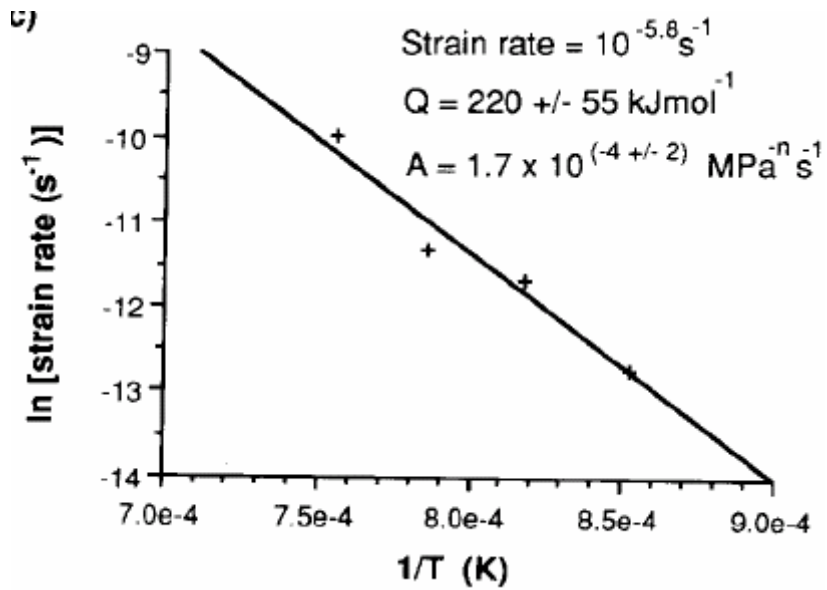
(Gleason & Tullis, 1995)

	Q (kJ/mol)	A (MPa^{-n}s^{-1})	n
Luan & Paterson (1992)	152	4e-10	4
Gleason & Tullis (1995)	223	1.1e-4	4
Paterson & Luan (1990)	135	6.5e-8	3.1
Hirth et al. (2001)	135	6.30957e-12	4
Rutter & Brodie (2004)	242 ± 24	logA = –4.93 ± 0.34	2.97 ± 0.29

Currently used quartz flow laws
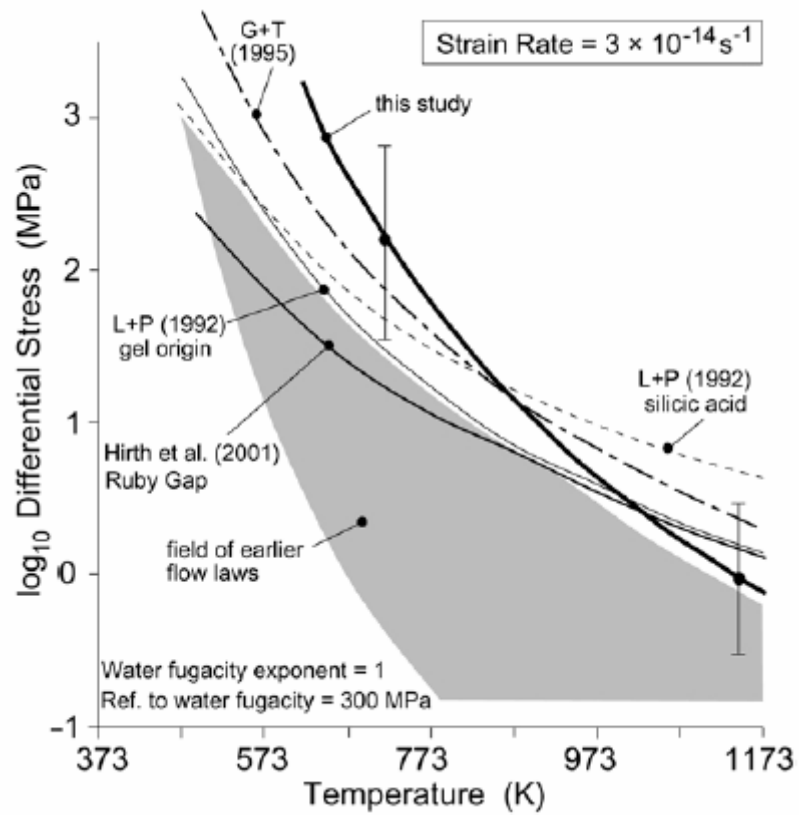
extrapolations (Rutter & Brodie, 2004)

b)

Shear Stress (MPa)

this study (1-2% melt)
Koch et al., 1989
Shelton & Tullis, 1981
Jaoul et al., 1984
this study (no melt)
Kronenberg & Tullis, 1984
Parrish et al., 1976

(Gleason & Tullis, 1995)

$Q = 135$ kJ/mol, $n = 4$, $m = 1$

$\dot{\varepsilon} = 5\times10^{-14}\text{s}^{-1}$

regime 1

$7\times10^{-15}\text{s}^{-1}$

regime 2

regime 3

10^{-15}s^{-1}
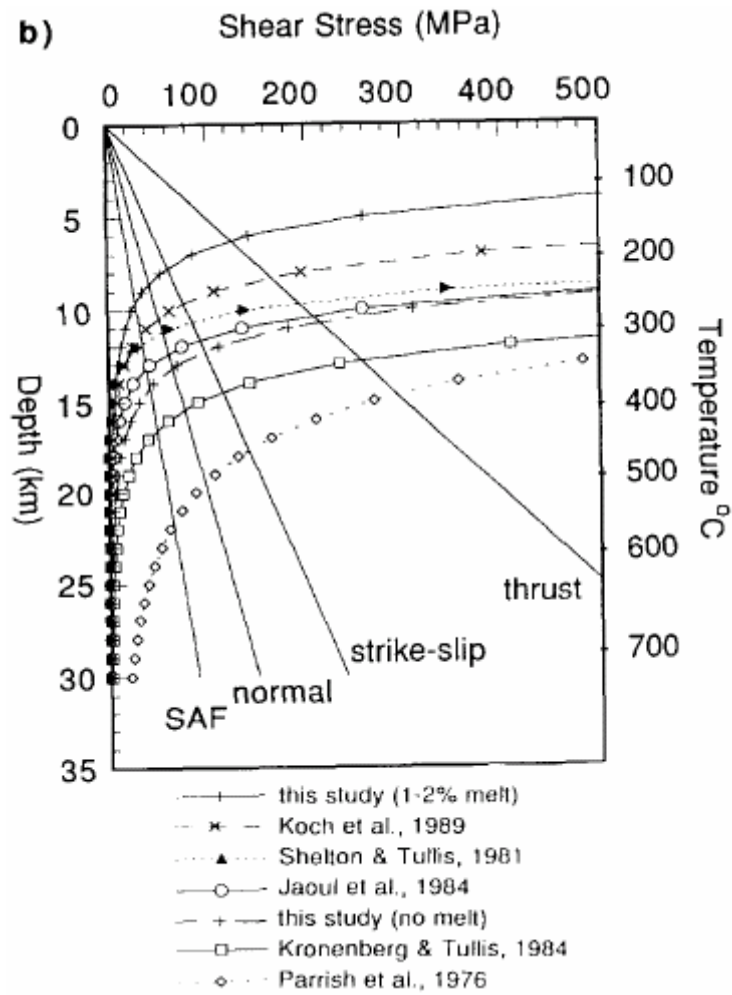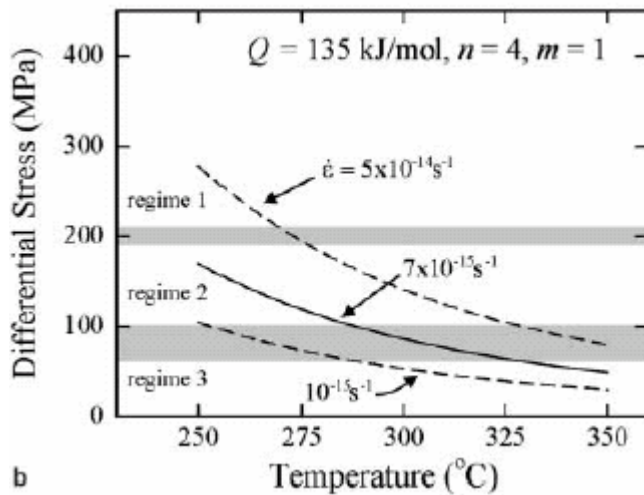
strain rates for Ruby Gap duplex (Hirth et al., 2001)

Quartz Crystallography
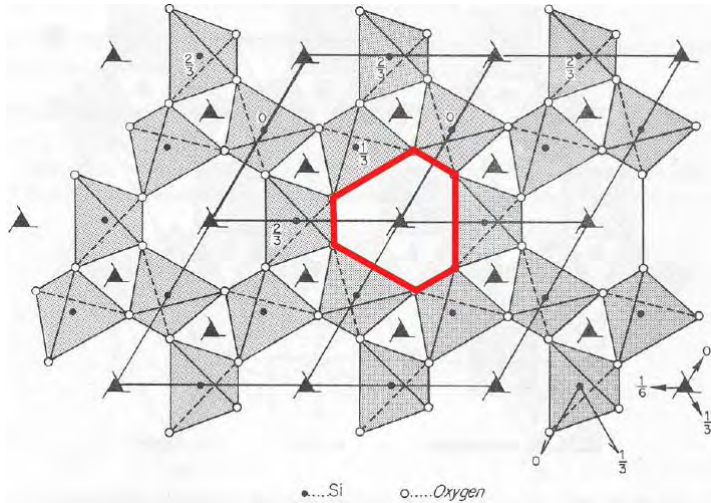
alpha quartz is trigonal and has L- and R-handed forms (projection down [0001] from Wei, 1935). Slip in quartz requires breaking Si–O bonds and should be hard. In fact, dry quartz *is* very strong.
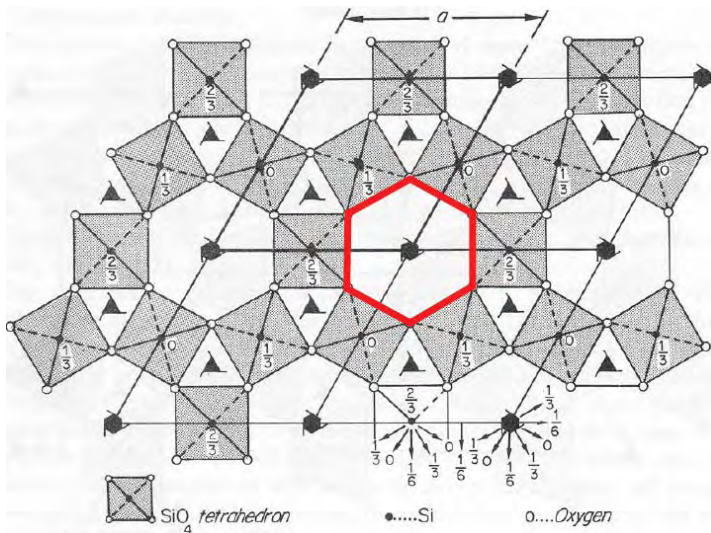
beta quartz is hexagonal (projection down [0001] from Deer et al., 1963).
At crustal pressures requires T>700–800°C (the equilibrium is T(°C) = 573 + 260P(GPa); Coe & Paterson, 1969).
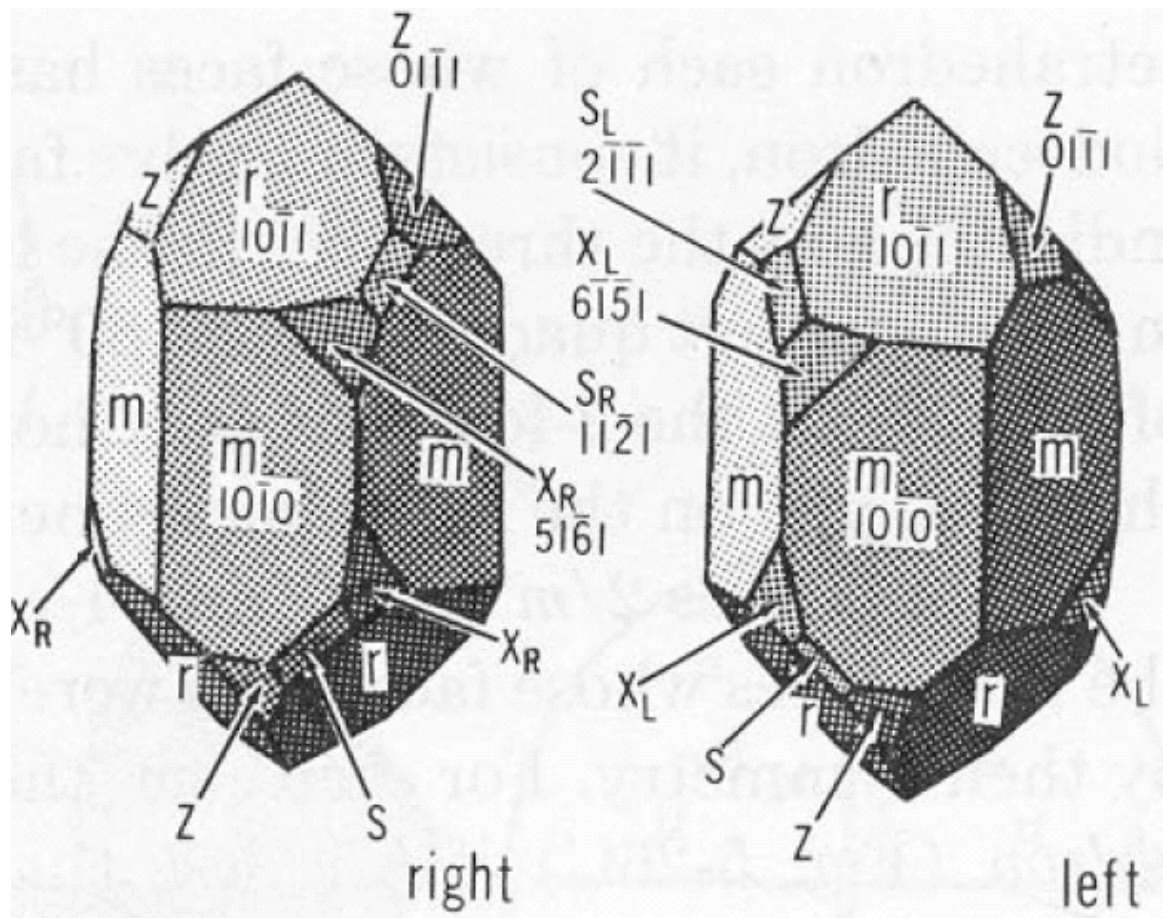
Quartz morphology (Bloss, 19xx)

EQUAL – AREA NET

(Linker et al., 1984)

× POLES TO PLANE
⊙ DIRECTION
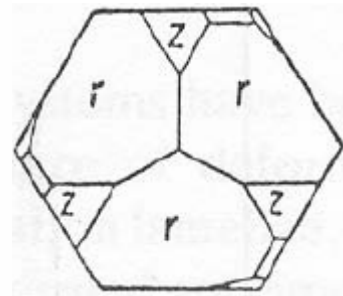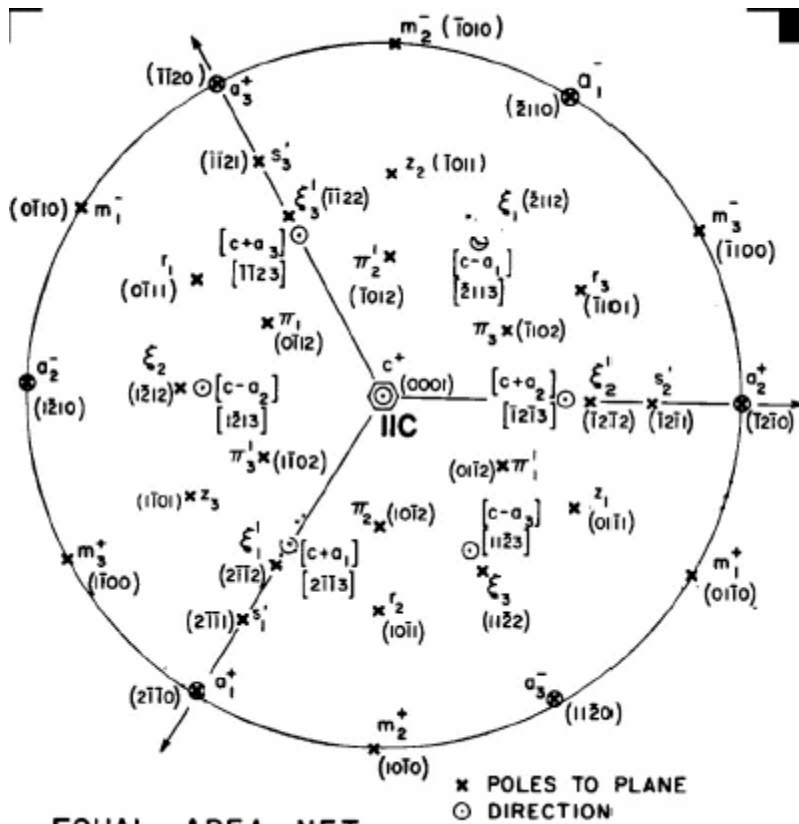
Quartz faces

c	(0001)	basal pinacoid	
m	$\{10\bar{1}0\}$	1st-order prism	c ^ m = 90°
a	$\{11\bar{2}0\}$	2nd-order prism	c ^ a = 90°
r	$\{10\bar{1}1\}$	positive rhomb	c ^ r ≈ 52°
z	$\{01\bar{1}1\}$	negative rhomb	c ^ z ≈ 52°
x		trigonal trapezohedron	
ξ	$\{11\bar{2}2\}$	trigonal bipyramid	c ^ ξ ≈ 48°
s or ξ'	$\{11\bar{2}1\}$	trigonal pyramid	c ^ s ≈ 63°
π	$\{01\bar{1}2\}$	rhombohedra	c ^ π ≈ 32°
d or π'	$\{10\bar{1}2\}$	rhombohedra	c ^ d ≈ 32°
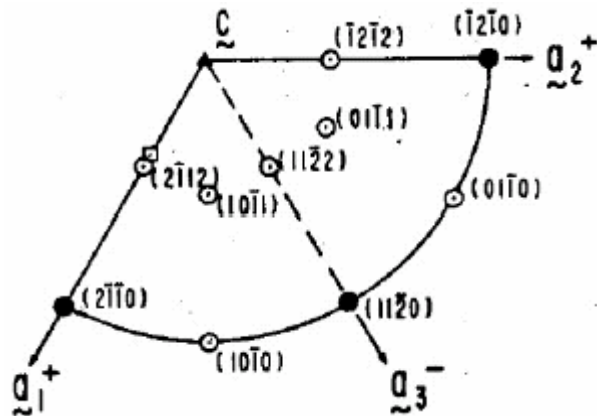
Minimum for trigonal symmetry (alpha quartz) (Linker & Kirby, 1981). Used for inverse pole figures (IPF)

Slip Systems in Quartz
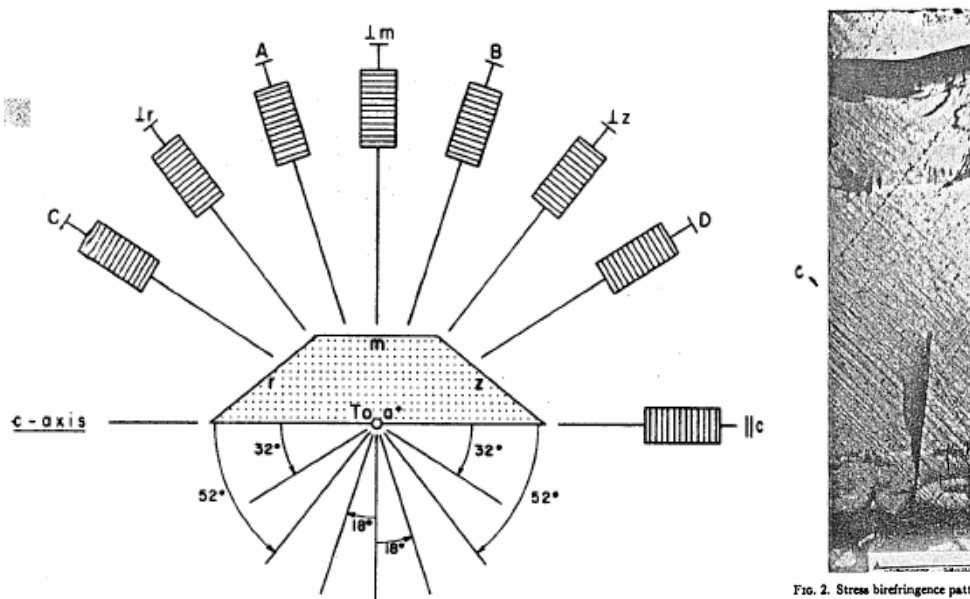
Fig. 4. Diagram representing the crystallographic orientations of the eight types of samples used in the experiments. The crystal is viewed towards the positive end of an a-axis.

Fig. 2. Stress birefringence pattern after 3% plastic strain at a strain rate of 10^{-4} sec^{-1} at 900°C. Compression axis 45° to [0001], microscope axis perpendicular to (1100). (Bar scale=1.0 mm).

Quartz single crystals have been compressed in a variety of orientations to induce slip (Christie et al., 1964; (Baeta & Ashby, 1969)

Slip systems identified in alpha quartz

<a>(c)	$\langle 1\bar{2}10 \rangle$ (0001)	basal plane in a direction
<a>{z}	$\langle 1\bar{2}10 \rangle$ $\{01\bar{1}1\}$	negative rhomb in a direction
<a>{r}	$\langle 1\bar{2}10 \rangle$ $\{01\bar{1}\bar{1}\}$	positive rhomb in a direction
<a>{m}	$\langle 1\bar{2}10 \rangle$ $\{01\bar{1}0\}$	1st-order prism in a direction

$<a>\{\pi'\}$ $\quad \langle 1\bar{2}10 \rangle \{01\bar{1}2\}$ rhombohedra in a direction

$[c]\{m\}$ $\quad [0001]\{10\bar{1}0\}$ 1st-order prism in c direction

$[c]\{a\}$ $\quad [0001]\{11\bar{2}0\}$ 2nd-order prism in c direction

$<c+a>\{m\}$ $\quad \langle 1\bar{2}13 \rangle \{10\bar{1}0\}$ 1st-order prism in c+a direction

$<c+a>\{z\}$ $\quad \langle 11\bar{2}3 \rangle \{\bar{1}011\}$ negative rhomb in c+a direction

$<c+a>\{\xi\}$ $\quad \langle 11\bar{2}3 \rangle \{\bar{2}112\}$ trigonal bipyramid in c+a direction

(Blacic & Christie, 1984)
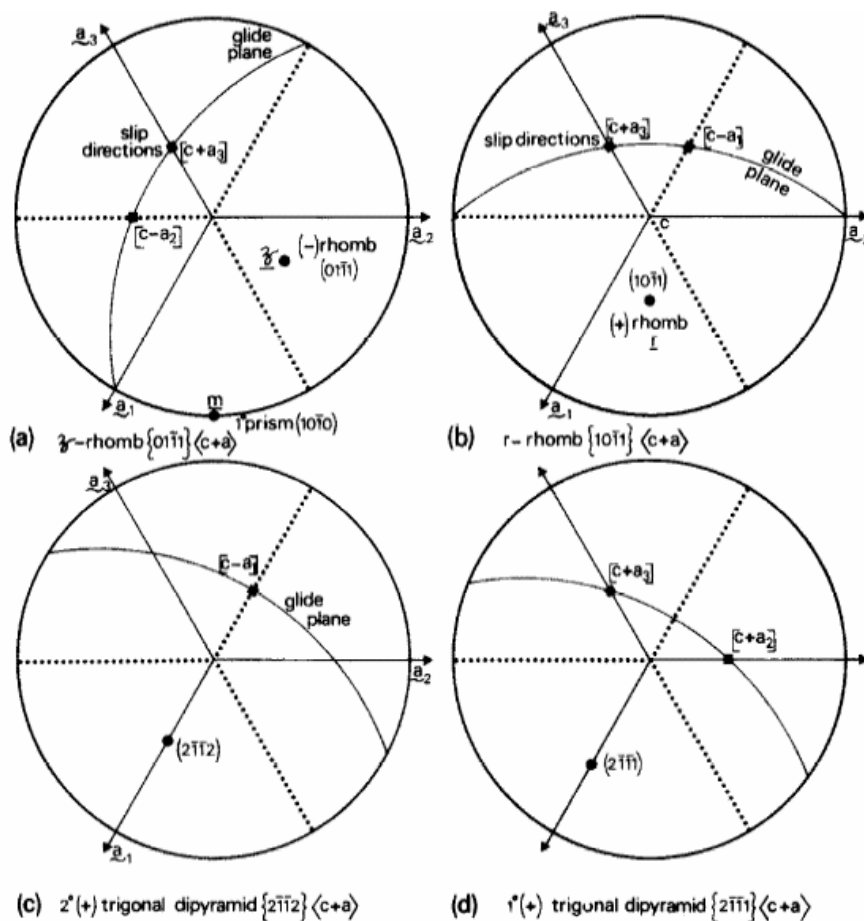
Stereonet representations of slip systems (Lister et al., 1978)

Symmetrically equivalent sets of glide systems

$\{10\bar{1}0\}$	$\langle c + a_2 \rangle$	$\equiv$	$\{10\bar{1}0\}$	$\langle c - a_2 \rangle$
$\{10\bar{1}1\}$	$\langle c - a_1 \rangle$	$\equiv$	$\{10\bar{1}1\}$	$\langle c + a_3 \rangle$
$\{01\bar{1}1\}$	$\langle c + a_3 \rangle$	$\equiv$	$\{01\bar{1}1\}$	$\langle c - a_2 \rangle$
$\{2\bar{1}\bar{1}2\}$	$\langle c - a_1 \rangle$	$\equiv$	$\{11\bar{2}2\}$	$\langle c + a_3 \rangle$
$\{2\bar{1}\bar{1}1\}$	$\langle c + a_2 \rangle$	$\equiv$	$\{11\bar{2}1\}$	$\langle c - a_2 \rangle$
$\{2\bar{1}\bar{1}1\}$	$\langle c + a_3 \rangle$	$\equiv$	$\{11\bar{2}1\}$	$\langle c - a_1 \rangle$

(Lister et al., 1978)

Influence of basal vs. rhombohedral slip on orientation of a axes
Rhombohedral planes contain only one possible <a> slip direction, whereas the basal plane contains 3 <a> directions. This means that the rhomb plane aligns || to the slip direction and forces the orientation of the a axes...not true for basal glide. Slip on the first-order prisms is also special because it allows slip of two $\{10\bar{1}0\}$ forms in two different <a> directions (Schmid & Casey, 1986)
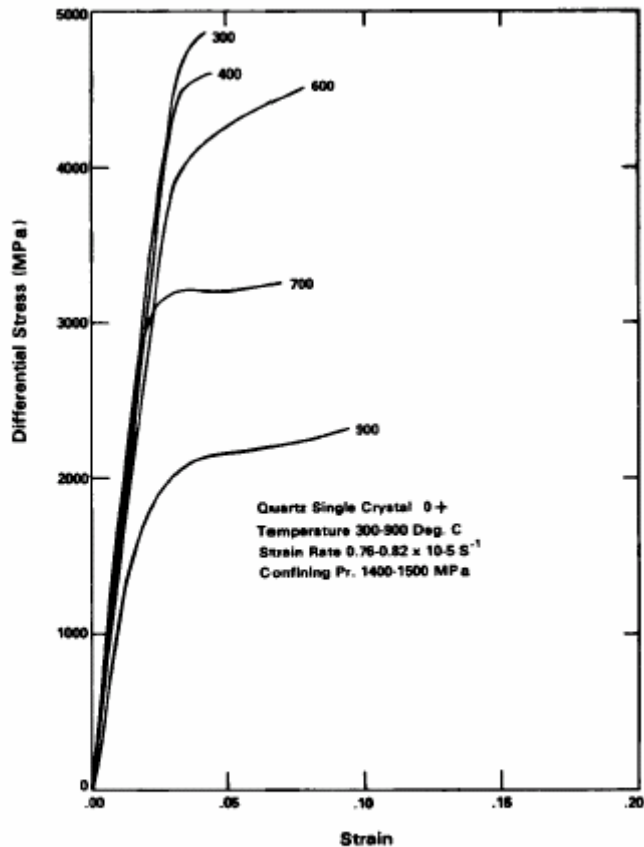

Fig. 2. Stress-strain curves for dry natural quartz single crystals deformed in the 0^+ orientation (see text). Confining pressure is ~1500 MPa and strain rate is ~10^{-5} s^{-1} for all tests.

Plastic flow of dry natural quartz crystals occurs only at high P and high T. Flow strengths approach the theoretical yield strength at T as high as 1000°C. Dislocation glide occurs on several planes with b = $1/3\langle 2\bar{1}\,\bar{1}0\rangle$ and b = [0001] (Blacic & Christie, 1984)

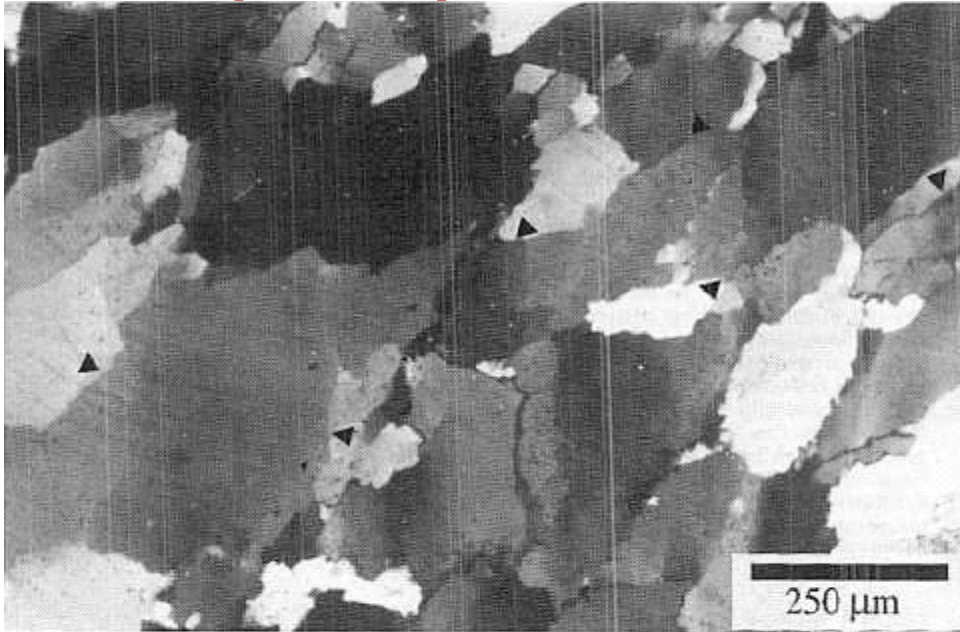## Microstructures produced in experiments and nature

Figure 1. Transmission light micrograph of deformation lamellae (arrowed) in naturally deformed quartzite.

deformation lamellae in quartz (Drury, 1993)

$\vec{g} = 10\bar{1}1$
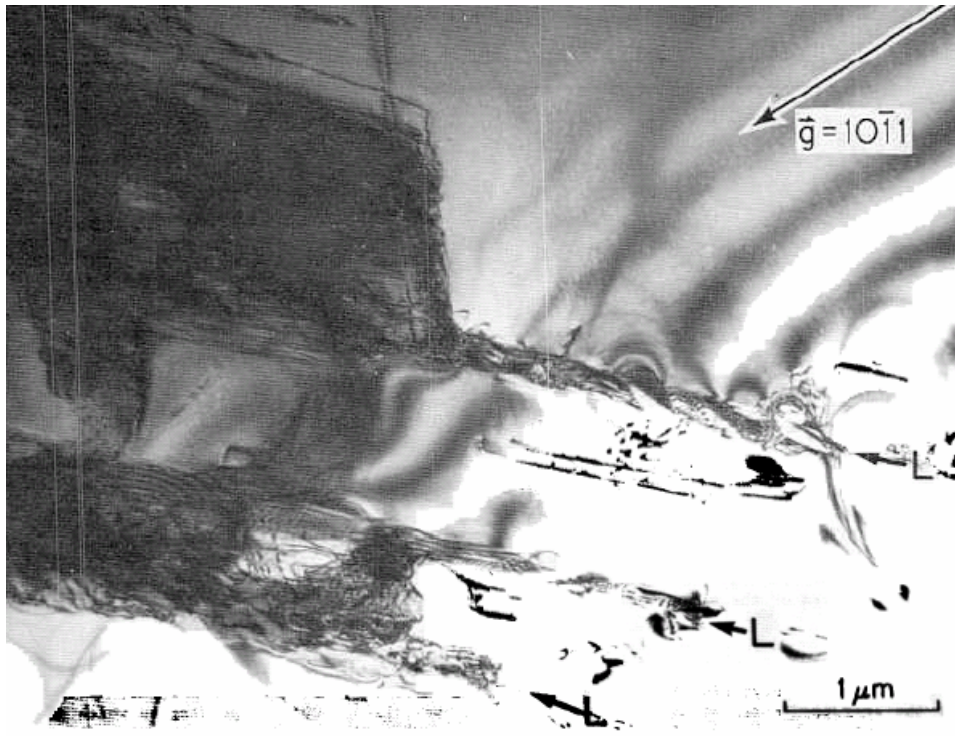
Fig. 1. Transmission electron micrograph of deformation lamella in dry quartz. Bright-field micrograph showing three basal lamellae and associated polygonal dislocation loops ($b = <1120>$). Straight dislocation segments are parallel to low-index zone axes. Crystal was compressed ~3% normal to ($10\bar{1}1$) at 1500 MPa pressure, 750°C at a strain rate of 10^{-6} s^{-1}; yield stress was approximately 3500 MPa. (Courtesy of A. J. Ardell and J. M. Christie, unpublished data, 1983)

deformation lamellae (Blacic & Christie, 1984)
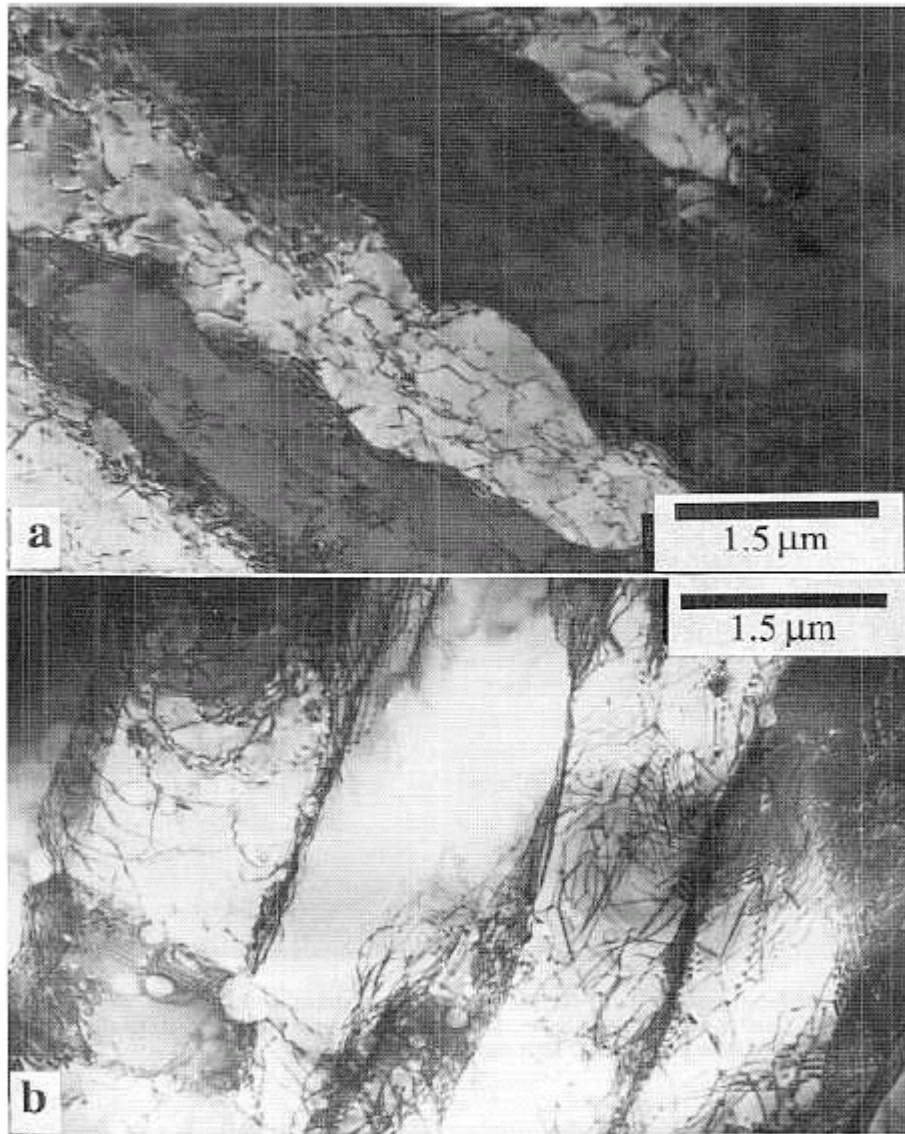
Figure 5. TEM micrographs of deformation lamellae substructures. Lamellae are defined by elongated subgrains with irregular walls. Subgrains contain a high density of free dislocations and in the case of quartz many fluid inclusions. (a) Al 5% Mg deformed in the exponential creep regime. (b) Quartz from the Bayas fault zone (Blenkinsop and Drury 1988).

deformation lamellae in quartz are defined by dislocation bands, elongate subgrains, subgrain walls and bubbles (Drury, 1993)

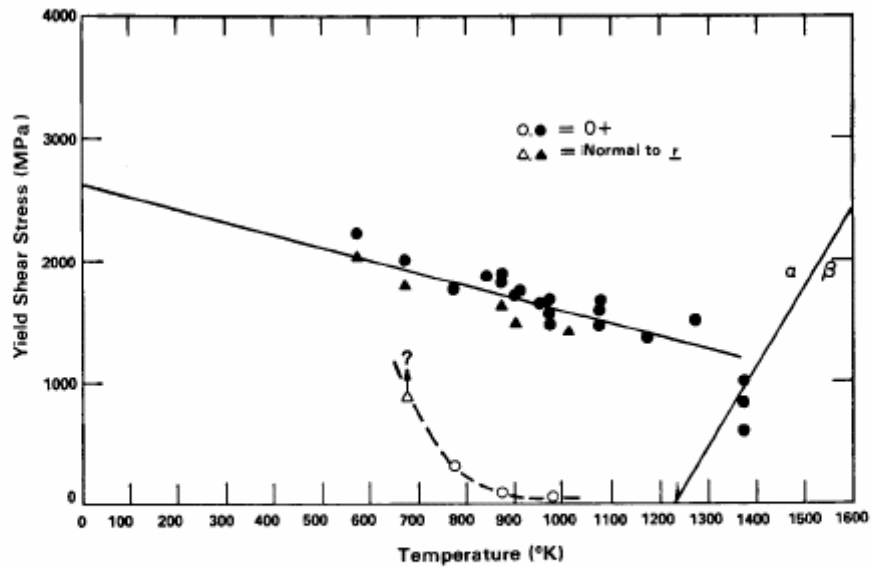Fig. 3. Yield shear stress resolved on the (0001) <11$\bar{2}$0> glide system as a function of temperature. Yield is defined as the point where the stress-strain curve first deviates from linear elastic behavior. Confining pressure is ~1500 MPa and strain rate ~10^{-5} s^{-1} for natural crystals (solid symbols). Synthetic crystal data (open symbols) are from Hobbs et al. [1972]; confining pressure 300 MPa, strain rate ~1 x 10^{-5} s^{-1}.

CRSS on <a>(c) slip system at 10^{-5} s^{-1} (Blacic & Christie, 1984)

Flow-law parameters for two common slip systems (Linker & Kirby, 1981)

$\{21\bar{1}0\}$ [c] slip   **$\{10\bar{1}0\}$<a> slip**

92 kJ/mol   213 kJ/mol
n = 3   n = 5.3

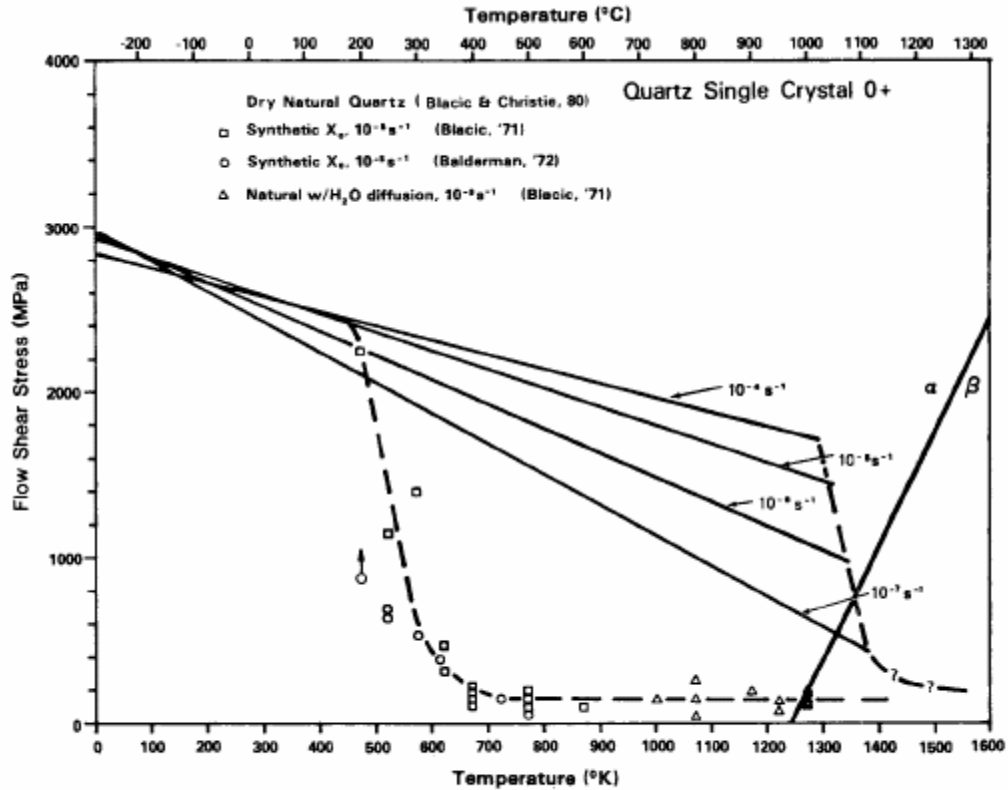Plus, <a> is much easier to operate than <c+a> (Linker et al., 1984)

Fig. 4. Flow shear stress versus temperature for dry and hydrolytically weakened natural quartz crystals at several strain rates, and synthetic quartz crystal, X-0, at 10^{-5} s^{-1} strain rate. Confining pressure is ~1500 MPa for all data except those of Balderman [1972] which are at 200–500 MPa.

In marked contrast to dry crystals, synthetic crystals with high in-grown H2O contents and dry natural crystals heat treated in a hydrous environment at high P are anomalously weak (Blacic & Christie, 1984).

TABLE 2. Flow Law Parameters for α Quartz Single Crystals: $\dot{\varepsilon} = A\sigma^n \exp(-Q/RT)$

Water Content, H/10⁶ Si	ln A, MPa⁻ⁿ s⁻¹	n	Q, kJ/mol	Source
20 (natural)	-96.7 ± 12.3	12.6 ± 1.8	62.2 ± 11.9	1
4300 (synthetic, X-0)	-10.5 ± 0.3	3.6 ± 0.2	132.3 ± 14.7	2
4300 (synthetic, X-0)	...	3.5 ± 0.5	163.3 ± 21	3
370 (synthetic, X-507)	-13.6	3.0 ± 0.2	93.3 ± 4.2	4
900 (synthetic, X-41)	...	3.4 ± 0.6	163 ± 9	5

Here $\dot{\varepsilon}$ = axial strain rate, σ = axial differential stress, T = degrees Kelvin, and R = gas constant. Sources: (1) this work; (2) Balderman [1974]; (3) Kirby and McCormick [1979]; (4) Linker and Kirby [1981]; (5) Kirby [1977].

n and Q very different for wet and dry quartz (Blacic & Christie, 1984).
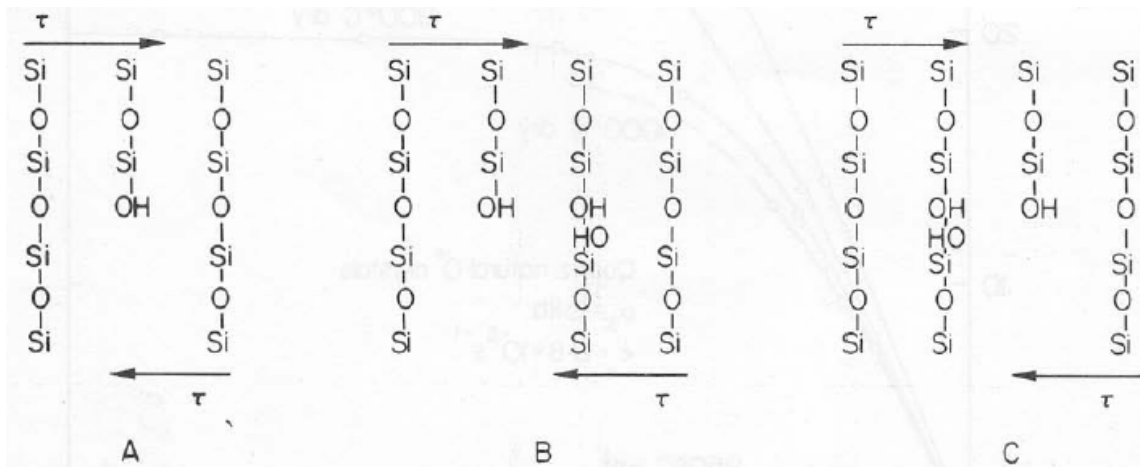
Hydrolytic weakening

Fig. 5.31. Schematic model of the Frank–Griggs mechanism for hydrolytic weakening:

(A) Sessile hydrolyzed edge dislocation with anhydrous neighbours

(B) The right-hand side neighbouring Si–O bond has been hydrolyzed by arrival of a H_2O molecule and a hydrogen bond is formed

(C) The hydrogen bond can easily be broken under shear stress and reforms with the OH at the dislocation edge. As a result the dislocation moves to the right

(Griggs, 1967)

264 Lecture 3

**Deformation Regimes in Quartz: Experiments**

Regime **1** (Hirth & Tullis, 1992). At lower temperatures and faster strain rates dislocation climb is difficult and recovery is accommodated by grain boundary migration recrystallization. Samples are the strongest and show strain weakening. Irregular and patchy undulatory extinction. Grain boundaries appear diffuse and have very fine-grained recrystallized grains. High densities of tangled, straight dislocations (up to 10^{16} m^{-2}) that show no subgrain boundary development suggest the rate of dislocation production is greater than the rate of recovery by climb. The recrystallized grains may nucleate via a bulge mechanism or via a cell misorientation mechanism. After they are nucleated, these recrystallized grains grow by strain-induced grain boundary migration.
High-strain samples show inhomogeneous flattening of original grains, and extensive (20–30%) recrystallization. The recrystallized grains have a large variability in dislocation density. Because the recrystallized matrix is weaker than the work-hardened original grains, the strain is accommodated predominantly within the recrystallized regions. Thus after 55% shortening, many of the original grains remain equant (Fig. 4e). A steady state flow stress can only be achieved after a sample is completely recrystallized.
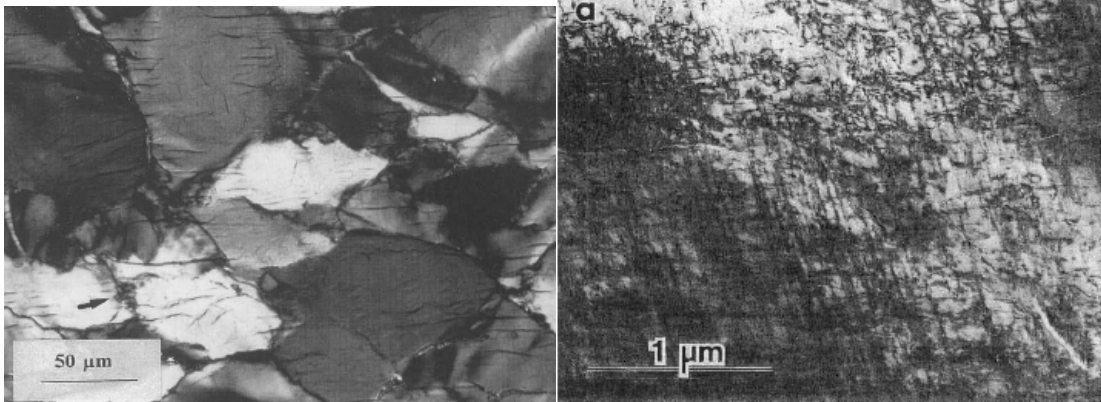
Regime 1. 20% shortening at 700°C and 10^{-6} s^{-1}; patchy undulatory extinction and diffuse grain boundaries; straight and tangled dislocations (Hirth & Tullis, 1992).
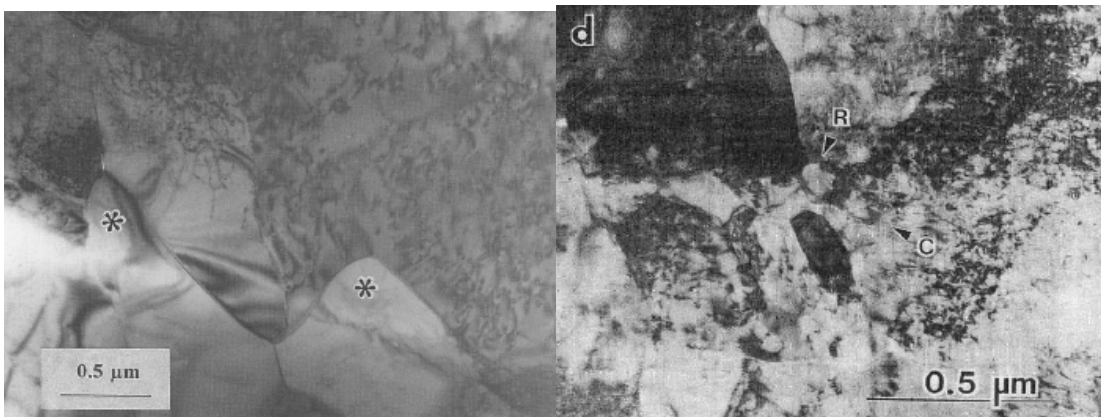
Regime 1. 20% shortening at 700°C and 10^{-6} s^{-1}; initiation of BLG; very small cells (C) and recrystallized grains (R) (Hirth & Tullis, 1992).
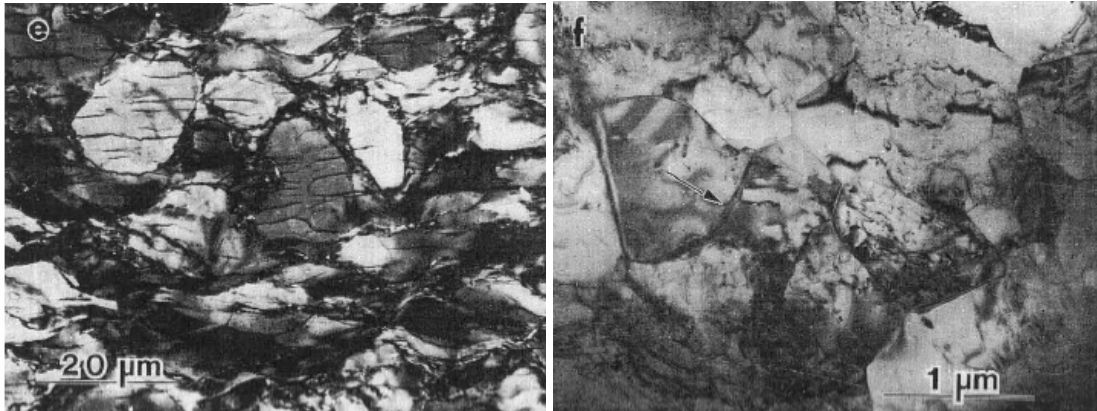
45% shortening at 850°C and 10^{-5} s^{-1}; irregular patchy extinction, inhomogeneously flattened grains and extensive grain-boundary migration; recrystallized region showing variable dislocation densities and local strain-induced grain-boundary migration (Hirth & Tullis, 1992). TEM image shows neoblasts replacing grain with dislocation tangles.

Large porphyroclasts, inhomogeneous deformation, patchy and undulatory extinction, deformation lamellae, kink bands, large irregular subgrains (Stipp et al., 2002)
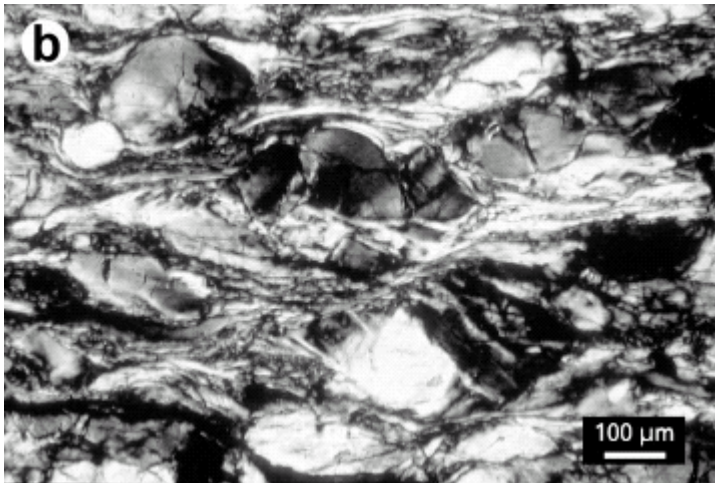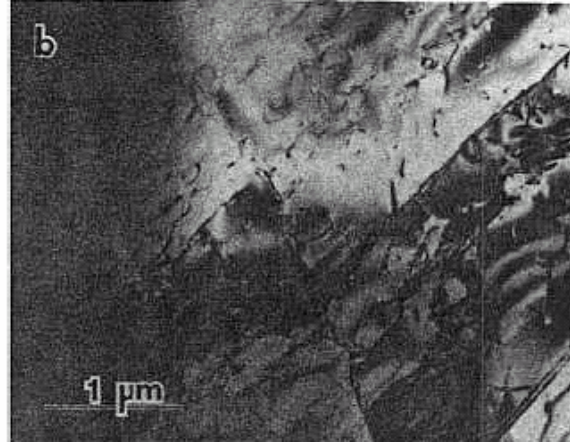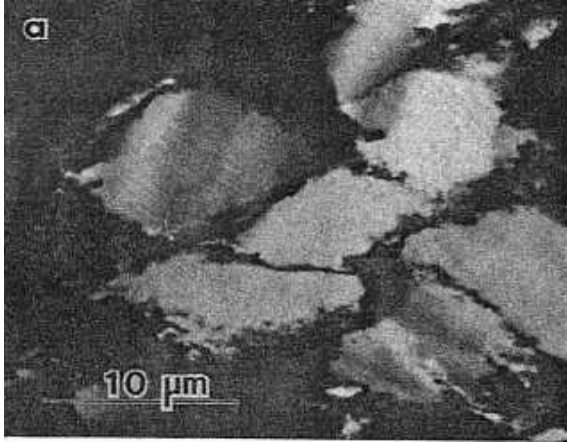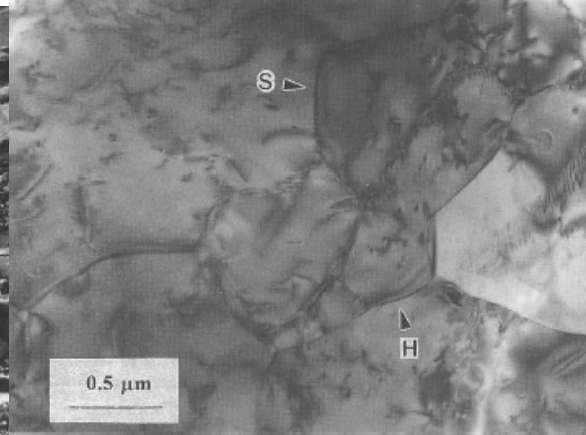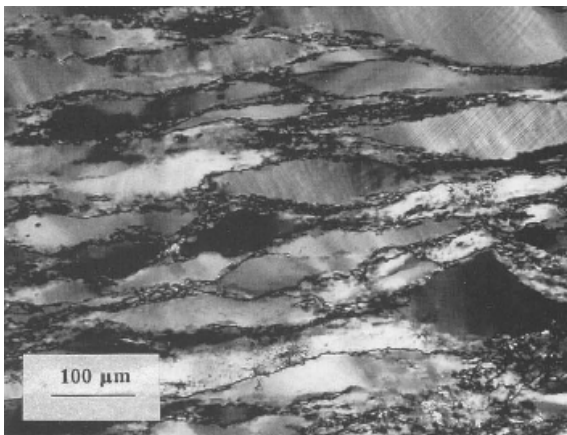

Regime 1, 60% strain

Regime 2 (Hirth & Tullis, 1992). With an increase in T or a decrease in strain rate, dislocation climb becomes sufficiently rapid to accommodate recovery. Grains exhibit sweeping undulatory extinction, optically visible subgrains and subbasal deformation lamellae defined by planar regions of higher dislocation density and elongate subgrains. Free dislocation density is much lower than regime 1 and dislocations are arranged into low-energy subgrain boundaries. Recrystallization occurs predominantly by progressive subgrain rotation. Free dislocation density of the recrystallized grains is the same as original grains SGR does not result in strain weakening because the recrystallized grains

have about the same dislocation density as the original grains from which they formed; thus achievement of a steady-state microstructure is not required for steady state flow.

Core-and-mantle structures, ribbon grains, subgrains same size and recrystallized grains, relatively straight grain boundaries (Stipp et al., 2002)
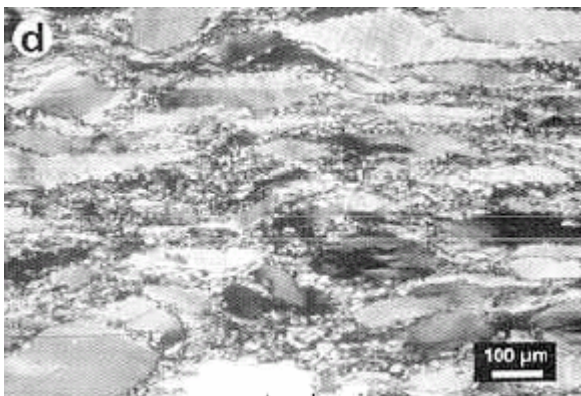

Regime 2, 30% strain

Regime 2, 60% strain at 800°C and 10^{-6} s^{-1}. TEM image shows recrystallized grains similar to subgrains.

Regime 2, 50% shortening and *simple shear* at 800°C and 10^{-5} s^{-1} (Tullis et al, 2000)

(Stipp et al., 2002)

***Regime* 3** (Hirth & Tullis, 1992). Increased rate of grain-boundary migration; recrystallization occurs by both grain-boundary migration and SGR. Original grains exhibit a core-and-mantle structure with optically visible subgrains that are larger than regime 2. Free dislocation density within the subgrains is lower than regime 2. The driving force for GBM may be due in part to a difference in the free dislocation density between grains, however the energy associated with the subgrain boundaries is also important. With the operation of two recrystallization mechanisms, samples in regime 3 become completely recrystallized at lower strains than regime 2 or regime I. Achievement of a steady state flow stress is not dependent on the achievement of a steady state microstructure.

Broader grain-size distribution, lobate and interfingering grain boundaries, island grains, no relict porphyroclasts; chessboard extinction at highest T (Stipp et al. 2002)
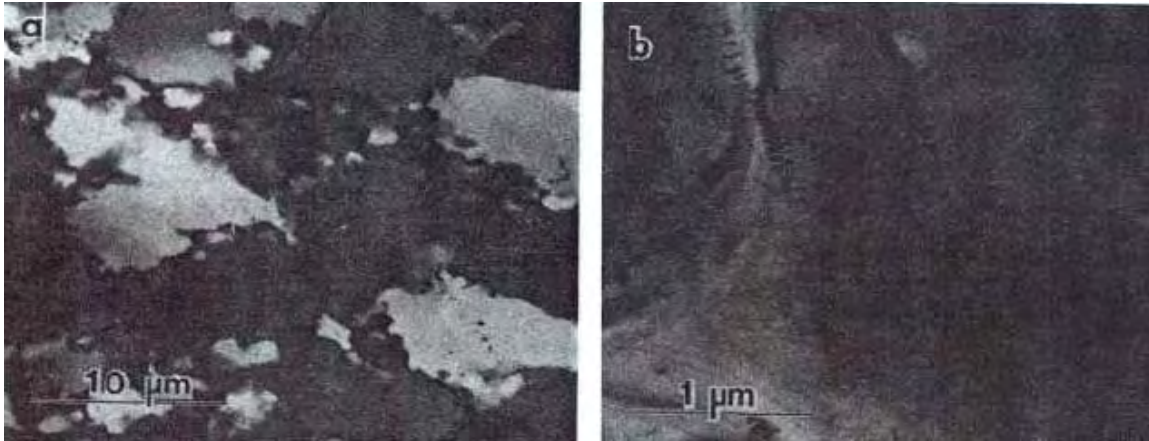
Regime 3, 35% strain
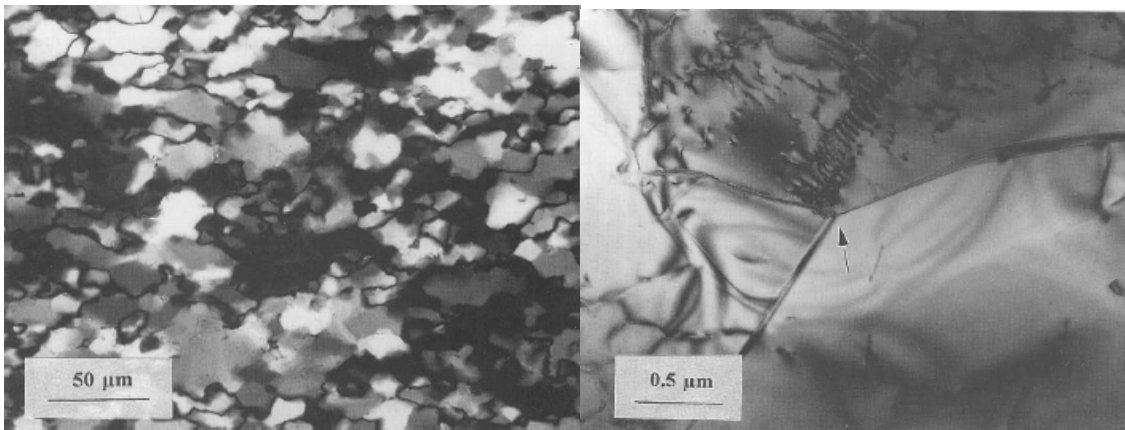
Regime 3, 60% strain at 900°C and 10^{-6} s^{-1} . TEM image shows cusp (arrow) at grain boundary indicating that interfacial energy is an important driving force. Recrystallized grain is larger than subgrain.

***Transition from regime 1 to regime* 2.** Caused by an increase in the rate of climb. While interiors of grains in regime 1 exhibit high densities of tangled dislocations with straight segments, interiors of grains in regime 2 show subgrain boundaries and a lower density of curved free dislocations. With a constant driving force, an increase in T results in an exponential increase in grain-boundary velocity. Because the transition to regime 2 occurs with increasing T (and therefore increasing grain-boundary mobility), the lack of grain-boundary migration in regime 2 indicates that the driving force for migration must be lower and this must be because of the uniform dislocation density of the recrystallized and original grains. Gradients in dislocation density are most likely to develop when few slip systems are operative. The transition to regime 2 may correspond to the enhanced activity of prism slip. Increased activity of prism slip is suggested by the more uniform grain flattening.

***Transition from regime 2 to regime* 3.** Microstructures show that dislocation climb remains sufficiently rapid to accommodate recovery and that the rate of grain-boundary migration is faster. The grain-boundary mobility is greatest in regime 3, however, the transition to regime 3 can occur with a decrease in strain rate at constant temperature

(mobility), suggesting that the velocity of grain-boundary migration increases due to an increase in driving force. An increase in the driving force may arise from an increase in energy associated with subgrain boundaries. Microstructural observations clearly show the migration of grain boundaries preferentially into subgrain dislocation networks. Transition to regime 3 may occur when the flow stress is low enough that the energy associated with subgrain boundaries becomes a significant portion of the driving force for grain-boundary migration. The relative influence of the subgrain boundaries is greater at low flow stresses because the strain energy associated with the free dislocations decreases as the dislocation density decreases.

Regime 1 BLG: bulging recrystallization	Regime 2 SGR: subgrain-rotation recrystallization	Regime 3 GBM: grain-boundary migration recrystallization
irregular & patchy undulatory extinction inhomogeneous flattening of porphyroclasts numerous deformation bands large, irregular subgrains very fine grained neoblasts along grain boundaries sutured & serrated grain boundaries strain concentrated in neoblasts	sweep undulatory extinction ribbon porphyroclasts core-and-mantle texture subgrains & deformation lamellae subgrains & recrystallized grains of similar size subgrains have different degrees of misorientation some subgrains *inside* porphyroclasts no grain boundary bulging relatively straight grain boundaries	lobate, interfingering grain boundaries more grain size variation than R2 at lo strain, core-and-mantle texture with larger subgrains than R2 at hi strain, no relict porphyroclasts chessboard extinction island grains and dissection microstructures

**Deformation Regimes in Quartz: Borrego Springs Mylonite**
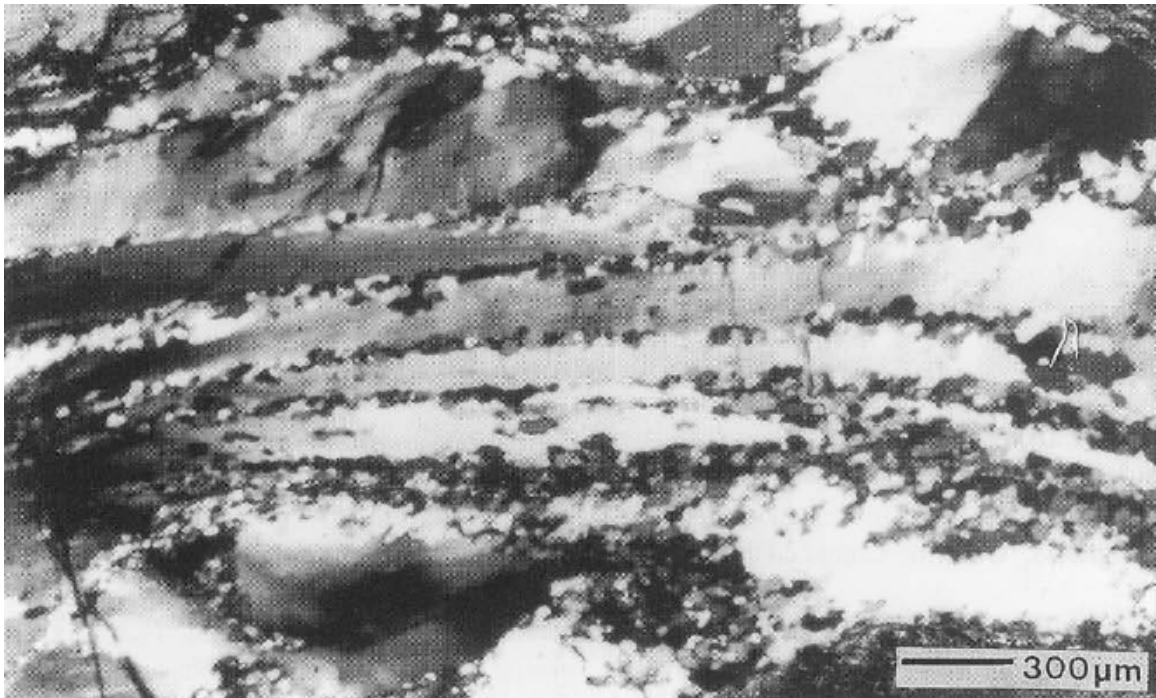
Regime 2. Greenschist-facies Borrego Springs mylonite. Quartz ribbons show undulatory extinction and minor subgrain formation (Simpson, 1998)
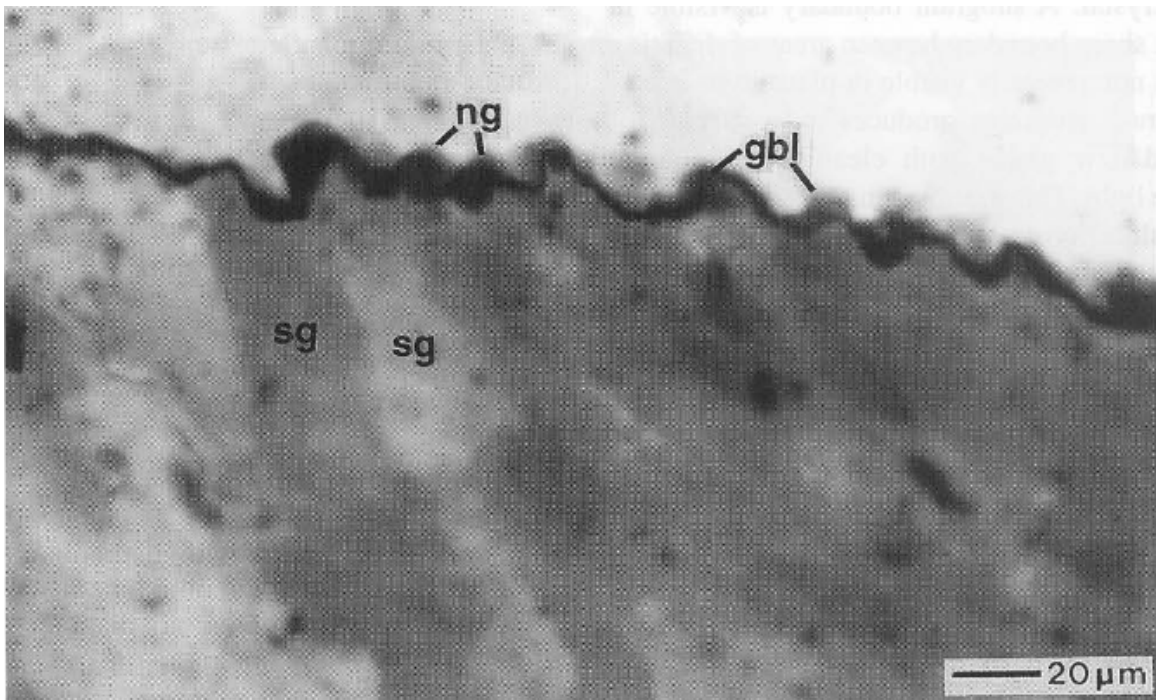
Regime 2. Enlargement of above showing size difference between subgrains (sg) and GBM lobes (gbl) and associated GBM neoblasts (ng) (Simpson, 1998)

**Deformation Regimes in Quartz: Heavitree Quartzite Australia**
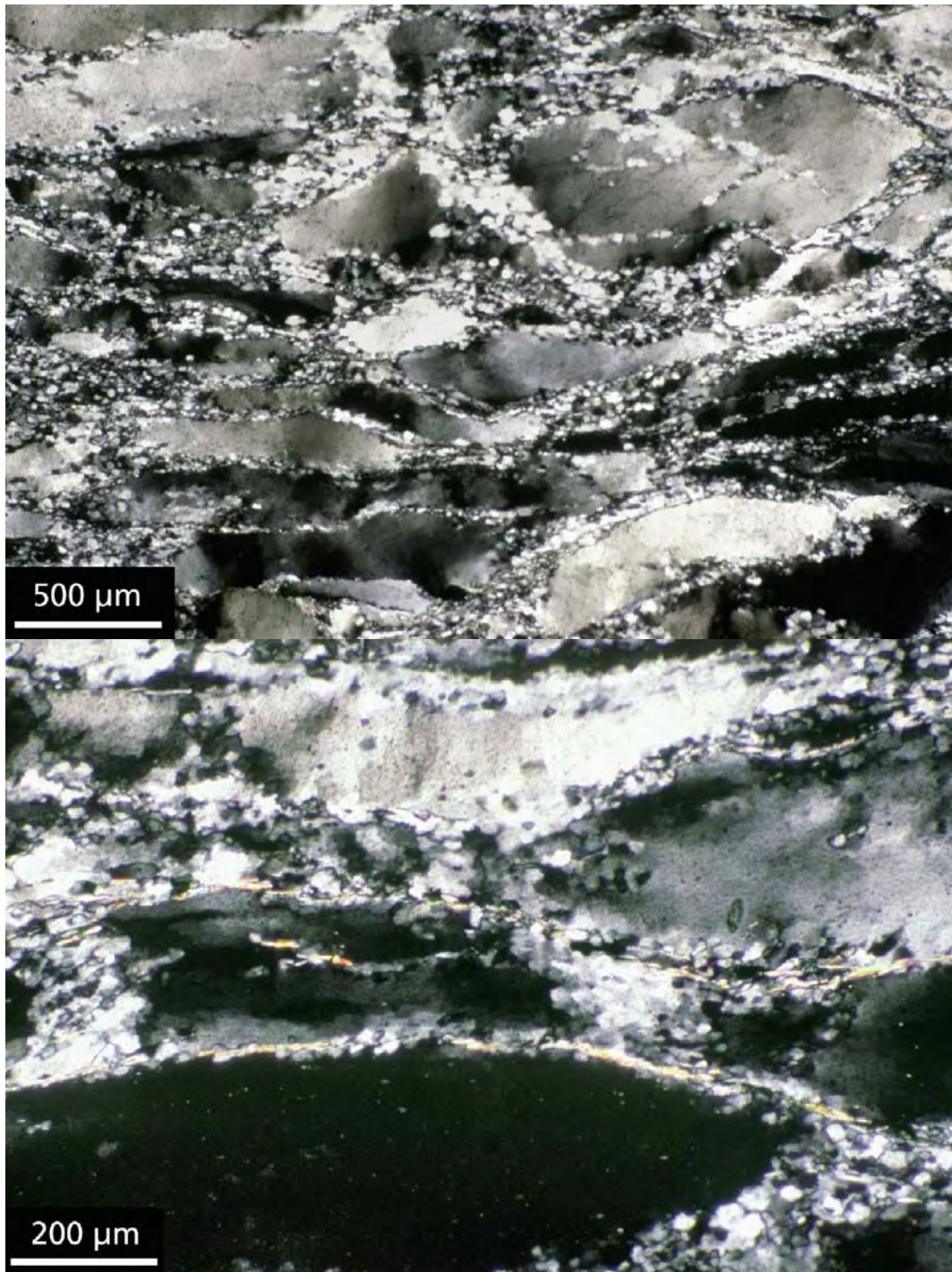
Regime 2. Heavitree quartzite deformed at greenschist conditions with subgrain rotation recrystallization. Original detrital quartz grains are flattened and stretched and show severe undulatory extinction due to the development of subgrains by lattice rotation. The large grains are surrounded by a mantle of recrystallized grains, ~50 mm in size, which formed by subgrain rotation. (Tullis et al, 2000)

Regime 2. Heavitree quartzite deformed at greenschist conditions by simultaneous subgrain rotation recrystallization and solution–precipitation. Detrital quartz grains are flattened, stretched, and bent in a fine-grained quartz-mica matrix. A NE-SW shear band deforms the dominant foliation and indicates top-to-the-left sense of shear. (Tullis et al., 2000)

Deformation Regimes in Quartz: Ruby Gap Duplex
Three creep regimes in Ruby Gap duplex in Oz (Hirth et al., 2001).
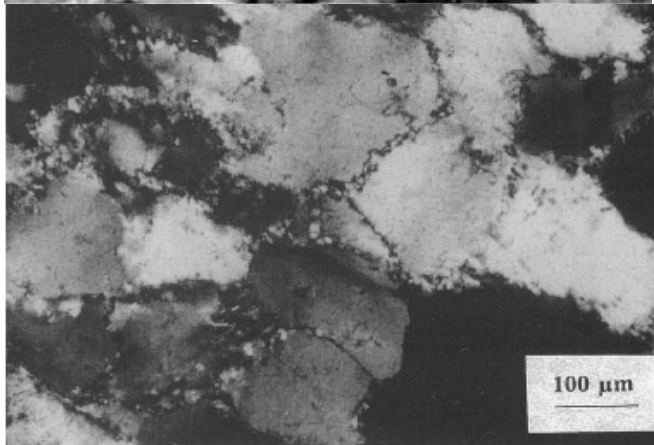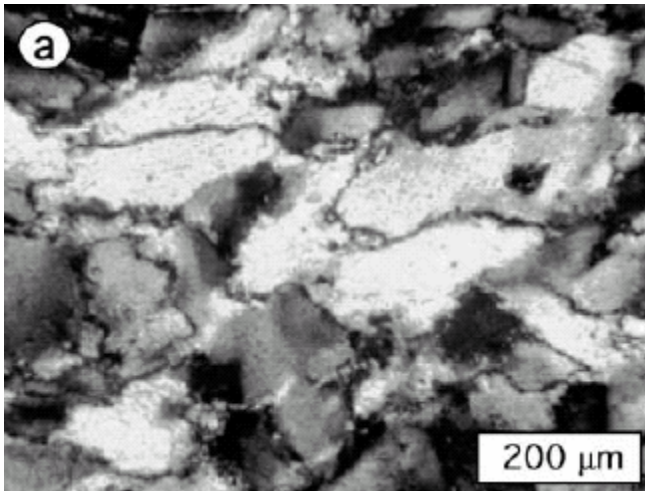
Regime 1: irregular, patchy undulatory extinction, numerous deformation bands, and very fine-grained recrystallized grains along GB; climb is difficult and recrystallization occurs by GB bulging (Hirth et al., 2001).
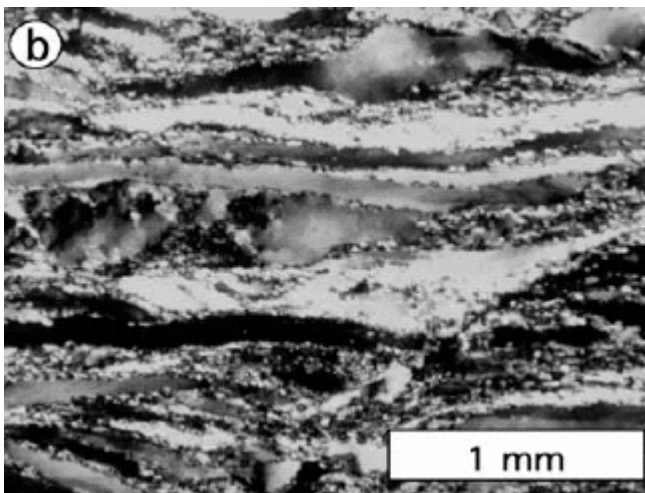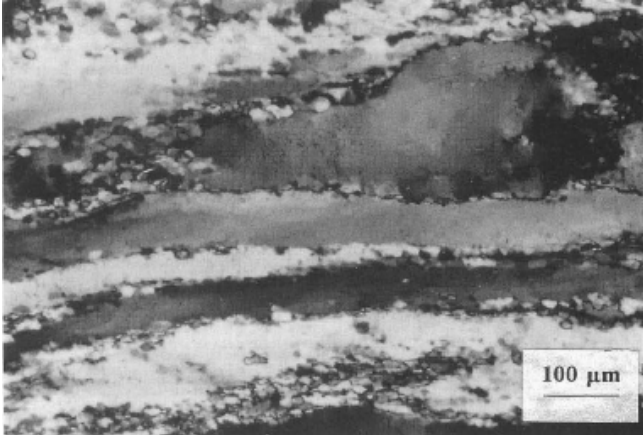
Regime 2: flattened quartz grains with optically visible subgrains and recrystallized grains along GB; recovery is accommodated by dislocation climb and recrystallization occurs by SGR (Hirth et al., 2001).
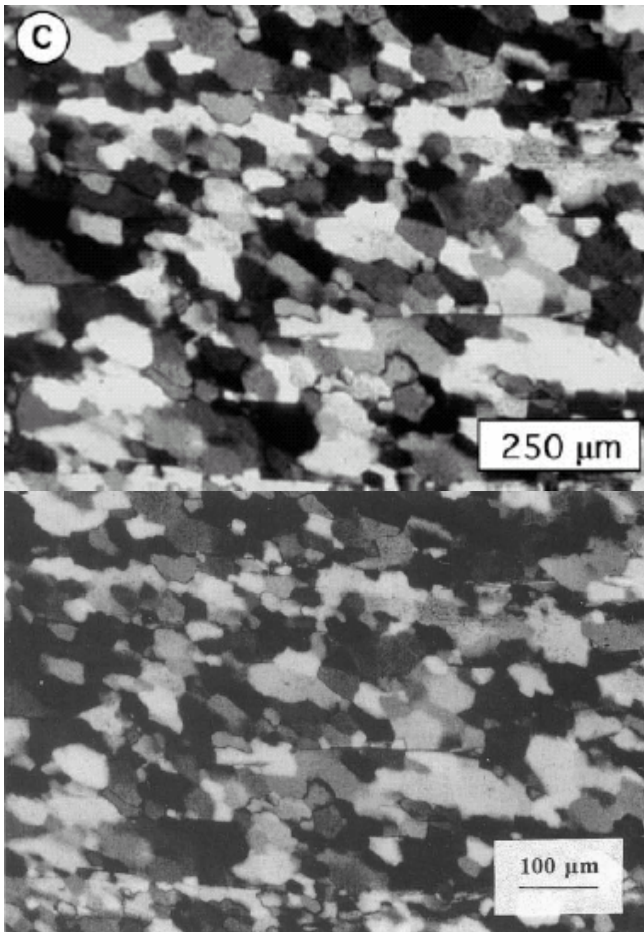
Regime 3: completely recrystallized with oblique SPO defined by recrystallized grains; recovery is accommodated by dislocation climb and recrystallization occurs by GBM (Hirth et al., 2001).
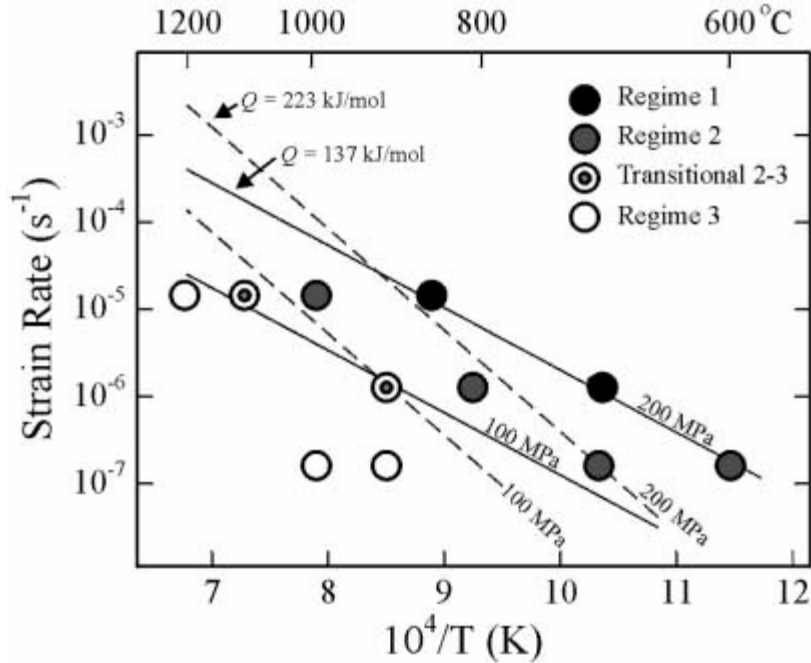
Experimental results of Hirth & Tullis (1992). The transitions between deformation regimes are a function of T and σ. Solid lines show "with melt" law of Gleason & Tullis (1995).

b
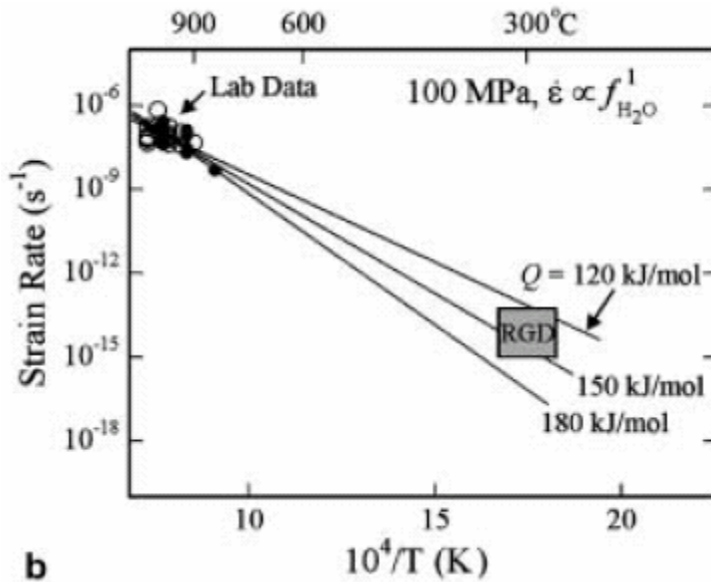
Extrapolation of lab data to Ruby Gap duplex (Hirth et al., 2001). Best fit is log(A) = − 11.2 ± 0.6 MPa^{-n}/s and Q = 135 ± 35 kJ/mol with m=1 and n=4 for

$$\dot{\varepsilon} = A f_{H_2O}{}^m \sigma^n \exp(-Q/RT)$$

where f_{H_2O} is the fugacity of H_2O (in Pa). Here is a table of fugacity coefficients from Tödheide (1972), summarized from the calculations of Burnham et al. (1969).

P, kbar	at $T=100°C$	200°C	300°C	400°C	500°C	600°C	700°C	800°C	900°C	1000°C
					Fugacity coefficients					
1.0	0.002	0.024	0.105	0.263	0.459	0.632	0.762	0.848	0.905	0.940
1.5	0.002	0.020	0.088	0.219	0.389	0.557	0.700	0.807	0.883	0.930
2.0	0.002	0.019	0.082	0.202	0.361	0.523	0.671	0.788	0.875	0.932
2.5	0.002	0.020	0.081	0.197	0.351	0.510	0.660	0.786	0.880	0.945
3.0	0.002	0.020	0.083	0.199	0.353	0.512	0.664	0.795	0.895	0.964
3.5	0.002	0.022	0.087	0.206	0.361	0.523	0.678	0.813	0.917	0.990
4.0	0.003	0.024	0.092	0.216	0.376	0.540	0.700	0.838	0.947	1.020
4.5	0.003	0.027	0.100	0.229	0.395	0.564	0.728	0.871	0.982	1.055
5.0	0.003	0.030	0.109	0.245	0.418	0.594	0.762	0.909	1.024	1.096
6	0.005	0.038	0.132	0.287	0.478	0.668	0.848	1.004	1.124	1.193
7	0.007	0.050	0.163	0.343	0.556	0.763	0.956	1.121	1.246	1.315
8	0.009	0.066	0.205	0.414	0.654	0.881	1.088	1.262	1.391	1.460
9	0.014	0.088	0.259	0.504	0.776	1.024	1.246	1.428	1.561	1.631
10	0.020	0.119	0.330	0.618	0.925	1.195	1.432	1.621	1.755	1.826

To calculate f_{H2O}, multiply pressure by the fugacity coefficient from this table. For example, at 300 MPa and 500°C, the fugacity of H_2O is 300 * 0.353 = 106 MPa.

To apply flow laws determined in pure shear to simple shear, we assume (following Nye, 1953) that the deformation is isochoric and that the third invariant of the deviatoric stress tensor is unimportant. This gives

$$\dot{\gamma} = A f_{H_2O}{}^m \left(\sqrt{3}\right)^{n+1} \left(\frac{\sigma_1 - \sigma_3}{2}\right)^n \exp(-Q/RT)$$

(Schmid et al., 1978).

Deformation Regimes in Naturally Deformed Quartz: Tonale fault zone
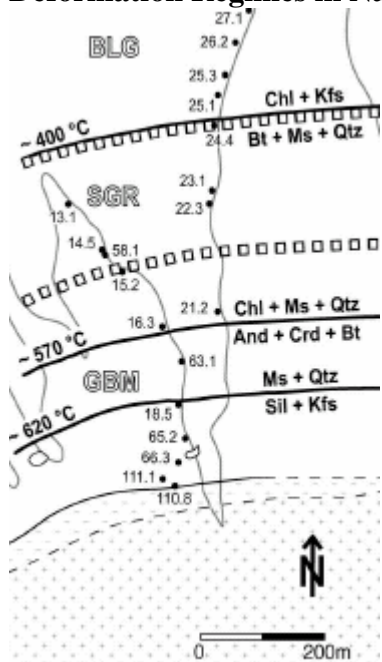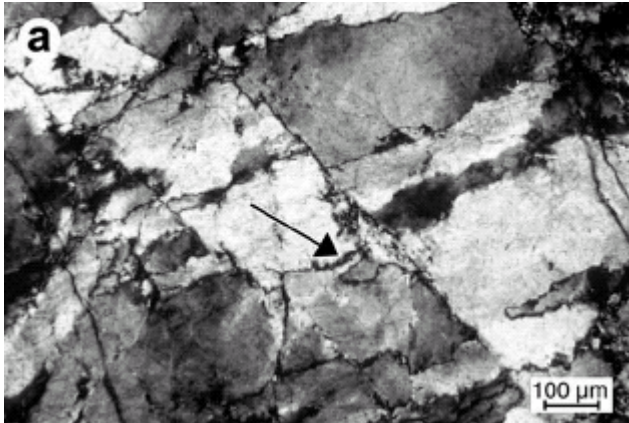
cataclasis at 250°C (Stipp et al., 2002)
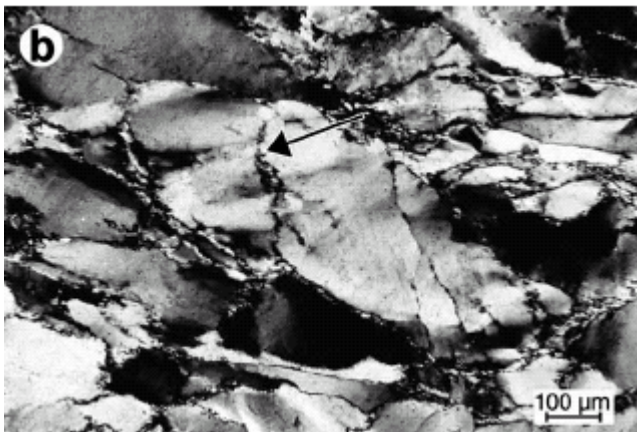
Regime 1 BLG at 300°C; sutured and serrated GB with recrystallized bulges (arrow) (Stipp et al., 2002)

Regime 1 BLG at 310°C porphyroclasts show undulatory extinction and serrated grain boundaries (Stipp et al., 2002)
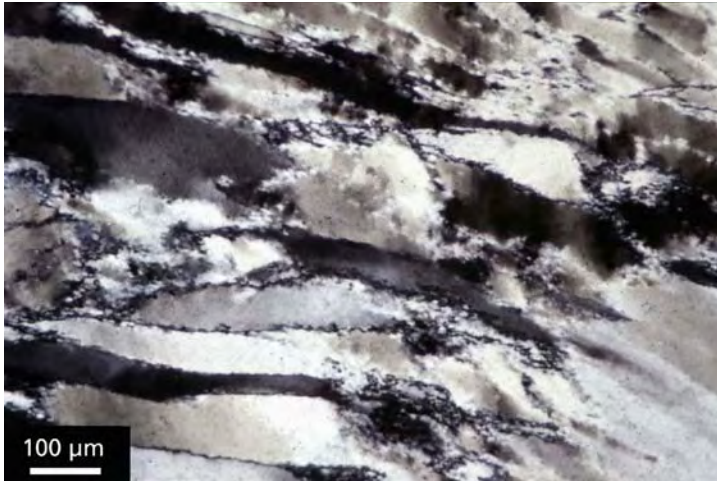
Regime 1 BLG at 340°C; elongate porphyroclast with bulging recrystallization, undulatory and patchy extinction (Stipp et al., 2002)
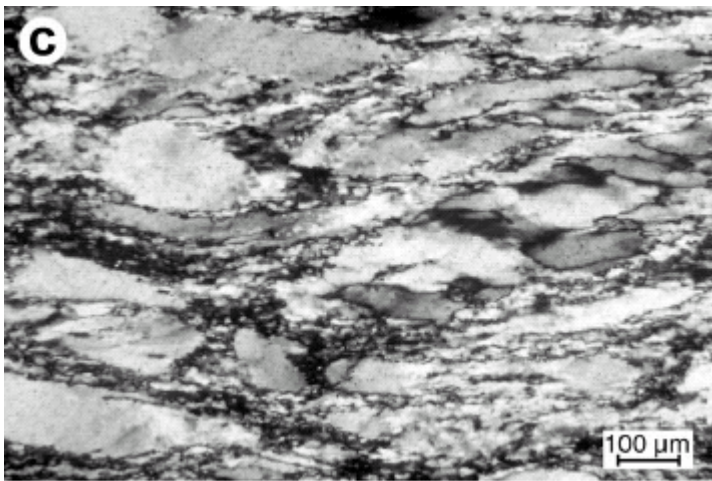

Regime 1 BLG at 370°C : recrystallization along serrated grain boundaries of porphyroclasts (core-and-mantle structure) (Stipp et al., 2002)
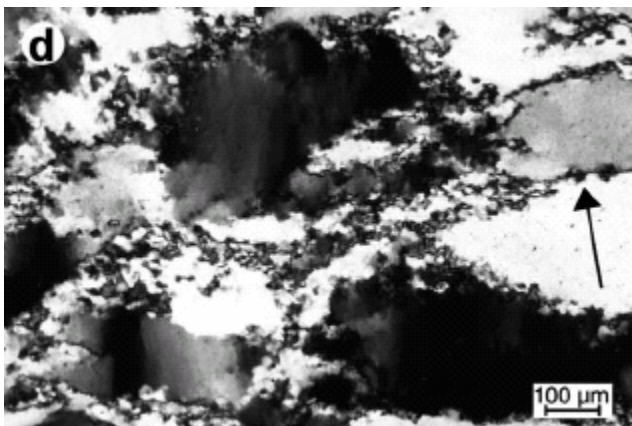
Regime 1 BLG at 400°C increased recrystallized grain size; sutured grain boundaries with bulges (arrow) suggest BLG dominant (Stipp et al., 2002)
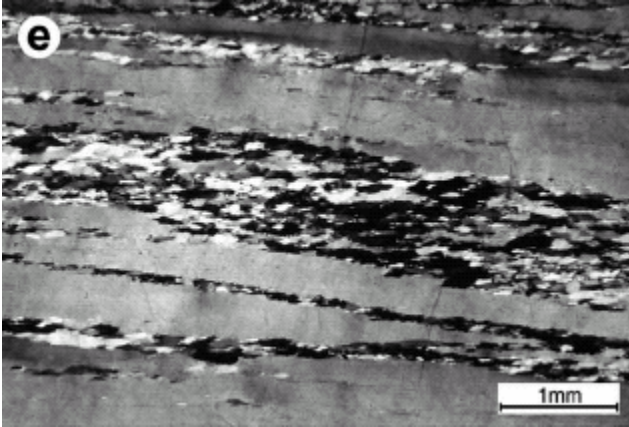
Regime 2 SGR at 490°C: ribbon grains. recrystallized grains form an oblique second foliation(Stipp et al., 2002)
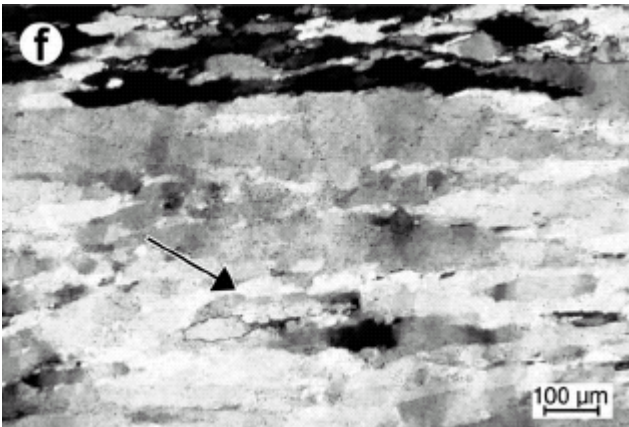
Regime 2 SGR at 490°C: polygonization due to progressive subgrain rotation; recrystallized grains are same size as subgrains (Stipp et al., 2002)
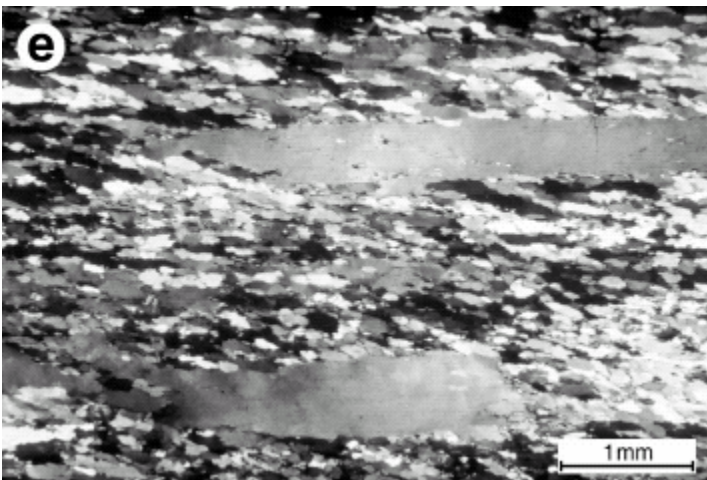
Regime 2 SGR at 510°C : polygonization and recrystallization of ribbons
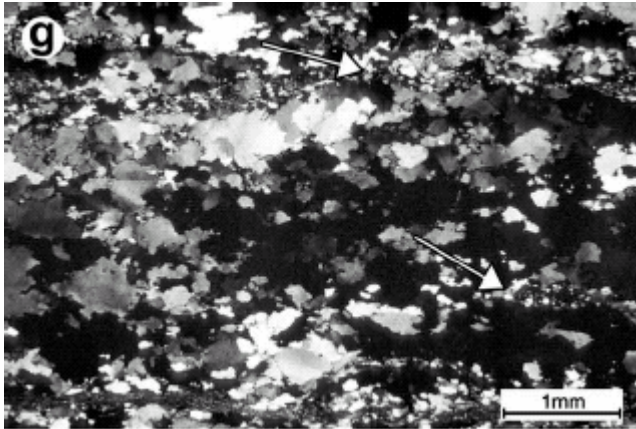
Regime 3 GBM at 560°C: irregular grain shapes, sizes and boundaries due to increased grain-boundary migration (Stipp et al., 2002)
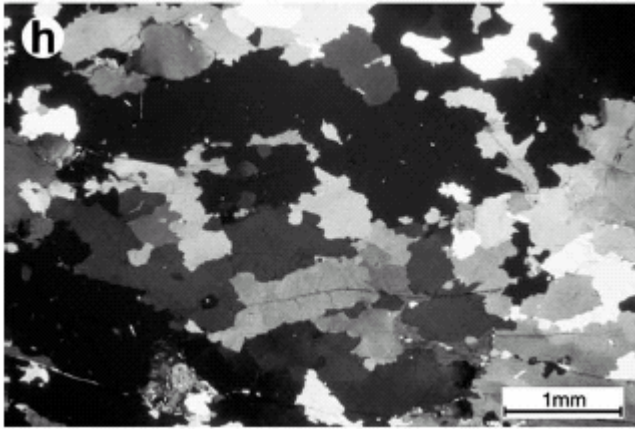
Regime 3 GBM at 650°C amoeboid grains with high-amplitude sutures, coarse recrystallized grains and dissection microstructures (Stipp et al., 2002)
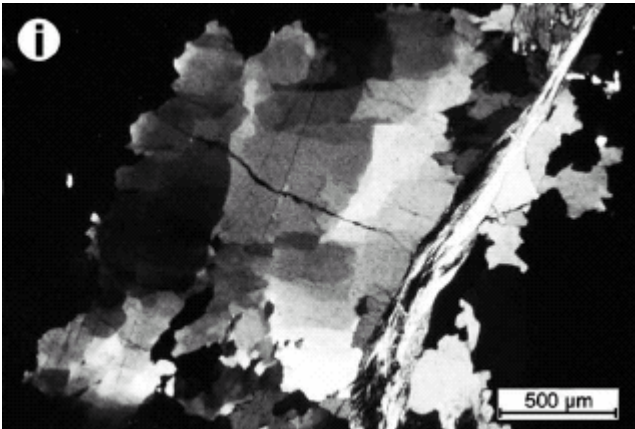
Regime 3 GBM @ 650°C chessboard extinction with subgrain boundaries parallel to basal and prism planes (Stipp et al., 2002)
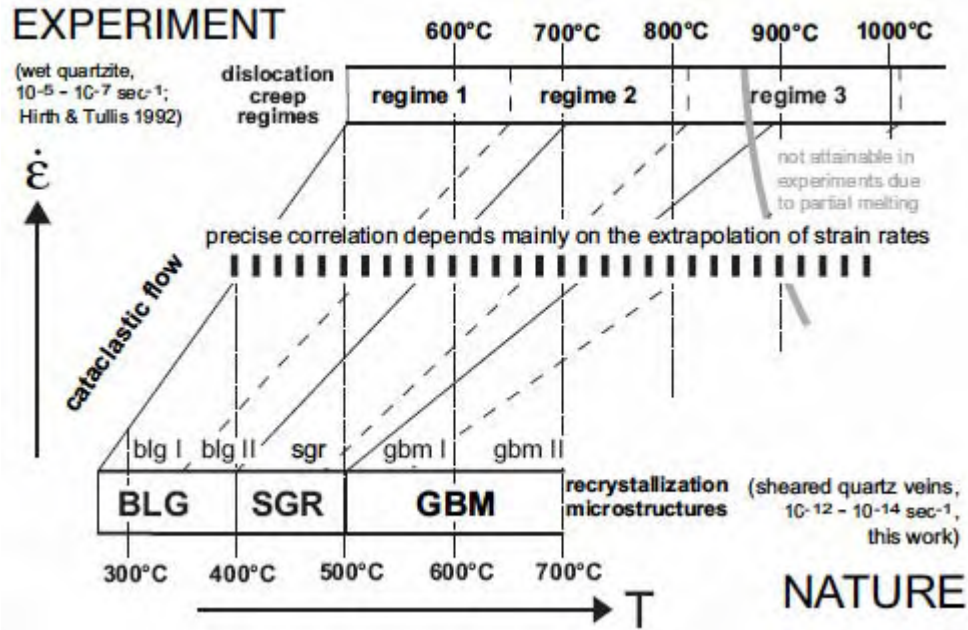
Correlation between experimental and natural T and strain rates (Stipp et al., 2002)
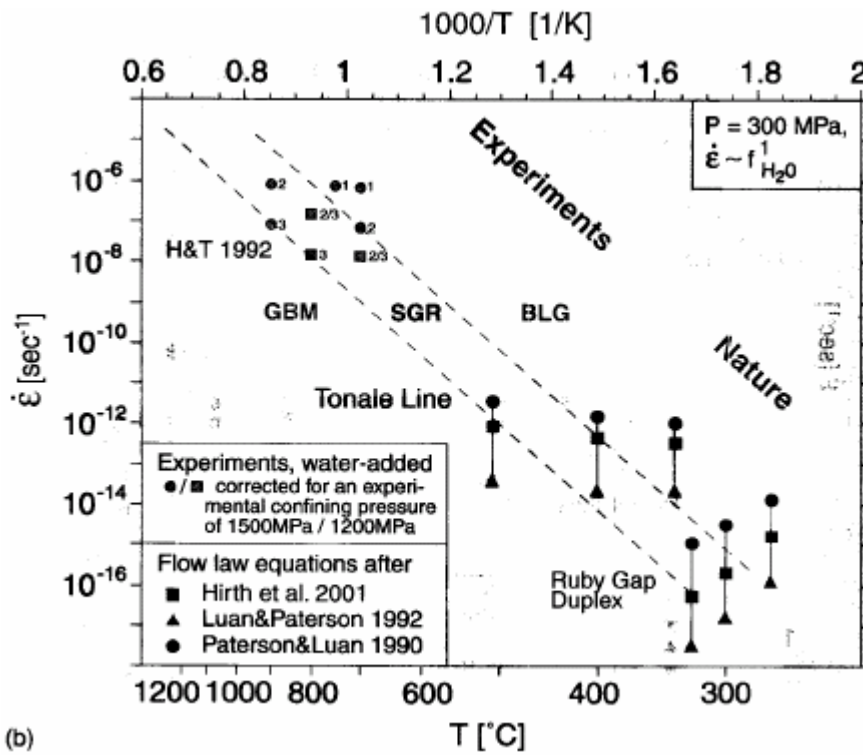
(b)

Correlation between experimental and natural T and strain rates (Stipp et al., 2002)

Lattice-Preferred Orientations (LPO)

Asymmetric patterns develop because one orientation is oriented favorably for slip and does so homogeneously without recrystallizing while the other orientation is unfavorably oriented for slip, does so heterogeneously and recrystallizes. The favorably oriented grains therefore grow and consume their more-deformed neighbors.
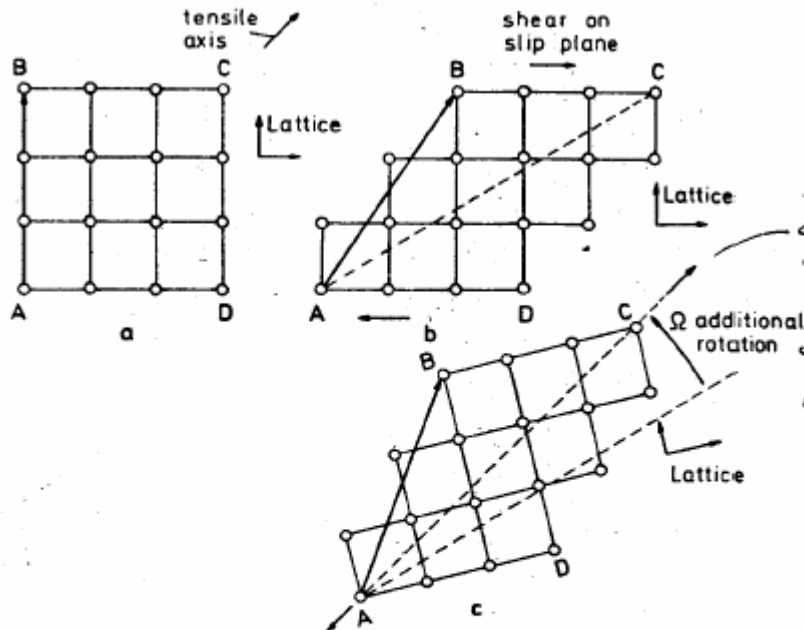
Fig. 5.5 a-b A shear γ on a slip plane does not cause the lattice to rotate, although a material vector may rotate (vector AB e.g.).
b-c An additional rotation – which also causes the crystal lattice to rotate – will bring the crystal in a position corresponding to the strain forced upon it : e.g. pure elongation in the direction AC.

(Christian, 1981)
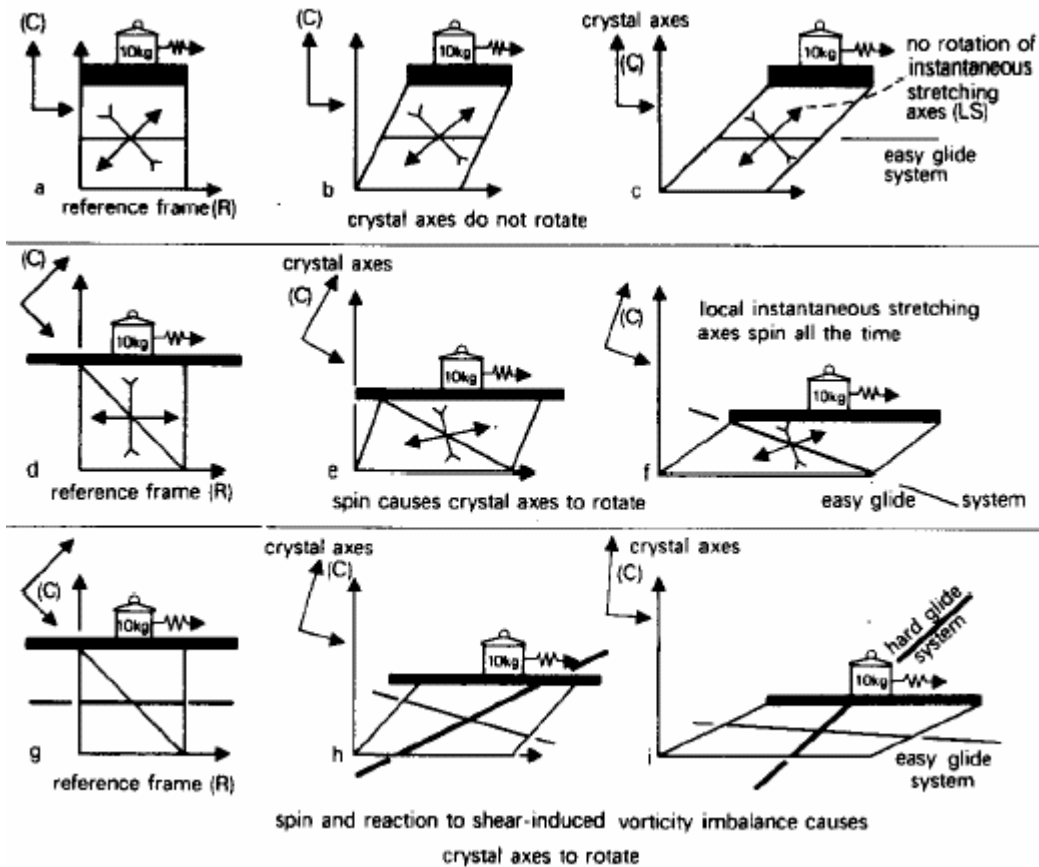
Rotation of crystal lattice in response to applied stress. (top) slip system ‖ to shear; no rotation of crystal axes. (middle) single slip system. (bottom) two slip systems (Lister, 1982)

Types of Typical Quartz LPOs
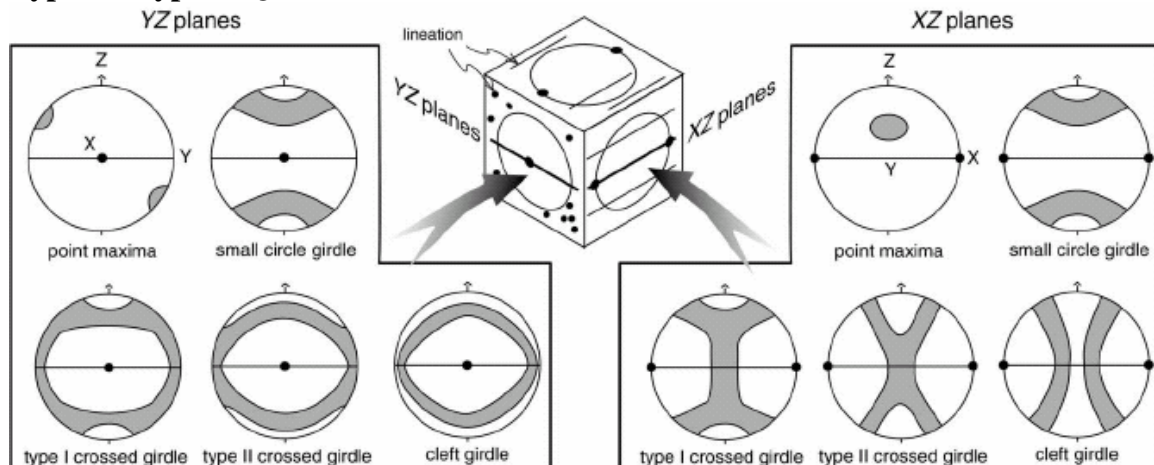
(Llana-Fúnez, 2002)

Examples of Fabric Types from Nature (Schmid & Casey, 1986)

c　　　　　a　　　　　m　　　　　r & z
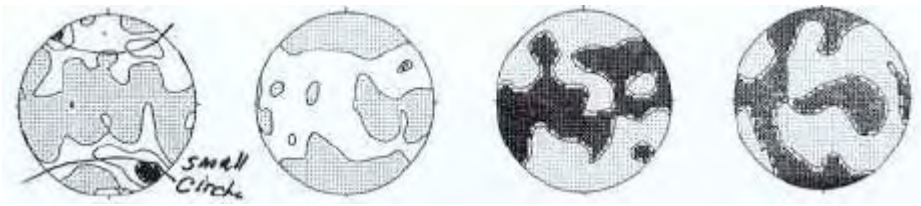
C-axis small-circle (granulite)
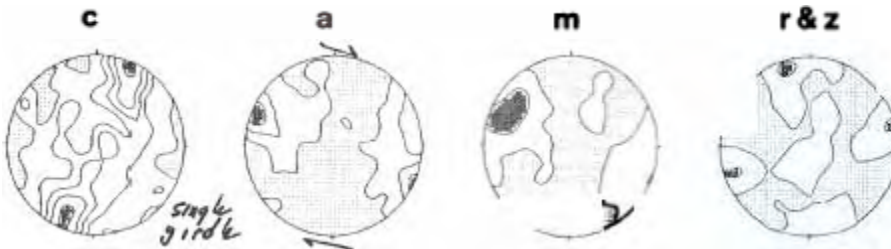
C-axis point maximum at Z (lower greenschist; predominantly basal slip)
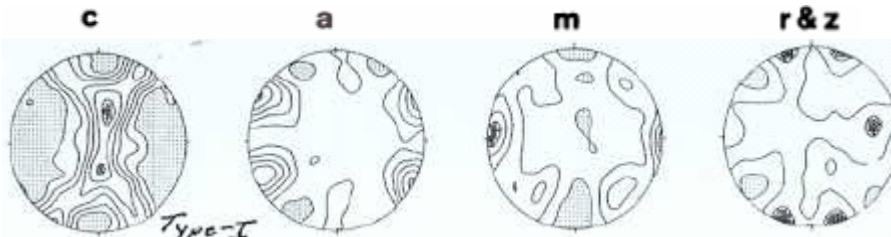
Type-I (I-beam) c-axis girdle (lowermost greenschist)
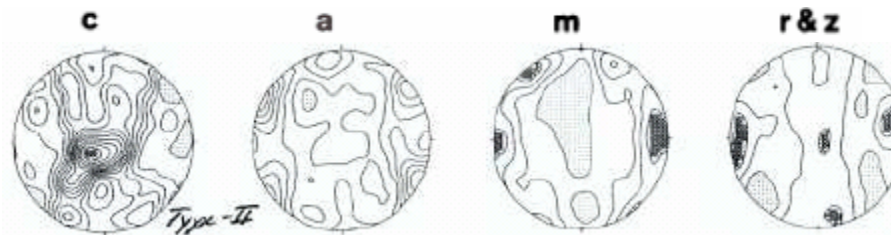
Type-II (X) crossed c-axis girdle; a-axis maxima indicate departures from plane strain. a-axis small circles around X imply constriction
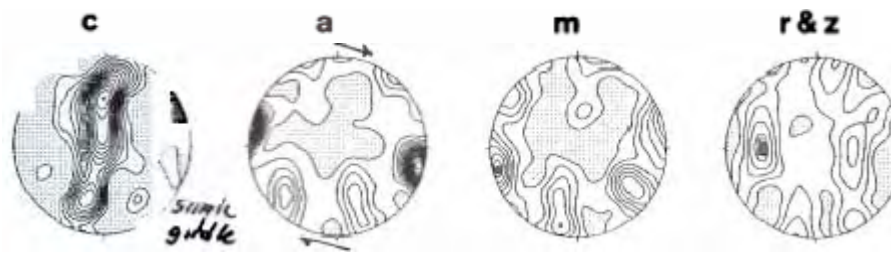
Single c-axis girdle and a-axis maximum near-X (greenschist; primarily by rhomb slip, with minor basal <a> and prism <a>)

c   a   m   r & z
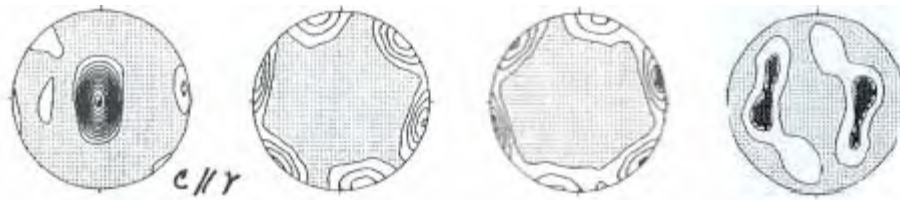
C-axis maximum parallel to Y (no basal slip; prism slip important)

LPO Development: Tonale fault zone
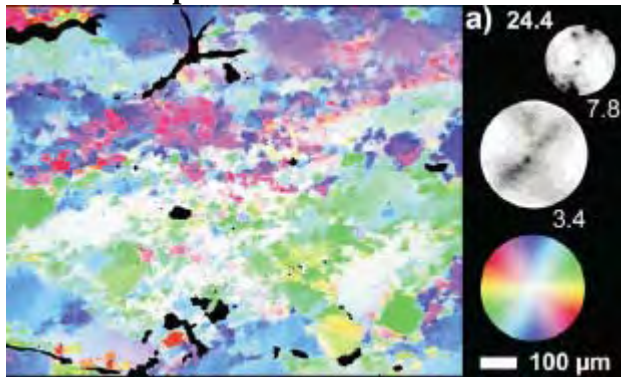
Regime 1 (BLG) LPO
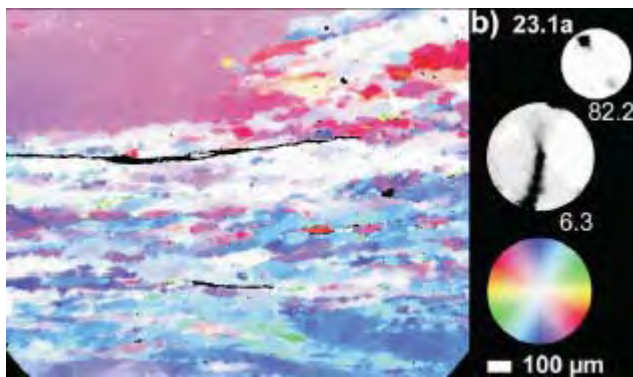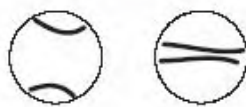
Regime 2 (SGR) LPO
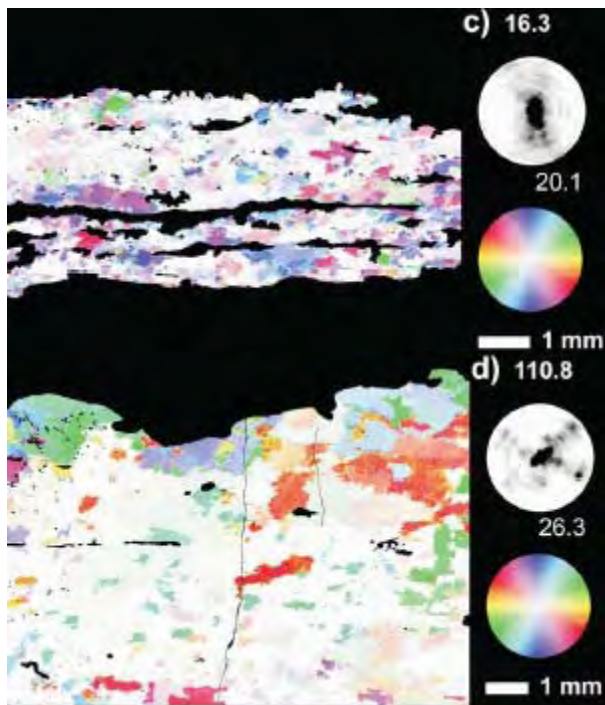
Regime 3 (GBM) LPO

(Stipp et al., 2002)

Regime 1. BLG: bulging recrystallization

irregular & patchy ux
ihomogeneous flattening of p'clasts
some subgrains
neoblasts of variable size
undulose grain boundaries
strain is conceentrated in neoblasts

Regime 2. SGR: subgrain rotation recrystallization

sweeping ux
ribbon p'clasts
core & mantle texture
sumgrains & deformation lamellae
subgrains have different degrees of misorentation
no grain-boundary bulging
subgrains all of similar size
some subgrains INSIDE p'clasts
relatively straight grain boundaries

Regime 3. GBM grain-boundary migration recrystallization

locate, interfingering grains
more grain size variation than R2
no relict p'clasts
chessboard extinction

Summary of criteria for identifying regimes.

Active Slip Systems Depend on Temperature
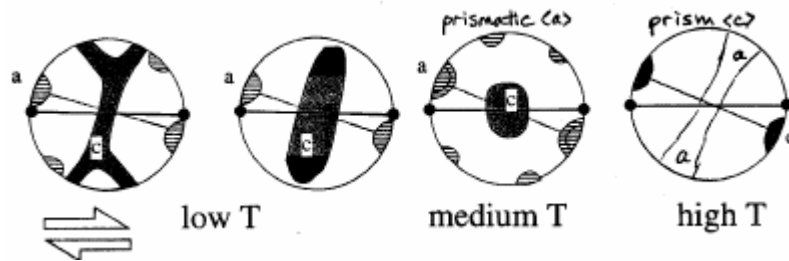
(Passchier & Trouw, 1996)

Von Mises Criterion

Deformation of a polycrystal leads to internal stresses because of unequal slip on different slip systems. As these stresses rise, deformation on other slip systems becomes possible and grains must deform to accommodate the imposed strain and their neighbors. For isochoric deformation, the 6 independent components of the strain tensor are reduced to 5 because $\varepsilon_{11} + \varepsilon_{22} + \varepsilon_{33} = 0$. Because the operation of one slip system produces only one independent component of the strain tensor, 5 independent slip systems are needed to achieve an arbitrary strain (von Mises, 1928). A corollary of the von Mises criterion is that because 5 independent slip systems are able to produce an arbitrary strain a crystal cannot possess more than 5 independent slip systems (Groves & Kelly, 1963).

Relaxation of this constraint comes from
1) dislocation climb wherein the motion of vacancies causes volume change (Groves & Kelly, 1969). For dislocations of a given Burgers vector, the addition of the strain components due to climb produces two independent strain components. In quartz, for example, a general strain can be achieved by adding climb to a set of three slip systems.
2) grain-boundary migration (Means & Jessell, 1986)
3) may not actually be necessary that *all* grains undergo the same strain
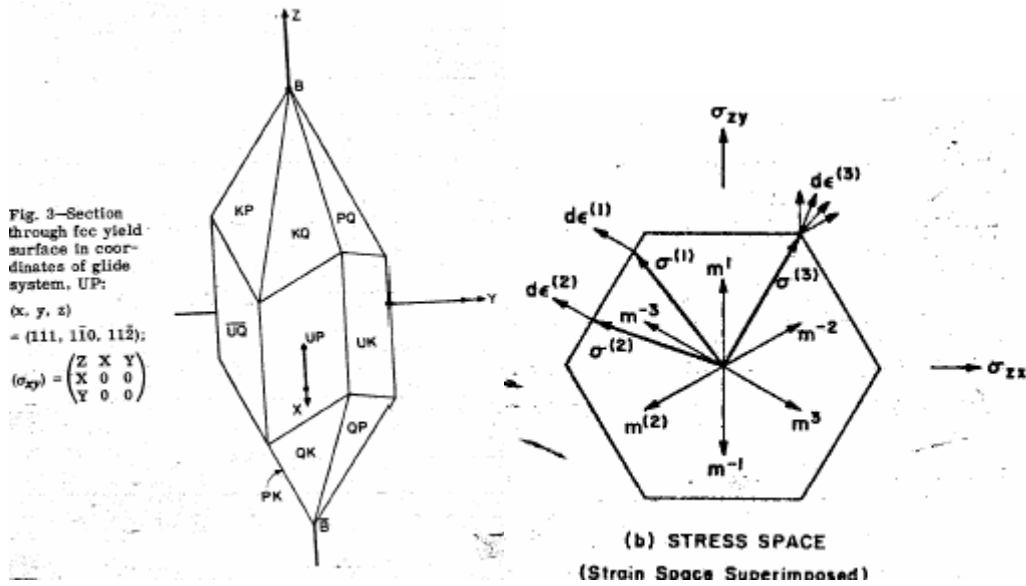4) formation of kink bands allows for shortening parallel to slip plane

A theory for crystal plasticity must know either stresses or strains within the polycrystal . Sachs (1928) assumed that all grains in the rock undergo the same imposed stress. Individual grains are treated as though they are free to deform independently. Schmid's law is used to determine the activated slip system. Because this uses only 1 slip system, Sachs' theory cannot be applied to rocks.
Taylor (1938) assumed that all grains in the rock undergo the same imposed strain. The stress in each crystal is the CRSS and stress compatibility among grains is therefore violated. To calculate the rotation of a grain produced by slip, the displacement gradient of the imposed strain is known, the orientation of the crystal is known and the CRSS's of the various slip systems are known: this yields 5 linear equations with n unknowns, where n is the number of slip systems. If there are more than 5 possible slip systems, a choice must be made, based, for example, on minimization of work. This is not a problem for rocks.
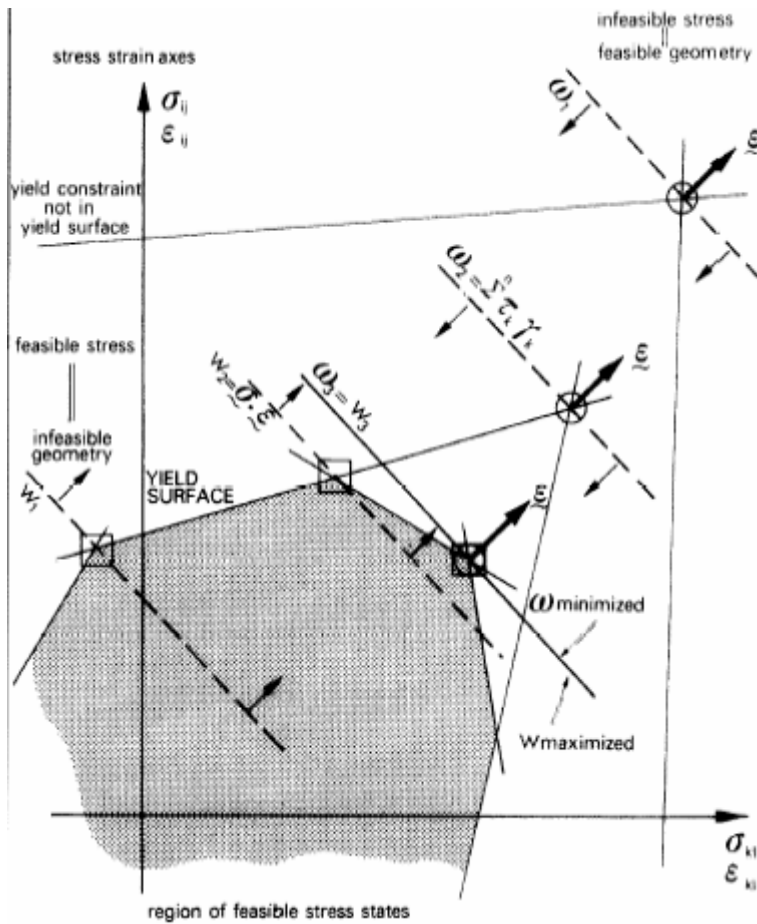
Bishop & Hill (1951) chose a "maximum work" approach involving a tangent to the yield surface.
Neither the Sachs nor the Taylor hypothesis accurately described behavior of a polycrystal because stress equilibrium and geometrical compatibility are not assured.

Yield Locus

Fig. 3—Section through fcc yield surface in coordinates of glide system, UP:

(x, y, z)

$= (111, 1\bar{1}0, 11\bar{2})$;

$(\sigma_{xy}) = \begin{pmatrix} Z & X & Y \\ X & 0 & 0 \\ Y & 0 & 0 \end{pmatrix}$

(b) STRESS SPACE
(Strain Space Superimposed)

Yield surface in real space and in stress space (Kocks, 1970)

Yield surface in stress space. Thick arrow shows imposed strain; thin arrows show optimized work function. The imposed strain and available slip systems constrain slip system activity (Lister et al., 1978)

Lister's Taylor–Bishop–Hill model for LPO development in quartzites

Potential glide systems for α-quartz

Glide plane	Glide direction	Multi-plicity	Opposite senses equivalent	Relative critical shear stresses for models			
				I	II	III	IV
c (0001) basal	a ⟨1̄21̄0⟩	3	yes	1.00	1.00	1.00	1.00
m {101̄0} prism	a ⟨1̄21̄0⟩	3	yes	*	*	0.01	0.60
	c ⟨0001⟩	3	no	*	*	*	1.00
	c + a ⟨1̄21̄3⟩	6	no	*	*	*	2.00
r {101̄1} (+) rhomb	a ⟨1̄21̄0⟩	3	yes	4.00	2.00	*	1.50
	c + a ⟨1̄1̄23⟩	6	no	5.00	2.00	2.00	2.00
z {011̄1} (−) rhomb	a ⟨1̄21̄0⟩	3	yes	*	2.05	*	1.55
	c + a ⟨1̄1̄23⟩	6	no	*	2.05		2.05
{21̄1̄1}, {112̄1} trigonal dipyramid	c + a₂ ⟨1̄21̄3⟩	6	no	*	*	*	*
	c + a₃ ⟨1̄1̄23⟩	6	no	*	*	*	*
{21̄1̄2}, {112̄2} trigonal dipyramid	c + a ⟨1̄1̄23⟩	6	no	*	*	*	*

*denotes that the CRSS value is sufficiently high to prevent activation of the system.

(Lister et al., 1978)
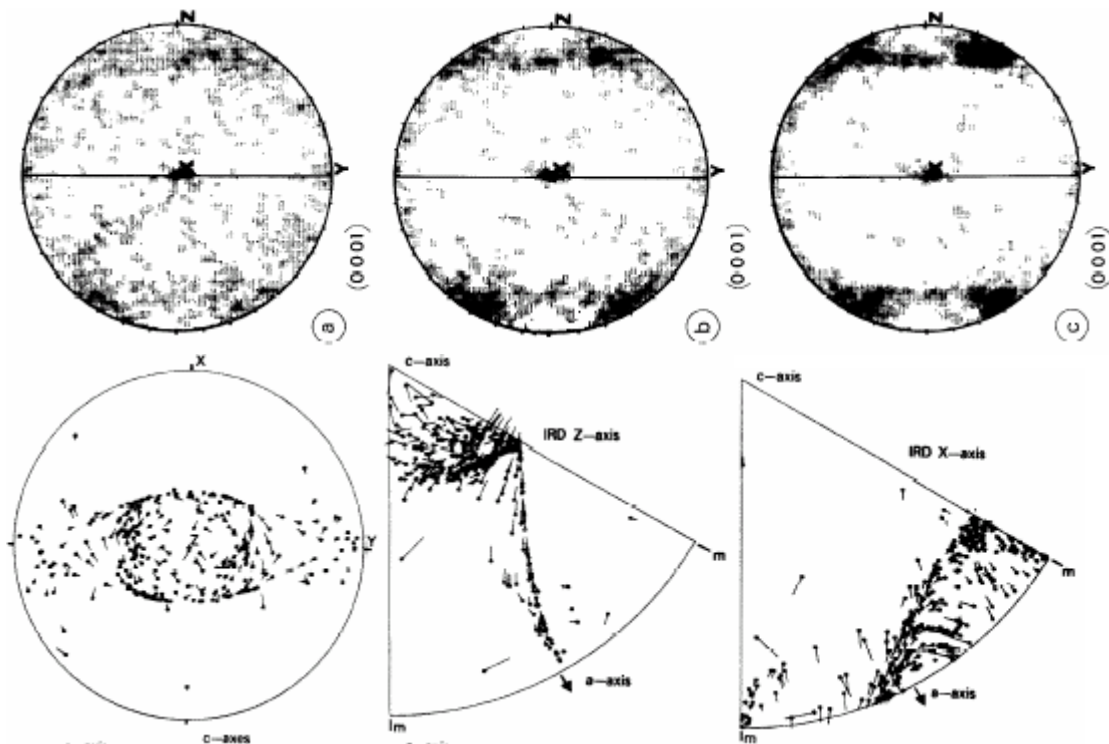
An example of how individual c axes rotate during the model. Plane strain, model I quartzite (basal + r-rhomb): (top) three stages of c axis rotation. (bottom): c axis rotation; IPF of Z-axis rotation and IPF of X-axis rotation (Lister et al., 1978).
Lister et al. showed that 40% shortening is sufficient to overprint existing LPO.

Fabric intensity related to strain in natural quartzite
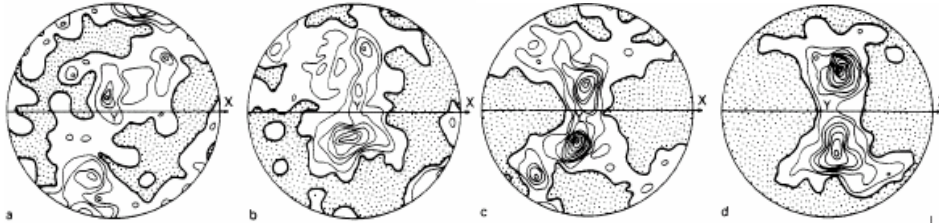
Shear strain increases from 0.2 to 2.5 from L to R (Hara et al., 1973)
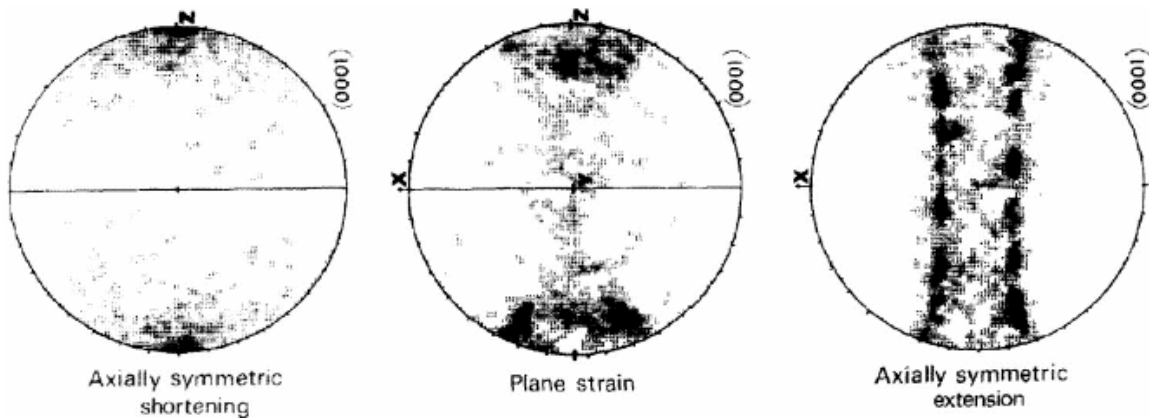
Computed effect of strain path for model I quartzite (Lister et al., 1978). In coaxial strain paths there is a simple relationship between strain symmetry and the pattern of quartz c- and a-axis fabrics that develop, the fabric strengthening but not changing in pattern with increasing strain).

LPO Depends on Which Slip Systems are Active
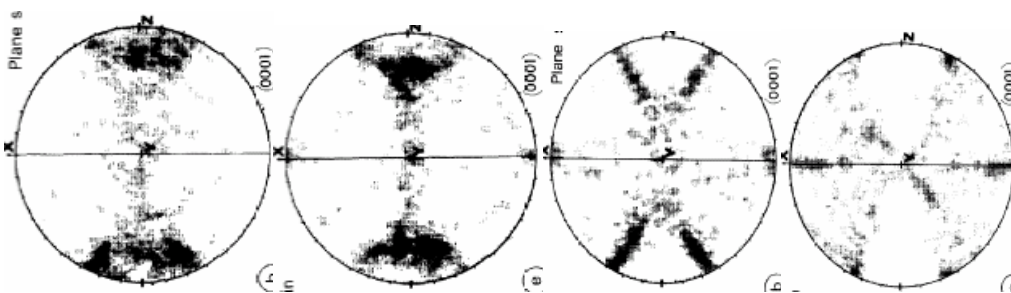
computed effect of different slip systems for plane strain. model I (basal + r-rhomb), model II (basal + z-rhomb), model III (basal +prism +r-rhomb), model IV (basal + prism + r-rhomb + z-rhomb) (Lister et al., 1978)
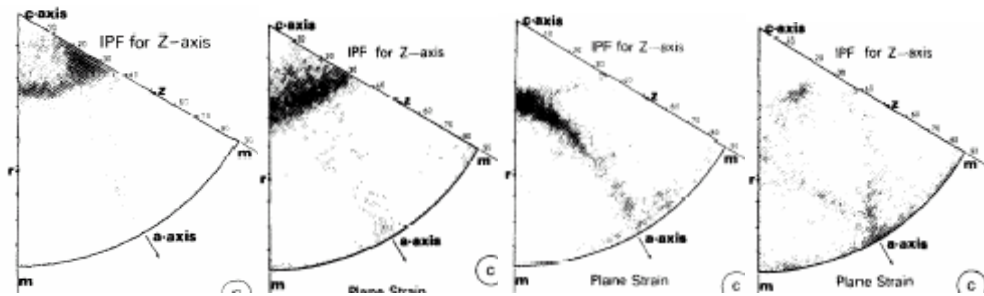
ditto, but IPF

LPO Can Be Used to Assess Strain Path
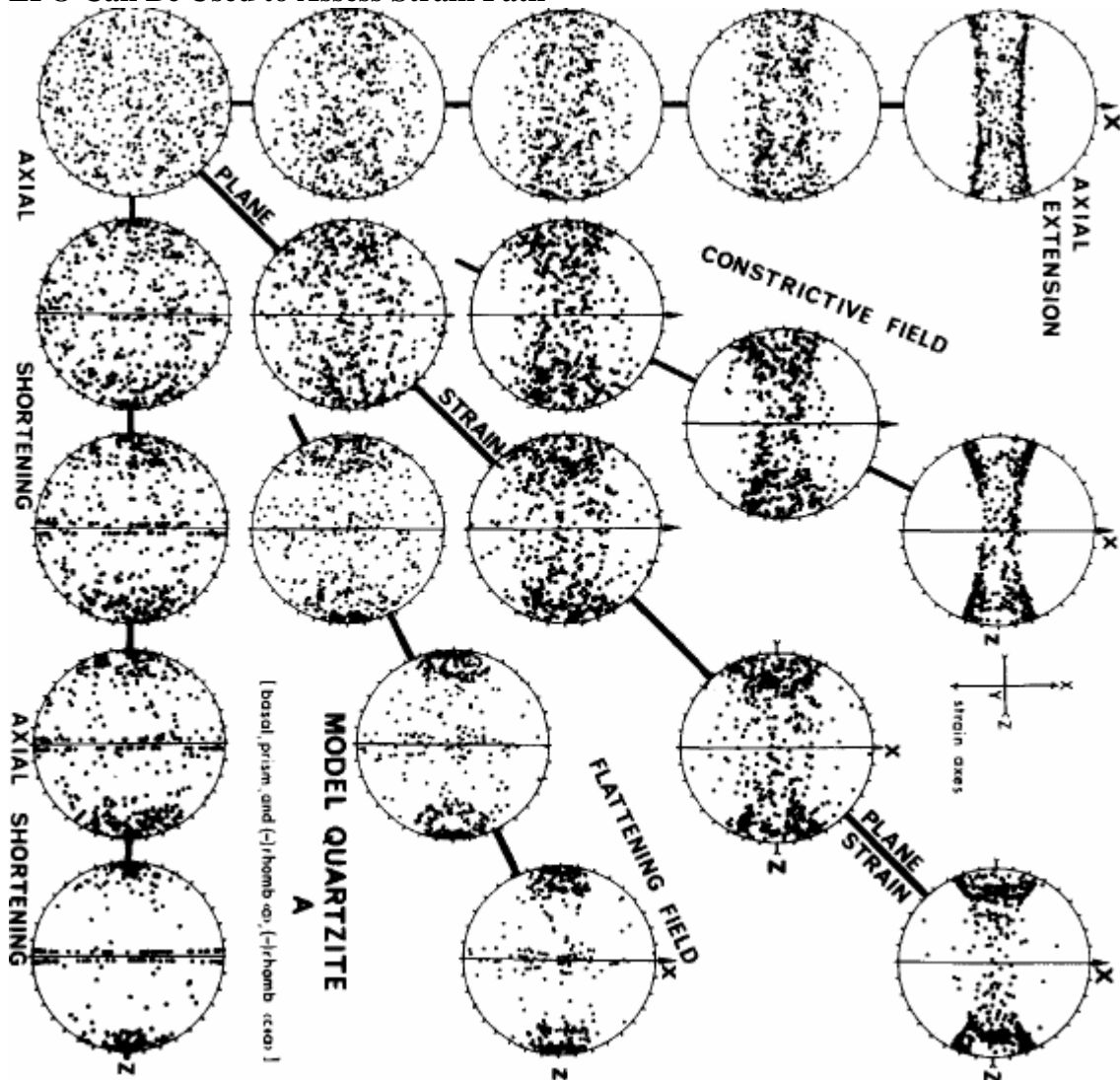
Evolution of fabric with strain for model quartzite with soft basal and hard r-rhomb and prism (Lister & Hobbs, 1980)
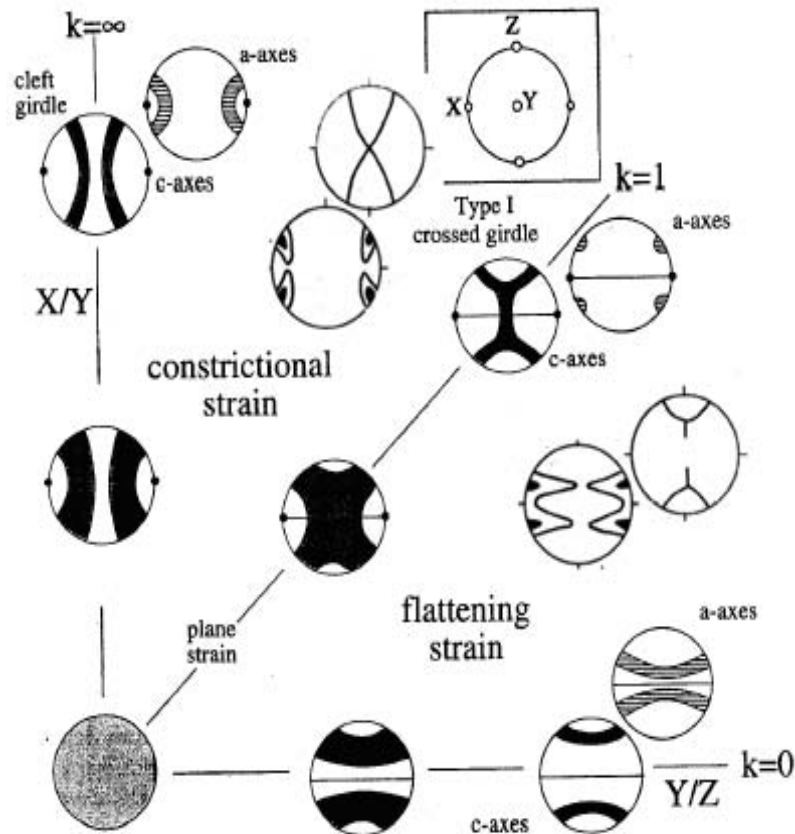
Summary diagram: LPO can be used to assess strain symmetry where no other markers are available (after Schmid & Casey, 1986; Passchier & Trouw, 1996)

LPO Can Be Used to Assess Whether Strain History is Coaxial or Non-coaxial
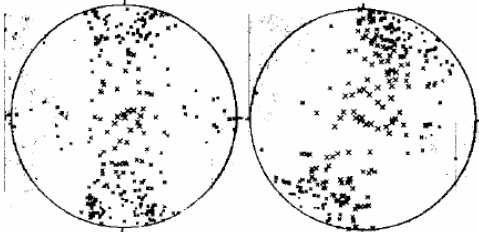
self-consistent theory pure shear and simple shear (Wenk et al., 1989)

In simple shear, grains do not rotate to a final orientation, but rather continue to rotate with accumulating strain. The grains rotate quickly when they are not in the preferred orientation, and rotate slowly while they are in the preferred orientation. Thus a steady state LPO is maintained.

Experiments Show Fabric Asymmetry Related to Non(coaxiality)
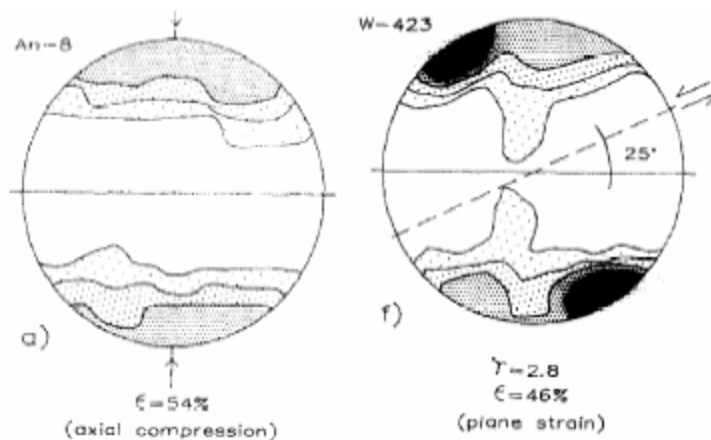
axial compression vs. near-simple shear (Dell'Angelo & Tullis, 1989)
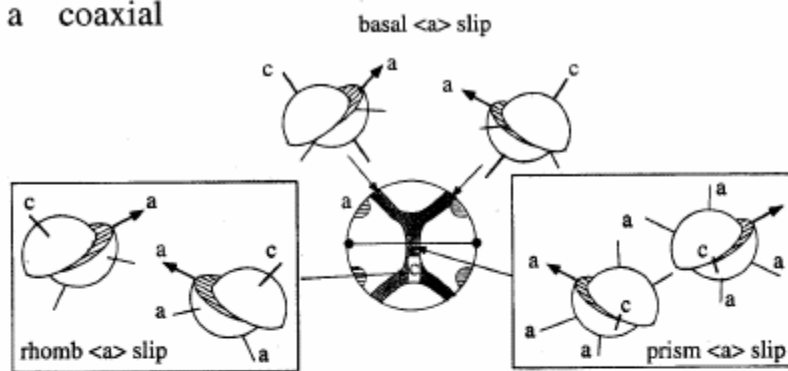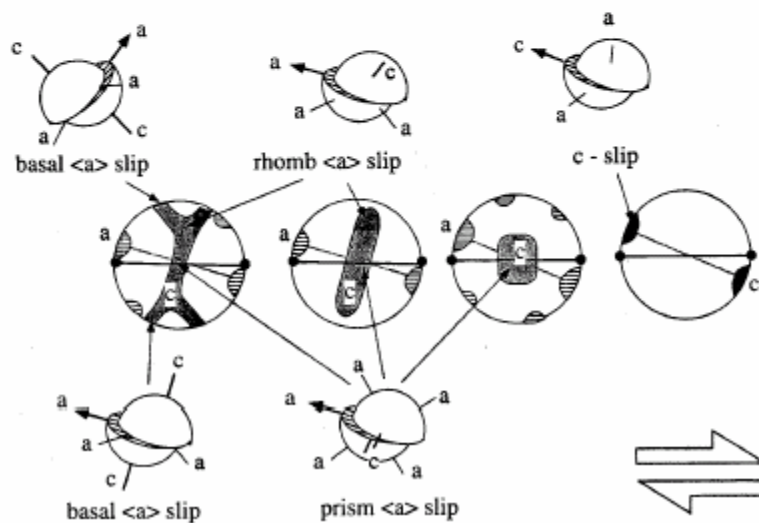
(Passchier & Trouw, 1996)

Evolution of Fabric Skeleton with Non-coaxial Strain

non−coaxial component of strain path increasing

or: increasing strain in simple shear
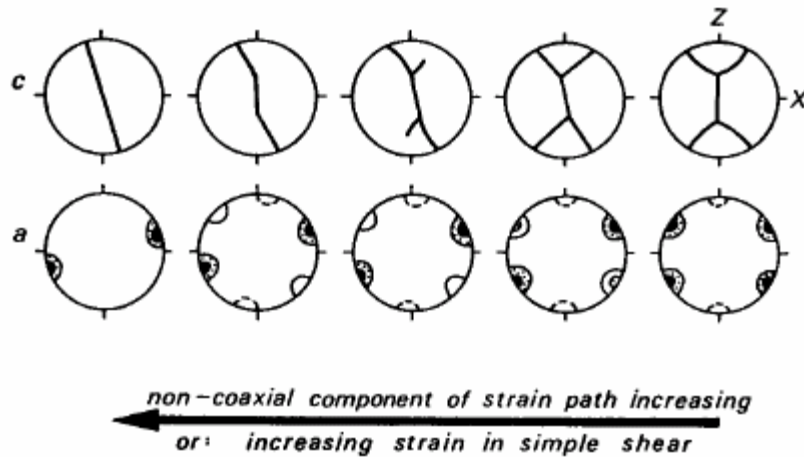
(Law, 1990; after Schmid & Casey, 1986).

The development of a crystallographic fabric is a function of strain path, magnitude of finite strain, and slip systems (Law, 1990)
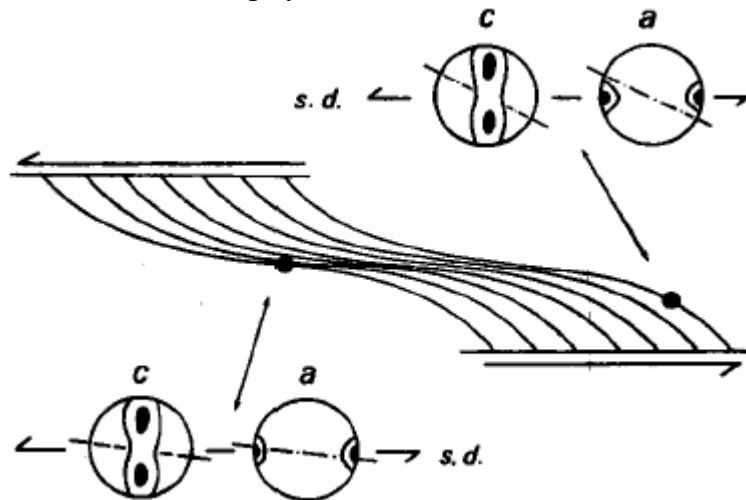
In non-coaxial strain paths the skeletal outlines of crystal fabrics remain in a constant orientation with respect to the imposed kinematic framework, although the fabric intensity changes with increasing strain magnitude. Thus it is the kinematic framework (and ultimately the imposed stress field) together with available crystal slip systems, rather than finite strain, that controls the orientation and pattern of crystal fabric. (Law, 1990). The asymmetry between the a-axis maximum and the foliation can be used as a sense of shear indicator. Tempting to use as a quantitative marked of strain magnitude, but usually under-predicts the shear strain.

Assessment of Strain Path Symmetry in the Earth: Tarskavaig
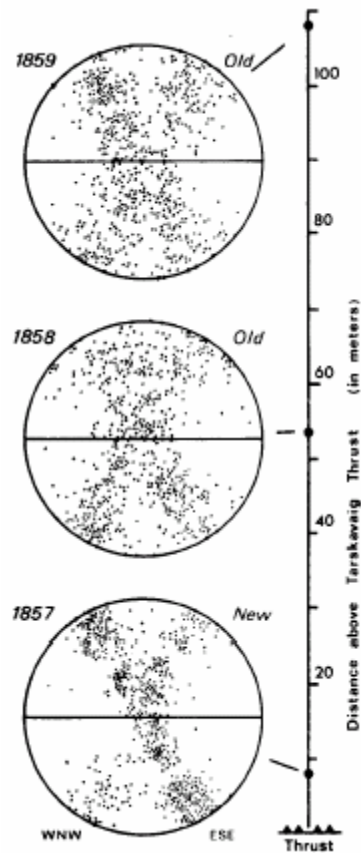
greenschist-facies Tarskavaig thrust shows increasing asymmetry downward toward basal thrust (Law & Potts, 1987)

Assessment of Strain Path Symmetry in the Earth: Torridon
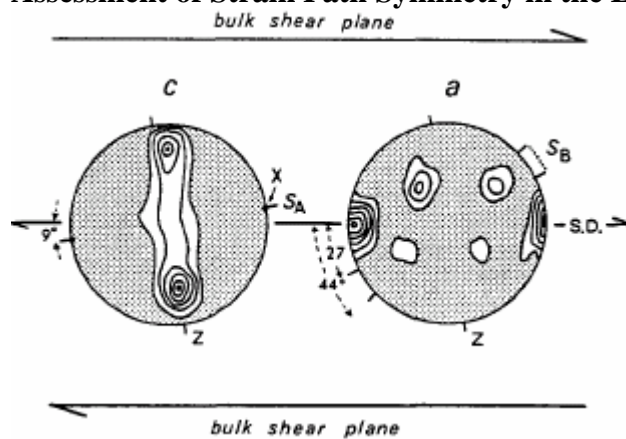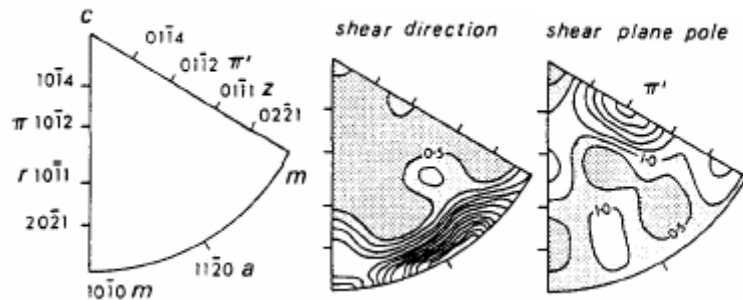
A single vein subjected to simple shear shows girdle of c axes with 2 maxima, single a axis maximum, shear direction parallel to <a> and shear plane parallel to the r-rhomb (Law et al., 1990)

Assessment of Strain Path Symmetry in the Earth: Moine
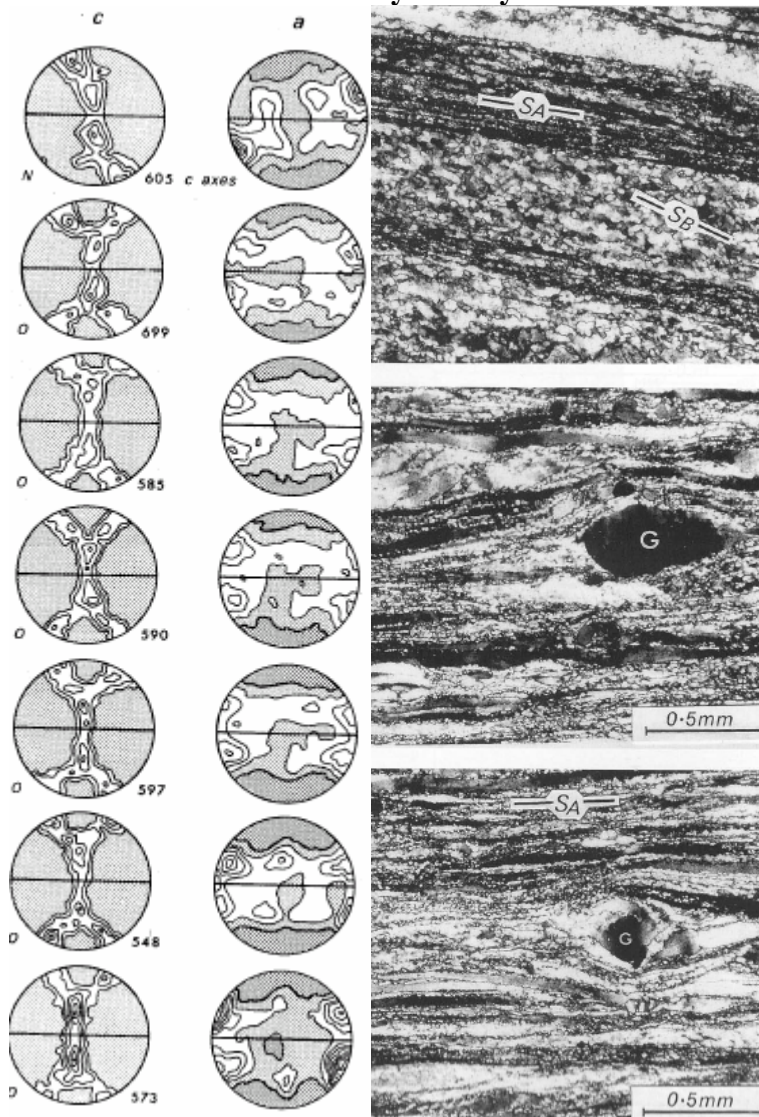
vertical section beneath Moine thrust shows increasing asymmetry right at thrust (Law et al., 1986)

Assessment of Strain Path Symmetry in the Earth: Tauern Window
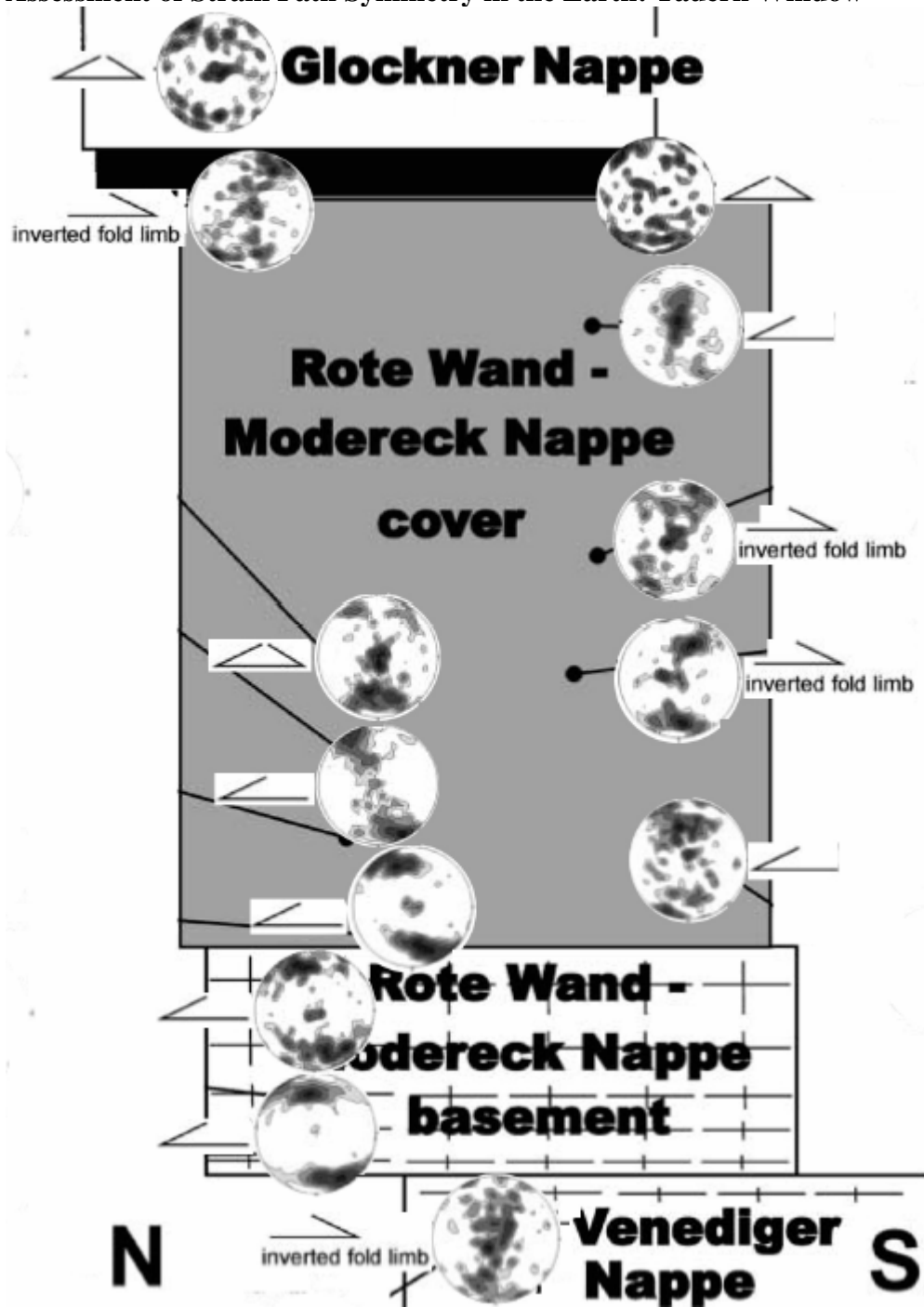
(Kurz et al., 2001)

Assessment of Strain Path Symmetry in the Earth: Cap de Creus
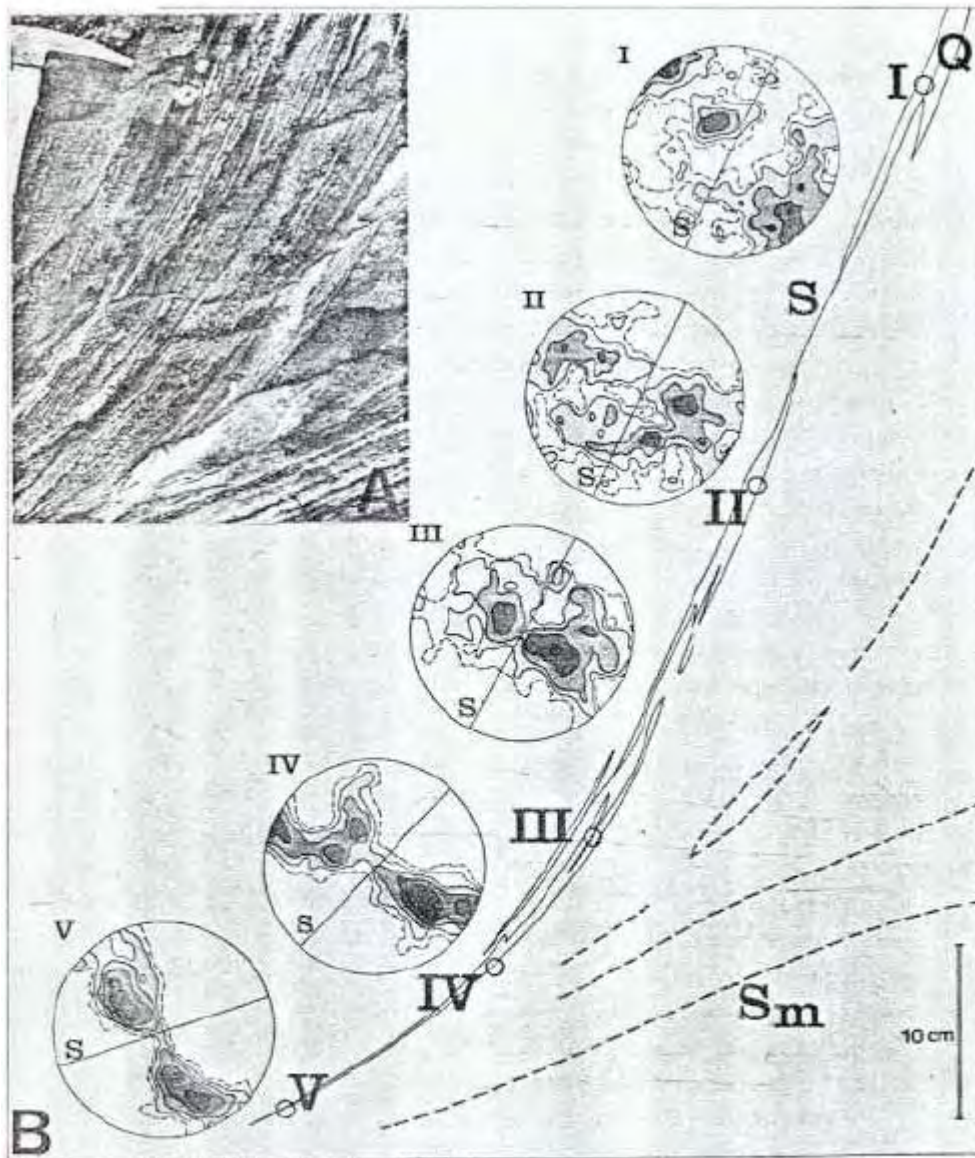
Fig.2 Progressive development of the c-axis fabric at the margin of a shear zone. A. The outcrop from which the quartz specimens in B where selected. The progressive bending of the earlier metamorphic schistosity into approximate parallelism with the trend of the shear zone is shown. B. Development of the c-axis fabric with increasing shear strain. (Lower hemisphere, 200 grains, contours: 0.5-1-2-4-8 %, Sm = mylonite foliation, S = schistosity of the country rock. Approximate shear strains are: I = 0.25, II = 0.3, III = 0.5, IV = 1.2 and V = 8).

Fabric intensity and asymmetry development (Carreras et al., 1977)

Assessment of Strain Path Symmetry in the Earth: Solidus Temperatures
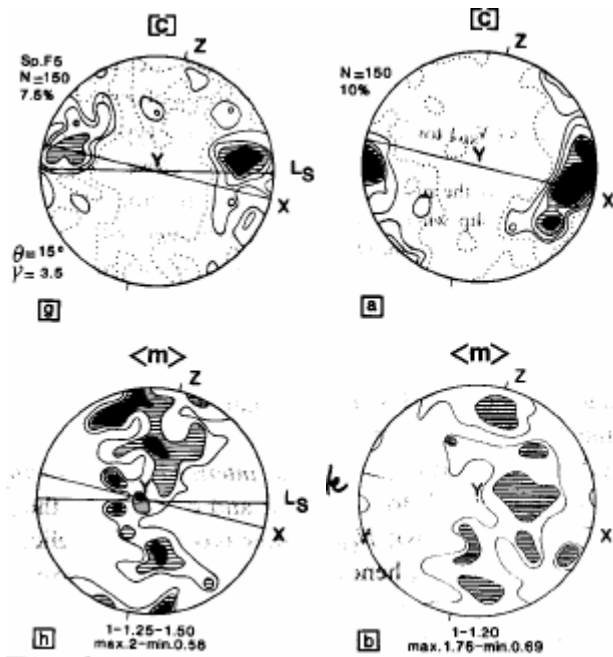
700–800°C granite shows LPO with [c] parallel to shear direction. (0001) tilt boundaries and free dislocations with b=[0001] (Blumenfeld et al., 1986)

Shape Preferred Orientations (SPO)
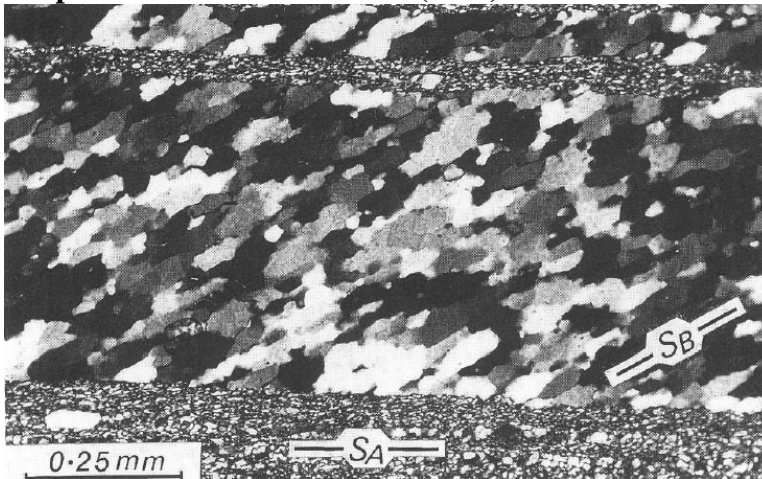
Oblique SPO (Law, 1998)
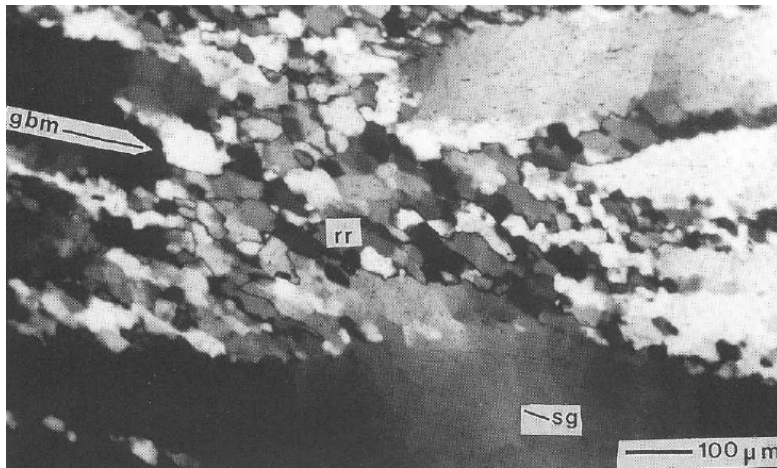
Regime 2 from Orocopia Schist (Simpson, 1998)

Shape Preferred Orientations: East Humboldt Range
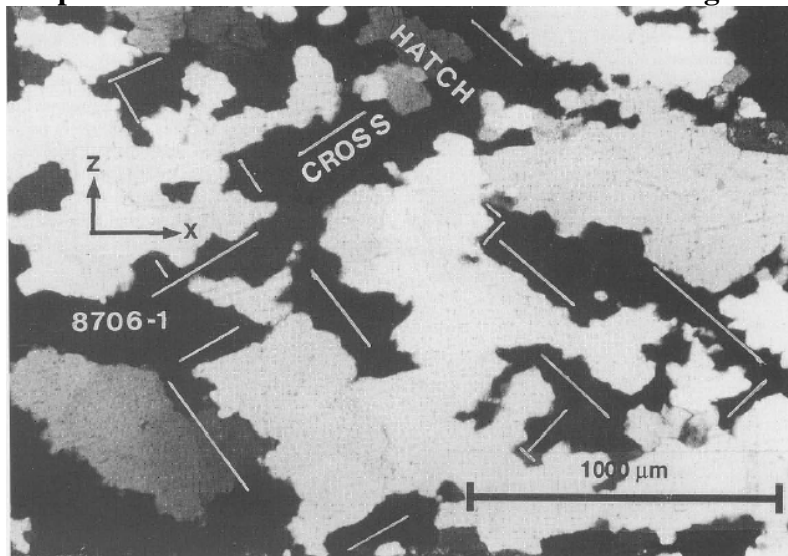
Gneissic quartzite from E Humboldt Range. Regime 3 GBM. Cross-hatch texture is characteristic of high T; white lines show orientations of basal planes. (McGrew & Casey, 1998)

Upper Domain

Lower Domain

300°-4°

8727-3

1.0 mm

8727-3

S

Z

X

1000 μm

C-axes
8727-3

Z

a

S

C

S=292
27
3004

X

b

a

S

Minimum: 0.00
Maximum: 13.8

Contours:
1.0, 2.0, 3.0, 4.0,
5.0, 6.0, 7.0, 8.0, 9.0,
10.0, 11.0, 12.0, 13.0

Poles to m
8727-3

Z

b

a

a,b

a

Minimum: 0.00
Maximum: 7.1

a-axes
8727-3

Z

b

a

a,b

b

Equal Area
Upper Hemisphere
Projections

Minimum: 0.00
Maximum: 7.0

Poles to r&z
8727-3

z a,b

a,b

X

Minimum: 0.00
Maximum: 4.8
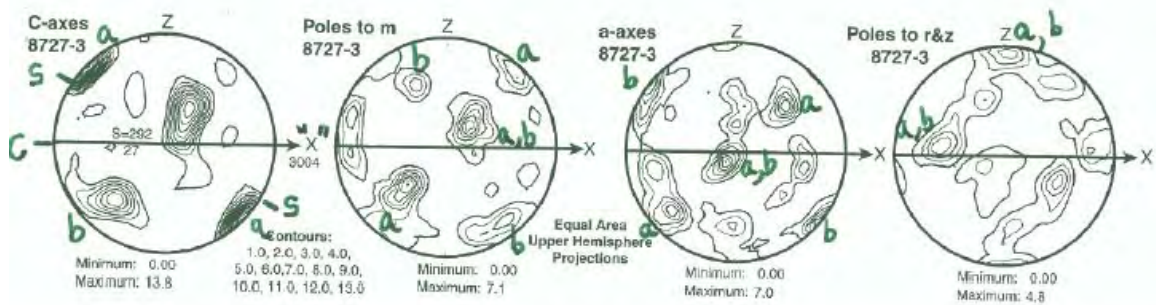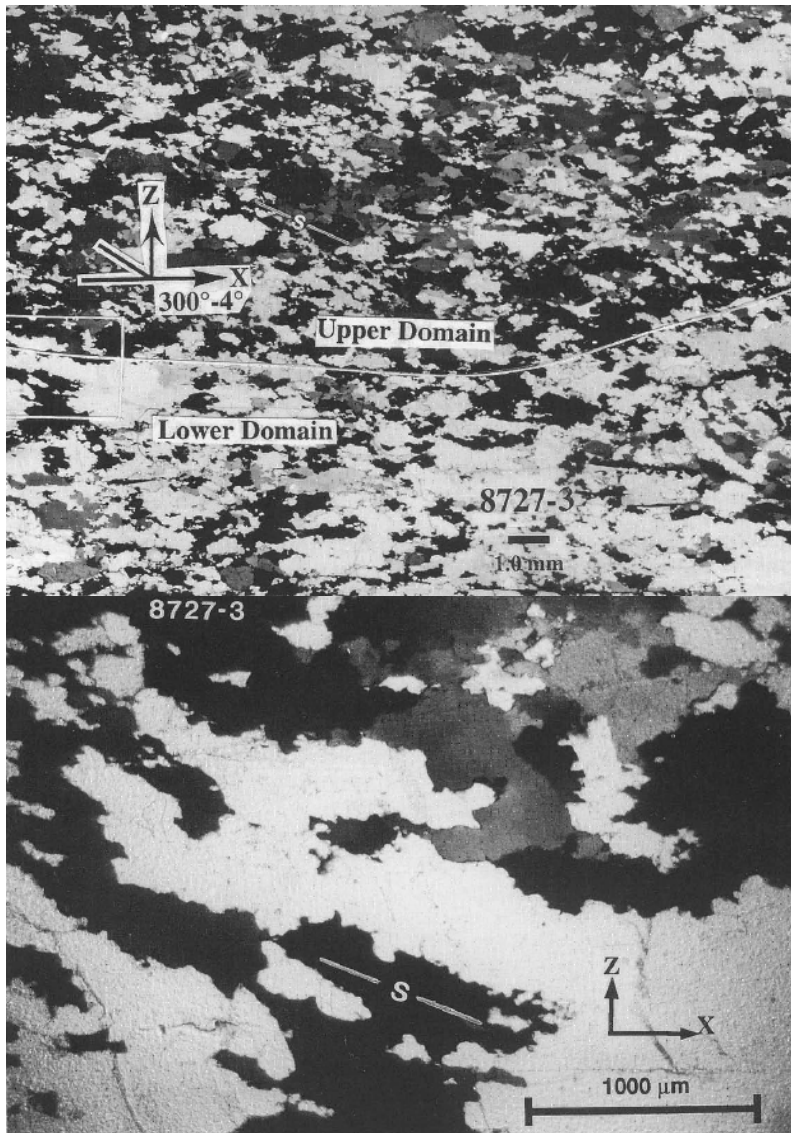
Asymmetric fabrics in gneissic quartzite from E Humboldt Range. Regime 3 GBM. Rhomb slip. (McGrew & Casey, 1998)

Diffusion Creep and Grain-Boundary Sliding

Diffusion Creep Mechanisms

Three diffusion creep mechanisms (Evans & Kohlstedt, 1995):
- volume diffusion
- grain-boundary diffusion
- grain-boundary reactions
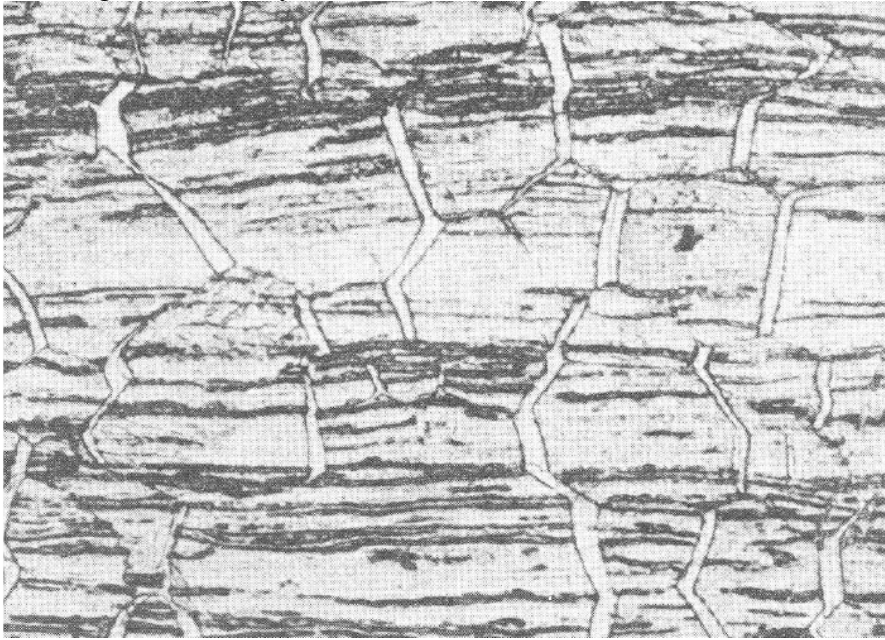
diffusion creep in Zr alloy (Poirier, 1985)

Volume-Diffusion Creep or Nabarro–Herring Creep
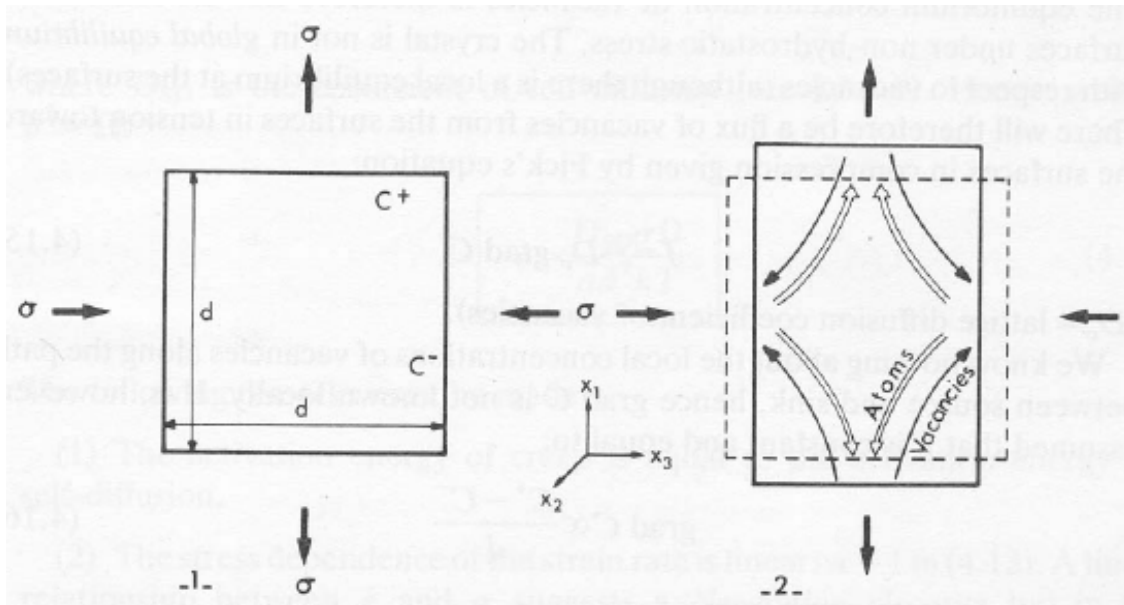
Fig. 4.10. Nabarro-Herring creep. Cubic crystal subjected to a pure shear; vacancies flow from the faces in tension where their concentration C^+ is higher, to the faces in compression where their concentration C^- is lower. Matter flows in the opposite sense (see text)

(Nicolas & Poirier, 1976). A nonhydrostatic stress field gives rise to different vacancy concentrations on crystal faces of different orientations. This is important only if flux of vacancies is large, i.e., at high T and for small grain sizes (Poirier, 1985)

$$\dot{\varepsilon} = 14\left(\frac{\sigma\Omega}{RT}\right)\frac{D_{SD}}{d^2}$$

where D_{SD} is self diffusion and Ω vacancy volume ($\sim b^3$) (Nicolas & Poirier, 1976; Evans & Kohlstedt, 1995). Note that volume-diffusion creep is Newtonian (actually Bingham in that there is a threshold stress below which no creep occurs) and grain-size dependent, neither of which are true for dislocation creep.
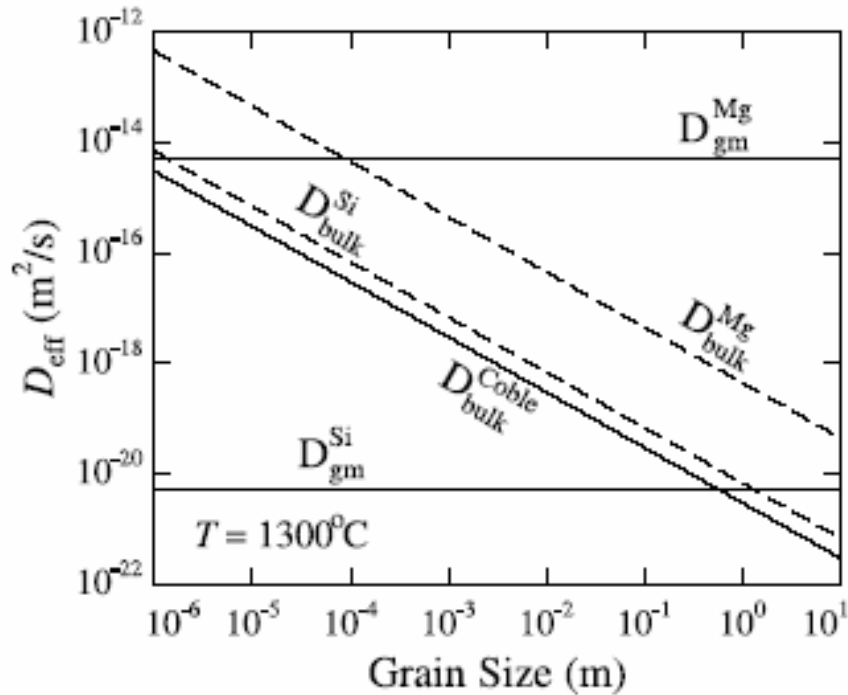
Diffusion creep in olivine is limited by grain-boundary diffusion of Si. This diagram shows that volume diffusion of Si (D_{gm}) is slower than grain boundary diffusion of Si (D^{Coble}) for grain sizes <1 m. Thus, volume diffusion (N–H) creep cannot occur in the mantle for grain sizes < 1 m (Hirth & Kohlstedt, 2003)

Grain-Boundary Diffusion Creep or Coble Creep

$$\dot{\varepsilon} = 44\left(\frac{\sigma\Omega}{RT}\right)\frac{\delta D_{GB}}{d^3}$$

where D_{GB} is GB diffusion, δ is the grain boundary width, and Ω vacancy volume (Nicolas & Poirier, 1976; Evans & Kohlstedt, 1995). Note that grain-boundary diffusion creep is Newtonian and grain-size dependent, neither of which are true for dislocation creep. Because the activation energy for grain boundary diffusion is less than that for volume diffusion, GBD creep can occur at lower temperatures.
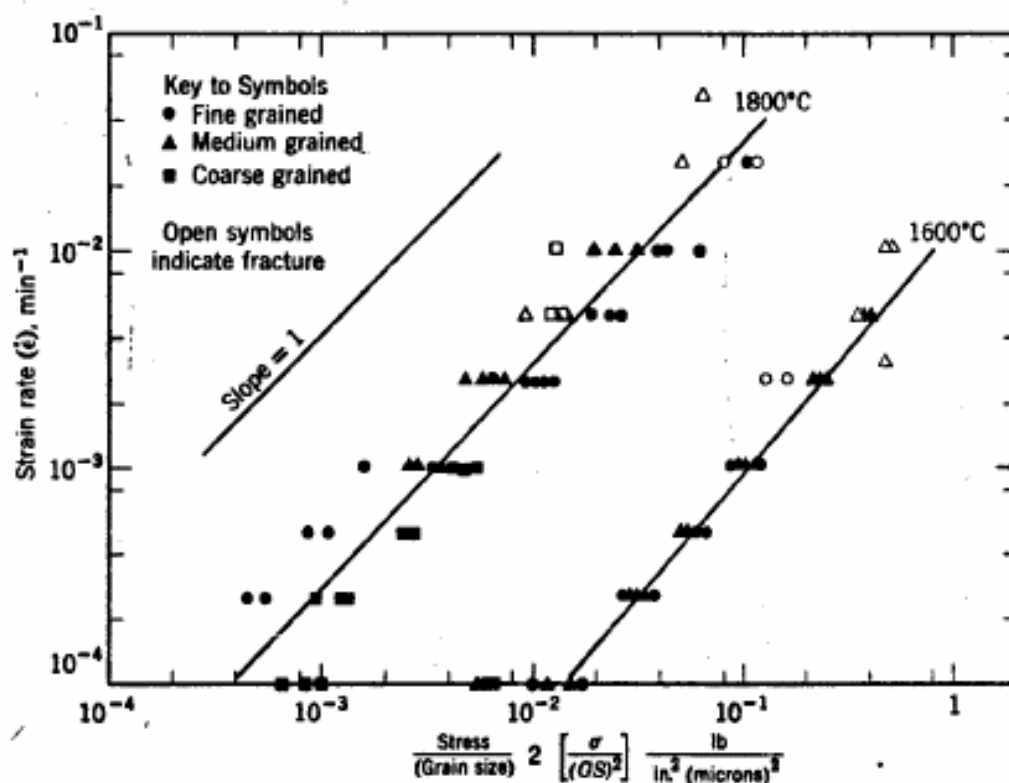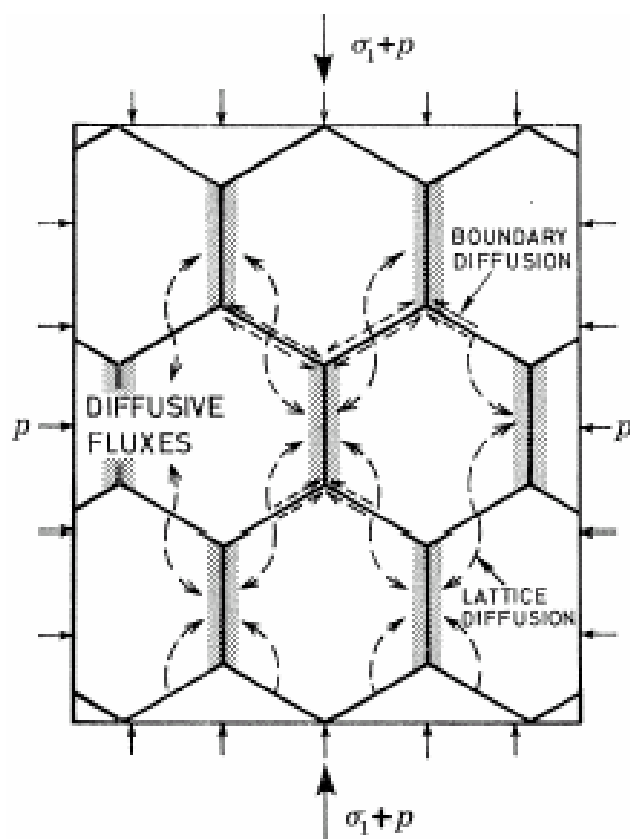
Fig. 18.3 Strain rate versus stress divided by grain size squared for polycrystalline alumina [Folweiler (9)].

Works for Al (Coble, 1965)

Grain-Boundary Sliding (GBS)
During pure Coble or Nabarro–Herring creep, grains must change shape, lengthening the transport path. If the transport path is to remain as small as possible, the grains must remain equant. If the grains are to remain equant and in contact, grain-boundary sliding must occur.
\
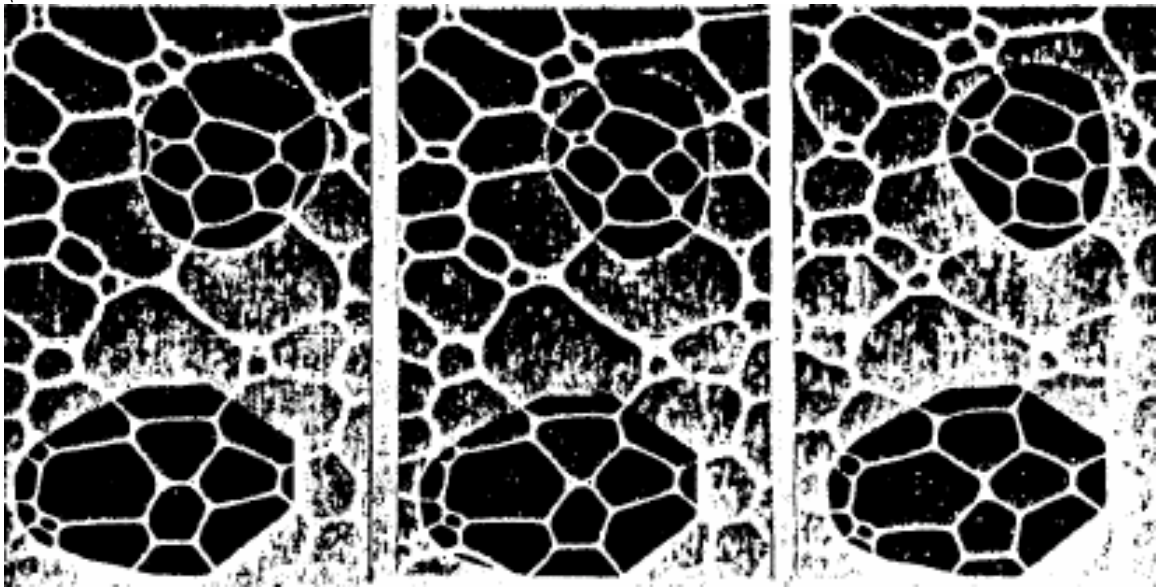
grains in an emulsion changing neighbors (Ashby & Verrall, 1977). Grains can slide past one another if material continuity is provided by dislocation creep or diffusion creep.
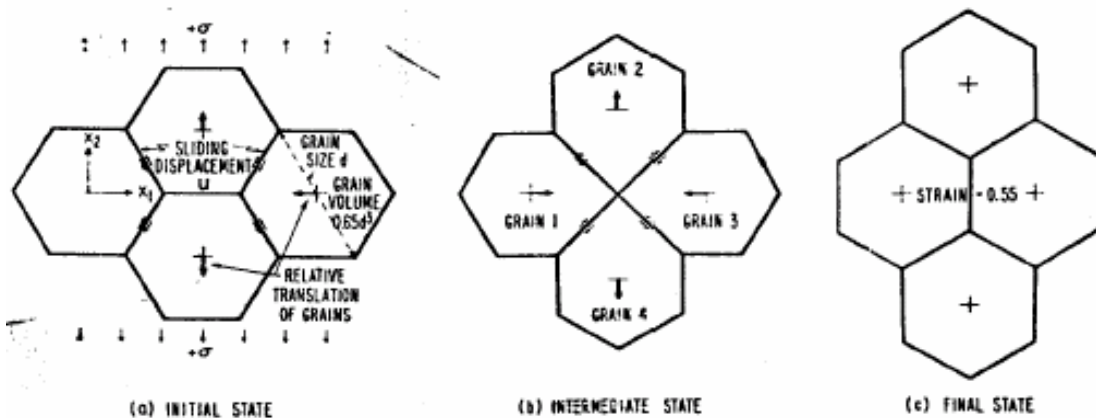
Diffusion-accommodated GBS: grains switch neighbors and do not change shape. This is a fundamental difference from Coble or Nabarro–Herring creep (Ashby & Verrall, 1977)
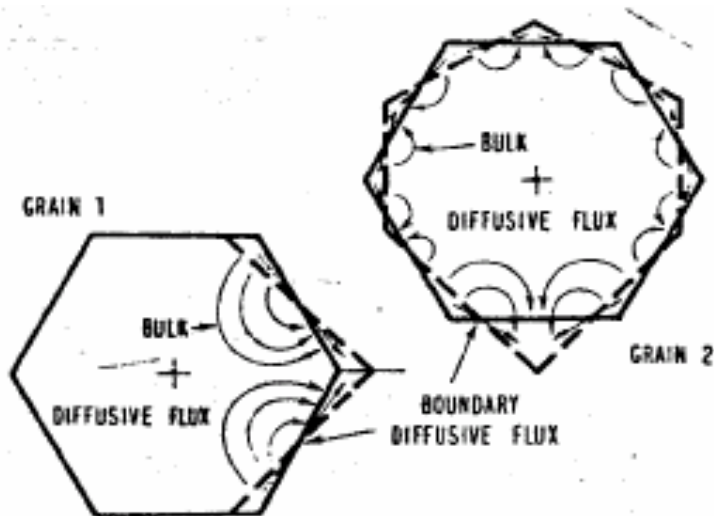
accommodation strains required when grains switch neighbors (Ashby & Verrall, 1977)
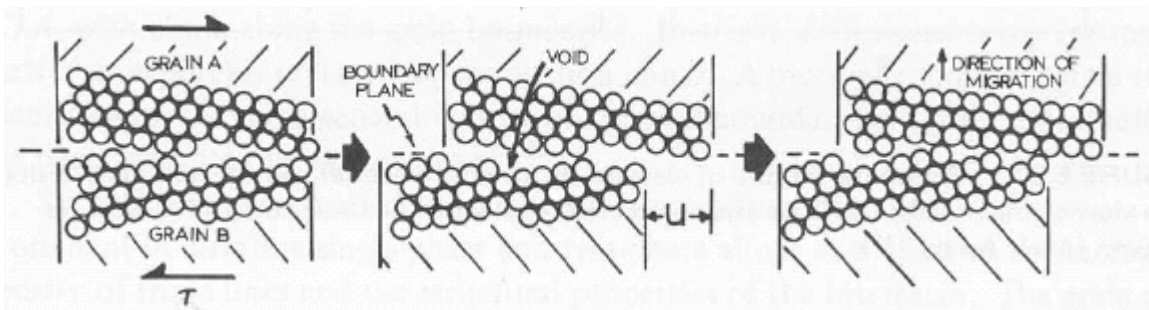
(Murr, 19xx)

Microstructural criteria for identifying GBS:
- equant grains (helps grains to rotate; Sherby, 1984)
- diamond or rectangular grains (grain boundaries can be subjected to high shear stress; Sherby, 1984)
- continuous alignment of grain boundaries over several grain diameters
- grain boundaries decorated with voids or a second phase (second phase helps maintain a fine grain size; Sherby, 1984)
- grain size comparable or smaller than the equilibrium subgrain size (possibly because of pinning by voids or a second phase)
- misorientations between adjacent grains are random and span all possible angles, whereas grains related by dislocation creep tend to have preferred, relatively low–moderate angle misorientations
- weak LPO (Fliervoet et al., 1997)
- both strong and weak phases in a rock have equant shapes, whereas one would expect the weak phase to be squished in dislocation creep (Stünitz & Fitz Gerald, 1993)
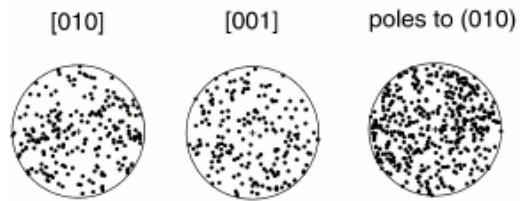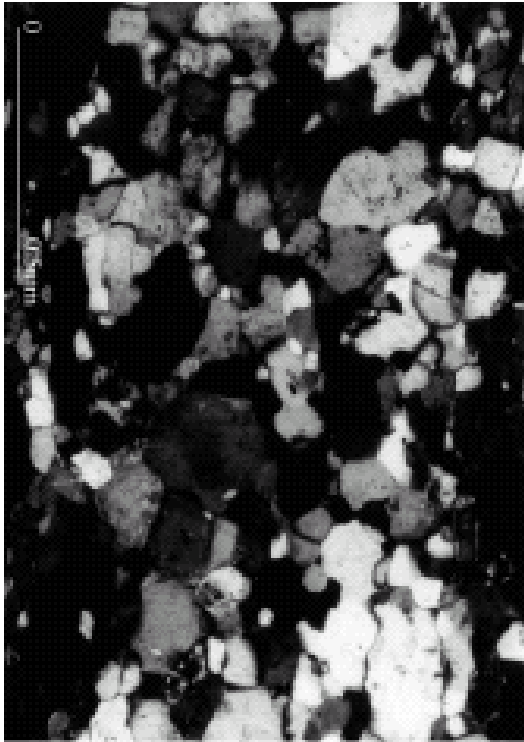
amphibolite-facies 100–250 µm anorthosites show no LPO, suggesting GBS (Lapworth et al., 2002)
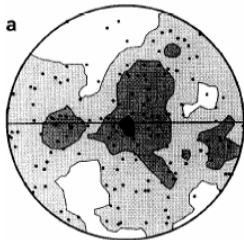
(quartz [0001] shown) quartzofeldspathic mylonite zones at greenschist facies and amphibolite facies have equant µm-sized grains with a weak LPO, suggesting GBS (Fliervoet et al., 1997)
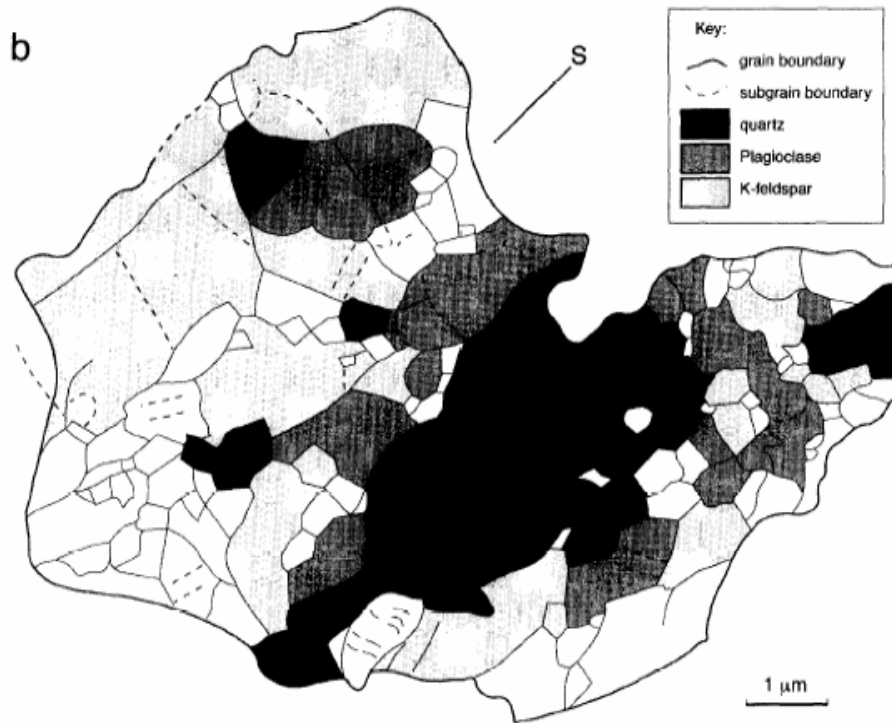
aligned grain boundaries over several grain diameters (Fliervoet et al., 1997)
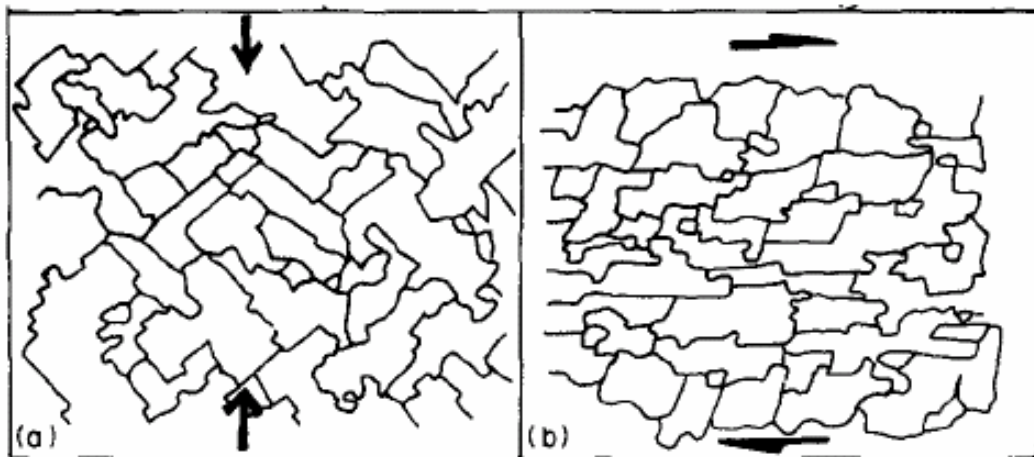
Fig. 4. Type M diamond and tabular grain structures. (a) Coaxial deformation and (b) simple shear deformation.

(Drury & Humphreys, 1988)
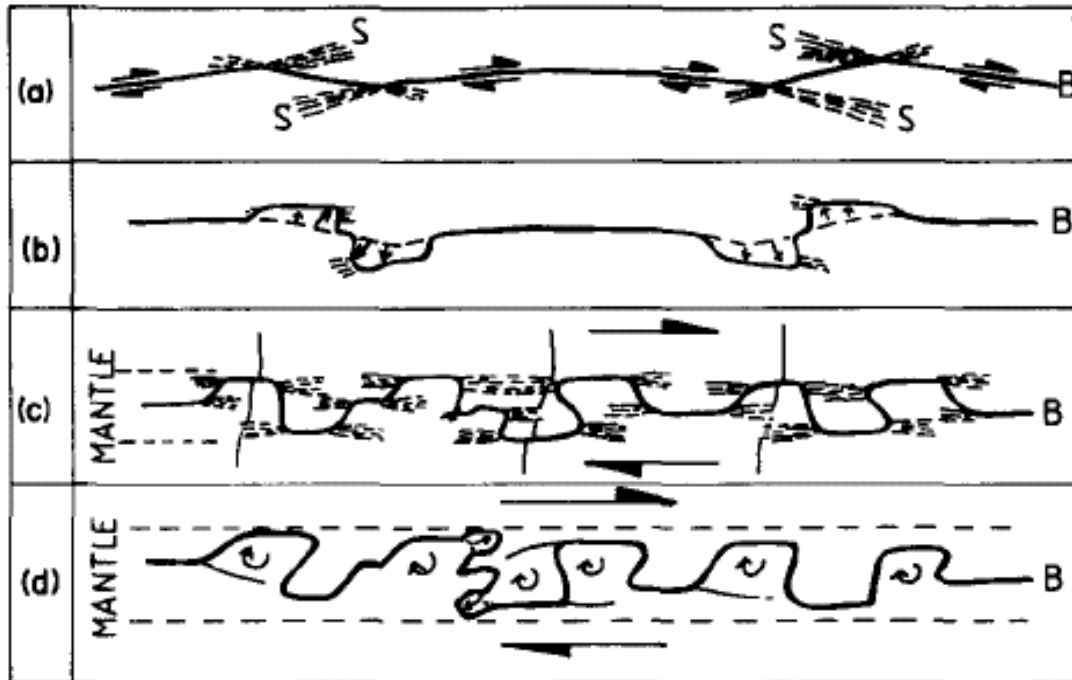
Fig. 2. Mechanism of formation of asymmetric bulges. (a) Deformation at the grain boundary B is accommodated by sliding and by non-uniform intragranular strain S adjacent to irregularities. (b) Local grain-boundary migration consumes zones of high defect density S, producing asymmetric bulges. The initial asymmetry depends upon the prior geometry of the irregularity. (c) Further deformation along the irregular boundary is accommodated by sliding along short segments and shear in the grain mantle. (d) Shear in the mantle modifies the shape of the bulges, amplifying the asymmetry of bulges with the same sense of shear as the sliding. Bulges with the opposite sense of asymmetry will be sheared to a more symmetrical geometry.

Sense of shear can be determined from rocks undergoing GBS. (Drury & Humphreys, 1988)
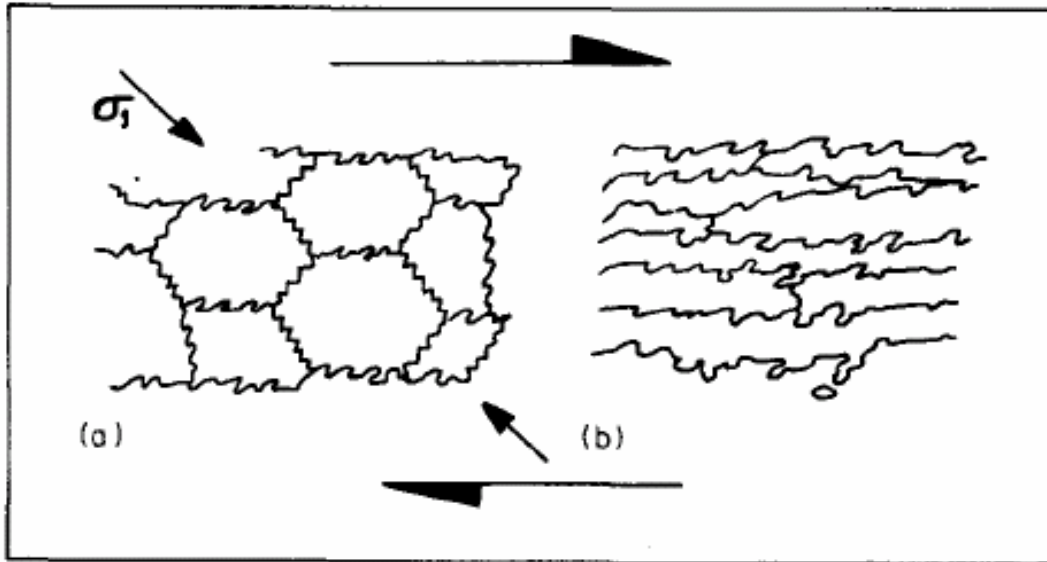
Fig. 3. Predicted geometry of grain-boundary bulges (developed by the mechanism shown in Fig. 2) for simple shear. (a) Low strain and (b) high strain.

Sense of shear can be determined from rocks undergoing GBS. (Drury & Humphreys, 1988)
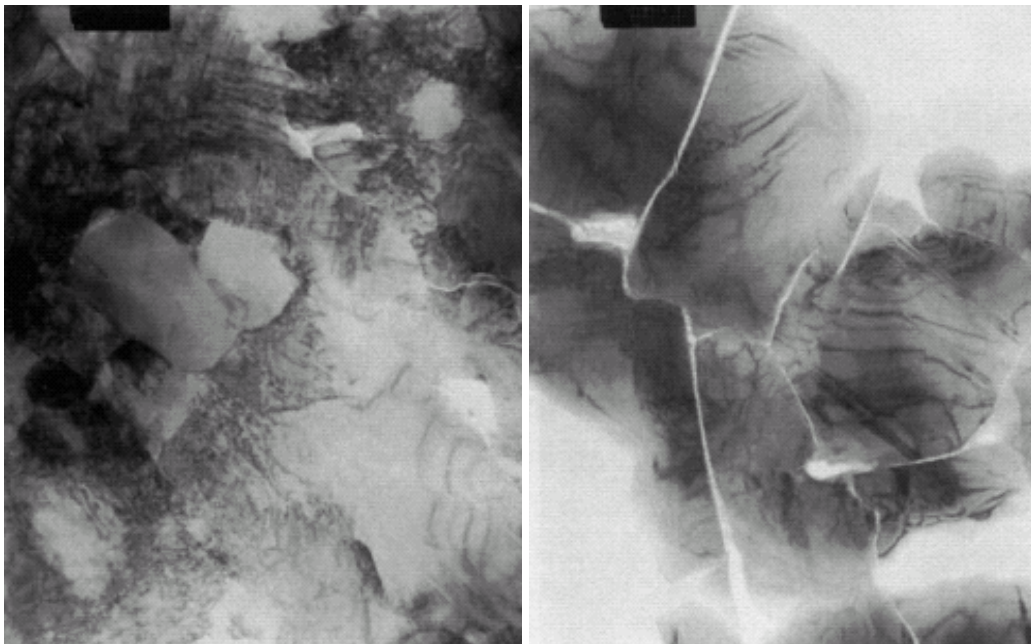
Addition of 0.9 wt% H_2O to a 2–10 µm albite causes a switch from (L) dislocation creep to (R) GBD creep. This was inferred from the lack of grain growth, lower dislocation density and presences of grain boundary pores (Tullis & Yund, 1991; 1996; Heidelbach et al., 2000)
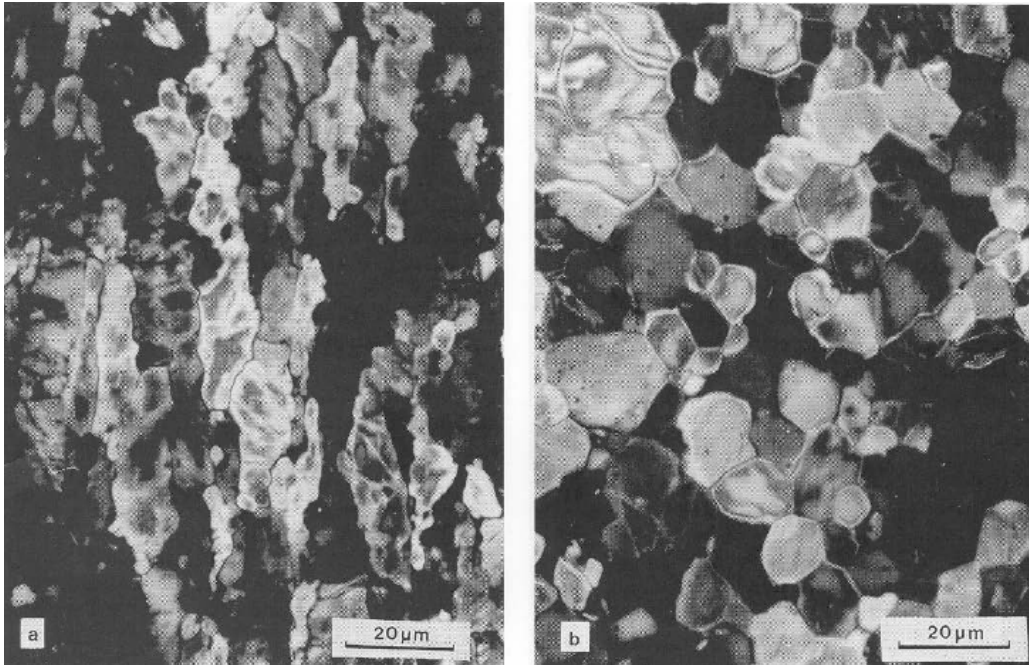
comparison of dislocation creep and diffusion creep fabrics in experimental marble (Walker et al., 1990)
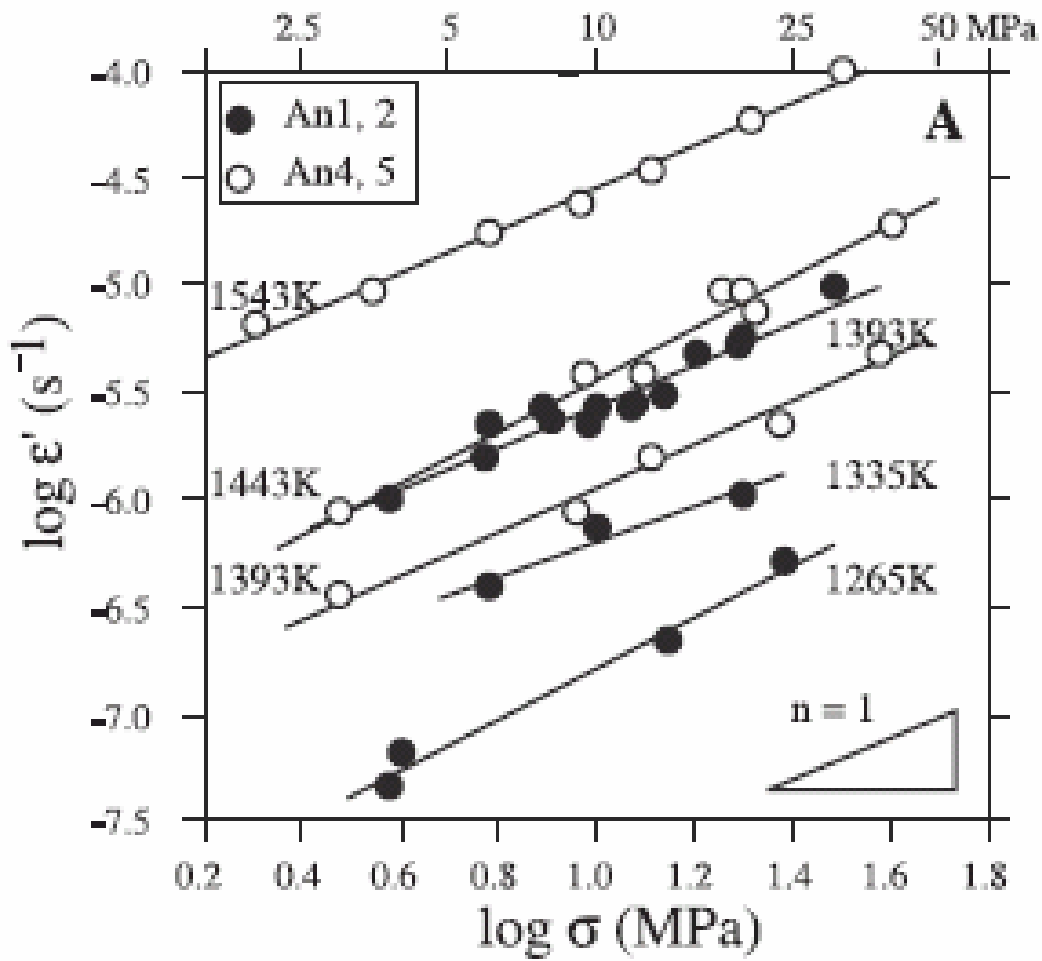
GBD creep in very fine-grained anorthite; note n = 1 (Dimanov et al., 2003)
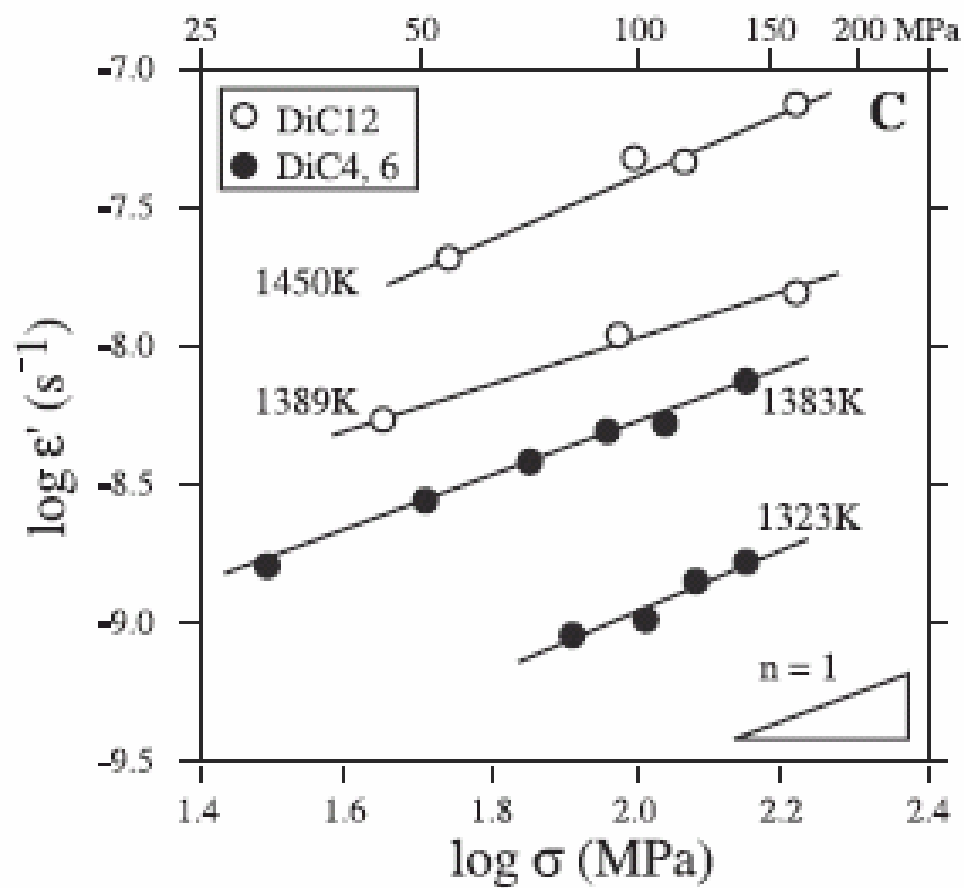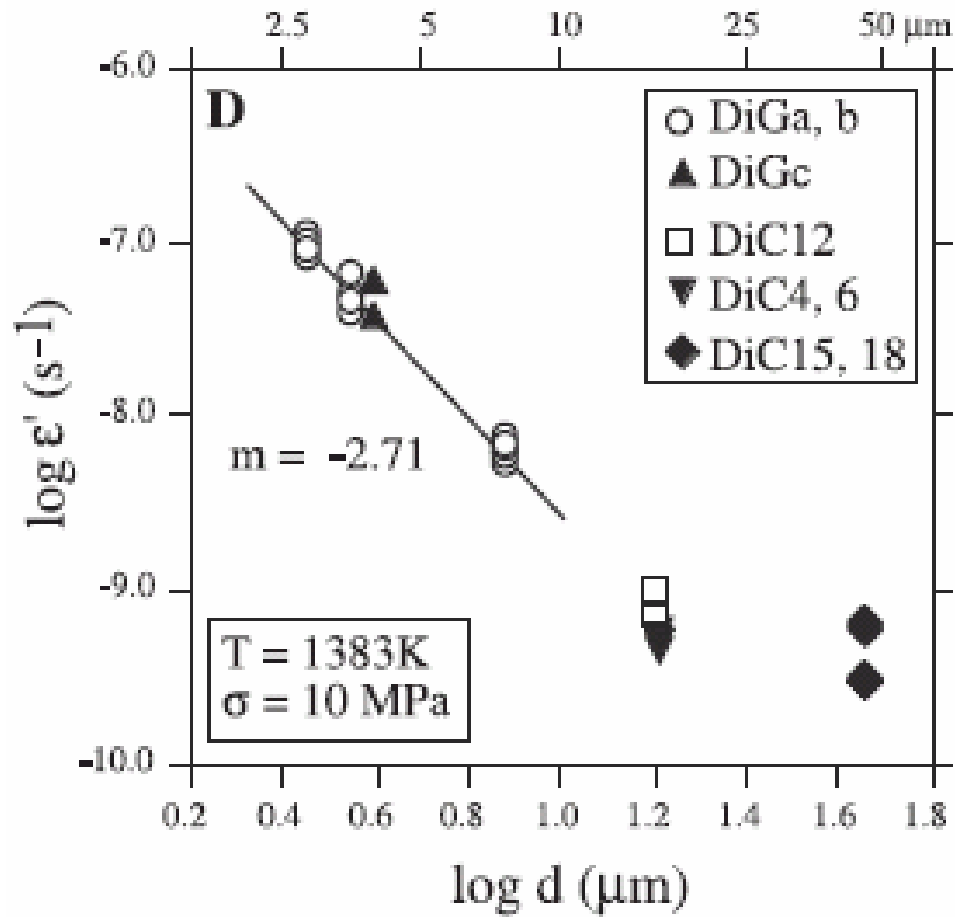
GBD creep in very fine-grained diopside; note n = 1 and m ~ 3 (Dimanov et al., 2003)

The plot shows:
- P = 450 MPa
- T = 1523 K
- σ = 26 MPa
- $a_{H_2O} \approx 1$
- m = -2.8

Axes: $\dot{\varepsilon}$ (s^{-1}) versus d (μm)
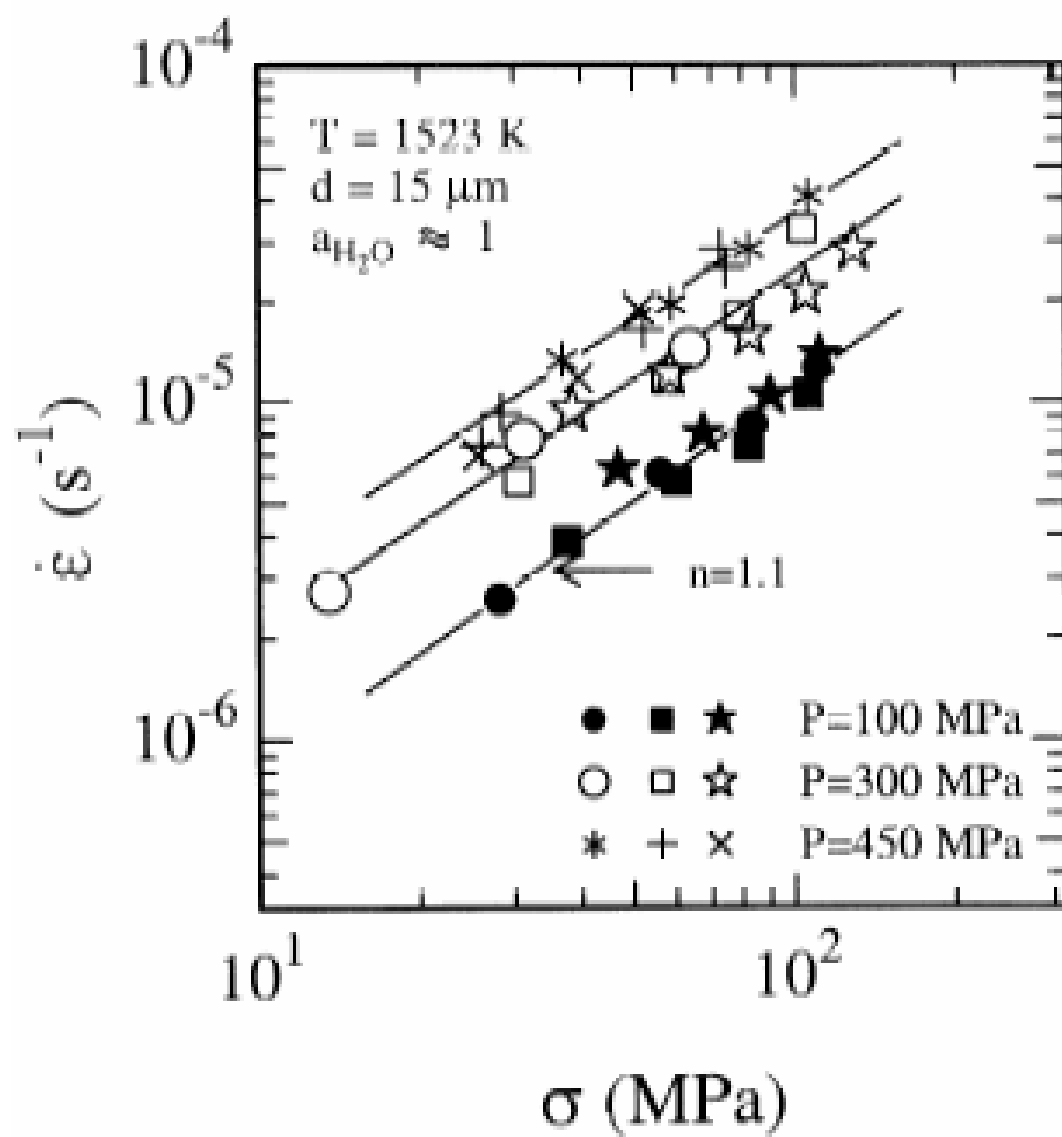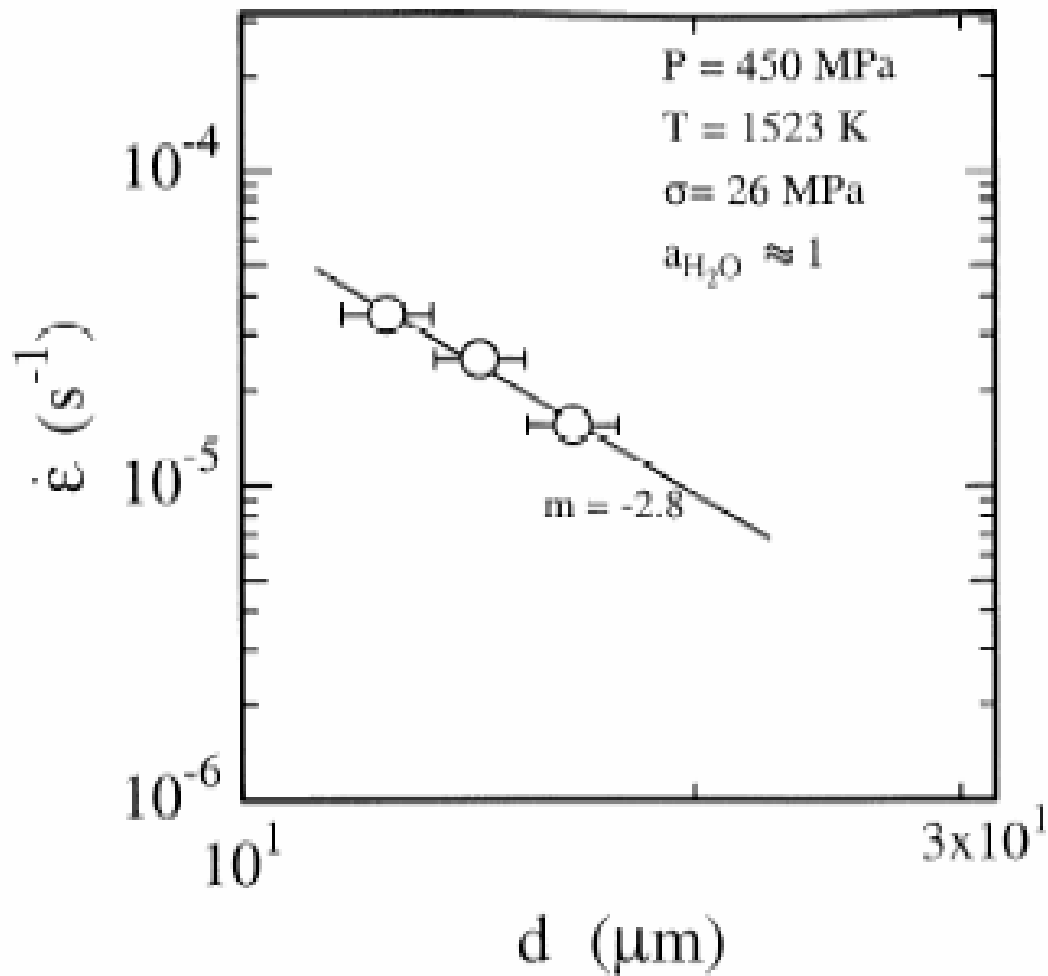
$$\dot{\varepsilon} = A \frac{\sigma^n}{d^m} f^r_{H2O} \exp(-Q/RT)$$

diffusion creep of olivine gives A = 1.3E5 μm^3 MPa$^{-1.8}$ s^{-1}, n=1.1, m = 3, r = 0.7, Q = 295 kJ/mol (Mei & Kohlstedt, 2000)

Grain-Size Sensitive (GSS) Creep, Grain-Size Insensitive (GSI) Creep & Deformation-Mechanism Maps
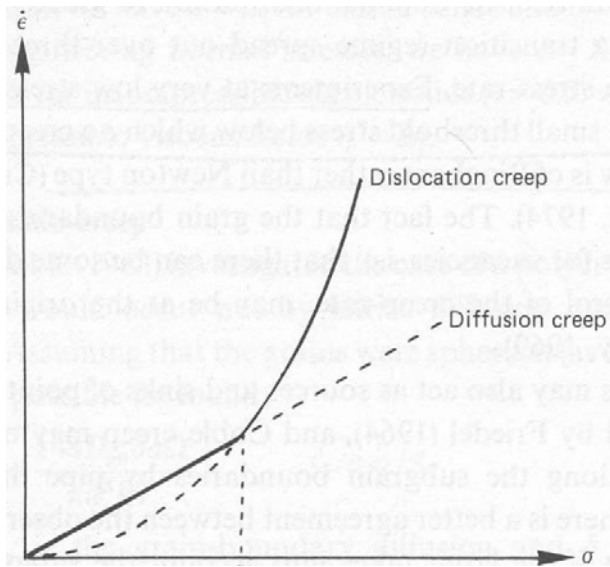
stress-strain diagram showing Newtonian behavior of diffusion creep and power-law behavior of dislocation creep. The transition from dislocation creep to diffusion creep is controlled by stress (diffusion creep is favored by lower stresses). It is also controlled by grain size because of diffusive length scale (diffusion creep is favored by smaller grain sizes) (Poirier, 1985)
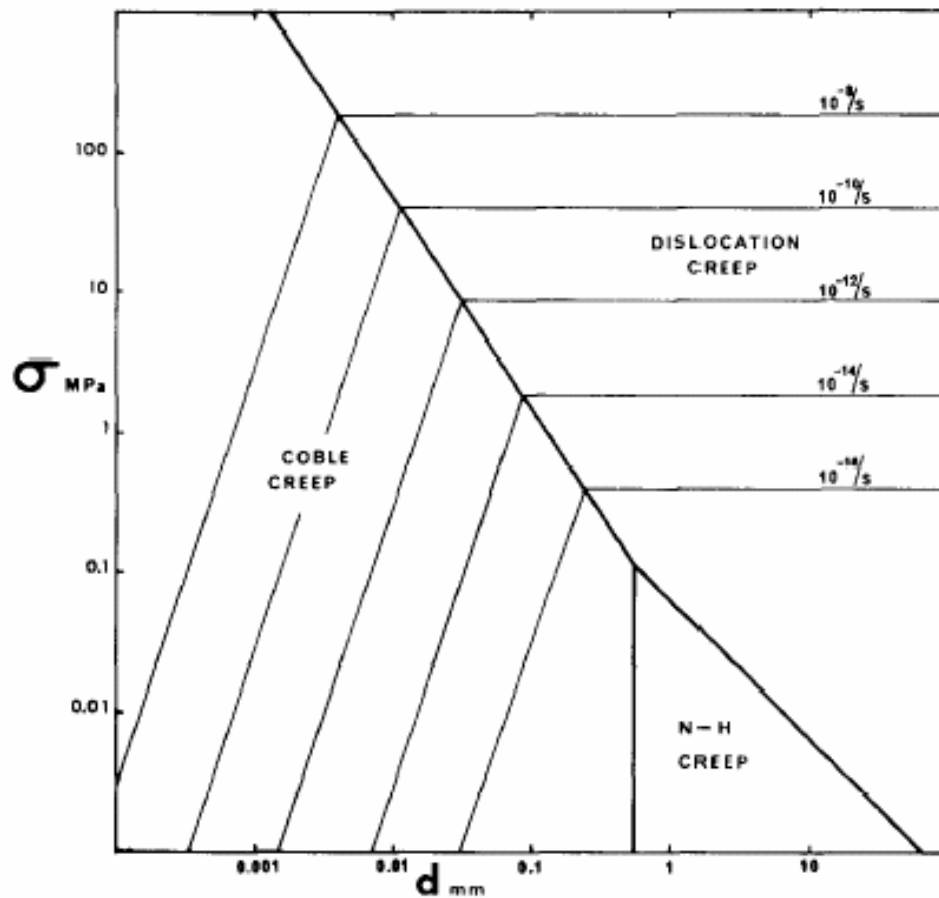
A deformation mechanism map for quartz at 500°C showing that grain-size sensitive creep at small grain sizes and low stresses gives way to grain-size insensitive dislocation creep at high stresses and large grain sizes (Etheridge & Wilkie, 1979)

(the word '[in]sensitive' refers to a dependence on the rate-limiting step. So, while dislocation creep *does* produce a specific grain size for a given stress, it is glide or climb that is rate limiting in dislocation creep, and not grain size) (G Hirth, pers comm., 2005)

Field-Boundary Hypothesis
Grain-size reduction by dynamic recrystallization during dislocation creep can cause a switch from grain-size insensitive dislocation creep to grain-size sensitive diffusion creep. Conversely, grain growth during diffusion creep can cause a switch to dislocation creep. The two mechanisms are independent and act in parallel, hence the faster controls deformation. The field boundary hypothesis posits that the grain size stabilizes along the boundary between the two fields: dislocation creep drives the grain size to smaller sizes through BLG and SGR and grain growth in the diffusion creep field drives the grains to coarsen (de Bresser et al., 2001). Deformation then is controlled by a combination of grain-size sensitive diffusion and grain-size insensitive dislocation mechanisms and the grain size organizes itself along the grain-size sensitive and grain-size insensitive boundary.

The boundary between grain-size sensitive and grain-size insensitive creep can be located with

$$\dot{\varepsilon} = (C+1)A\sigma^n \exp(-Q/RT)$$

and

$$\sigma = \sigma_{disl}(C+1)^{-1/n}$$

where C is the ratio of strain rate due to grain-size insensitive (dislocation) creep and grain-size sensitive creep and the rest are the usual dislocation creep parameters. This means that the (overall) strain rate is relatively insensitive to this ratio and that grain-size sensitive creep does not produce a major weakening.
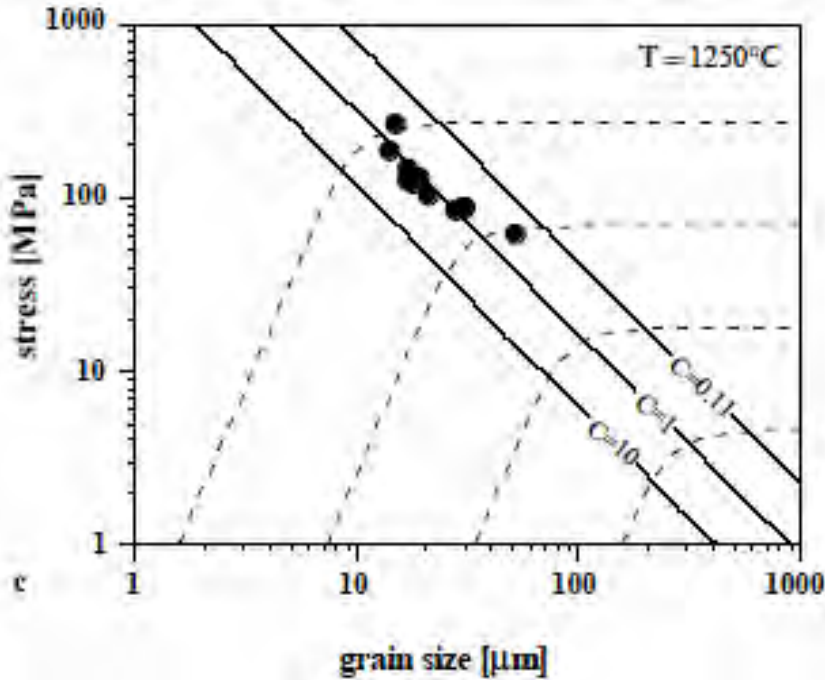
deformation mechanism map for olivine. C = ratio of dislocation-creep strain rate to dislocation-creep strain rate. Dashed lines are strain rates of 10^{-3}, 10^{-5}, 10^{-7}, and 10^{-9} s^{-1} (de Bresser et al., 2001)
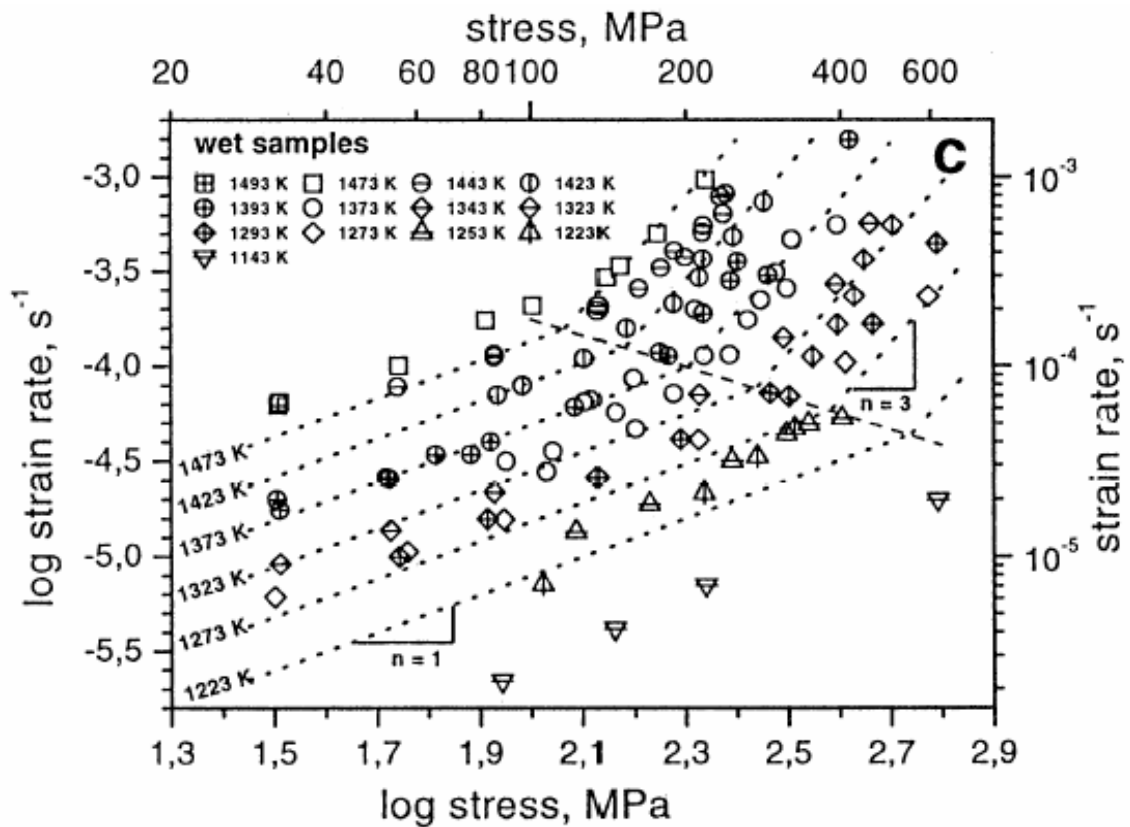
synthetic anorthite polycrystals of 3 µm define two regimes with n=1 and n=3 (Rybacki & Dresen, 2000)
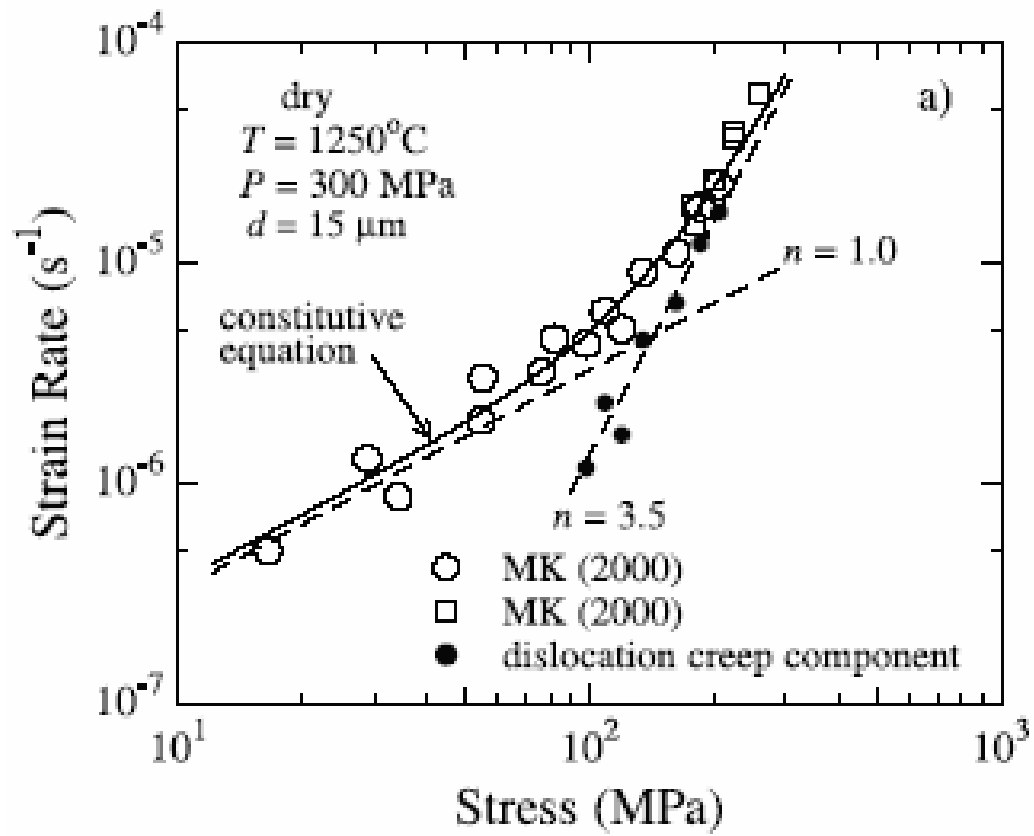
transition from diffusion creep to dislocation creep (Mei & Kohlstedt, 2000; Hirth & Kohlstedt, 2003)

a)

diffusion
creep

□ KFP (1986)
○ MK (2000)
△ HK (1995)
◊ HK (1995)
● CP (1984)

$[110]_c$

GBS

dislocation
creep

$[011]_c$

$T = 1250°C$
$\sigma = 150$ MPa

Strain Rate (s^{-1})

Grain Size μm

under dry conditions, between the diffusion creep regime and the dislocation creep regime is a regime of dislocation-accommodated GBS. (Hirth & Kohlstedt, 2003)
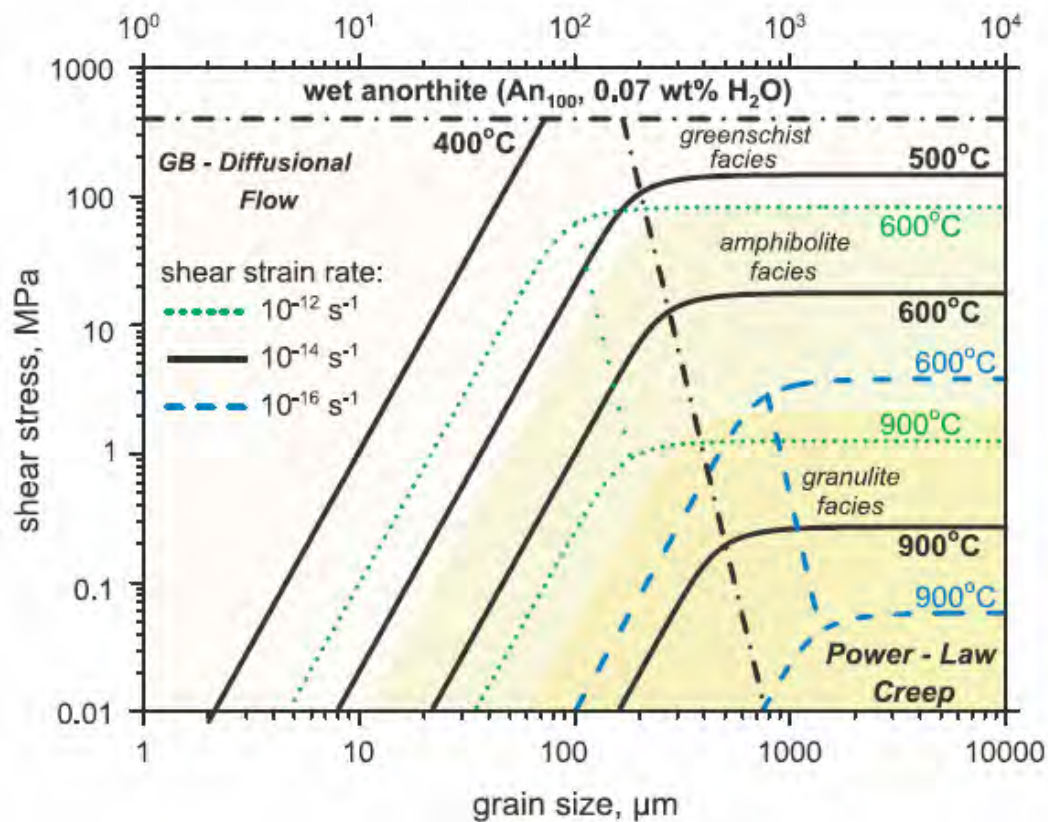
for wet anorthite, GBD creep dominates below 0.1–1.0 mm at 600°C and 10^{-14} s^{-1} (Rybacki & Dresen, 2004)
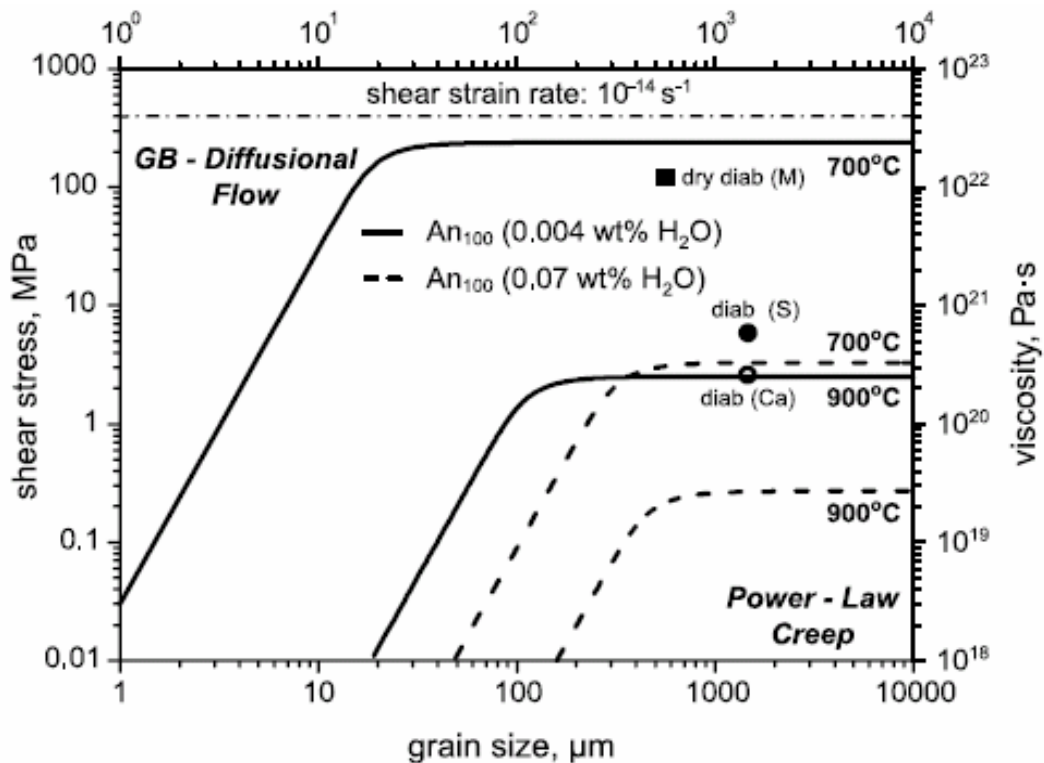
Fluid also catalyzes grain-boundary diffusion. This figure shows the difference in strength between wet rocks (solid lines) and dry rocks (dashed lines) (Rybacki & Dresen, 2004)
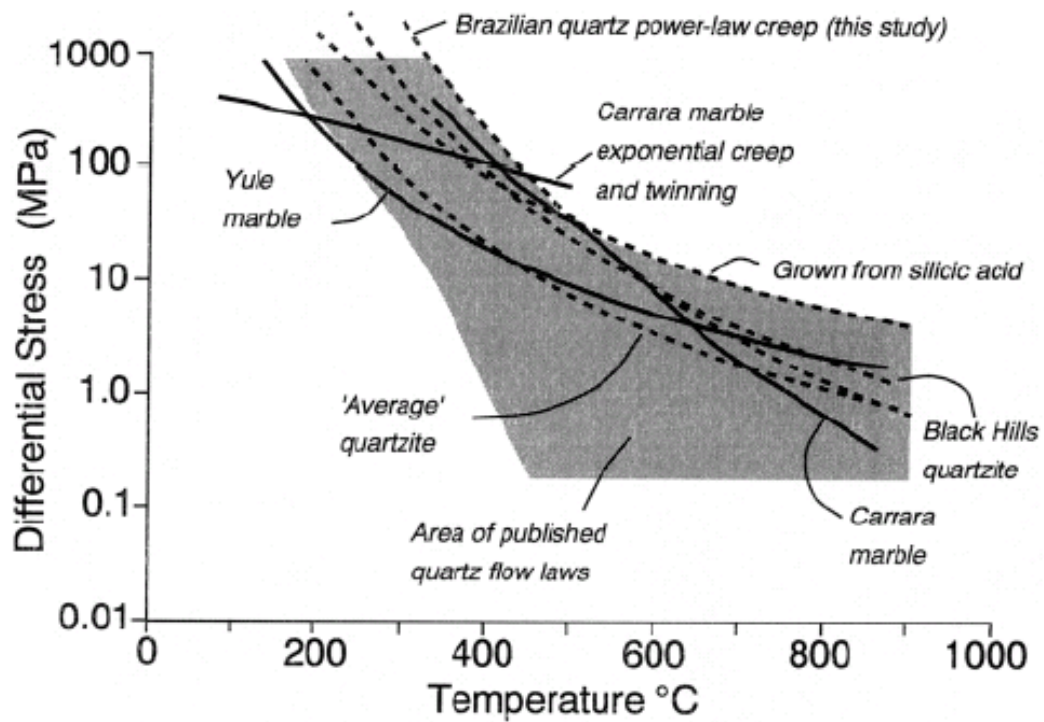
extrapolated flow laws for quartzite and marble overlap. How can this be? (Brodie & Rutter, 2000)
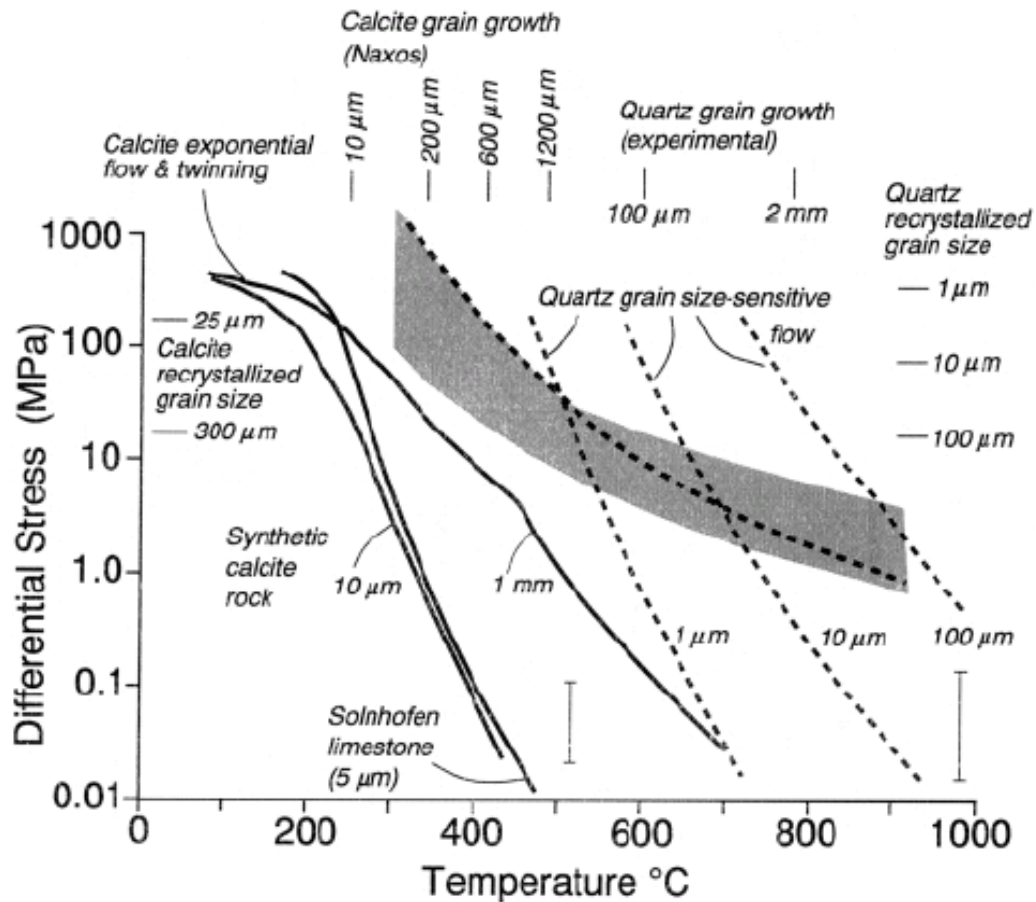
If grain-size-sensitive and grain-size-insensitive creep is compared, the predicted strength of marble is less than quartzite. Comparison of quartz (dashed) and marble (solid) at 3×10^{-14} s^{-1}. Marble is dominated by GSS from 1 μm to 1 mm, passing at high stress and low T into dislocation creep field. Gray field is quartz dislocation creep (Brodie & Rutter, 2000)
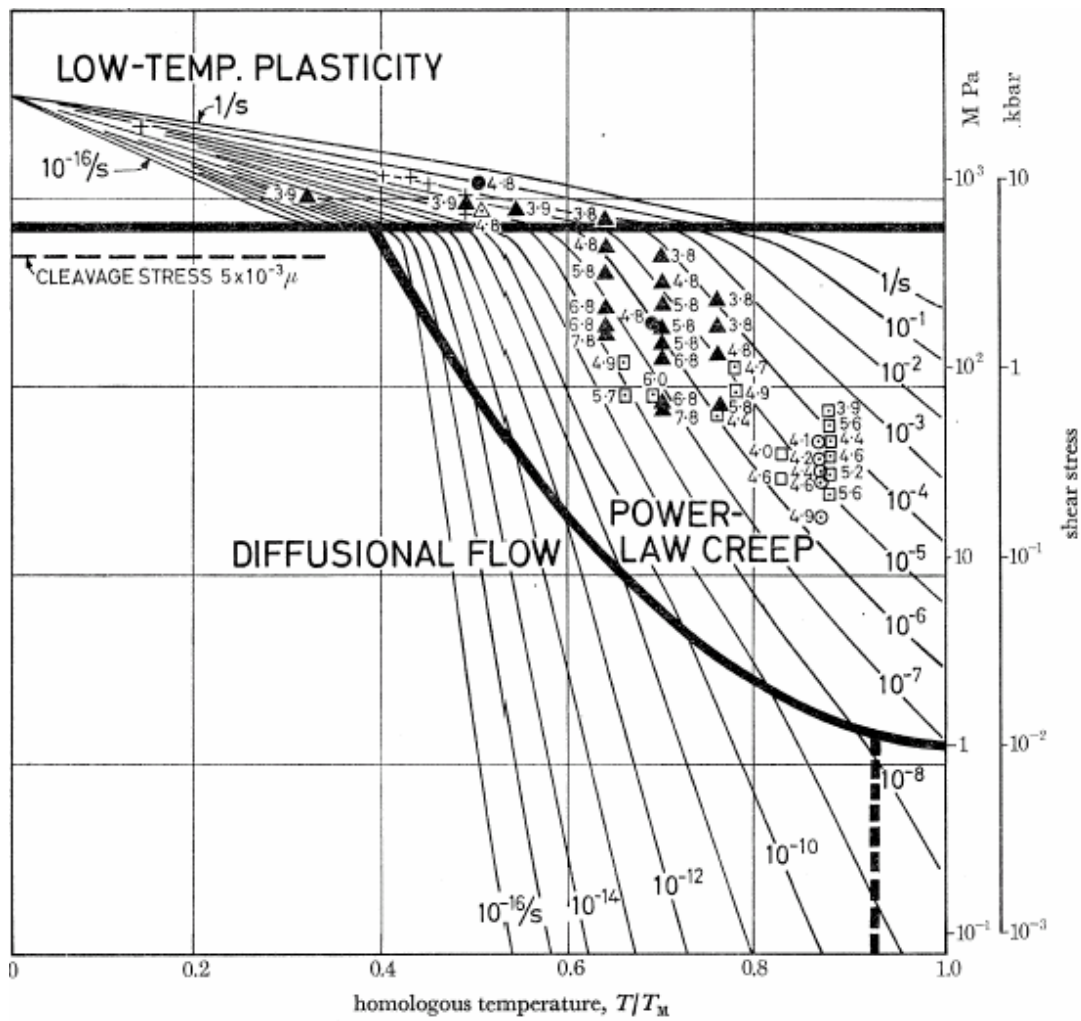
100 μm olivine (Ashby & Verrall, 1978)
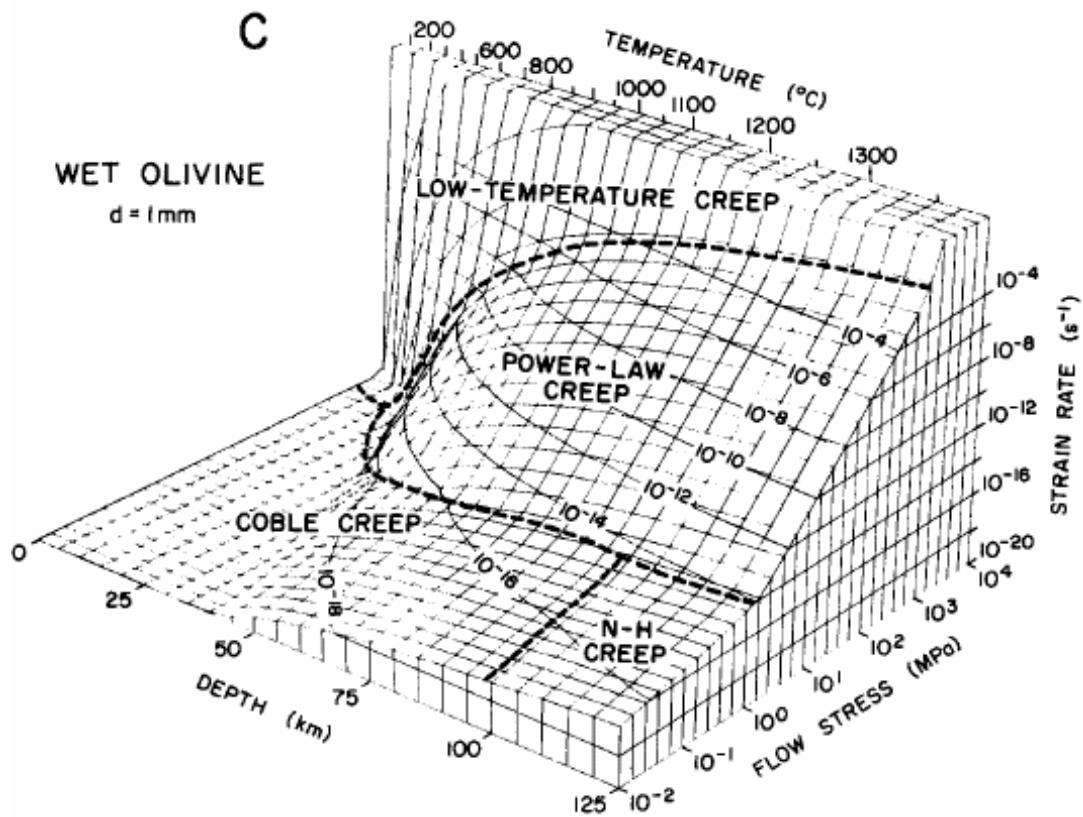
(Carter & Tsenn, 1987)
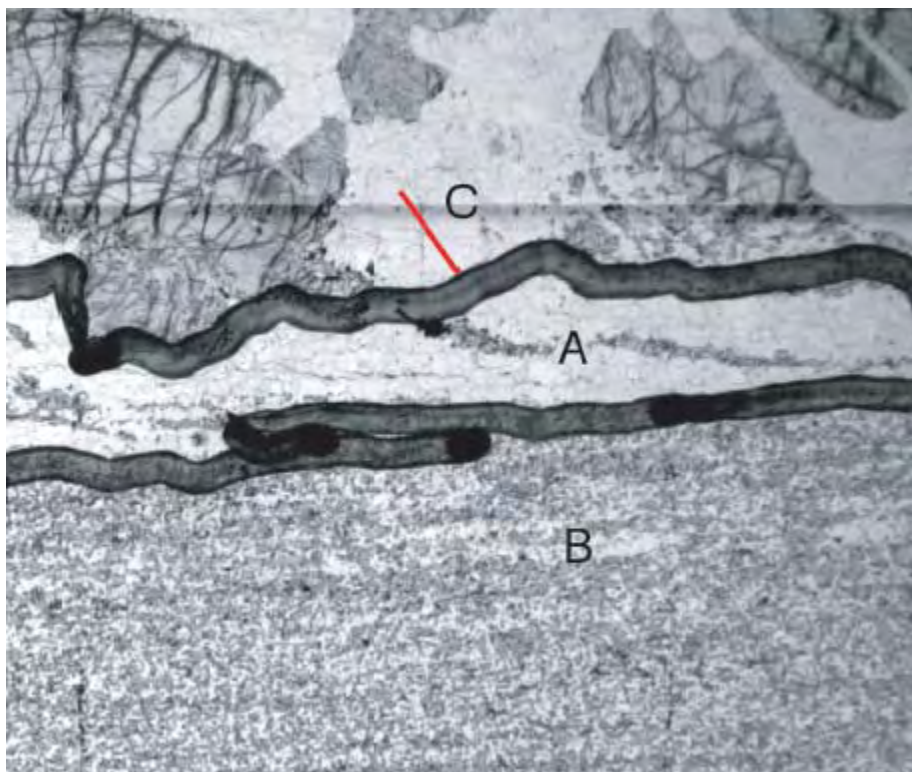
oceanic gabbro showing coarse-grained region (A) adjacent to fine-grained region where plagioclase is pinned by distributed clinopyroxene (Luc Mehl, pers. comm., 2005)
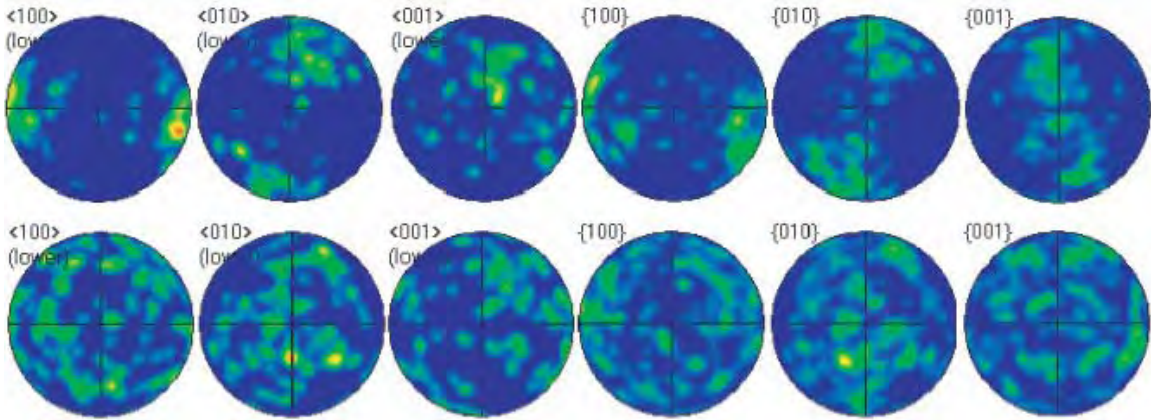
plagioclase LPO for (top) coarse-grained region A suggests [100](010) dislocation creep and (bottom) fine-grained region B suggests diffusion creep (Luc Mehl, pers. comm., 2005)
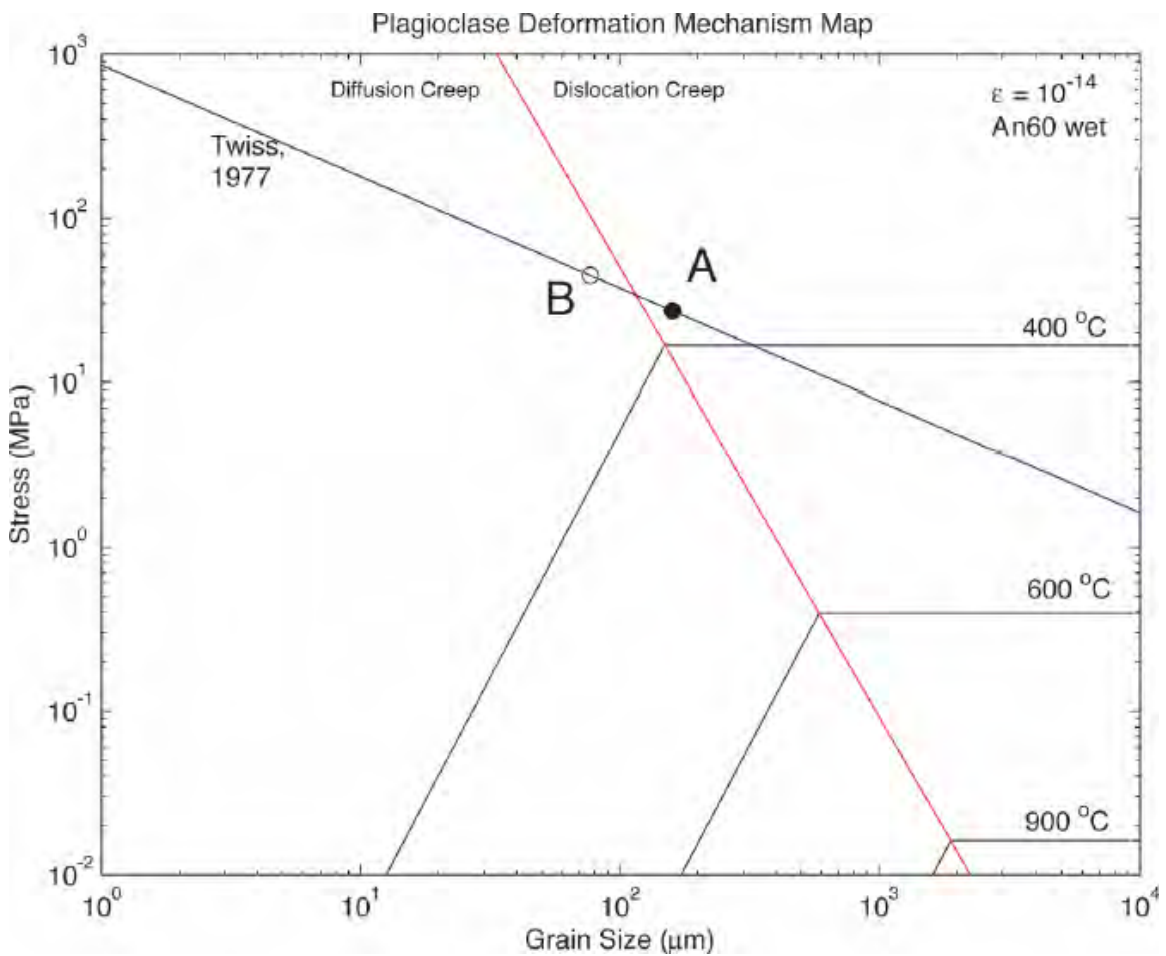
deformation mechanism map—based on wet An60 flow law parameters ignoring H_2O fugacity and Twiss [1977] piezometer—suggests that gabbro parts "A" and "B" lie in dislocation creep and diffusion creep fields, respectively (Luc Mehl, pers. comm.)

Initial Lithologic Stratification
(D ≤ 5 μm)

Pure Calcite

Calcite + 2% of 2 μm phases

Calcite + 5% of 0.3 μm phases

Pure Calcite

(a)

No Rheological Contrast

Pure Calcite

Calcite + 2% of 2 μm phases

Calcite + 5% of 0.3 μm phases

Pure Calcite

(b)

Metamorphic Stratification
(400°C, 100,000 yrs)

Pure calcite	D = 780 μm
2% of 2 μm phases	60 μm
5% of 0.3 μm phases	6 μm
Pure Calcite	780 μm

(c)

Rheological Stratification
(400° C, σ = 100 MPa)

	strain rate (1/s)	strain 100,000 yrs
Pure	8 E-15	0.03
2% of 2 μm	2 E-12	6
5% of 0.3 μm	2 E-9	6000
Pure	8 E-15	0.03

(d)

The presence of a second phase will force a rock to remain in GSS creep and be the weakest layer in a sequence (Olgaard, 1990)

quartz-feldspar mylonites wherein the feldspar grains have been comminuted during retrograde fracturing remain fine grained (3–30 µm) because of pinning (Stünitz & Fitz Gerald, 1993)

in natural peridotites deformed at <950°C, deformation is often concentrated in narrow zones; this may occur because of strain softening: the fine-grained material is weaker because grain-size sensitive deformation mechanisms take over (Drury et al., 1991). If the recrystallized grain size is controlled by stress (dislocation creep), there will be a T-dependent grain size below which grain-size sensitive creep will be dominant.
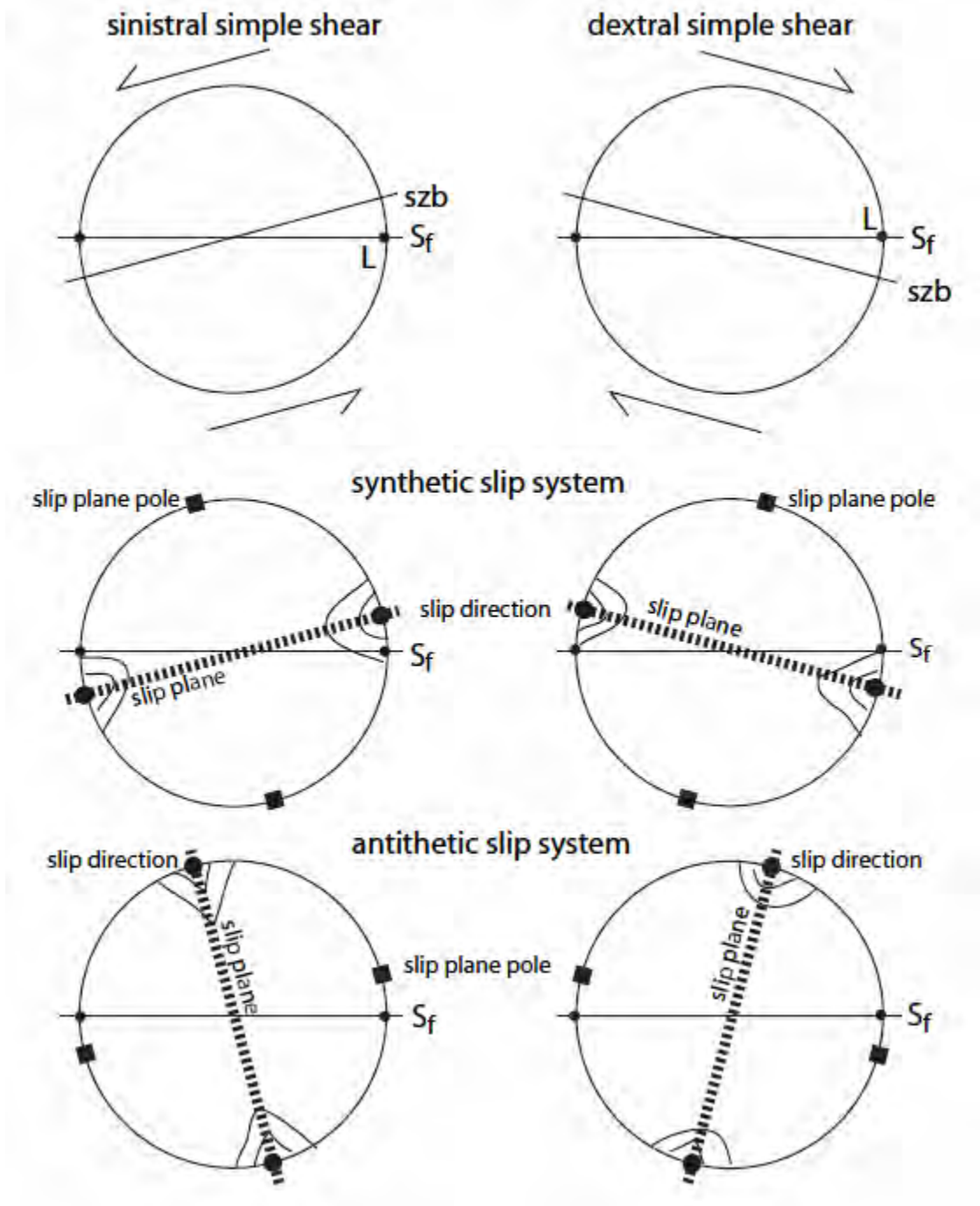
Guide to asymmetric fabrics (Idiot, 2005)

Plagioclase
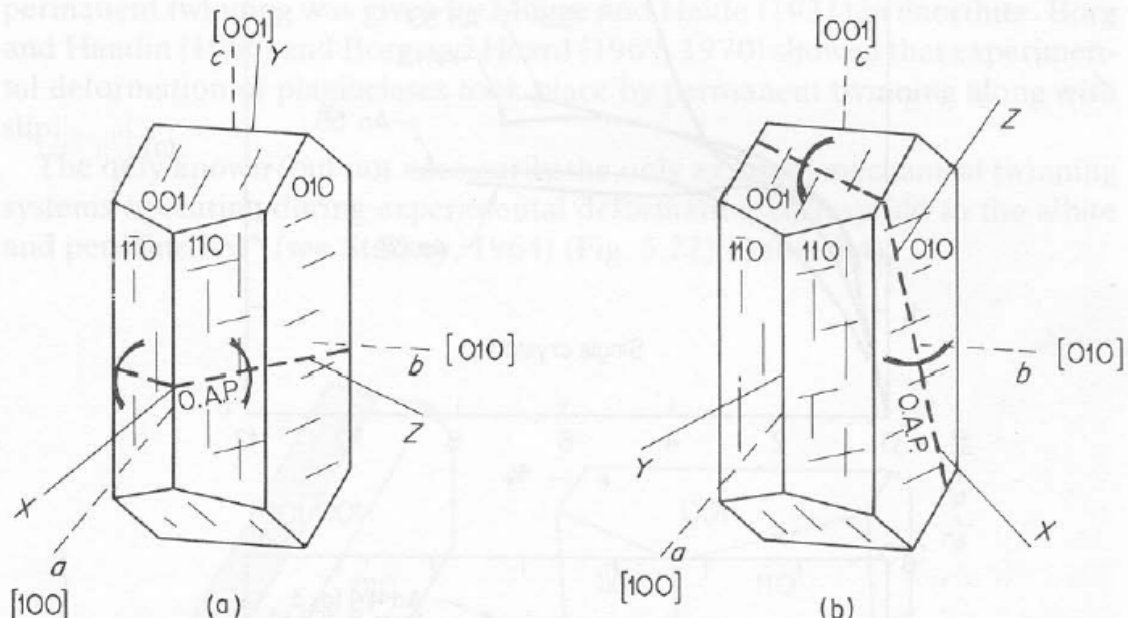
crystallography of low albite and anorthite (Nicolas & Poirier, 1976)

dominant: [001] in (010)

secondary: [100] in (010), (001)
              [101] in (010)
              [201] in (010)
              1/2 [110] in (001), (1$\bar{1}\bar{1}$)
              1/2 [1$\bar{1}$0] in (001), (11$\bar{1}$)
              1/2 [111] in (10$\bar{1}$)
              1/2 [1$\bar{1}$1] in (10$\bar{1}$)

tentative: 1/2 [112] in (11$\bar{1}$)
              1/2 [1$\bar{1}$2] in (110)
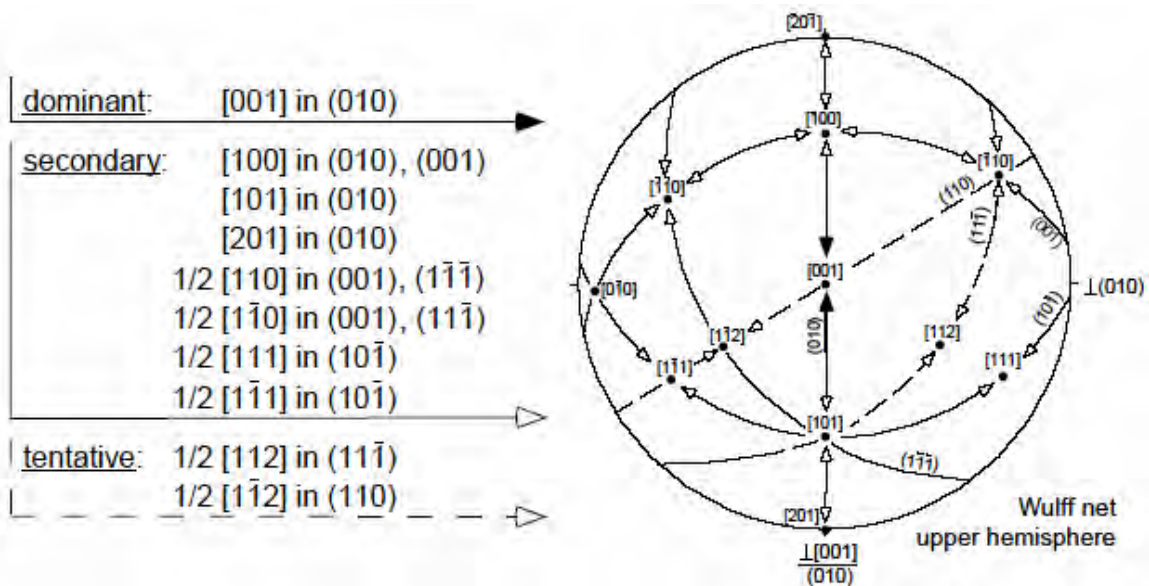
Slip systems in intermediate plagioclase ($C\bar{1}$ space group) after Marshall and McLaren (1977), Olsen & Kohlstedt (1984), Montardi & Mainprice (1987). Inverse pole figure after Burri et al. (1967), with pole to (010) to the east and [001] in the center pointing up (Kruse et al., 2001)
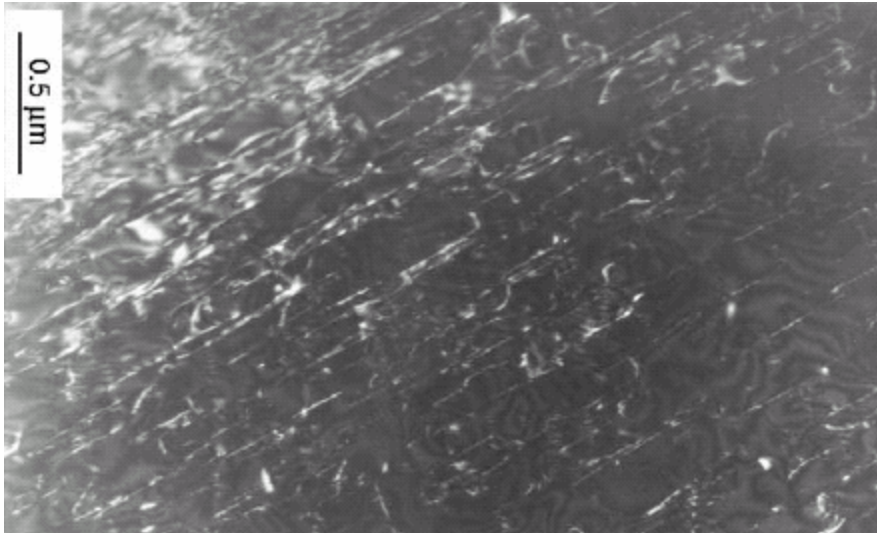
dislocations from [001](010) slip plus less <110>(001) to {111} (Stünitz et al., 2003)

Twin Laws in plagioclase (Borg & Heard, 1970)

	albite	pericline
K1 (slip plane)	{010}	rhombic section
N1 (slip line)	irrational	<010>

(the rhombic section is an irrational plane that contains [010] and intersects (010) in a line normal to [010])

(a) Albite twin   (b) Pericline twin
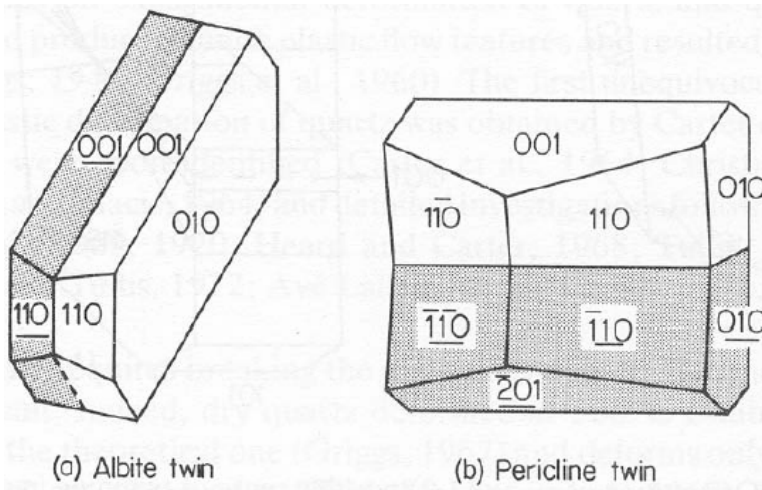
(Nicolas & Poirier, 1976)
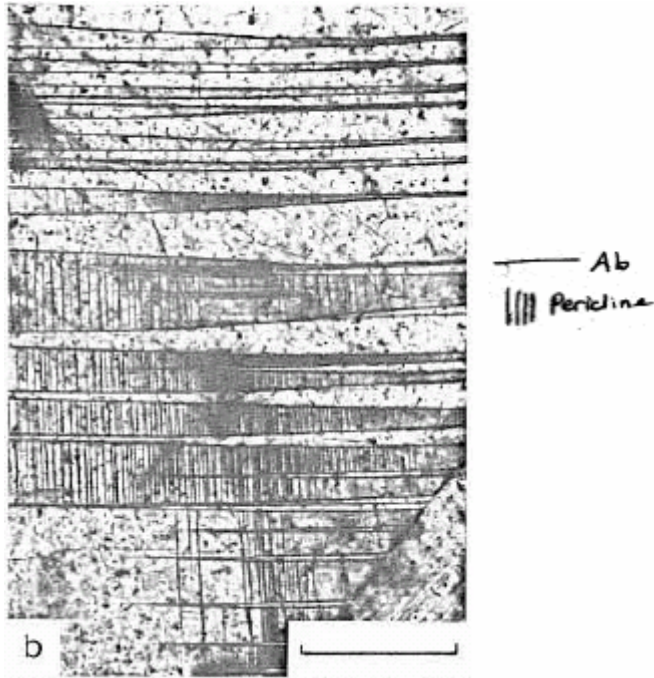
albite and pericline mechanical twins (Brown & Macaudière, 1986)

Experimentally Deformed Plagioclase

Comparison of quartz and plagioclase deformation in aplite at 10^{-6} s^{-1} strain rate (Dell'Angelo & Tullis, 1996)

T (°C)	quartz	plagioclase
700	regime 1	semi-brittle. Homogeneous flattening by grain-scale faulting. Straight dislocations and mechanical twins
800	regime 2	semi-brittle to regime 1. Grains homogeneously flattened by twinning, grain-scale faulting and dislocation glide.
900	regime 3	regime 2?. Inhomogeneous deformation of grains; tangled straight dislocations and variable dislocation density
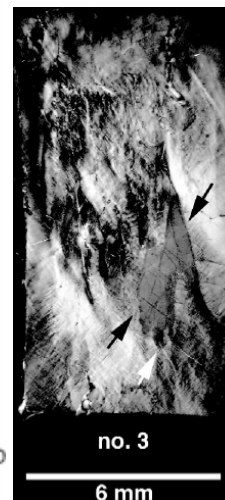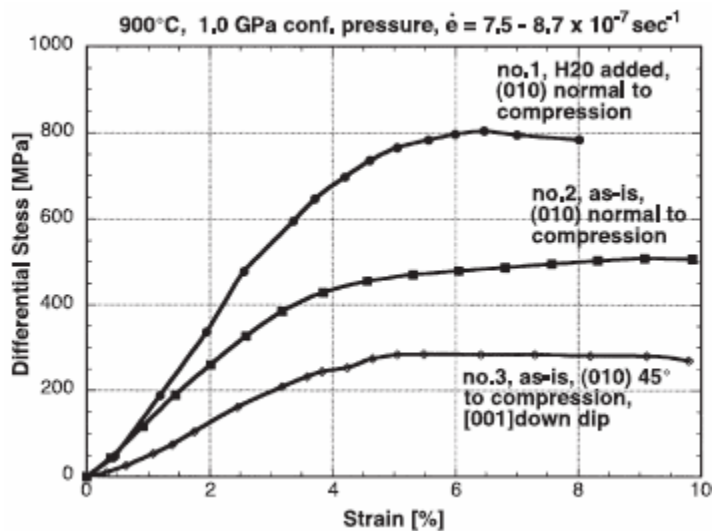
Experiments on plagioclase single crystals (Stünitz et al., 2003)
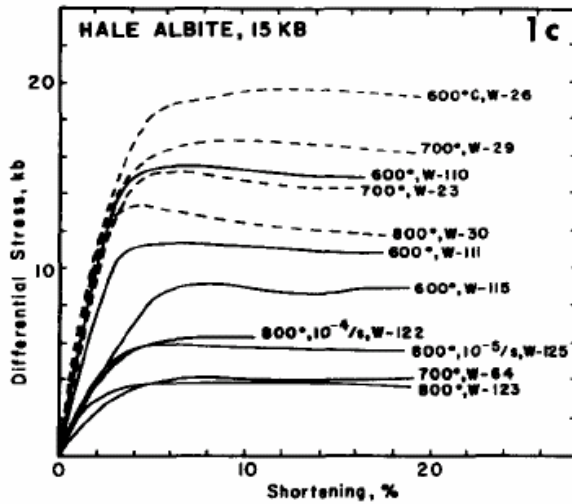
Water weakening has a significant effect on Hale albite (dry, dashed; wet , solid) (Tullis & Yund, 1980)
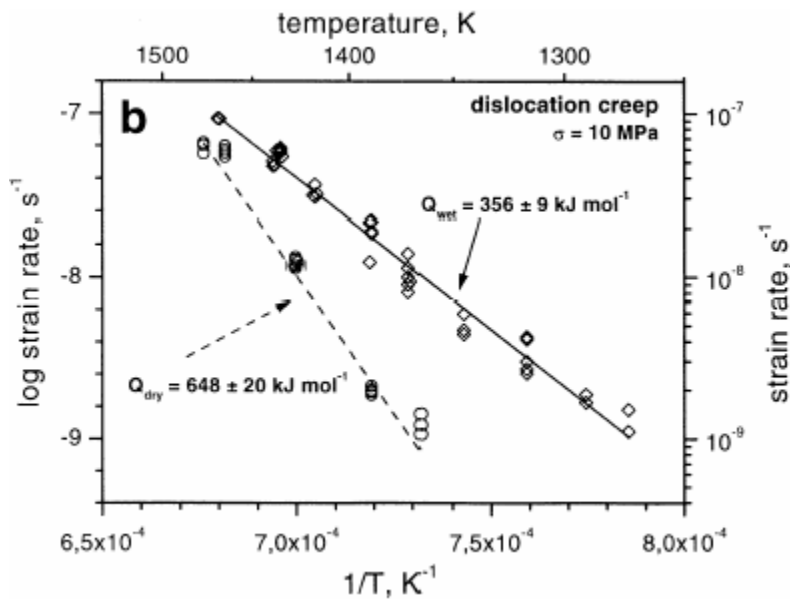
wet and dry synthetic 3 μm anorthite polycrystals define two dislocation creep regimes of different activation energy, Q (Rybacki & Dresen, 2000)

	n	Q (kJ/mol)	log A	m	wt% H_2O	ref
dislocation creep						
An_{100}	3.0 ± 0.4	648 ± 20	12.7 ± 0.6	0	.004	Rybacki & Dresen (2000)
An_{100}	3.0 ± 0.2	356 ± 9	2.6 ± 0.3	0	.07	Rybacki & Dresen (2000)
An_{60}	3	235 ± 13	-1.5 ± 0.5	0	.3	Dimanov
An_{100}	3	332 ± 23	3.4 ± 1.0	0	.2	Offerhaus et al. (2001)
An_{00}	3.4	234	-5.62	0	?	Shelton, 1981; Tullis et al., 1991

diffusion creep						
An_{100}	1.0 ± 0.1	467 ± 16	12.1 ± 0.6	3	.004	Rybacki & Dresen (2000)
An_{100}	1.0 ± 0.1	170 ± 6	1.7 ± 0.2	3	.07	Rybacki & Dresen (2000)
An_{60}	1	153 ± 15	1.1 ± 0.6	3	.3	Dimanov
An_{100}	1	193 ± 25	3.9 ± 1.1	3	.2	Offerhaus et al. (2001)

flow law creep parameters for synthetic plagioclase aggregates,

$$\dot{\varepsilon} = A\sigma^n d^{-m} \exp(-Q/RT) \text{ (Rybacki \& Dresen, 2004)}$$
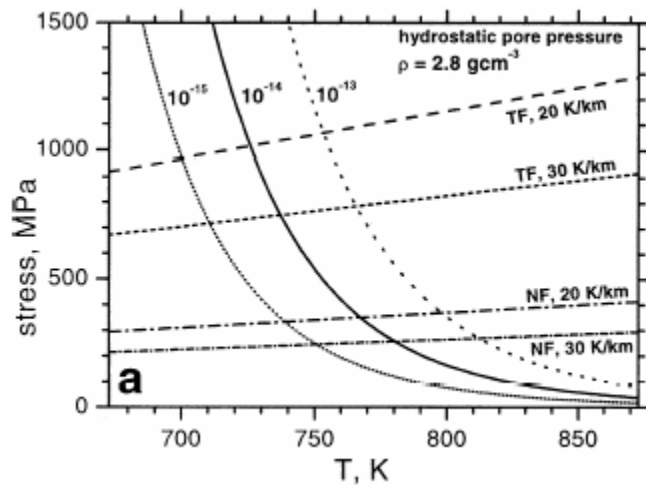
extrapolation of wet anorthite dislocation creep data. For example, at 100 MPa and 500°C, a strain rate of $\sim 10^{-15}$ s^{-1} is predicted (Rybacki & Dresen, 2000)

Experimentally Deformed Plagioclase Textures
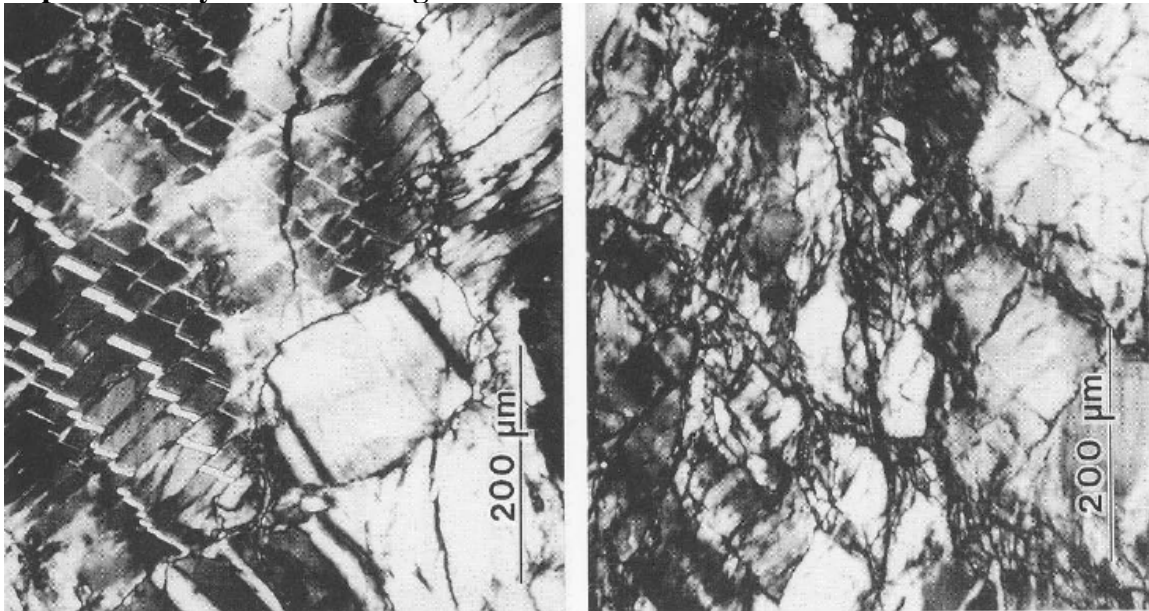
cataclastic feldspar deformed at 300°C 10^{-5} s^{-1} (Tullis & Yund, 1998)
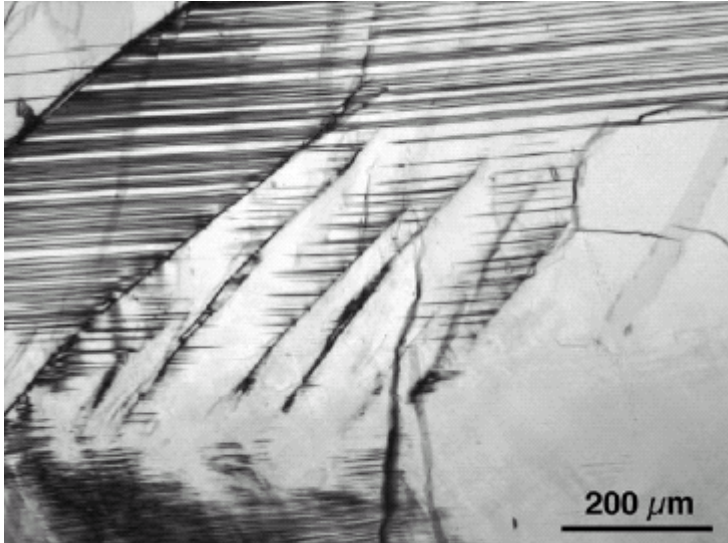
Fracturing almost always accompanies dislocation creep of plagioclase in nature, even at 700–900°C, and fracturing appears to be a precursor to dislocation generation. This was seen experimentally (Stünitz et al., 2003)
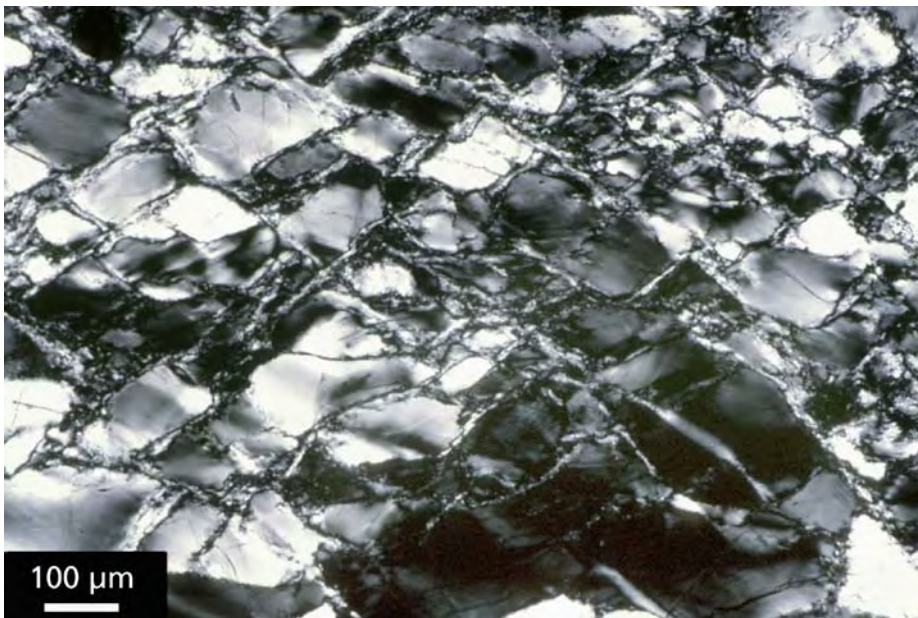
Hale albite shortened 56% at 1000°C and 10^{-6} s^{-1}; Regime 1 (Tullis et al., 2000)
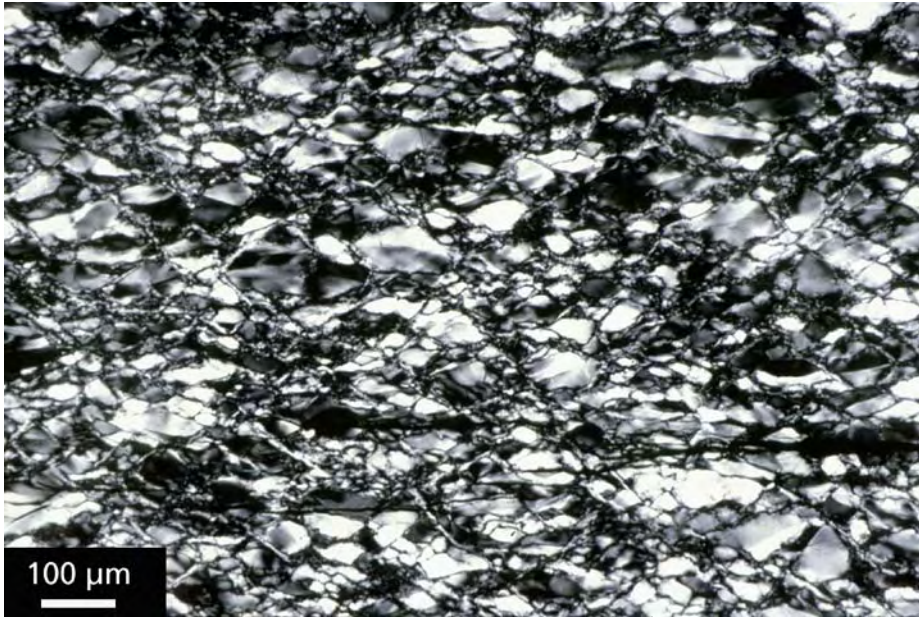
Tanco albite shortened 52% at 1100°C and 10^{-5} s^{-1}; Regime 1 (Tullis et al., 2000)
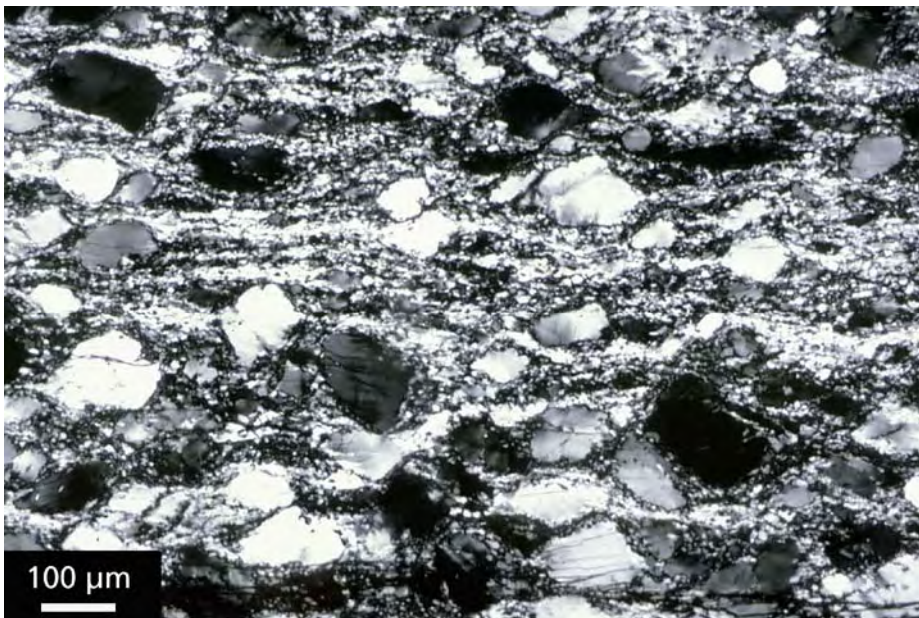
Hale albite shortened 70% at 1100°C and 10^{-6} s^{-1}; Regime 1 (Tullis et al., 2000)
porphyroclasts separated by very fine grains

Naturally Deformed Plagioclase
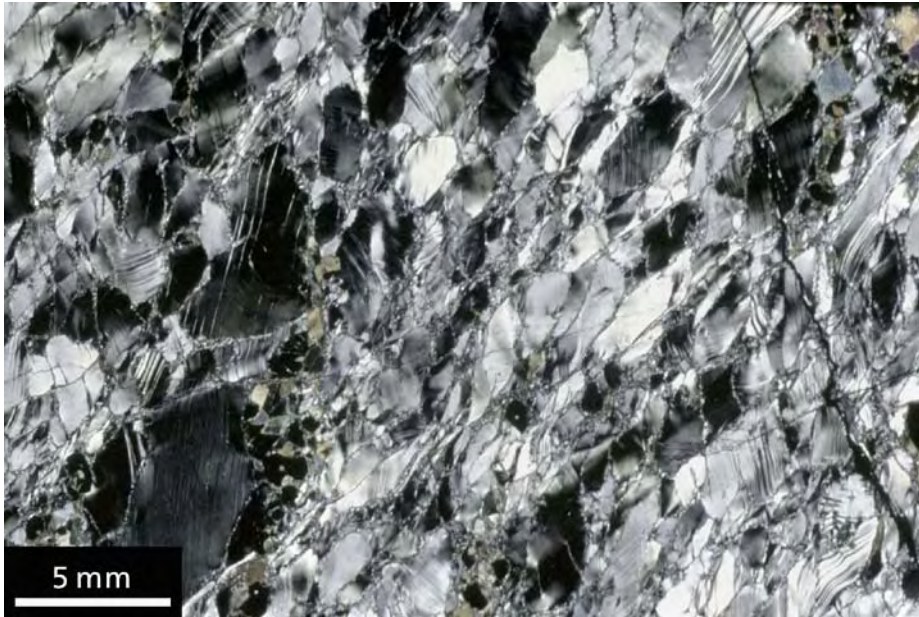
Jotun anorthosite weakly deformed at 700°C and regime 2 (Tullis et al., 2000)
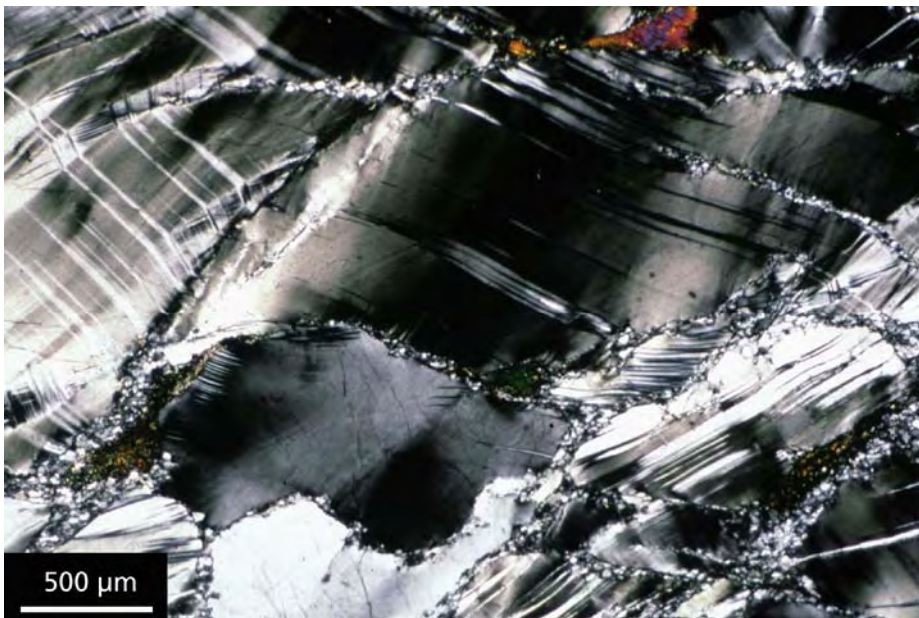
detail of above (Tullis et al, 2000)
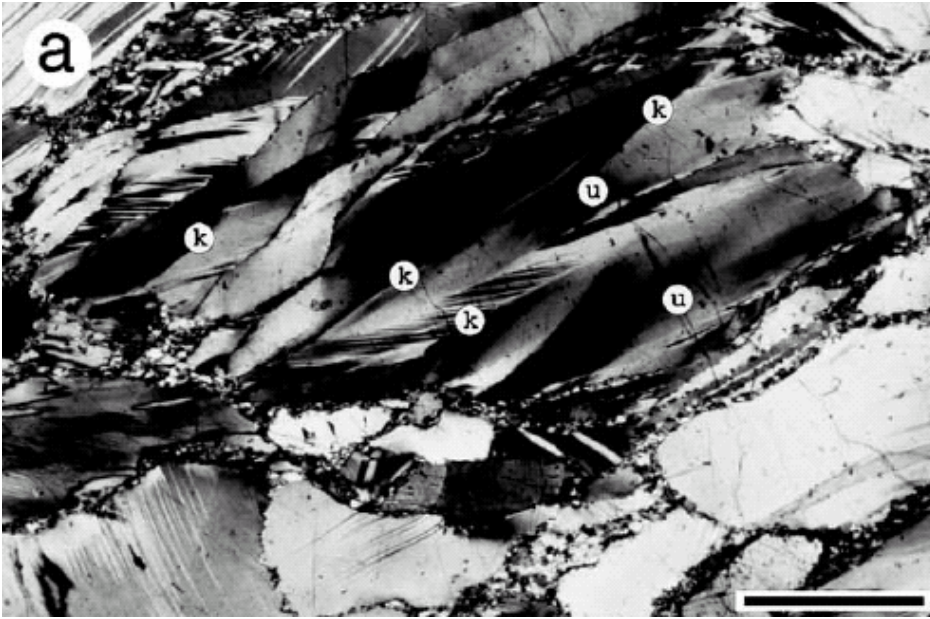
Jotun 700°C (u) undulatory extinction and (k) kink bands (Kruse et al., 2001)
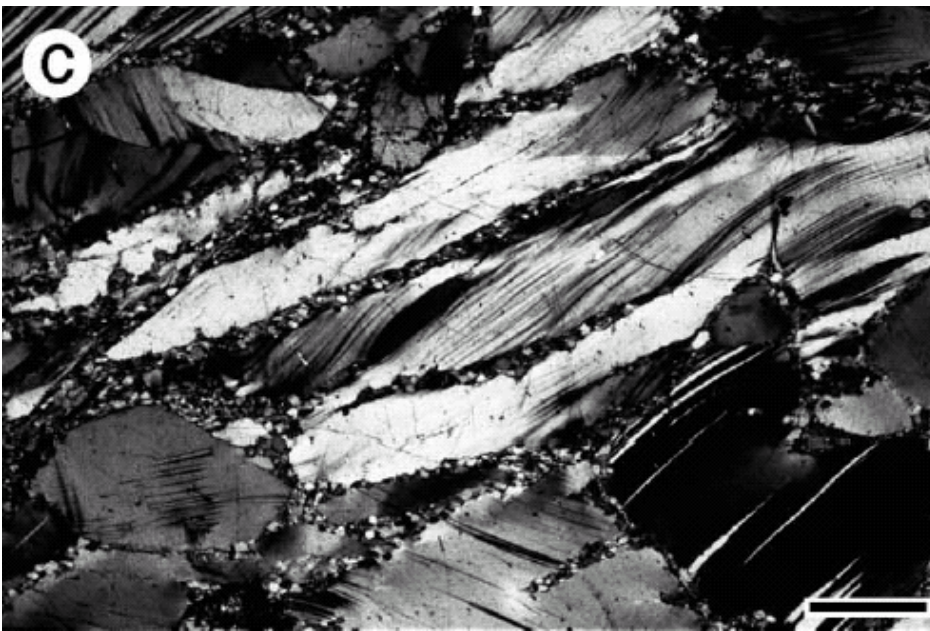
Jotun 700°C core-and-mantle recrystallization texture (Kruse et al., 2001)
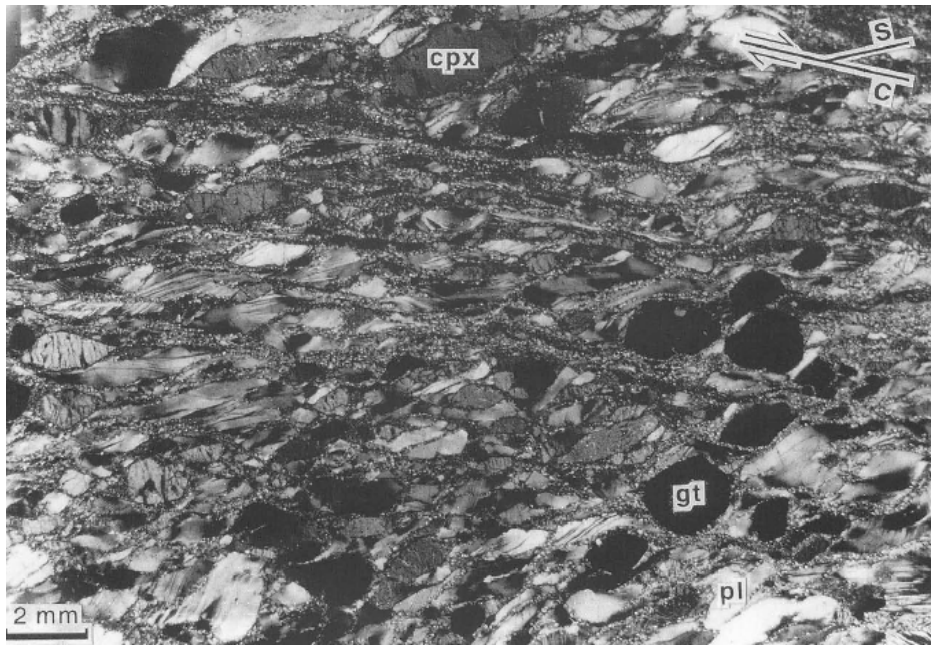
Jotun nappe amphibolite-facies anorthosite mylonite with recrystallized plagioclase C planes (Ji, 1998)
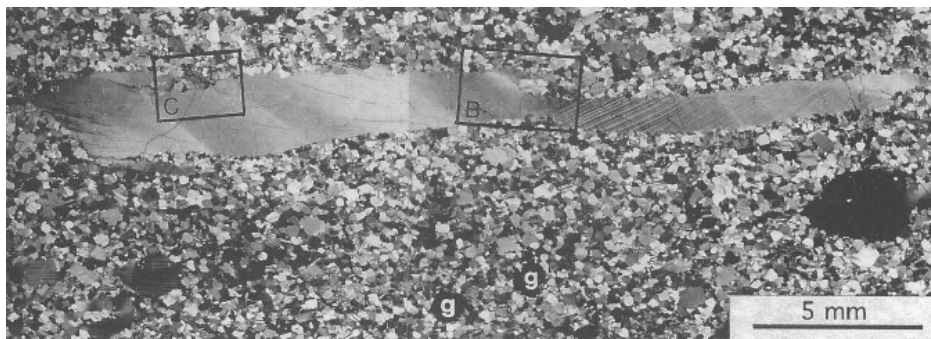
Jotun nappe granulite-facies mylonite (Olesen, 1998). Ribbon porphyroclast oriented favorably for twinning, seen clearly by (010) planes.
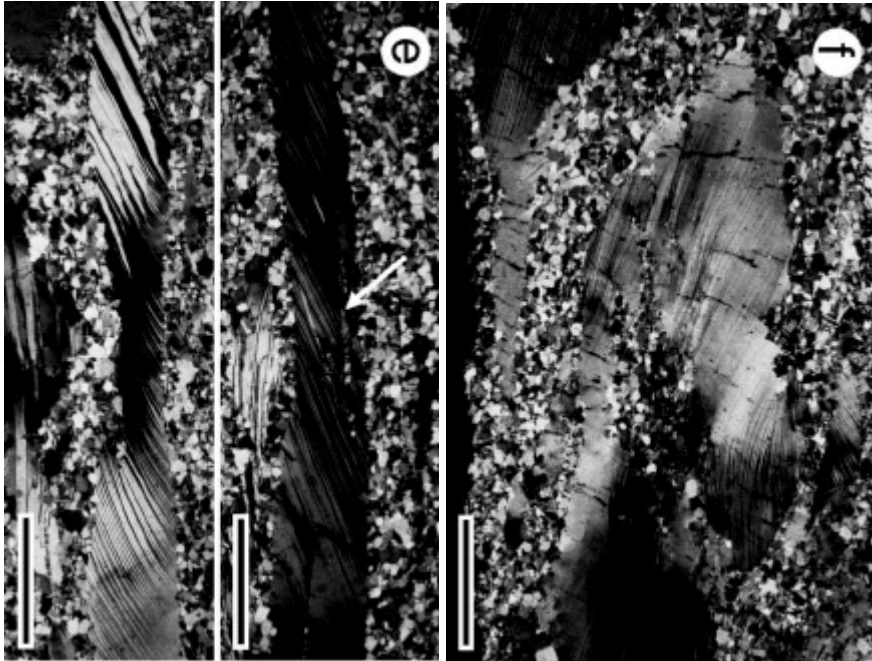
Jotun 700°C porphyroclasts (L) oriented for easy slip on (010)[001] are flattened and have straight grain boundaries whereas porphyroclasts (R) not oriented for easy slip on (010)[001] show inhomogeneous flattening, irregular grain boundaries and microfractures (Kruse et al., 2001)

Jotun anorthosite moderately deformed at 700°C; regime 2 (Tullis et al., 2000)

detail of above (Tullis et al., 2000)

Jotun anorthosite strongly deformed at 700°C; regime 2 (Tullis et al., 2000)
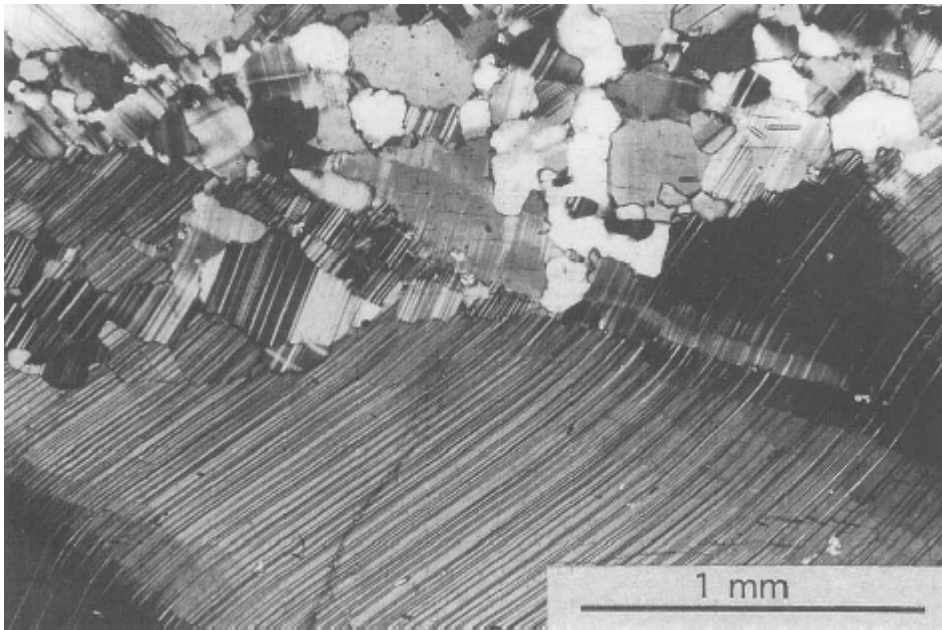
Jotun nappe granulite-facies mylonite showing kinking and SGR; (010) (albite) twin planes visible (Olesen, 1998).
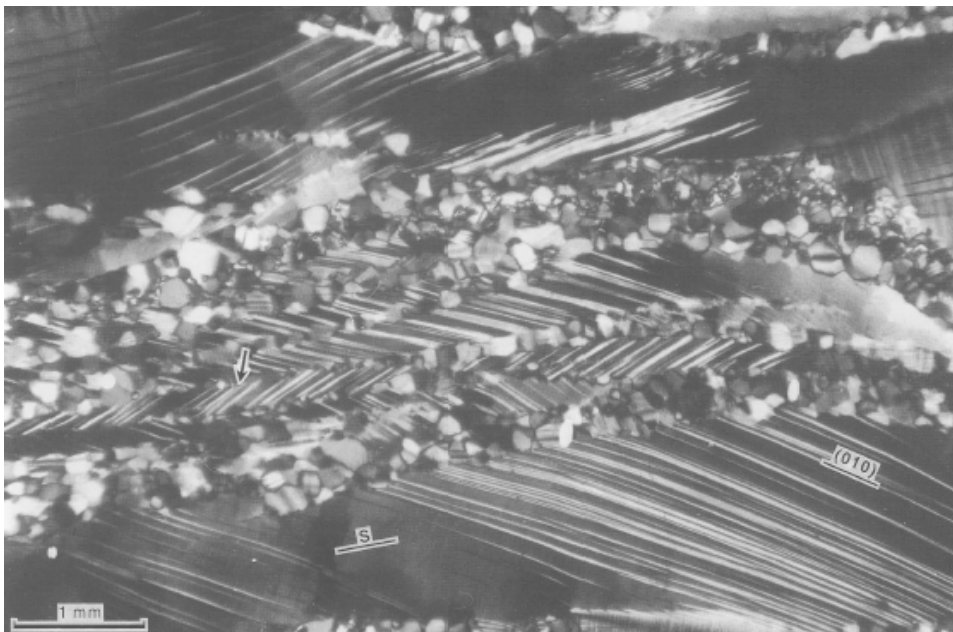
recrystallization of plagioclase kink bands formed by (010)[001] slip (Ji, 1998)
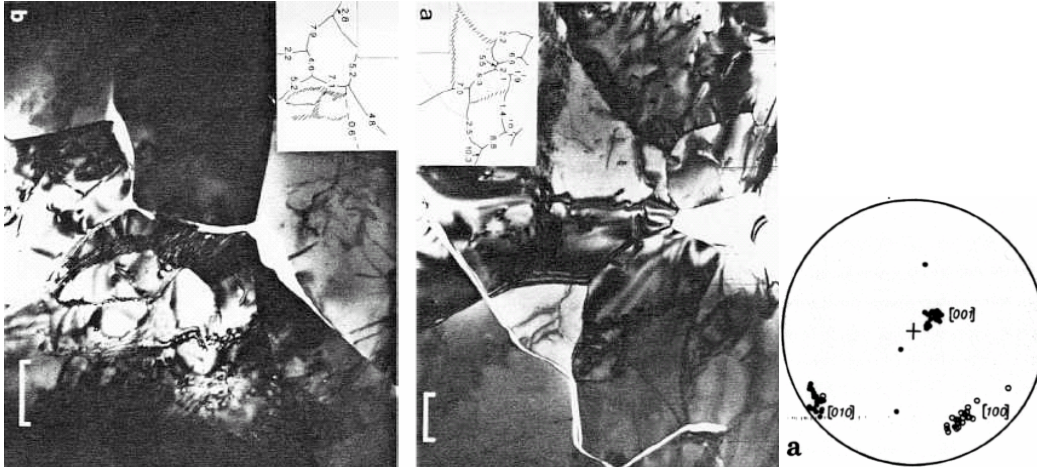
albite deformed at ~400°C in the Franciscan complex shows SGR (Fitz Gerald et al., 1983).
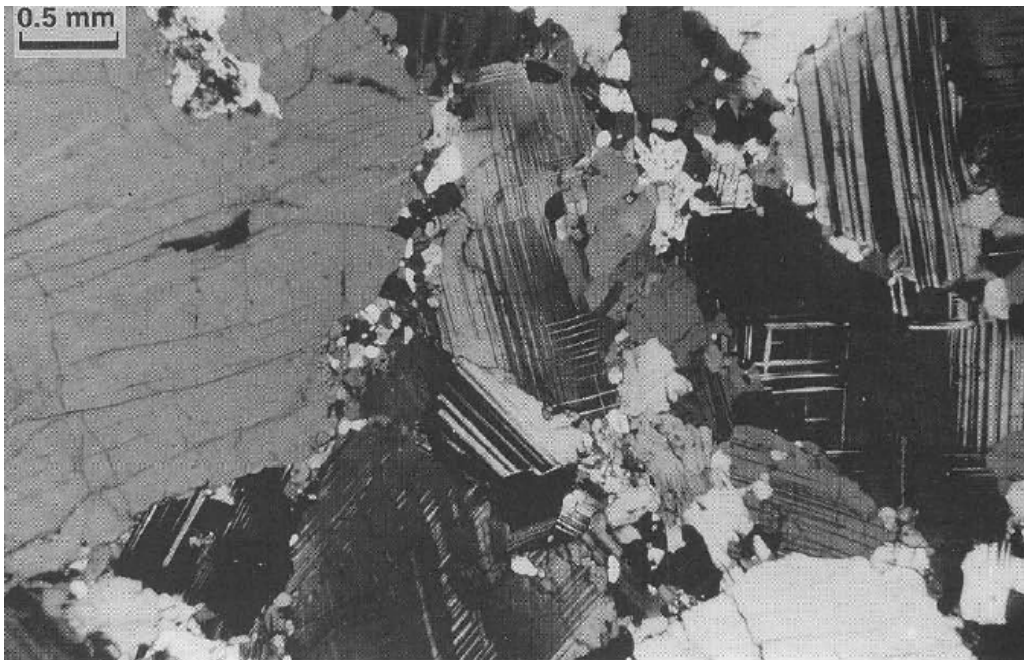
Core and mantle texture in plagioclase (Brown & Macaudiére, 1998)
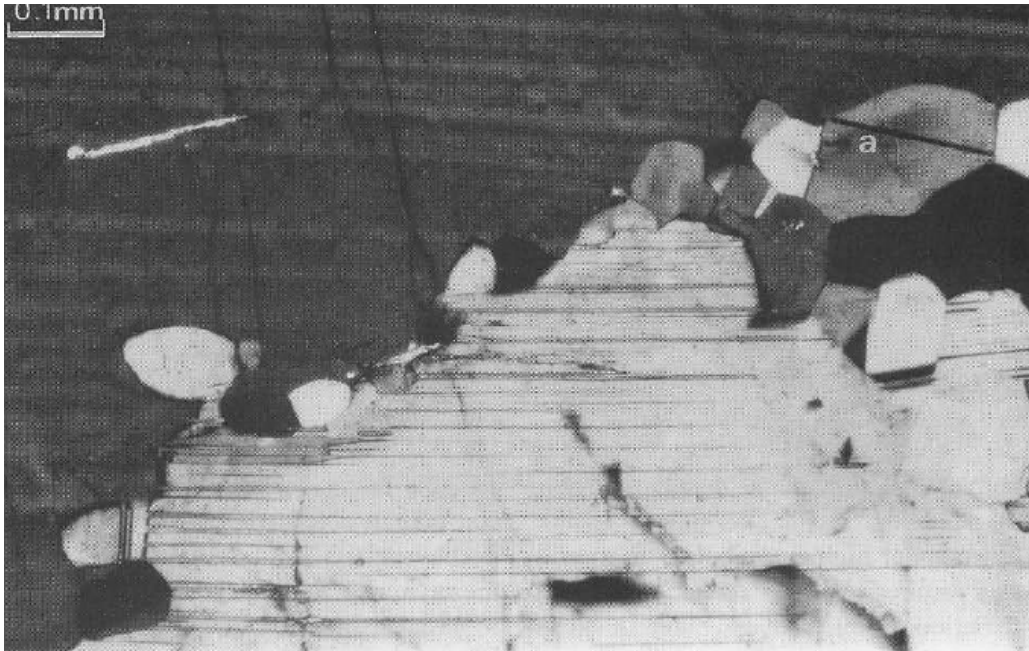
GBM of plagioclase (Brown & Macaudiére, 1998)
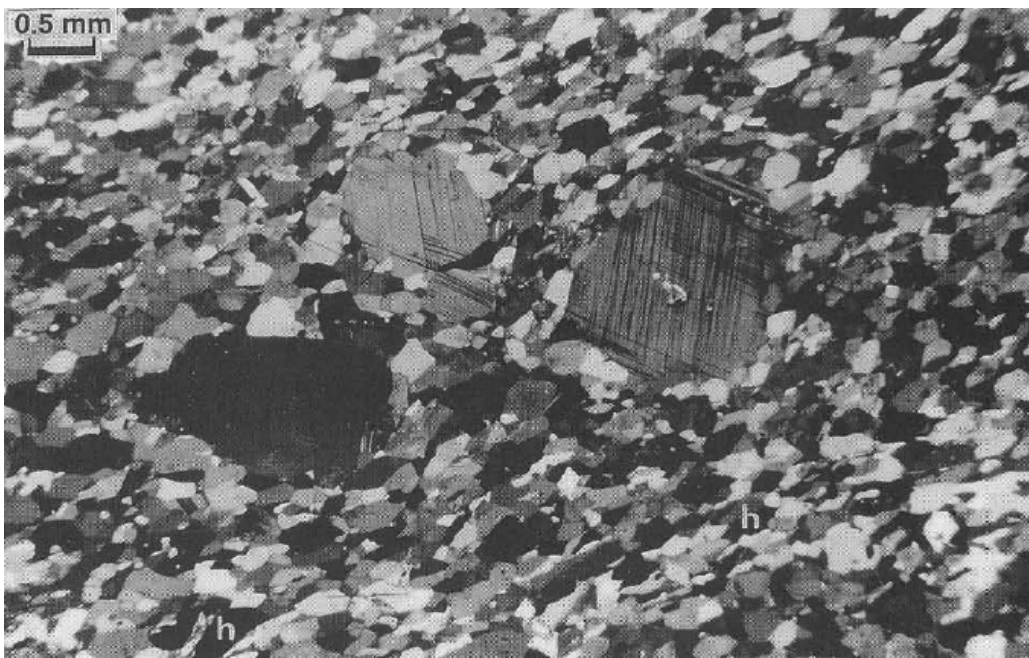
Mostly recrystallized plagioclase (Brown & Macaudiére, 1998)
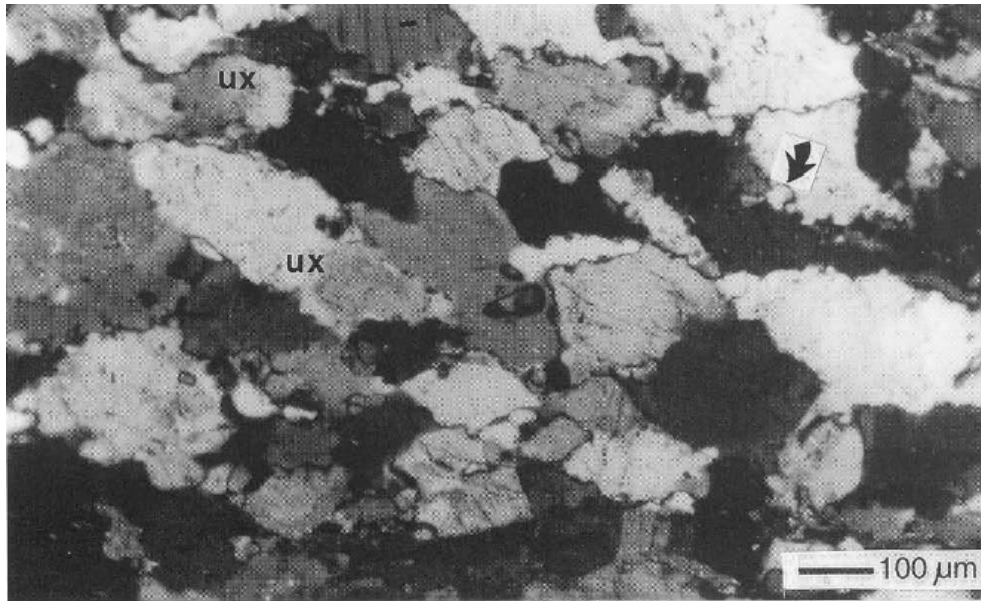
GBM in plagioclase (Simpson, 1998)
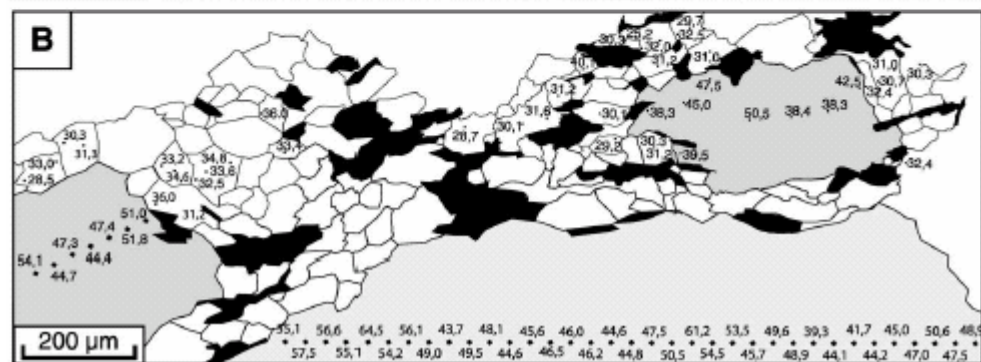
Bergell tonalite lower amphibolite facies. Deformation of plagioclase by dislocation creep and recrystallization by neocrystallization of grains of different composition (Rosenberg & Stünitz, 2003)
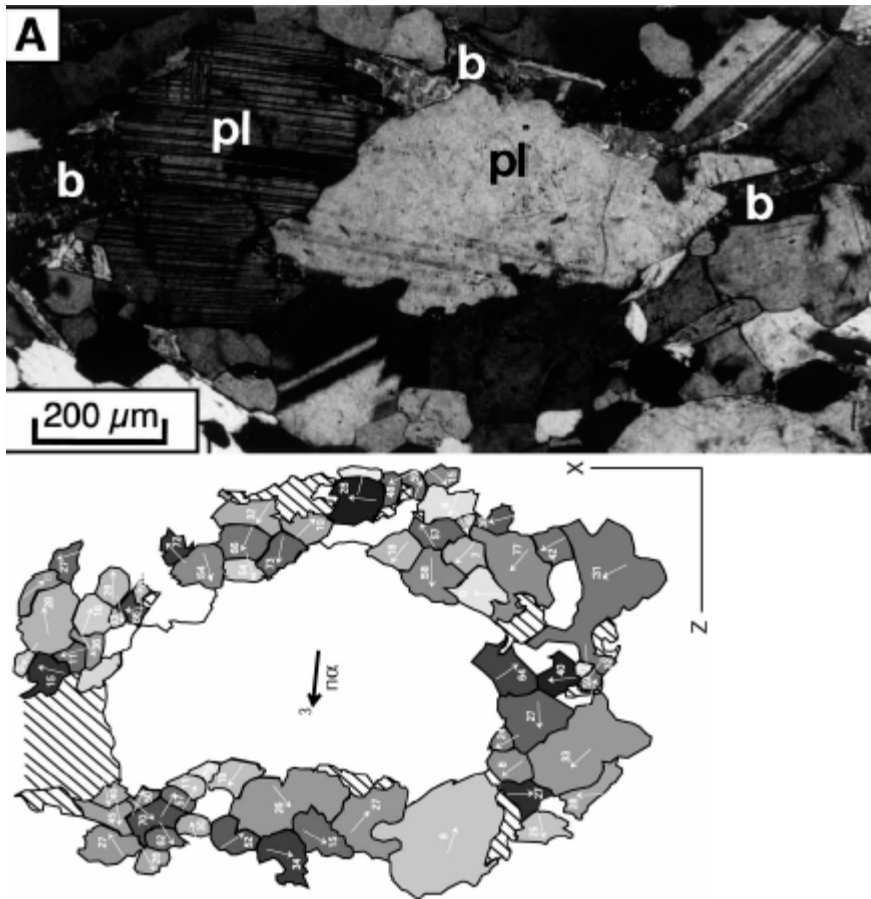
Bergell tonalite upper amphibolite facies. Deformation by diffusion-accommodated GBS and recrystallization by SGR + GBM (Rosenberg & Stünitz, 2003)

Experimentally Produced Plagioclase Lattice Preferred Orientations
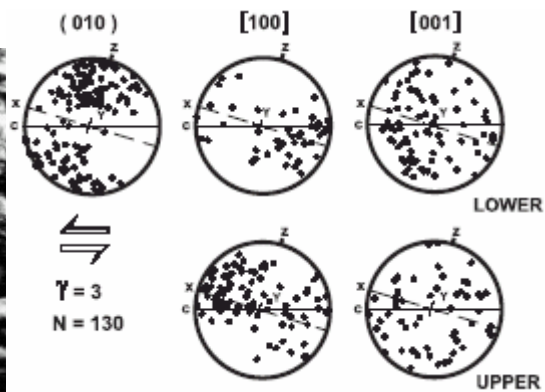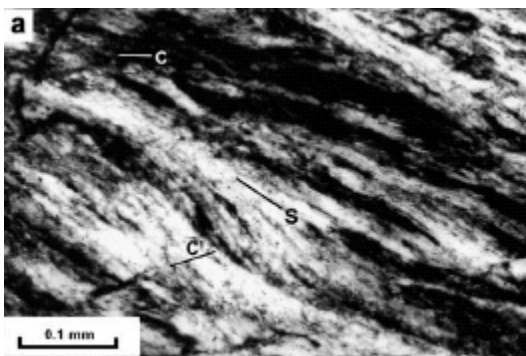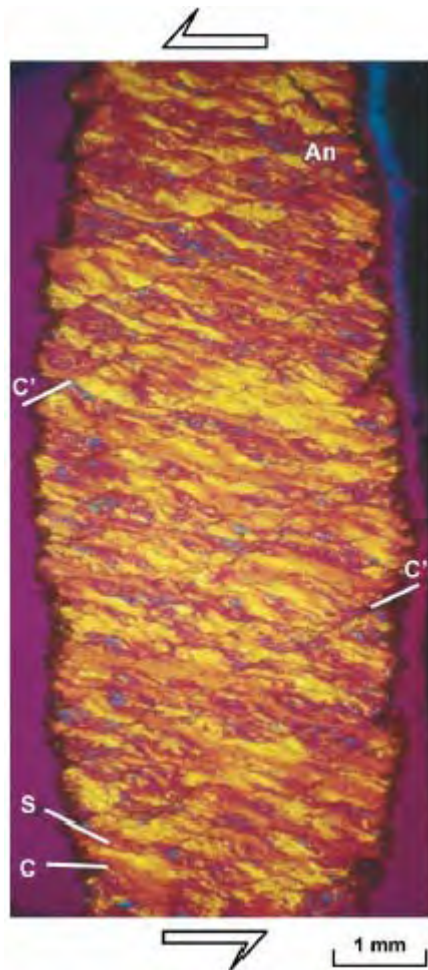
plagioclase deformed in torsion at 1100°C and 10^{-4} s^{-1} ; yellow grains have (010) parallel to shear plane and [100] parallel to X (Ji et al., 2004)
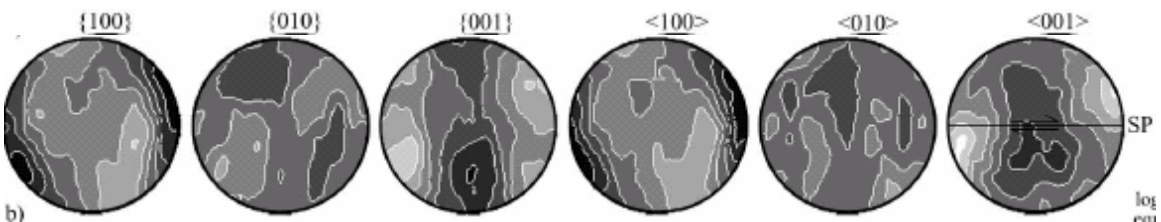
plagioclase dextrally sheared at 10^{-4} s^{-1} and 900°C slipped on <100>{001}(Heidelbach et al., 2000)

Natural Plagioclase Lattice Preferred Orientations
Comparatively few have been measured because it is difficult.
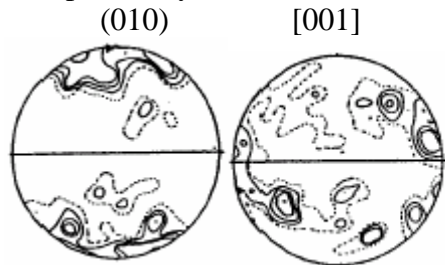
(010)   [001]

plagioclase [001] (010) slip at 800°C (Ji & Mainprice, 1990)
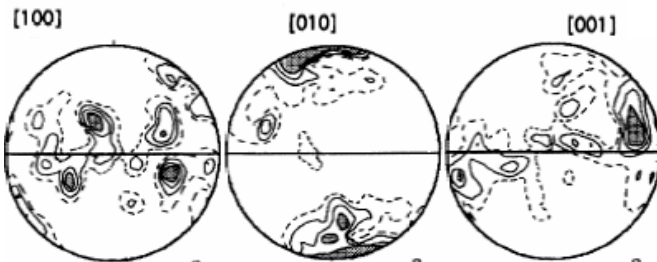
[100]   [010]   [001]

plagioclase from mafic mylonite suggests sinistral [001](010) (Ji et al., 1993)
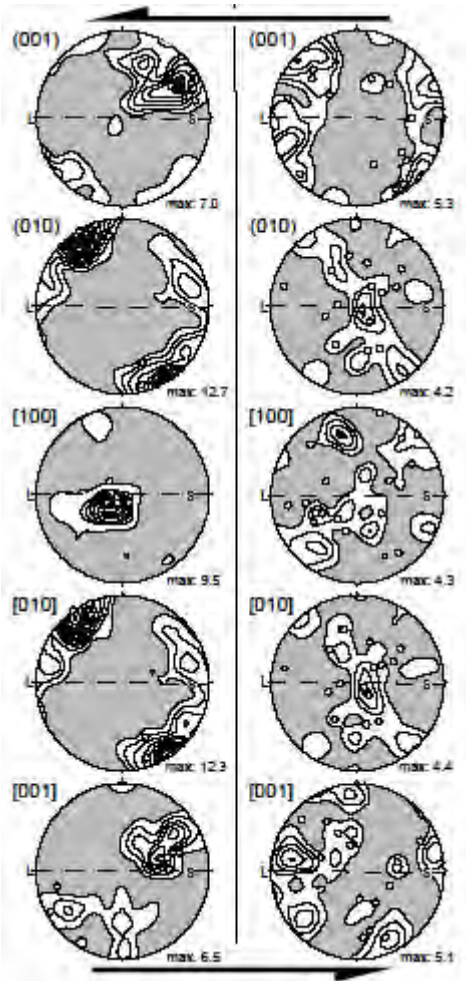
Jotun 700°C porphyroclasts (L) oriented for easy slip on (010)[001] show (010) and [001] oriented at a high Schmid factor, whereas porphyroclasts (R) not oriented for easy slip on (010)[001] show [100](001) (Kruse et al., 2001)

Olivine
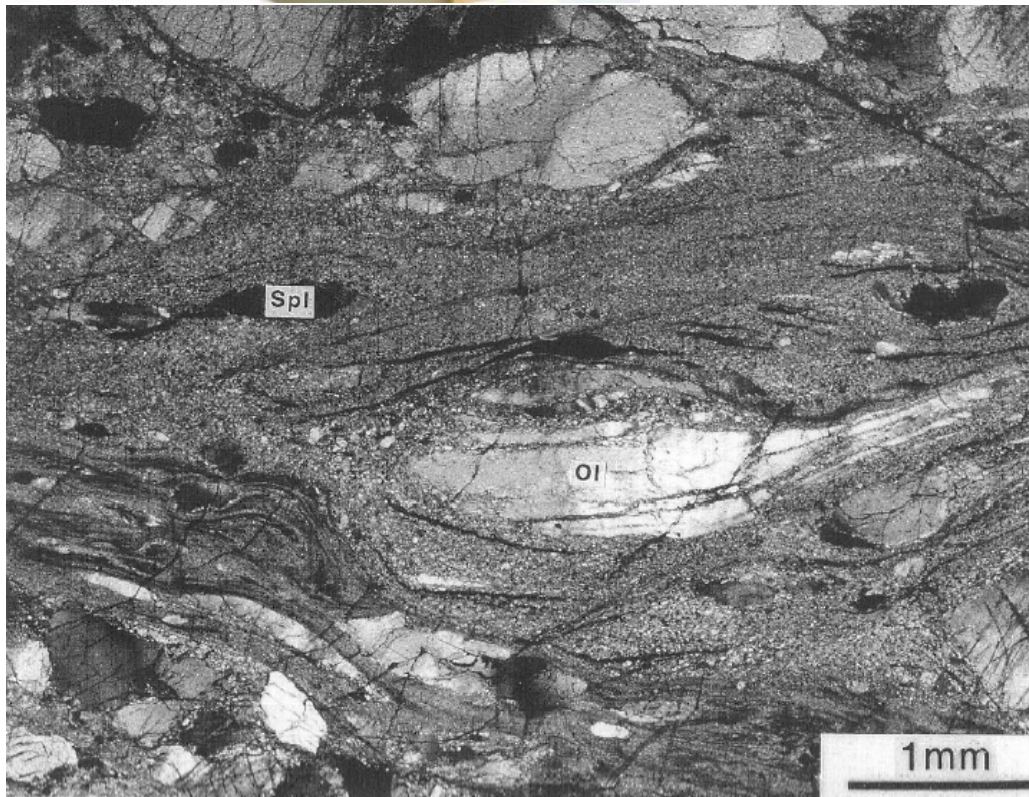
porphyroclasts of olivine and pyroxene in very fine grained matrix of recrystallized olivine and clinopyroxene (Brodie, 1998)
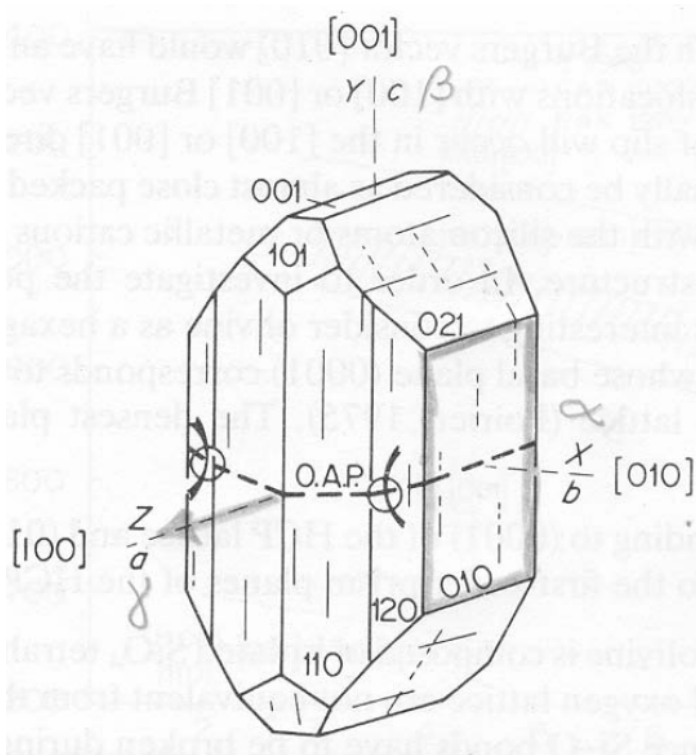
(Nicolas & Poirier, 1976)
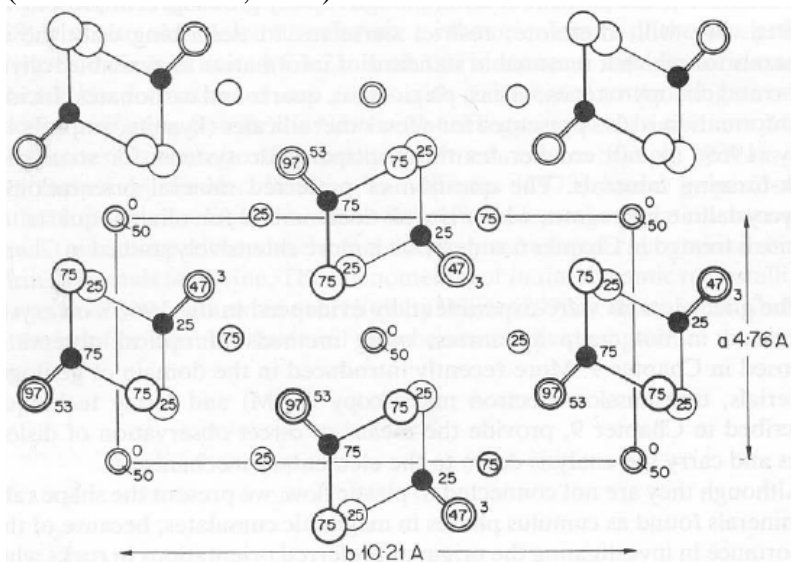
Projection on (001). Olivine is composed of isolated tetrahedral; slip on any plane other than (010) requires breaking Si–O bonds (Nicolas & Poirier, 1976)

olivine slip systems; fontsize indicates prevalence (Nicolas & Poirier, 1976)

low T, high é	med T, med é	high T, low é
(100)[001]	{110}[001]	(010)[100]
{110}[001]	(100)[001]	{0kl}[100]
(100)[010]	(100)[010]	{110}[001]
		(001)[100] elevated H_2O?

		{101}[010]

T	slip system
800	[001](100), [001]{110}, [001] (010), [010](100), [100](010)
1000	[001](100), [001]{110}, [100](001), [100](010)
>1150	[001](010), [100](010)

experimentally observed olivine slip systems (Tommasi et al., 2000)

Experimentally Deformed Olivine
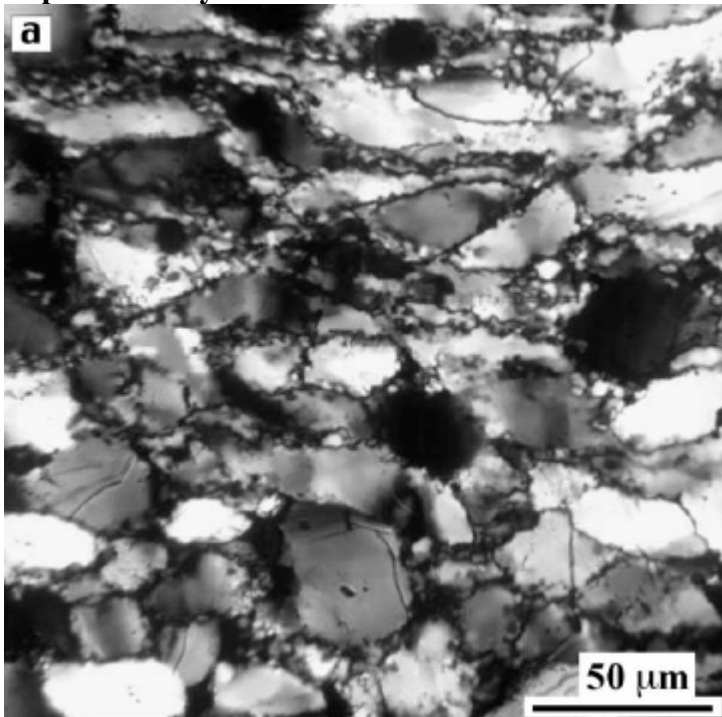
Regime 2 olivine in simple shear 1200°C 10^{-4} s^{-1} (Lee et al., 2002)
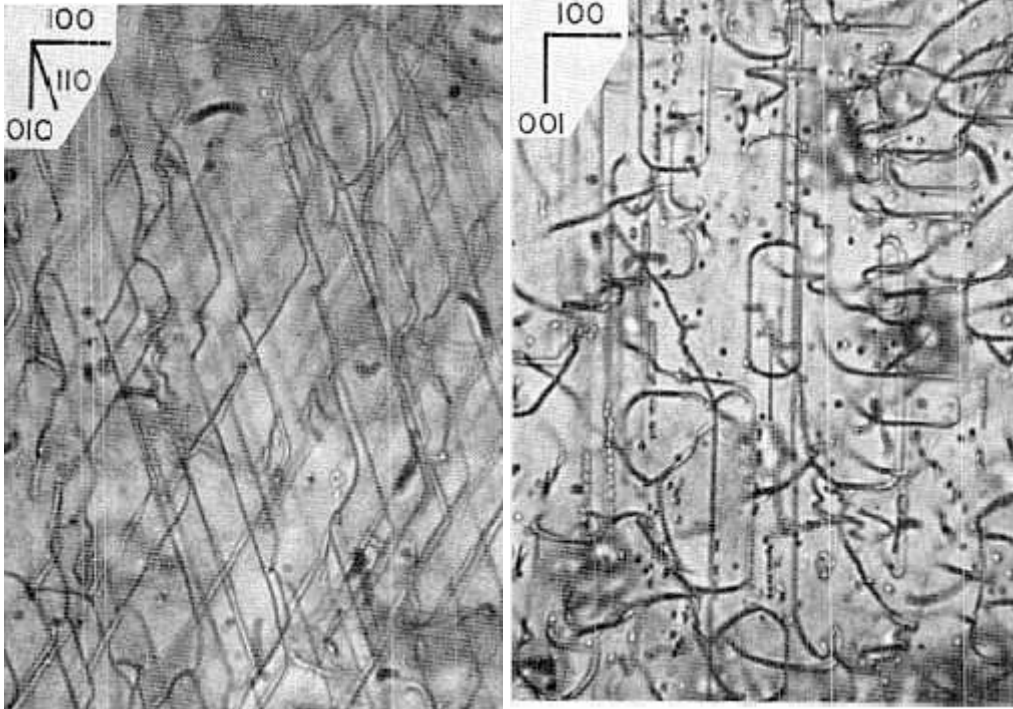
(001) plane shows short screw segments and long edge segments in the <110> directions; (010) plane shows glide loops composed of long and straight edges and short and bent screws (Darot & Guéguen, 1981)
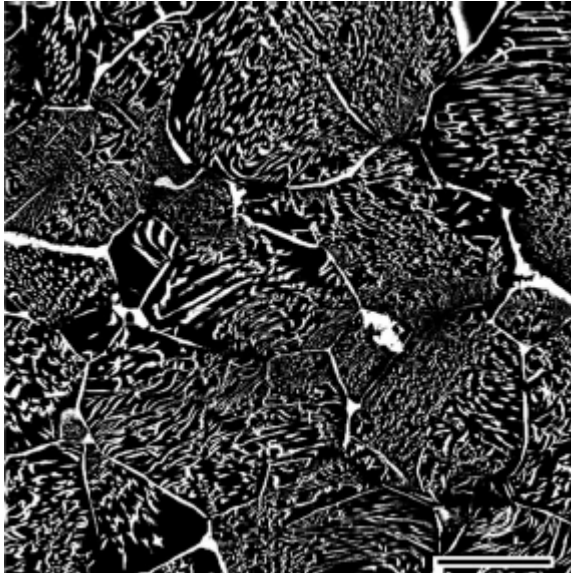
(Jung & Karato, 2001)

Naturally Deformed Olivine
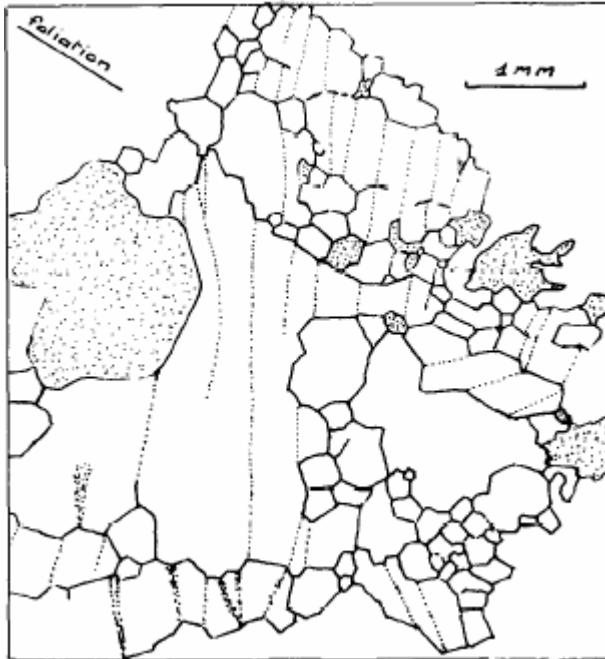
kinking and SGR are important in olivine (Nicolas et al., 1971)
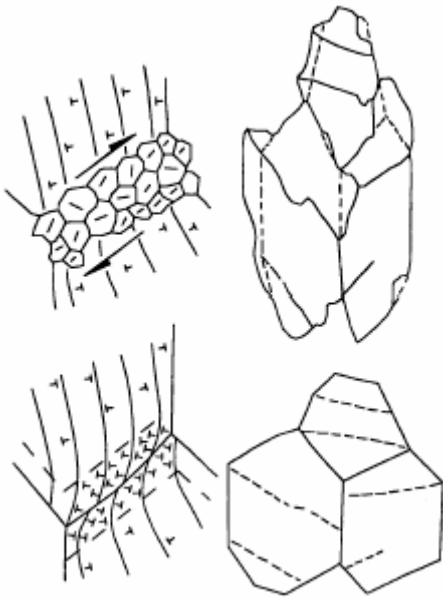
(L) At low T/high stress, olivine recrystallization is by local grain boundary bulging and subgrain rotation. (R) At high T/low stress olivine recrystallization is by subgrain rotation throughout grains and by extensive GBM (Drury et al., 1991)

Naturally Deformed Olivine Textures and Lattice Preferred Orientations
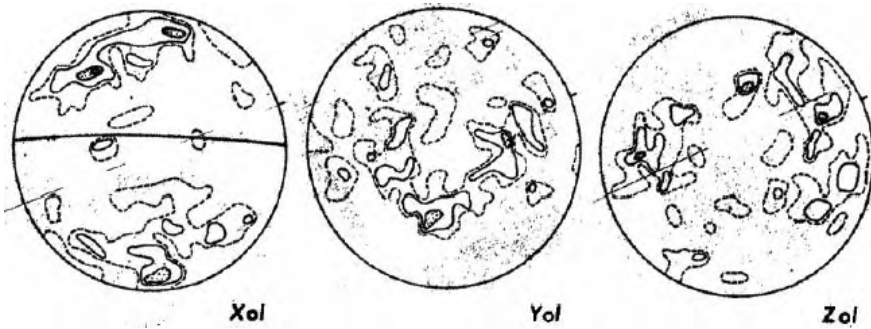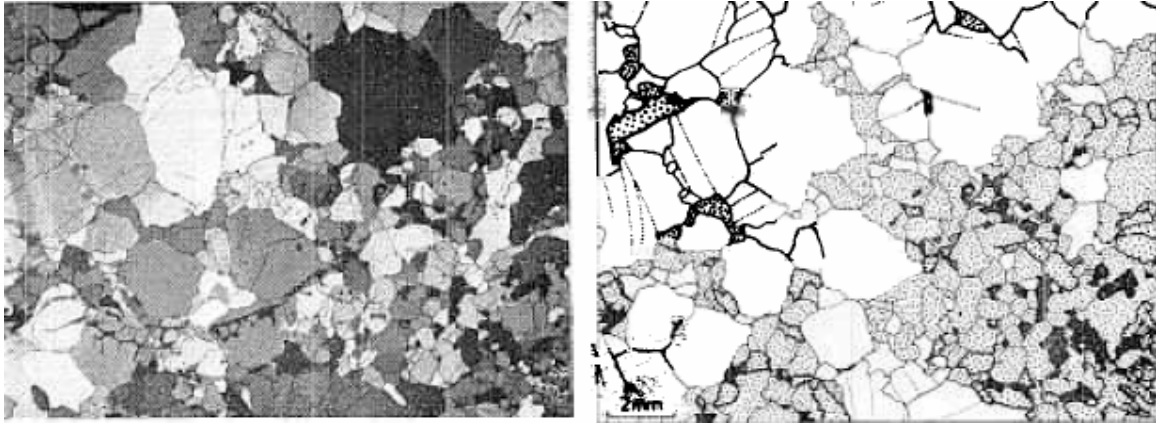
"protogranular" texture: no visible foliation or lineation coarse grains with few KBBs and subgrains. LPO implies [001](100) slip. (orthopyroxene dashed, clinopyroxene heavy dots, spinel black) (Mercier & Nicolas, 1975) "A"
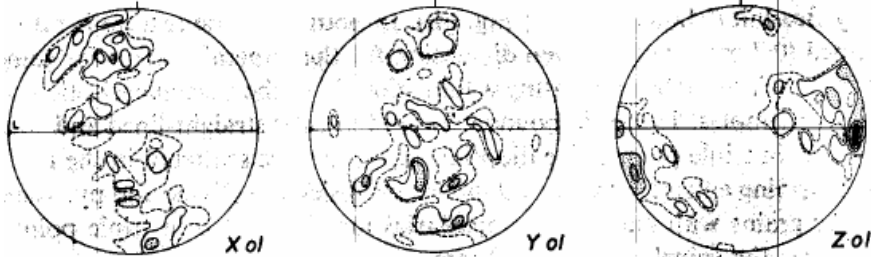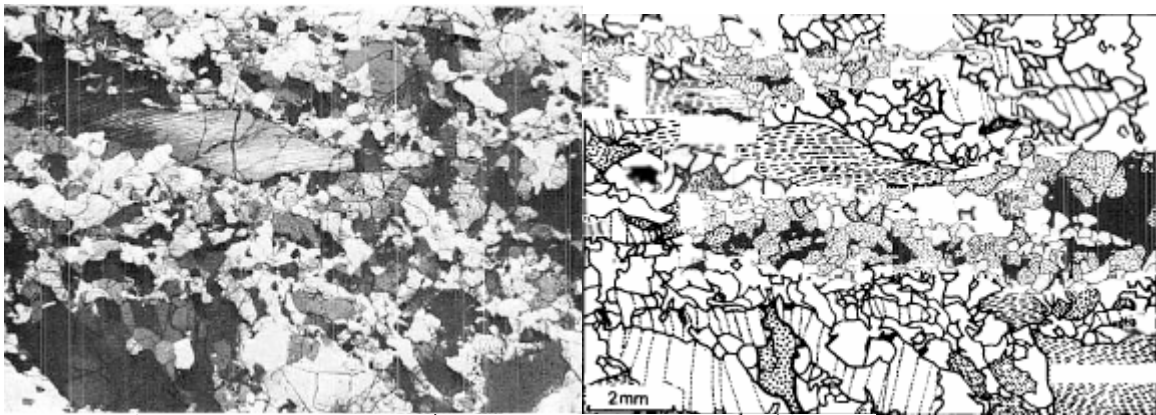
"porphyroclastic" texture: olivine and enstatite porphyroclasts with extensive kink bands and some polygonization and small equant, strain-free grain-boundary neoblasts formed by SGR. LPO implies [001](100) slip (Mercier & Nicolas, 1975) "C' "
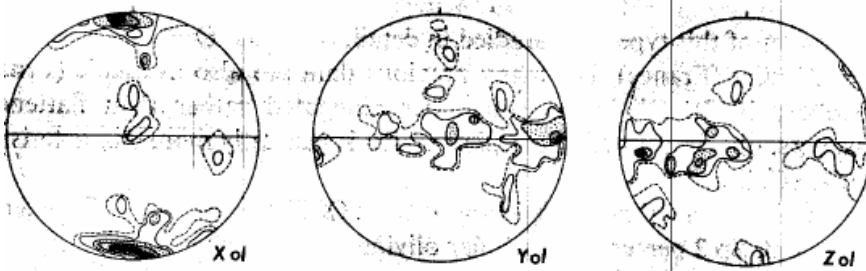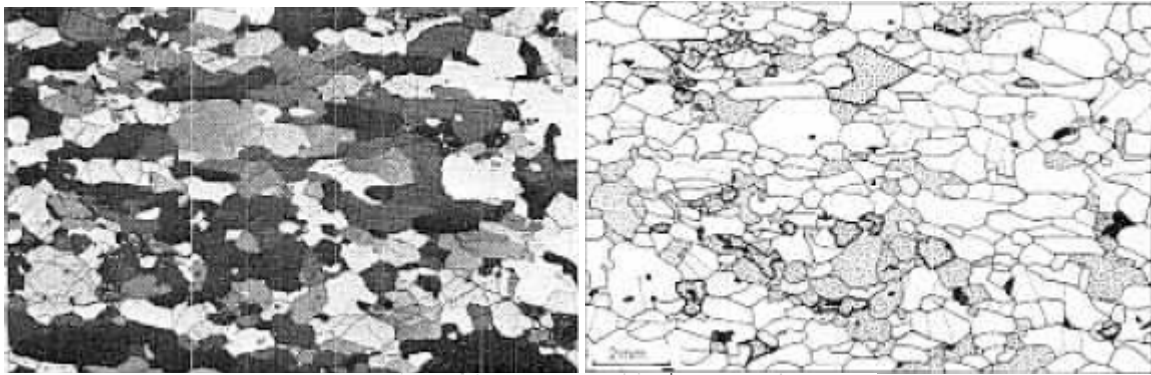
"tabular equigranular" texture: tabular grains with straight GB and 120° triple junctions, some are kinked porphyroclasts with ragged grain boundaries, others are smaller strain-free neoblasts. LPO implies [001](100) + [010](100) slip (Mercier & Nicolas, 1975) "C"
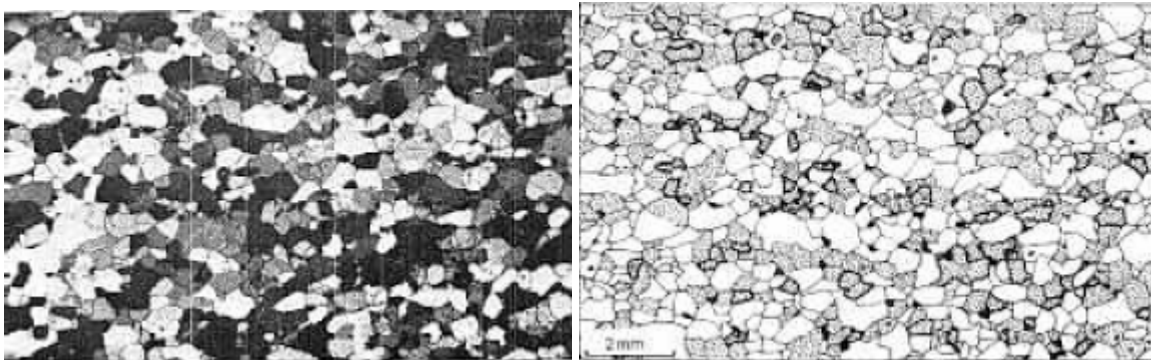
"mosaic equigranular texture": equant grains with straight GB and 120° triple junctions. Weak LPO implies grain boundary sliding (Mercier & Nicolas, 1975)

Laboratory Mechanical Data
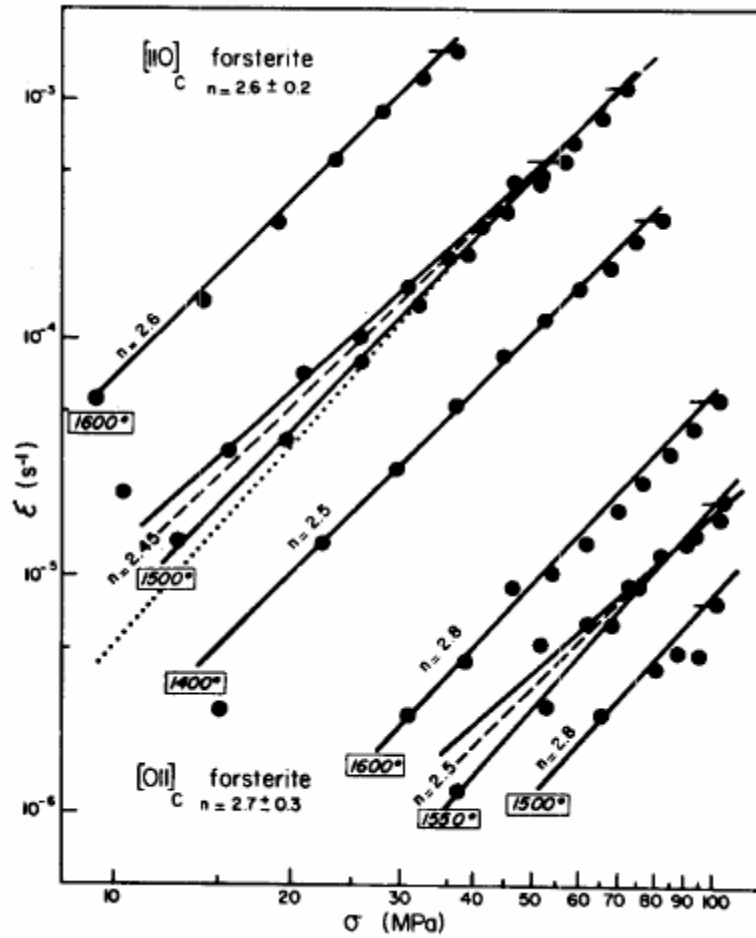
n=3 for single crystals compressed down [110] (Darot & Guéguen, 1981)

General flow law for olivine single crystals:

$$\dot{\varepsilon} = A\sigma^n f_{O_2}^m a_{opx}^q \exp(-Q/RT)$$

each slip system is associated with specific power law parameters, where a_{opx} is the orthopyroxene activity; Q = 250–1000 kJ/mol, n = 3.5 ± 0.1 and m = 0.0–0.4 (Bai et al., 1991)

ANITA BAY DUNITE - RELAXATIONS
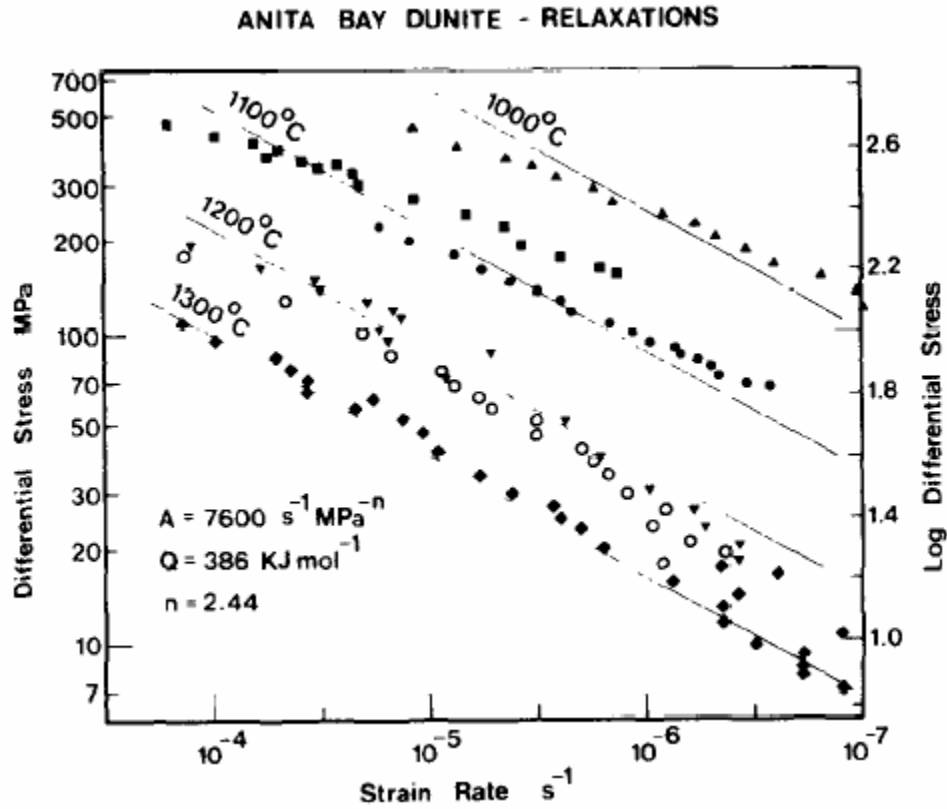
(Chopra & Paterson, 1981)

	$\log_{10}A$ $(s^{-1} MPa^{-n})$	n	Q $(kJ\ mol^{-1})$
Åheim dunite, constant $\dot{\epsilon}$	2.62 ± 0.18	4.48 ± 0.31	498 ± 38
Anita Bay dunite, constant $\dot{\epsilon}$ ($\sigma > \sim 100$ MPa)	3.98 ± 0.17	3.35 ± 0.17	444 ± 24
Anita Bay dunite, relaxation ($\sigma < \sim 100$ MPa)	3.88 ± 0.43	2.44 ± 0.18	386 ± 27

(Chopra & Paterson, 1981)
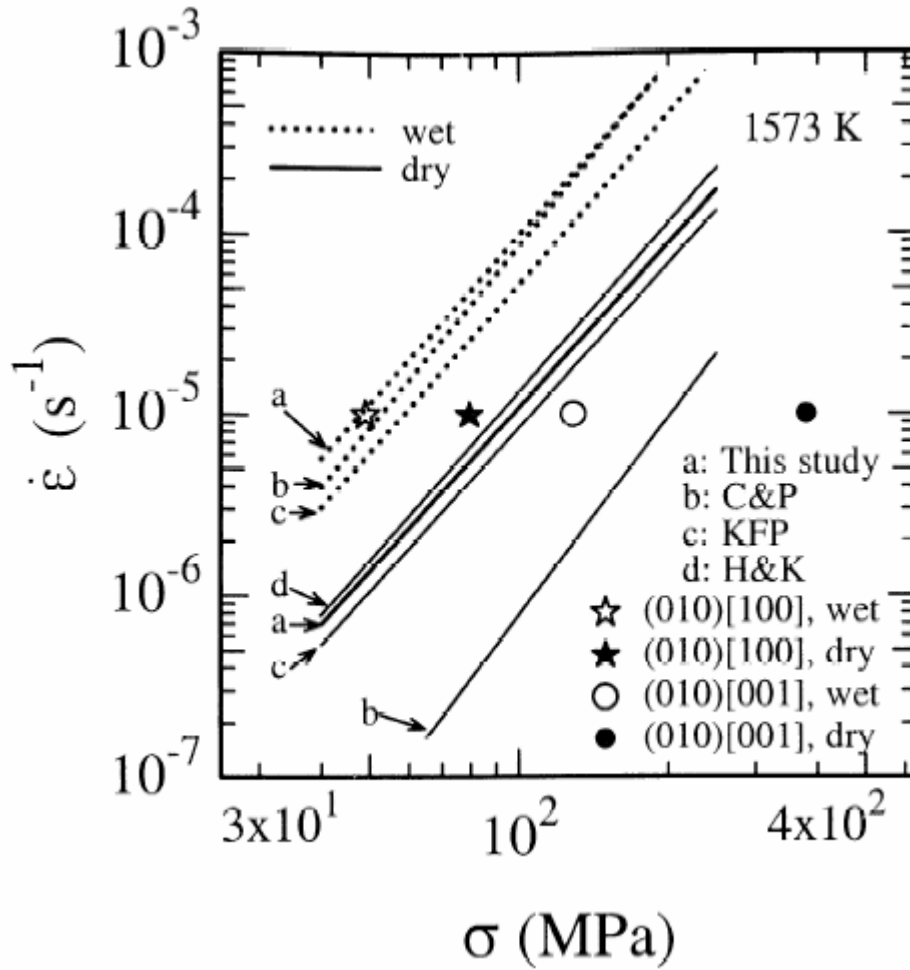
comparison of single-crystal and rock data (Mei & Kohlstedt, 2000). Assessment of single crystal and polycrystal data indicate that n = 3.5 ± 0.3 under wet and dry conditions (Hirth & Kohlstedt, 2003)
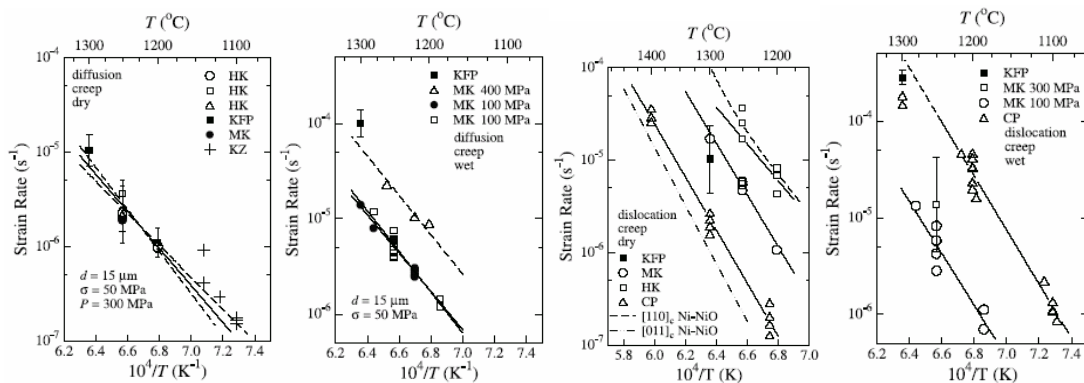
activation energies for dry diffusion creep 375 ± 50 kJ/mol, wet diffusion creep 375 ± 75 kJ/mol, dry dislocation creep 530 ± 4 kJ/mol, and wet dislocation creep 520 ± 40 kJ/mol (Hirth & Kohlstedt, 2003)
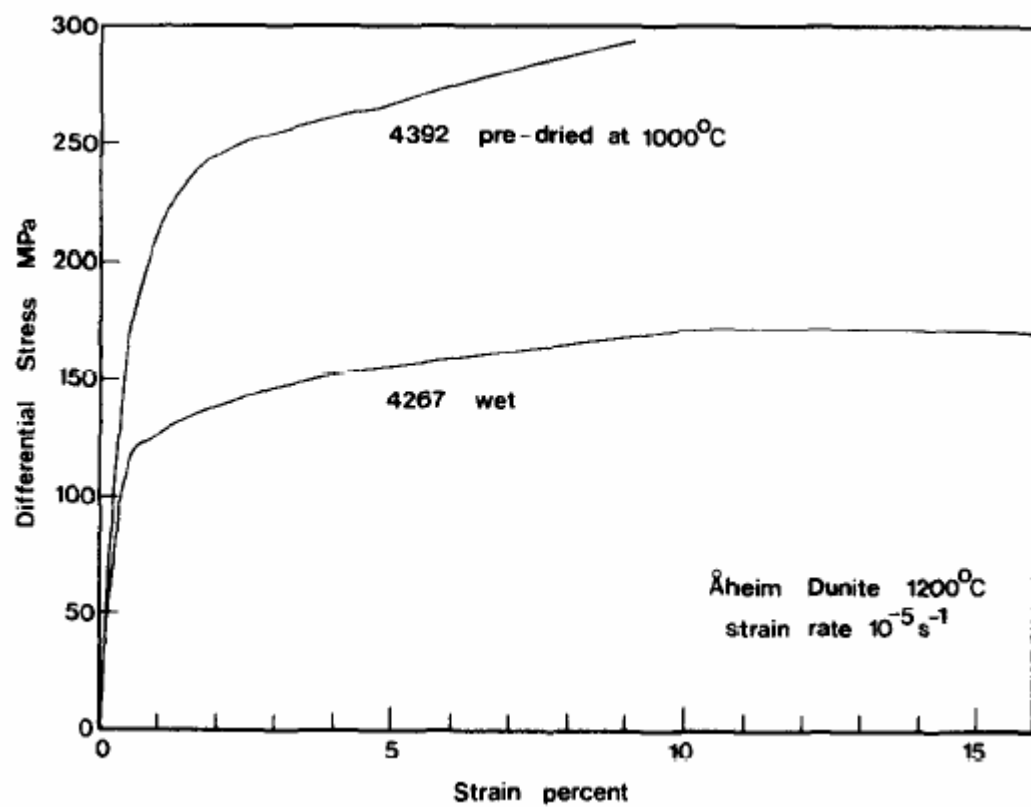
hydrolytic weakening (Chopra & Paterson, 1981).
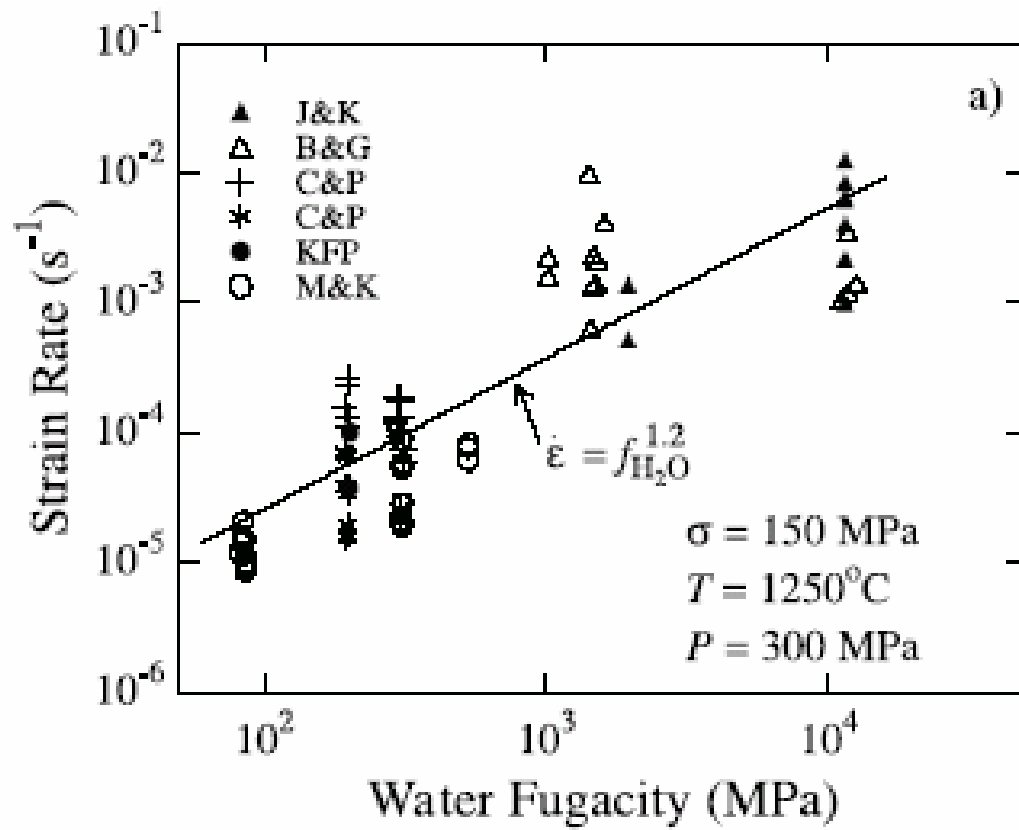
effect of f_{H2O} (Hirth & Kohlstedt, 2003)
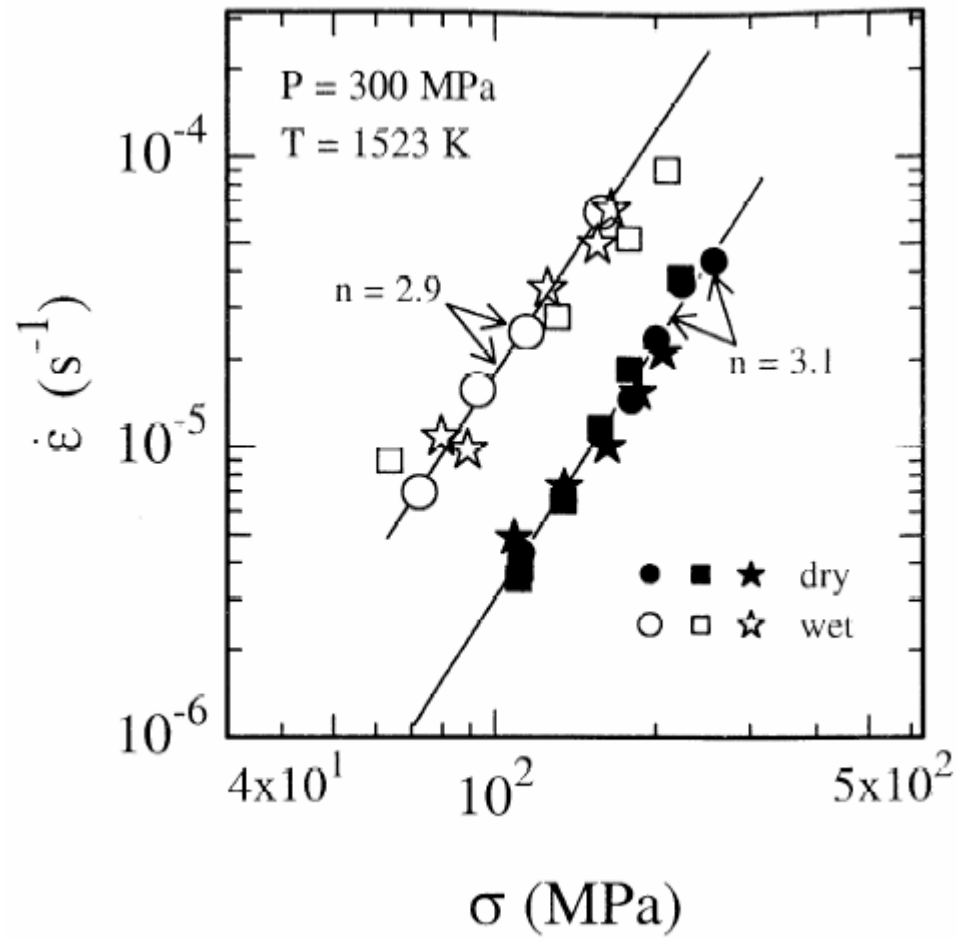
$$\dot{\varepsilon} = A \frac{\sigma^n}{d^m} f_{H2O}^r \exp(-Q / RT)$$

Dislocation creep of olivine polycrystals gives A = 4.6E3 μm^3 $MPa^{-3.7}$ s^{-1}, n=3, m = 1, r = 0.69, Q = 470 kJ/mol (Mei & Kohlstedt, 2000)
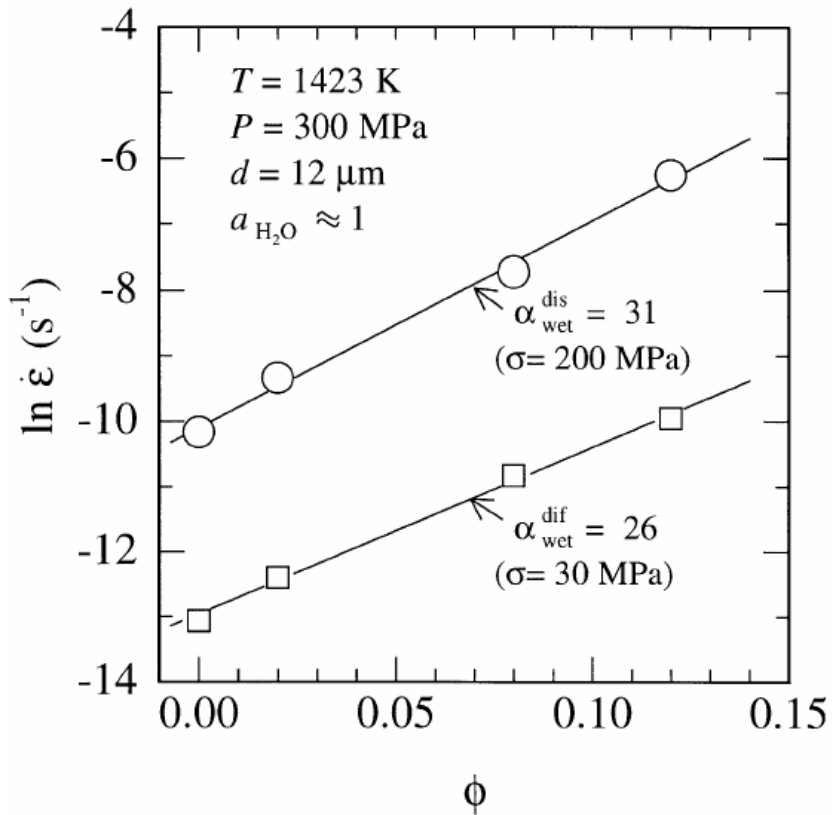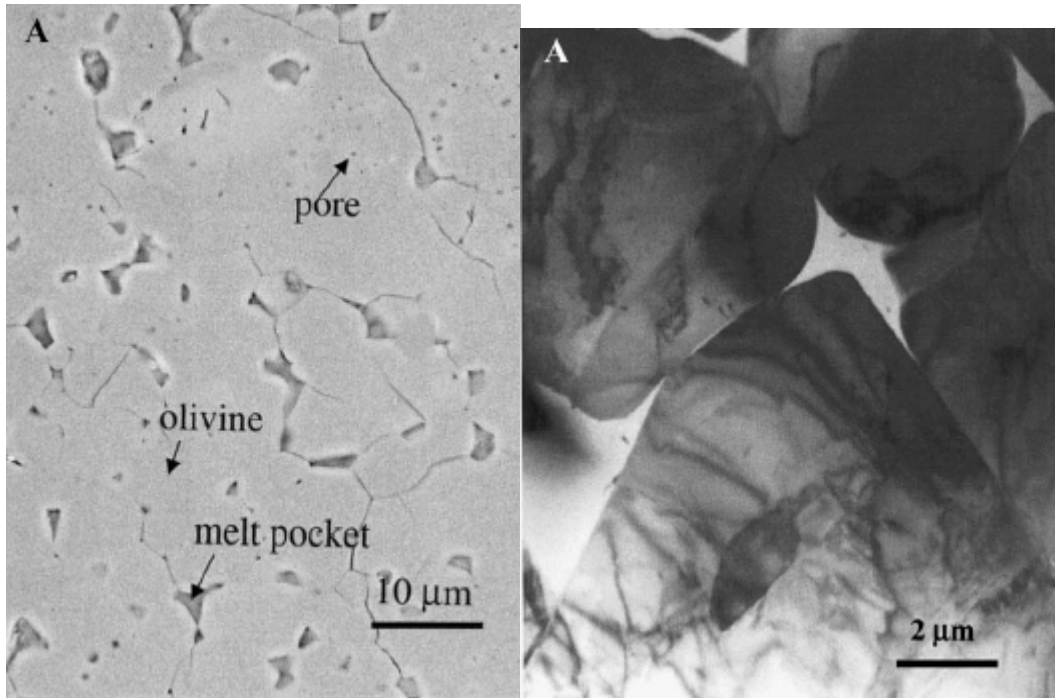
deformation of partially melted dunite in both the diffusion creep and dislocation creep regimes (Mei et al., 2002)
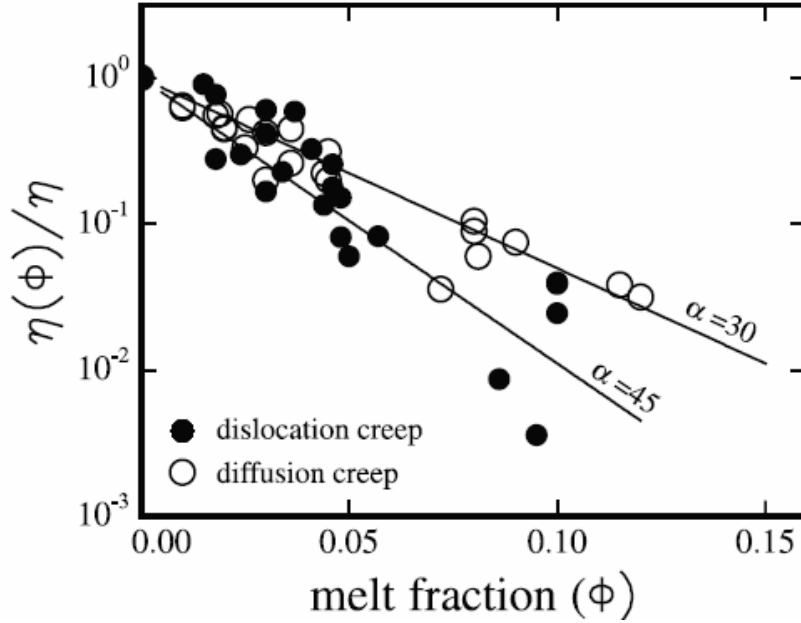
effect of melt is such that $\alpha = 25$–30 in the diffusion creep regime and 30–45 in the dislocation creep regime in dunite, and ~20 and ~25 in lherzolite (perhaps because orthopyroxene does not wet as well and sucks up some melt, reducing the effect) (Hirth & Kohlstedt, 2003)

Table 1: Rheological Parameters for Equation (1).

	A^a	n	p	r^b	α	E^* (kJ/mol)	V^* (10^{-6} m^3/mol)
dry diffusion	1.5×10^9	1	3	-	30	375 ± 50	2-10
wet diffusion	$2.5\times10^{7\,d}$	1	3	0.7–1.0	30	375 ± 75	0-20
wet diffusion (constant C_{OH})^c	1.0×10^6	1	3	1	30	335 ± 75	4
dry dislocation	1.1×10^5	3.5 ± 0.3	0	-	30-45	530 ± 4	(see Table 2)
wet dislocation	1600	3.5 ± 0.3	0	1.2 ± 0.4	30-45	520 ± 40	22 ± 11
wet dislocation (constant C_{OH})^e	90	3.5 ± 0.3	0	1.2	30-45	480 ± 40	11
dry GBS, T>1250°C	4.7×10^{10}	3.5	2	-	30-45	600^f	(see Table 2)^g
dry GBS, T<1250°C	6500	3.5	2	-	30-45	400^f	(see Table 2)^g

^{a}For stress in MPa, f_{H_2O} in MPa (or C_{OH} in H/10^6Si) and grain size in µm.
^{b}Uncertainty in r is correlated with uncertainty in V^*
^{c}Example calculation for $C_{OH} = 1000$ H/10^6Si, d = 10 mm, T = 1400°C, P = 1 GPa, σ = 0.3 MPa:
$\dot\varepsilon = (1.0\times10^6)*(0.3)^1*(10,000)^{-3}*(1000)^1*\exp[-(335000+10^9*4\times10^{-6})/(8.314*1673)] = 7.8\times10^{-15}$/s
^{d}Value for A is given for $r = 1$.
^{e}Example calculation for $C_{OH} = 1000$ H/10^6Si, T = 1400°C, P = 1 GPa, σ = 0.3 MPa:
$\dot\varepsilon = (90)*(0.3)^{3.5}*(1000)^{1.2}*\exp[-(480000+10^9*11\times10^{-6})/(8.314*1673)] = 2.5\times10^{-12}$/s
^{f}The activation energy for GBS is assumed to be that for slip on (010)[100], which changes with increasing temperature [Bai et al., 1991]. The values given here include the effect of temperature on oxygen fugacity.
^{g}The value for V^* is assumed to be the same as that for dislocation creep.

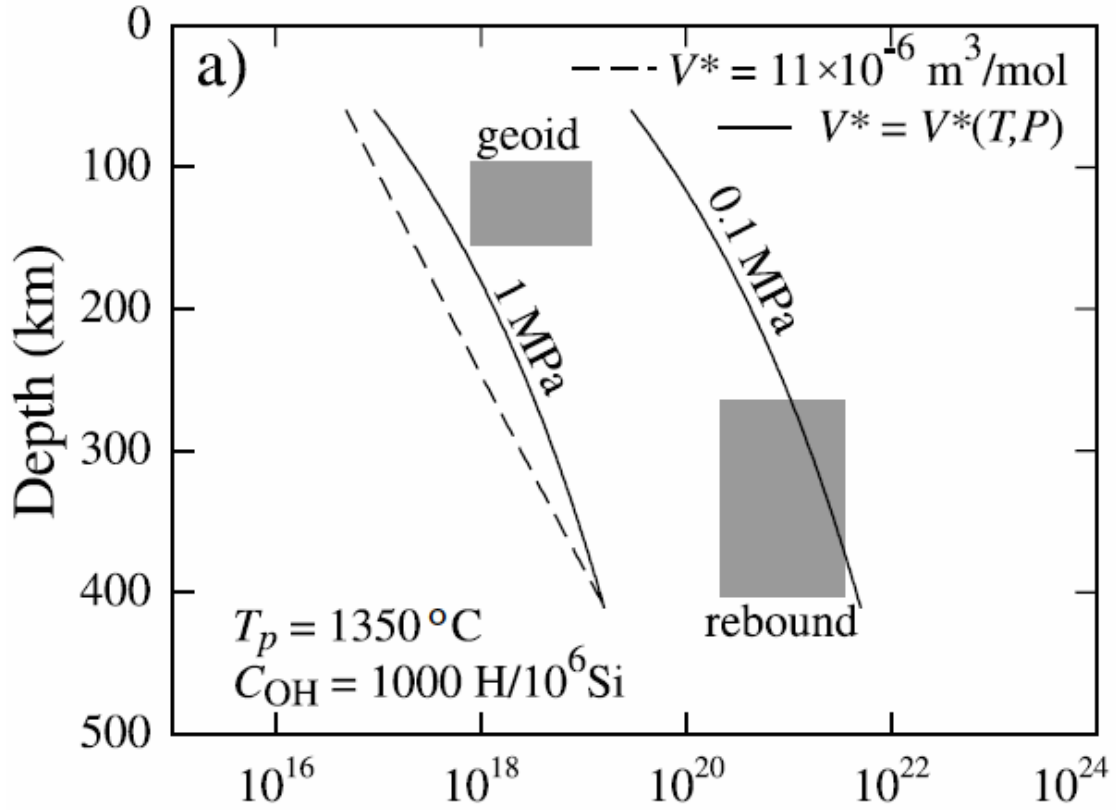$$\dot\varepsilon = A\frac{\sigma^n}{d^p}\exp(\alpha\phi)f_{H2O}^r \exp\left(\frac{E^* + PV^*}{RT}\right)$$

where α is and ϕ is melt fraction (Hirth & Kohlstedt, 2003)

water concentration C_{OH} in olivine is

$$C_{OH} = A_{H_2O}\exp\left[-\left(E_{H_2O} + PV_{H_2O}\right)/RT\right]f_{H_2O}$$

where $A_{H2O} = 26$ ppm H/MPa, $E_{H2O} = 40$ kJ/mol, $V_{H2O} = $ 1E-5 m^3/mol (Hirth & Kohlstedt, 2003).

Extrapolation to Earth

a)

$V^* = 11 \times 10^{-16}$ m^3/mol

$V^* = V^*(T,P)$

geoid

0.1 MPa

1 MPa

$T_p = 1350\,°C$

$C_{OH} = 1000$ H/10^6Si

rebound

viscosity for adiabatic mantle with T = 1350°C (dashed line is constant V* and boxes are estimates from geoid and glacial rebound) (Hirth & Kohlstedt, 2003)
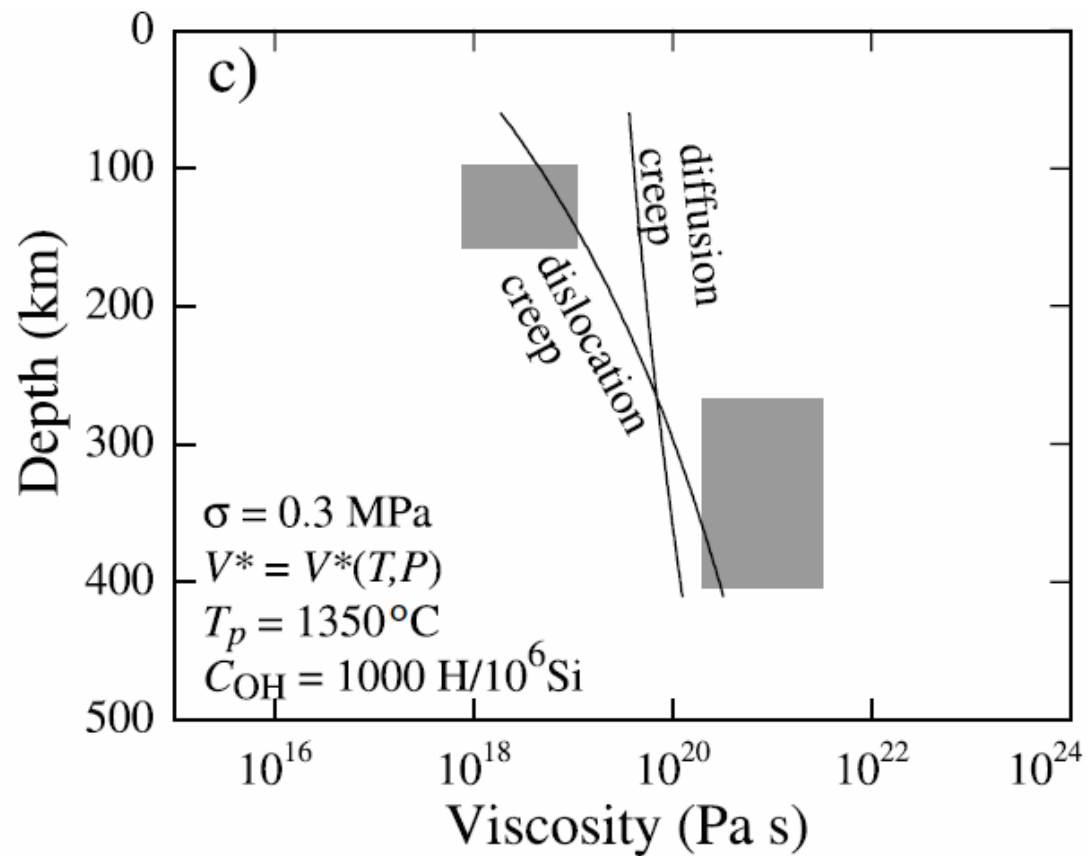
dislocation creep for 0.3 MPa compared with diffusion creep for grain size of 10 mm (the probable grain size of the upper mantle); transition to diffusion creep is predicted at depth of >250 km (Hirth & Kohlstedt, 2003)
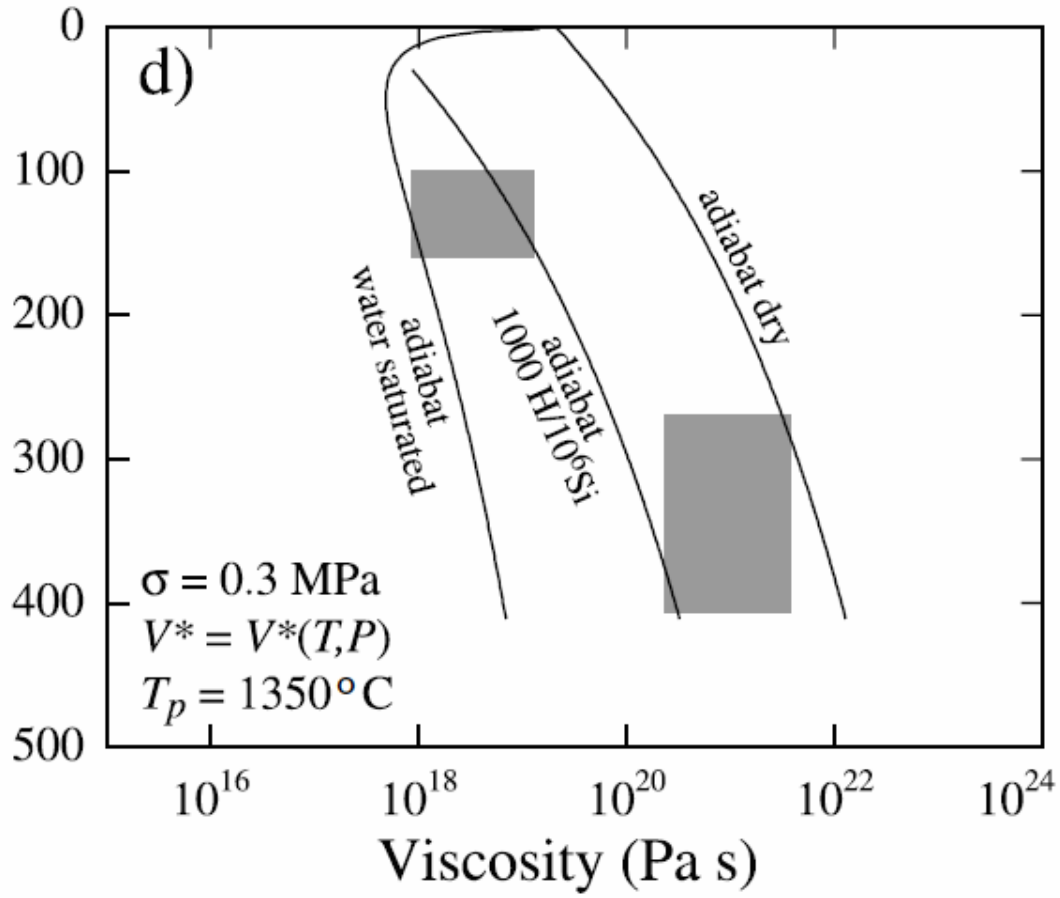
comparison of dry and H$_2$O-saturated adiabats (Hirth & Kohlstedt, 2003)
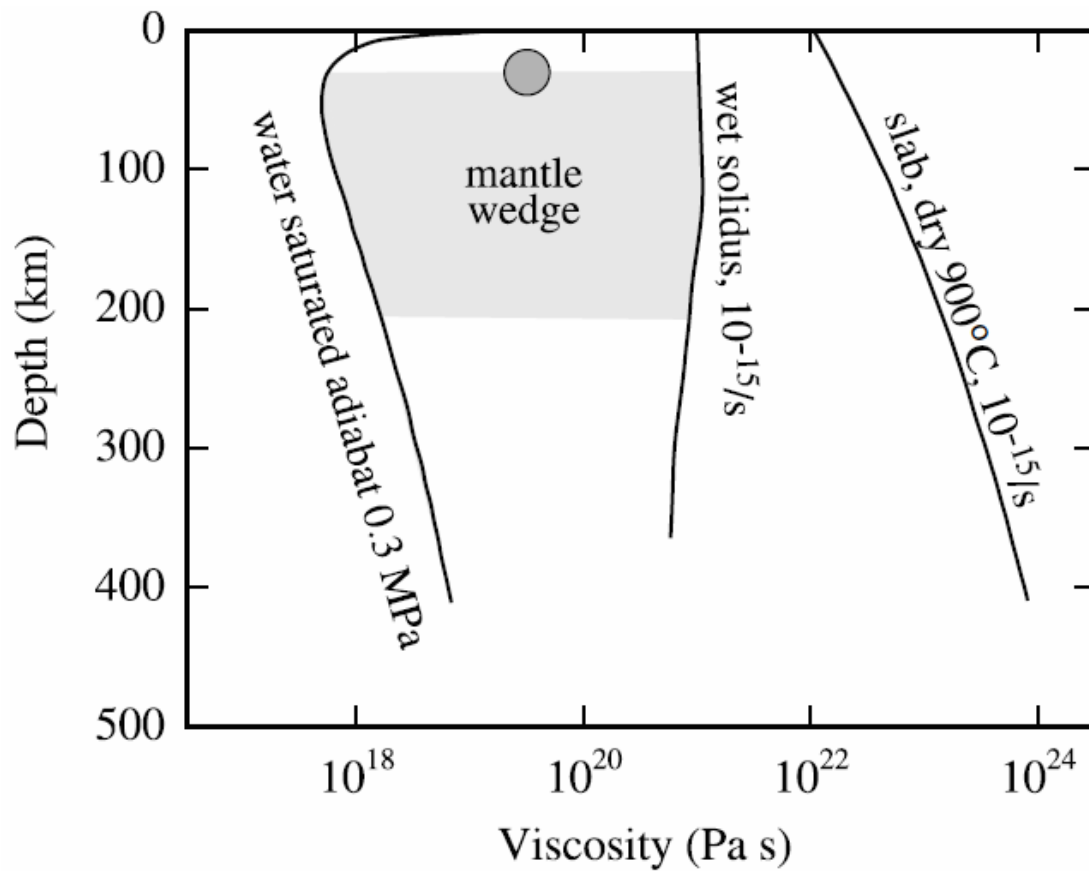
viscosities predicted for subduction-zone mantle wedges (Hirth & Kohlstedt, 2003)

Experimentally Produced Olivine Lattice Preferred Orientations
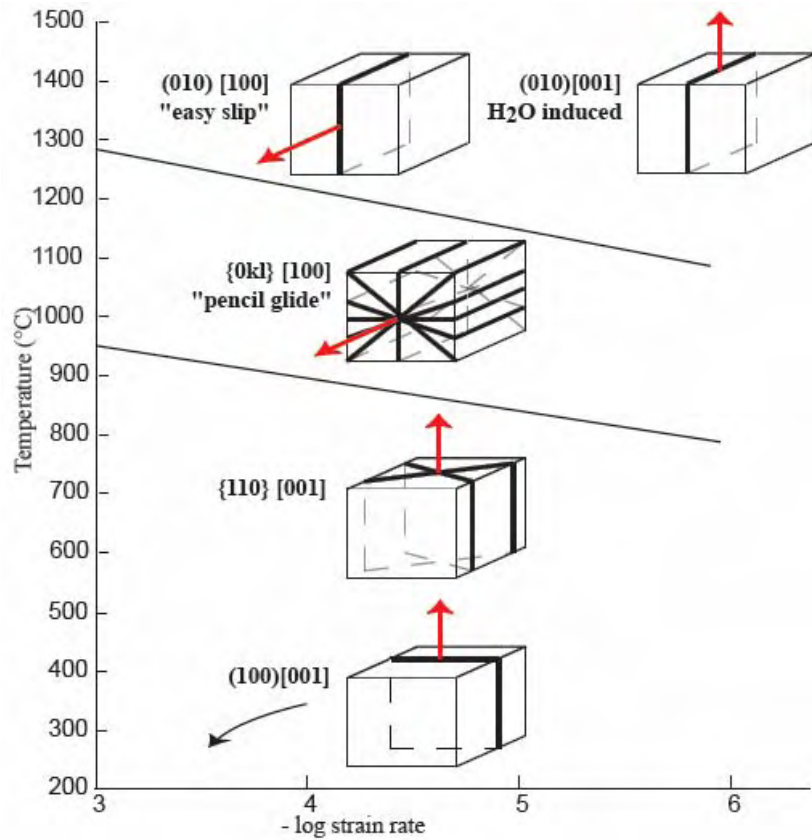
(from Luc Mehl, after Carter & Avé Lallement, 1970).
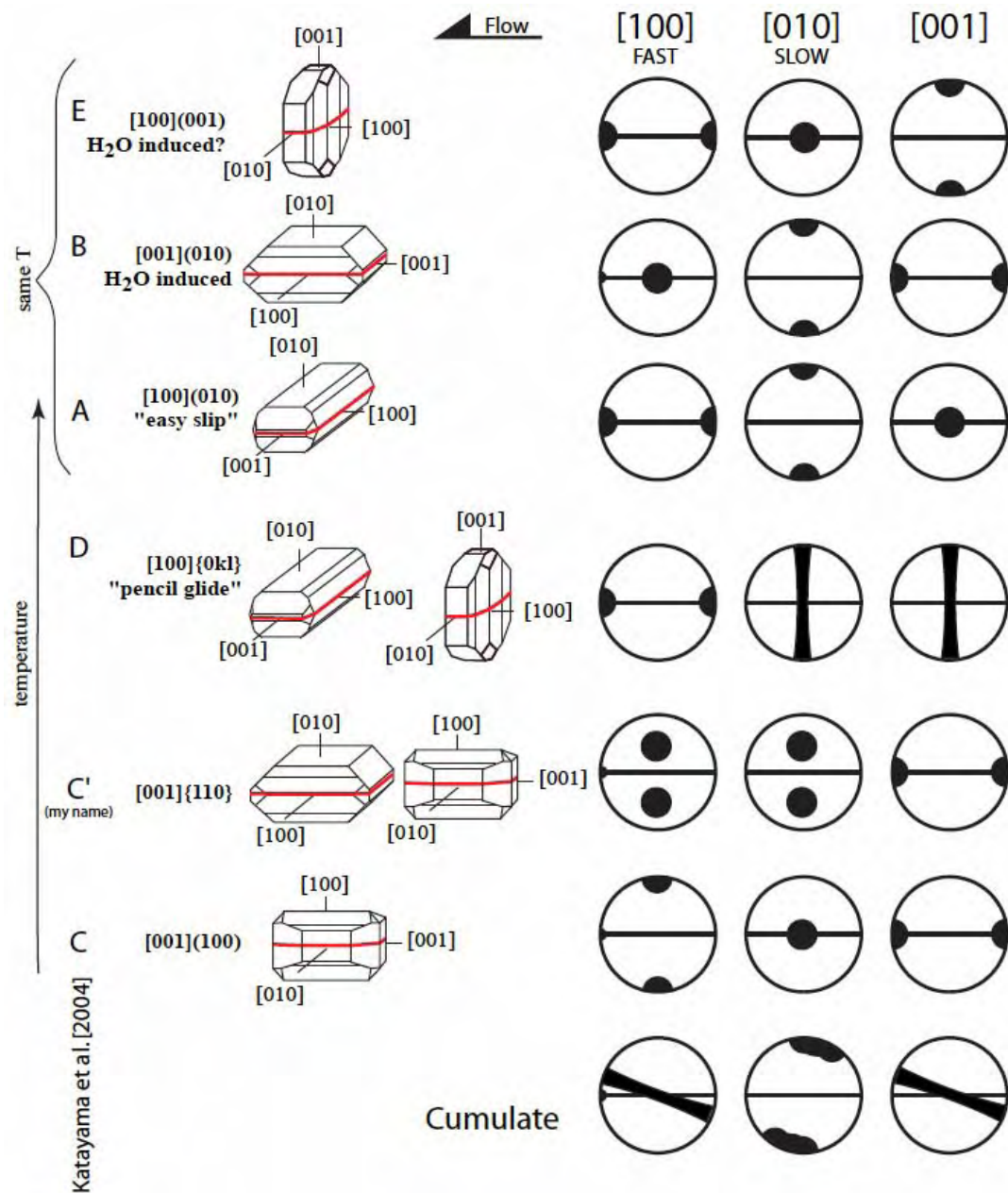
(after Luc Mehl)
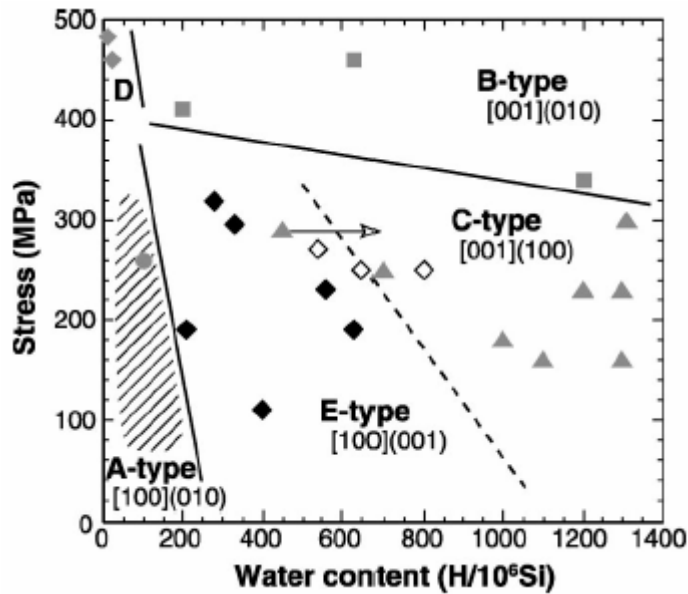
[*Jung and Karato*, 2001] conducted 14 dunite simple-shear experiments at 1400–1570 K, 200–1300 ppm H/Si, shear strain rate = 5E–6 to 1E–3 s^{-1}, σ = 160–460 MPa. They reported four fabric types, which they equated with different σ and H contents. This was subsequently updated by Katayama et al. (2004), who added a fifth type

Easy Glide (Type "A"; Katayama et al., 2004) [100](010) high-T, low-stress
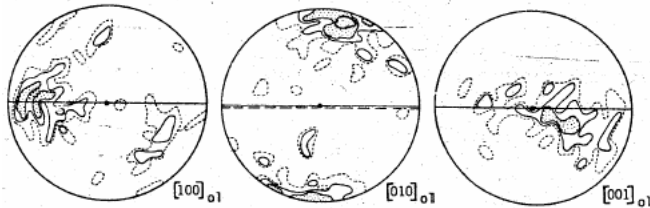
dextral shear at Lanzo (Boudier et al., 1978) "A"
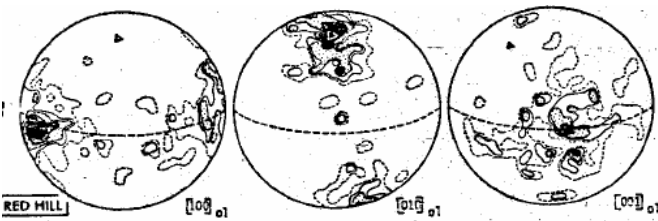
Red Hill (Nicolas et al., 1981) "A"
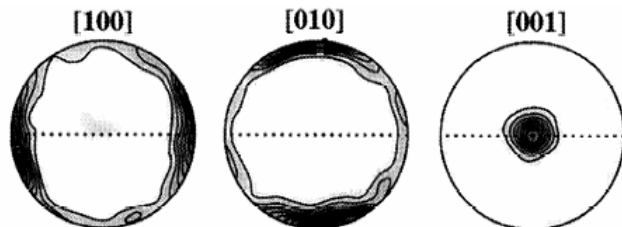
kimberlite (Tommasi et al., 2000) "A"
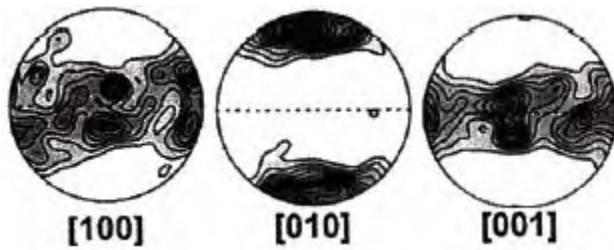
experimentally deformed dunite (Nicolas et al., 1973)
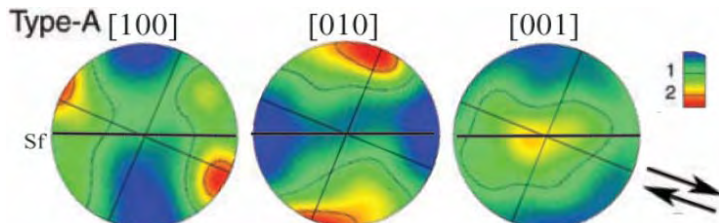
Experimental [100](010) slip (Zhang & Karato, 1995; Jung & Karato, 2001) "A"
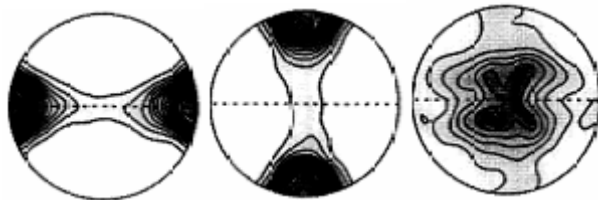
pure shear simulation of "high-temperature" slip [100](010) and [100](001) (Tommasi et al., 2000) "A"
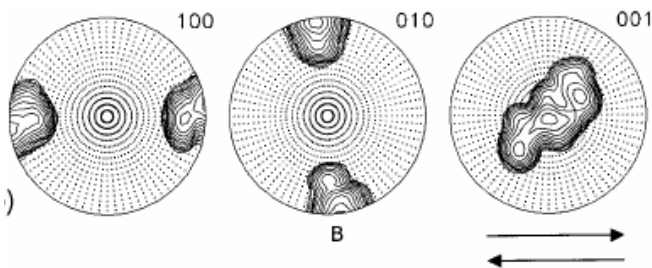
calculated pattern (Wenk & Tomé, 1999) "A"
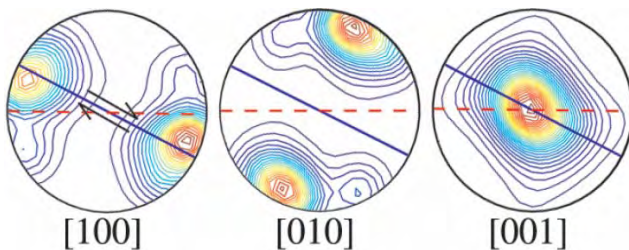
theoretical model of above (Kaminski & Ribe, 2001) "A"

Low-T, high-stress (Type "C") [001](100) and "C' " [001]{110}
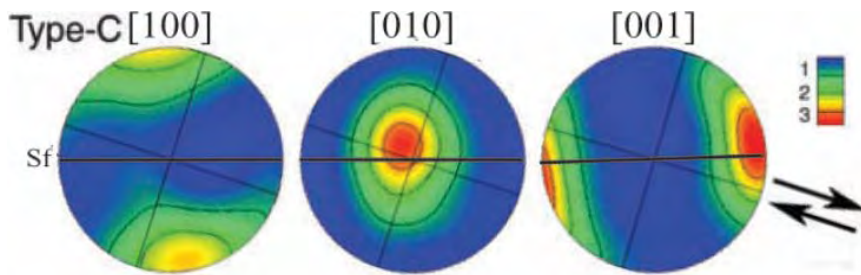
Type C: [001] ≈ lineation, [100] ⊥ foliation—[001](100) slip (Jung & Karato, 2001) (not known in nature [*Ismail and Mainprice*, 1998]) #6
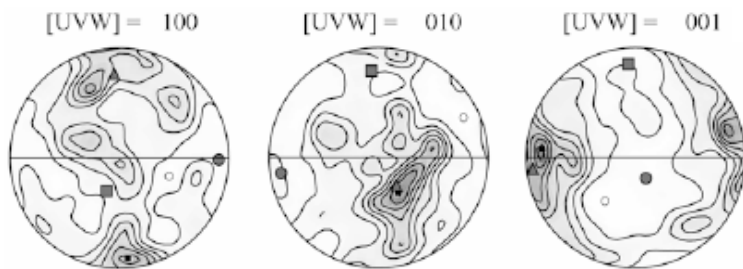
Cima di Gagnone (Frese et al., 2003) "C"

pure shear simulation of "low-temperature" slip [100](001), [001](100), [001]{110}, [100](010) (Tommasi et al., 2000) "C"
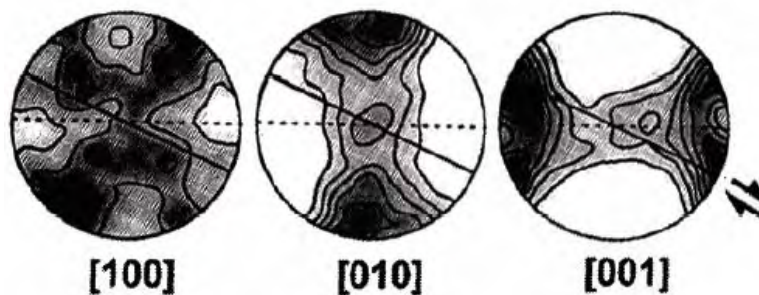
simple shear simulation of "low-temperature" slip [100](001), [001](100), [001]{110}, [100](010) (Tommasi et al., 2000) "C"

H$_2$O-Induced (Type "B"; Katayama et al., 2004) [001](010)
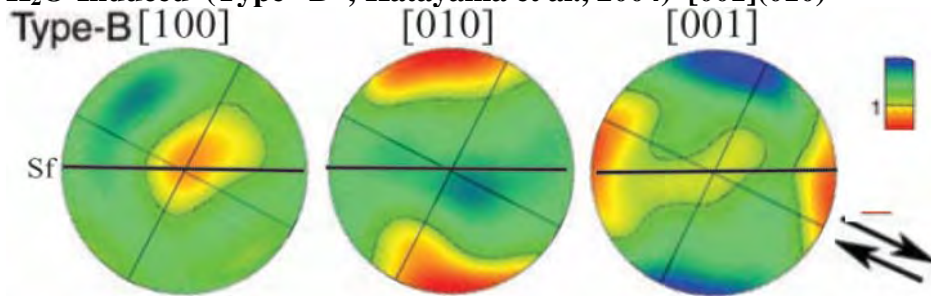
Type B: [001] ≈ lineation, [010] ⊥ foliation—[001](010) slip (Jung & Karato, 2001) (not known in nature [*Ismail and Mainprice*, 1998]) "B"
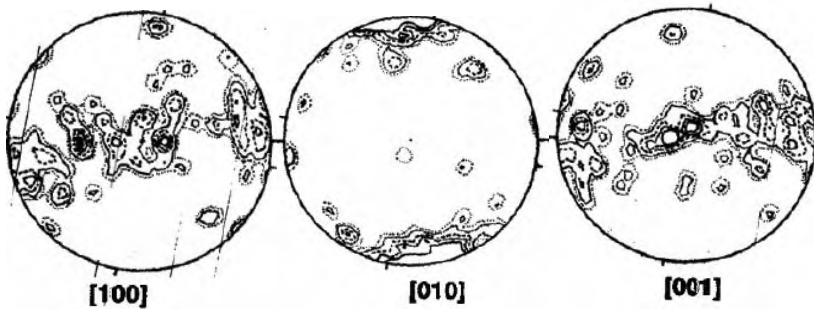
Hessian xenolith implying [h0l](010) (Wedel et al., 1992) "A"+"B"
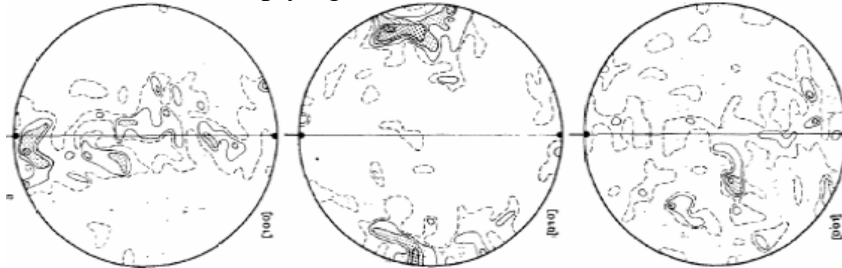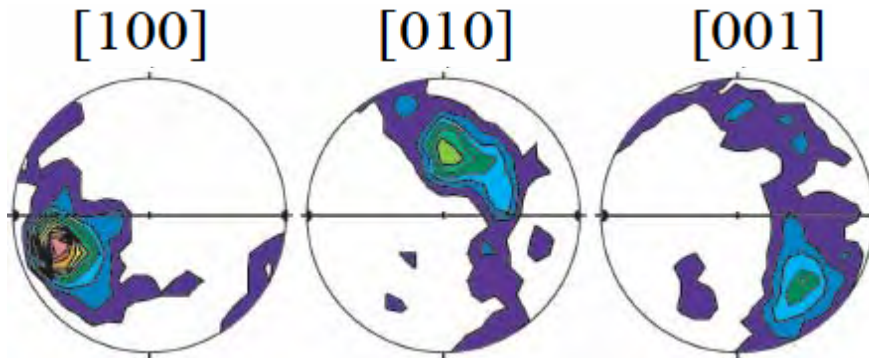

New Caledonia (Prinzhofer et al., 1980) "A"+"B"
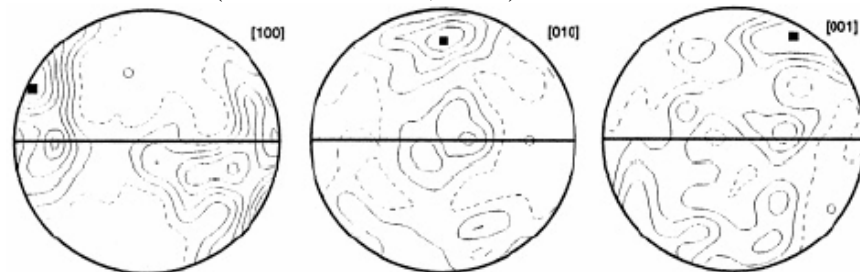
unspecified location (Type 3): all three axes form girdles, with a [100] girdle in the XY plane, implying [100](0kl) slip (Ismail & Mainprice) "A" + "E"
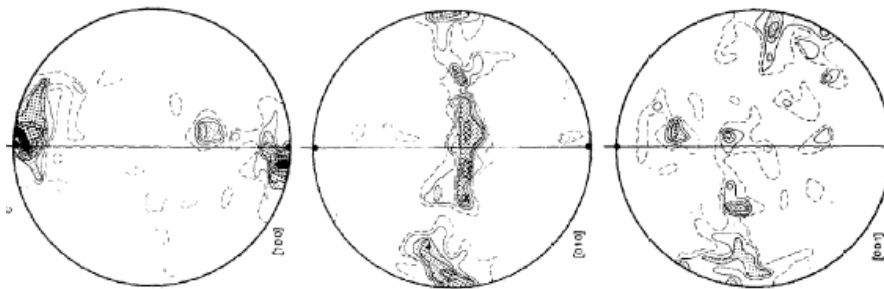

"Pencil Glide" (Type "D"; Katayama et al., 2004) [100]{0kl}

a [100] b [010] c [001]

Sf γ ~ 4
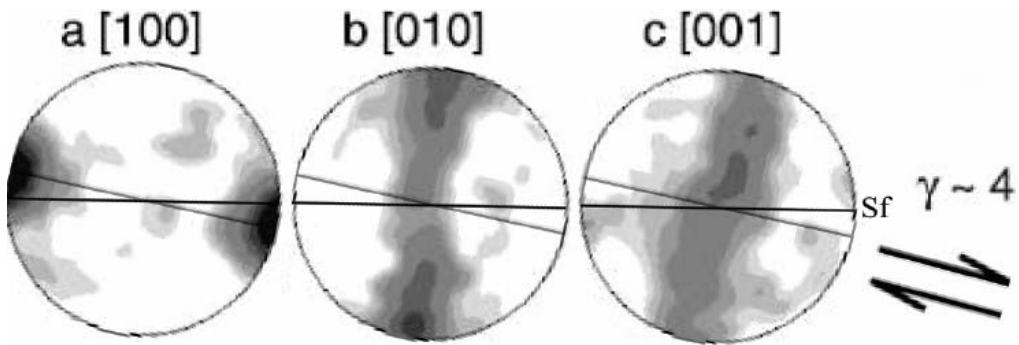
[*Bystricky et al.*, 2000] dunite torsion experiments at 1200°C, <30 ppm H/Si, 10^{-4} s^{-1}, σ = 200–300? MPa. Neoblasts showed [100] || shear direction, and the other directions are girdles, implying [100]{0kl} slip (Type D of [*Jung and Karato*, 2001] and Type 2 of [*Ismail and Mainprice*, 1998]). "D"
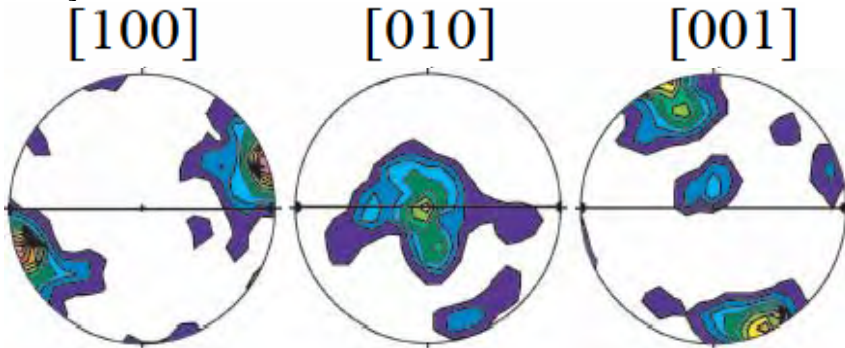

[100] [010] [001]

[100]{0kl} (Mehl et al., 2003) "D"

New Caledonia (Prinzhofer et al., 1980) "D"

[100] [010] [001]
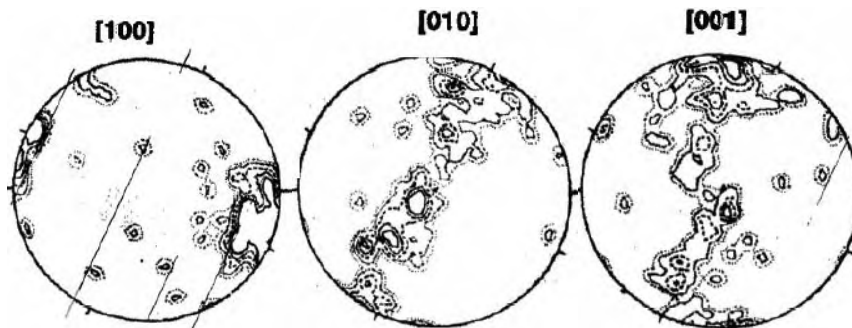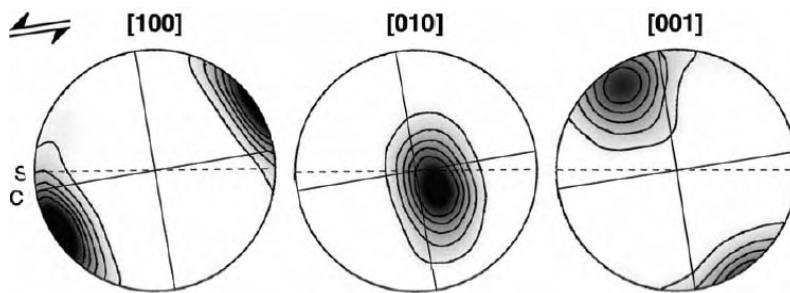
Hessian xenolith (Wedel et al., 1992) "D"

H₂O-Induced? (Type "E" ; Katayama et al., 2004) [100](001)

may be the result of "wet" conditions and grain-boundary migration [*Tommasi et al.*, 2000]
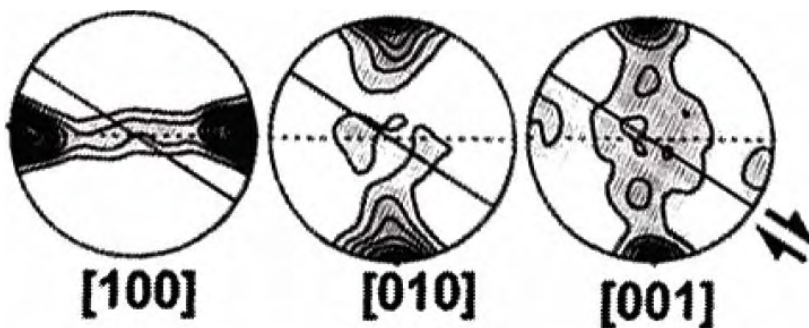

sinistral [100](001) observed in nature (Mehl et al., 2003) "E"
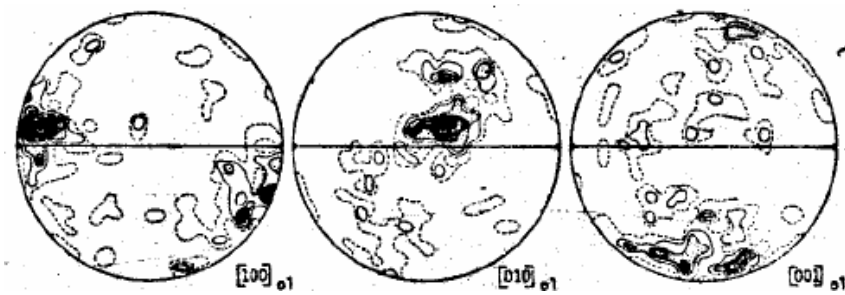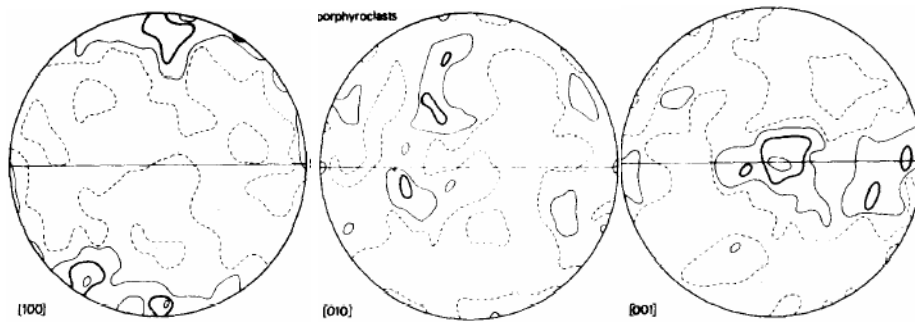

dextral Mariana (Nicolas et al., 1980) "E"

"E" fabric produced experimentally at ~ 200 MPa, 10^{-4}–10^{-5} s^{-1} and ~500 ppm H (Katayama et al., 2004) "E"
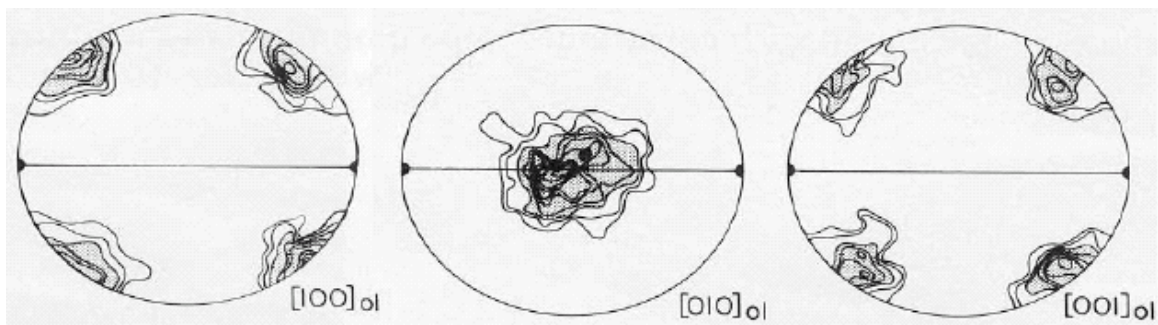
simple shear simulation of "high-temperature" slip (Tommasi et al., 2000) "A"

Other Observed Fabrics

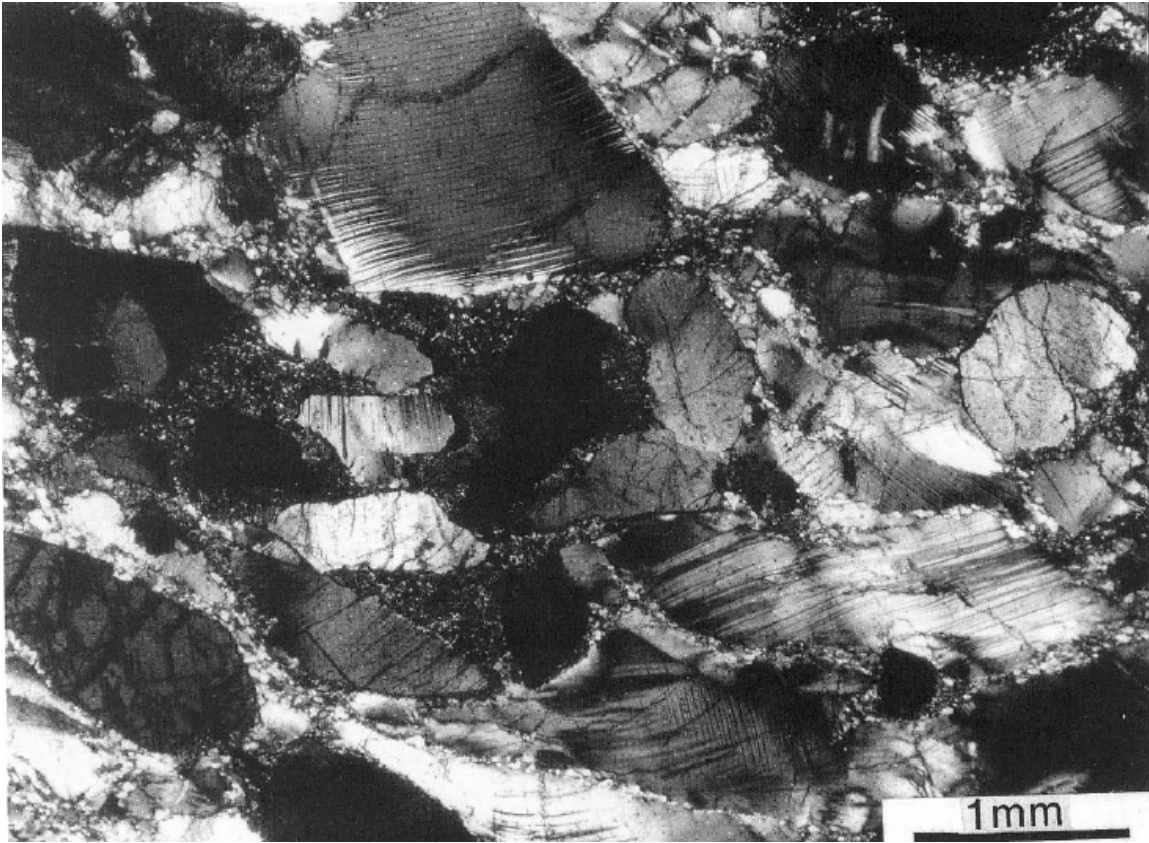

Alpe Arami implying [010](100), but quite weak (Buiskool Toxopeus, 1977) unknown type
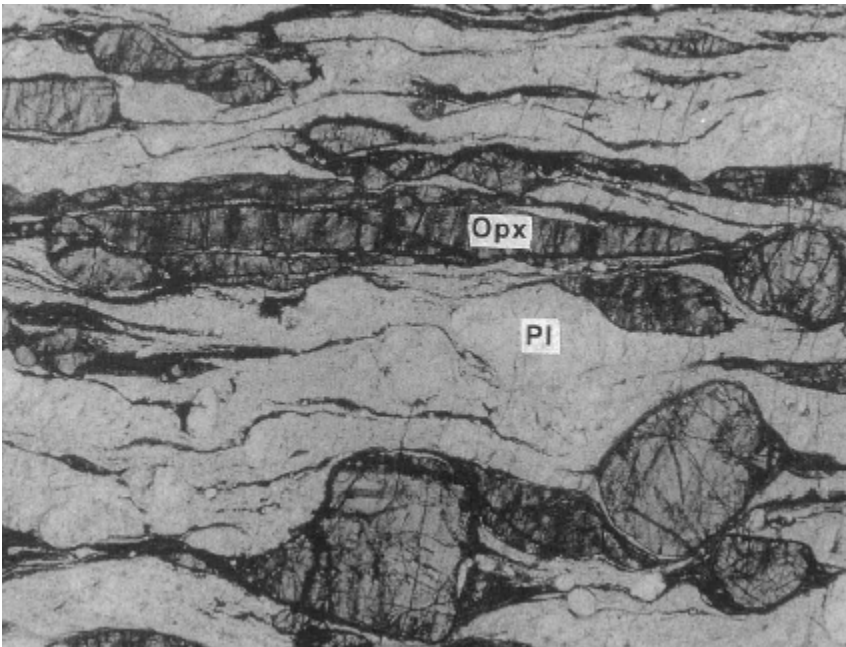

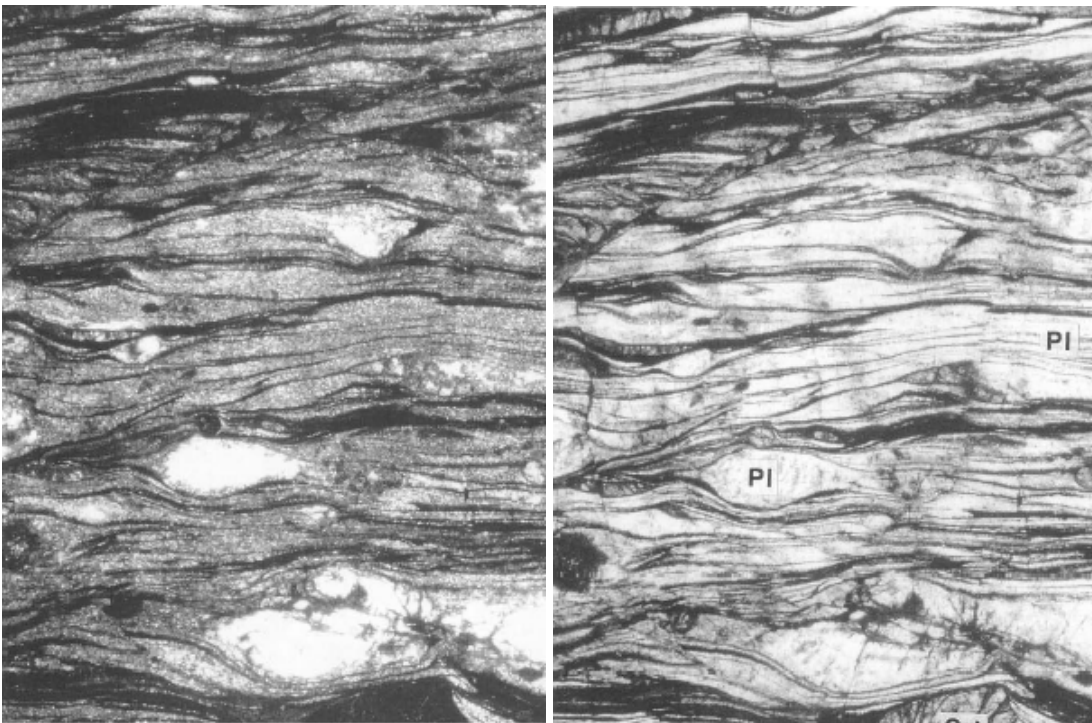kimberlite (Mercier et al., 1985)

Mafic Rocks

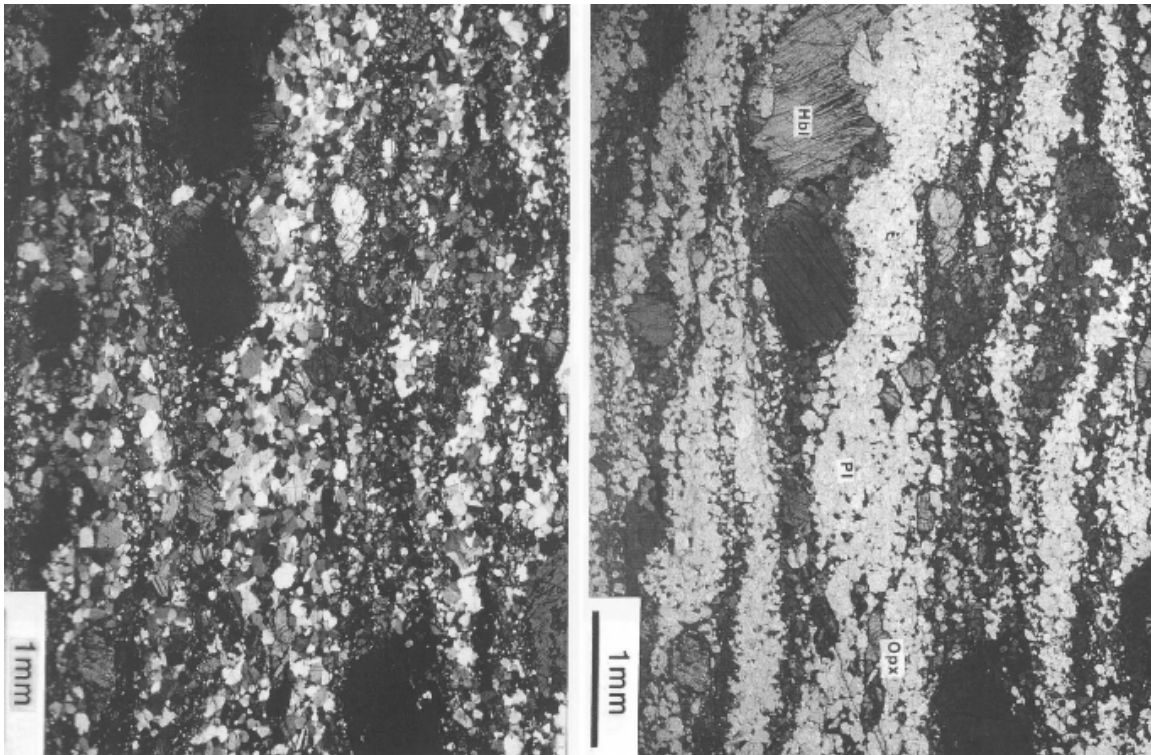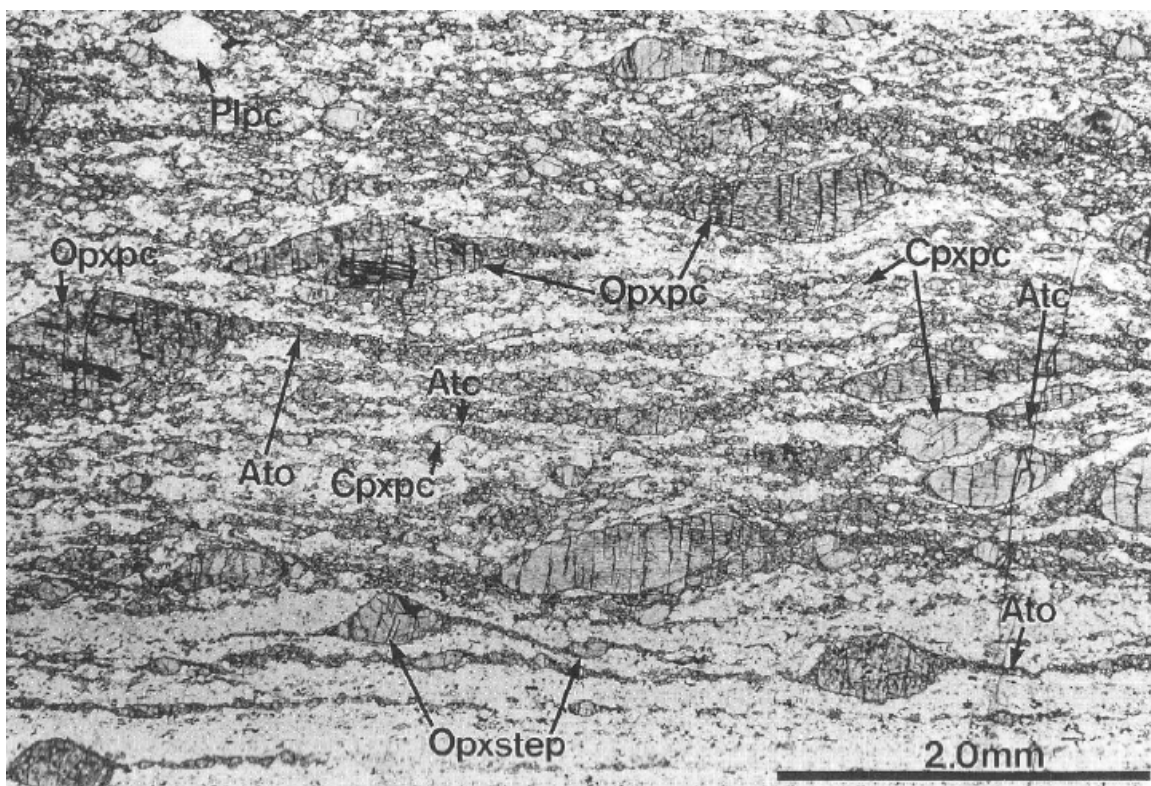protomylonitic gabbro (Regime 2) (Brodie, 1998)

plagioclase recrystallized to very fine grain size; orthopyroxene locally elongated by slip (Brodie, 1998)
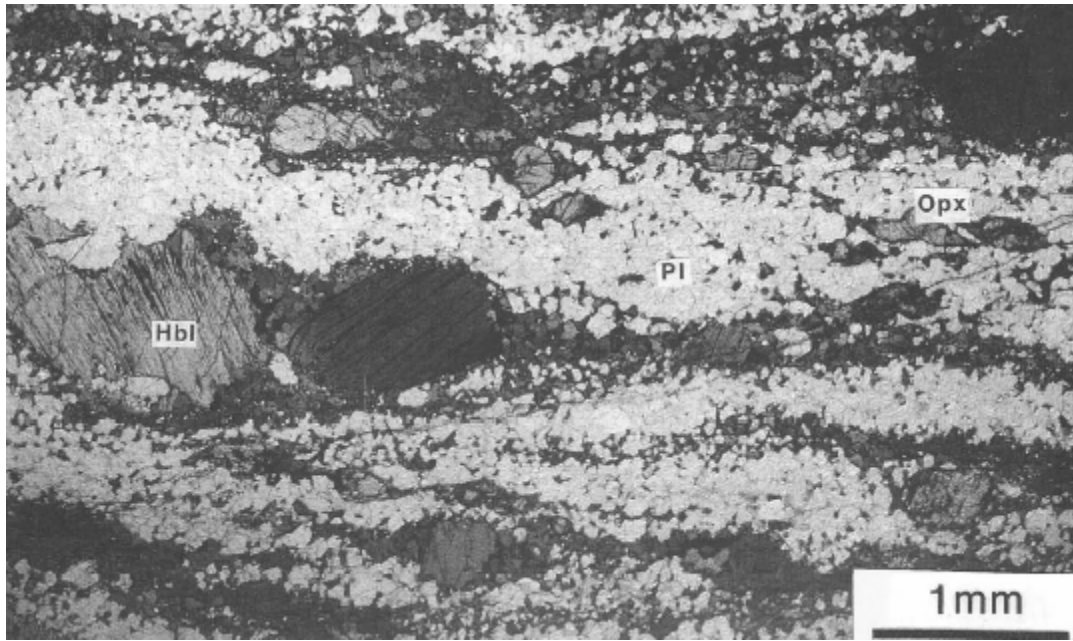

plag recrystallized to very fine grain size; opx locally elongated by slip (Brodie, 1998)
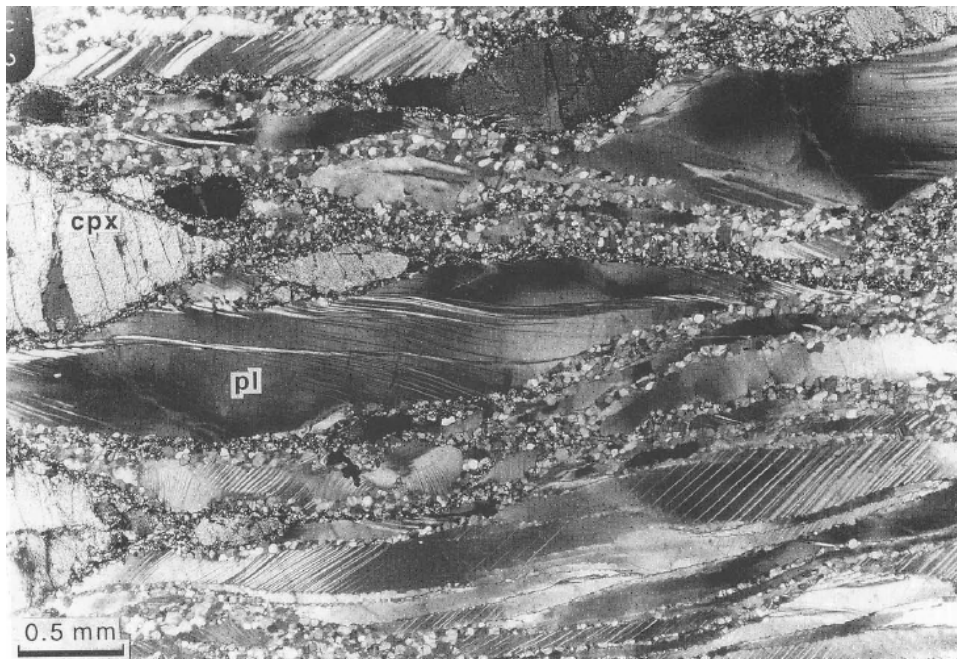
granulite-facies mafic rock, Kohistan arc (Brodie, 1998)

asymmetric tails (Ato) on orthopyroxene porphyroclasts (Opxpc). asymmetric tails (Atc) on clinopyroxene porphyroclasts (Cpxpc). (Toyoshima, 1998)

(Brodie, 1998)

S–C anorthosite mylonite Jotun. plag ribbons show deformation twins, undulatory extinction; clinopyroxene recrystallized to very fine grained amphibole (Ji, 1998)

Jotun nappe amphibolite-facies anorthosite mylonite with plagioclase ribbon porphyroclasts showing undulatory extinction, twinning and clinopyroxene recrystallized into amphibole (Ji, 1998)
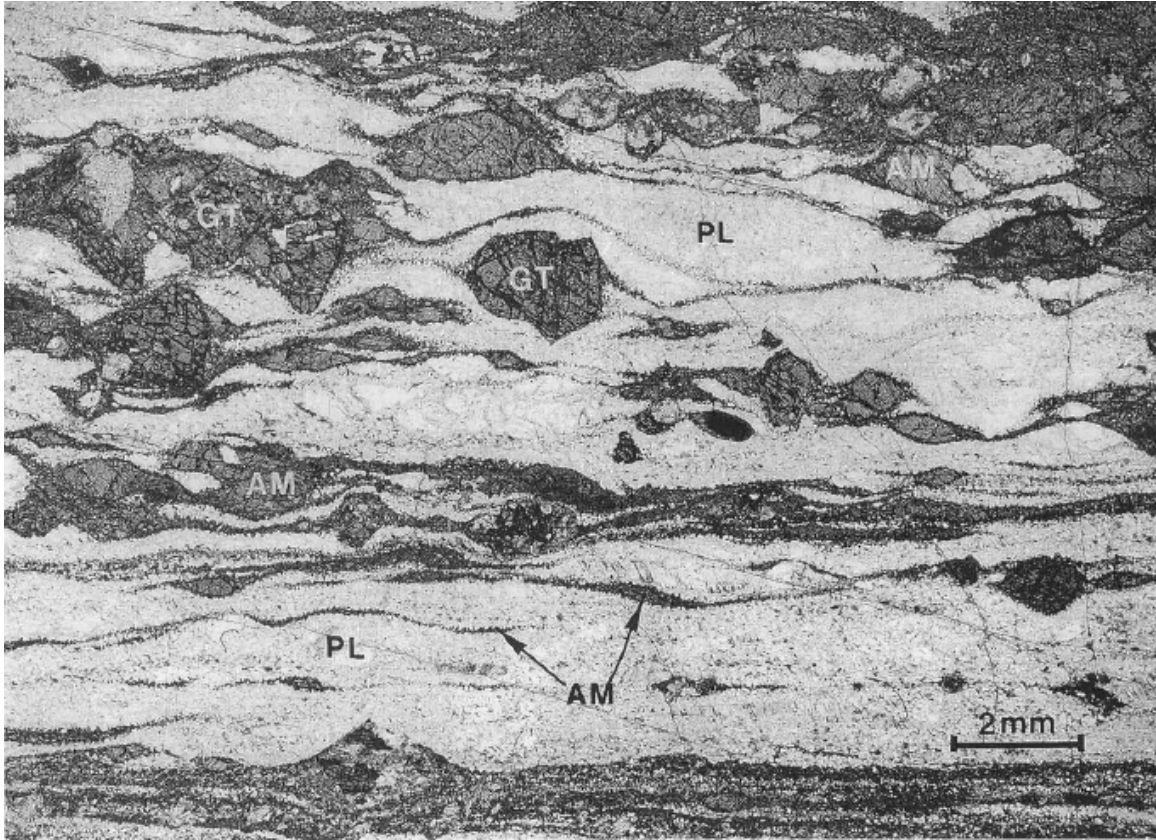
Jotun nappe strained 350% at 600°C (Boullier & Guéguen, 1998). Plagioclase 50 µm, amphibole 10 µm. Small grains have no LPO, interpreted as GBS.
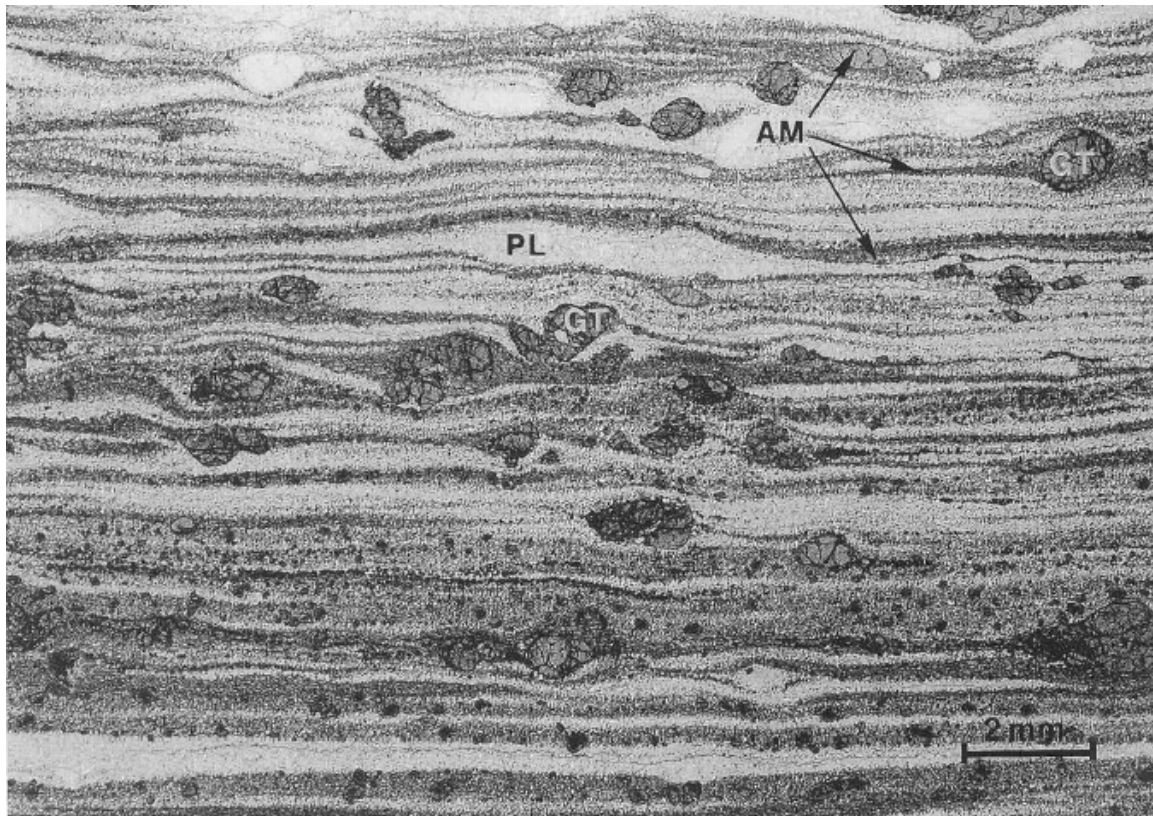
Jotun nappe strained 1000% at 600°C (Boullier & Guéguen, 1998). Plagioclase 50 µm, amphibole 10 µm. Small grains have no LPO, interpreted as GBS.

Various flow laws for mafic rocks

rock	A	n	Q (kJ/mol)	ref
amphibolite	1.1±0.3e–4	3.7±0.3	244±18	Hacker & Christie, 1990
basalt	5.3e–9	5.4±0.2	263±20	Hacker et al., 1992
dry diabase	1900	4.5±0.3	500±30	Mackwell et al., 1995
diabase	1.6e–4	3.4	259	(Shelton, 1981; Tullis et al., 1991)
orthopyroxene granulite	2.5e2	5.5±0.6	265±6	Ross & Wilks, 1996
eclogite	$10^{3.3±0.9}$	3.4±0.2	480±30	Jin et al., 2001
Adirondack granulite	8e-3	3.0	243	Wilks & Carter, 1990
Pikwitonei granulite	1.4e4	4.2	445	Wilks & Carter, 1990
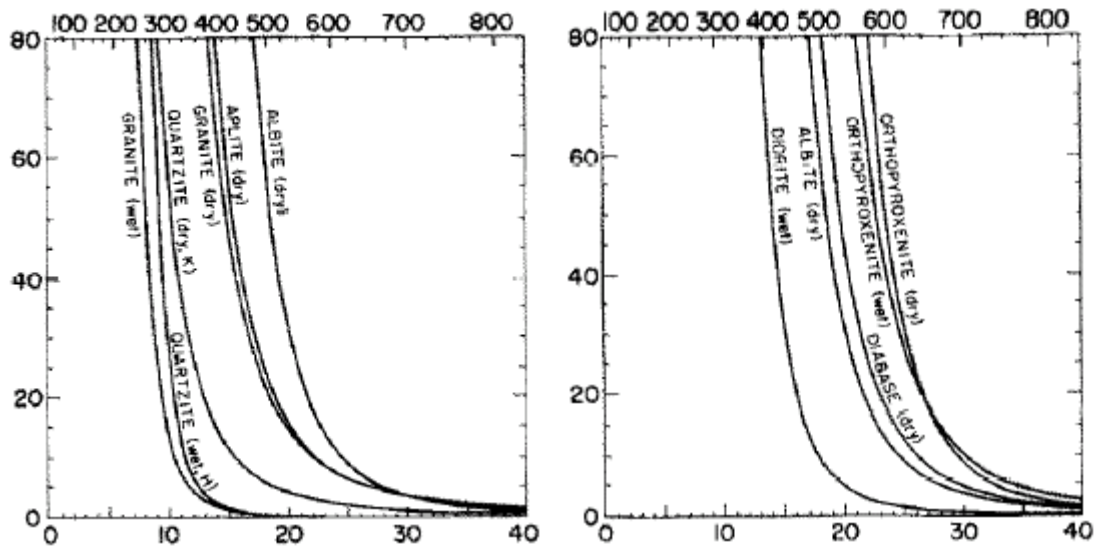
flow stresses (MPa; vertical axis) for (L) felsic and (R) mafic crustal rocks at 10^{-14} s^{-1} (ordinate is z (km)) (Carter & Tsenn, 1987)
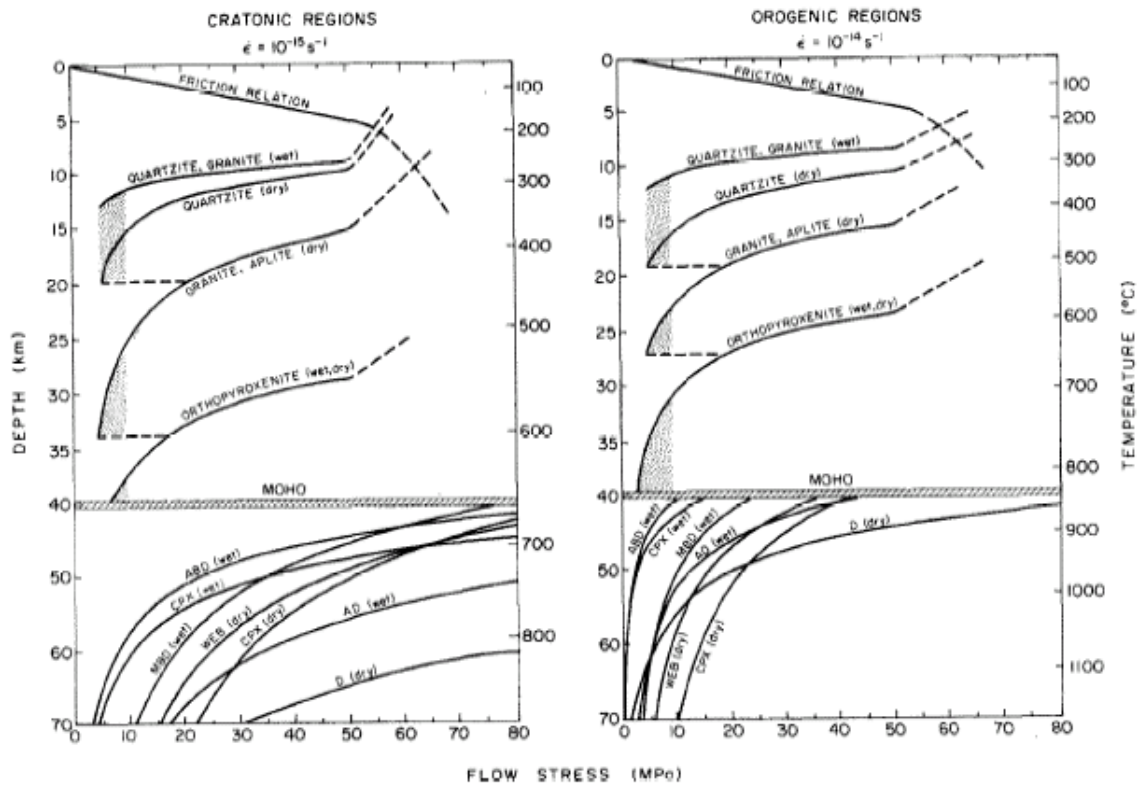

10^{-14} s^{-1} (ordinate is flow stress (MPa)) (Carter & Tsenn, 1987)
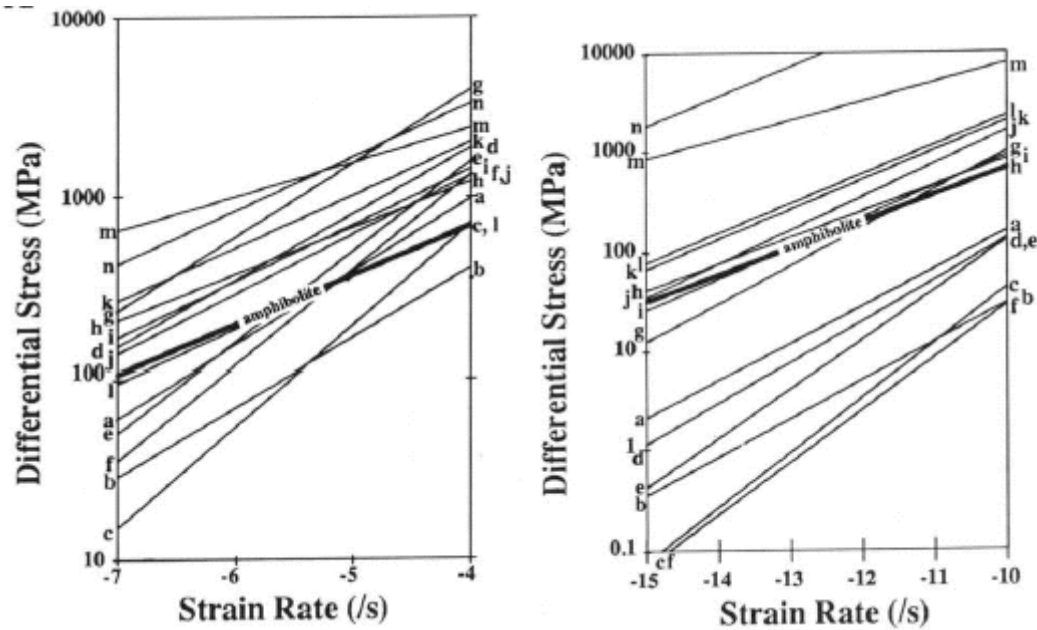
a: wet quartzite (Koch, 1983); b: wet quartzite (Kronenberg & Tullis, 1984); c: wet quartzite (Hansen & Carter); d: dry quartzite (Koch, 1983); e dry quartzite (Shelton & Tullis, 1981); f: dry quartzite (Hansen & Carter, 1982); g: quartz diorite (Hansen & Carter, 1982); h: albite rock (Shelton & Tullis, 1981); j: diabase (Caristan, 1982); k: diabase (Shelton & Tullis, 1981); l: diopsidite (Shelton & Tullis, 1981); m: diopsidite (Kirby & Kronenberg, 1984); n: wet dunite (Chopra & Paterson, 1981). (from Hacker & Christie, 1990)

Orthopyroxene
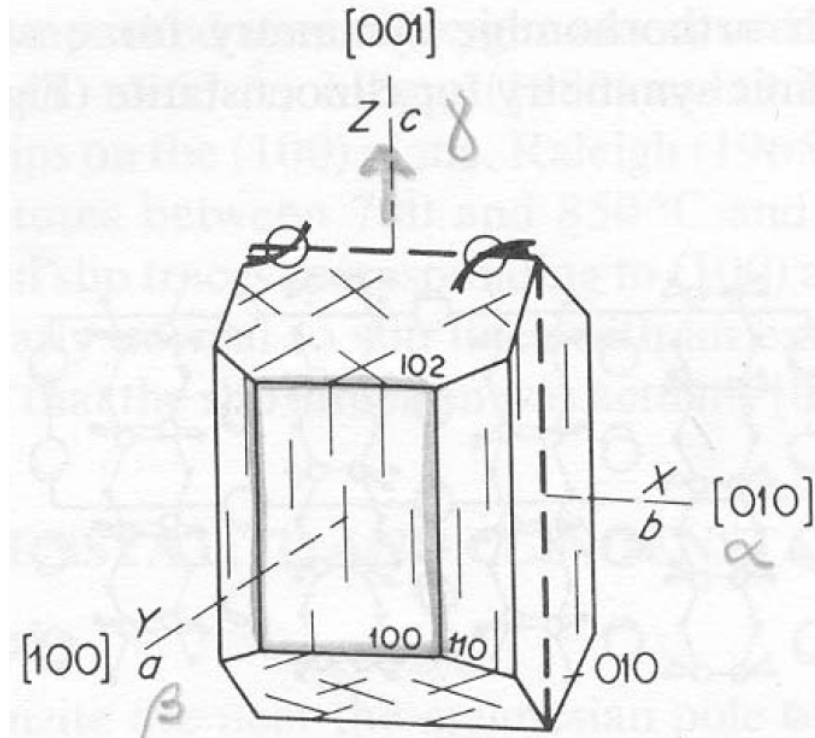
crystallography of orthopyroxene. Inosilicate chains are parallel to c. Exsolution of Ca-rich clinopyroxene ("diopside", higher birefringence) lamellae along (100)

● Silicon ○ Oxygen ◑ Magnesium
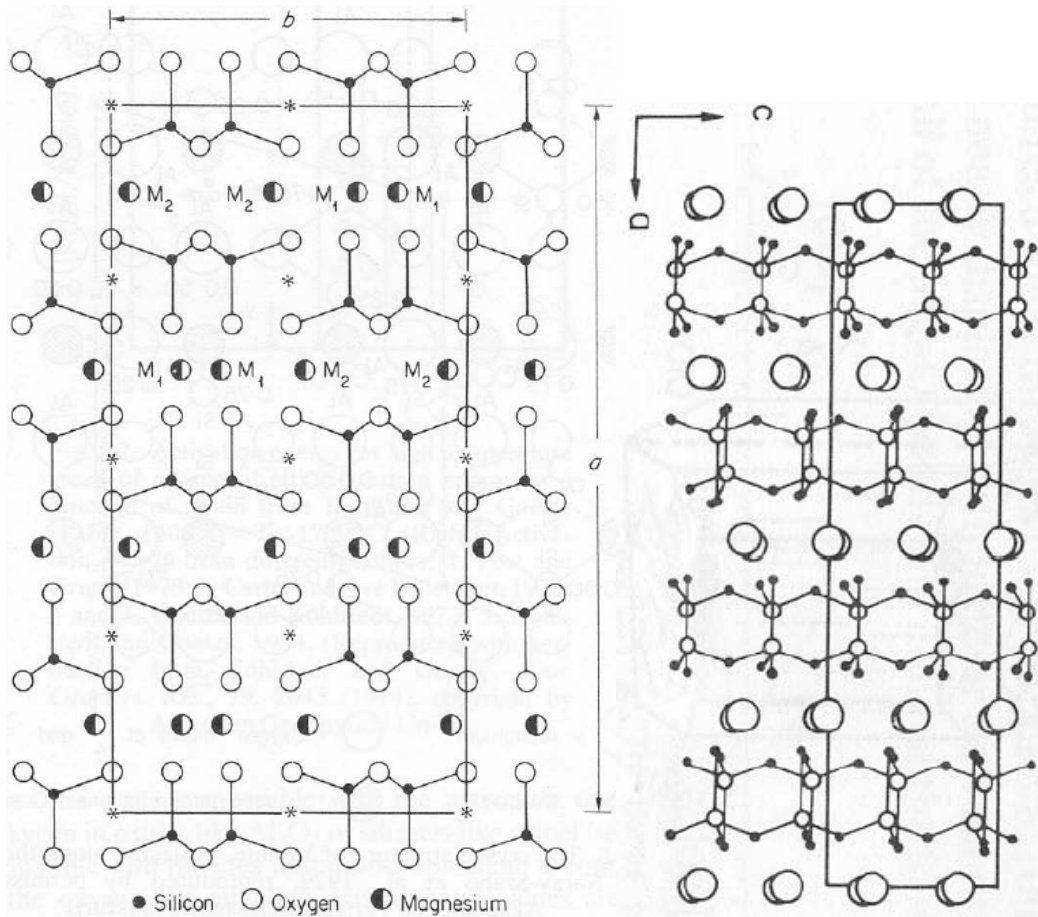
a = 18.2 Å (impossible)
b = 8.8 Å (possible)
c = 5.2 Å (likely)
(100) looks weak
(010) looks strong and is parallel to chains
(001) looks strong and would involve breaking inosilicate chains

[001](100) only known easy glide system in orthopyroxene (van Duysen et al., 1985)
[010](100) possible
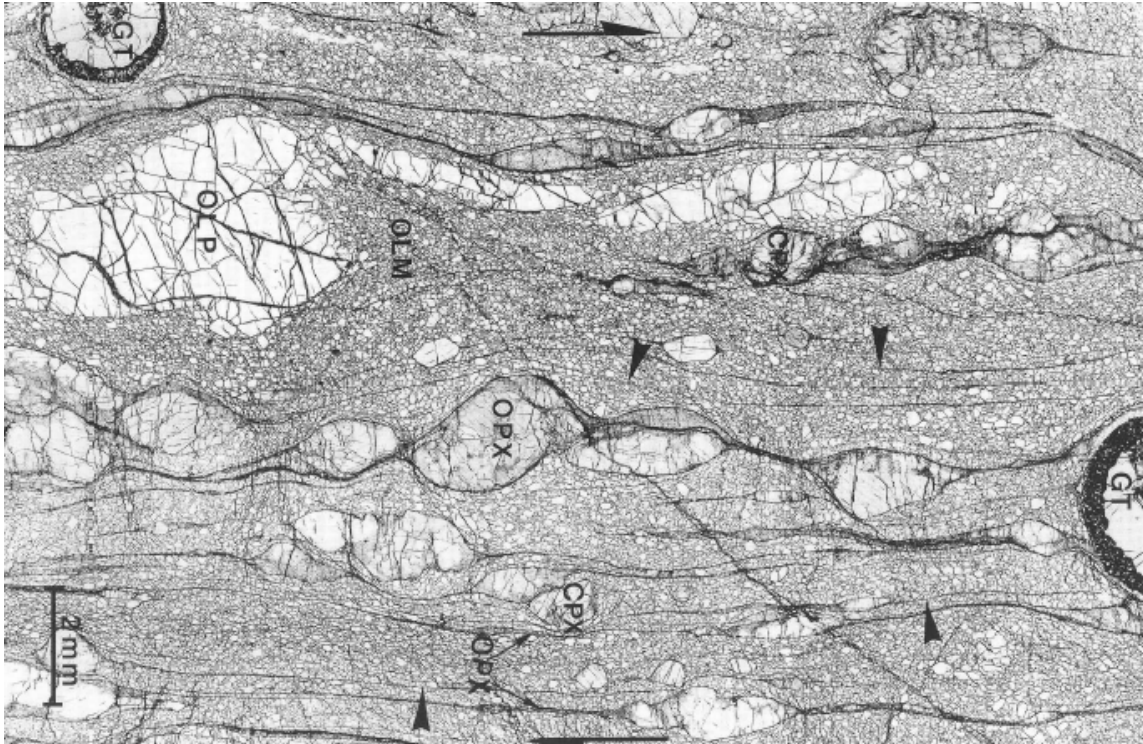[100](010) unlikely—oxygens bump together
[001](010) maybe?
[100](001) unlikely
[010](001) unlikely
what about [001]{210} or [120]{210}? ({210} is cleavage plane)
Shape preferred orientation based on morphology would look like [001](100) slip

twins on [001](100) by 13.3° (Coe & Kirby, 1975)

Lesotho kimberlite deformed at 200 km and 1400°C. All olivine recrystallized except one porphyroclast (OLP). Opx records 840% strain by necking. Fine-grained opx is unoriented, lacks subgrains and has moderate dislocation density of 5E7 cm^{-2}, but opx porphyroclasts show strong fabric (Boullier & Guéguen, 1998)
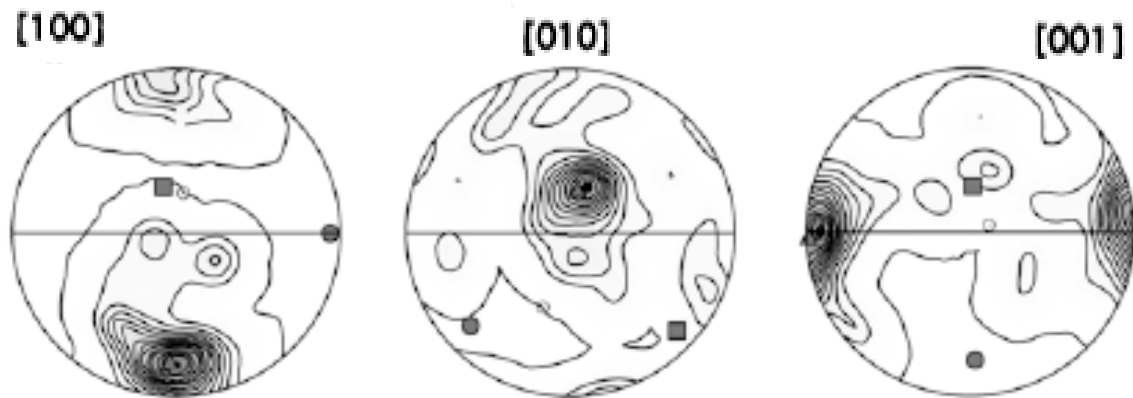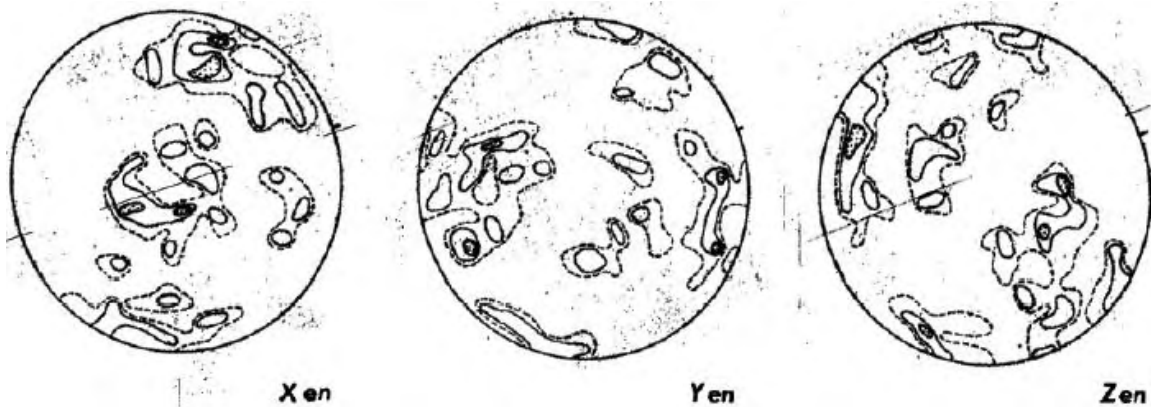

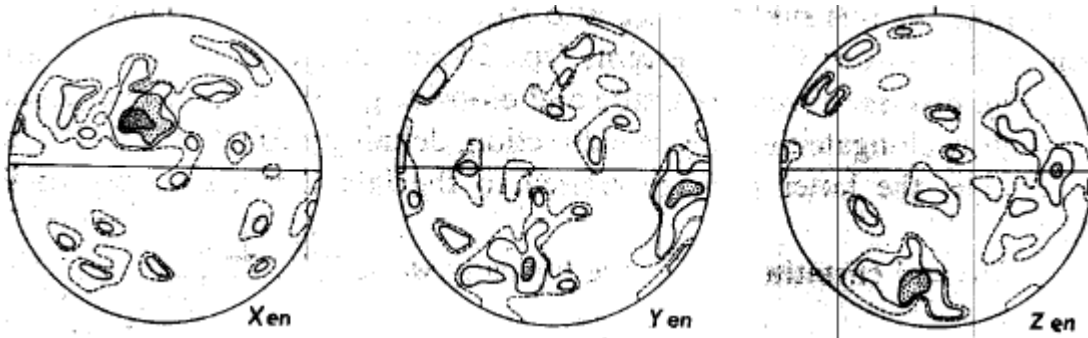[001](100), expected. Cima di Gagnone orthopyroxene (Frese et al., 2003)
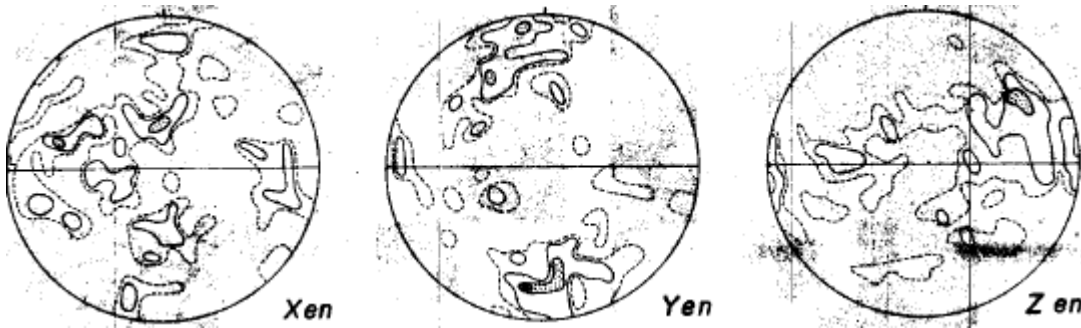
porphyroclastic texture. enstatite LPO implies [001](010) slip (Mercier & Nicolas, 1975)
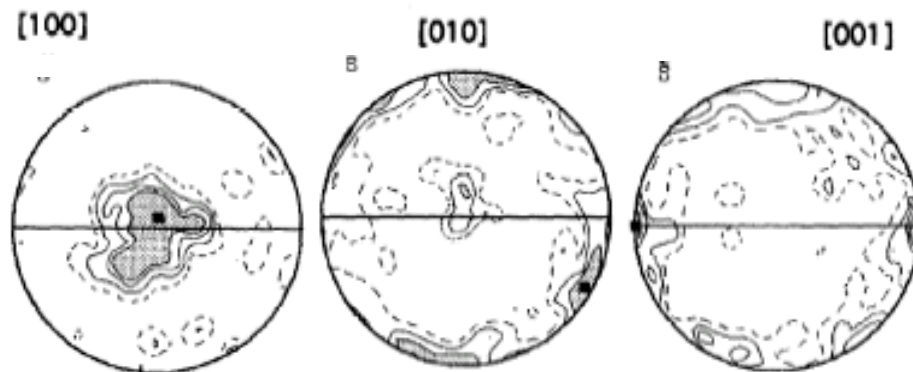

tabular equigranular texture enstatite LPO (Mercier & Nicolas, 1975); implies [001](010) or [001]{210} slip???

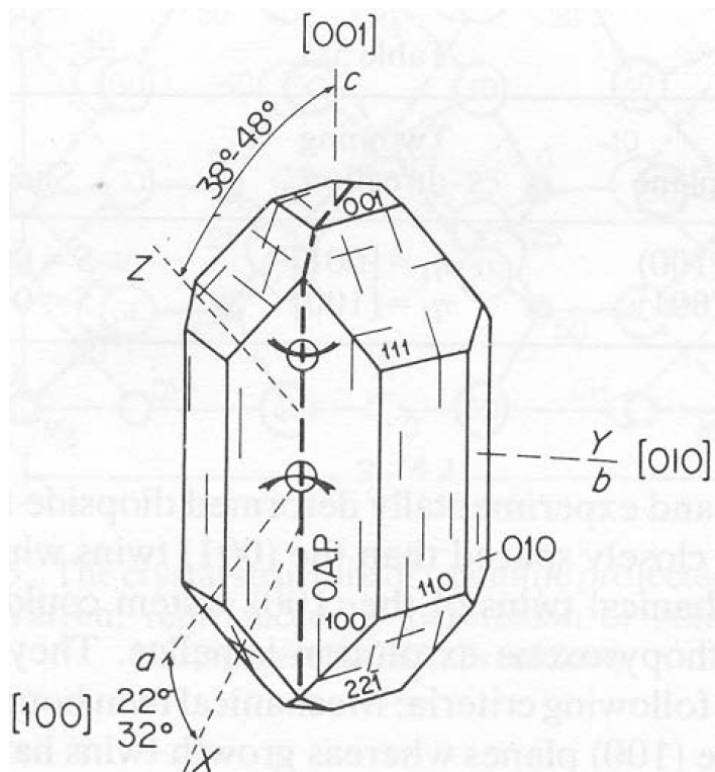protogranular texture: enstatite LPO suggests [010](100) slip. (Mercier & Nicolas, 1975)

mosaic equigranular texture. enstatite LPO implies [010](001) slip (Mercier & Nicolas, 1975)

unusual orthopyroxene LPO in mafic mylonite suggesting highly improbable [001](010) slip (Ji et al., 1993)

Clinopyroxene

crystallography of clinopyroxene (Nicolas & Poirier, 1976). Exsolution of Ca-poor orthopyroxene ("enstatite"; lower birefringence) lamellae *approximately* along (100)

Clinopyroxene Experiments

Clinopyroxenite shortened 52% at 1100°C and 10^{-5} s^{-1} ; regime 2 (Tullis et al., 2000)

Clinopyroxenite shortened 32% at 1200°C and 10^{-6} s^{-1} ; regime 3 (Tullis et al., 2000)

Activation energies for websterite are 382 kJ/mol wet 326 kJ/mol dry (Avé Lallement, 1978). Clinopyroxenite flow law:

$$\dot{\varepsilon} = 14.8 \pm 1e4 \sigma (MPa)^{3.3 \pm 0.5} \exp(-\frac{490 \pm 80 kJ/mol}{RT})$$

(Boland & Tullis, 1986).
Clinopyroxene flow law:

$$\dot{\varepsilon} = 16 \sigma (MPa)^{3.4} \exp(-\frac{335 kJ/mol}{RT})$$

(Shelton, 1981; Tullis et al., 1991)

Clinopyroxene Preferred Orientations

Experiments

low T (<800°C	med T (800–1000°C)	high T (>1000°C)	
	[001]{110} is easier than ½<a±b>{110}	½<a±b>{110} is easier than [001]{110}	Raterron et al., 1994
mechanical twinning on (100) and (001)	[001](100) is easiest and [100](010) and ½<110>{1$\bar{1}$0} are less easily activate	½<110>{1$\bar{1}$0} slip is favored	Bascou et al., 2002

Slip Systems Observed in Nature:
common, down to 450°C
½<1 $\bar{1}$ 0>{110} (Philippot et al., 1992) (Skrotzki, 1994) (Bascou et al., 2002)
[001](100) (Philippot et al., 1992) (Skrotzki, 1994) (Bascou et al., 2002)

less common
[001]{110} (Philippot et al., 1992) (Bascou et al., 2002)
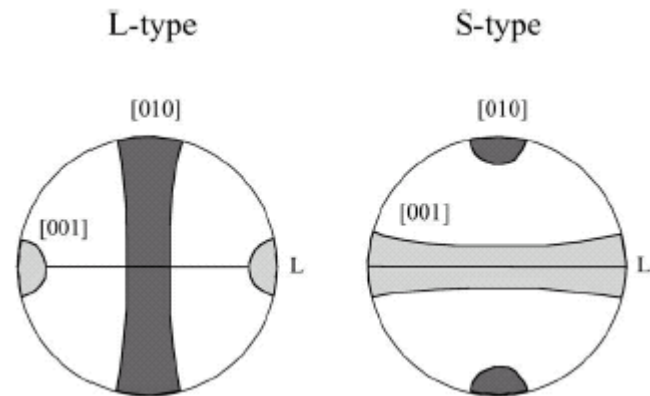½[001](010) (Philippot et al., 1992)
[010](100) (Skrotzki, 1994)
[100](010) (Skrotzki, 1994)
½<112>{110} (Skrotzki, 1994)
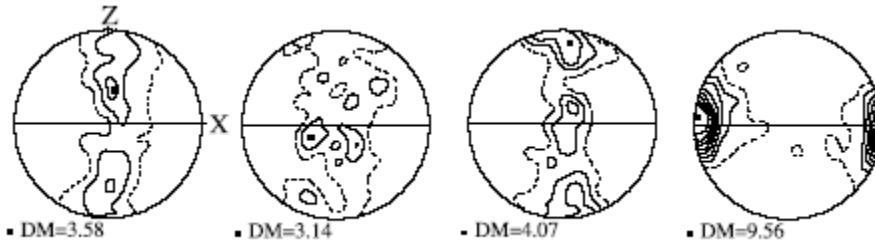<101>(010) (Skrotzki, 1994)
<111>{110} (Skrotzki, 1994)

Classification of clinopyroxene fabrics (Helmstaedt et al., 1972). L-type implies
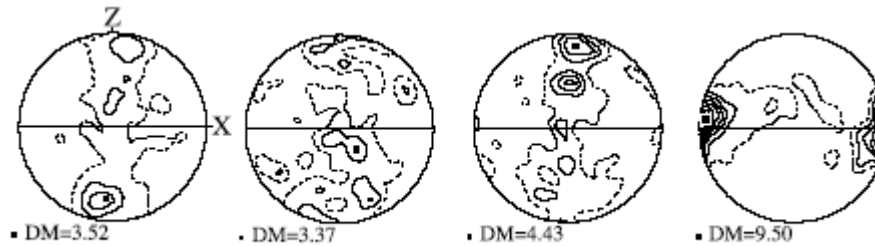[001](hk0). S-type implies [u0w](010)

Examples of the L-type fabric
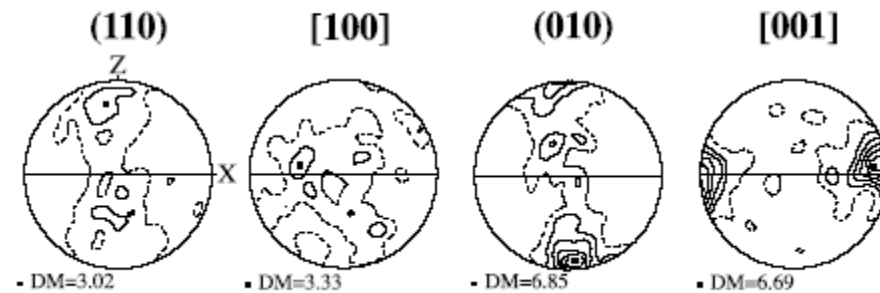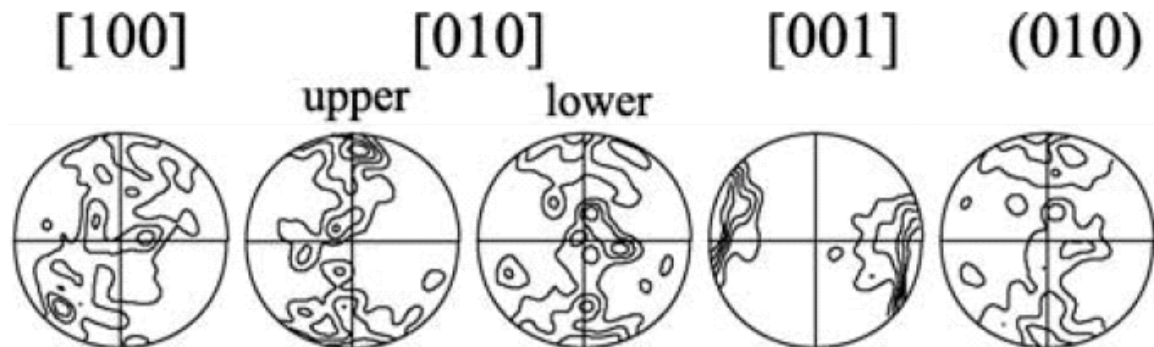

Alpe Arami eclogites, sample AB.E
(Bascou et al., 2002)

DM=3.58   DM=3.14   DM=4.07   DM=9.56

Nordfjord (WGR) eclogites, sample B6

(Bascou et al., 2002)

DM=3.52   DM=3.37   DM=4.43   DM=9.50

Sulu eclogites, sample SL50

(Bascou et al., 2002)

[100]   [010]   [001]   (010)

upper   lower

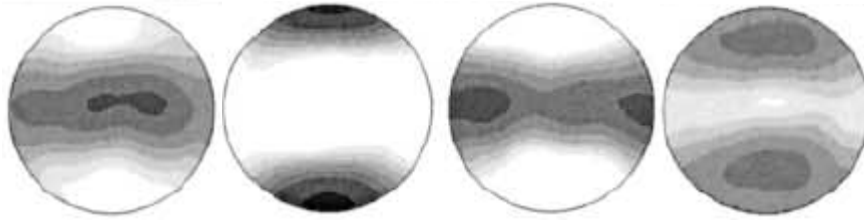650–700°C eclogite (L type) developed in the C2/c ordered structure (Brenker et al., 2002)

Examples of the S-type fabric

(110)   [100]   (010)   [001]
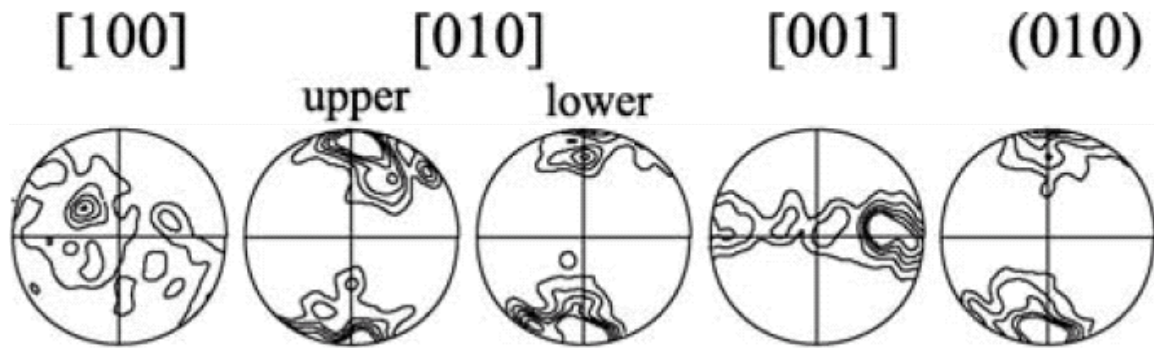

DM=2.15   DM=2.99   DM=5.69   DM=3.51
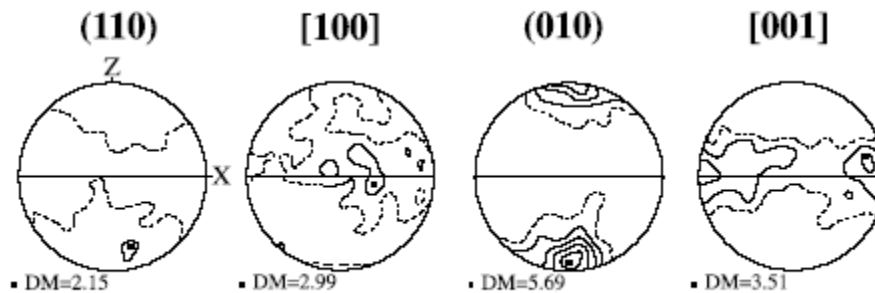
Gourma eclogites, sample S522

(Bascou et al., 2002)

a*(100)   b[010]   c[001]   (110)

Armorican Massif eclogite (Mauler et al., 2001)

[100] [010] [001] (010)

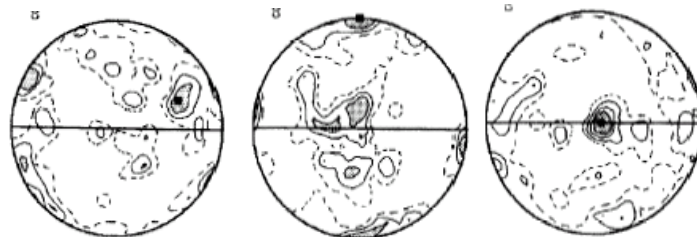upper lower

>750°C eclogite (S type) developed in the P2/n ordered structure (Brenker et al., 2002)
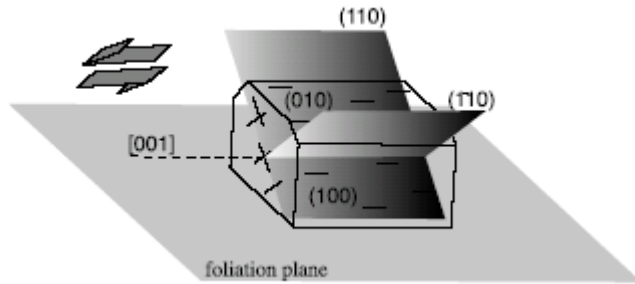
Other fabrics

= 50
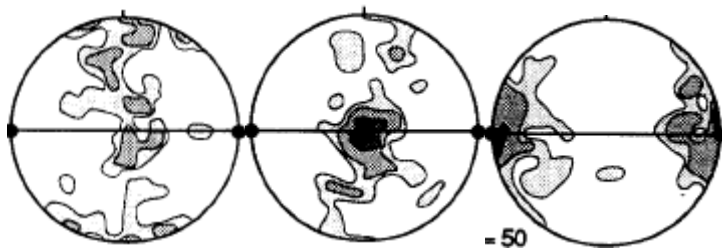
[001](100) fabric in Monviso eclogite (Philippot & van Roermund, 1992)


'[001] close to Y' mafic granulite mylonite implies [100](010) slip (Ji et al., 1993)

In spite of the LPOs suggesting [001](010) slip, dislocations indicating activity on this slip system are generally not observed. Instead, these LPO's can be explained by [001]{110}:

foliation plane

The (010) maximum develops because the {110} planes are well oriented for slip and *not* because (010) is slipping (Bascou et al., 2002)
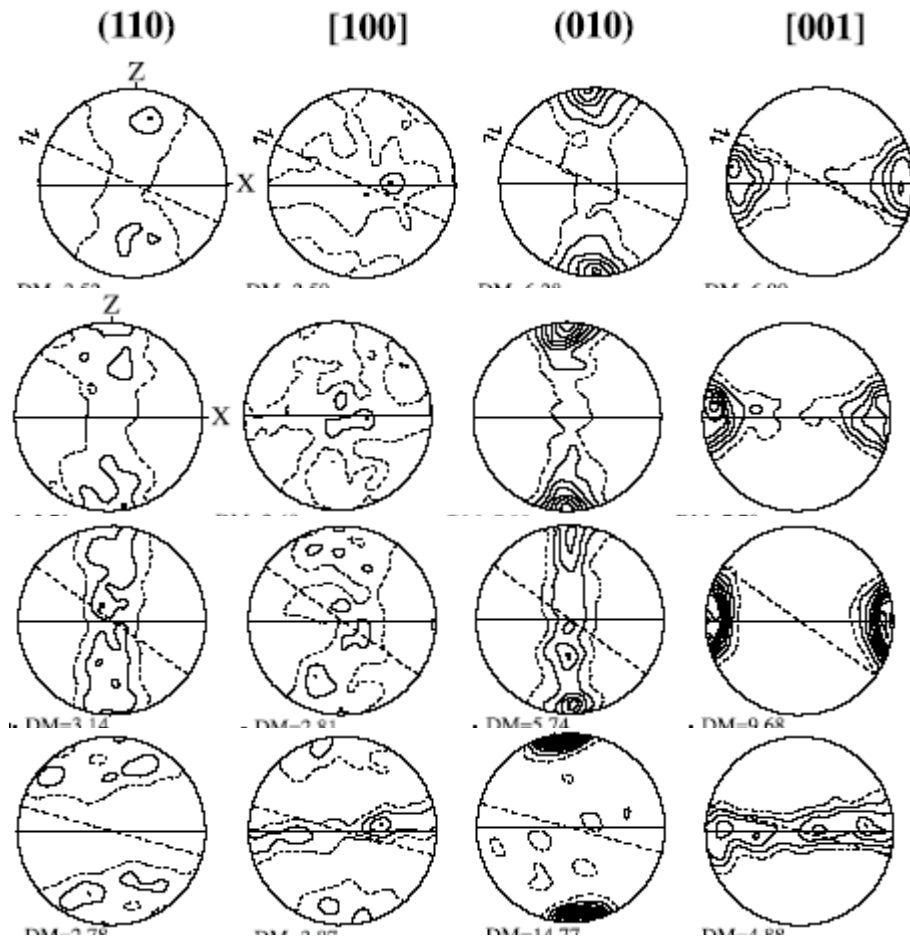
viscoplastic modeling ((top) simple shear, pure shear, transtension, and (bot) transpression) of [001](100), [1 $\bar{1}$ 0]{110} and [001]{110} slip (Bascou et al., 2002)
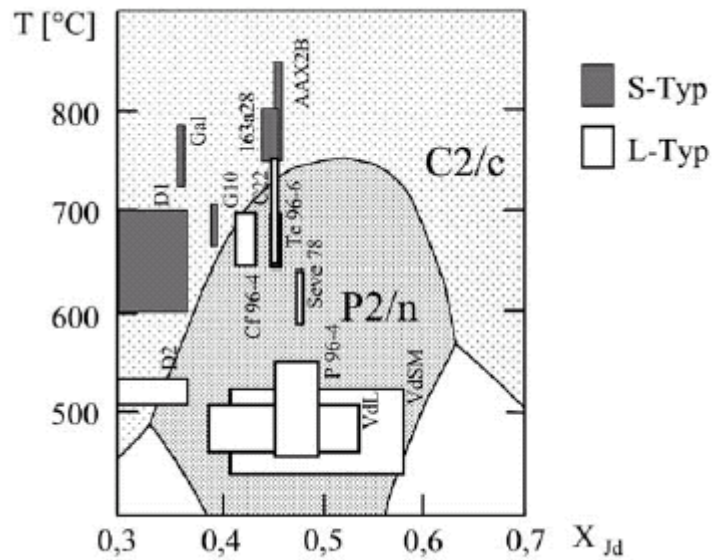
S-type LPO's develop in C2/c structure and L-type in P2/n structure (Brenker et al., 2002)
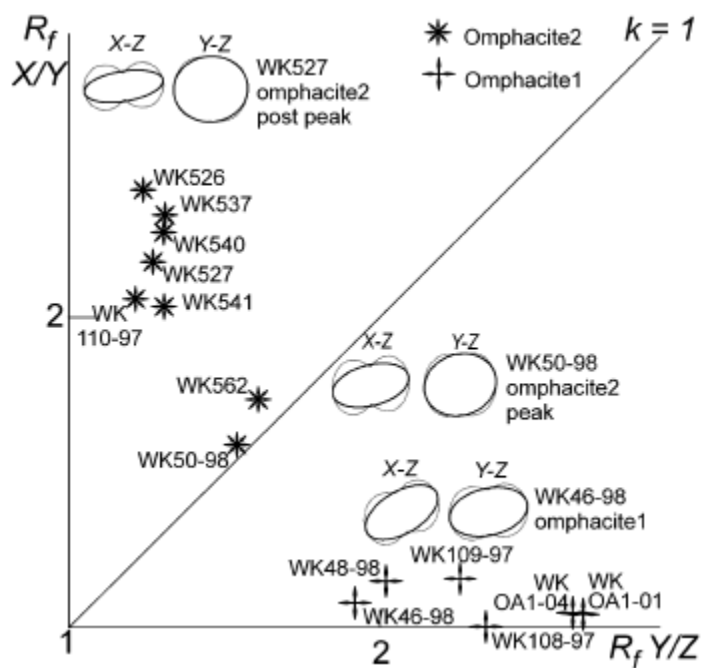
eclogites from the Tauern Window have textures indicating flattening to constrictional strains (Kurz, 2005)

The LPO's are "compatible with this", indicating [001](100) slip (Kurz, 2005). Actually, the top row is barely statistically significant.
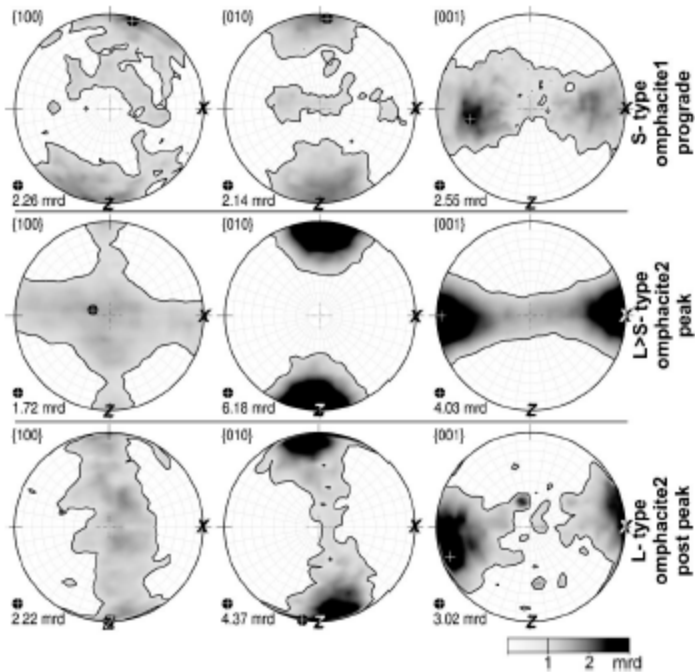
Hornblende

TABLE 1. Potential Slip Systems in Amphibole

	[100]	[010]	[001]
(100)	X	Possible, but a unit Burgers vector would be 18 Å.	Easy slip system, with Burgers vector of 5 Å.
(010)	Requires tetrahedra to rub past one another.	X	Easy slip system, with Burgers vector of 5 Å.
(001)	Require I-beam chains to break.	Require I-beam chains to break; unit Burgers vector would be 18 Å.	X

"X" indicates combinations in which the potential slip direction does not lie in the slip plane.

(Hacker & Christie, 1990)

($\bar{1}$01)[$\bar{1}$0$\bar{1}$] twinning

(100)[00$\bar{1}$] twinning
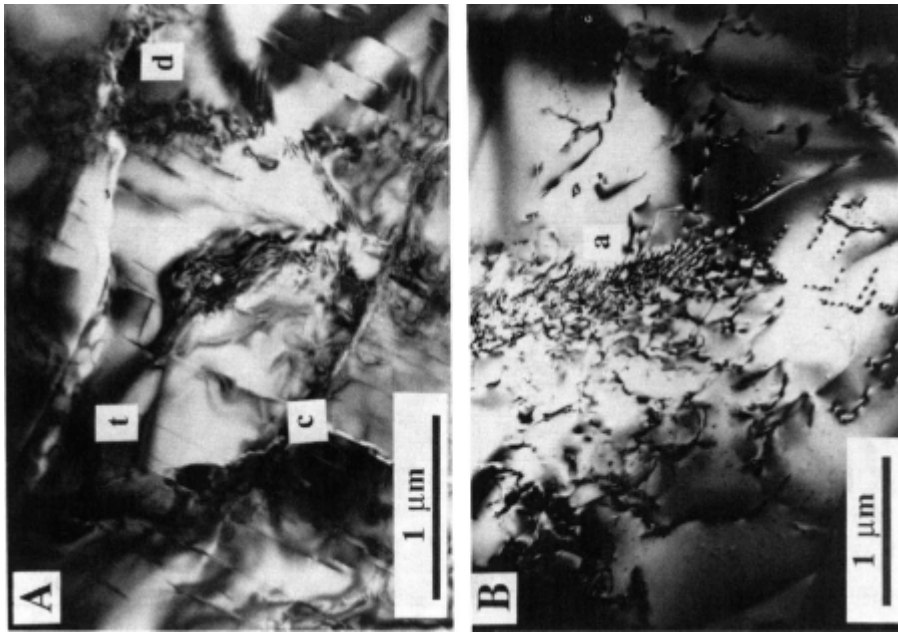
[001]

(001)[100] slip, breaks I-beams

(010)[100] slip, tetrahedral rubbing; (100)[010] slip, b=18Å

[0$\bar{1}$0]

[100]

{hk0}[001] "easy" slip
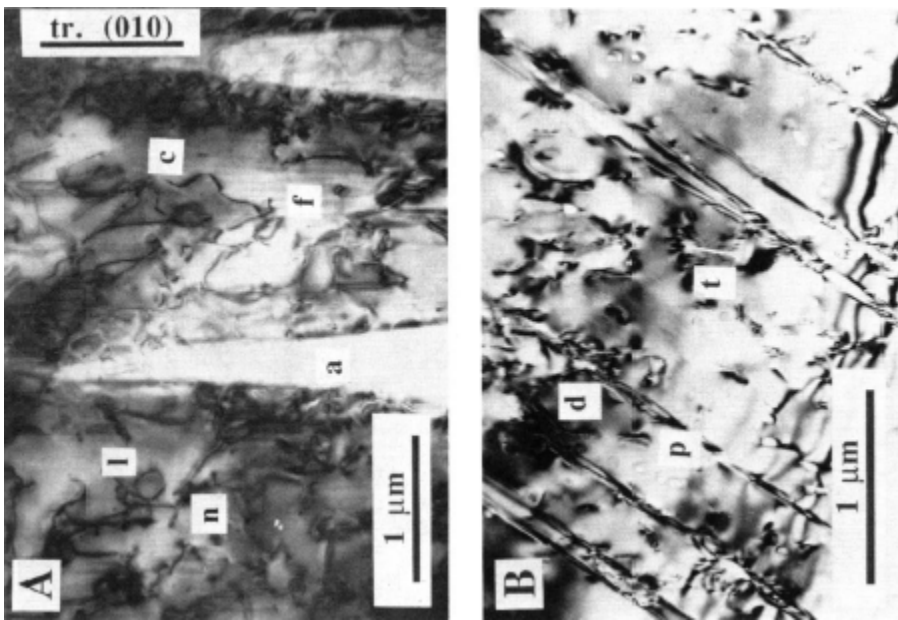
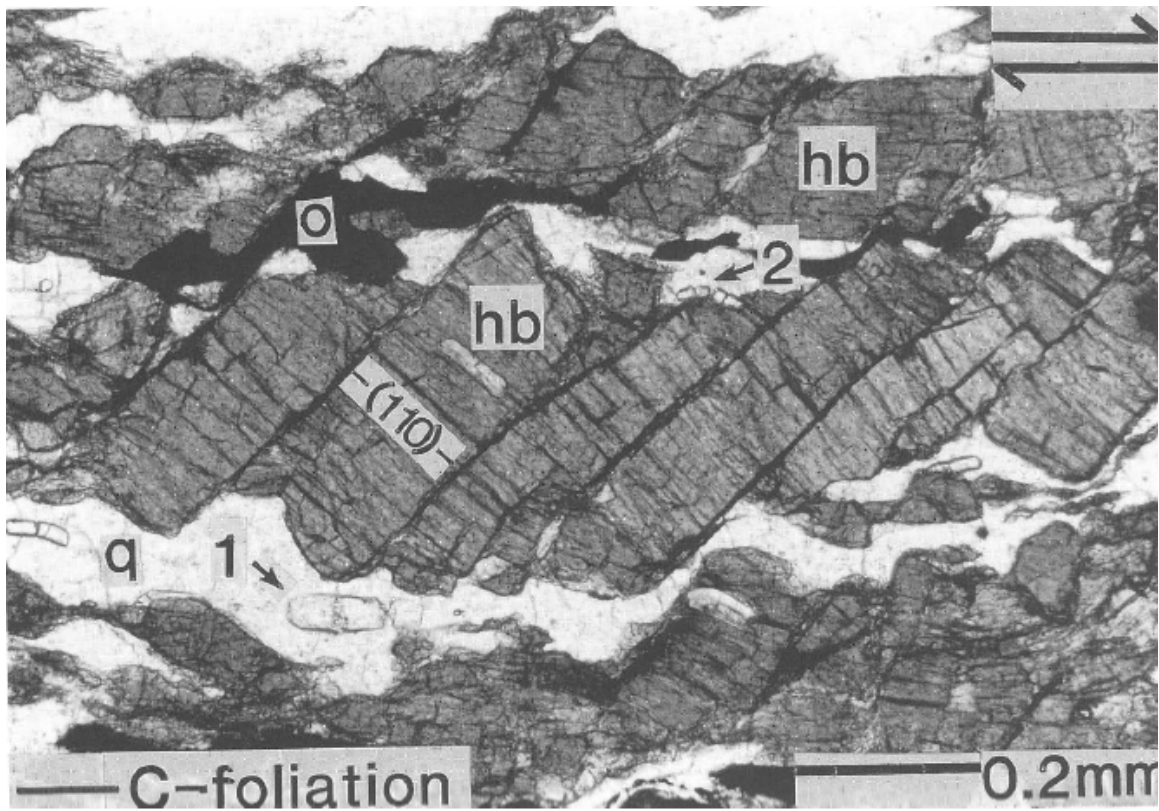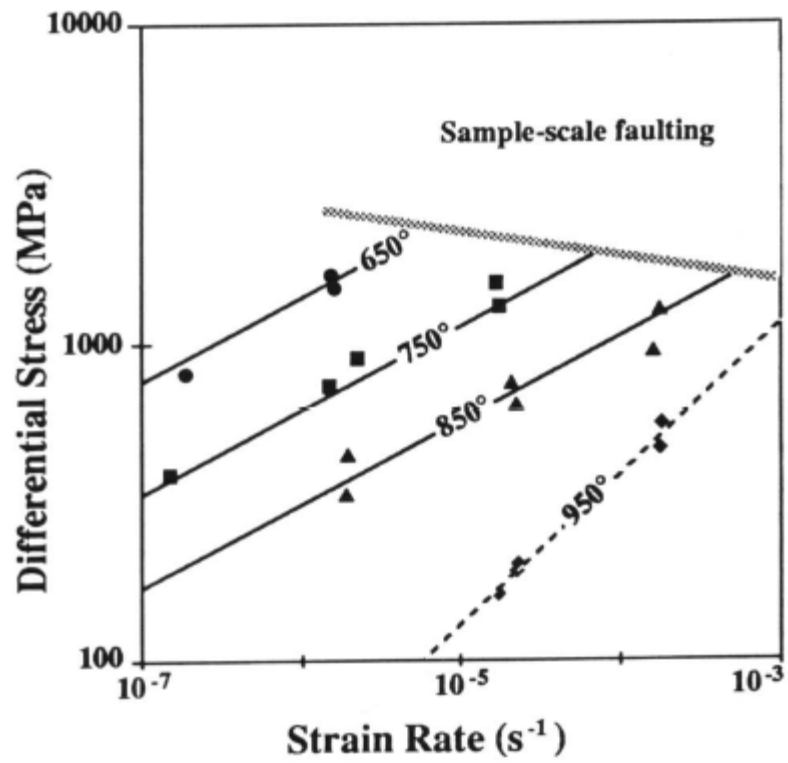(001)[010] slip, breaks I-beams
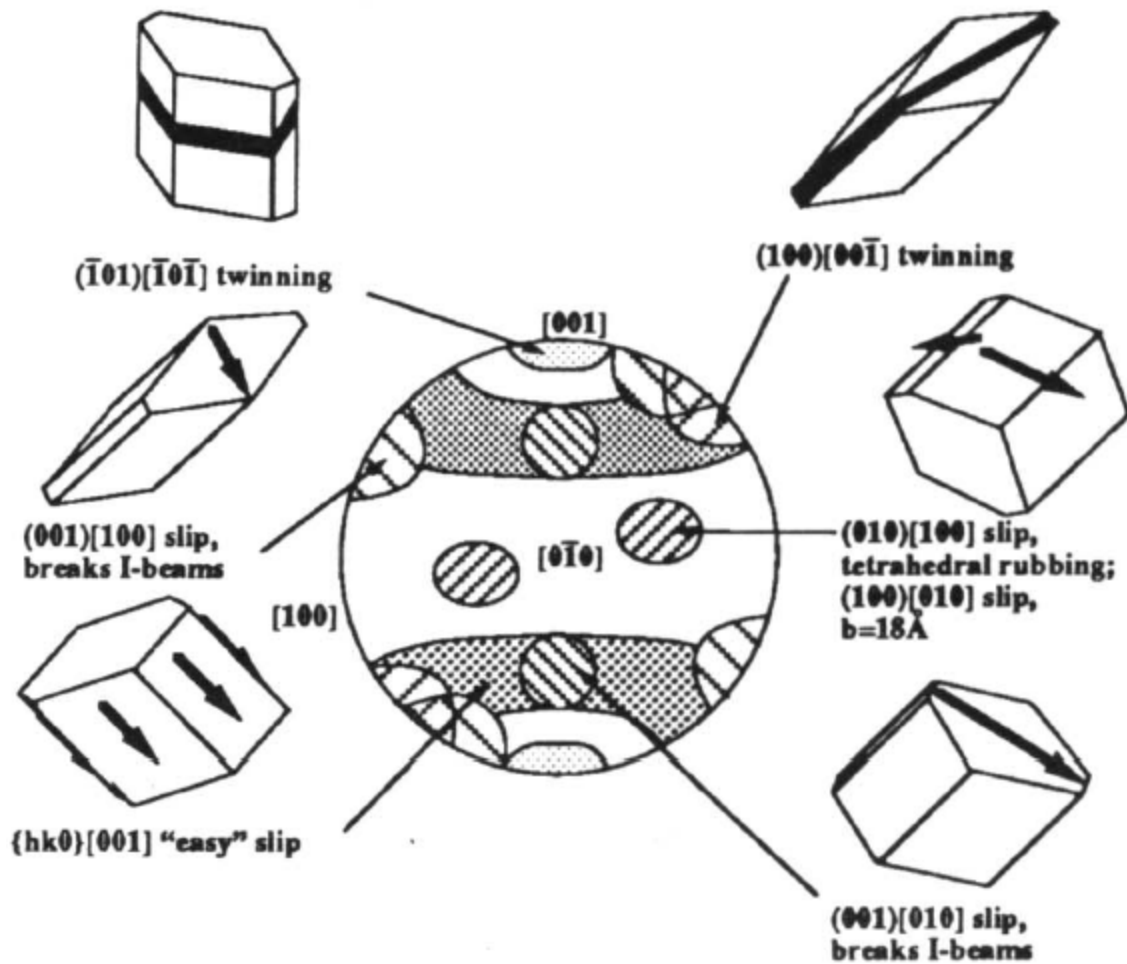
(Hacker & Christie, 1990)
In experimentally deformed hornblende (Rooney et al., 1973, 1974), the main deformation mechanism is ($\bar{1}$01) twins and [001](100) slip, with minor [001](010), [100](010) and [100](001) (Morrison-Smith, 1976)

low T amphibole deformation (Hacker & Christie, 1990)

high T amphibole deformation (Hacker & Christie, 1990)

Babaie & LaTour (1998)
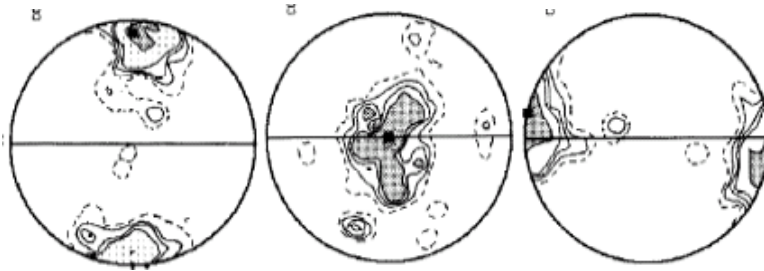
amphibole LPO in mafic mylonite implies [001](100)(Ji et al., 1993)

Garnet Lattice Preferred Orientations
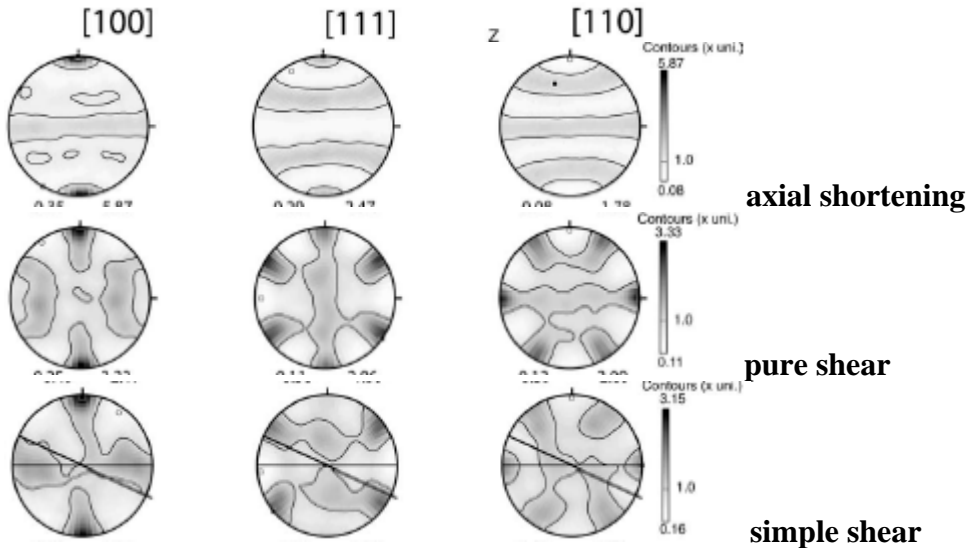
axial shortening

pure shear

simple shear

There are 66 possible slip systems in garnet, with <111>{110} the most common.
Calculated LPOs for garnet (Mainprice et al., 2004).
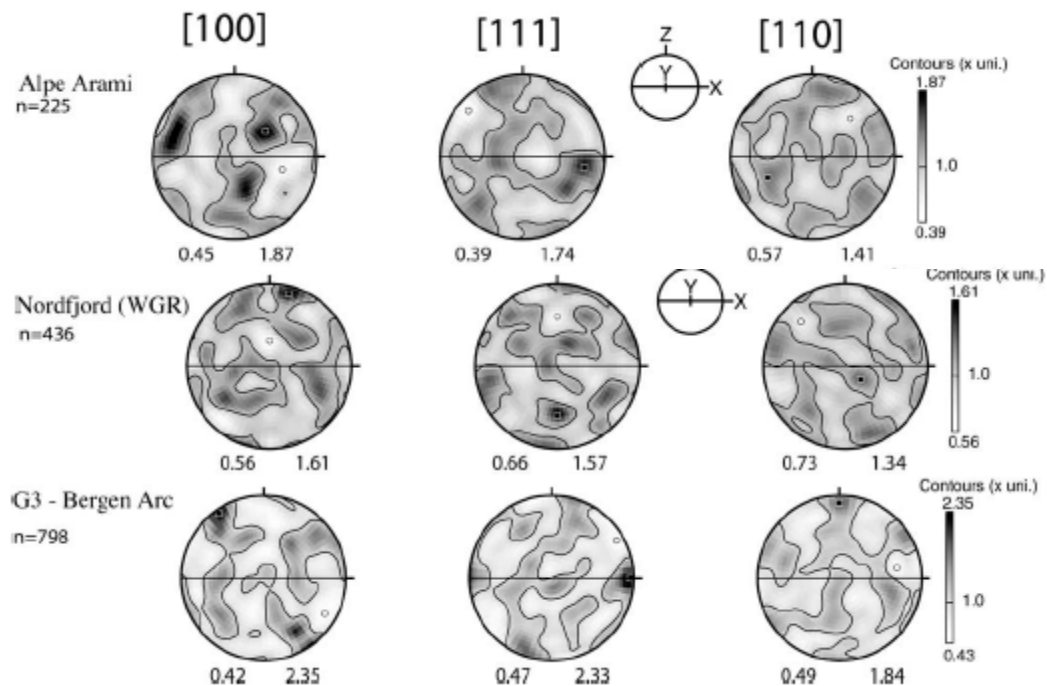
Natural garnet fabrics are weak implying grain boundary sliding or simply reflecting the abundance of garnet slip systems (Mainprice et al., 2004).

Calcite
Naturally Deformed Marbles

coarse-grained Palm Canyon marble showing twinning, kinking, and grain-boundary recrystallization (Erskine & Wenk, 1998)
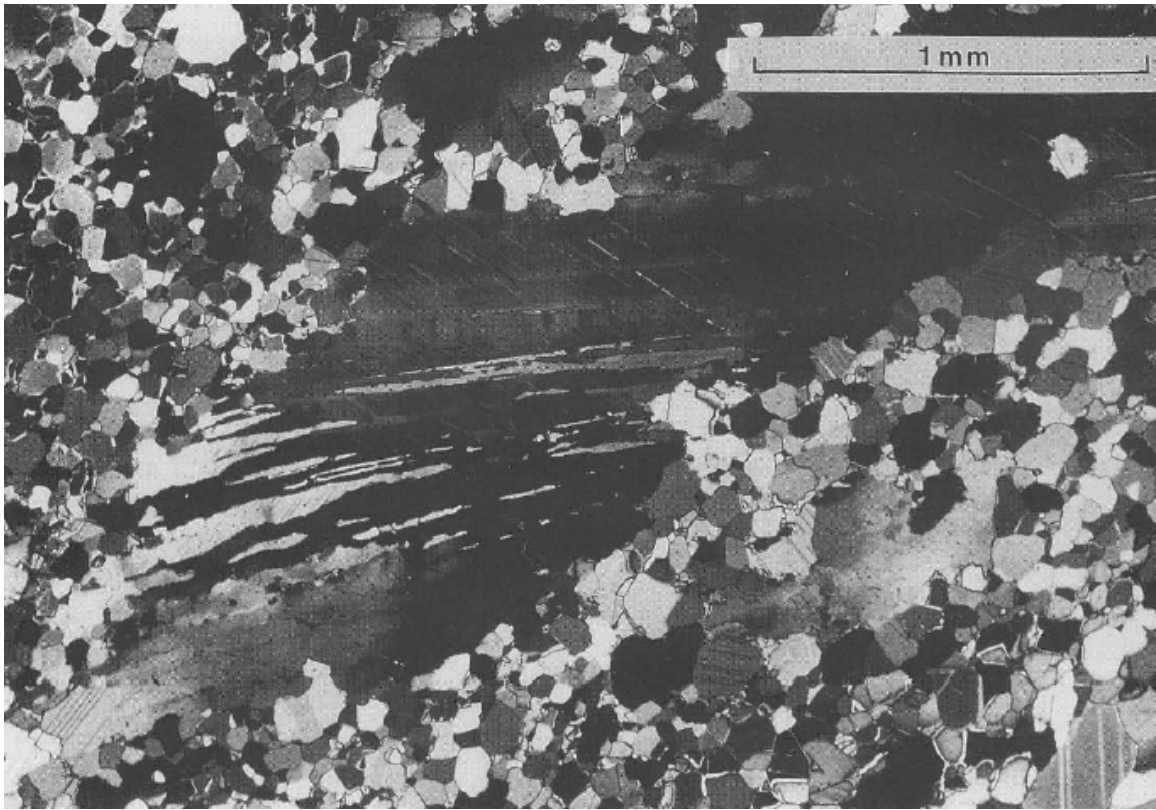
Greenschist-facies marble mylonite with partially recrystallized twinned porphyroclasts in sea of strain-free neoblasts (Vernon, 1998)
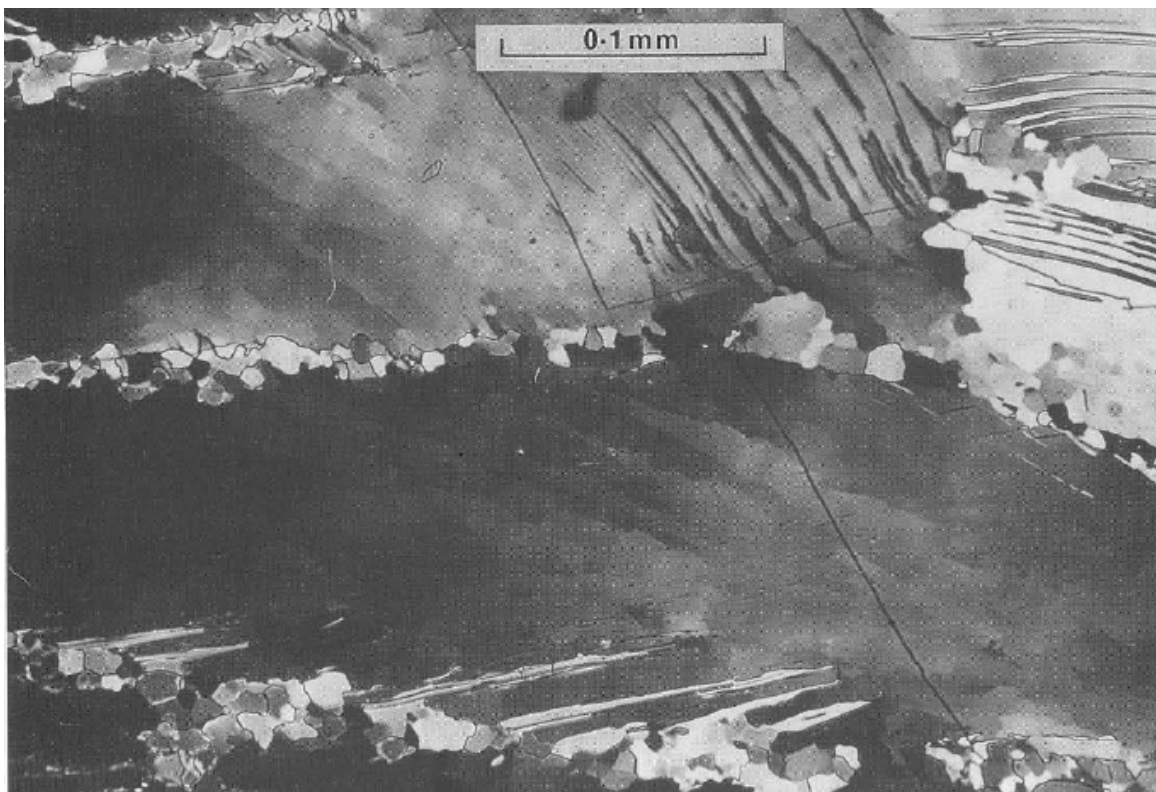
Preferential recrystallization along grain boundaries in calcite (Vernon, 1998)
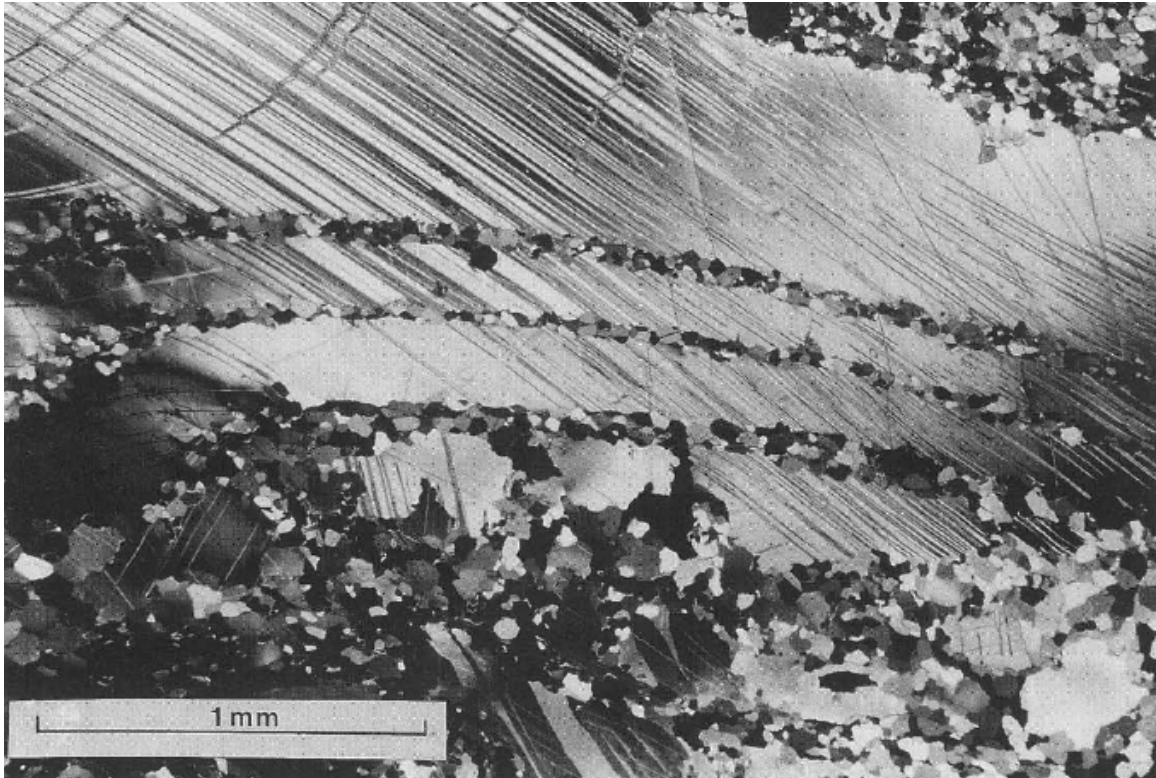
Preferential recrystallization along twins or KBB in calcite (Vernon, 1998)

Porphyroclast with subgrains formed by SGR and strain-free neoblasts formed by GBM (Vernon, 1998).
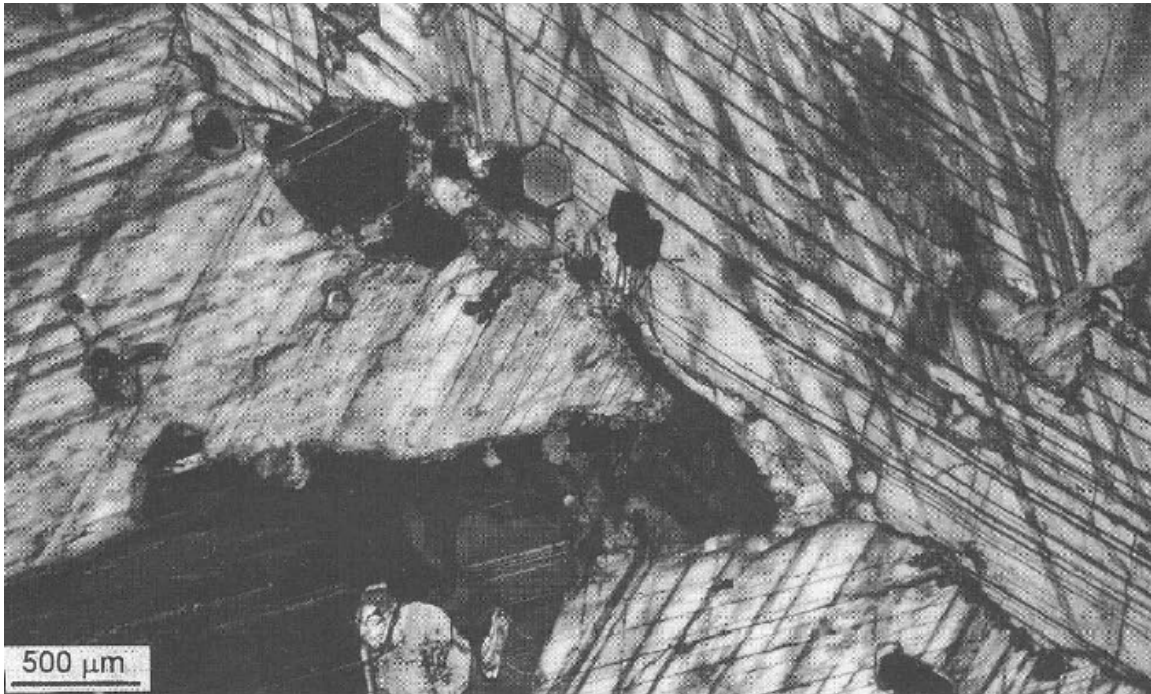
Bancroft shear zone, 475°C (van der Pluijm and Busch, 1998). Protolith
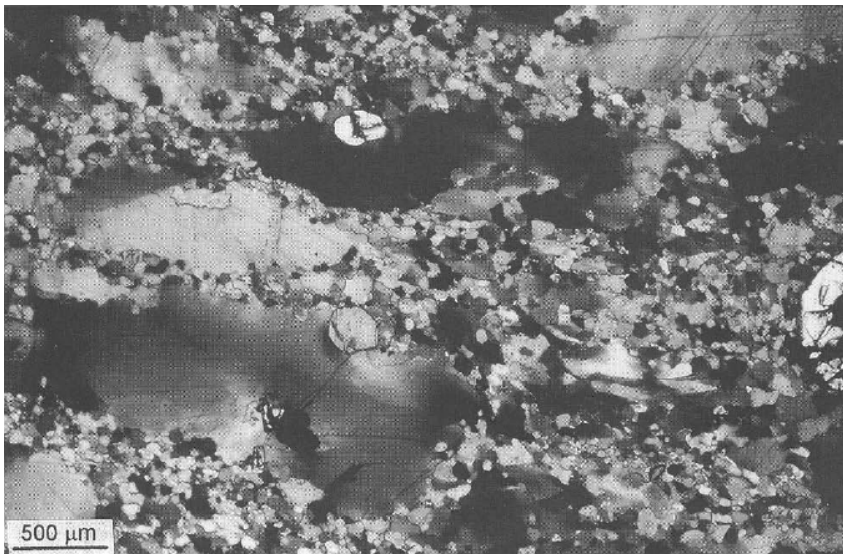
Bancroft shear zone (van der Pluijm and Busch, 1998). Protomylonite composed of mm size calcite porphyroclasts with irregular boundaries and undulatory extinction surrounded by equant, strain-free neoblasts.
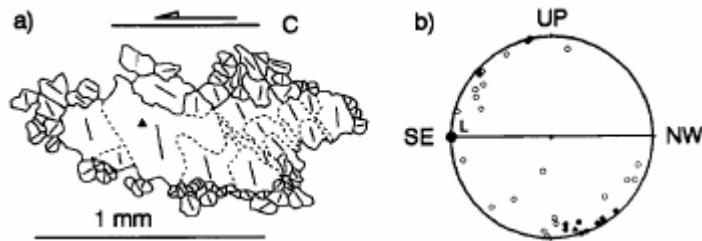
family of subgrains formed by SGR (Busch & van der Pluijm, 1995)
Angular misorientations of neoblasts with respect to porphyroclasts indicates SGR.
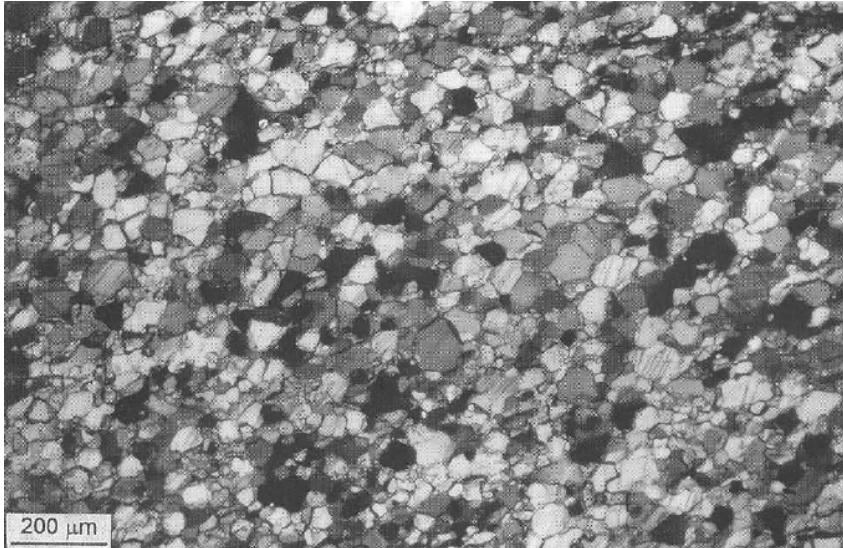
Bancroft shear zone (van der Pluijm and Busch, 1998). Coarse (50 µm) mylonite with nearly random LPO interpreted and GBS.
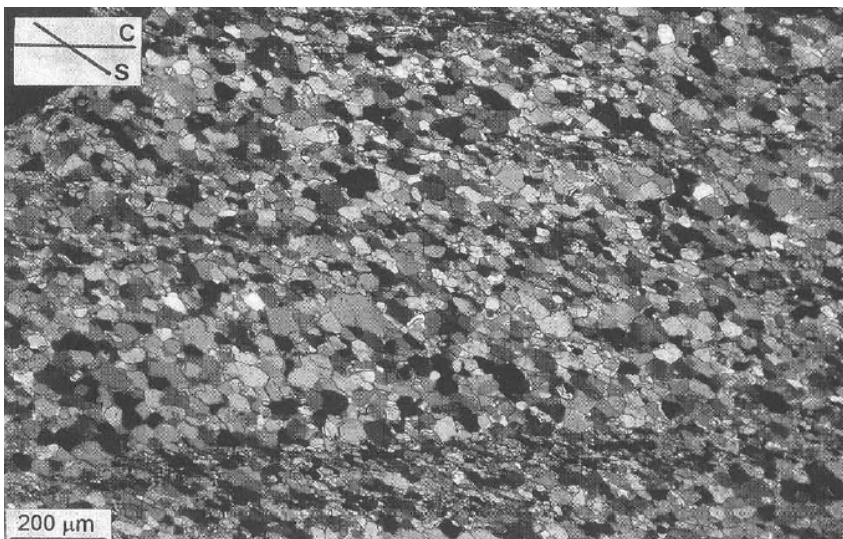
Bancroft shear zone (van der Pluijm and Busch, 1998). S–C mylonite has stronger SPO aligned 30° to shear plane. Bimodal grain size: C planes defined by very fine grained crystals.
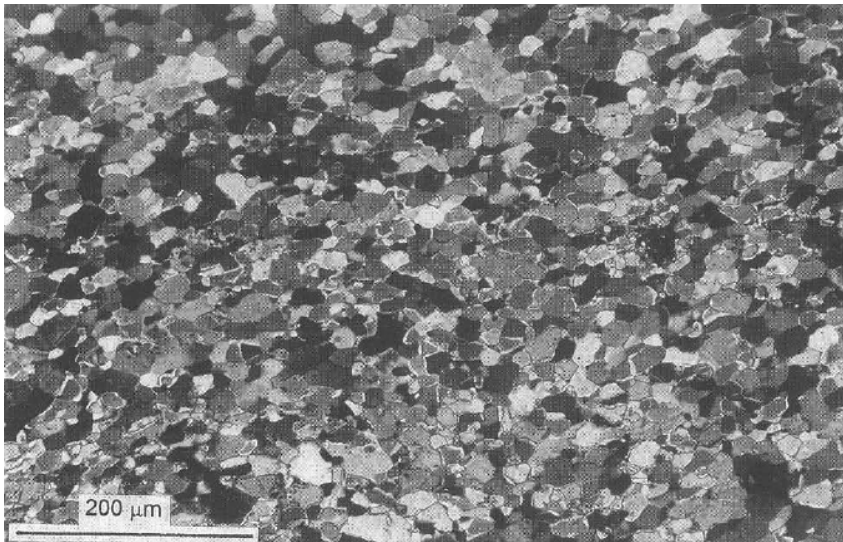
Bancroft shear zone (van der Pluijm and Busch, 1998). Ultramylonite (25 µm)
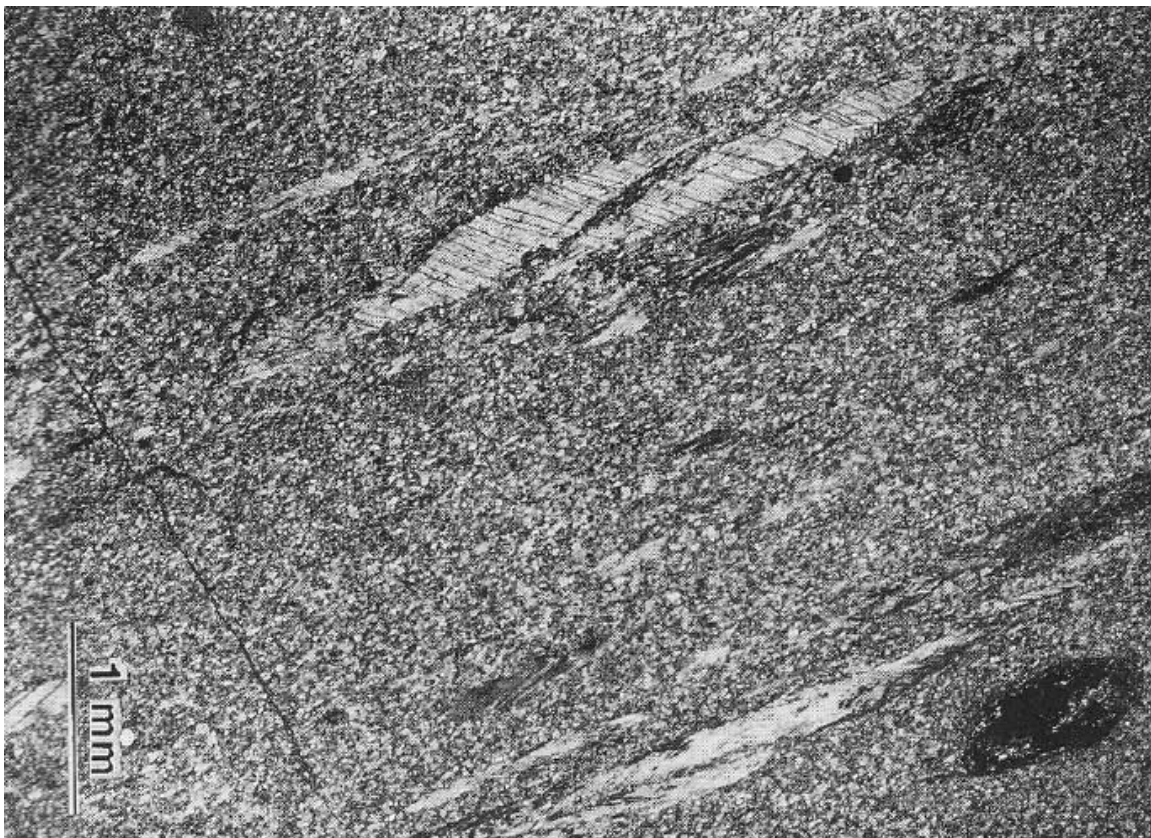
near-complete recrystallization of coarse-grained Palm Canyon marble (Erskine & Wenk, 1998)
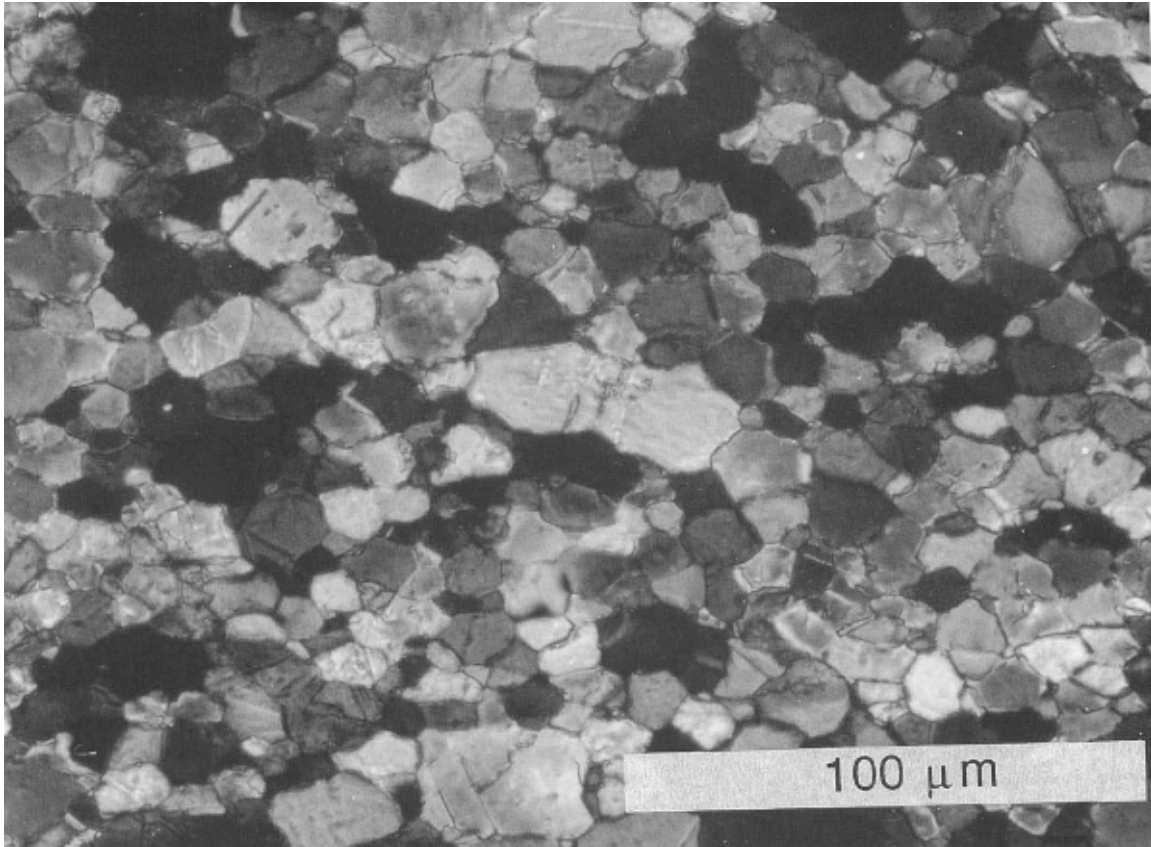
Burlini et al. (1998) Fine-grained marble mylonite with weak SPO and no LPO from Pakistan.

Calcite Crystallography
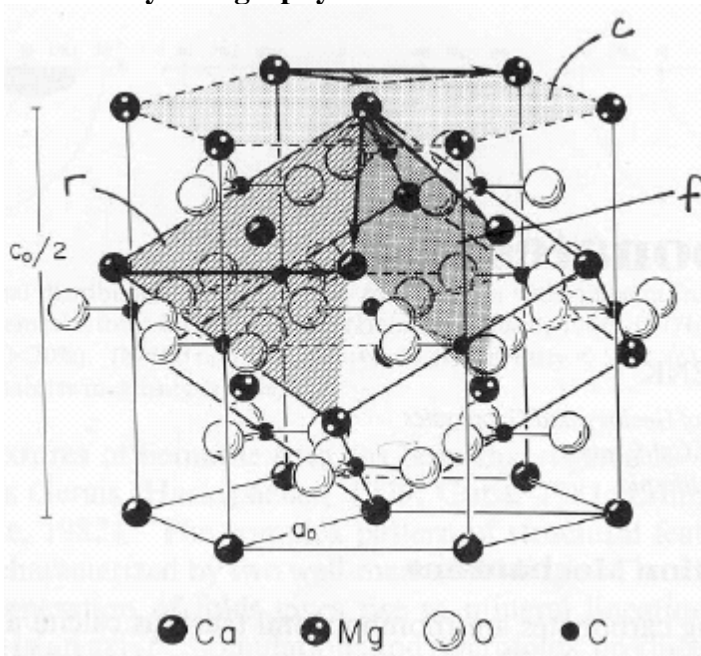
dolomite (Wenk, 1985). *e* is the negative rhomb, *r* is the positive rhomb (Wenk, 1985)

a = 4.99 Å
c = 17.06 Å
c ^ r = 44.5°
c ^ e = 26.25°
e ^ e' = 45°
r ^ r' = 75°
e ^ r = 38°
 (Turner, 1949)
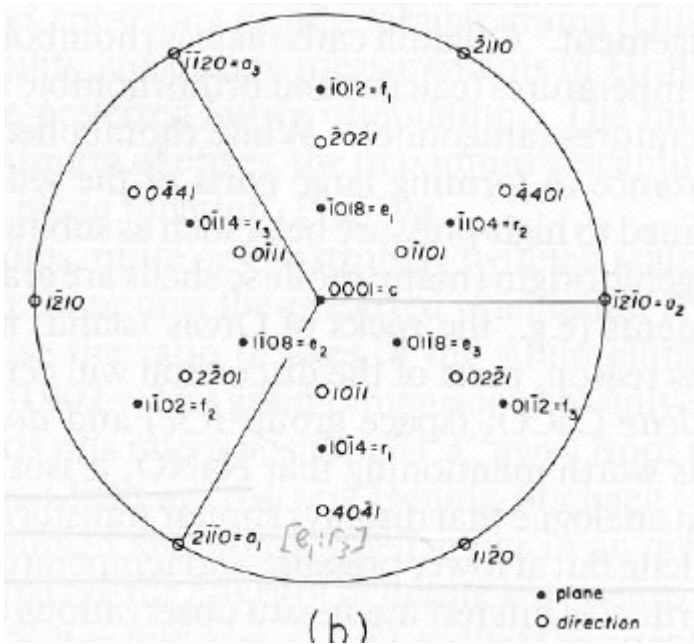
complete pole figure (Wenk, 1985)
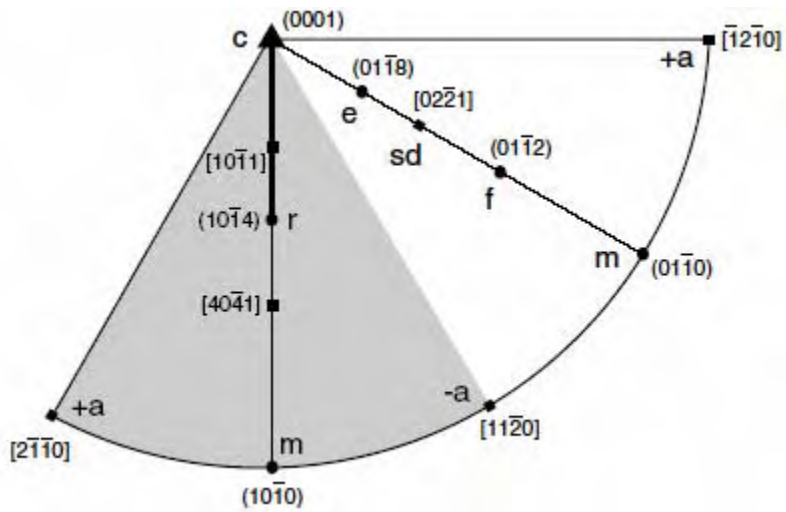
minimum pole figure (Pieri et al., 2001)

slip systems in calcite (Nicolas & Poirier, 1976; De Bresser & Spiers, 1997; Pieri et al., 2001)

plane	direction	
twining		
e^+ $\{\bar{1}018\}$	sd $<40\bar{4}1>$	
r^+ $\{10\bar{1}4\}$	sd $<\bar{2}021>$	minor importance
f^- $\{\bar{1}012\}$	sd $<\bar{1}01\bar{1}>$	minor importance
slip		
r^- $\{10\bar{1}4\}$	sd $<\bar{2}021>$	
r^+ $\{10\bar{1}4\}$	a $<\bar{1}2\bar{1}0>$	
f^- $\{\bar{1}012\}$	sd $<\bar{2}201><0\bar{2}2\bar{1}>$	
f^+ $\{\bar{1}012\}$	sd $<2\bar{2}01><02\bar{2}1>$	
f^- $\{\bar{1}012\}$	sd $<\bar{1}01\bar{1}>$	
f^+ $\{\bar{1}012\}$	sd $<10\bar{1}1>$	
c $\{0001\}$	a $<\bar{1}2\bar{1}0>$	
a $\{\bar{1}2\bar{1}0\}$	sd $<\bar{2}021>$	minor importance
m $\{10\bar{1}0\}$	a $<\bar{1}2\bar{1}0>$	minor importance
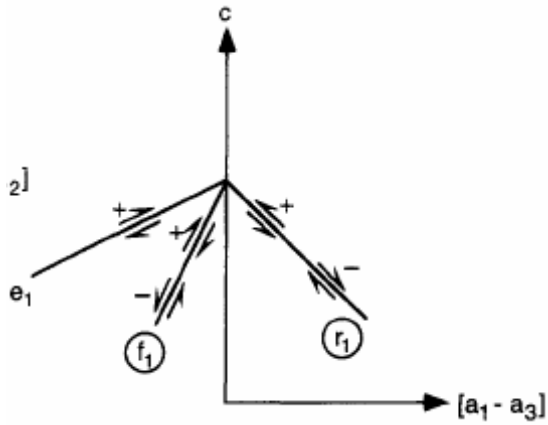
(De Bresser & Spiers, 1997, after Turner et al., 1954)
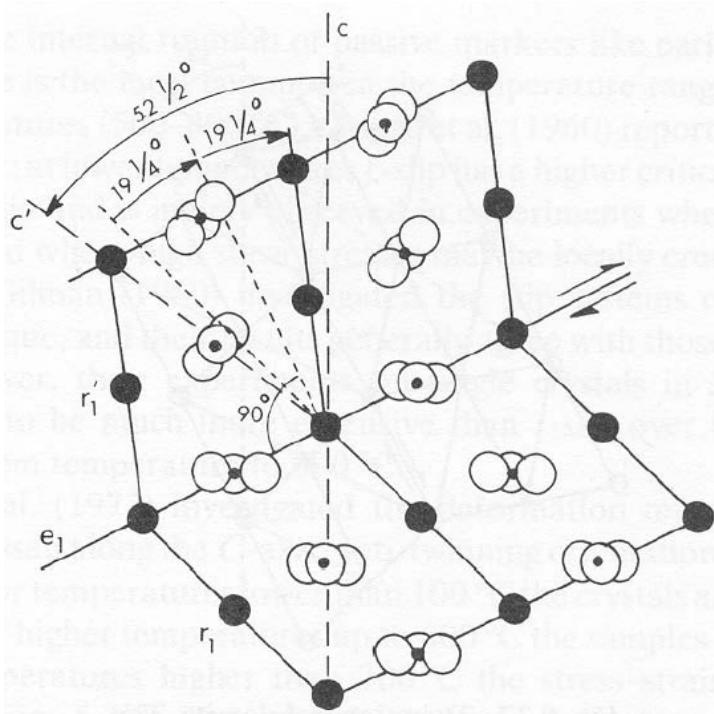
e twinning in calcite occurs along the 'negative rhomb' planes; there are 3 crystallographically distinct *e* planes in (trigonal) calcite (Nicolas & Poirier, 1976)

Experimental Mechanical Data: Single Crystals
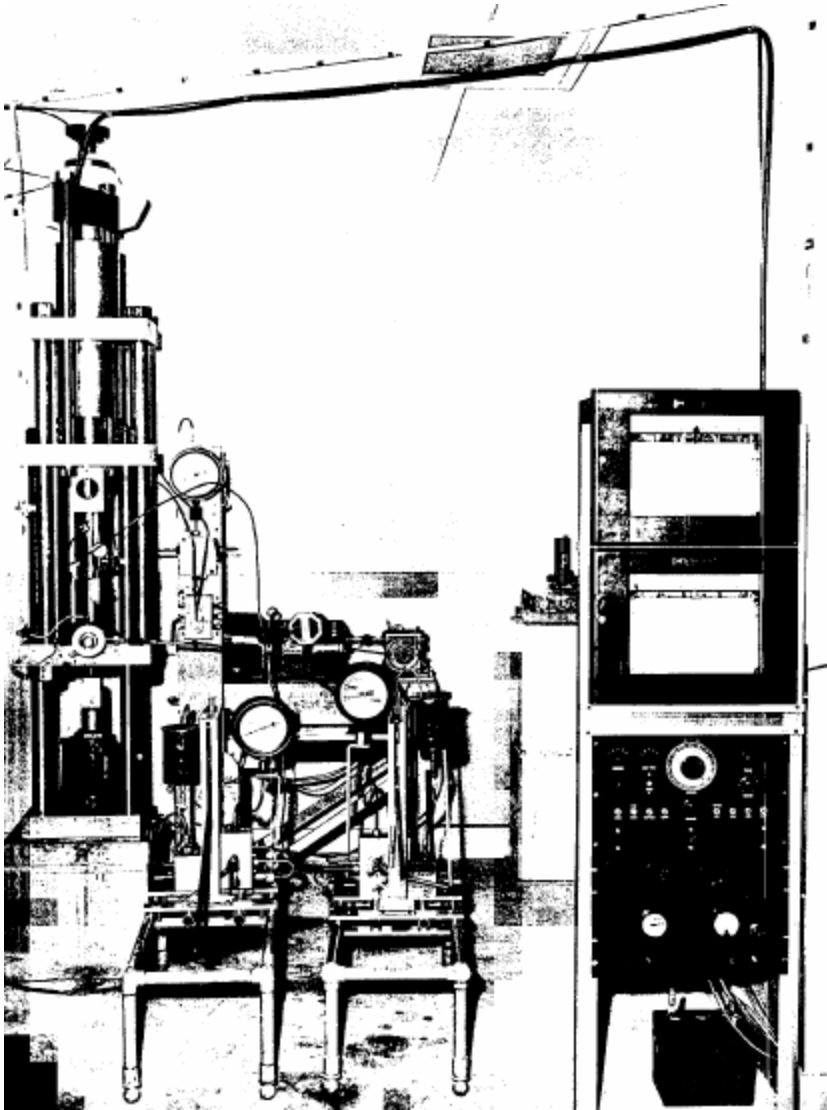
some of the first high T rheology tests were carried out on marble (Griggs & Miller, 1951)
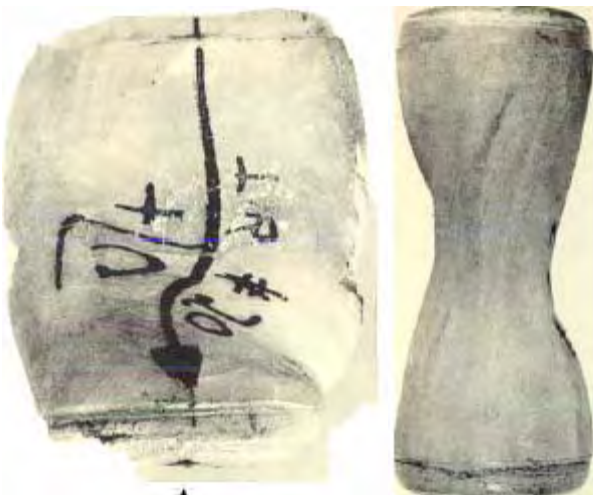
shortened and extended single calcite crystals—exterior (Turner et al., 1954)
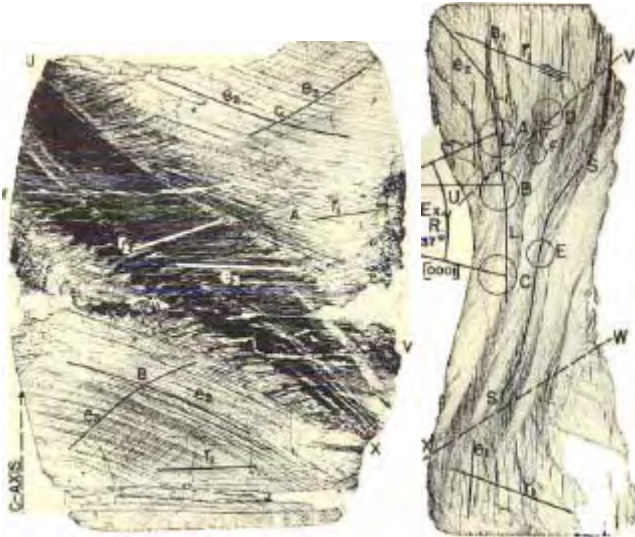
shortened and extended single calcite crystals—interior (Turner et al., 1954)
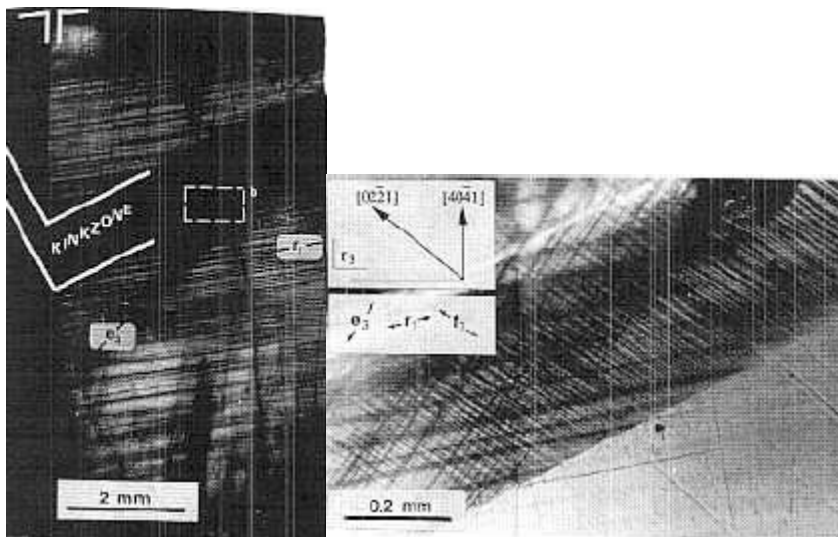
single crystal experiments are used to measure mechanical properties of individual slip systems (De Bresser & Spiers, 1990)
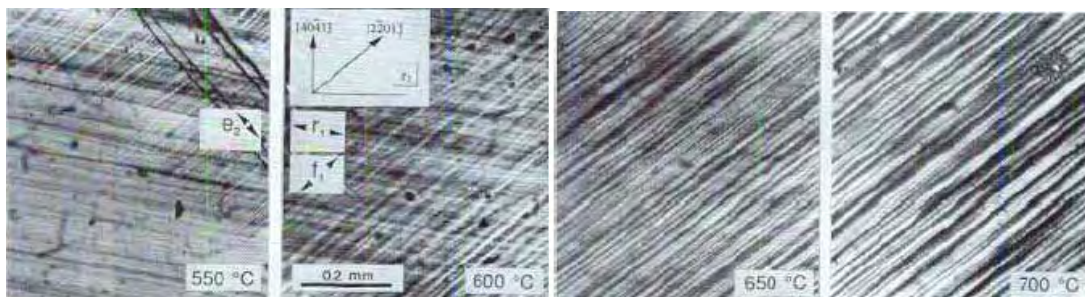
The transition from dominantly *r* slip at 550°C (left) to *f* slip at 700°C (right) as seen in a single crystal (De Bresser & Spiers, 1990)
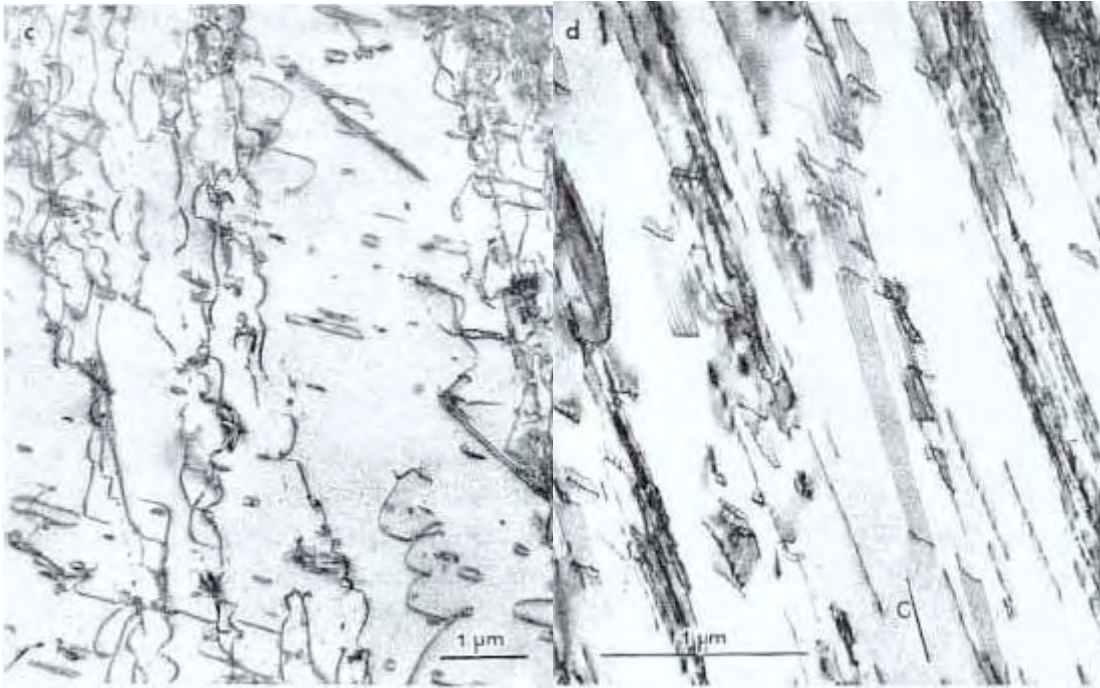
800°C loops and (0001) stacking faults induced by c slip at 420°C (Barber et al., 1981)
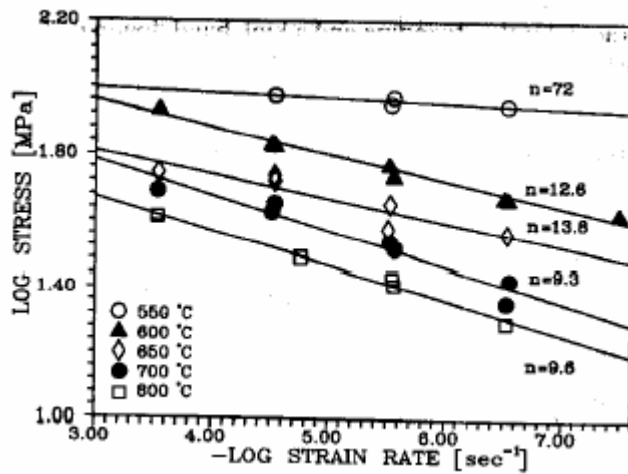
Stress exponents for calcite single crystals vary as a function of temperature (De Bresser & Spiers, 1990)
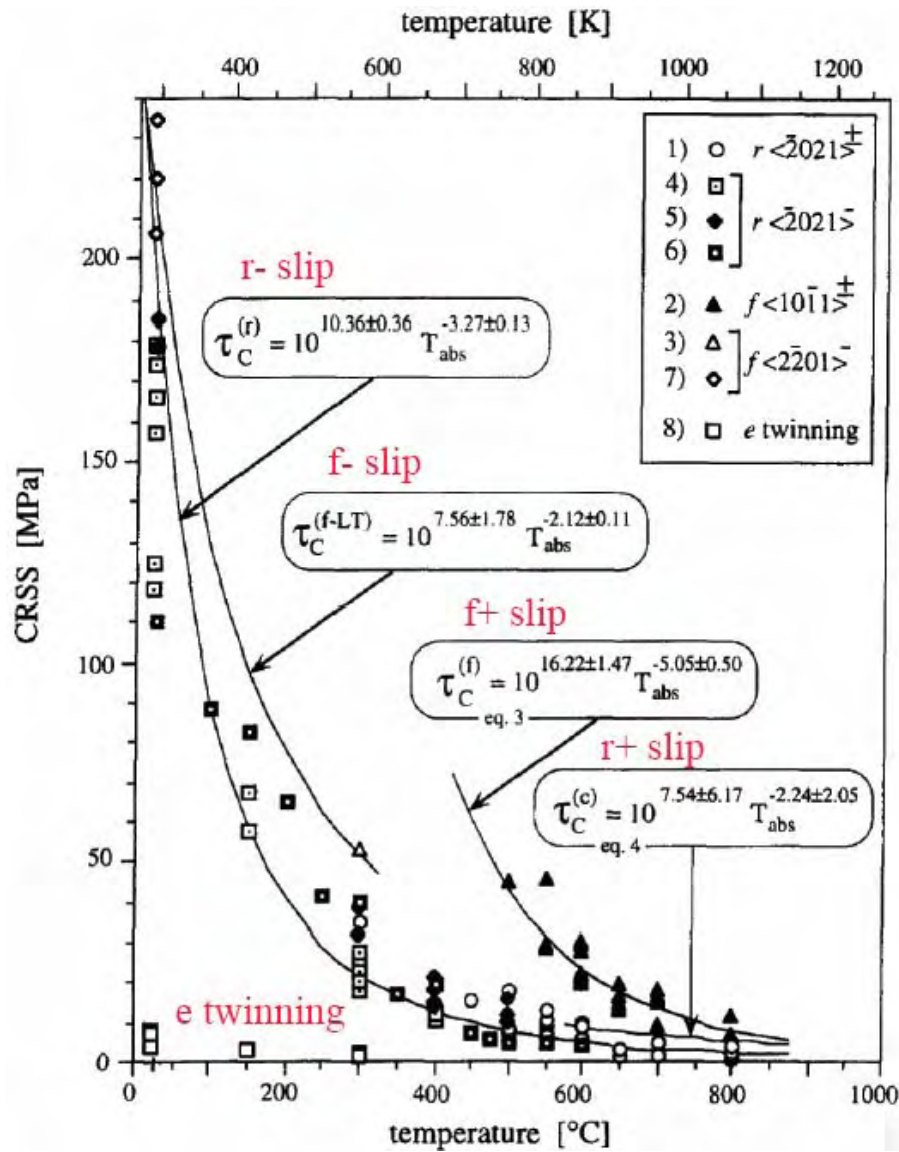
critical resolved shear tress for *e* twinning, *r* slip, *f* slip and *c* slip at 10^{-5} s^{-1} (De Bresser & Spiers, 1997)

General observation for single crystals (De Bresser & Spiers, 1997):
- low T regime with
  - $<40\bar{4}1>\{\bar{1}018\}$ *e* twinning
  - $<\bar{2}021>\{10\bar{1}4\}$ *r* slip
  - $<2\bar{2}01>\{\bar{1}012\}$ *f* slip
- high T regime with
  - $<\bar{2}021>\{10\bar{1}4\}$ *r* slip
  - $<10\bar{1}1>\{\bar{1}012\}$ *f* slip
  - $<\bar{1}2\bar{1}0>\{0001\}$ *c* slip
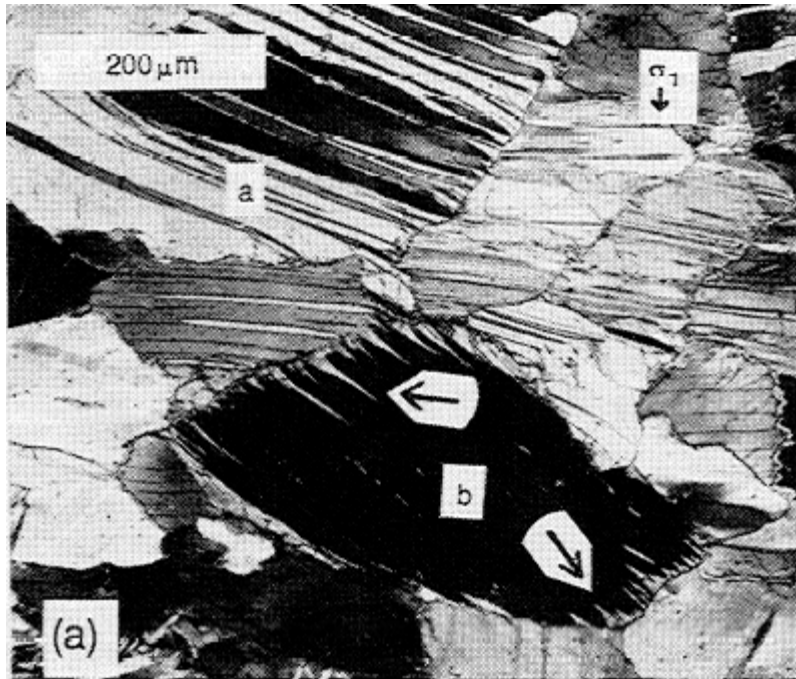
(Rutter, 1995)

twinning occurs along 3 *e* planes at very low CRSS of 2–12 MPa (Burkhard, 1993)

maximum strain from complete *e* twinning is 29% theoretically and closer to 15% in marble (Wenk, 1985)

Experimental Mechanical Data: Rocks
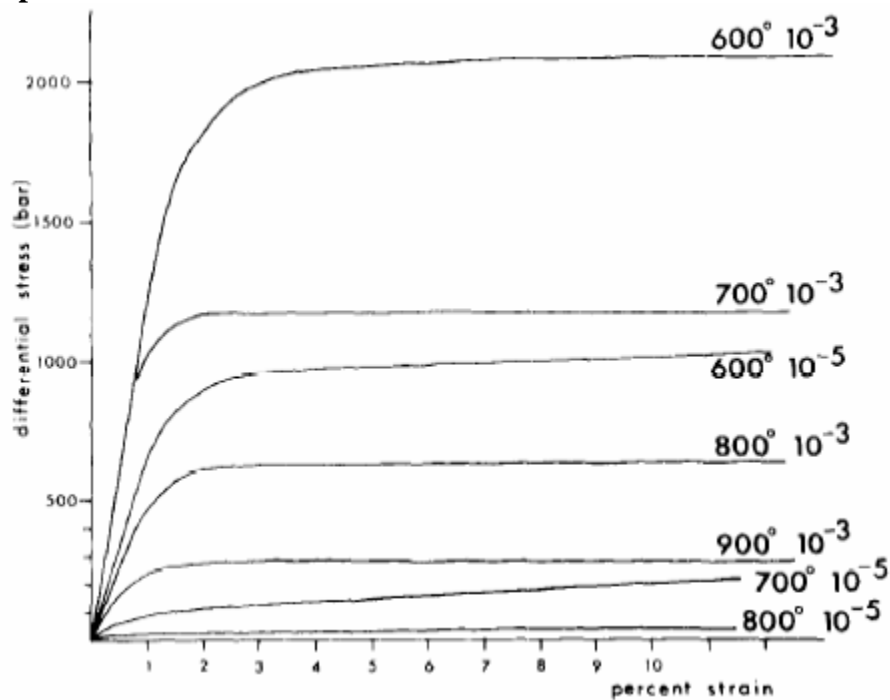
Solnhofen limestone (Schmid et al., 1977)
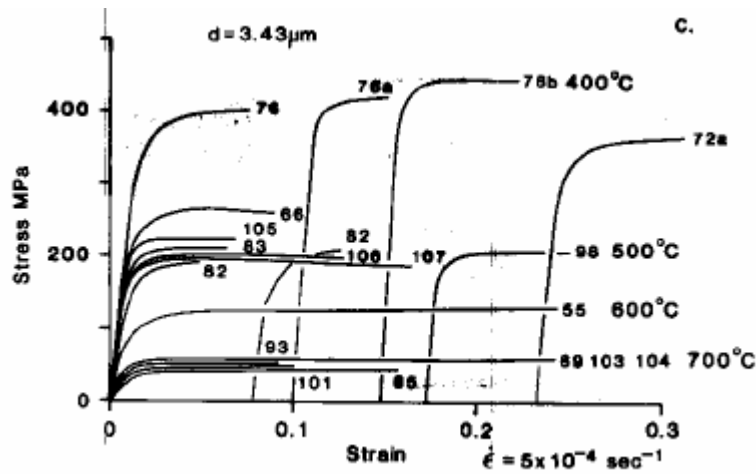
mechanical tests on synthetic marble (Walker et al., 1990)
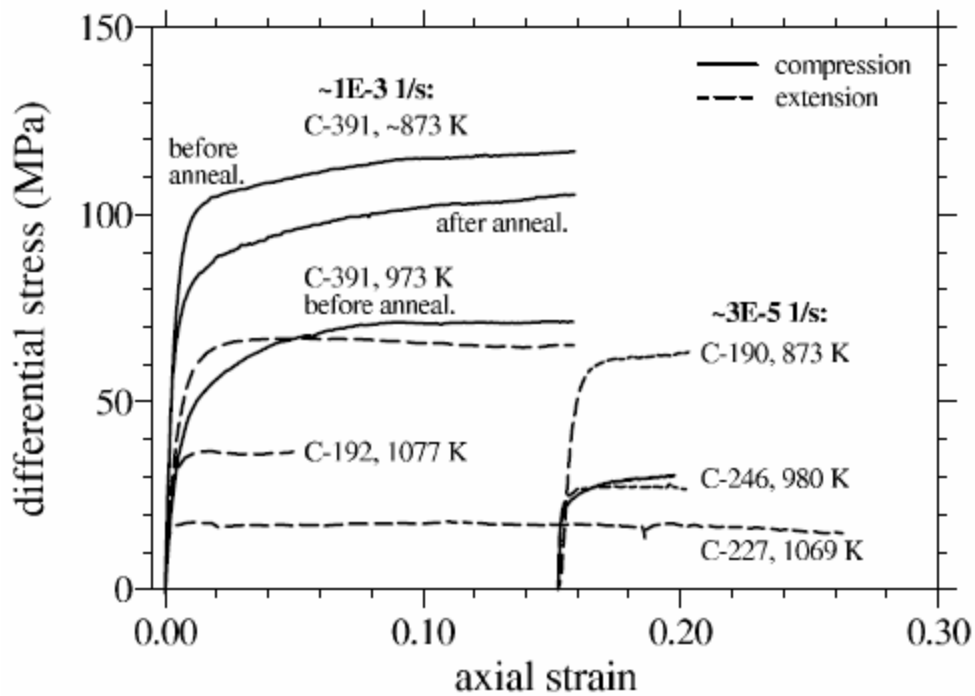
mechanical tests on synthetic marble (Renner et al., 2002)
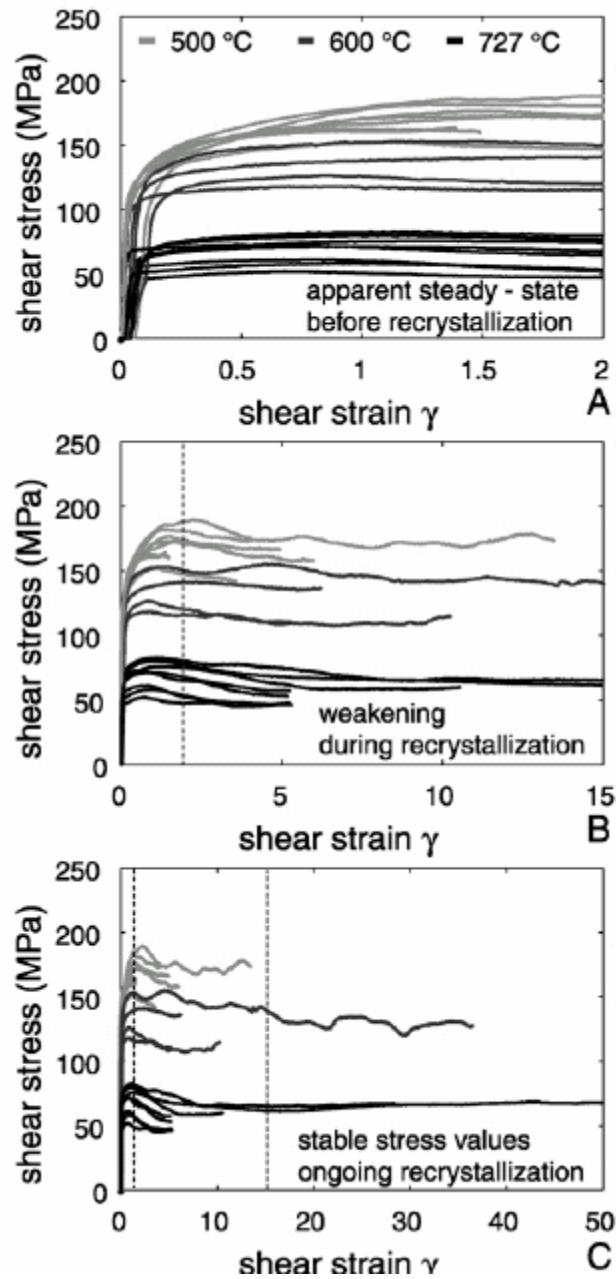
stress to different strains in Carrara marble (not changes in scale), showing mechanical effect of secondary recrystallization (Barnhoorn et al., 2004)
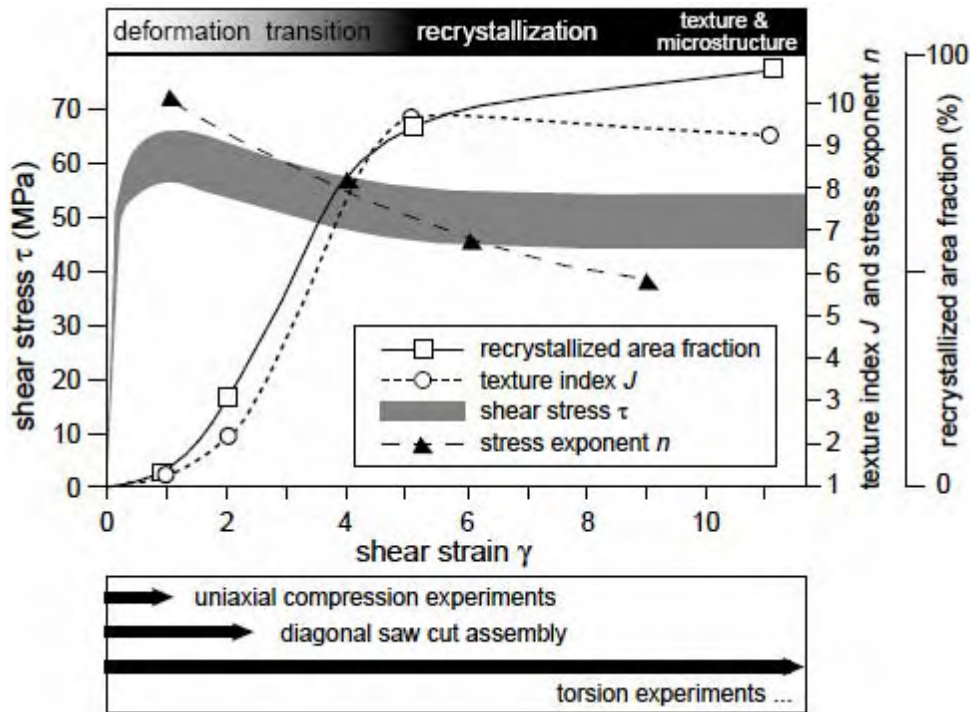
importance of torsion experiments (Pieri et al., 2001)
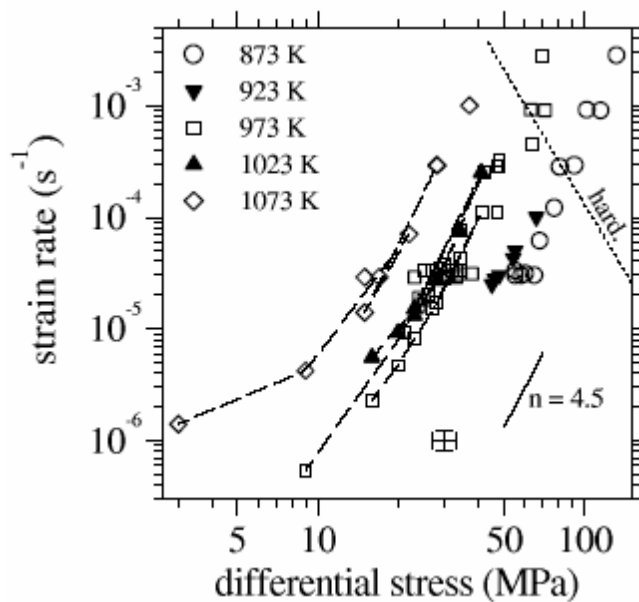
synthetic calcite aggregates show n = 4.5 at 600–800°C ('hard' = strain hardening regime) (Renner et al., 2002)
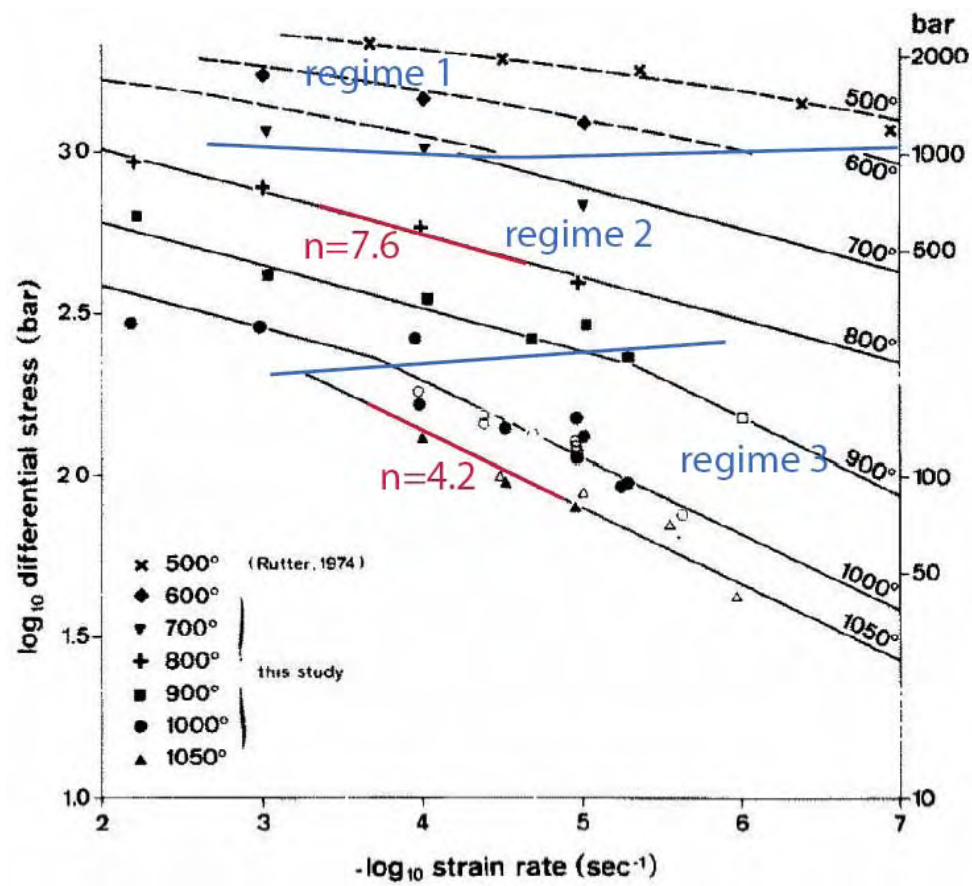
Carrara marble deformation regimes (Schmid et al., 1980)
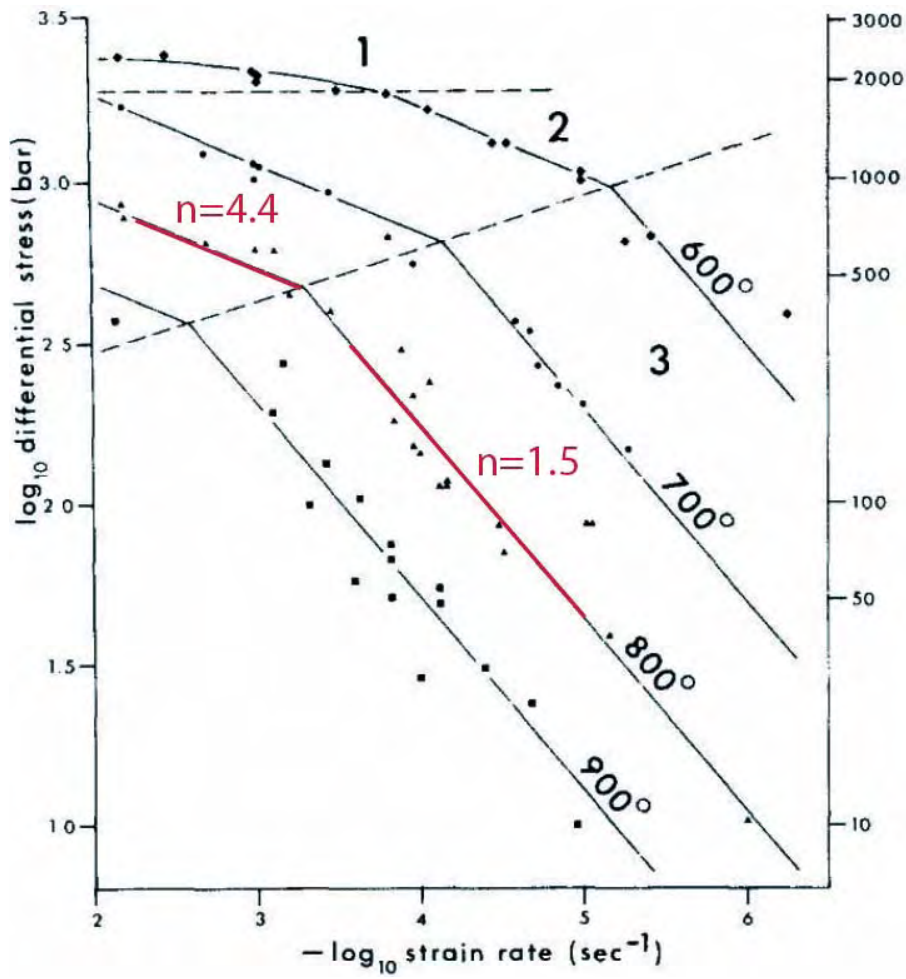
Solnhofen limestone deformation regimes (Schmid et al., 1977)
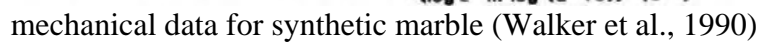
mechanical data for synthetic marble (Walker et al., 1990)
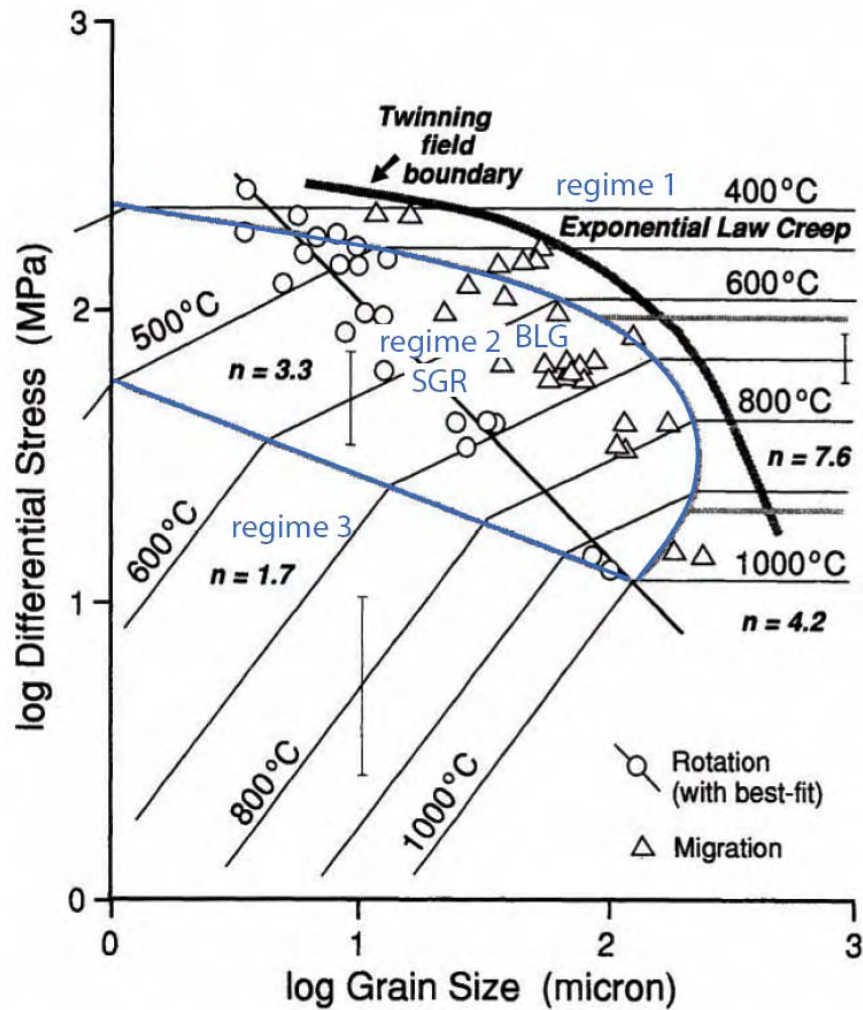
deformation mechanism map for 10^{-5} s^{-1} showing grain-size sensitive and grain-size insensitive fields (Rutter, 1995)
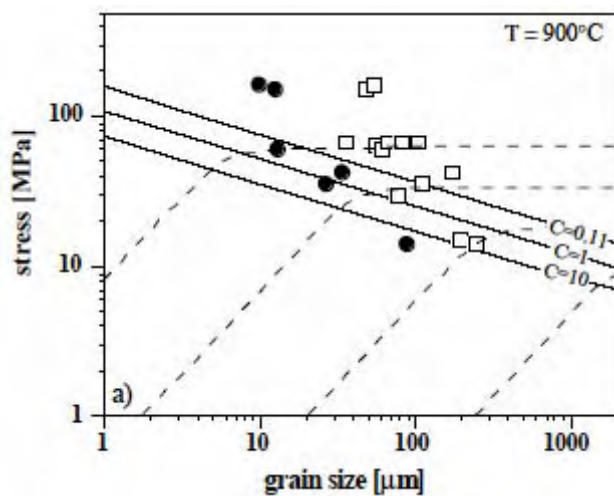
deformation mechanism map for calcite showing grain-size sensitive and grain-size insensitive fields. C = ratio of dislocation-creep strain rate to dislocation-creep strain rate. Dashed lines are strain rates of 10^{-2}, 10^{-4}, 10^{-6}, and 10^{-8} s^{-1} (de Bresser et al., 2001)
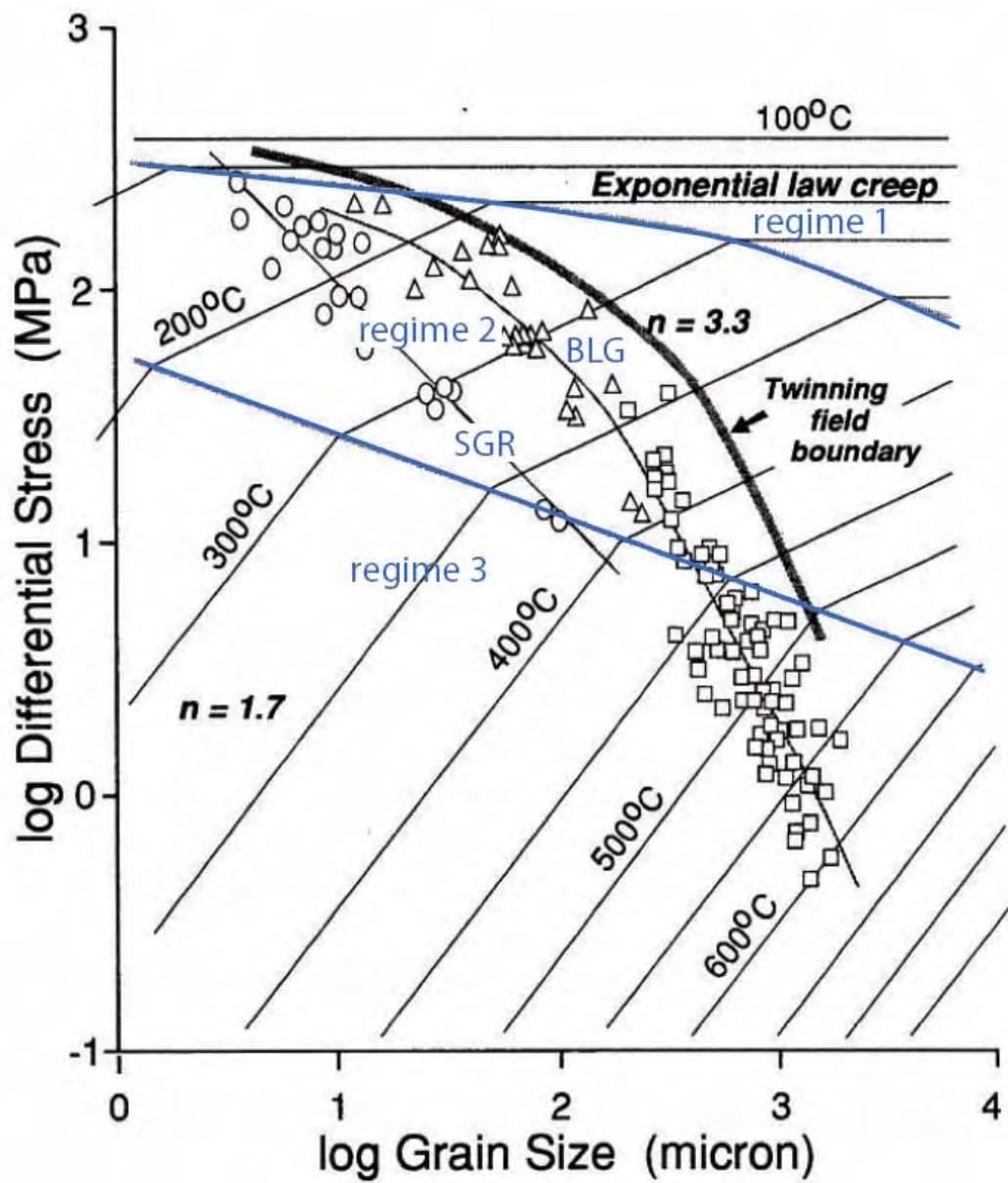
deformation mechanism map for $3*10^{-14}$ s^{-1} (Rutter, 1995)

	log A	Q	n	m	ref
Solnhofen R2	3.4	287 ± 17	4.4 ± 0.44	0	Schmid et al. 1977
Solnhofen R3	4.3	205 ± 10	1.5 ± 0.1	–2.5 (est.)	Schmid et al. 1977
Yule	-3.7 ± 0.8	261 ± 12	8.2 ± 0.4	0	Heard & Raleigh 1972
Carrara R2	3.1	418 ± 42	7.6 ± 0.8	0	Schmid et al. 1980
Carrara R3	8.1	427 ± 46	4.2 ± 0.4	0	Schmid et al. 1980
Synthetic	2.00	190	3.33	–1.34	Walker et al. 1990
Synthetic	4.93	190	1.67	–1.87	Walker et al. 1990

Flow law parameters (all in MPa, µm; after Brodie & Rutter, 2000)

Twinning regime 1 is different: exponential relationship of Rutter (1974) (also fits Schmid et al. data):

$$\dot{\varepsilon} = 5.9E5s^{-1} \exp\left(\frac{-259kJ/mol}{RT}\right) \exp\left(\frac{\sigma}{11.4MPa}\right) \text{ Carrara}$$

Twinning Regime 1 (Schmid et al., 1980; 1987)
Regime 1 is characterized by *e* twinning with minor *r* slip of grains that cannot twin. It is characteristic of Solnhofen at T < 400°C and Carrara at T ≤ 600°C.
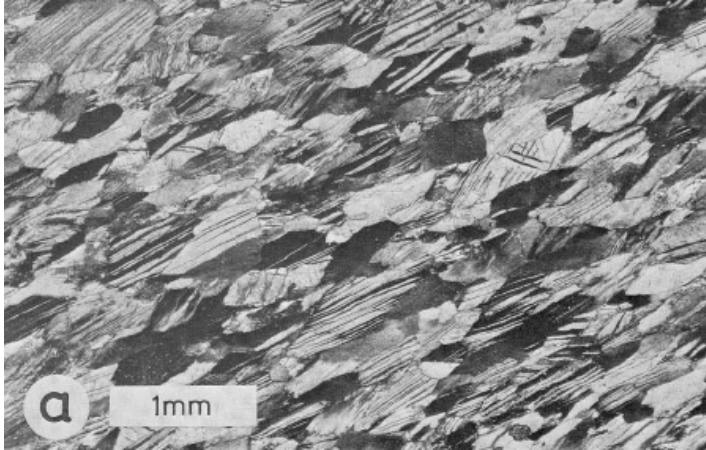
twinning and grain flattening (Schmid et al., 1987)
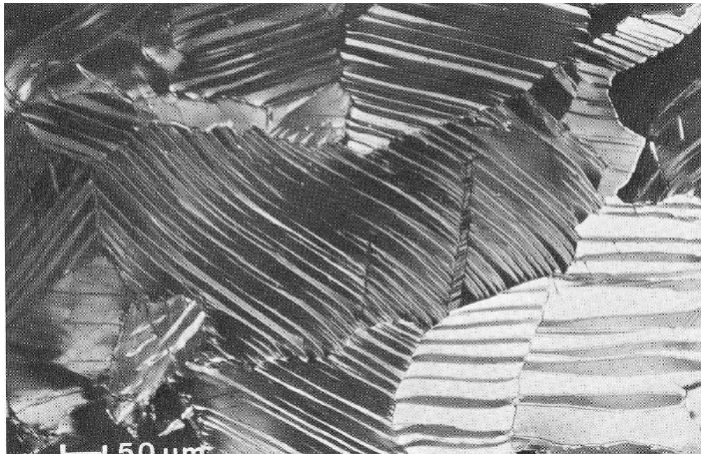
mechanical twinning(Schmid et al., 1980)
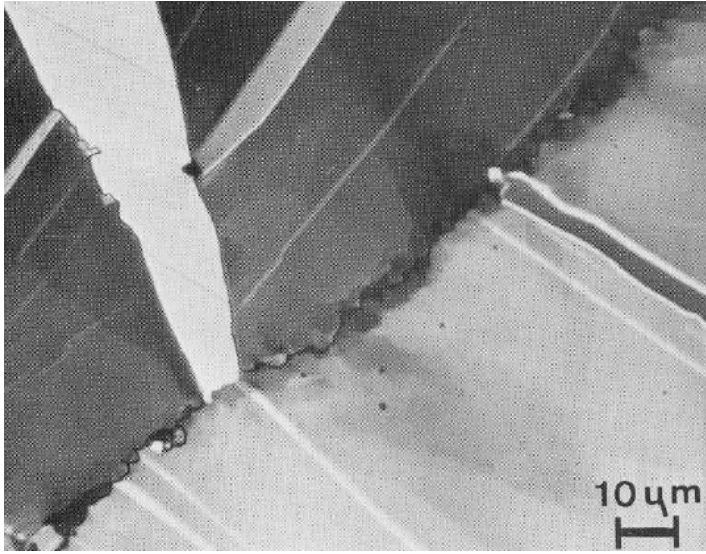
minor recrystallization along grain boundaries(Schmid et al., 1980)
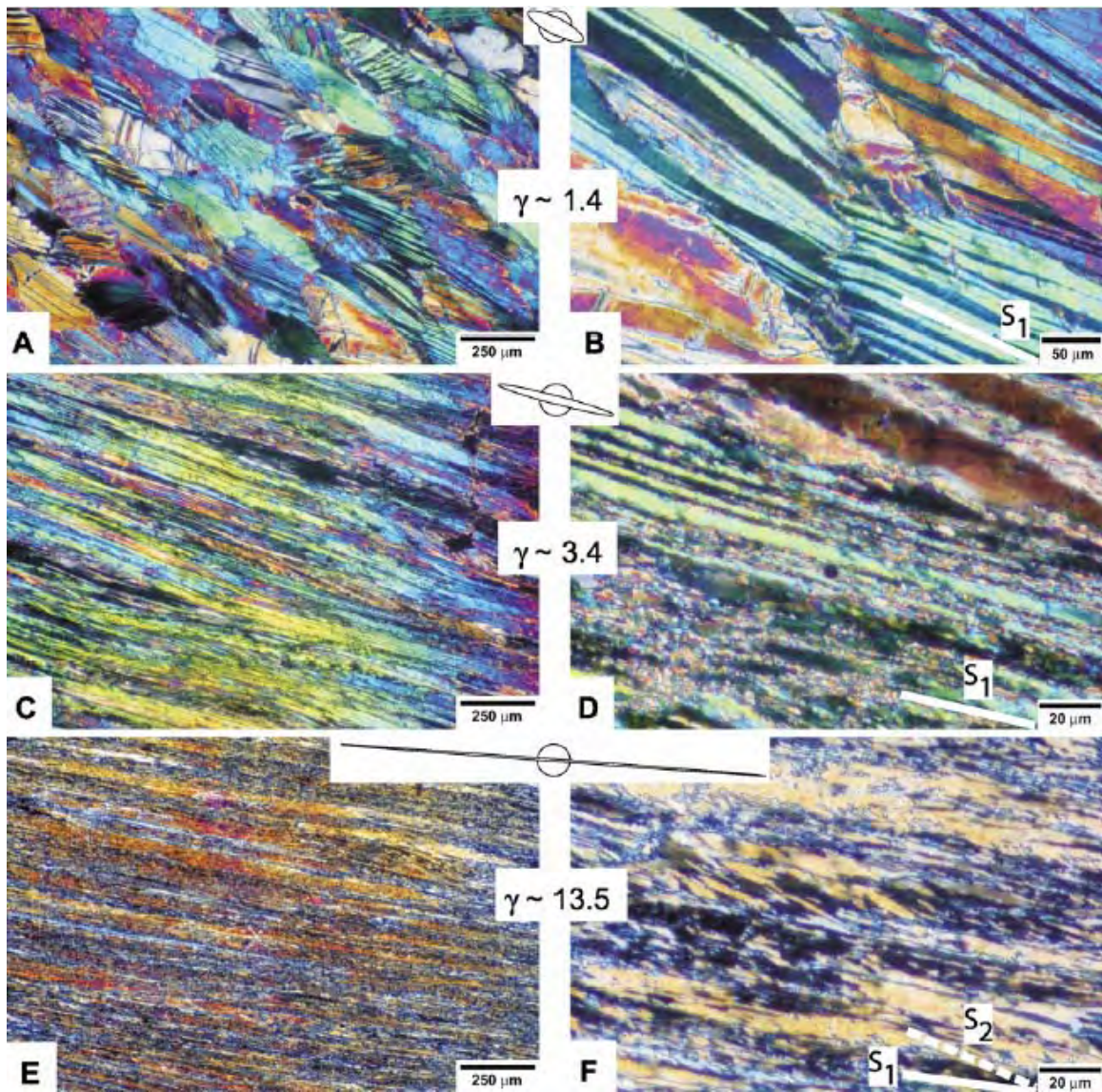
Carrara marble textures at 500°C; A&B) twinning, no recrystallization; C&D) very heavy twinning, small recrystallized grains at twin boundaries; E&F) more pervasive recrystallization (Barnhoorn et al., 2004)

Twinning rotates the *c* axis 52° toward the compression direction—but (important!) not because of compensatory rotation induced by dislocation glide.
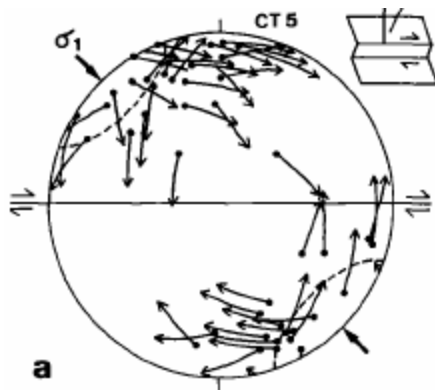
arrows show *opposite* sense of rotation of c axes from twinning (i.e., from twinned to pre-twinned orientation; Schmid et al., 1987). Twinning occurs at minor strains in response to *stress*, so the LPO's must be interpreted differently.
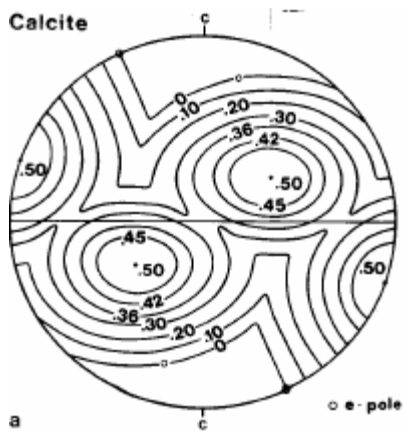
Schmid factor for calcite *e* twinning (Jamison & Spang, 1986). A grain whose c axis is within ~26° of the compression axis cannot twin.
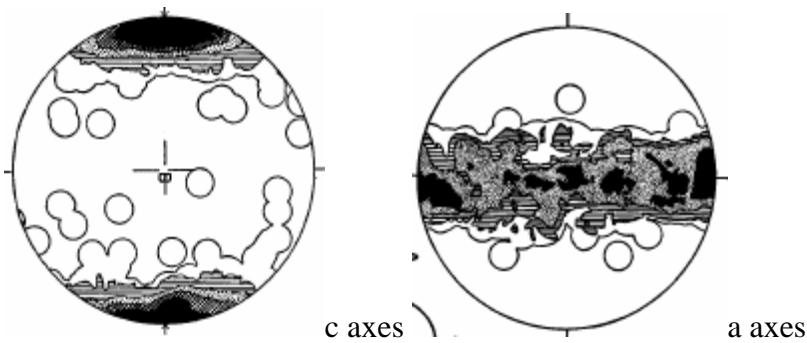
LPO formed from uniaxial shortening and simple shear at 400°C in Yule Marble (Turner et al., 1956)
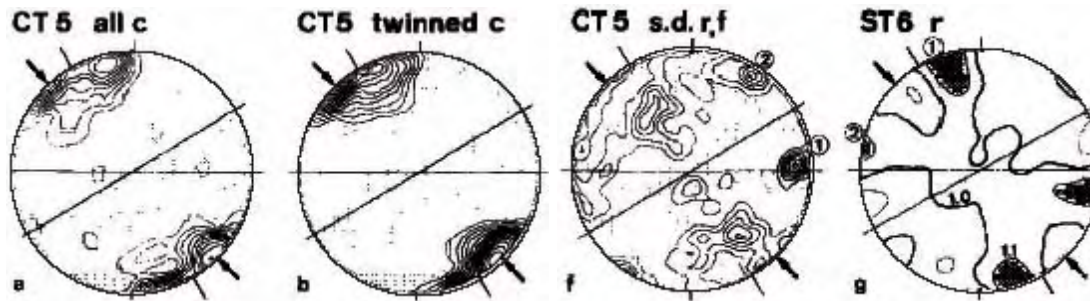
Carrara marble LPOs produced in twinning regime. a) *c* axes of all grains; b) *c* axes of twinned grains; f) slip direction for *r* and *f* planes; g) poles to *r* planes. Note deflection of *c* in the "opposite" sense expected for *glide* on the *e* plane because deformation is by twinning rather than slip. One set of *r* planes is aligned for synthetic slip, the other for antithetic slip (Schmid et al., 1987)
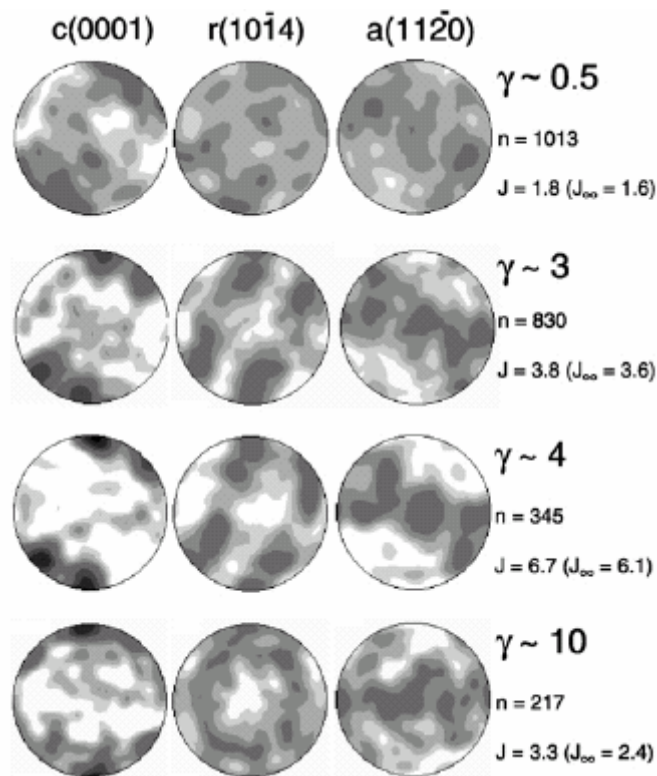
Carrara marble sinistral torsion at 500°C; SZB is horizontal; two *c*-axis maxima at $\gamma \leq 4$ replaced by three at $\gamma = 10$ (Barnhoorn et al., 2004). Note how $\gamma = 0.5$ has "wrong" asymmetry and *c* axes for $\gamma = 10$ look symmetric.

c(0001)   r(10Ī4)   a(11Ž0)

γ ~ 2
n = 949
J = 2.9 (J∞

γ ~ 4
n = 764
J = 3.7 (J∞

γ ~ 9
n = 698
J = 4.1 (J∞

γ ~ 32
n = 3875
J = 42.1 (J,
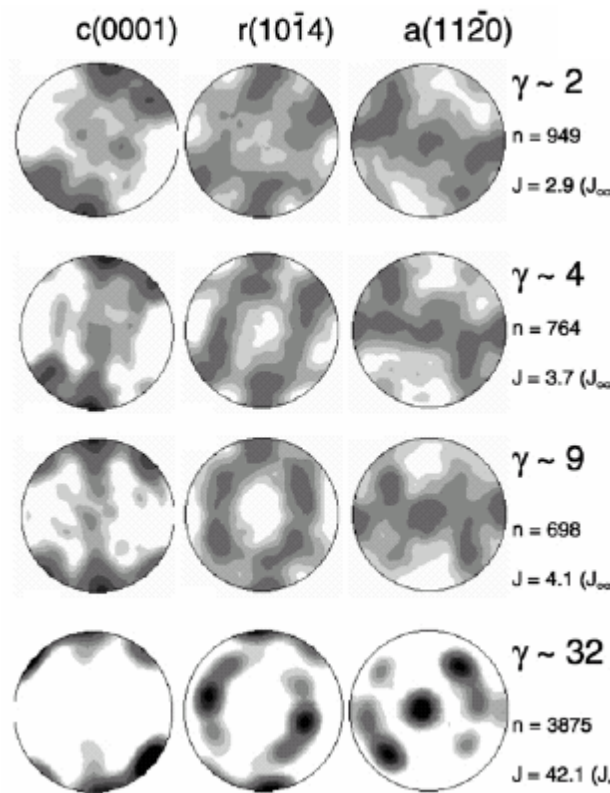
Carrara marble sinistral torsion at 600°C; SZB is horizontal; two *c*-axis maxima at γ ≤ 4 replaced by three at γ ≥ 9 (Barnhoorn et al., 2004). Note how different the γ = 32 is from the 500°C experiments and reversal in asymmetry between γ = 9 and γ = 32.

Slip Regime 2 (Schmid et al., 1977; 1980; 1987)
Regime 2 is characteristic of Solnhofen limestone at T ≥ 400°C and Carrara marble at T ≥ 700°C. This difference in T between these 2 rocks occurs because twinning is more difficult in fine-grained rocks where grain boundaries interfere with twinning. Typical microstructures produced by SGR include core-and-mantle texture, undulatory extinction, deformation bands, and elongate subgrains.

d   100μm
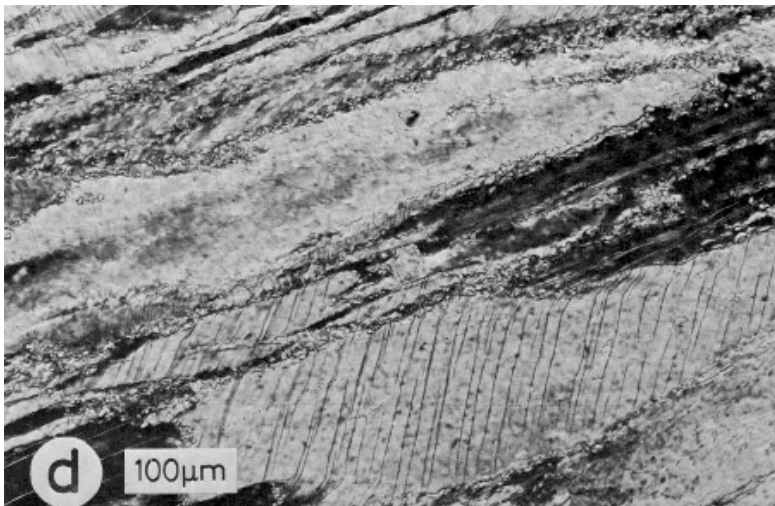
core-and-mantle textures indicative of SGR in Carrara marble (Schmid et al., 1987)

SGR and GBM in Carrara marble (Schmid et al., 1980)
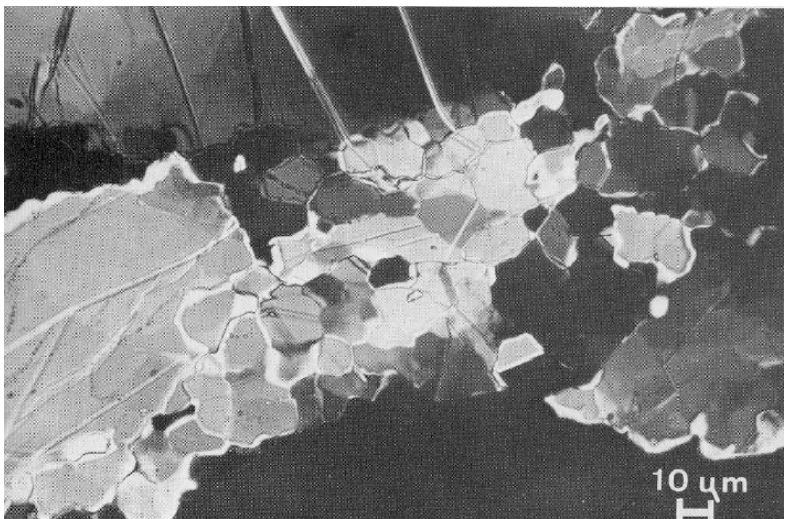
SGR and GBM in Carrara marble (Schmid et al., 1980)
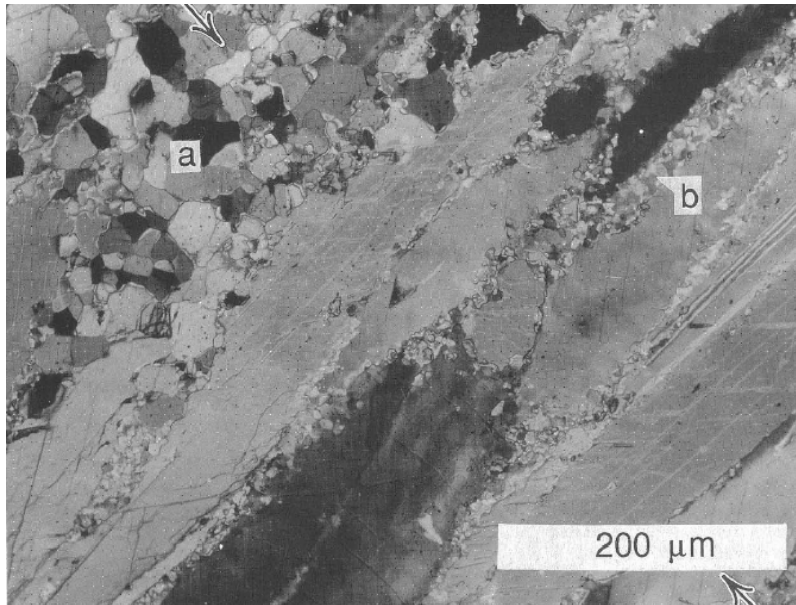
Rutter (1998) Marble extended 650% at 800°C and 250 MPa. Necklaces of small, neoblasts form by a combination of SGR (b) and GBM (a). The grain size from GBM is always larger than that formed by SGR.
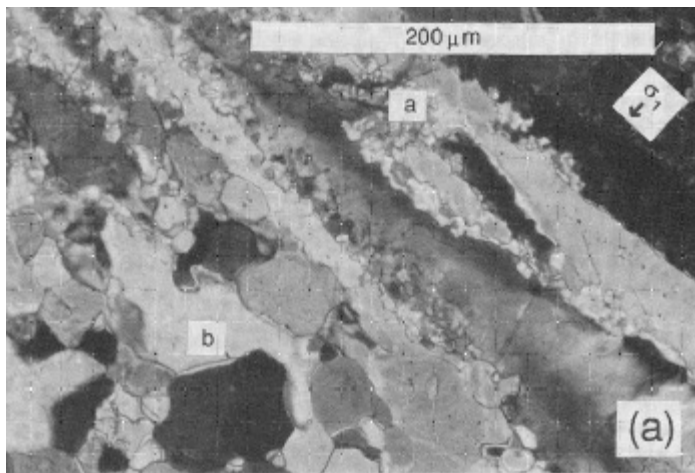
700°C 400% extension necklace of neoblasts produced by SGR and grain boundary bulging (Rutter, 1995)
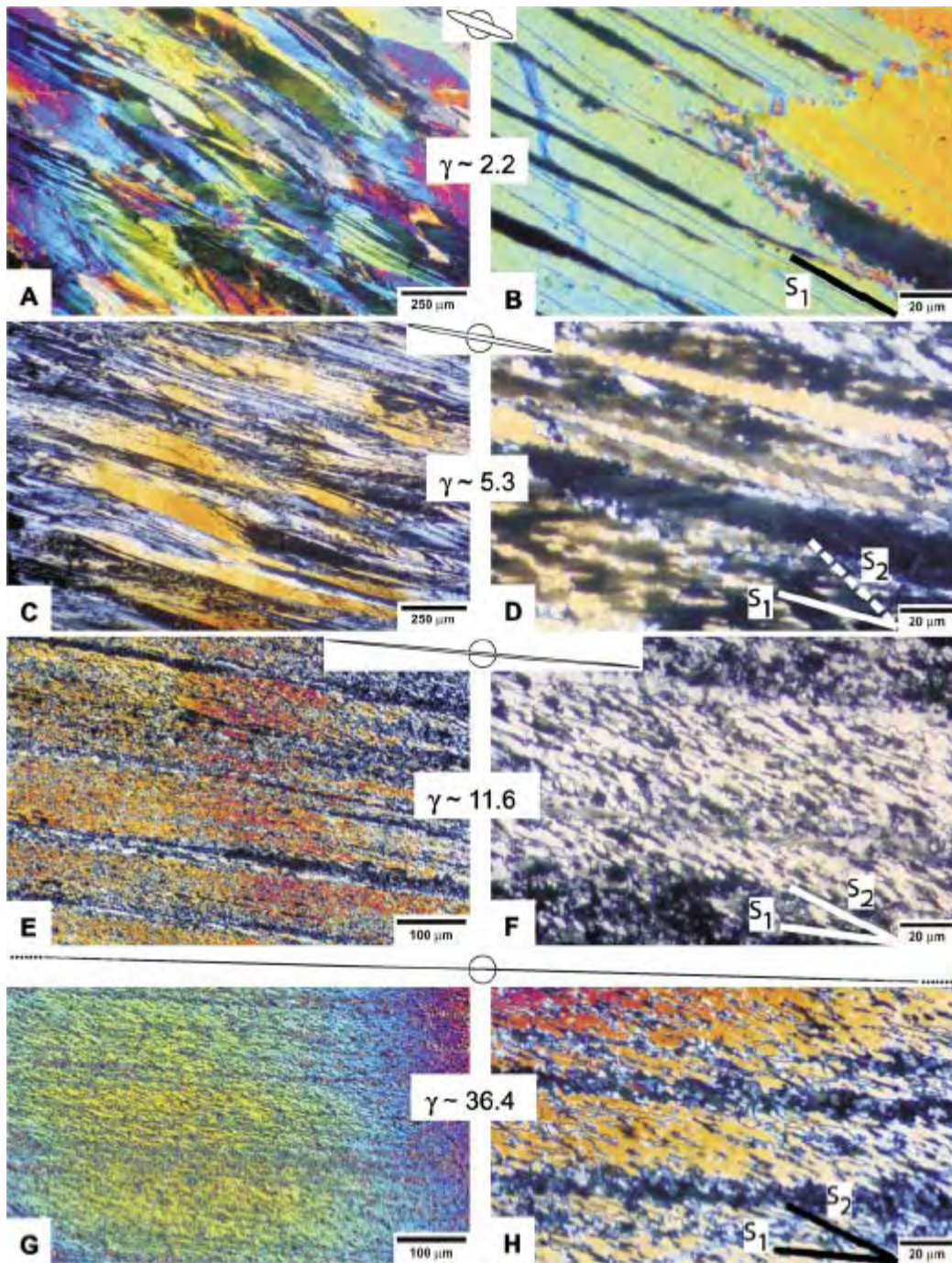
Regime 2Carrara marble textures at 600°C A&B) twins are less abundant and thicker than at 500°C; C&D) elongate grains have high-angle subgrains whose shape defines the sense of shear; E&F) 85% recrystallization, secondary foliation forming; G&H) complete recrystallization to secondary foliation (Barnhoorn et al., 2004)

γ ~ 0.8

γ ~ 5.2

γ ~ 10.5

γ ~ 29.1

γ ~ 50.4
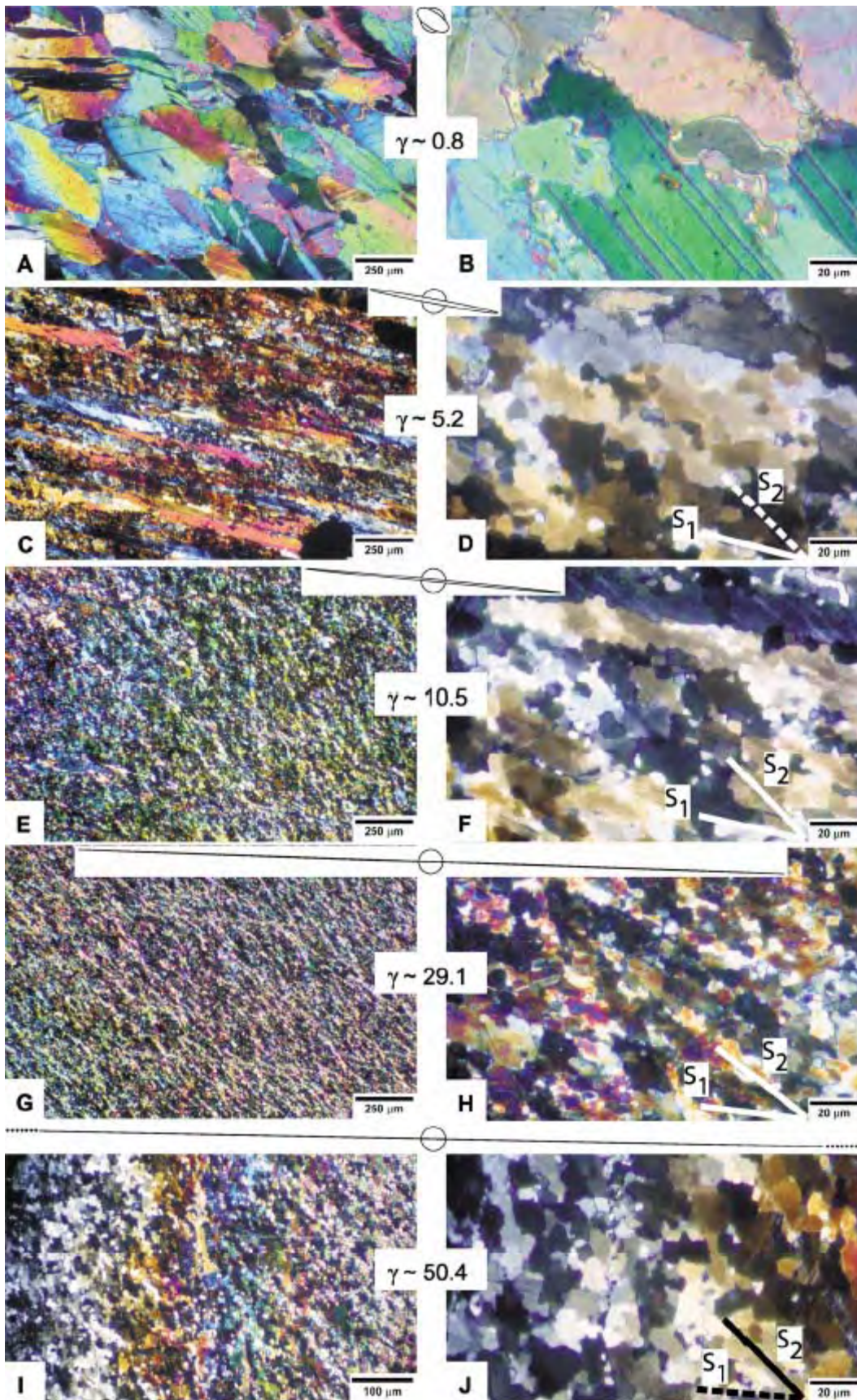
Regime 2 Carrara marble textures at 723°C. A&B) relatively few, thick twins with small recrystallized grains at grain boundaries; C&D) 75% recrystallization through SGR; E&F) complete recrystallization to second foliation; G&H) complete recrystallization to second foliation I&J) no further microstructural changes out to $\gamma = 50$ (Barnhoorn et al., 2004)
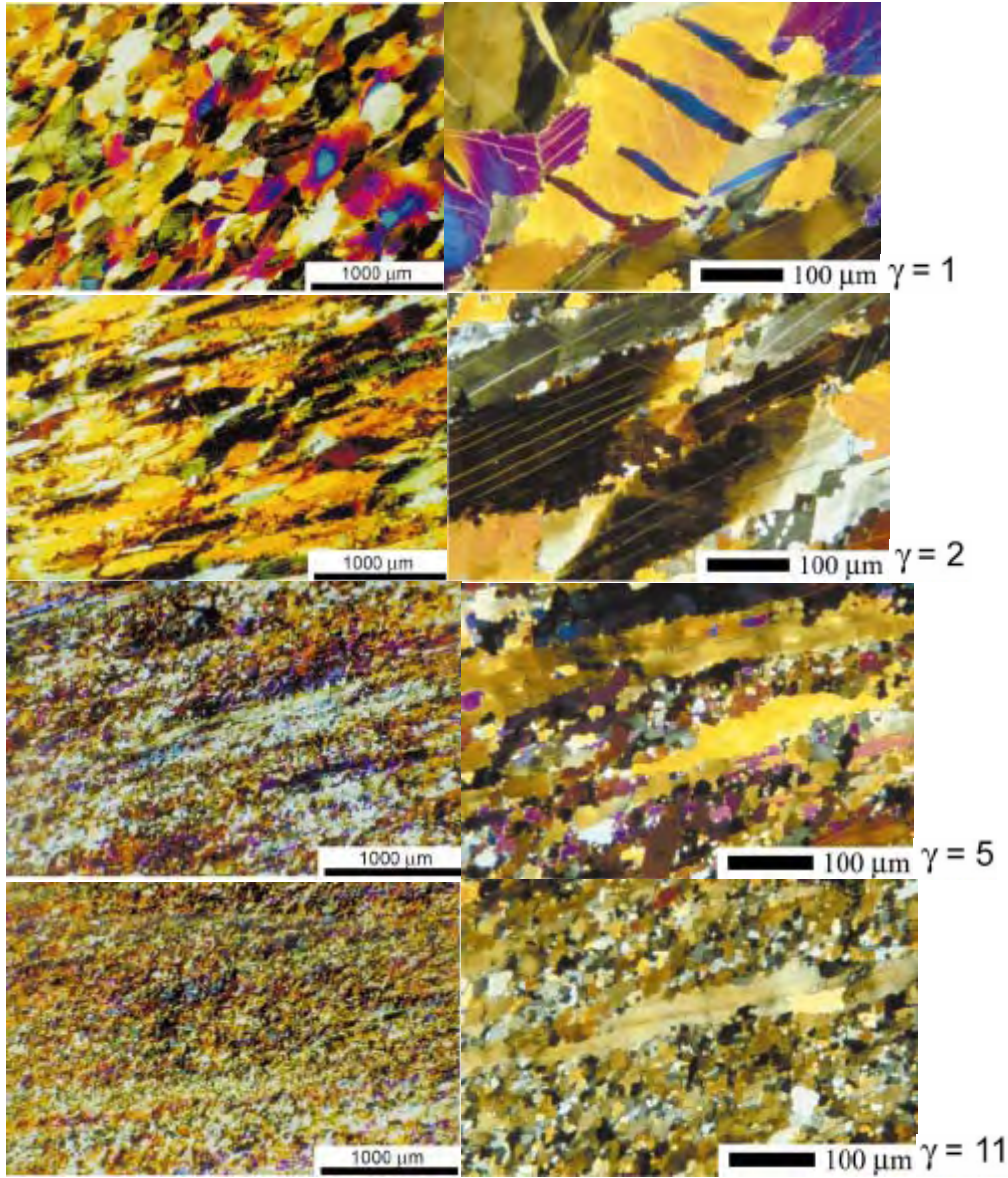
Regime 2 torsion experiments on Carrara marble at 723°C. Undulatory extinction, twinning, deformation bands, and grain boundary subgrains (Pieri et al., 2001)
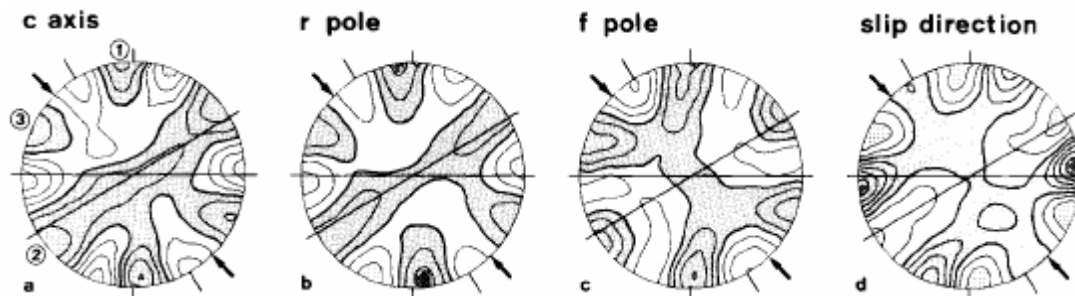
LPO for Solnhofen limestone at 500°C ("slip direction" is for *r* and *f* slip; Schmid et al., 1987). One set of *r* planes are oriented for easy slip and one set of *f* planes are oriented for easy slip. Note 3 orientations for *c* axes; position "1" may indicate basal <a> slip; position "2" comes from alignment of the *r* and *f* planes for easy slip and does not exist in the twinning regime because these grains are favorably oriented for twinning and thus removed in the twinning regime; position "3" corresponds to a favorable orientation for *r* slip. These positions remain stable with respect to the shear-zone boundary because the simple shear produced by glide in the crystal is exactly the imposed deformation. The *c* axis positions do rotate with respect to the foliation and have the "correct" sense of offset with respect to the sense of shear.
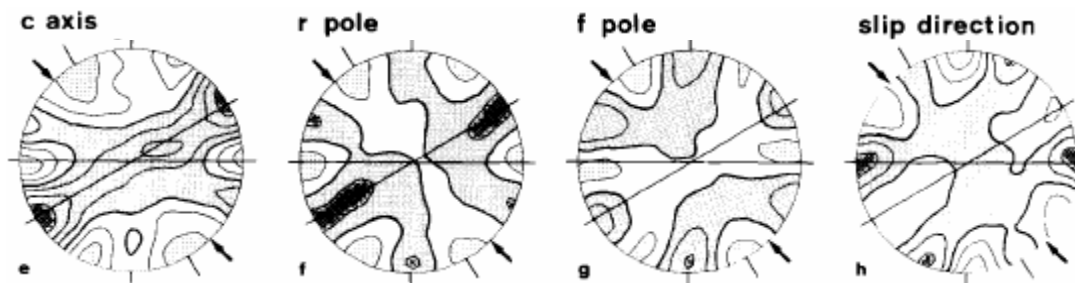
Solnhofen at 700°C (Schmid et al., 1987)
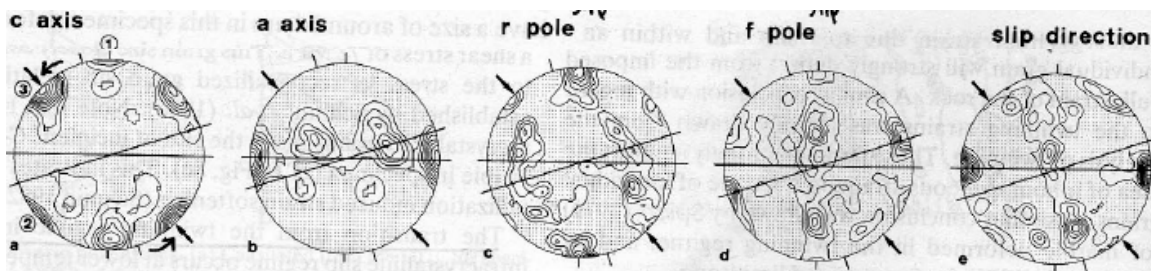
Carrara marble at 700°C. (Schmid et al., 1987)
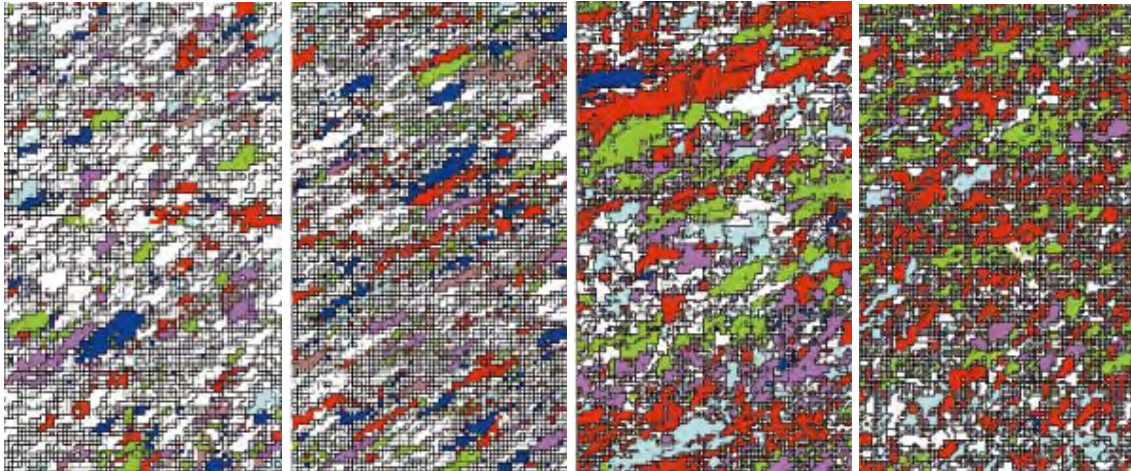
Regime 2 torsion experiments on Carrara marble at 723°C. AVA/OIM figures at γ = 1, 2, 5 and 11. Shape preferred orientation similar to finite strain ellipsoid (Pieri et al., 2001)
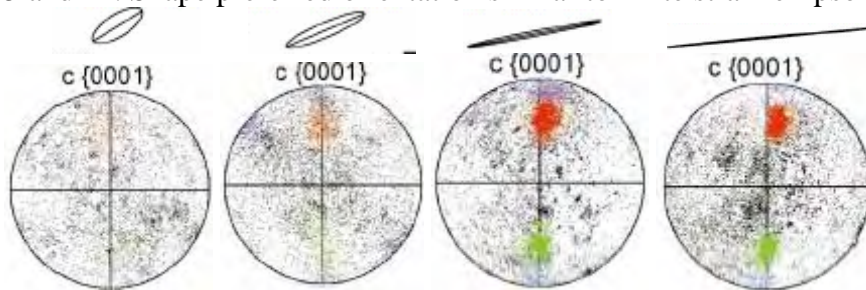
Regime 2 torsion experiments on Carrara marble at 723°C γ = 1, 2, 5 and 11. *c* planes align parallel to shear plane (Pieri et al., 2001)
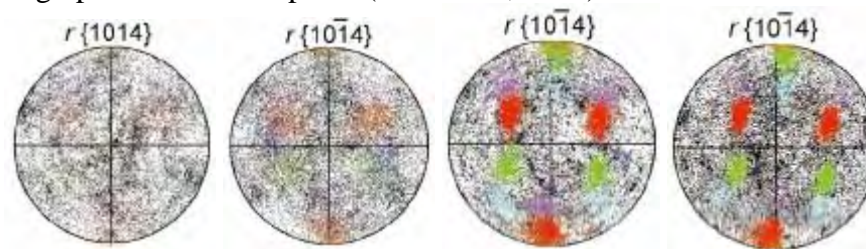
Regime 2 torsion experiments on Carrara marble at 723°C γ = 1, 2, 5 and 11. *r* planes align parallel to shear plane (Pieri et al., 2001)
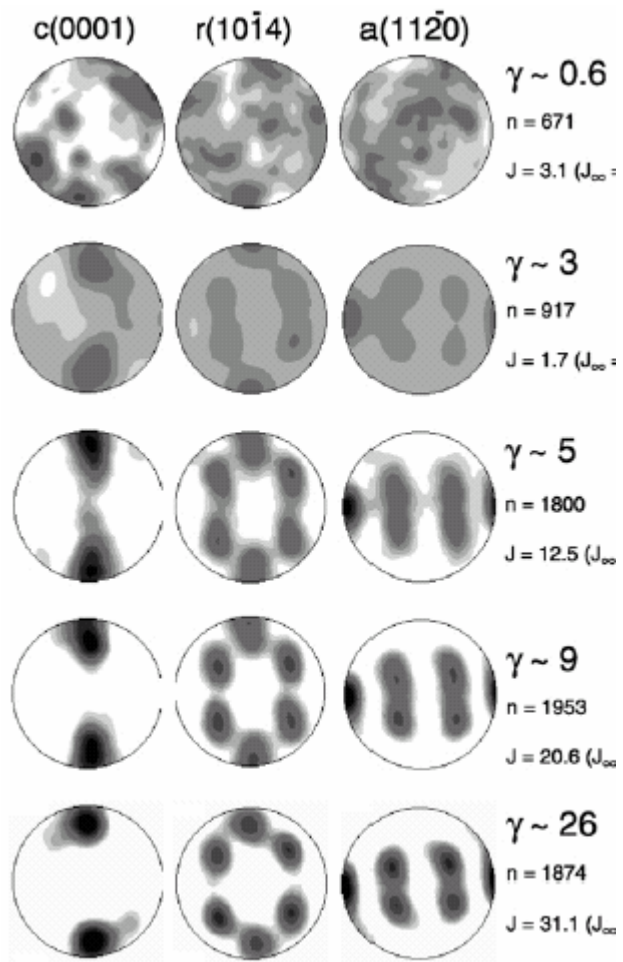
Carrara marble sinistral torsion at 723°C; shear-zone boundary is horizontal; beyond γ = 3, LPO strengthens but does not change (Barnhoorn et al., 2004)
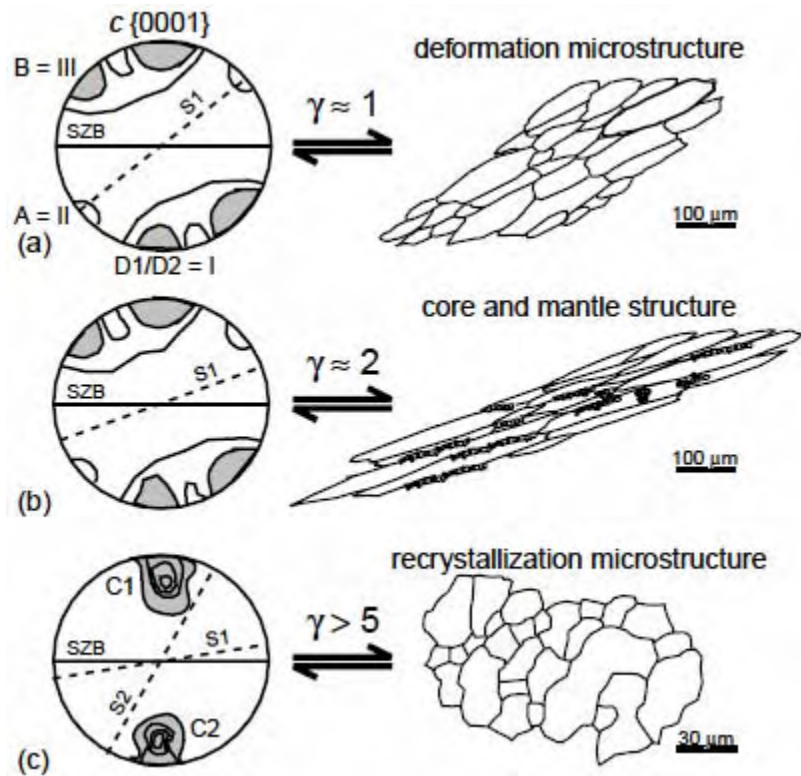
Regime 2 evolution of microstructure and LPO with shear strain. a) dislocation glide and grain flattening with minor bulging recrystallization; b) incipient dynamic recrystallization produces core-and-mantle texture by combination of SGR and GBM; c) complete recrystallization and development of second, oblique foliation accompanied by strain-invariant LPO (Pieri et al., 2001). Minimal fabric obliquity at small strains creates potential for misinterpretation of non-coaxial deformation as coaxial.
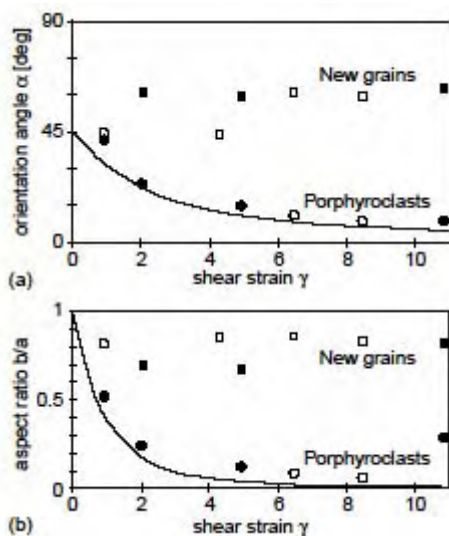
Regime 2 porphyroclast shape and shape preferred orientation track finite strain (Pieri et al., 2001)

Grain-Boundary Migration Regime 3C (Schmid et al., 1980; 1987)

Carrara marble at ≥800°C. GBM-accommodated recrystallization.
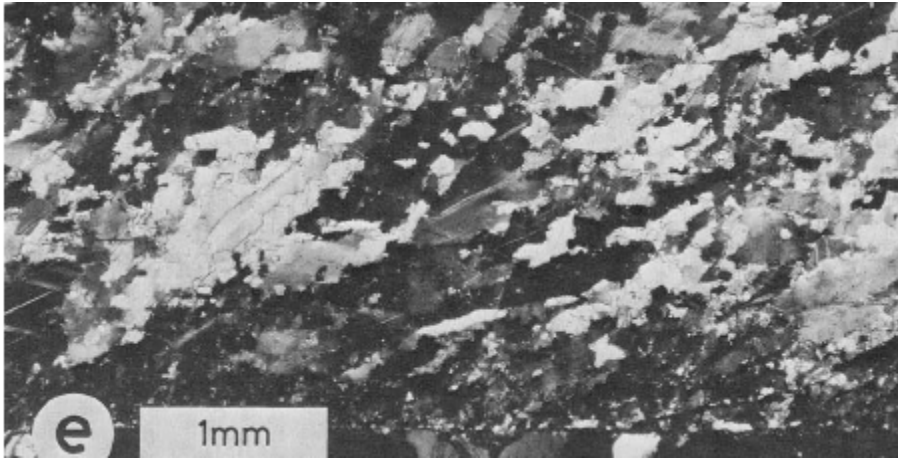
Carrara marble GBM regime 800°C (Schmid et al., 1987)
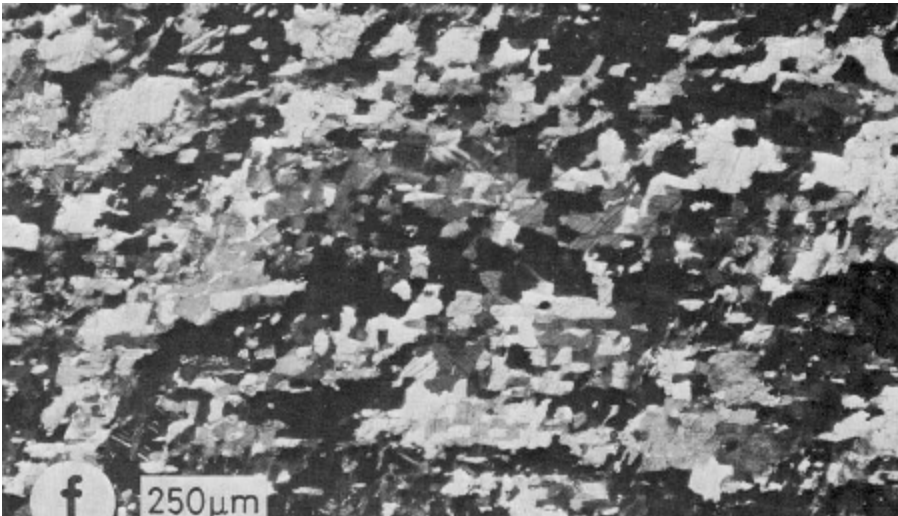
Carrara marble GBM regime 900°C; note strong alignment of grain boundaries (Schmid et al., 1987)
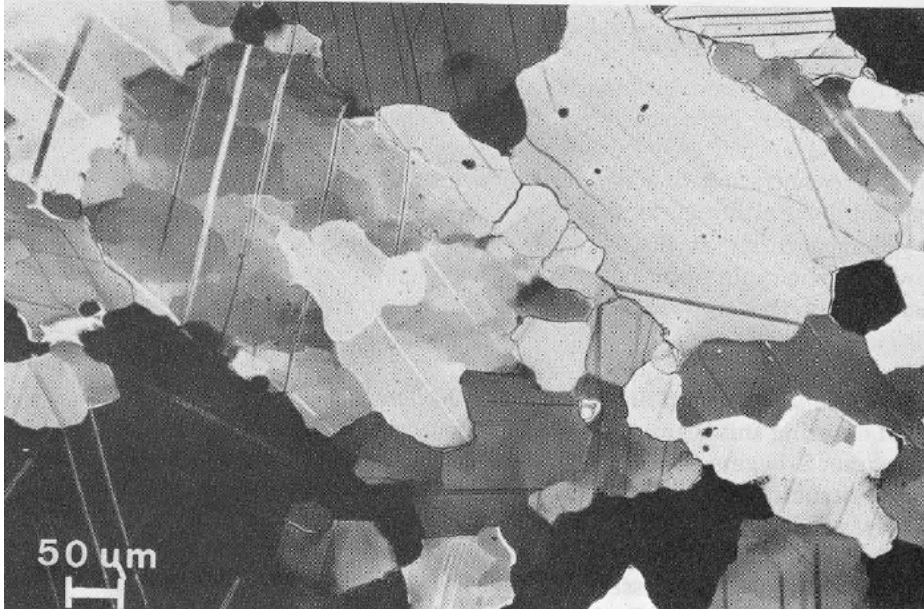
high-angle grain boundaries and low-angle subgrain boundaries (Schmid et al., 1980)
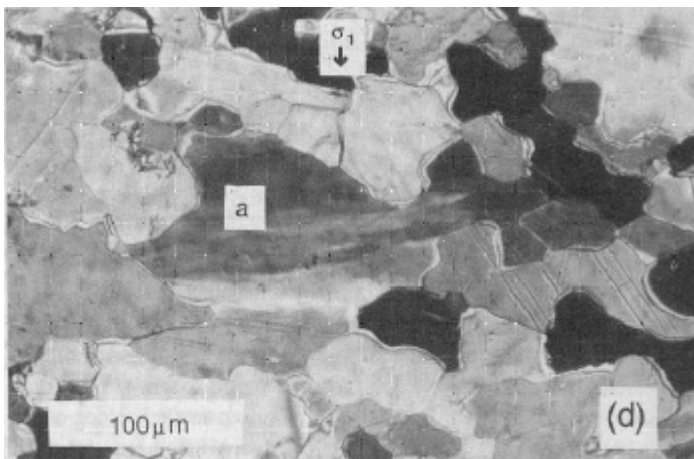
700°C GBM consuming strain grain "a" (Rutter, 1995)
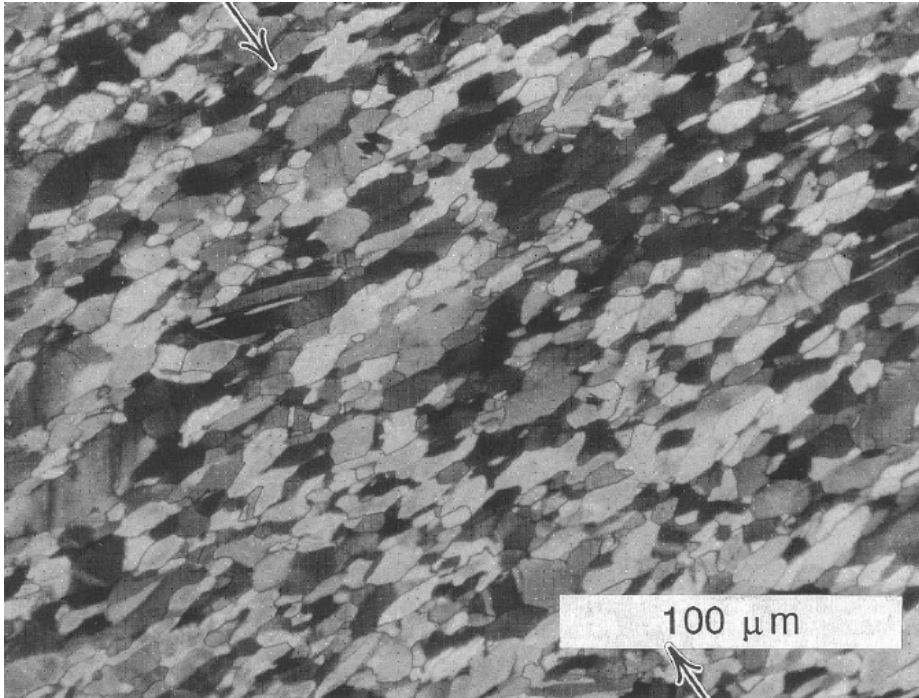
Rutter et al. (1998) Carrara marble experimentally shortened 30% at 500°C and 200 MPa and 10^{-4} s^{-1} has marked SPO and LPO formed by dislocation creep.

7 μm grain size, specimen extended heterogeneously at 700°C, n=3.3 grain-size sensitive flow.

Near neck, 600-1000% strain
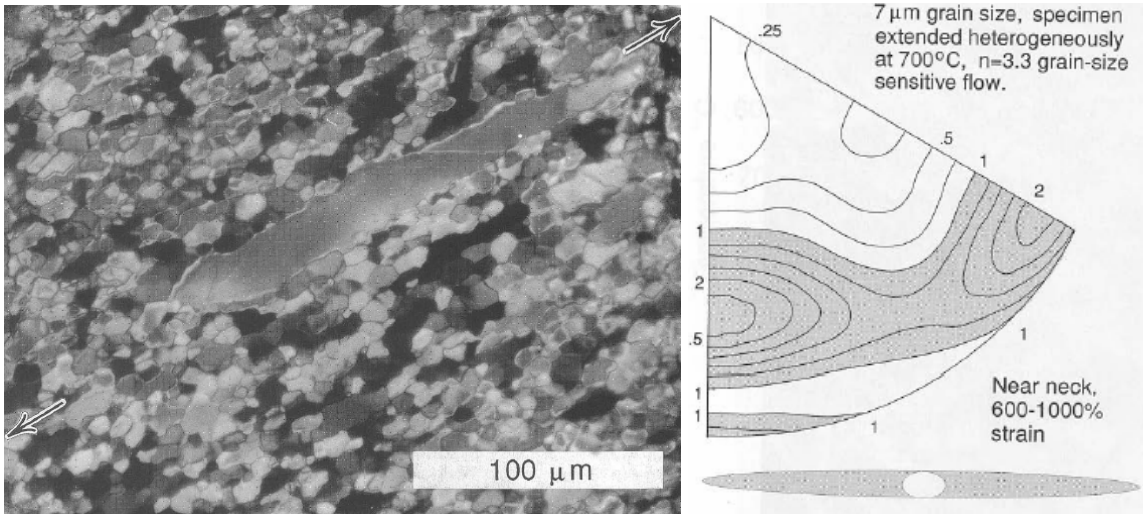
Rutter et al. (1998) Carrara marble experimentally shortened 1000% at 700°C and 250 MPa and 10^{-3} s^{-1} in grain-size sensitive regime. Porphyroclast deformed plastically and shape tracks bulk strain. Finer grains have only weak SPO but a strong LPO.

| c axis | a axis | r pole | f pole | slip direction |
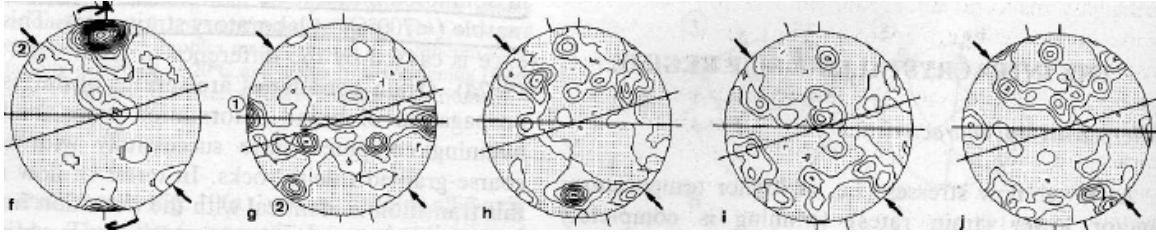
Carrara marble at 800°C shows <a>(0001) slip with minor r and f slip. (Schmid et al., 1987)
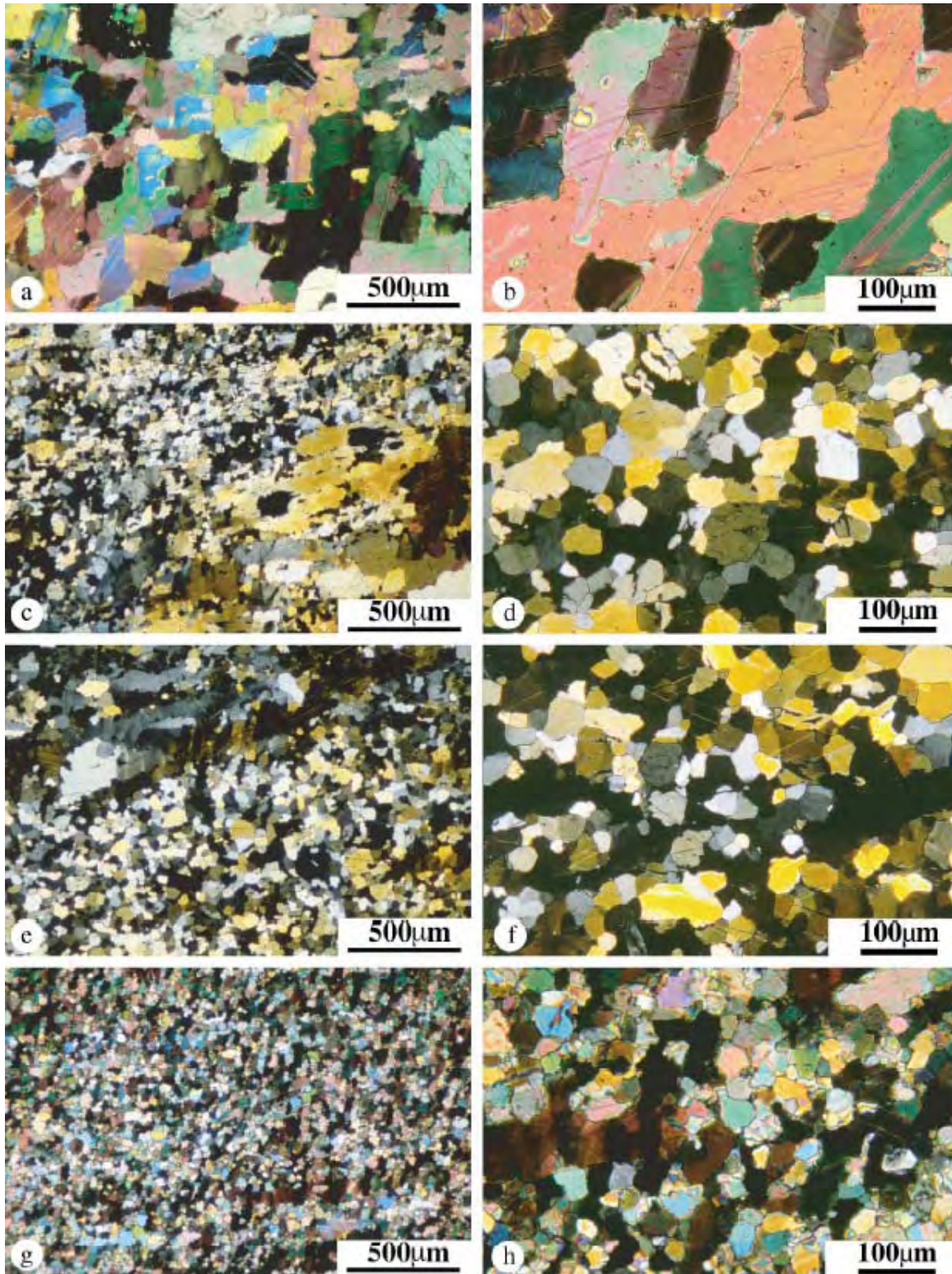
Regime 3 torsion experiments on Carrara marble at 823°C and γ = 1, 2, 5 and 11 (Pieri et al., 2001). Grain boundaries ∥ to shear plane and at 75° to shear plane; deformation bands, undulatory extinction, and subgrains. Weak SPO compared to 723°C.

Grain-Boundary Sliding Regime 3S (Schmid et al., 1977; 1980; 1987)
Solnhofen limestone at 700–900°C; not seen in Carrara marble
Regime 3S microstructures include straight grain boundaries and no shape preferred orientation. GBM leads to equilibrated grain boundaries but *no* grain growth.
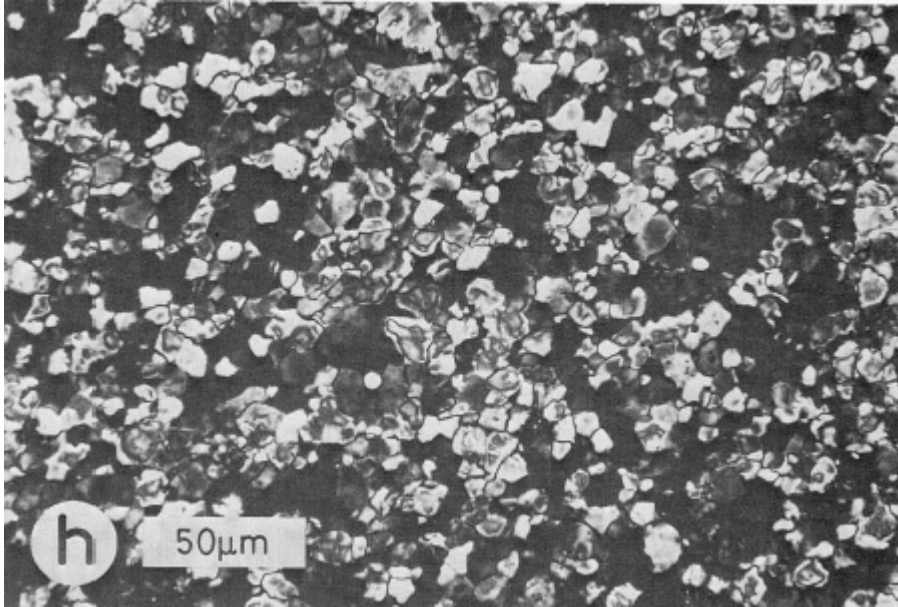
Solnhofen limestone GBS regime 900°C (Schmid et al., 1987)
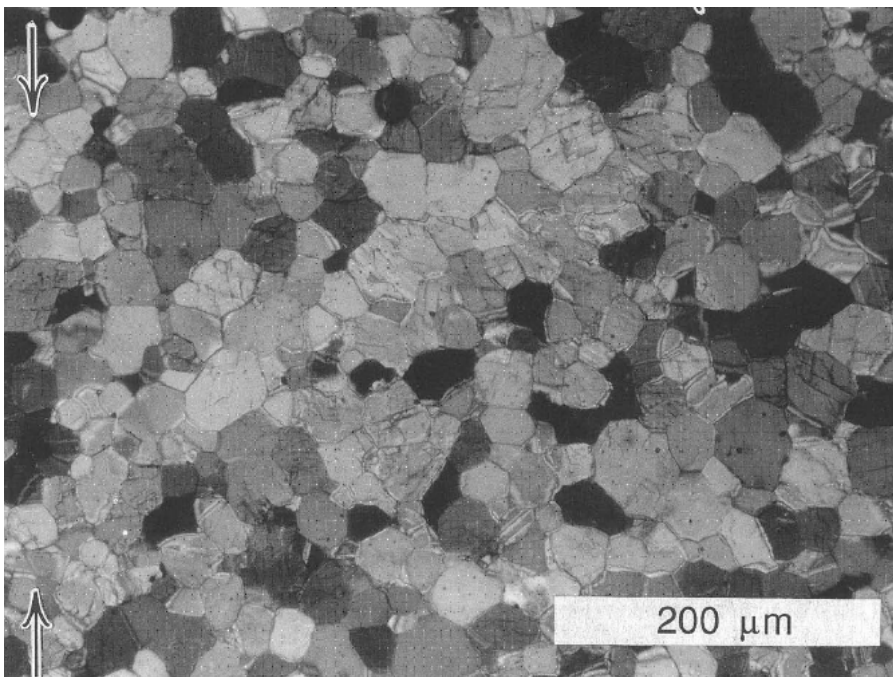
Rutter et al. (1998) Carrara marble experimentally shortened 30% at 700°C and 200 MPa and 10^{-6} s^{-1} has no SPO or LPO and deformed in grain-size sensitive regime.
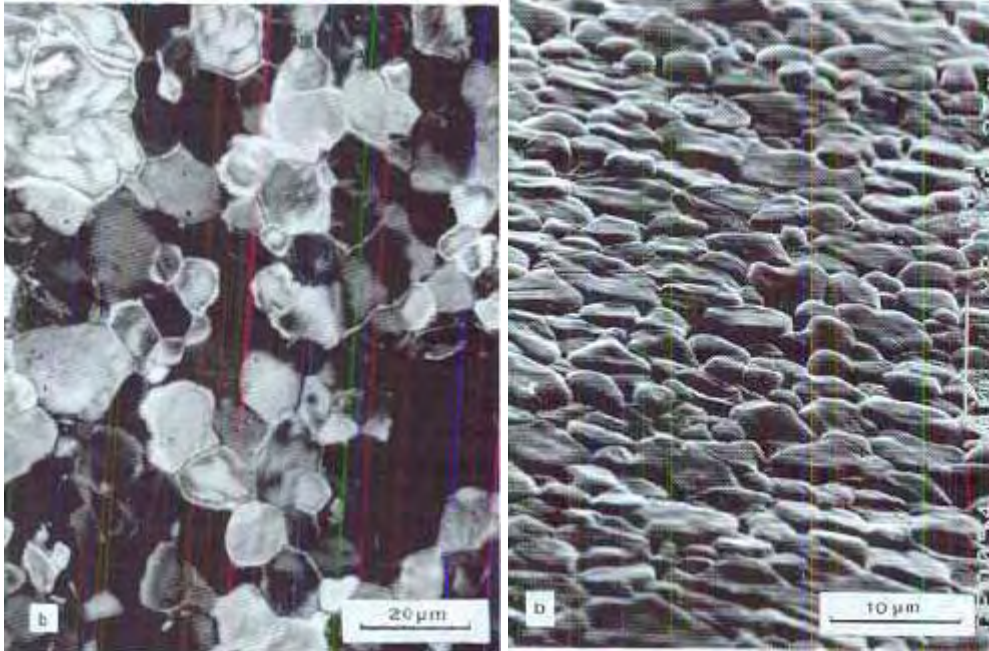
equant grains and displaced grains in split cylinder indicate GBS in synthetic marble (Walker et al., 1990)

displaced grains in split cylinder indicate GBS in Carrara marble (Rutter, 1995)
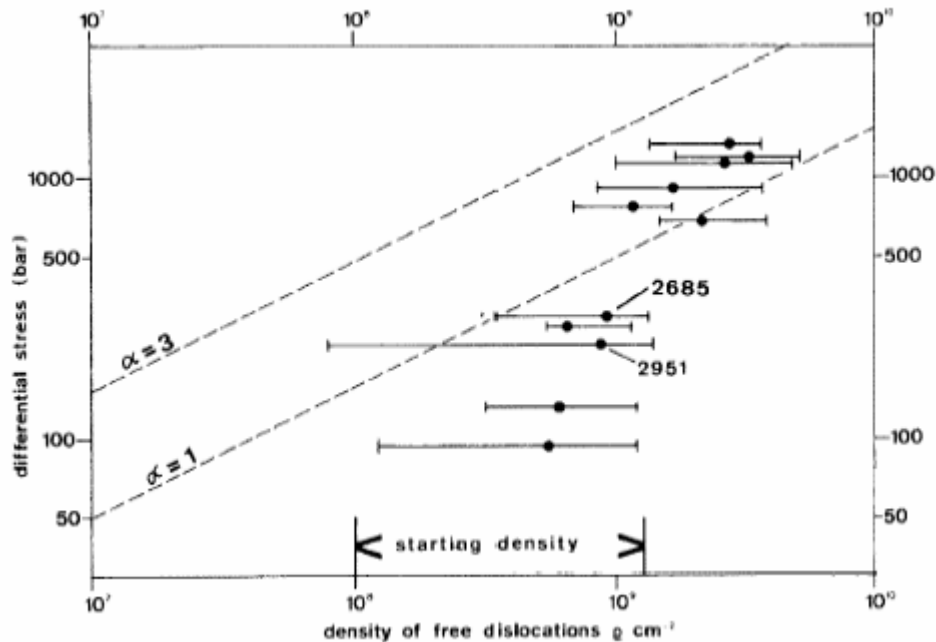
dislocation density does not depend on stress in GBS regime (Schmid et al., 1980)
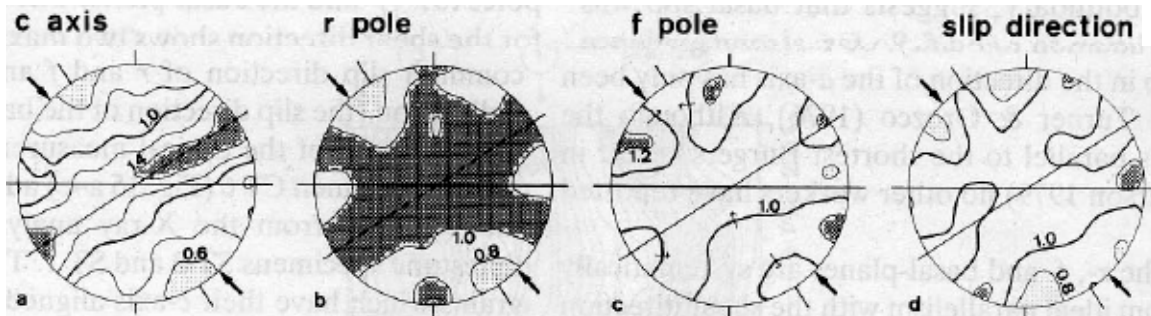
Solnhofen at 700°C (Schmid et al., 1987). LPOs are weak; *c* axis maxima "1" and "3" seen at lower T disappear and maximum "2" becomes a girdle that corresponds to positions for high resolved shear stress on *f* planes. The presence of slip means that diffusion is not needed; therefore glide-accommodated grain-boundary sliding.
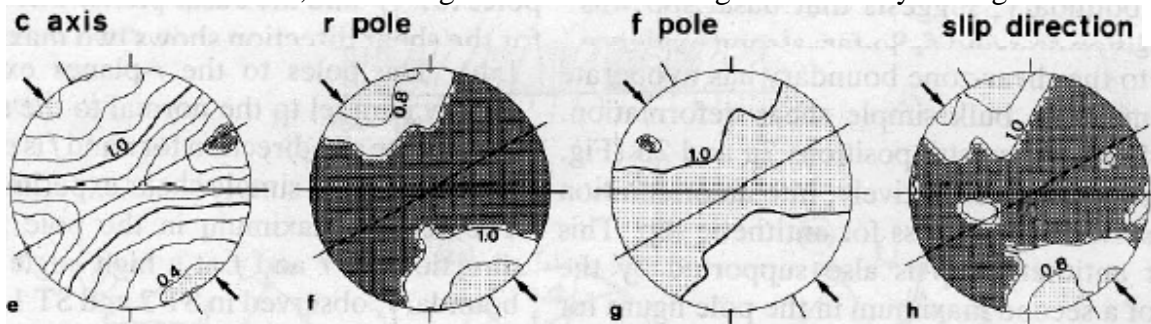
Solnhofen at 800°C (Schmid et al., 1987)
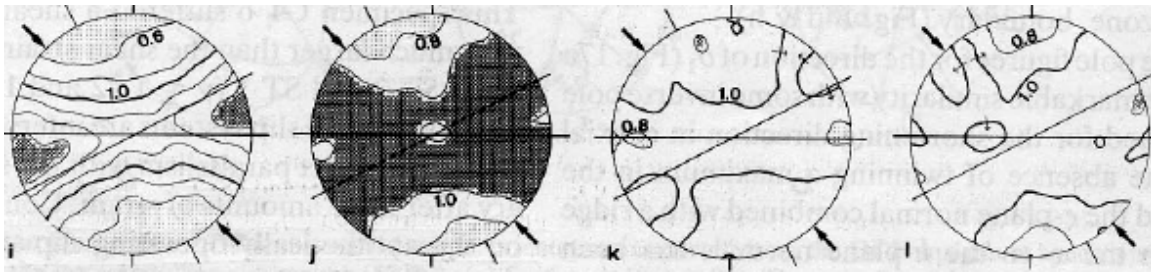
Solnhofen at 900°C (Schmid et al., 1987)

Modeling of Lattice Preferred Orientations
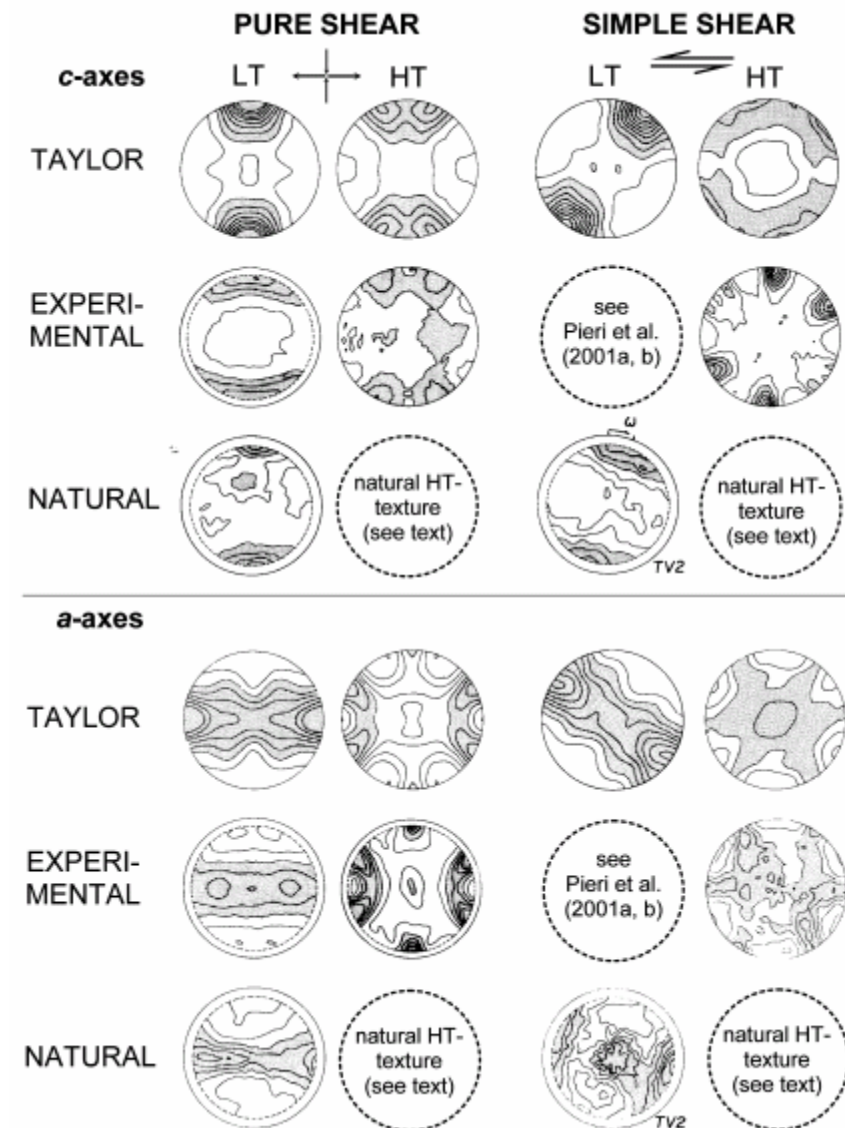
Summary of marble textures. LT = low temperature twinning regime 1; HT= high temperature dislocation creep regime 2 (Wenk et al., 1987; Leiss & Molli, 2003)
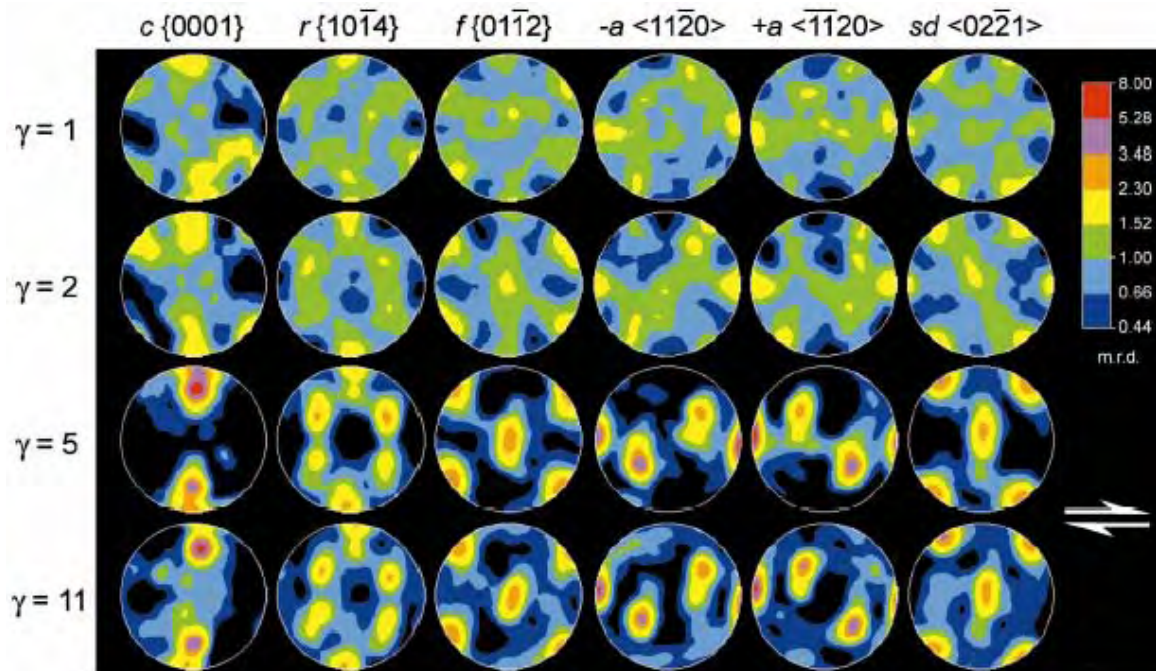
Carrara marble dataset for 723°C (Pieri et al., 2001)
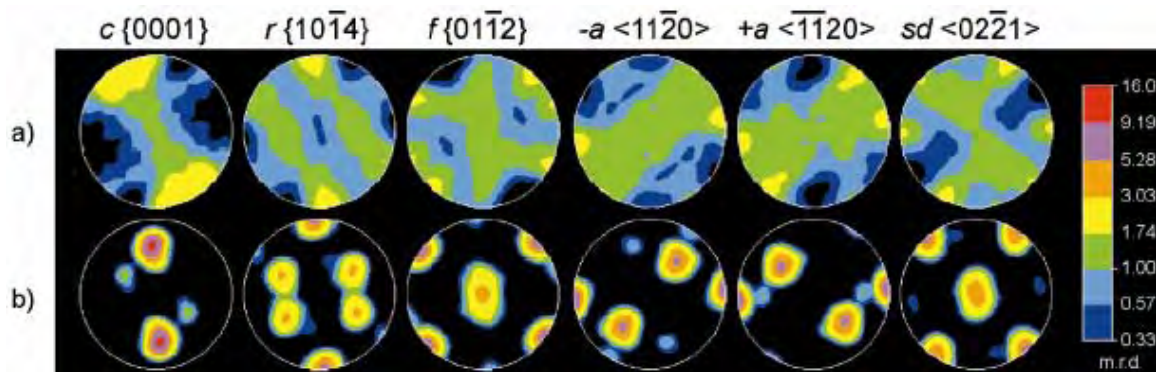
simulated LPOs for comparison with above; calculations assumed dominant <a>{r} slip plus f slip and c slip: a) without recrystallization (fits low-strain experimental samples well) and b) with recrystallization (fits high-strain experimental samples well) . Note alignment of <a> with shear direction and {r} with shortening direction (Pieri et al., 2001)

Summary of Experimentally Produced Calcite LPOs (SZB horizontal)
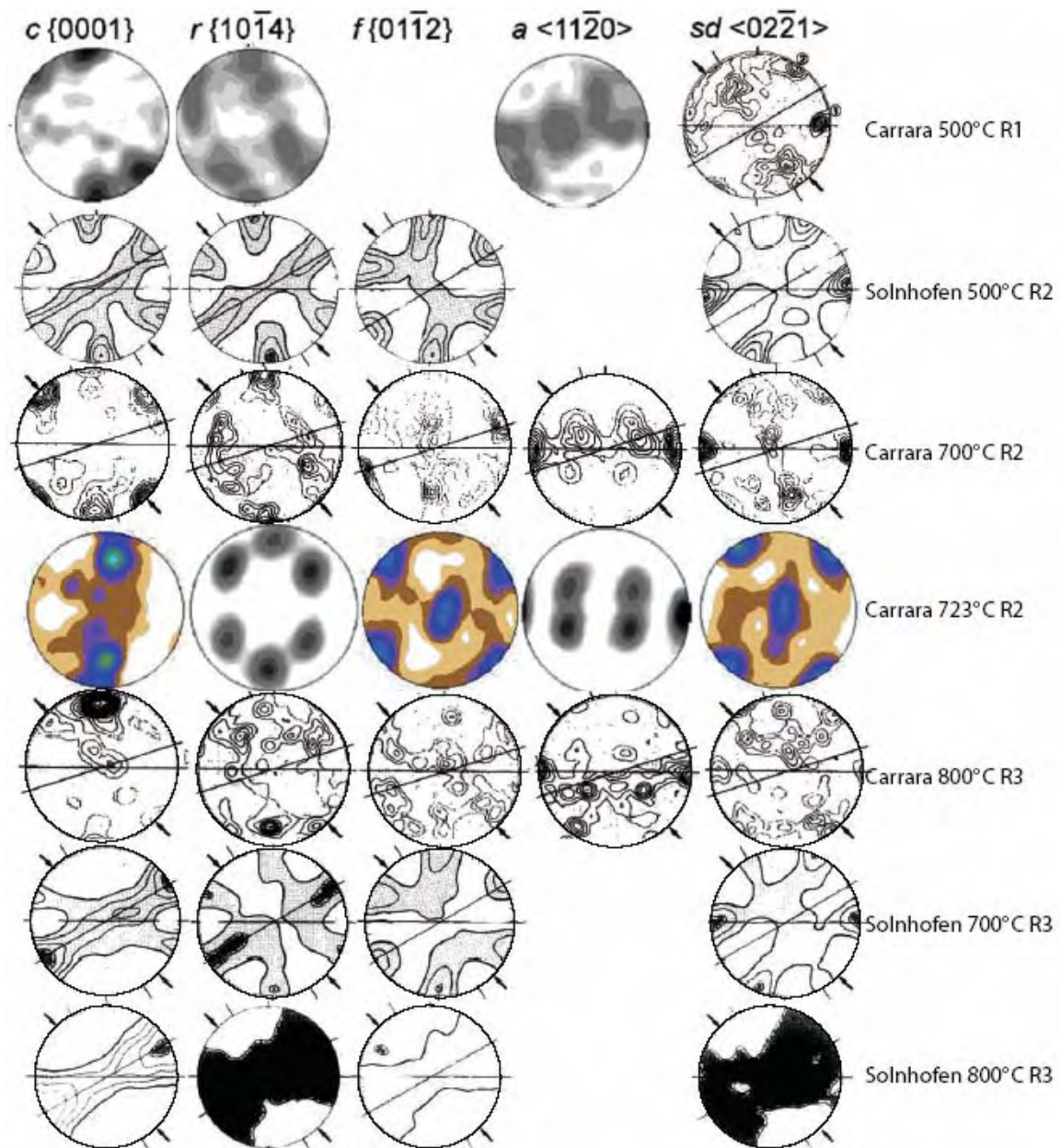
Summary of Experimentally Produced Calcite LPOs (foliation horizontal)

Column headers: c {0001} r {10$\bar{1}$4} f {01$\bar{1}$2} a <11$\bar{2}$0> sd <02$\bar{2}$1>

Row labels:
Carrara 500°C R1
Solnhofen 500°C R2
Carrara 700°C R2
Carrara 723°C R2
Carrara 800°C R3
Solnhofen 700°C R3
Solnhofen 800°C R3
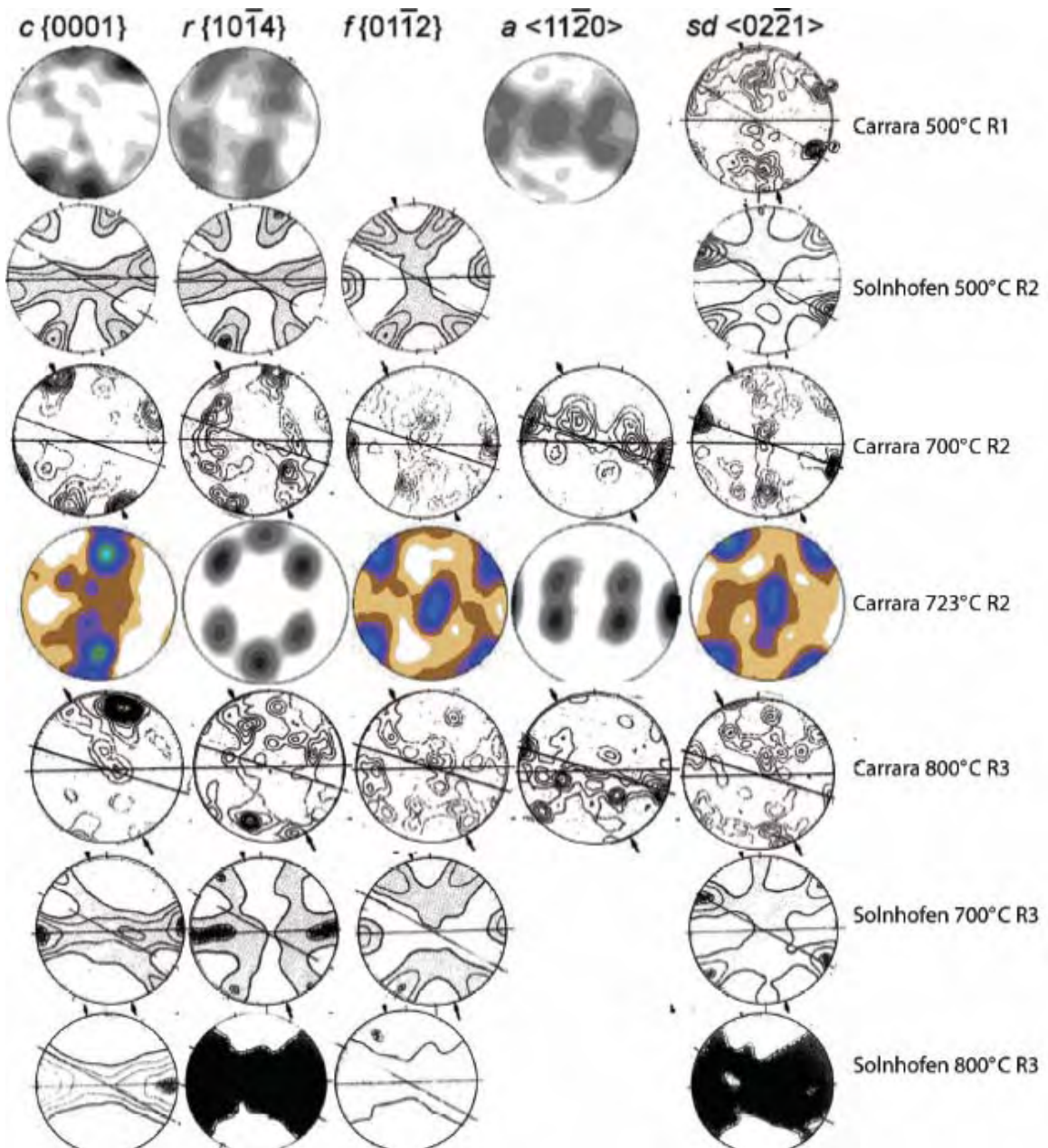
Natural Calcite Lattice Preferred Orientations
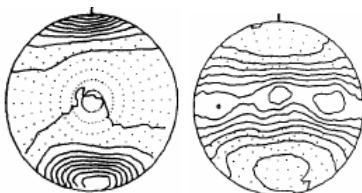
c and *a* axes pure shear in subgreenschist facies (Ratschbacher et al., 1991). Similar to R1 Carrara
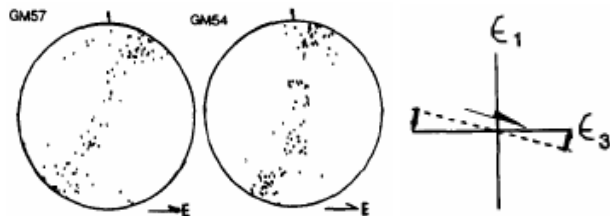
c axes dextral shear in subgreenschist facies (Ratschbacher et al., 1991). Similar to R2 Carrara
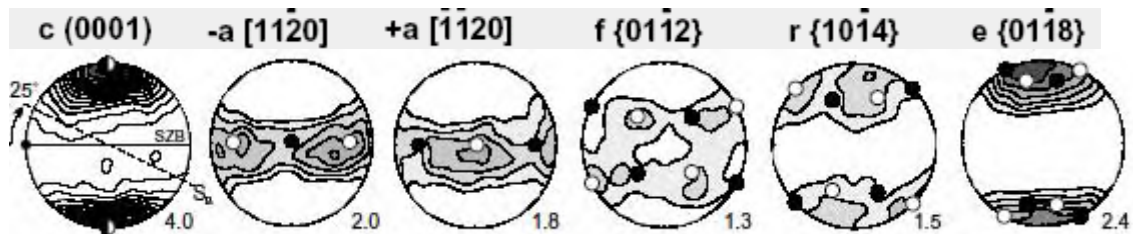
sinistral 300–350°C marble mylonite (Bestmann et al., 2000). Similar to R3 Carrara marble 800°C
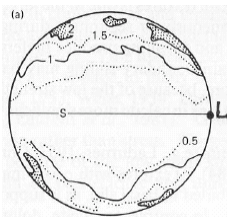
c axes, Morcles nappe (Wenk, 1985). Weak LPO suggests GBS—Solnhofen R3
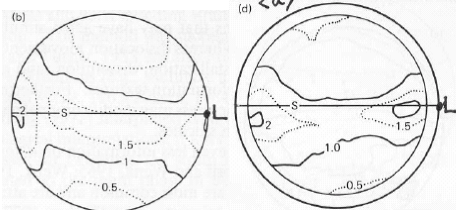
a axes, Lochstein mylonite and Palm Canyon (Wenk, 1985). Weak LPO suggests GBS—Solnhofen R3
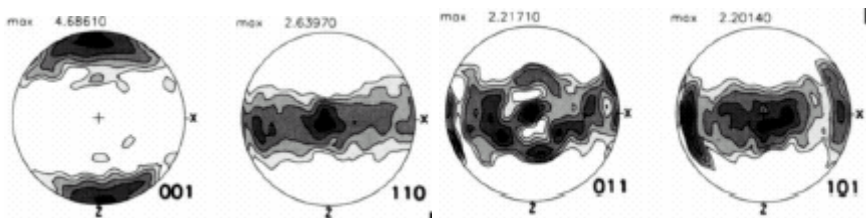
low-temperature fabric Tauern Window similar to Carrara R1 coaxial (Kurz et al., 2000); [001] = c; [110] = a; [100] poles to prisms; [101] and [011] poles to rhombs.
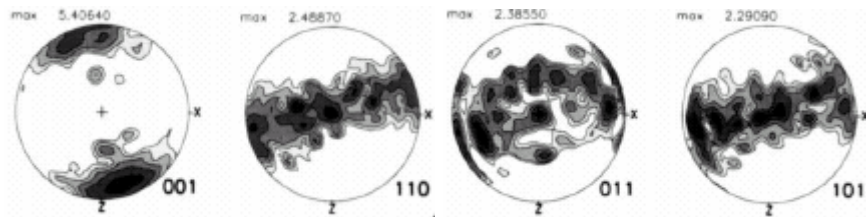
low-temperature asymmetric fabric Tauern Window similar to Carrara R1 dextral (Kurz et al., 2000)
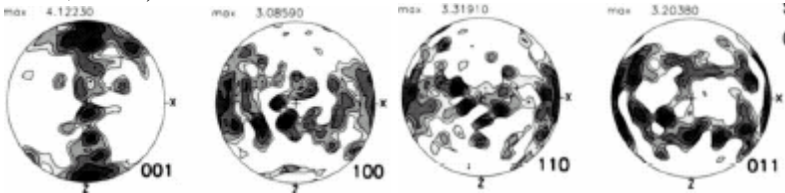
medium-temperature fabric Tauern Window similar to Carrara R2 (Kurz et al., 2000)
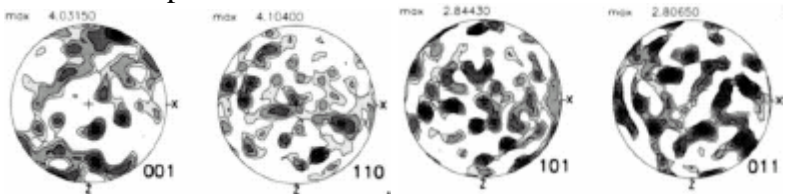
high-temperature fabric Tauern Window similar to Solnhofen R3 (Kurz et al., 2000)

Recent Advances in Flow Laws for Marble
1. Renner et al. (2002) Peierls relation
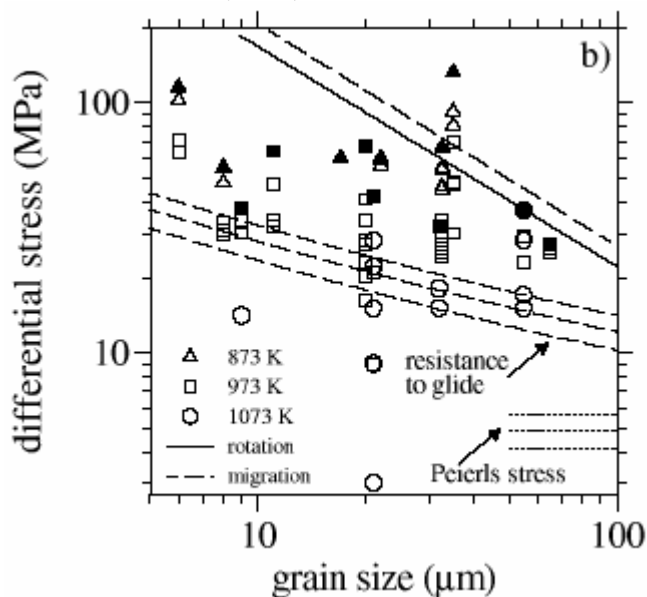
correlation between grain size and strength implies that standard dislocation creep models are inappropriate (Renner et al., 2002)
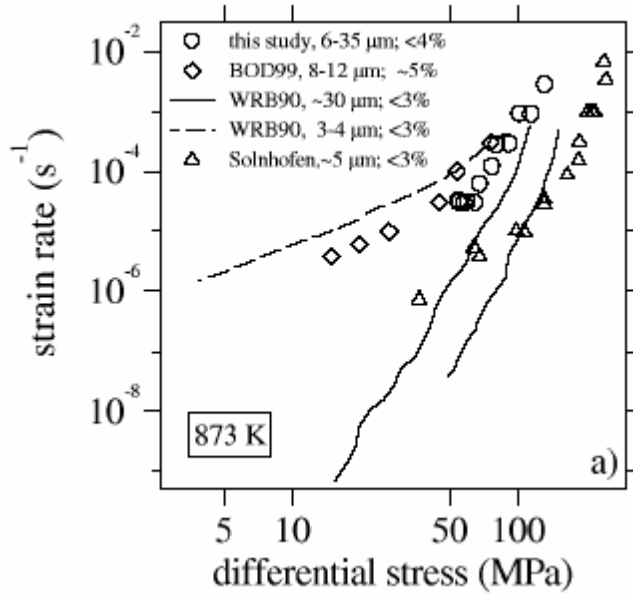
studies on marbles also show widely divergent strengths, again implying current models are inadequate (Renner et al., 2002).
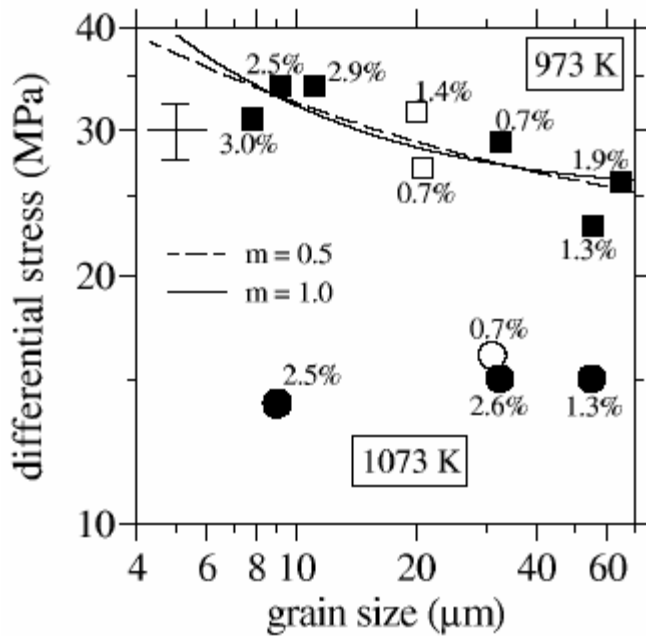
Unlike conventional dislocation creep assumptions, the stress supported by calcite depends on grain size, implying a Hall–Petch relationship (solid and dashed lines)

$$\sigma = \sigma_o + kd^{-m}$$

where m is between 0.5 and 1.0. Renner et al. (2002) tried to fit all mechanical data for marble using a Peierls relation:

$$\dot{\varepsilon} = A_P \sigma^2 \exp\left(\frac{\sigma}{\sigma_P}\right)\exp\left(-\frac{Q_P}{RT}\right)$$

where σ_P, the resistance to glide, is composed of an intrinsic Peierls stress and a backstress generated by, e.g., pileups in front of grain boundaries, that *depends on grain size*:

$$\sigma_P = (\Sigma_{P,0} + Kd^{-m})(T_m - T)$$

They were able to fit all calcite data using the following parameters:

$$\ln A_P = 10^{\pm 0.5} \ \mathrm{MPa}^{-2} \ \mathrm{s}^{-1}$$
$$\Sigma_{P,0} = 6.4 \ \mathrm{MPa \ k/K}$$
$$K = 115 \ \mathrm{MPa \ k/K \ \mu m}^{0.5}$$
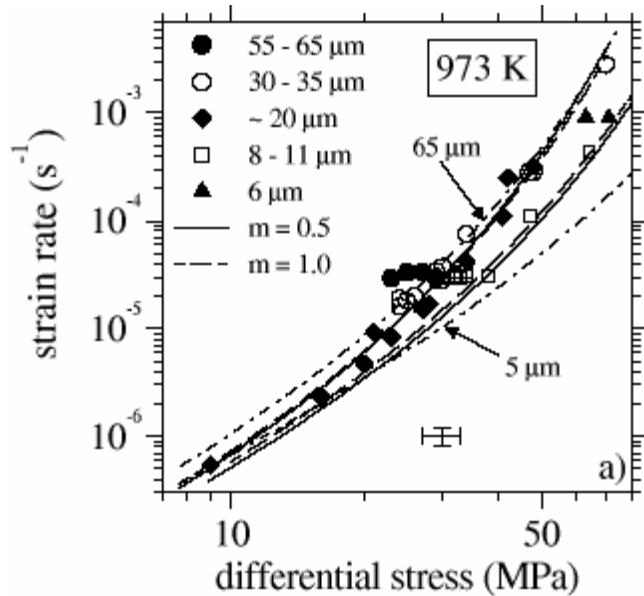
Their fit looks good for marble with a range of grain sizes (Renner et al., 2002)
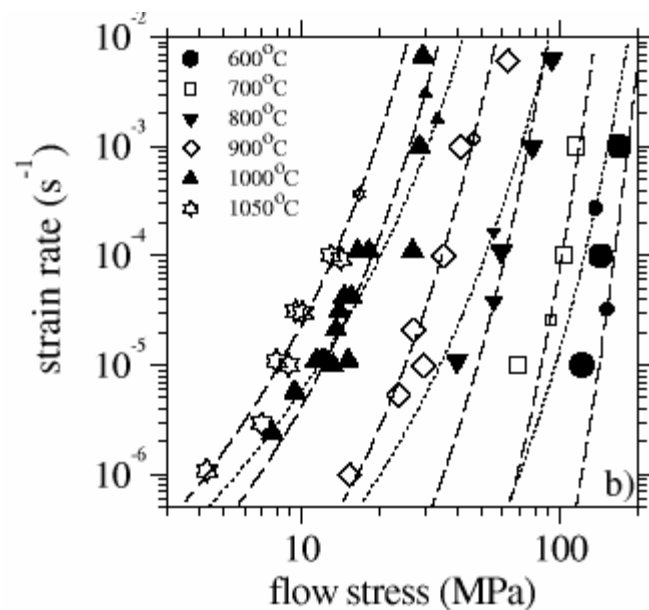
…and a range of temperatures (Renner et al., 2002)
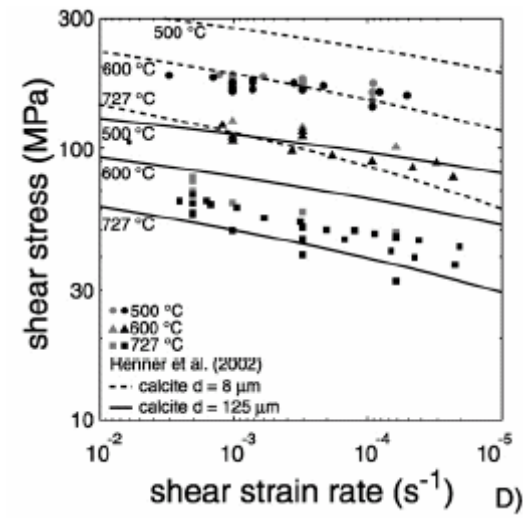
the torsion data of Barnhoorn et al. (2004) show a good fit to the Renner et al. (2002) model. The grain sizes shown correspond to Carrara marble initial grain size and recrystallized grain size (Barnhoorn et al., 2004)

2. De Bresser (2002) Creep Controlled by Cross-Slip of Screw Dislocations
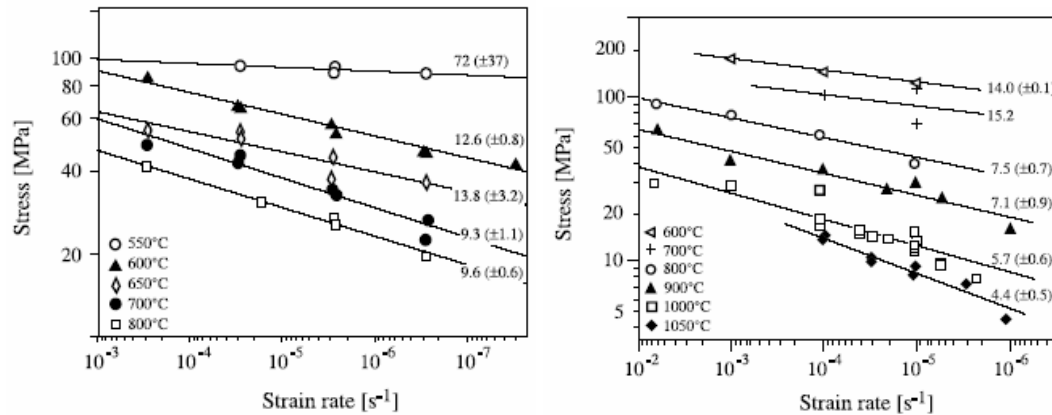
stress exponent for calcite single crystals (left) and marble (right). Calcite has large stress exponents in conflict with conventional models for dislocation creep, in which n = 3–4.5 (De Bresser, 2002).
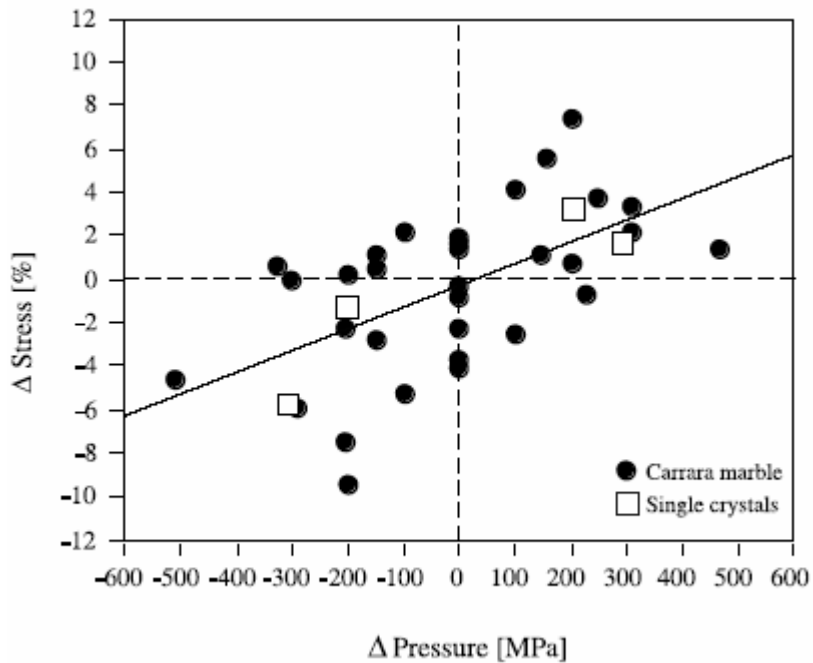
The pressure dependence of flow stress suggests that cross slip of dislocations, rather than dislocation climb, is the rate-controlling mechanism for calcite creep.
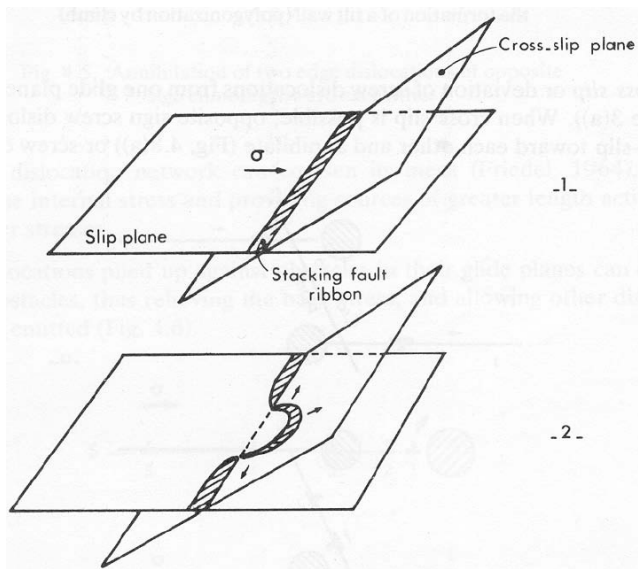
(Nicolas & Poirier, 1976).

In cross slip, screw dislocations glide onto planes other than the slip plane.
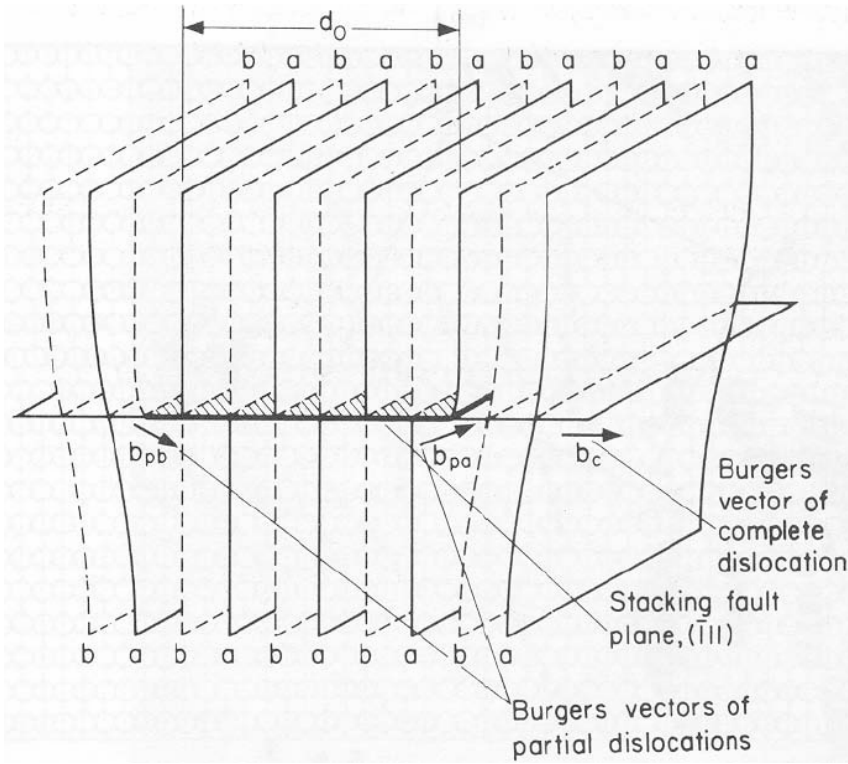
(Hull & Bacon, 1984).

Unlike climb, cross slip depends on stress and pressure because dislocations that have dissociated into partial dislocations separated by stacking faults must recombine to allow cross slip. Using a general flow law for cross-slip controlled creep (De Bresser, 2002):

$$\dot{\varepsilon} = K' \left(\frac{\sigma}{\mu} \right)^2 \exp\left[-\frac{\Delta U_{cs}(\sigma, P)}{kT} \right]$$

the ΔU term represents either an activation energy required to recombine the stacking fault:

$$\Delta U_{cs}(\sigma, P) = \Delta U_{cs} \left[\ln \frac{\sigma_{T=0}}{\mu_{T=0}} - \frac{\sigma_T}{\mu_T} \right]$$

or an activation barrier at zero applied stress, representing the concept that dissociation can occur in the absence of any applied stress:

$$\Delta U_{cs}(\sigma, P) = \Delta U_{cs} \left[1 - \frac{\alpha b \sigma}{\gamma} \right]$$
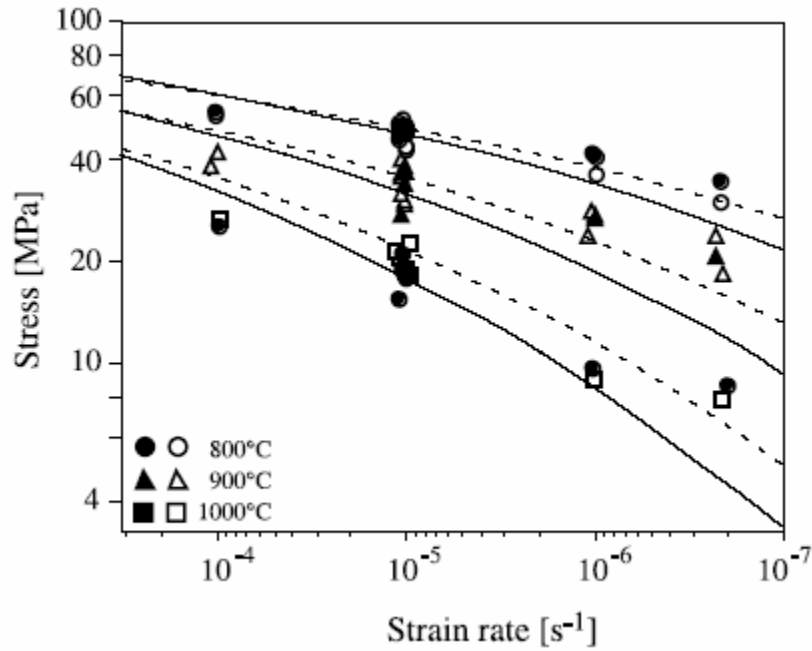
A fit to the marble dataset yields (De Bresser, 2002)

$$K' = 10^{6.32 \pm 0.04}$$
$$\gamma = 0.23 \text{ J/m}^2$$
$$\alpha = 2.2$$
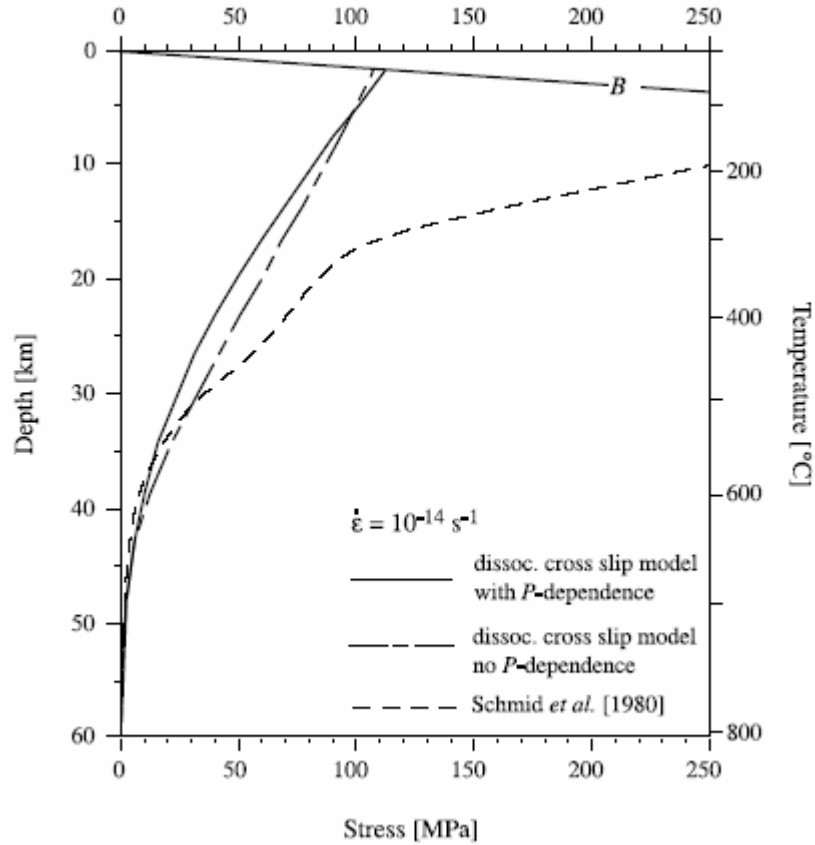
extrapolation to Earth (De Bresser, 2002)

Piezometry
Theory for Dislocation Density Dependence on Stress
The relationship between dislocation density and stress is based on the argument that if recovery is active, the dislocation density increases until the "back stresses" due to dislocation interactions matches the applied stress (Christie & Ord, 1980)

$$\rho = Bb^{-2}\left(\frac{\sigma}{\mu}\right)^2$$

where μ is the shear modulus, 65 GPa, and b the Burgers vector 0.5 nm.
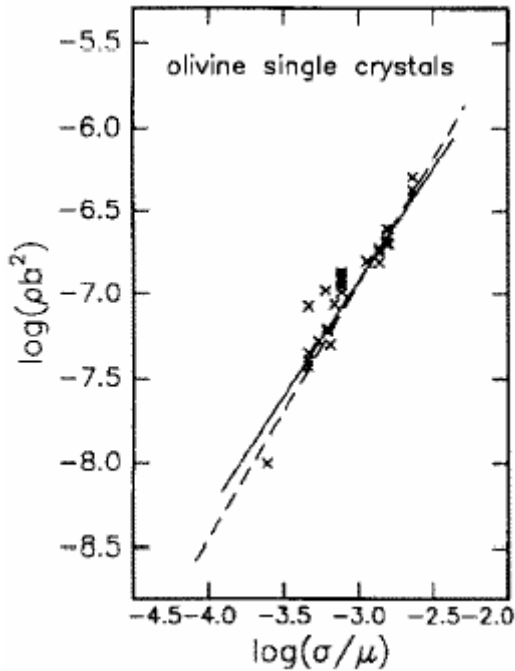
Olivine single crystals show B = 1.74E–3, and s = 1.37, regardless of T, f_{O2} or a_{opx} (Bai & Kohlstedt, 1992)

Theory for Grain Size Dependence on Stress
Recrystallized grain size has been observed to follow an empirical law:

$$\frac{d}{b} = K\left(\frac{\sigma}{\mu}\right)^{-p}$$

where d is grain size, b the Burgers vector, μ the shear modulus, and p (~1) and K are constants.

Small grains grow to reduce surface energy, but coarse grains recrystallize; together these processes produce a constant grain size.

Twiss (1977) assumed that there is a unique subgrain size where there is a balance between the energy of dislocations in grain boundaries and the dislocations in grain interiors. This model is flawed because of its lack of T dependence and lack of a

1

phenomenological basis (Poirier, 1985), however, and models only the smallest possible grains.

$$\left(\frac{d}{b}\right) = K\left(\frac{\sigma}{\mu}\right)^{-p} \exp\left(\frac{Q}{aRT}\right)$$

A more general piezometer equation has a T dependence (Ter Heege et al., 2005).
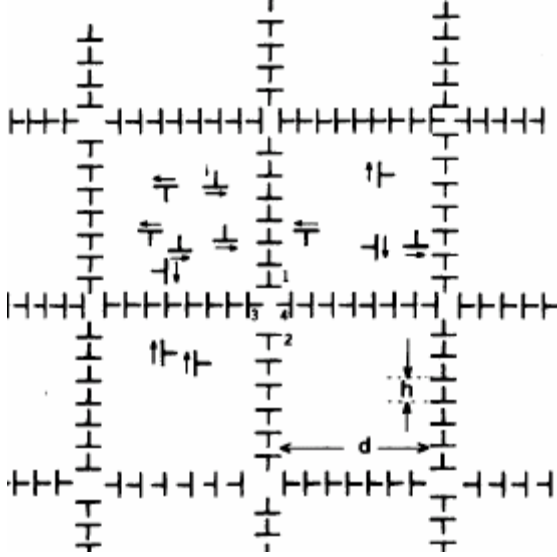
Edward et al. (1982) modeled a dynamic balance between the flux of dislocations gliding and climbing into subgrain walls and the climb-controlled annihilation of dislocations within the subboundaries. The relationship between subgrain size and flow stress is determined by the dislocation generation rate and mean slip distance (grain size) and the climb velocity in the subgrain wall:

$$d = K\sigma^{-n/4} \exp\left(\frac{Q_r - Q_d}{4RT}\right)$$

where Q_r is the activation energy of dislocation creep and Q_d is the activation energy for the diffusion process controlling climb in the subboundary. (Edward et al., 1982)

Derby & Ashby (1987) considered GBM with nucleation at grain boundary bulges. They considered that the grain size is such that within its volume there is one bulge nucleation event in the same time that a grain-boundary migrates through the volume. This is a balance between the rate of bulge nucleation and the mean grain boundary migration rate (Derby, 1990):

$$d = K\sigma^{-n/2} \exp\left(\frac{Q_v - Q_{gb}}{2RT}\right)$$

where Q_v and Q_{gb} are the activation energies lattice and grain boundary diffusion. Steady-state grain size is achieved by competition between neoblast formation by grain boundary bulging and grain growth.

Shimizu (1998) assumed instead that neoblasts form via SGR. A steady-state grain size develops due to a balance between the rate of nucleation and the radial growth rate of the neoblasts (similar to Derby & Ashby, 1987, but SGR rather than grain boundary bulging). The following is Shimizu's logic in detail. Assume that subgrains larger than some critical misorientation θ_c become nuclei and start to grow. Assuming a simple tilt boundary, the dislocation spacing around the nucleus is

$$b/\theta_c.$$

The flux of dislocation climb is

$$\rho u$$

where ρ is the dislocation density and u is their velocity. The time required for a subgrain to rotate sufficiently away from its host to become a nucleus is then

$$t = \theta_c/b\rho u$$

The climb velocity is

$$u = \frac{D_v \sigma b^3}{lkT} \; ; \; l = \frac{b}{2\pi}\ln\left(\frac{r}{b}\right)$$

where r is the dislocation spacing and D_v is the self diffusion coefficient:

$$D_v = C_v b^2 \upsilon \exp\left(-\frac{Q_v}{kT}\right)$$

where C_v is the vacancy concentration, υ the atomic vibration frequency and Q_v the activation energy for self diffusion. The nucleation rate $\dot{N}$ is written

$$\dot{N} = N / t$$

where N is the number of potential nucleation sites per unit volume for grain-boundary nucleation

$$N = \frac{6}{\pi d_{grain} d_{subgrain}^2}$$

The grain boundary mobility M is

$$M = \frac{bwD_{gb}}{kT}$$

where w is grain-boundary width and D_{gb} is grain-boundary diffusivity:

$$D_{gb} = C_{gb} b^2 \upsilon \exp\left(-\frac{Q_{gb}}{kT}\right)$$

where C_{gb} is the vacancy concentration in the grain boundary, and Q_{gb} the activation energy for self diffusion. The driving force for grain-boundary migration F is approximated as

$$F \approx \frac{3\gamma}{d_{subgrain}}$$

where γ is the sub-boundary energy, approximated as

$$\gamma = \left(\frac{\mu b^2}{2}\right)\left(\frac{\theta_m}{b}\right)$$

3

where the first term is the dislocation tension and the second is the density of dislocations in the sub boundary (θ_m is the sub-boundary misorientation). If the above equations are substituted into the equation for grain size

$$d = a\left(\frac{\dot{R}}{\dot{N}}\right)^{\frac{1}{4}}$$

(where $\dot{R}$ is the subgrain radial growth rate and a is a geometric term close to 1), the following relationship is obtained:

$$\left(\frac{d}{b}\right) = A\left(\frac{\sigma}{\mu}\right)^{-p}\left(\frac{D_{gb}}{D_v}\right)^{\frac{1}{m}} \quad \text{or} \quad \left(\frac{d}{b}\right) = A'\left(\frac{\sigma}{\mu}\right)^{-p}\exp\left(\frac{Q_{gb} - Q_v}{mkT}\right)$$

where

$$A = a\left(\frac{\pi K \alpha^2}{4}\frac{\theta_m \theta_c wl}{b^2}\right)^{\frac{1}{3}}, \; p = 4/3, \text{ and } m = 3$$

Note that p = 1.3 and that there is a T dependence
It is important that the post-Twiss models have a T dependence (de Bresser et al., 2001)
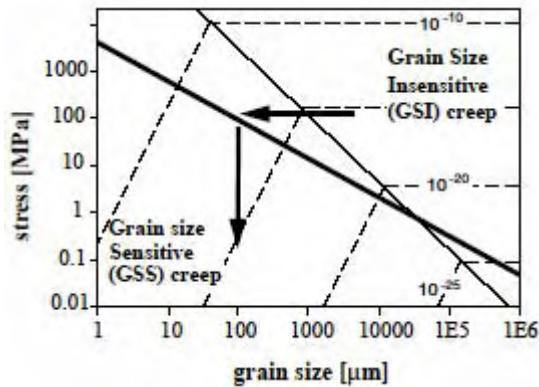
De Bresser et al. (1998) adopted a different strategy. They assumed that recrystallized grain size is that which falls along the diffusion creep and dislocation creep fields (field boundary hypothesis), with the grain size dictated by diffusion creep grain-size dependence.

Experimental Dataset
Use mean linear intercept method (Underwood, 1960) to determine grain size. The mean true grain size, D, is derived by assuming all grains are cubes, and this gives D = 3/2L (Smith & Guttman, 1953).
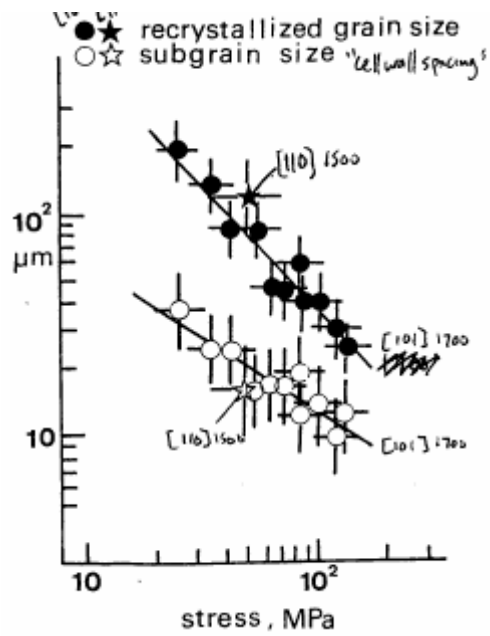
olivine single crystals (Karato et al., 1980).
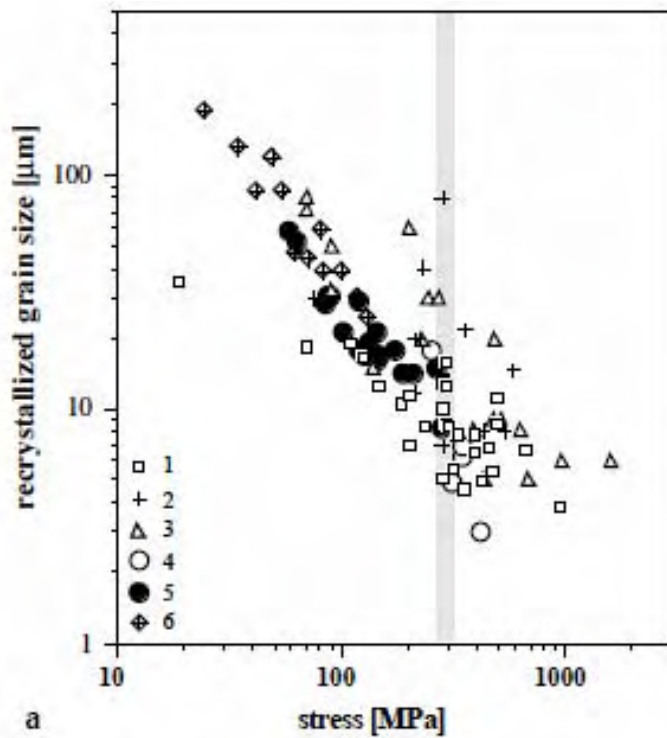
olivine dataset (de Bresser et al., 2001)

5
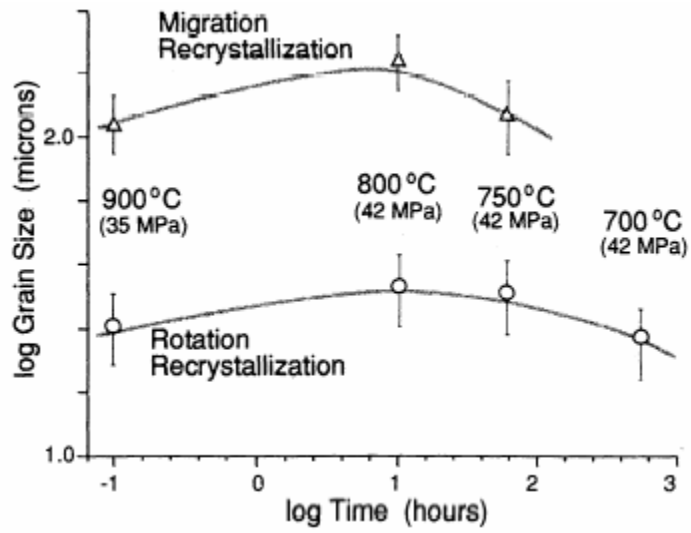
indication that grain size does not depend on strain rate or strain in marble (Rutter, 1995)
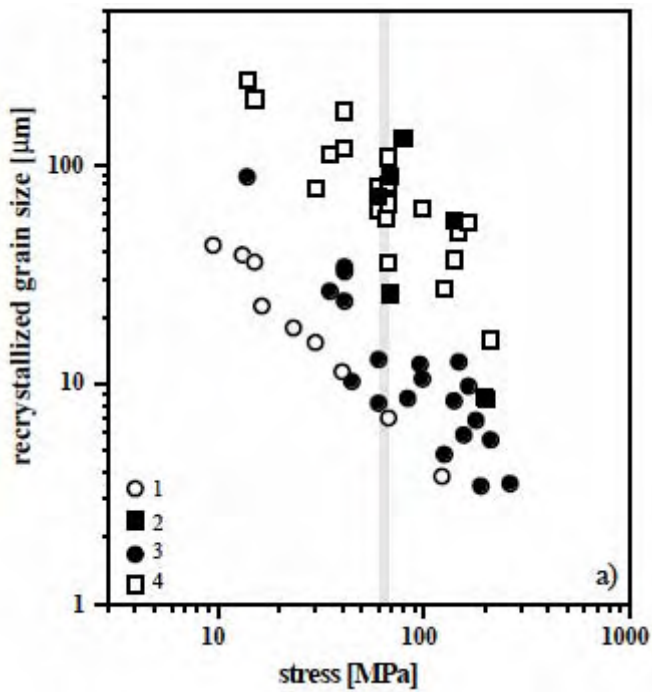
calcite dataset (de Bresser et al., 2001)

6
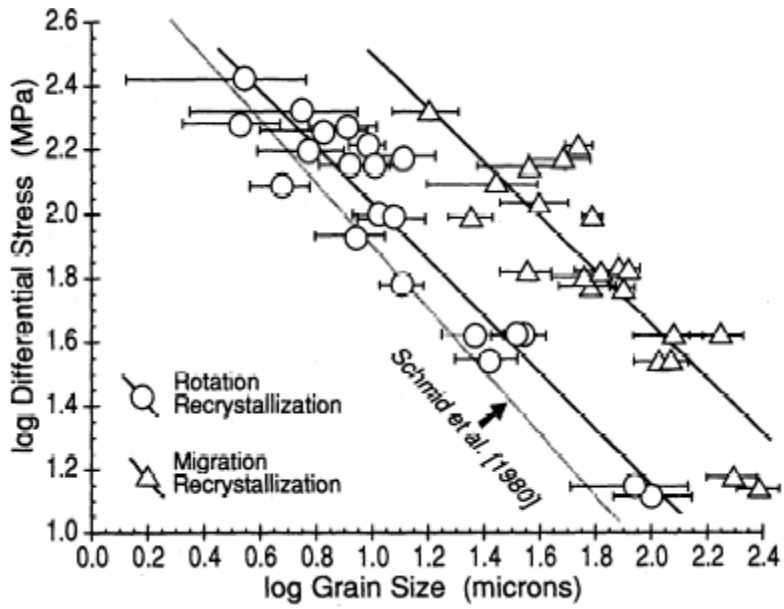
Carrara marble (Rutter, 1995)
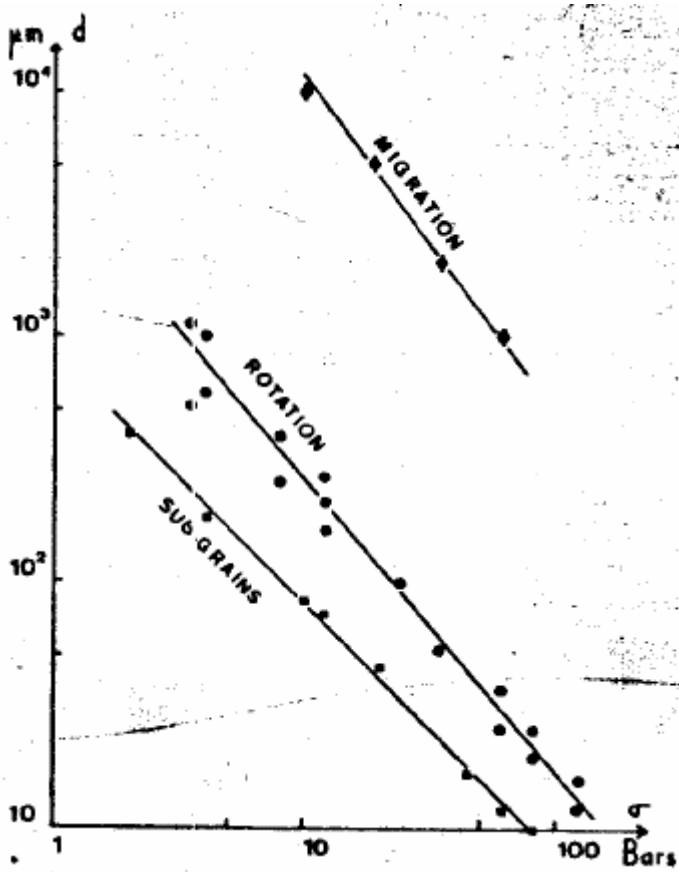
halite dataset (Guillope & Poirier, 1979)

7
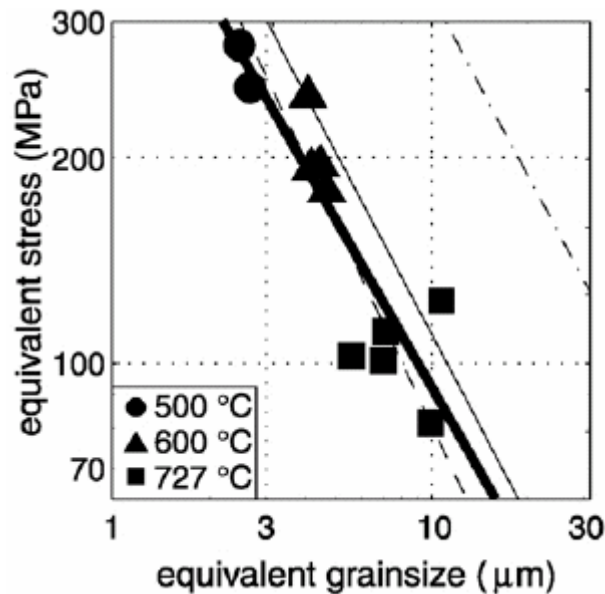
calcite torsion experiments. Solid line is SGR piezometer (Rutter, 1995), dash-dot is GBM recrystallization piezometer, dashed line piezometer of Schmid et al. (1987) (Barnhoorn et al., 2004). Heavy line is

$$\log \sigma \text{ (MPa)} = (-0.82 \pm 0.15) \log \text{(grain size, } \mu m) + 2.73 \pm 0.11$$
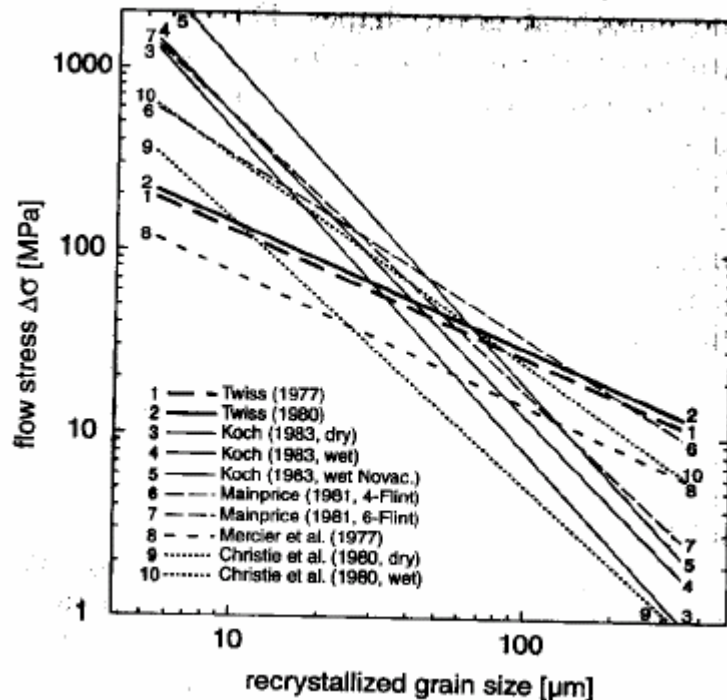
quartzite dataset. Experiments by Gleason and Tullis (1995) indicate that the Twiss (1977) piezometer is accurate at conditions near the transition between regimes 2 and 3. But De Bresser et al. (2000) note that the stresses calculated near the regime 2/3 transition should be considered minima because of possible T effects and post-deformation annealing. Post & Tullis (1999) noted that the Twiss (1977) piezometer may overestimate stress when recrystallization occurs by SGR (Regime 2).

8

Material	m1[a]	m2[b]	m3[c]	m4[d]	n	References
Albitic feldspar				0.66	3.1	Post and Tullis (1999)
Calcite (Carrara marble)			0.89		7.6	Schmid et al. (1980), regime 2
Calcite (Carrara marble)			0.97		4.2	Schmid et al. (1980), regime 3
Calcite (Carrara marble)			1.14	1.12	7.6	Rutter (1995); Schmid et al. (1980)
Olivine (Åheim dunite, wet)	0.59			1.19	4.48	Van der Wal (1993); Van der Wal et al. (1993); Chopra and Paterson (1984)
Olivine (Anita Bay dunite, wet)	0.42			0.88	3.35	Van der Wal (1993); Van der Wal et al. (1993); Chopra and Paterson (1984)
Olivine (San Quintin Baja, dry)	1.00	1.23			3.0	Mercier et al. (1977); Kirby and Raleigh (1973)
Olivine (Mt. Burnet dunite, wet)		0.89			3.0	Post (1977)
Olivine (Mt. Burnet dunite, wet)	0.69	0.82			3.0	Ross et al. (1980); Post (1977)
Olivine (Mt. Burnet dunite, dry)		0.75			3.6	Post (1977)
Olivine (Mt. Burnet dunite, dry)	0.62	1.27			3.8	Ross et al. (1980)
Olivine single crystals	0.67	1.18			3.6	Karato et al. (1980); Durham and Goetze (1977)
Quartzite (novaculite)				0.61	2.6	Bishop in: Post and Tullis (1999); Kronenberg and Tullis (1984)
Quartzite (wet Canyon Creek)		1.40			2.6	Mercier et al. (1977); Parrish et al. (1976)
Quartzite (flint, novac.)		0.59			2.65	Koch (1983); Hacker et al. (1990); Christie et al. (1980)

[a] Subgrains
[b] Unspecified recrystallization mechanism
[c] Rotation recrystallization
[d] Migration recrystallization

Developing Plot Complications in Recent Experiments

extant piezometers using $d = K\sigma^{-m}$ (de Bresser et al., 2001)
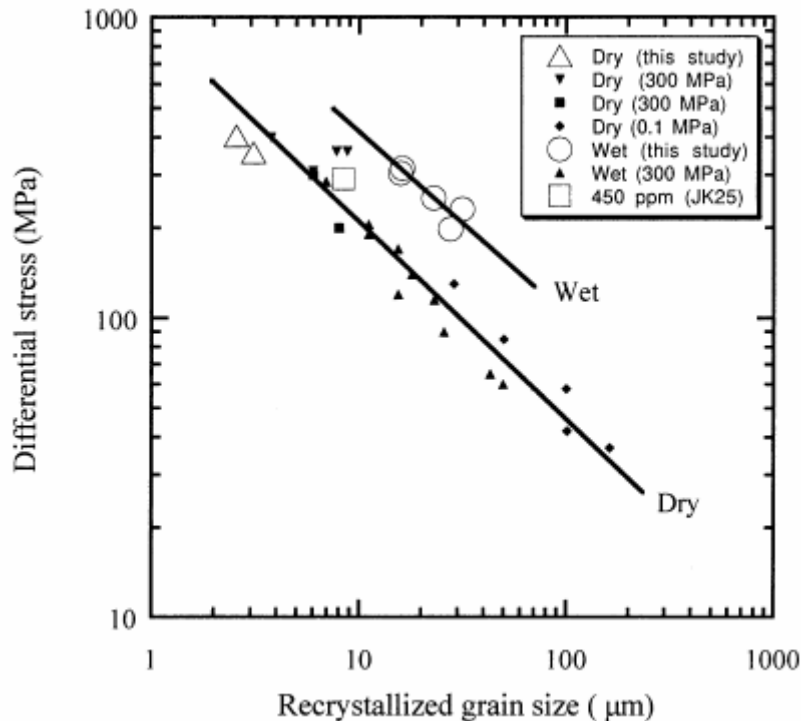
olivine with >800 ppm H/Si is 2–3X coarser, implying that adding water enhances GBM more than dislocation climb (Jung & Karato, 2001). This H concentration is less than that expected in the mantle, so piezometers need to be revised.

9
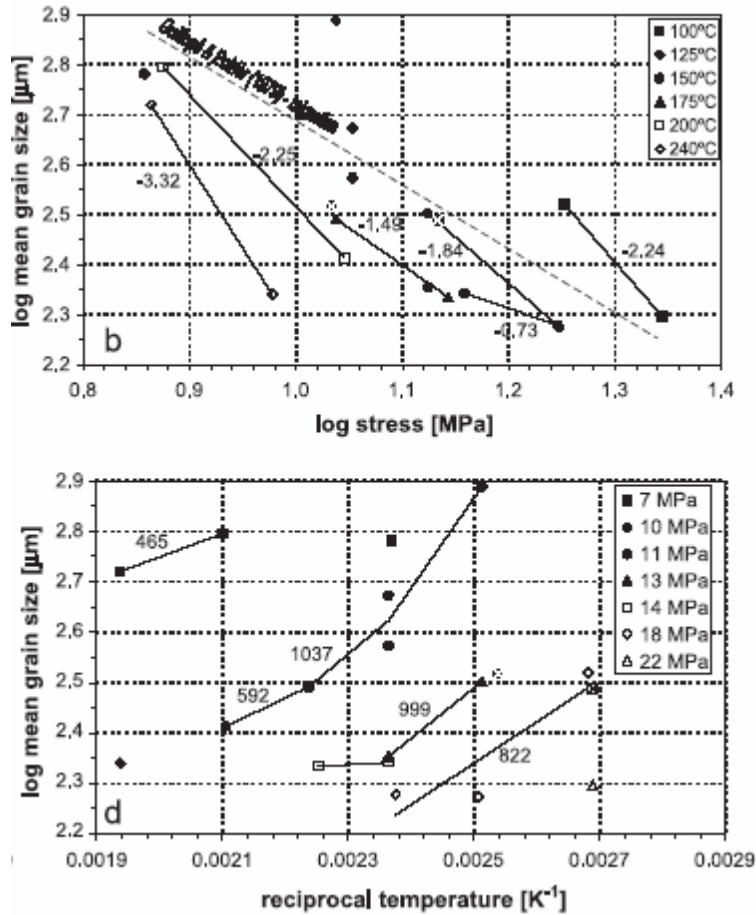
halite undergoing GBM recrystallization shows stress *and* temperature dependence (Ter Heege et al., 2005)

Study/authors	p (model)	ΔQ (model)	a (model)	p (value)	ΔQ/a (value)	log K
This study—median	–	–	–	1.40±0.17	7.7±2.1	0.43±0.18
This study—mean	–	–	–	1.85±0.23	14.2±2.8	−1.55±0.24
Guillopé and Poirier (1979)—migration	–	–	–	1.28	0	2.25
Guillopé and Poirier (1979)—subgrain rotation	–	–	–	1.18	0	1.12
Twiss (1977)	1.3≤p≤1.5	0	–	1.3≤p≤1.5	0	–
Derby and Ashby (1987)	n/2	Q_v-Q_{gb}	2	2.65±0.40	88–98 or 21.8±3.7[a]	–
Shimizu (1998)—grain boundary nucleation	1.25	Q_v-Q_{gb}	4	1.25	45–49 or 10.9±3.7[a]	–
Shimizu (1998)—intracrystalline nucleation	1.33	Q_v-Q_{gb}	3	1.33	60–66 or 14.5±3.7[a]	–
De Bresser et al. (1998)	(n−1)/m	Q_r-Q_d	m	1.43±0.40	14.5±3.7	–

halite experiments of Ter Heege et al. (2005) give *p* and *Q* that agree best with De Bresser et al. (1998) model.

10
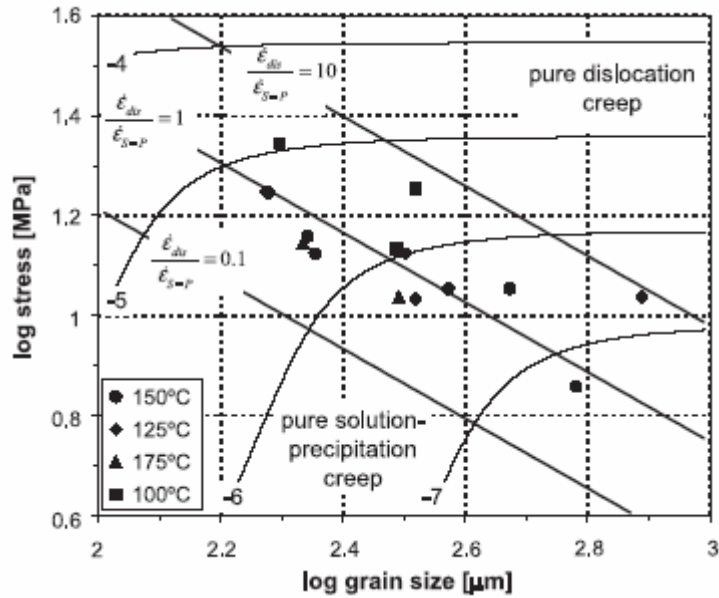
The location of the Ter Heege et al. (2005) dataset within the 'field boundary' between GSS and GSI creep on the deformation mechanism map for halite suggests that dynamic recrystallization constrains the grain size to lie in the boundary.

Applications of Piezometry

Grain size and stress (bars) in the Lanzo massif (Boudier & Nicolas, 1980)

xenoliths from continental extension zones (Avé Lallement et al., 1980)

xenoliths from cratons (Avé Lallement et al., 1980)

TABLE 2. Calculated Differential Stresses

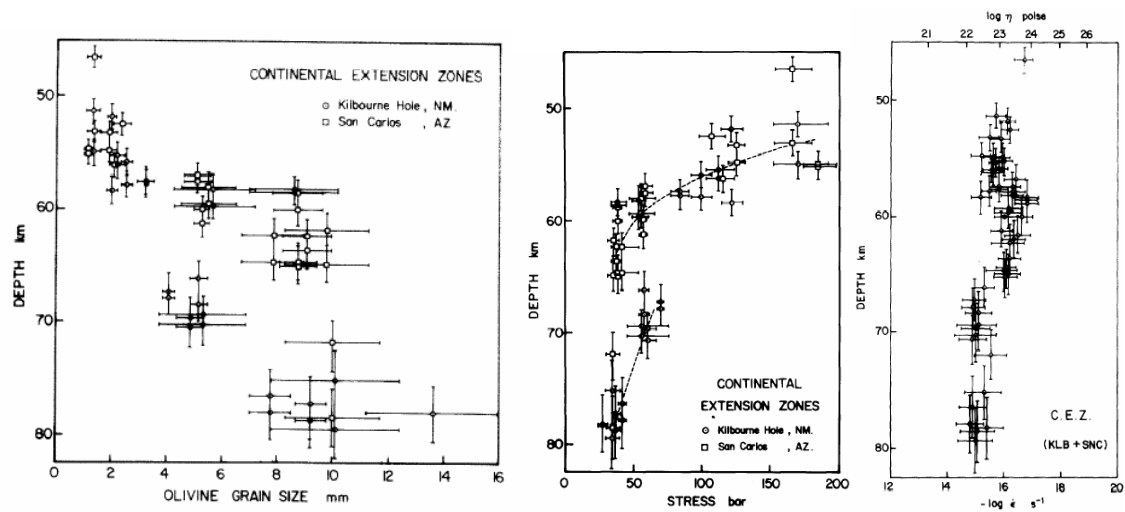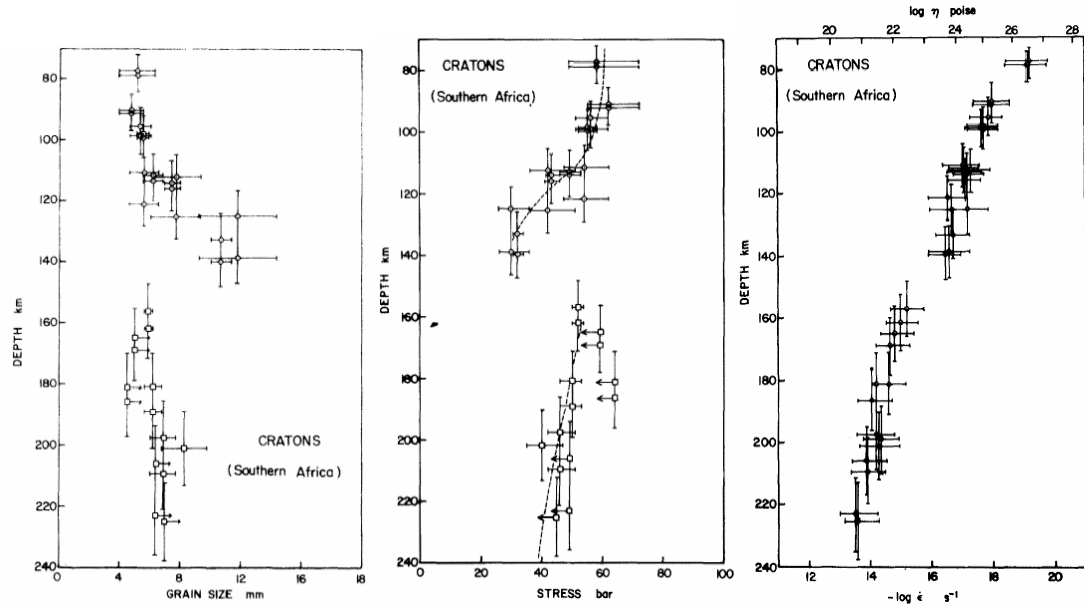| Sample	Grain Size $\bar{D}$, μm	Differential Stress (MPa)		
		Twiss [1977, 1980]	Mercier et al. [1977]	Koch[1] [1983]
Below Detachment Fault on North Side of Range				
Wh-5	61±4	41$^{+2}_{-1}$	20$^{+1}_{-1}$	34$^{+4}_{-4}$ $^{+17}_{-10}$
Wh-6	53±6	45$^{+4}_{-3}$	22$^{+2}_{-1}$	43$^{+10}_{-7}$ $^{+28}_{-15}$
Wh-8	56±6	44$^{+3}_{-3}$	21$^{+2}_{-1}$	39$^{+8}_{-6}$ $^{+25}_{-13}$
Wh-20	89±6	32$^{+2}_{-1}$	15$^{+1}_{-0}$	18$^{+2}_{-2}$ $^{+8}_{-5}$
Wh-23	106±6	28$^{+2}_{-1}$	14$^{+0}_{-1}$	13$^{+2}_{-1}$ $^{+6}_{-3}$
Wh-27	134±6	24$^{+2}_{-1}$	11$^{+1}_{-0}$	9$^{+1}_{-1}$ $^{+4}_{-3}$
Wh-29	162±6	21$^{+2}_{-1}$	10$^{+1}_{-1}$	6$^{+2}_{-1}$ $^{+4}_{-2}$
Wh-30	115±6	27$^{+1}_{-1}$	13$^{+1}_{-1}$	12$^{+1}_{-2}$ $^{+5}_{-4}$
Beneath Mylonitic Front on Southwest Side of Range				
Wh-40	51±4	47$^{+2}_{-3}$	23$^{+1}_{-1}$	46$^{+7}_{-6}$ $^{+25}_{-15}$
Wh-41	56±4	44$^{+2}_{-2}$	21$^{+2}_{-1}$	39$^{+5}_{-4}$ $^{+20}_{-12}$
Wh-42	39±3	56$^{+3}_{-3}$	28$^{+1}_{-2}$	72$^{+10}_{-8}$ $^{+41}_{-24}$
Wh-43	41±3	54$^{+2}_{-3}$	27$^{+1}_{-2}$	66$^{+9}_{-7}$ $^{+37}_{-21}$
Wh-44	34±4	62$^{+5}_{-5}$	31$^{+2}_{-3}$	91$^{+21}_{-16}$ $^{+65}_{-34}$
Wh-45	61±6	41$^{+3}_{-2}$	20$^{+2}_{-1}$	34$^{+6}_{-5}$ $^{+20}_{-12}$
Wh-47	41±3	54$^{+3}_{-2}$	27$^{+1}_{-2}$	66$^{+9}_{-7}$ $^{+37}_{-21}$
Wh-48	42±3	53$^{+3}_{-2}$	26$^{+2}_{-1}$	64$^{+18}_{-7}$ $^{+34}_{-21}$
Wh-49	33±3	63$^{+4}_{-4}$	31$^{+2}_{-2}$	96$^{+16}_{-14}$ $^{+60}_{-34}$
Wh-51	32±2	64$^{+3}_{-2}$	32$^{+1}_{-1}$	101$^{+11}_{-10}$ $^{+55}_{-32}$
Wh-53	50±4	47$^{+3}_{-2}$	23$^{+2}_{-1}$	47$^{+7}_{-5}$ $^{+27}_{-15}$
Wh-54	50±3	47$^{+2}_{-2}$	23$^{+1}_{-1}$	47$^{+6}_{-4}$ $^{+24}_{-14}$
Wh-57	57±5	43$^{+3}_{-2}$	21$^{+2}_{-1}$	38$^{+6}_{-5}$ $^{+21}_{-22}$

13

| T(°C)	D̄ (μm)	σ(MPa)	Shelton and Tullis (1981)	Hansen and Carter (1982)	Koch et al. (1989) "dry"	Hansen (1982)	Koch et al. (1989) "wet"	Kronenberg and Tullis (1984)	Jaoul et al. (1984)	Logarithm Effective Viscosity (Pa s)
			Mylonitic Gneisses With Average Final Grain Size, D = 37 μm							
500	20±2	223	$9.9^{+0.4\ +0.5}_{-0.5\ -0.5}$	$8.7^{+0.4}_{-0.4}$	$10.1^{+0.6\ +3.4}_{-0.6\ -3.6}$	$8.2^{+0.4}_{-0.4}$	$9.5^{+0.5\ +2.0}_{-0.6\ -2.1}$	$8.3^{+0.5\ +1.1}_{-0.6\ -2.1}$	$8.9^{+0.3\ +1.6}_{-0.3\ -1.9}$	$18.0^{+0.6\ +3.4}_{-0.6\ -3.6}$
450	37±1	96	$11.2^{+0.4\ +0.5}_{-0.4\ -0.5}$	$9.7^{+0.4}_{-0.4}$	$11.5^{+0.5\ +3.6}_{-0.6\ -3.6}$	$9.5^{+0.4}_{-0.4}$	$10.8^{+0.5\ +2.0}_{-0.6\ -2.1}$	$9.6^{+0.5\ +0.9}_{-0.6\ -1.9}$	$10.0^{+0.3\ +1.5}_{-0.3\ -1.7}$	$19.0^{+0.5\ +3.6}_{-0.6\ -3.6}$
400	37±1	96	$12.1^{+0.4\ +0.4}_{-0.4\ -0.5}$	$10.4^{+0.4}_{-0.4}$	$12.2^{+0.5\ +3.6}_{-0.6\ -3.6}$	$10.4^{+0.4}_{-0.4}$	$11.6^{+0.5\ +2.1}_{-0.6\ -2.2}$	$10.3^{+0.5\ +0.9}_{-0.6\ -2.0}$	$10.8^{+0.3\ +1.5}_{-0.3\ -1.7}$	$19.7^{+0.6\ +3.4}_{-0.6\ -3.6}$
			Mylonitic Gneisses With Average Final Grain Size, D = 55 μm							
520	27±3	134	$9.8^{+0.4\ +0.5}_{-0.5\ -0.6}$	$8.6^{+0.4}_{-0.4}$	$10.0^{+0.6\ +3.3}_{-0.6\ -3.5}$	$8.0^{+0.4}_{-0.4}$	$9.4^{+0.5\ +2.0}_{-0.6\ -2.1}$	$8.2^{+0.5\ +0.8}_{-0.5\ -1.8}$	$8.7^{+0.3\ +1.5}_{-0.4\ -1.8}$	$17.6^{+0.6\ +3.3}_{-0.6\ -3.5}$
460	55±3	43	$11.7^{+0.4\ +0.4}_{-0.4\ -0.5}$	$10.2^{+0.4}_{-0.4}$	$12.1^{+0.5\ +3.3}_{-0.6\ -3.5}$	$9.8^{+0.3}_{-0.4}$	$11.4^{+0.5\ +1.9}_{-0.5\ -2.0}$	$10.2^{+0.5\ +0.8}_{-0.5\ -1.8}$	$10.3^{+0.3\ +0.13}_{-0.3\ -0.15}$	$19.3^{+0.5\ +3.3}_{-0.5\ -3.5}$
400	55±3	43	$12.7^{+0.4\ +0.4}_{-0.4\ -0.5}$	$11.0^{+0.3}_{-0.4}$	$13.0^{+0.5\ +3.5}_{-0.6\ -3.7}$	$11.0^{+0.3}_{-0.4}$	$12.4^{+0.5\ +2.0}_{-0.5\ -2.1}$	$11.0^{+0.5\ +0.8}_{-0.5\ -1.9}$	$11.2^{+0.3\ +1.3}_{-0.3\ -1.5}$	$20.2^{+0.5\ +3.5}_{-0.6\ -3.7}$

Gleason & Tullis (1995) flow law indicates an order of magnitude slower strain rates than Koch et al. (1989)

(Stipp et al., 2002)
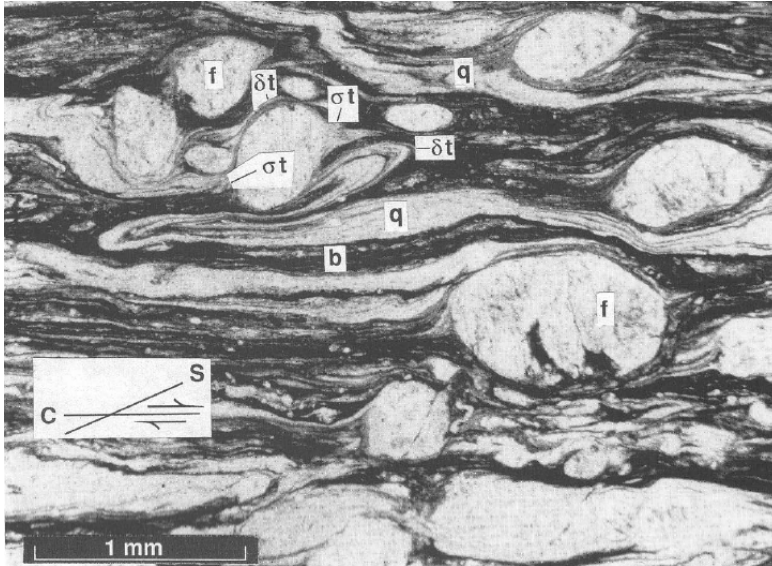

14
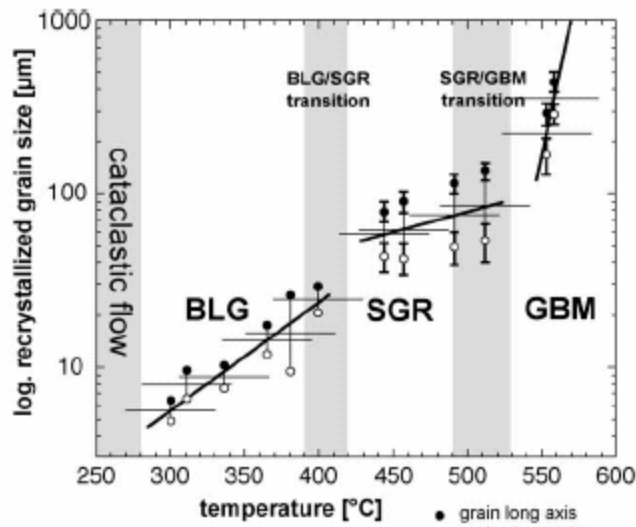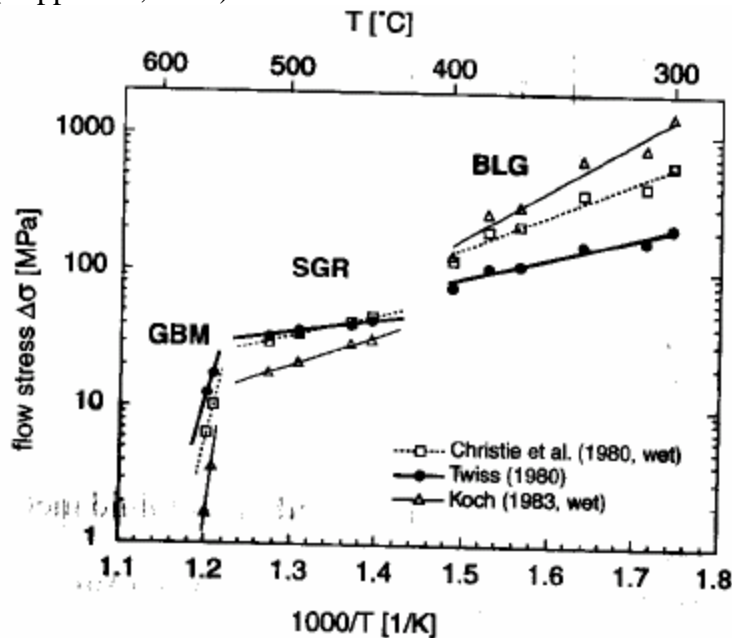
(Stipp et al., 2002)
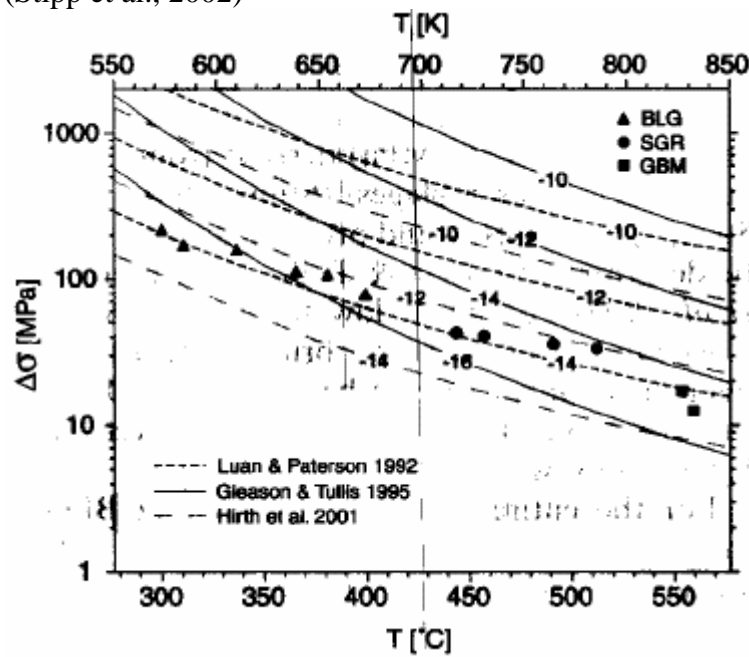
(Stipp et al., 2002)

## Rheology of Multiphase Rocks

Borrego Springs mylonite shows ductile (Regime 2) quartz and brittle feldspar (Simpson, 1998)

Catalina Mtns mylonite shows ductile (Regime 2) quartz and brittle feldspar with sigma and delta porphyroclasts (Davis et al., 1998)
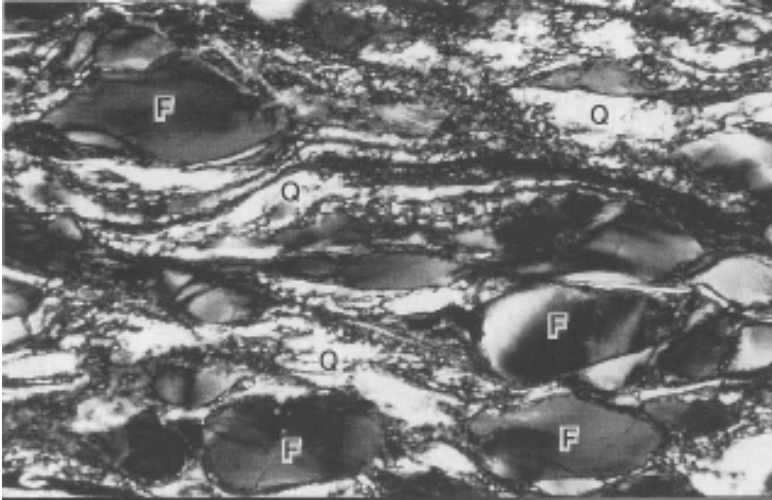

Enfield aplite shortened 35% at 725°C and 10^{-6} s^{-1} (Tullis et al., 2000). At these conditions quartzite deforms by BLG (regime 1) dislocation creep and is weaker than anorthosite, which deforms by cataclastic flow. This aplite shows that the isolated quartz was stronger than the feldspar, because in regime 1 dislocation creep, the recovery process is bulging recrystallization, which can only occur if there are quartz–quartz grain boundaries.

16
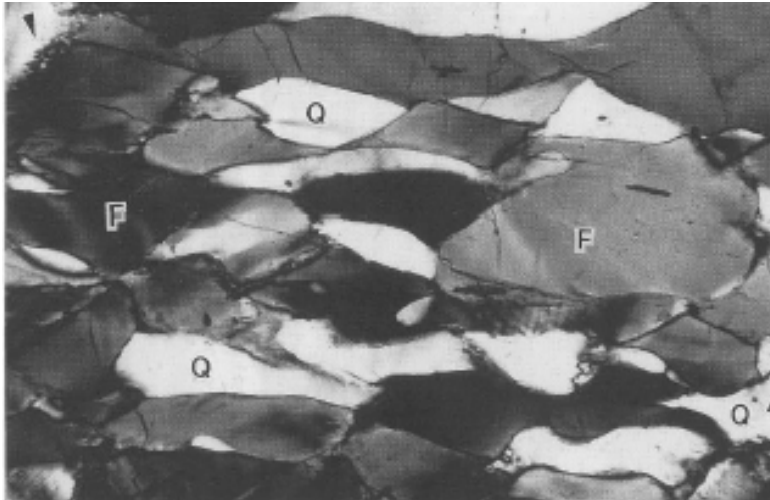
aplite shortened 40% at 900°C and 10^{-5} s^{-1}; quartz has subgrains, plagioclase has dislocation tangles (Dell'Angelo & Tullis, 1998).


100 µm

Enfield aplite shortened 60% at 900°C and 10^{-6} s^{-1}. Quartz deforms by SGR (regime 2) dislocation creep and the feldspars deform by BLG (regime 1) dislocation creep. Because dislocation climb is easy in quartz, it undergoes homogeneous flattening; some grains show sub-basal deformation lamellae, and recrystallized grains formed by SGR are observed especially along some grain boundaries. The feldspars are stronger and deform less homogeneously, including necking (Tullis et al., 2000)

17

aplite shortened 65% at 900°C and 10^{-5} s^{-1} (Dell'Angelo & Tullis, 1998)
feldspar has fine recrystallized tails, quartz highly flattened and undergoing SGR

Enfield aplite shortened 85% at 900°C, 10^{-6} s^{-1}; recrystallized ribbons of quartz, feldspar augen with tails (Tullis et al., 2000).
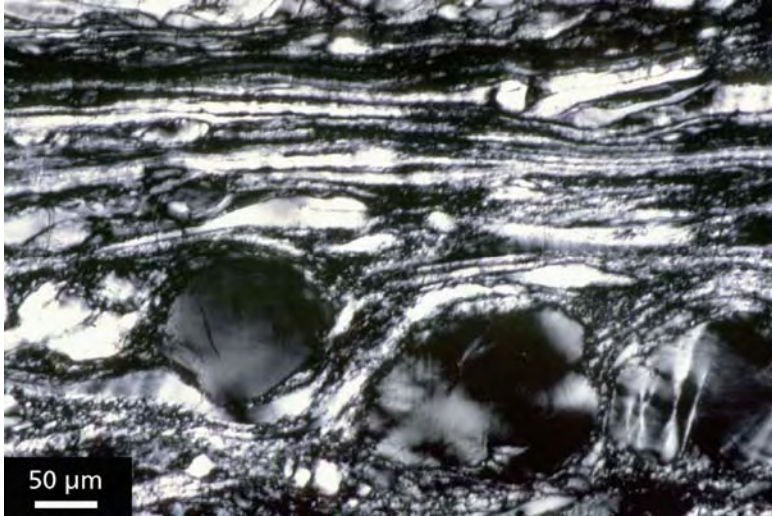
Enfield aplite shortened 40% and dextrally sheared ($\gamma = 2.4$) at 900°C, 10^{-5} s^{-1}; recrystallized ribbons of quartz, feldspar augen with tails (Tullis et al., 2000).
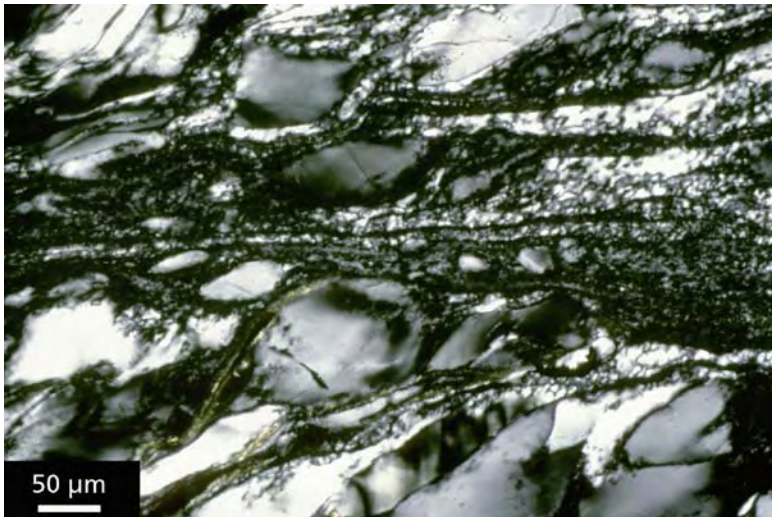

Enfield aplite shortened and dextrally sheared at 900°C and 10^{-6} s^{-1}; recrystallized grain size of quartz is larger than that of feldspar (Tullis et al., 2000)

19
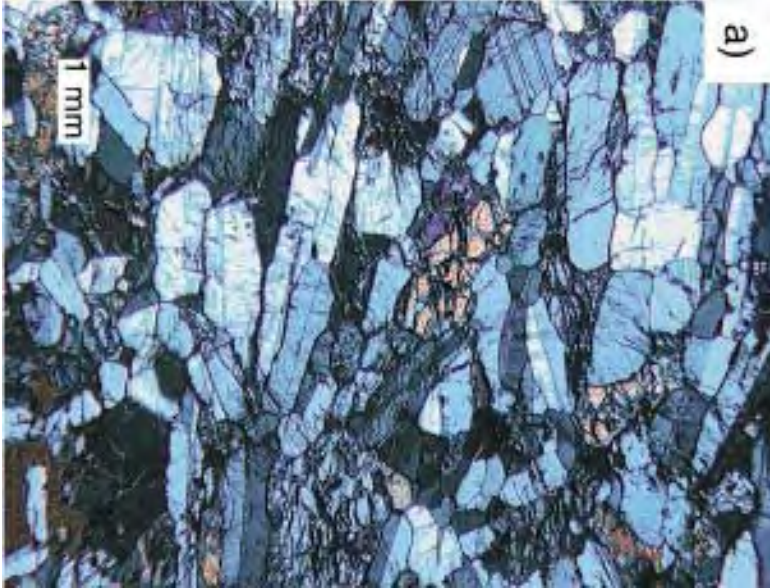
Some oceanic rocks deformed at hypersolidus conditions have undeformed pyroxene and plagioclase coexisting with crystal plastically deformed olivine. This is contrary to expectations for dislocation creep (Yoshinobu & Hirth, 2002):
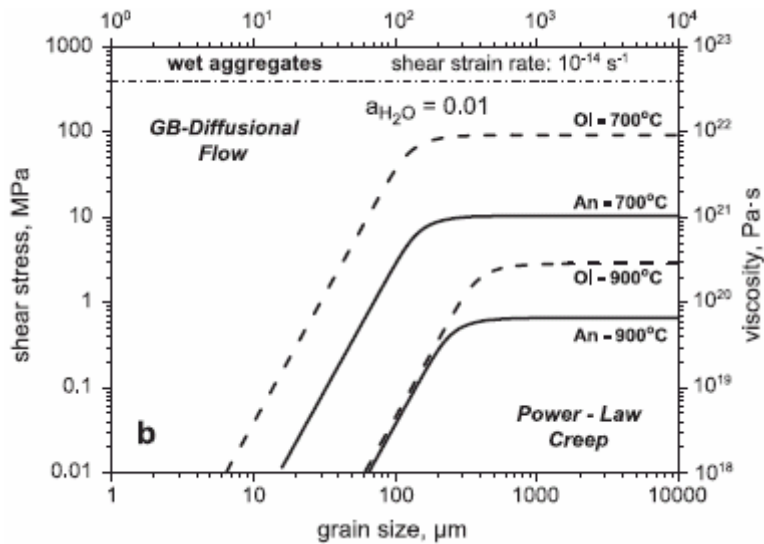
difference in strength between anorthite and olivine (Rybacki & Dresen, 2004)

20
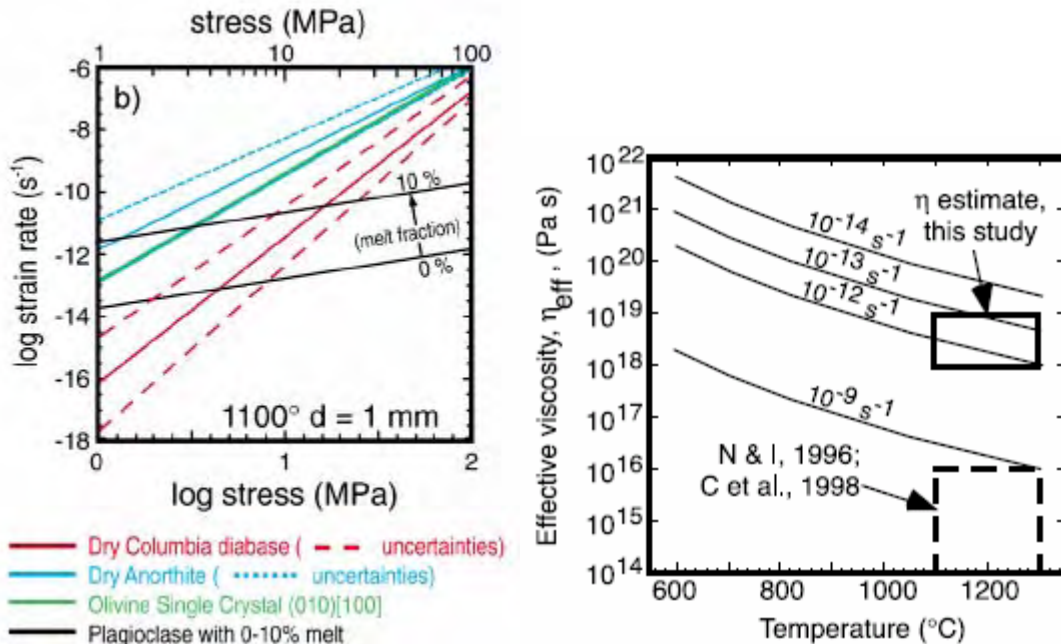
However, extrapolations suggest that olivine deforming by dislocation creep is weaker than plagioclase deforming by diffusion creep in the presence of 0–10% melt (Yoshinobu & Hirth, 2002).

General Behavior of Composite Materials
At high strains, the strength of a composite is expected to be dominated by the weak mineral.

Small amounts of a second phase can inhibit grain growth and force grain-size sensitive flow.
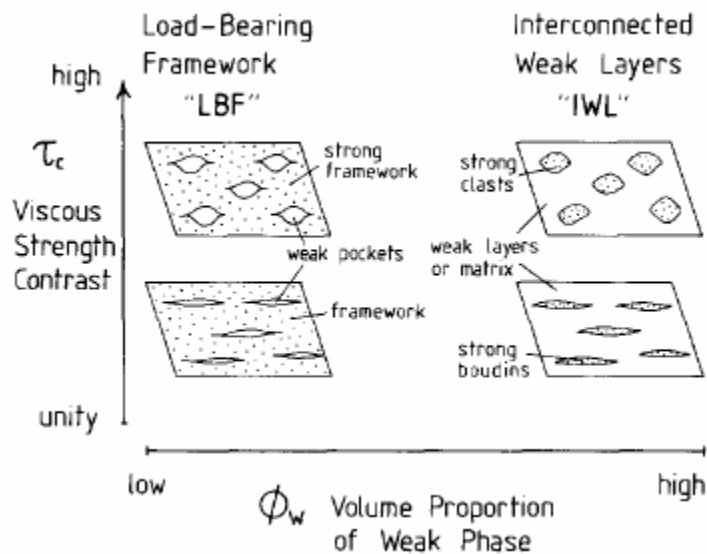
There are two basic types of rock microstructure:

i) LBF load-bearing strong phases with pockets of weak material. Characterized by uniform strain rate with stress concentrated in stronger material.

ii) ii) IWL interconnected layers of weak material with clasts of stronger material. Characterized by higher strain rate and sometimes higher stress in interconnected weak phase (Handy, 1994)

The shear strength of an LBF can be calculated as

$$\tau_{LBF} = \tau_w \phi_w + \tau_s \phi_s$$

where w and s are weak and strong (Handy, 1994). The shear strength of an IWL rock can be calculated as

$$\tau_{IWL} = \tau_w \phi_w^{1-x} + \tau_s \frac{(1-\phi_w^{1-x})}{(1-\phi_w)}$$

where

$$x = 1 - \frac{1}{\tau_c}$$

is the 'strain-rate concentration function', ϕ is volume fraction, and τ is octahedral shear stress (Handy, 1994).

A study based on finite-element modeling showed that

$$n_c = 10^{\phi_s \log n_s + \phi_w \log n_w}$$

$$Q_c = \frac{Q_w(n_c - n_s) - Q_s(n_c - n_w)}{n_w - n_s}$$

$$A_c = 10^{\frac{\log A_w(n_c - n_s) - \log A_s(n_c - n_w)}{n_w - n_s}}$$

parameters for flow laws of composites can be computed from the volume-weighted geometric means of the component parameters (c, composite; s, strong; w, weak; Tullis et al., 1991)

Interaction Between Deformation and Metamorphism
### Influence of Deformation on Phase Transformations (Brodie & Rutter, 1985)
- increase in point defects leads to diffusion
- increase in line defects leads to pipe diffusion
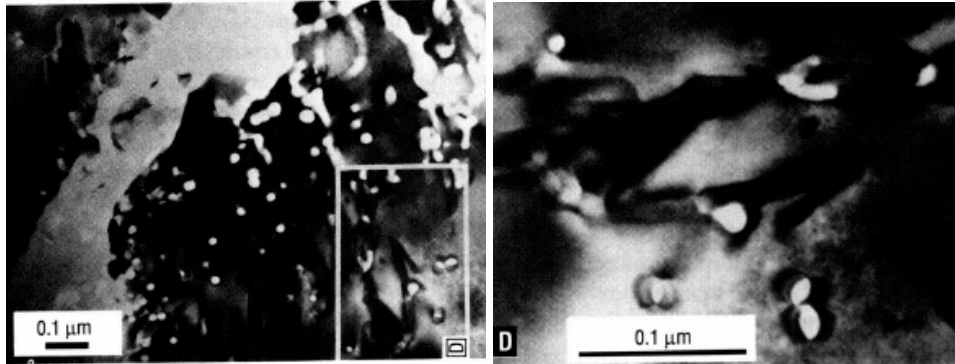
(Hacker & Christie, 1991)
- dynamic recrystallization can enable compositional change
- reduction in grain size increases grain surface

22

- 'shear heating' causes T increase
- cracking permits fluid infiltration, so
  - H_2O is a catalyst
  - reduces fluid pressure
  - permits hydration reactions to occur
  - permits longer reaction length scale
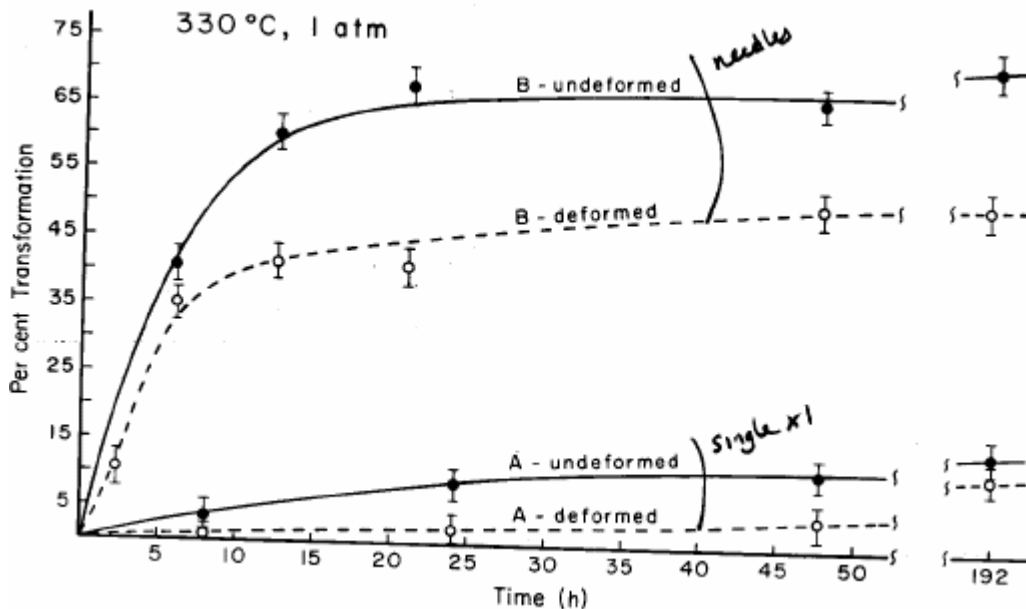
transformation of aragonite to calcite is enhanced by strong grain-size reduction caused by deformation (Snow & Yund, 1987)
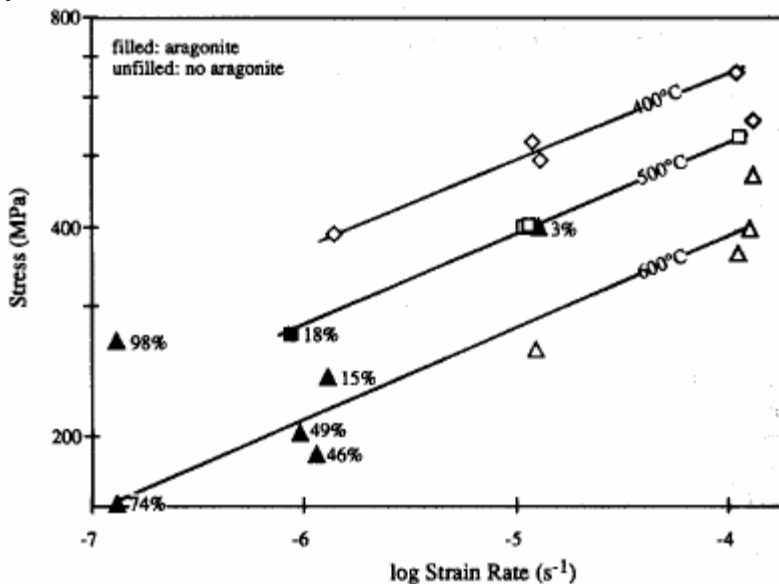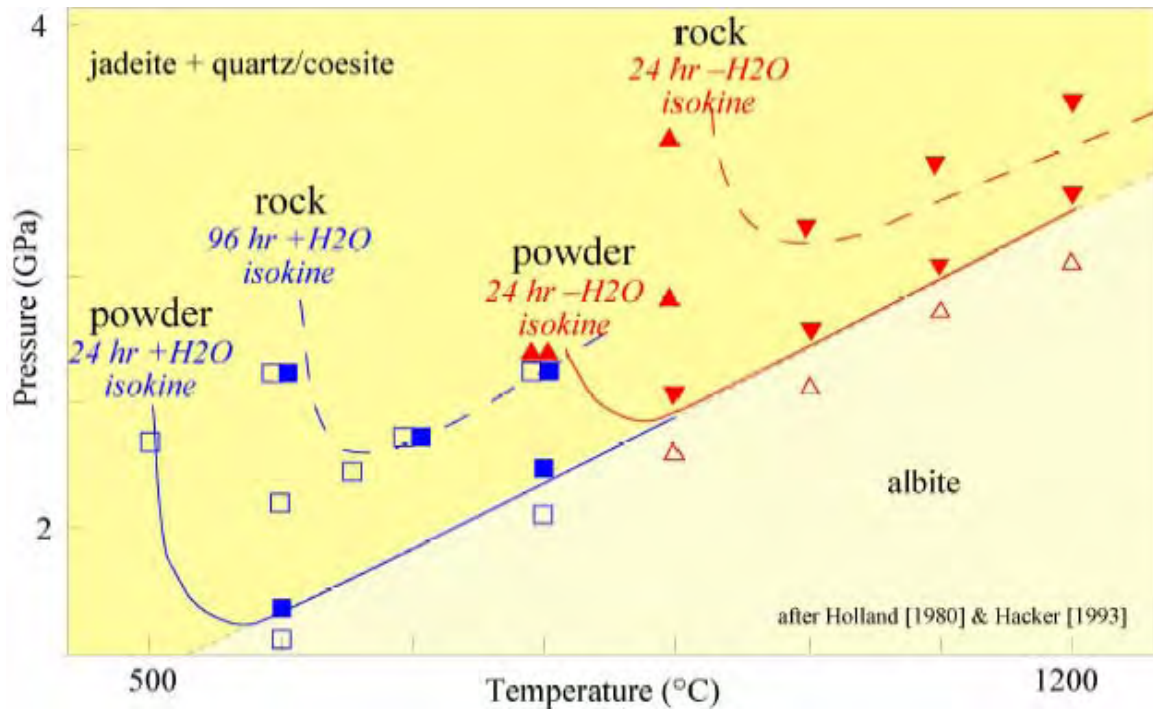

Fig. 8. Strength trends of samples containing aragonite (filled symbols) are not systematically stronger or weaker than strength trends of samples lacking aragonite (unfilled symbols). Percentages indicate average amount of aragonite present.
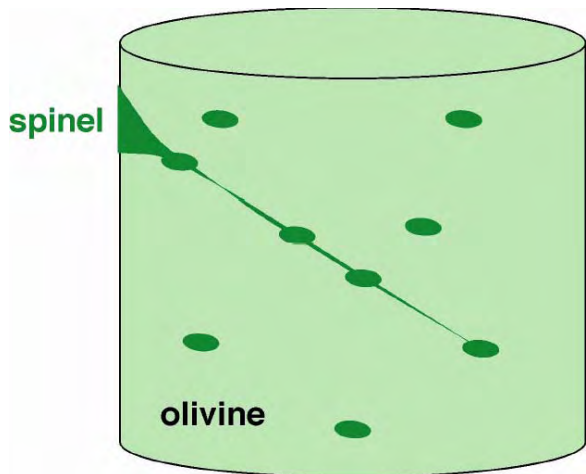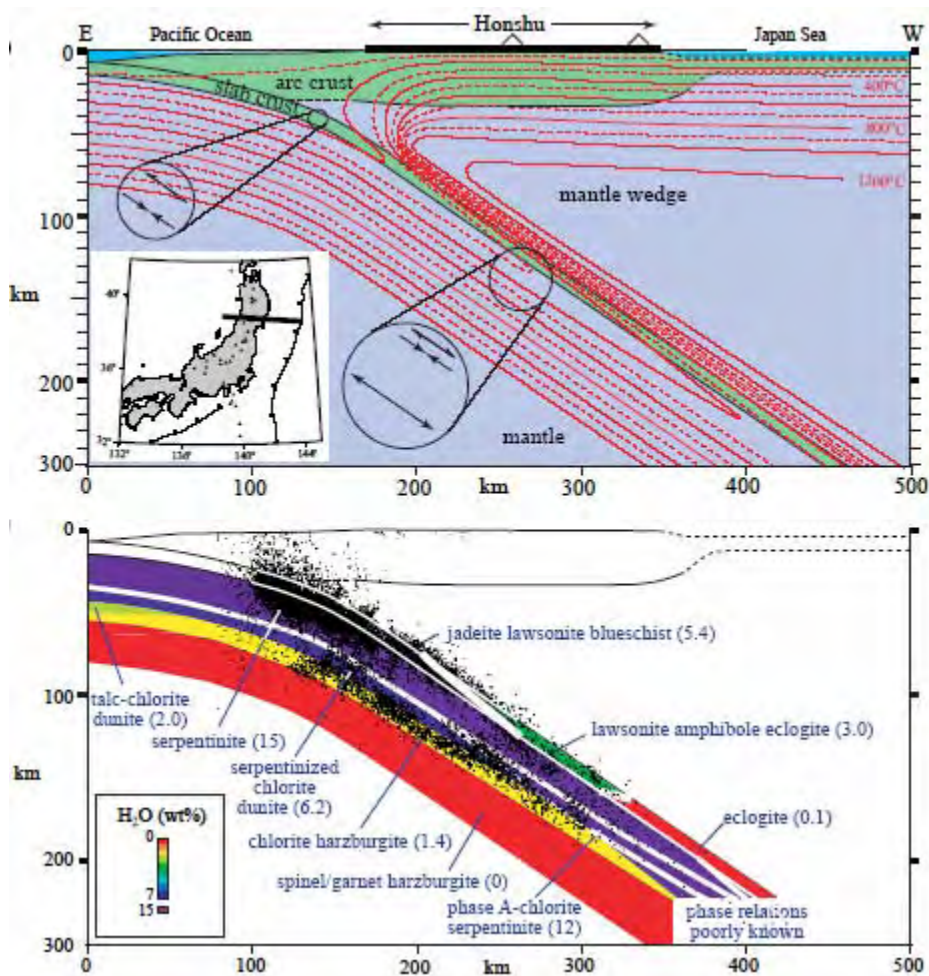
(Hacker & Kirby, 1993)

23

powdered albite transforms much faster than solid albite rock; H_2O also causes a marked acceleration in reaction rate
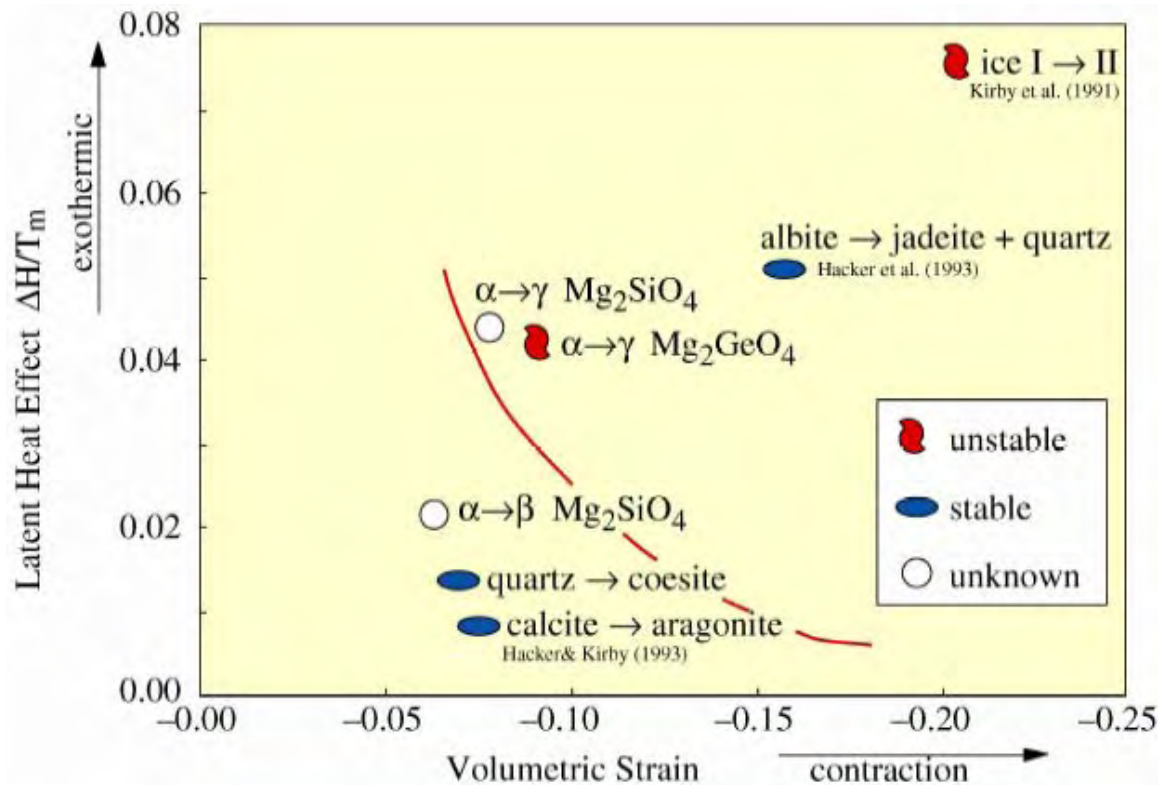
reactions with large contractions and large latent heat affects induce unstable faulting
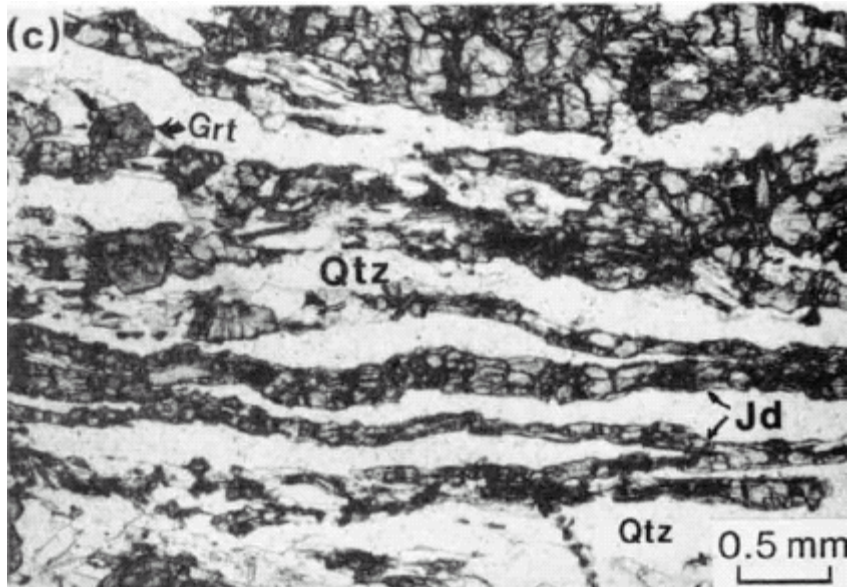
24

the transformation of olivine to spinel *may* be the cause of deep-focus earthquakes

dehydration *may* be the cause of deep-focus earthquakes (Hacker et al., 2003)

Influence of Phase Transformations on Deformation (Brodie & Rutter, 1985)
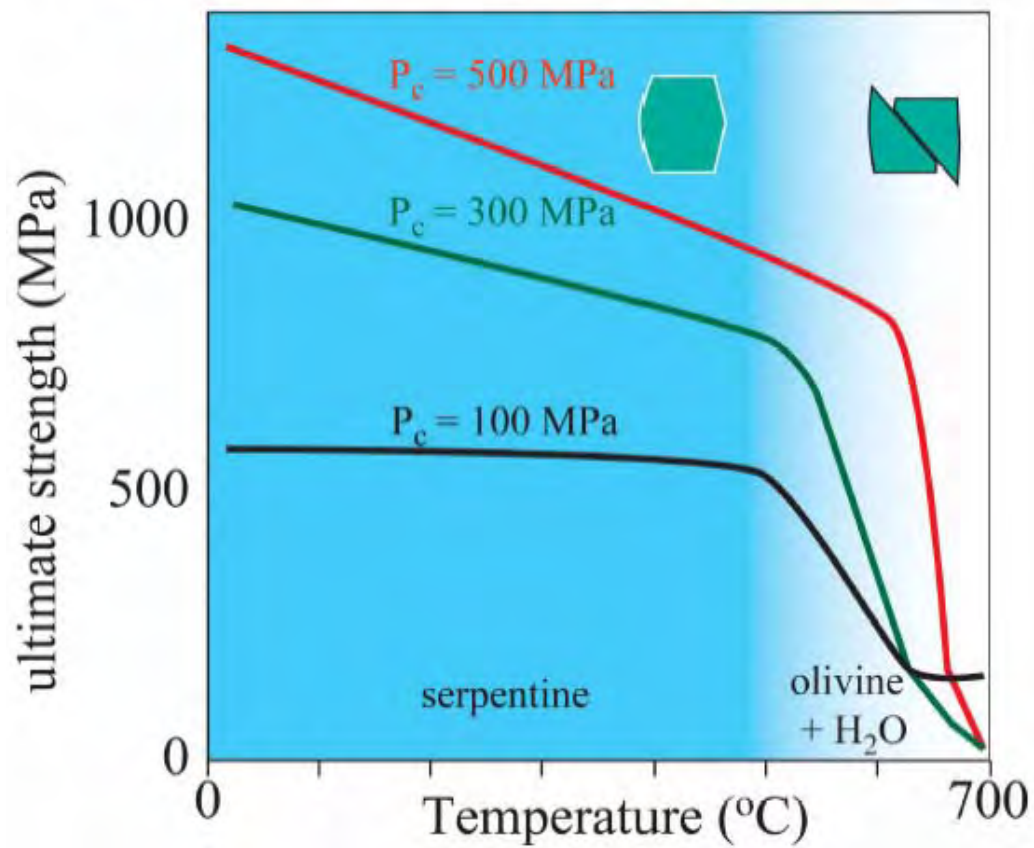- fine grain size may enable grain-size sensitive creep

fine-grained jadeite (Rubie, 1990)

- coarse grain size may force dislocation creep
- release of fluid may cause dehydration embrittlement
- $\Delta V_{reaction}$ may drive diffusion creep
- point defect chemistry change

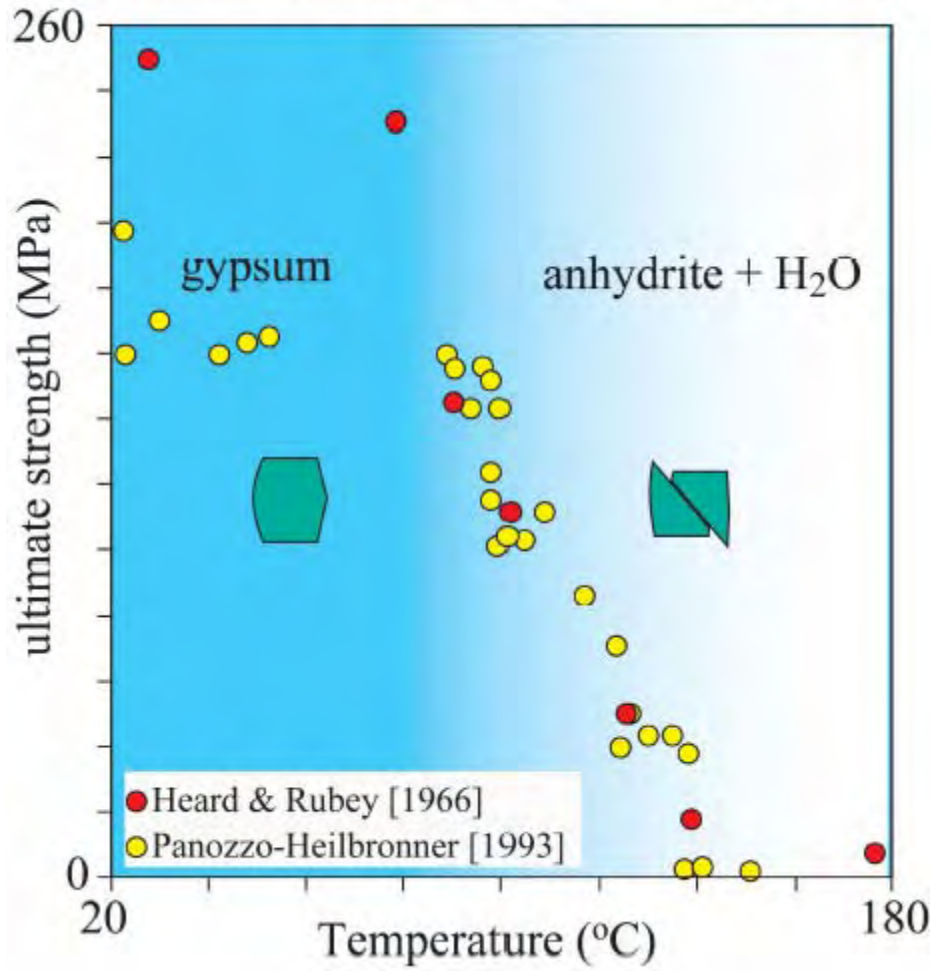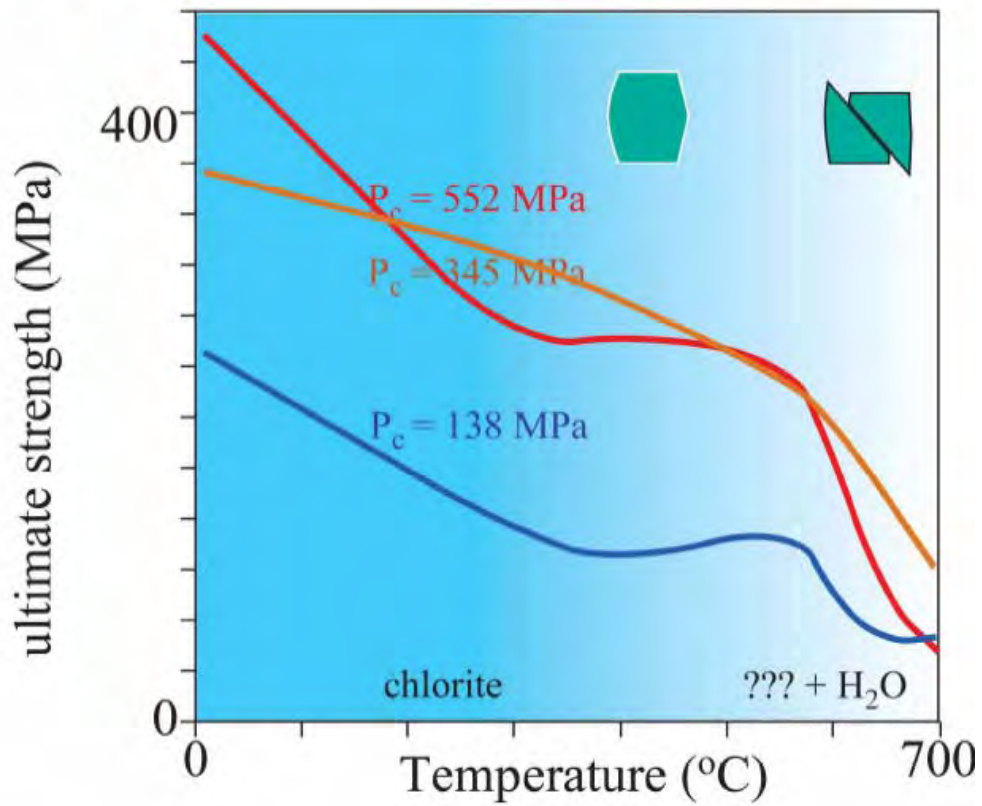**Dehydration Embrittlement**

Serpentinite Dehydration Embrittlement

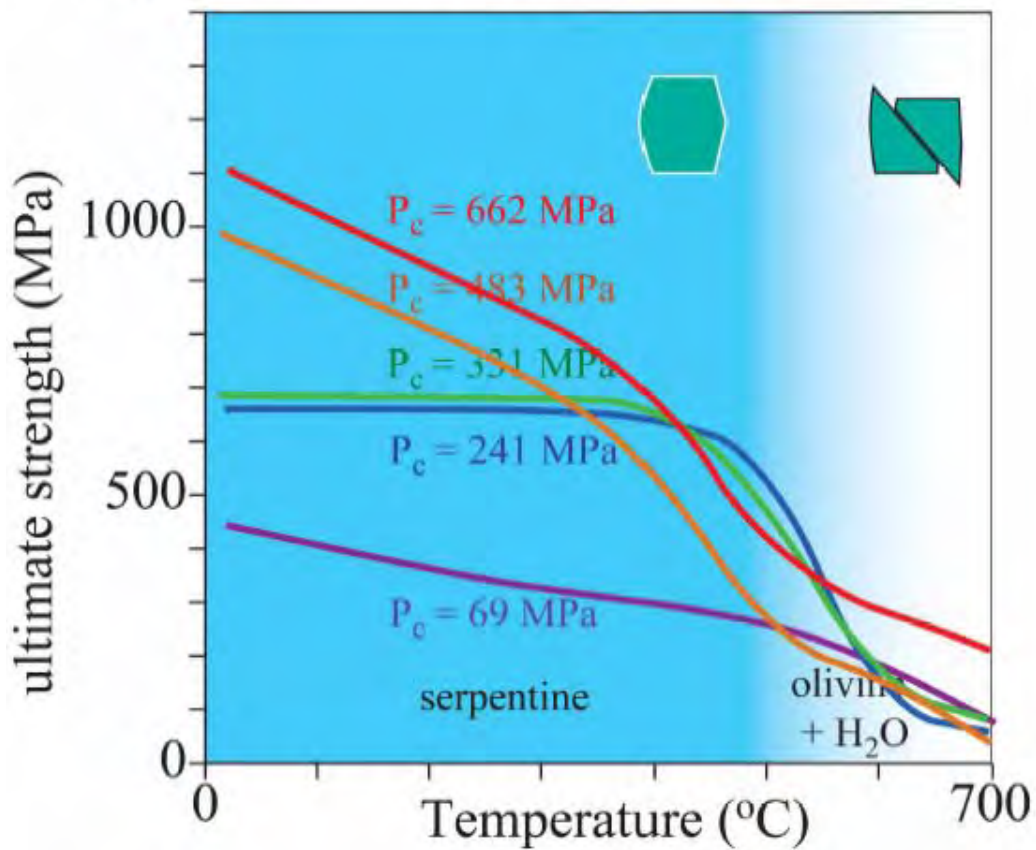(Raleigh & Paterson, 1965)

Gypsum Dehydration Embrittlement

28

Chloritite Dehydration Embrittlement

(Murrell & Ismail, 1976)

29

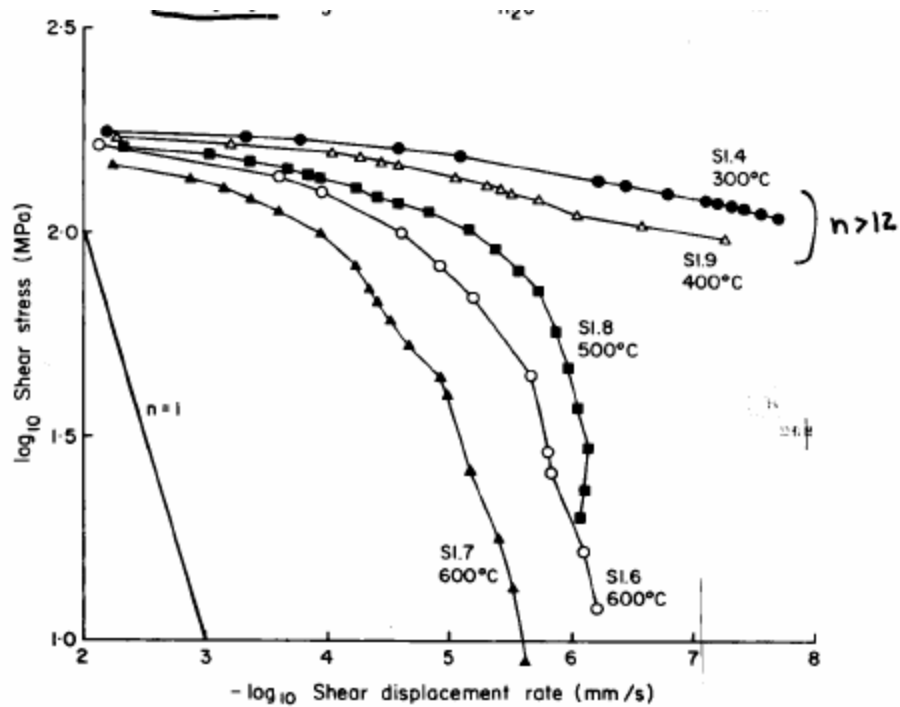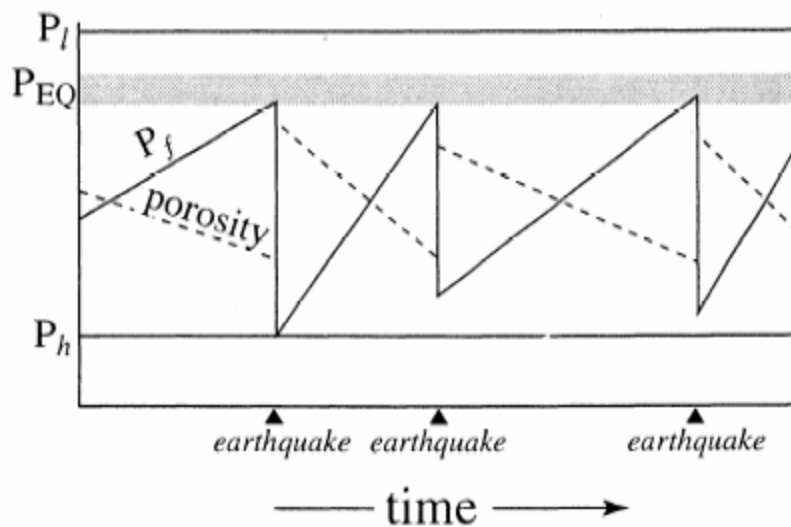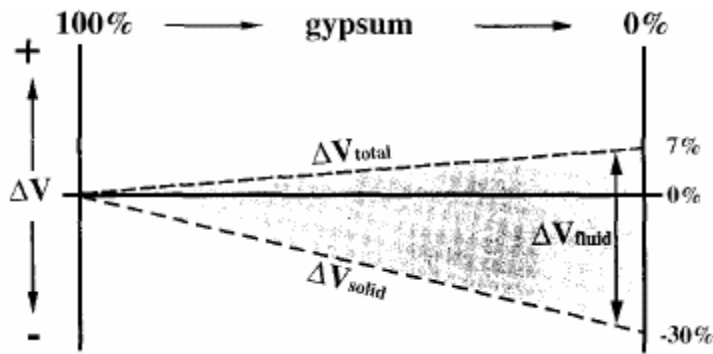# Serpentinite Dehydration Embrittlement

(Murrell & Ismail, 1976)

serpentine → olivine + H_2O, showing concentrated dehydration products along shear zone (Rutter & Brodie, 1988)

serpentine → olivine + H_2O, showing strength decrease with increasing T (Rutter & Brodie, 1988)

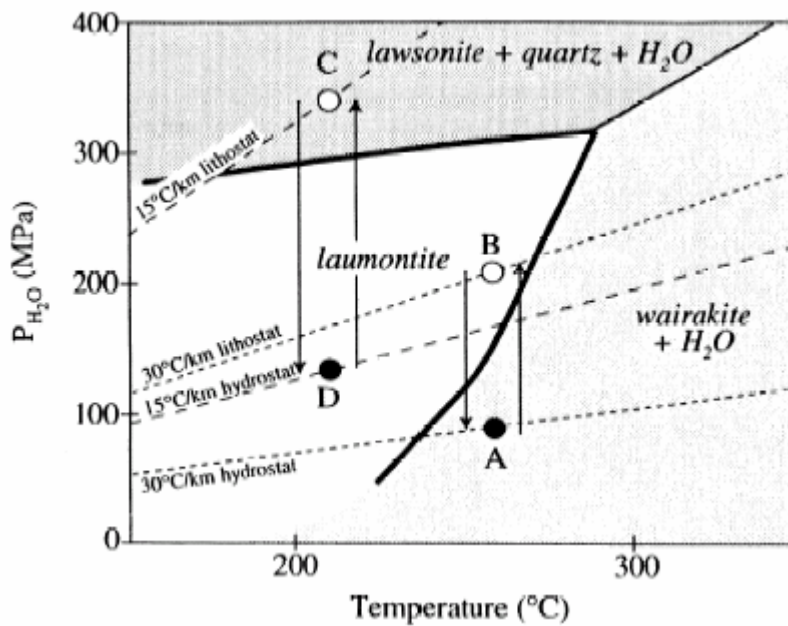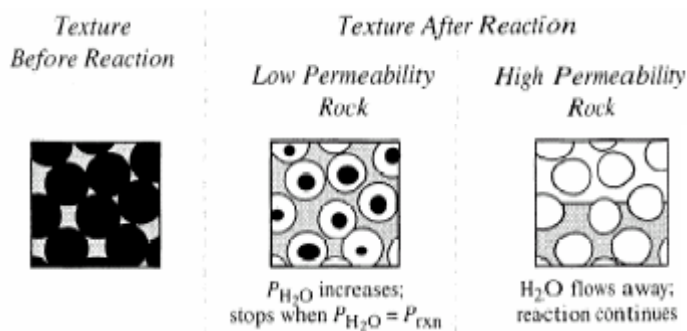(Hacker, 1997)

$$\Delta V_{fluid} + \Delta V_{solid} = \Delta V_{total}$$
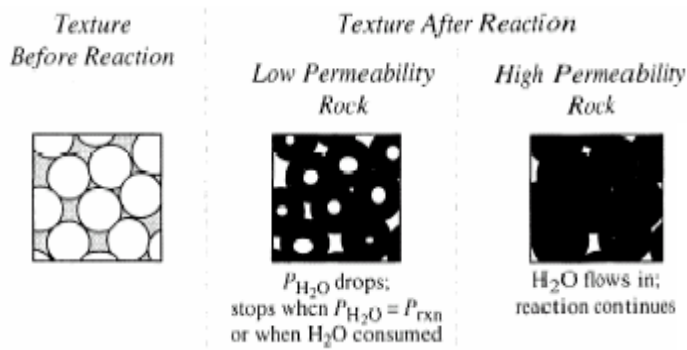$$+37\% \quad + \quad -30\% \quad = \quad +7\%$$
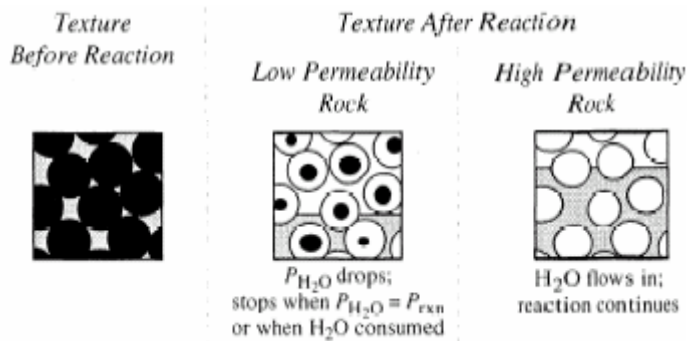
gypsum –> anhydrite + H_2O (Olgaard et al., 1995)
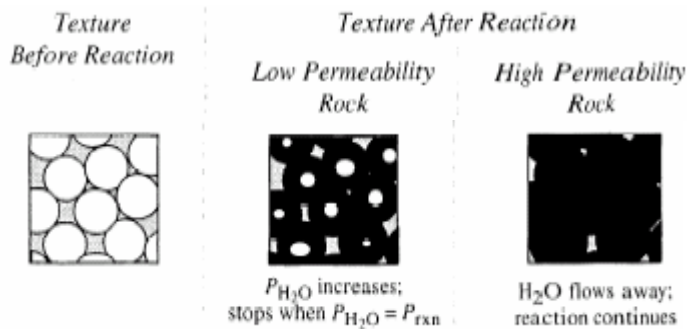

(Hacker, 1997)

laumontite → wairakite + H_2O. Fluid-dominated dehydration reaction driven by decreasing P_{H_2O}. Reaction produces excess H_2O; outflow required for continued reaction.

32

Texture Before Reaction

Texture After Reaction

Low Permeability Rock — P_{H_2O} drops; stops when $P_{H_2O} = P_{rxn}$ or when H_2O consumed

High Permeability Rock — H_2O flows in; reaction continues

wairakite + H_2O –> laumontite. Fluid-dominated dehydration reaction driven by increasing P_{H_2O}. Reaction consumes H_2O; inflow required for continued reaction.

Texture Before Reaction

Texture After Reaction

Low Permeability Rock — P_{H_2O} drops; stops when $P_{H_2O} = P_{rxn}$ or when H_2O consumed

High Permeability Rock — H_2O flows in; reaction continues

laumontite → lawsonite + quartz + H_2O. Solid-dominated dehydration reaction driven by increasing P_{H_2O}. Reaction produces excess porosity; inflow required for continued reaction.

Texture Before Reaction

Texture After Reaction

Low Permeability Rock — P_{H_2O} increases; stops when $P_{H_2O} = P_{rxn}$

High Permeability Rock — H_2O flows away; reaction continues

lawsonite + quartz + H_2O → laumontite. Solid-dominated dehydration reaction driven by decreasing P_{H_2O}. Reaction consumes porosity; outflow required for continued reaction.

laumontite → wairakite + H_2O. Fluid-dominated dehydration reaction driven by decreasing P_{H_2O}. Reaction produces excess H_2O; outflow required for continued reaction.

33
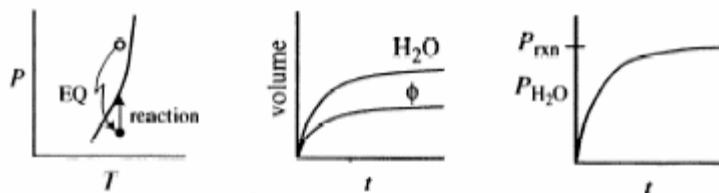
wairakite + H_2O –> laumontite. Fluid-dominated dehydration reaction driven by increasing P_{H2O}. Reaction consumes H_2O; inflow required for continued reaction.
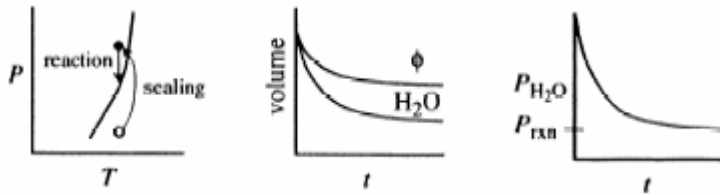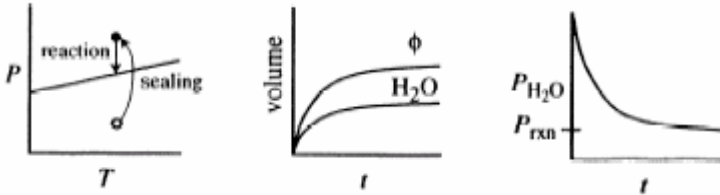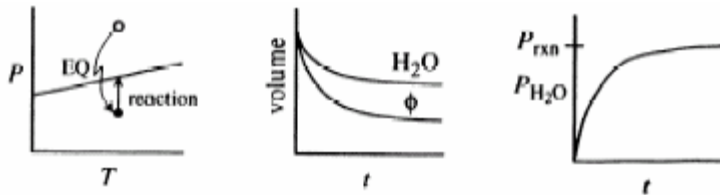

laumontite → lawsonite + quartz + H_2O. Solid-dominated dehydration reaction driven by increasing P_{H2O}. Reaction produces excess porosity; inflow required for continued reaction.


lawsonite + quartz + H_2O → laumontite. Solid-dominated dehydration reaction driven by decreasing P_{H2O}. Reaction consumes porosity; outflow required for continued reaction.

Partially Molten Rocks

A partially melted rock can be approximated as a suspension of rigid spheres in a Newtonian viscous melt (Einstein, 1906; Roscoe, 1952):

$$\frac{\eta_{rock+melt}}{\eta_{melt}} = (1.35C - 0.35)^{-2.5}$$

This equation gives a near-rigid material at $C = 0.26$, which corresponds to close packing of spheres:
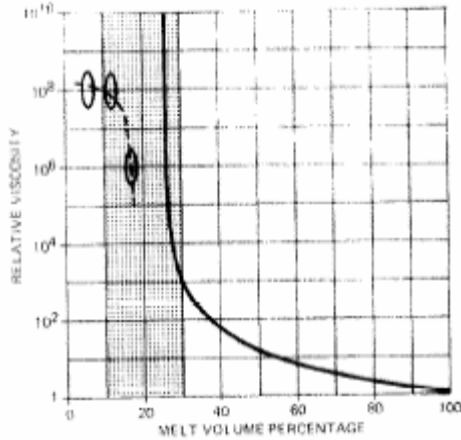
(dashed curve is Westerly Granite data) (Arzi, 1978). More realistic is to consider interactions among the solid particles, and melt/solid interaction. The idea of a rheologically critical melt percentage (RCMP) is based on the idea that at some melt fraction the solid particles will be forced to interact and produce a load-supporting framework.

A more realistic RCMP for uniform grain sizes is ~40%, corresponding to the 'random packing density', where particles *begin* to interact. This number will be smaller if the grain sizes are non-uniform. Cataclastic flow with minimal dislocation glide. Melt is drawn from grain boundaries of all orientations to grain boundaries parallel to the compression direction.
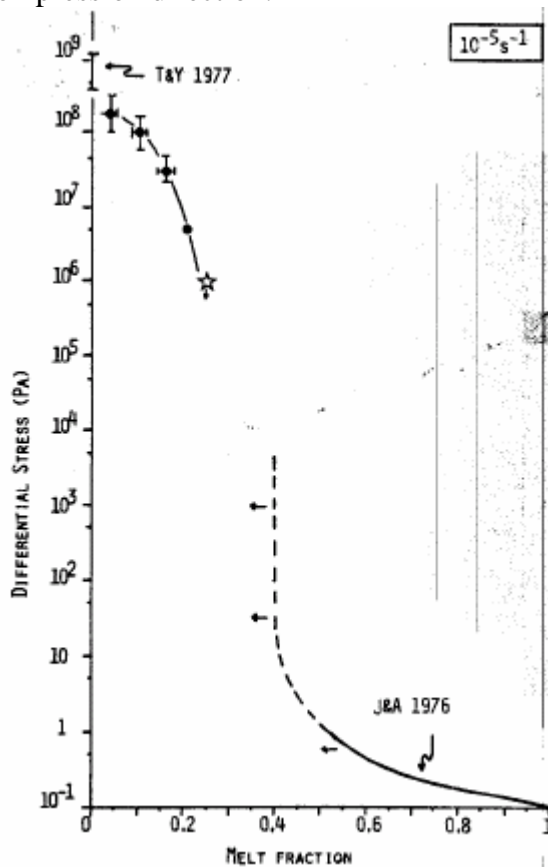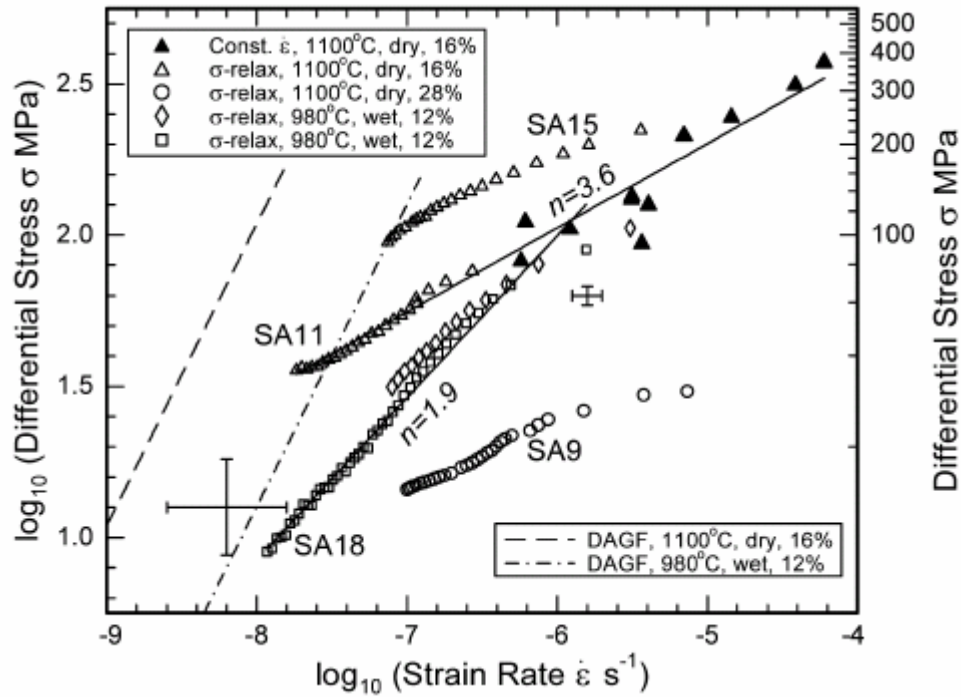
(van der Molen & Paterson, 1979)
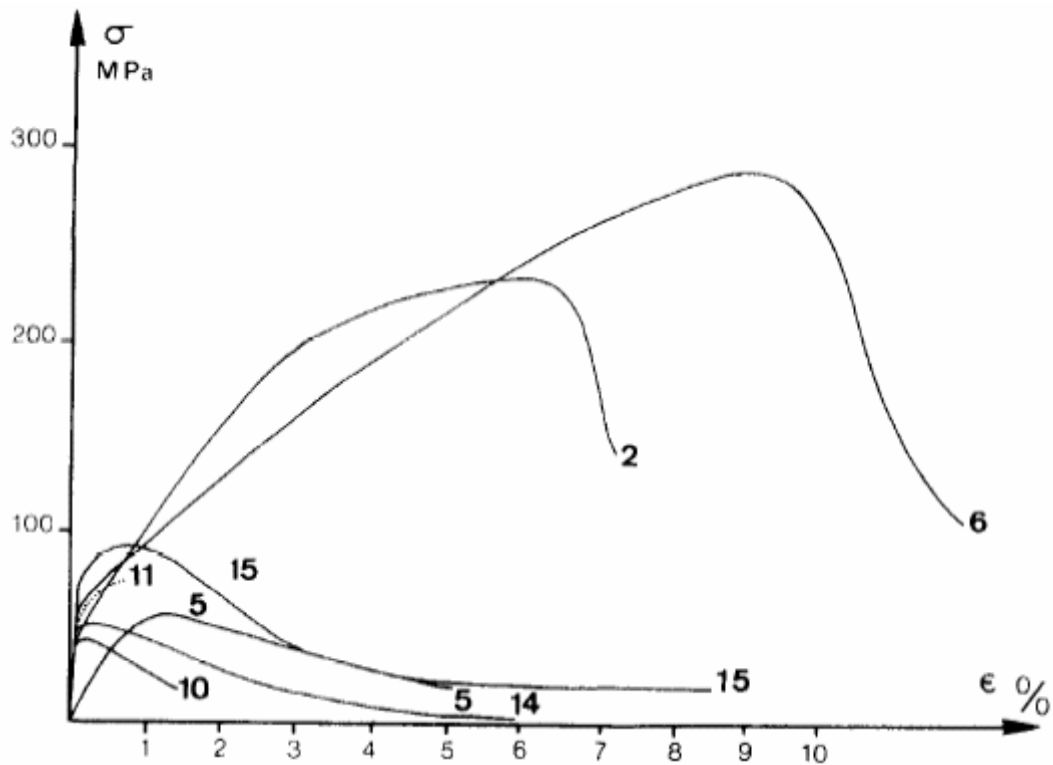
partially molten aplite (Paquet et al., 1981)
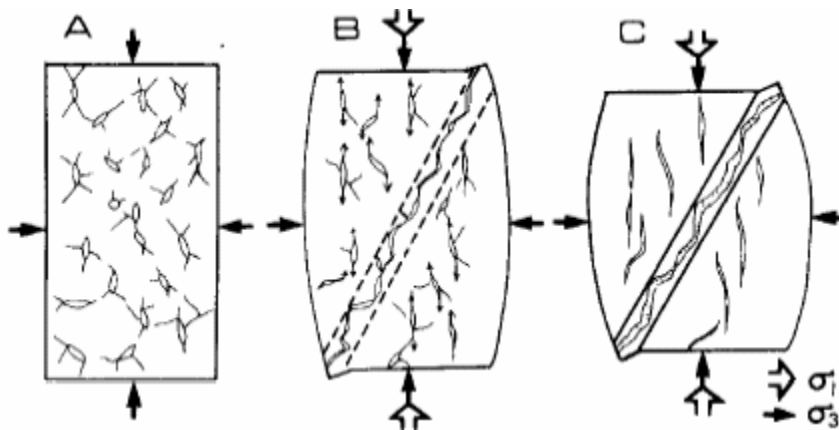
textural evolution of partially melted sample during shortening (Paquet et al., 1981)

deformation can cause melt to change from isolated triple-junction pockets to grain boundaries (Gleason et al., 1999)

Melting causes 'melt-fracturing' at low T and diffusion enhancement at high T

36

partially molten synthetic granite shows n > 1, suggesting that cracking or dislocation motion, and not diffusion, controls the deformation (Mecklenburgh & Rutter, 2003)

37

Electron Back-Scatter Diffraction (EBSD)
Electromagnetic radiation (light, electricity, magnetism) is an energy wave that is composed of an electric field component and a magnetic field component. The electric and magnetic fields oscillate at right angles to each other and the combined wave moves in a direction perpendicular to both of the electric and magnetic field oscillations.
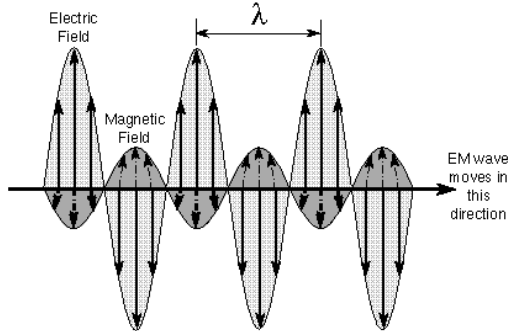
Electromagnetic waves travel through a vacuum at 2.99792E8 m/s (the speed of light).

In the early part of the 20th century Albert Einstein found a relationship between the energy of a light wave and its frequency:

$E = h\nu = hc/\lambda$

where h is the Planck constant (6.62618E-34 J s), ν is frequency, c is the speed of light, and λ is wavelength.

Scanning electron microscopy

In the SEM, a beam of electrons is scanned across a specimen surface in synchrony with a cathode ray tube (CRT) display. Interaction between this beam and the specimen results in a variety of emission signals. Different detectors within the SEM monitor the intensity variation of these emission signals, which determines the observed image intensity (contrast).

A typical SEM consists of an electron gun; a narrow central column down which electrons pass through a sequence electromagnetic lenses, beam defining apertures and a set of scan coils; and a specimen chamber which also houses detectors required to collect the various signals emitted from the target specimen.


Electron Gun.   Electron Lenses.
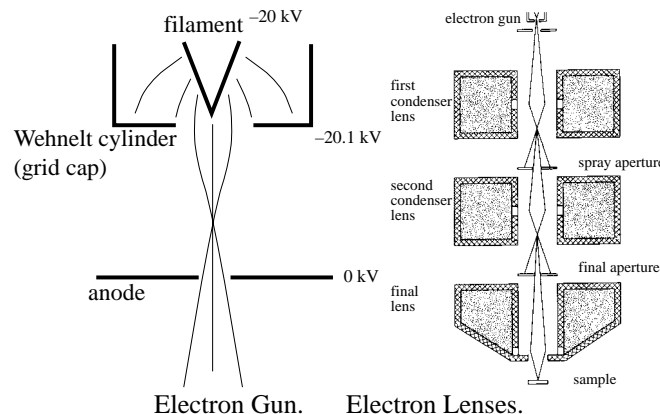
Electron–Optical Column

The source of electrons consists of an electron gun, which is most commonly a tungsten wire heated to 2700K which gives off electrons by thermionic emission. The electrons accelerate toward an anode (held at positive bias of typically 5–15 kV) and then pass through a series of electromagnetic lenses that refine the size and shape of the beam. Each lens consists of a wire coil, through which an electric current is passed, wound on an iron core with a central hole (the optic axis) through which the electron beam passes. The minimum size of the beam is controlled mainly by spherical aberration, which results because electrons far from the optic axis travel farther than those on axis and are bent differently by the lenses; as described below, the minimum beam size is always smaller than the effective beam size. (Other kinds of lens aberration are chromatic aberration, in which electrons of different accelerating voltages (wavelengths) are bent different amounts by the lens; and astigmatism, which is anisotropy in the lens.) The current reaching the sample is measured by a Faraday cup, which is typically a piece of carbon inserted temporarily into the beam path. Any images generated will be sharpest when the beam is focused exactly on the sample surface.

Sample–Beam Interaction
Electrons that hit a sample penetrate some distance into the sample before either bouncing elastically off of a nucleus, being deflected by nuclei or being absorbed by losing energy in (a series of) collision with valence electrons. The pathway followed by electrons in a material thus looks somewhat chaotic but depends on the energy of the incident electrons and the atomic number of the material. It is this pathway that dictates the effective size of the beam on/in the sample.
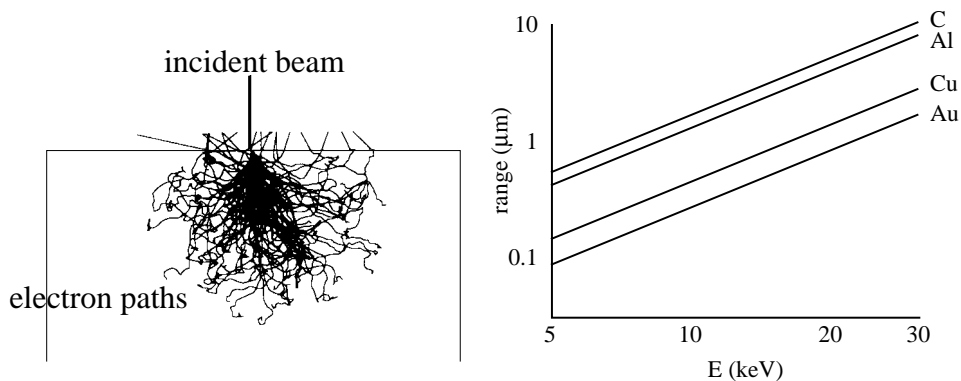
Sample–Beam Interaction.   **Sample Penetration By Beam.**

Image Formation
The beam is rastered (or swept) across the sample by deflection-scan coils situated within the final lens. The scanned electron beam dwells on a point on the specimen surface for an instant, determined by the scan rate. During this time, the electrons interact with the specimen, resulting in a number of very different emission signals. At any one instance, there is only one ray between the gun and the specimen. If a CRT is scanned in synchronism with the scanned electron beam, each CRT picture element (pixel) is equivalent to an individual point on the specimen surface. Thus, the brightness observed for each pixel is determined by the intensity of the electron-specimen emission signal at each point on the specimen. This results in an image of the specimen, the exact nature of

which depends on the characteristics of the electron-specimen interaction and emission signal.

Magnification of an specimen image in the SEM is a very simple process. Whereas the area of specimen scanned by the electron beam can be easily varied from several mm^2 to only a few mm^2, the size of the CRT screen remains constant. nevertheless, the one-to-one relationship between specimen point and CRT pixel is maintained, resulting in magnification of the specimen image as the area scanned is reduced. The lowest magnification is limited by the distance over which the beam can be rastered without distortion of the image; the maximum magnification is governed by the diameter of the beam and beam–sample interactions.

Secondary Electron Imaging
Incident electrons collide elastically with valence electrons, producing 'secondary' electrons (generally defined as those with energies <50 eV). Some fraction of these secondary electrons near the sample surface will escape the sample and can be collected on a detector and used to form an image. Because of the very low energies of secondary electrons, only those formed within the upper few nm of the sample surface can actually escape and form an image.
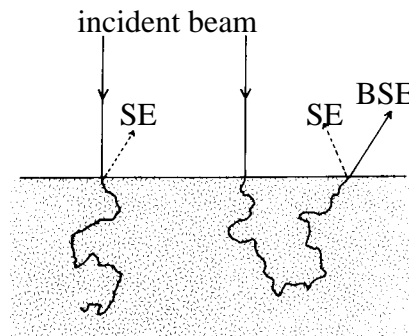
Secondary and back-scattered electrons.

Back-Scattered Electron Imaging
Some electrons hitting a sample will miss all the electrons of an atom and strike the nucleus. Because of the huge difference in mass between the electron and the nucleus, the electron will ricochet off elastically with very little energy loss. Some fraction of these electrons will ricochet free of the sample. These 'back-scattered' electrons can be collected on a detector and used to form an image. The fraction of incident electrons that leave the sample via elastic interactions with nuclei depends on atomic number. Because of the high energies of back-scattered electrons, those 'formed' within the upper μm of the sample surface can actually escape and form an image.
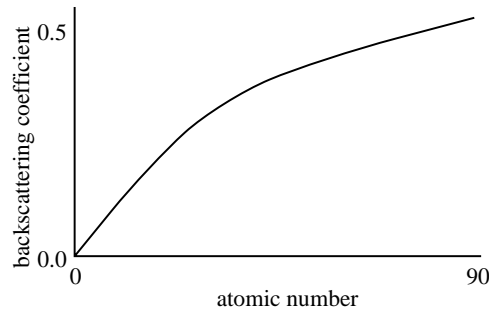
Fraction of BSE depends on atomic number.

Diffraction

Diffraction arises from constructive interference of coherent radiation, typically x-rays or electrons. When radiation is scattered elastically off the surface of a crystal (which has 3D periodicity), in certain directions the scattered rays may be in phase and interfere constructively; this is diffraction.
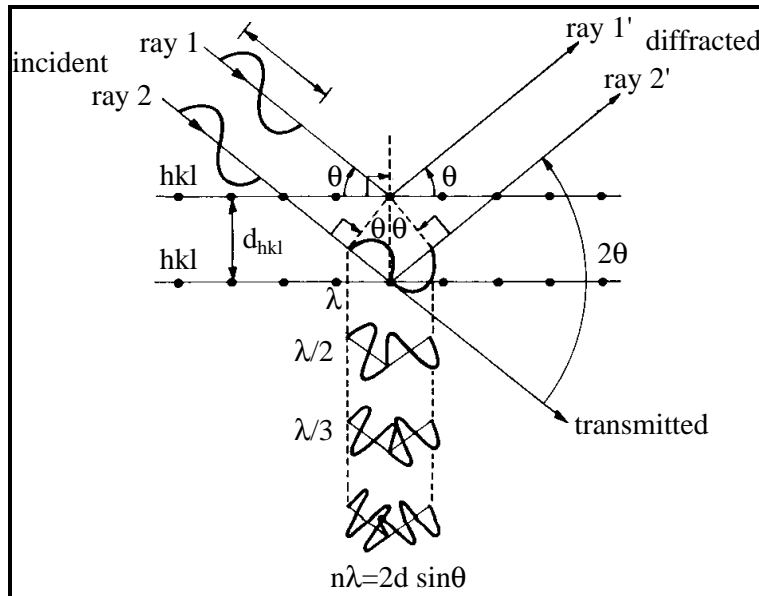
Diffraction of radiation by the periodic structure of a crystal.

The conditions for diffraction are:

1) the angle θ between the diffracting (hkl) plane and the incident beam is equal to the angle between the diffracting (hkl) plane and the diffracting beam;
2) the incident beam, diffracted beam, and normal to the diffracting plane are coplanar
3) rays scattered from successive (hkl) planes differ in path length by an integral number of wavelengths.

This relationship is described by Bragg's Law:

$n\lambda = 2d_{hkl}sin\ \theta$

where n is the order of the diffracted beam, d is the interplanar spacing of the (hkl) planes, and θ is the angle between the incident beam and the diffracting planes.

The Reciprocal Lattice

How could you create a representation of the diffraction properties of a 3D crystal without simply drawing all the possible diffracting planes and labeling their interplanar **d** spacings and their interplanar angles? You might, for example, want to represent all the orientations to which a diffractometer must be rotated to access all the diffractions coming from a 3D crystal. It seems like the representation of the diffraction properties of a 3D object must be something with three dimensions. Rather than draw each plane, we can simplify by using a vector orthogonal to the plane to represent each plane; the magnitude of each vector is chosen to be d_{hkl}—or the spacing between the (hkl) planes.

d_{110} is a vector drawn from the origin perpendicular to the plane and equal in magnitude to the lattice spacing.

Unfortunately, using d_{hkl} vectors and starting them all from the origin results in severe crowding of the higher order planes:

A two-dimensional section of vectors perpendicular to planes with magnitude equal to the interplanar spacing.
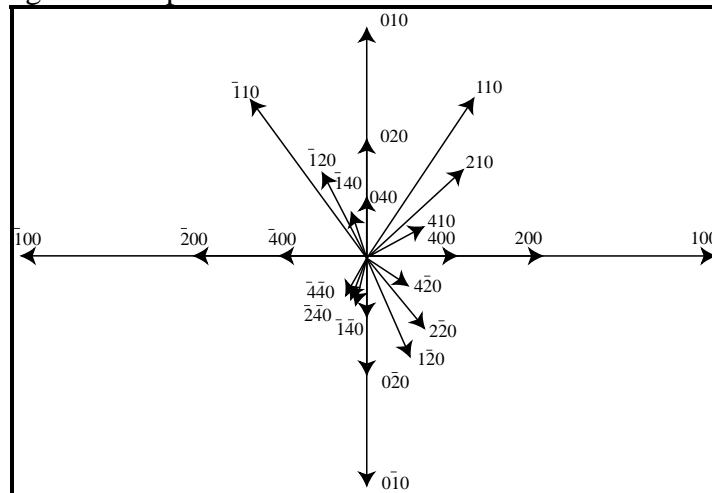
If instead we plot only the tip of each vector and choose the magnitude of each vector as $d^*_{hkl} = 1/d_{hkl}$, we get a manageable and surprisingly orderly representation of the diffraction symmetry of the crystal.

So, we can easily determine where to orient a diffractometer to get a particular diffracted beam: the positions are in Å^{-1} and the reciprocal angles differ from the real angles by 180°. Conversely, if we can generate a reciprocal lattice by diffraction, we can determine the diffraction symmetry of the crystal.
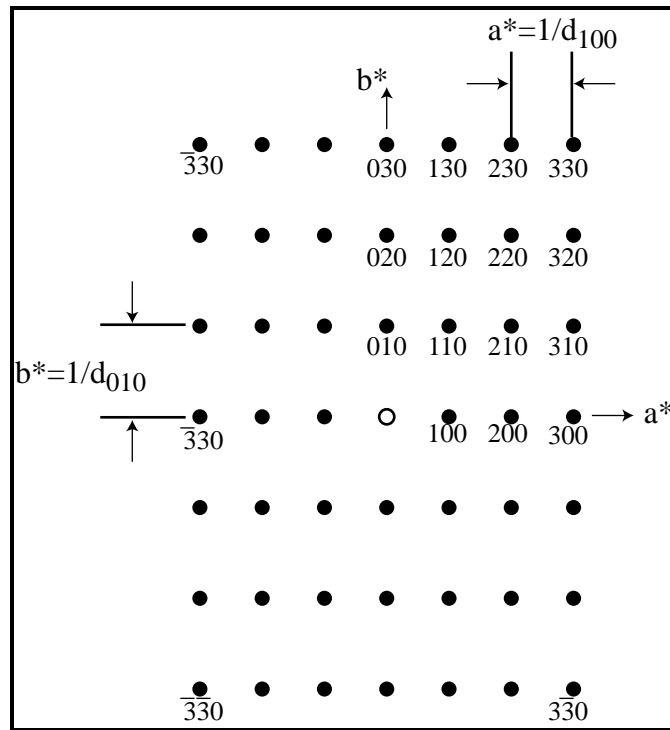
The reciprocal lattice for an orthorhombic [001] zone.
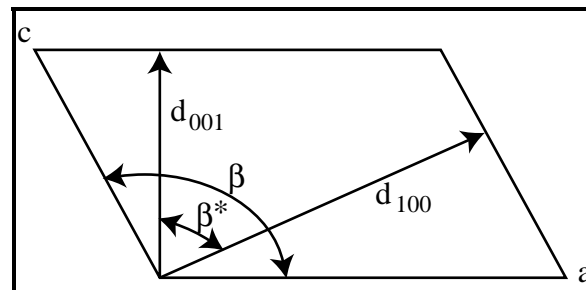
The *ac* plane of a monoclinic cell showing the relation between the lattice vectors and d_{hkl} vectors.

Kikuchi Lines

Normal TEM diffraction patterns composed of reciprocal lattice reflections are produced by electrons scattered elastically from the material. As the crystal thickness increases, however, more primary beam electrons lose small amounts of energy (50 eV) via interaction with the sample, producing a broader diffraction spot. Eventually, the crystal becomes so thick that the electrons are essentially rediffracted within the crystal as if they were at a new point source.
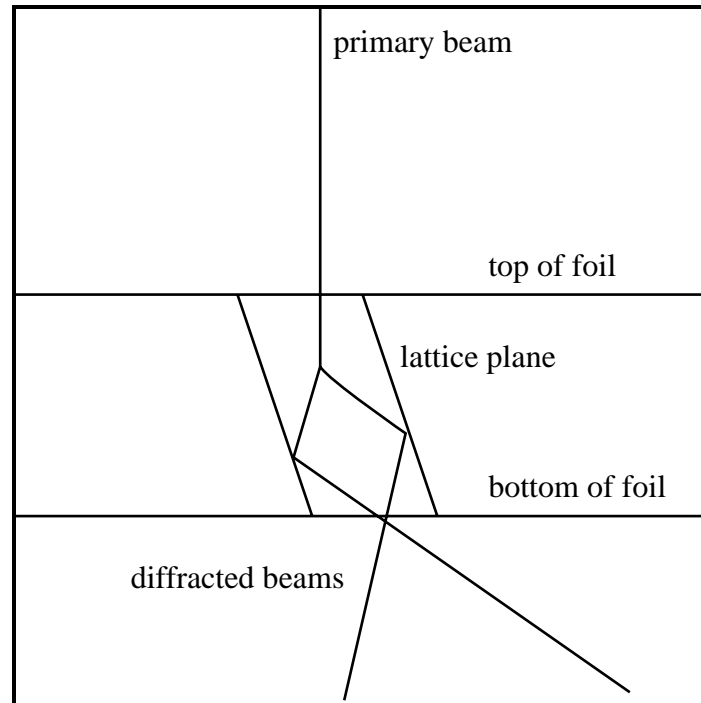
Cross-section of geometry of diffraction to form Kikuchi lines.

The electrons scattered inelastically then diffract, producing lines (that are weakly curved), rather than spots. These Kikuchi lines can be indexed to give crystal lattice orientation information.

Electron Back Scatter Diffraction

A second technique that takes advantage of Kikuchi lines is electron back scatter diffraction (EBSD). In this technique, electrons that are back-scattered off a sample at a shallow angle are analyzed for crystal orientation information. The sample is prepared either by electropolishing or colloidal silica (0.02 µm) polishing and then placed in an SEM. The primary beam is directed onto the sample surface and electrons that diffract off the surface are collected by a CCD camera and passed to software that indexes the Kikuchi lines to determine the orientation of the crystal (using a Hough transform, which transforms lines into points).The sample is moved beneath the beam to make a complete orientation map of the sample down to the scale of the electron beam (~1 µm).
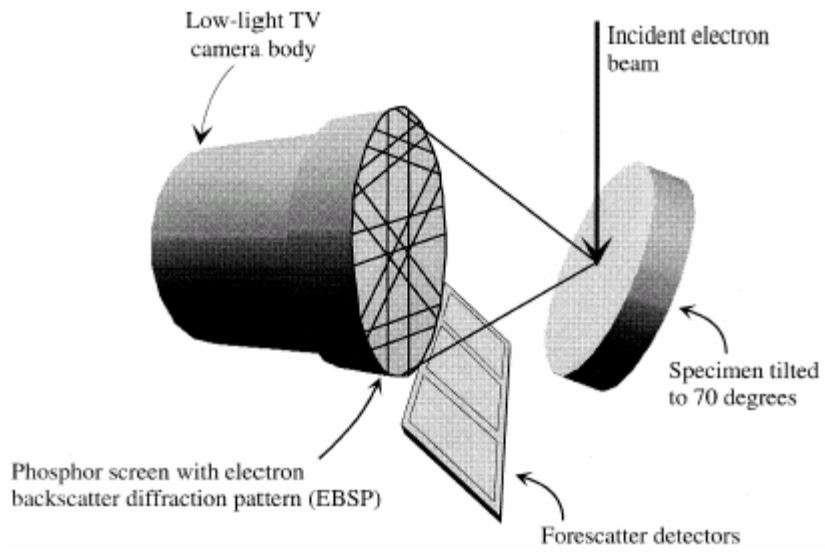
(Prior & Trimby, 1999)
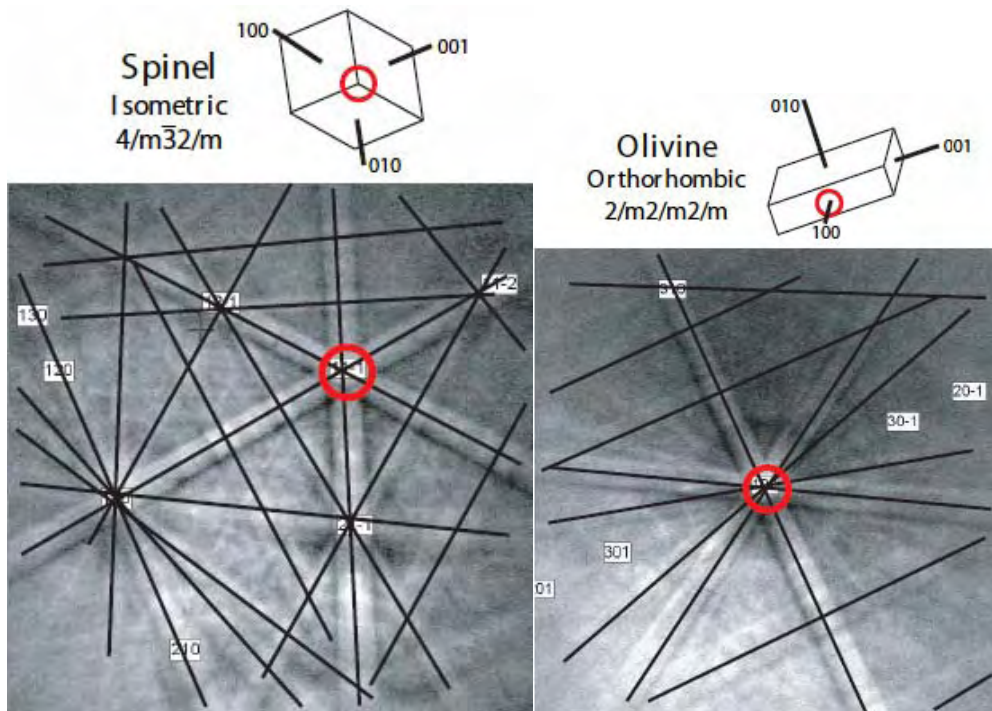
(from Luc Mehl)
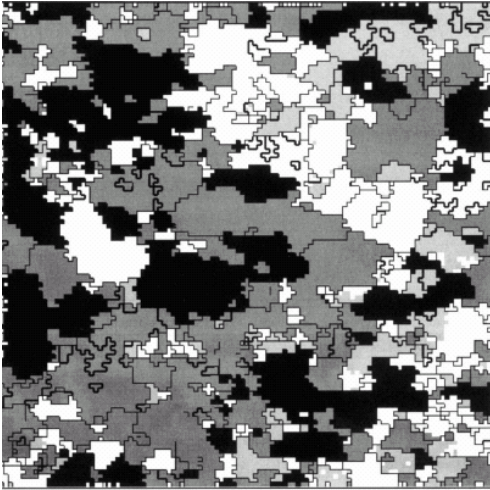
grains and subgrains (Neumann, 2001)
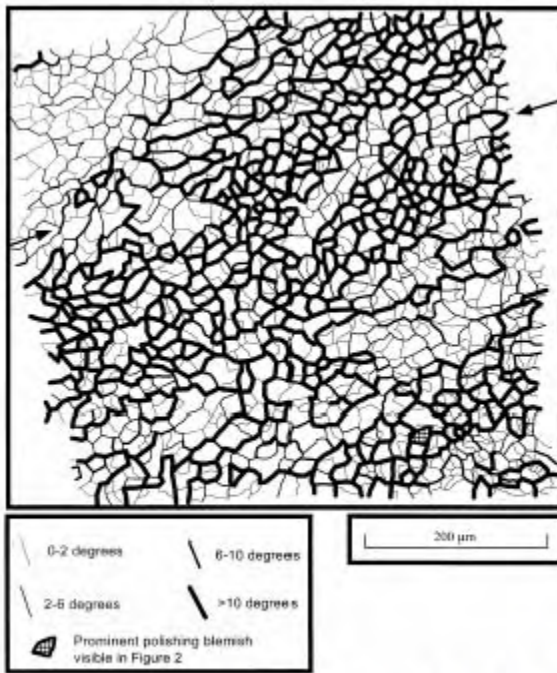
Fig. 3. Misorientation map of the area shown in Fig. 2. The
misorientation map (Prior & Trimby, 1999)
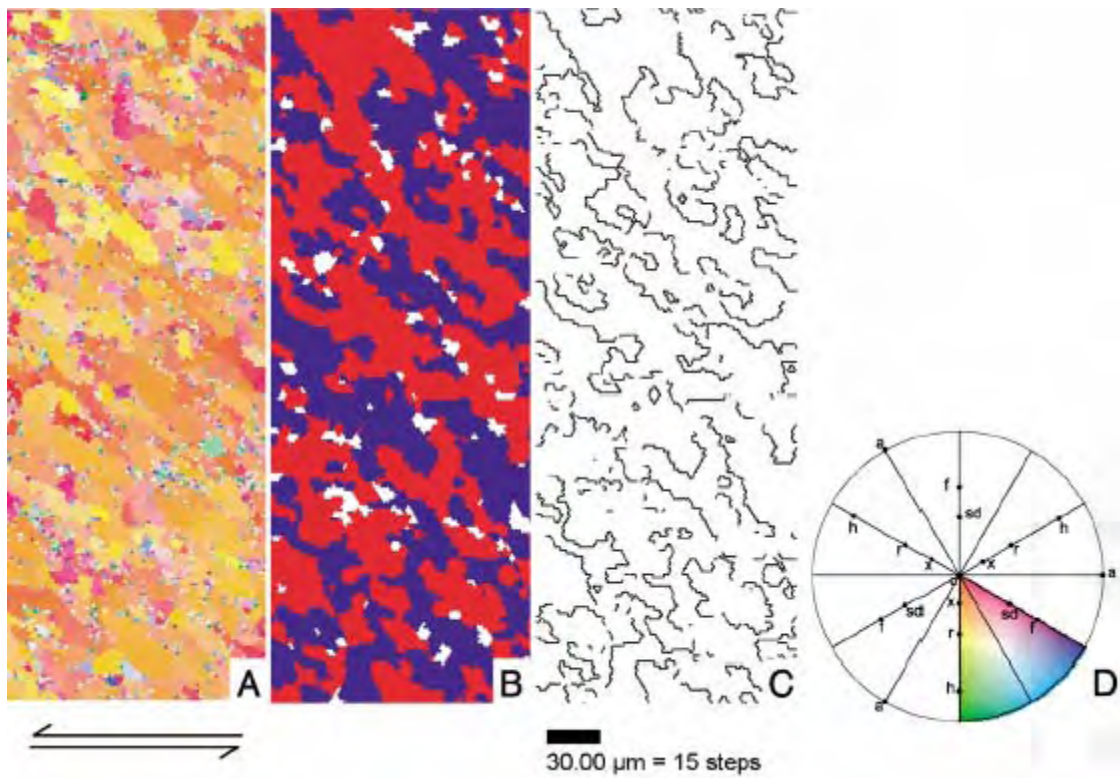
calcite torsion (Barnhoorn et al., 2004)
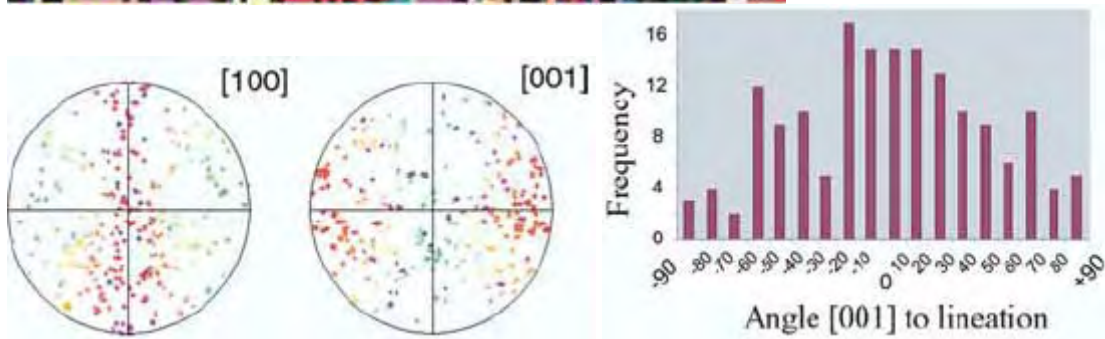
olivine (Frese et al., 2003)
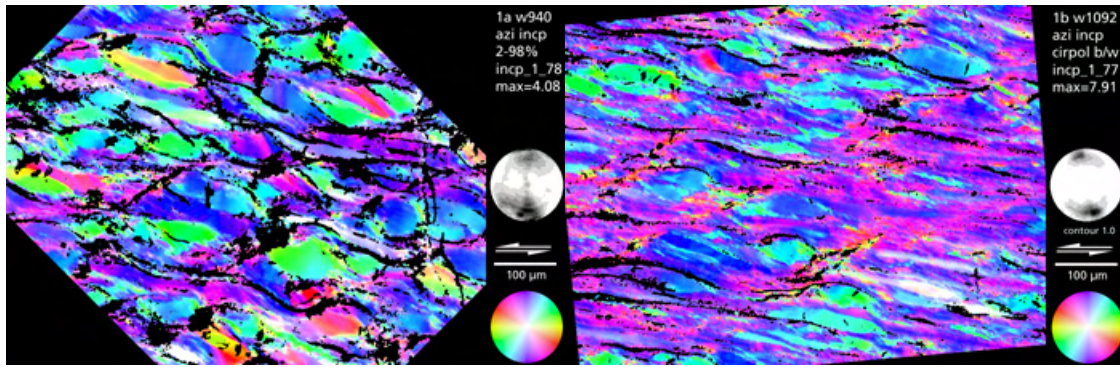
Regime 1, high and low strain (http://pages.unibas.ch/earth/micro/)
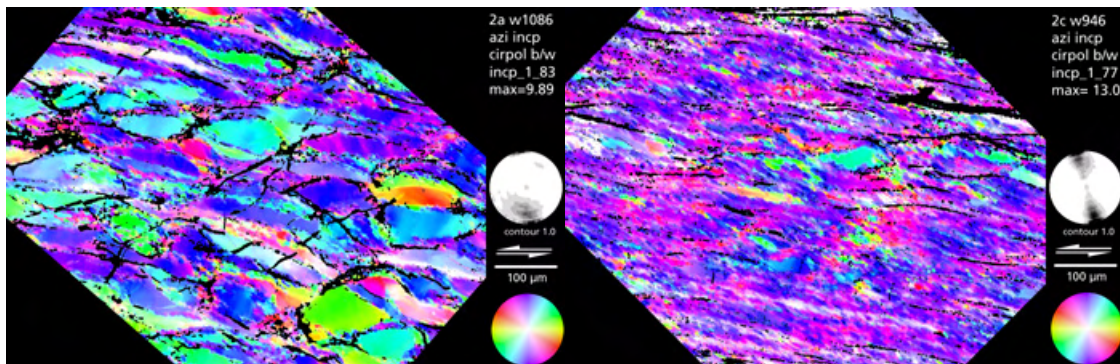
Regime 2, high and low strain (http://pages.unibas.ch/earth/micro/)
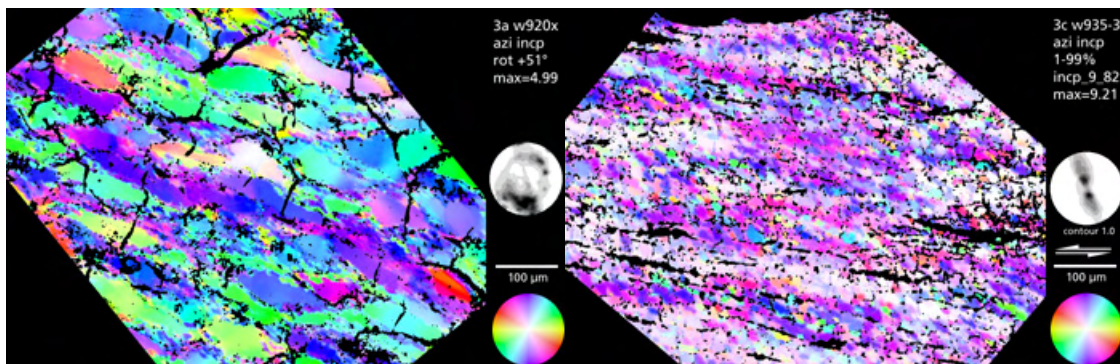
Regime 3, high and low strain (http://pages.unibas.ch/earth/micro/)
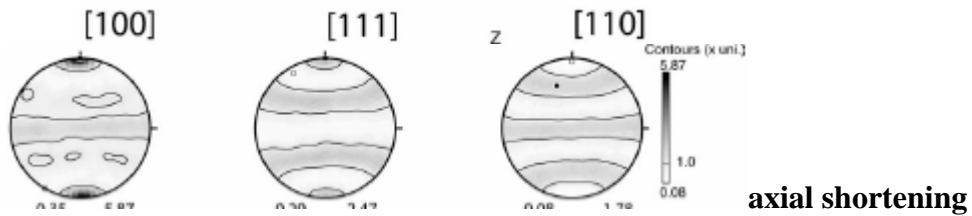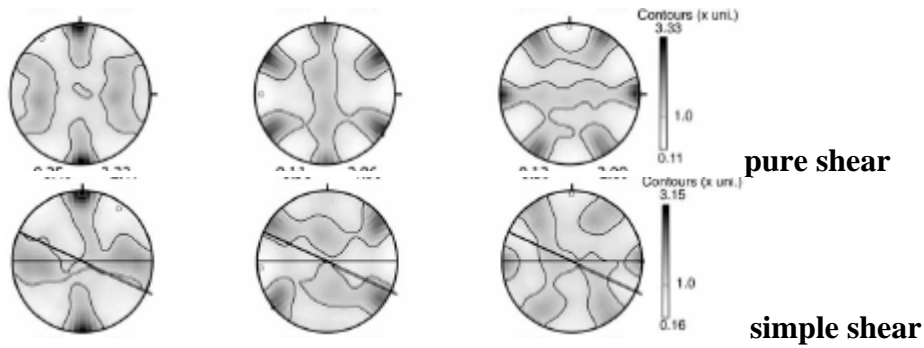
Garnet Lattice Preferred Orientations

axial shortening

pure shear

simple shear

There are 66 possible slip systems in garnet, with <111>{110} the most common. Calculated LPOs for garnet (Mainprice et al., 2004).
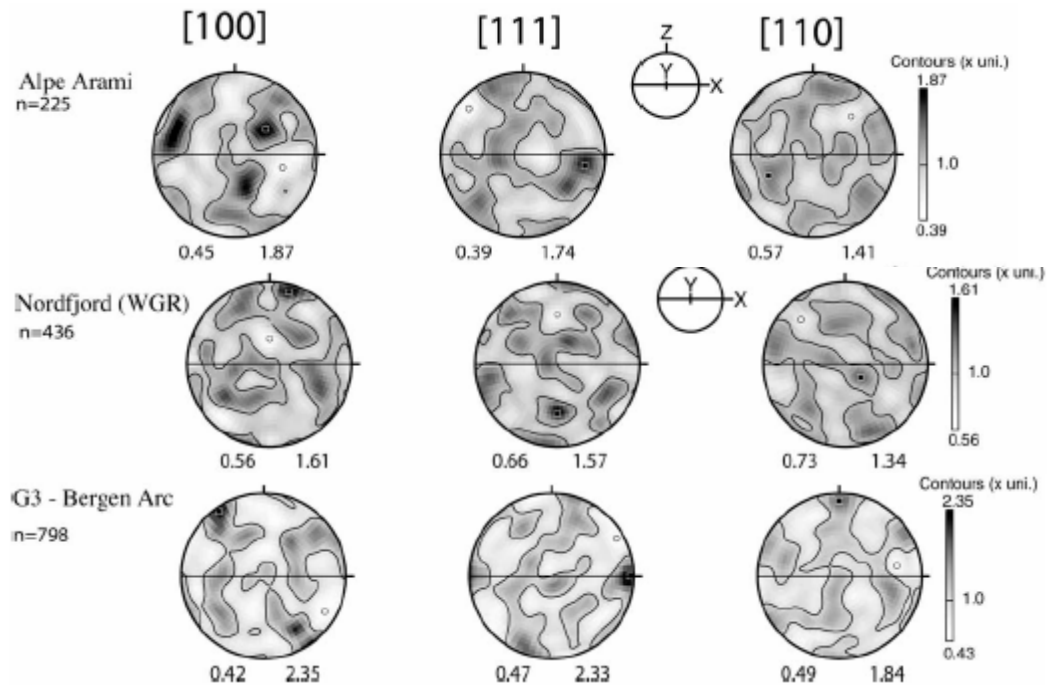
Natural garnet fabrics are weak implying grain boundary sliding or simply reflecting the abundance of garnet slip systems (Mainprice et al., 2004).

Rayleigh–Taylor Instabilities and the Strength of the Mantle
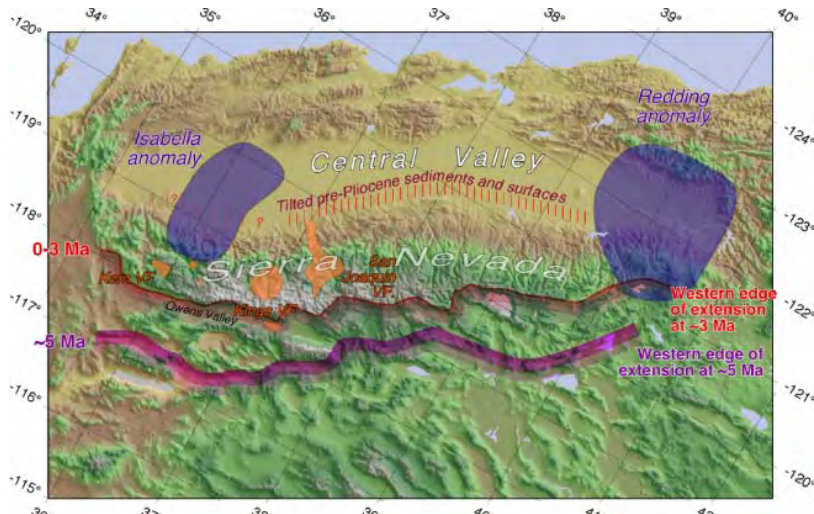
Xenoliths erupted show eclogitic +garnet clinopyroxenite root to Sierra Nevada persisted until ~10 Ma when it was replaced at ~3.5 Ma by spinel peridotite. Sierra Nevada is remarkably cold; if heat flow plus xenolith temperatures of 925°C at 130 km are extrapolated, the Miocene lithosphere was ~190–200 km thick. This lithosphere would have been ~200 kg/m^3 denser than underlying asthenosphere.
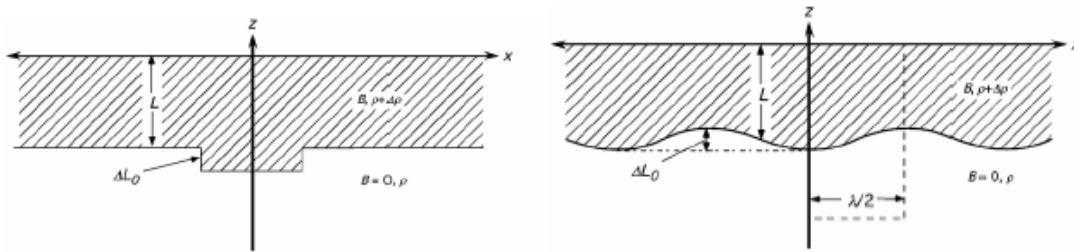
(Molnar & Jones, 2004). Rayleigh–Taylor instabilities are counteracted by thermal diffusion and the nonlinear relationship between stress and strain rate; if the instability can grow fast enough it can be treated as a R–T instability.
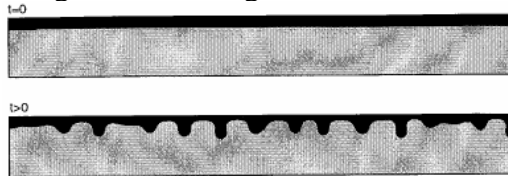
(Jull & Kelemen, 2001). Consider a power law

$$\tau_{ij} = B\dot{E}^{(1-n)/n}\dot{e}_{ij}$$

where $\dot{E}$ is the second invariant of the strain-rate tensor $\dot{e}_{ij}$:

$$\dot{E}^2 = 0.5\Sigma_{i,j}\dot{e}_{ij}\dot{e}_{ij}$$

$$B = A^{-1/n}\exp\left(\frac{Q}{nRT}\right)$$

and dimensionless time and distance are:

$$t' = \frac{t}{(B/\Delta\rho gL)^n}$$

$$L' = z/L$$

The effective viscosity becomes

$$\eta = \frac{B}{2}\dot{E}^{(1-n)/n}$$

or

$$\eta = \frac{\sigma}{\dot{\varepsilon}} = \sigma^{(1-n)}A^{-1}\exp\left(\frac{Q}{RT}\right)$$

for dislocation creep.
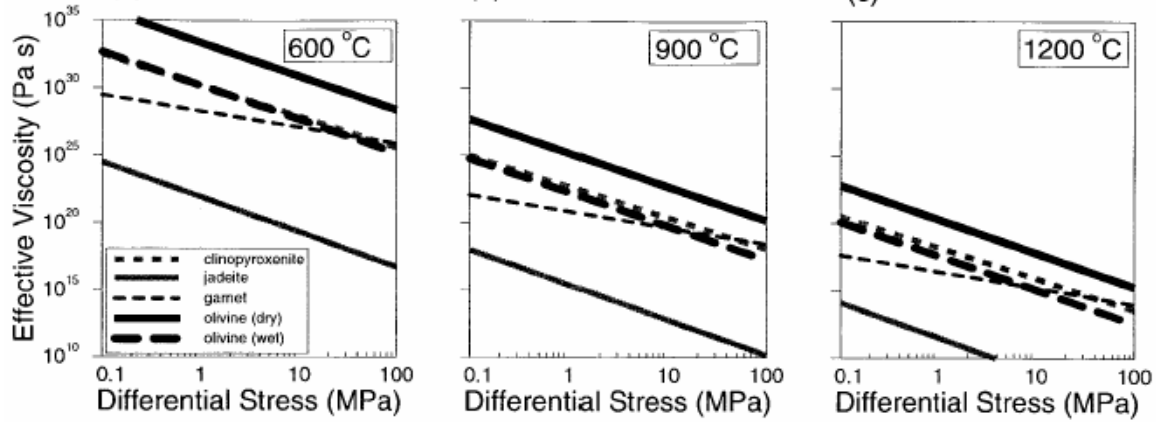
(Jull & Kelemen, 2001).

For a layer of Newtonian viscosity with a perturbation of ΔL_o:

$$\Delta L'(t') = \frac{\Delta L'_o(1 + \tanh(t'/4))}{1 - (1 + \Delta L'_o)\tanh(t'/4)}$$
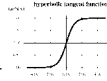
This equation goes blows up when $(1 + \Delta L'_o)\tanh(t'/4) = 1$. We can rewrite this to show *when* this blow up occurs as

$$t'_b(\Delta L'_o) = 4\tanh^{-1}\left(\frac{1}{(1 + \Delta L'_o)}\right) = 2\ln\frac{2 + \Delta L'_o}{\Delta L'_o}$$

Because we know that this time is ~7 Ma, this can be recast as viscosity:

$$\eta = \frac{\Delta\rho g L t_b}{4\ln\dfrac{2 + \Delta L'_o}{\Delta L'_o}}$$

For $\Delta L'_o = 0.01$, 0.1 or 1 (i.e., 1.6, 16 and 160 km), $v = 3.3$–16 x 10^{21} Pa s. The same can be done for nonlinear rheology:
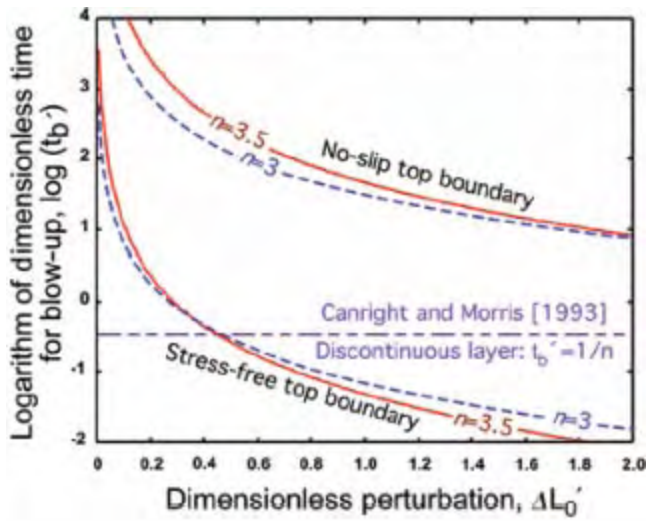
indicating B values of 0.8–5.6 x 10^{12} Pa s$^{1/3.5}$ (Molnar & Jones, 2004)
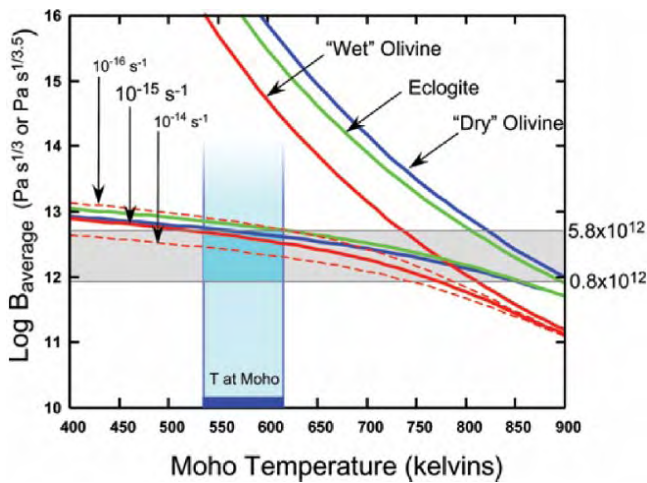
Coincidence between the calculated B values and an extrapolation of the high-stress olivine creep law of Evans 7 Goetze (1979) for 10^{-14}–10^{-16} s^{-1} gives confidence that the flow law and the R–T rationale are OK. This corresponds to stresses of 40–290 MPa (Molnar & Jones, 2004)

For convective instability of the base of an arc,
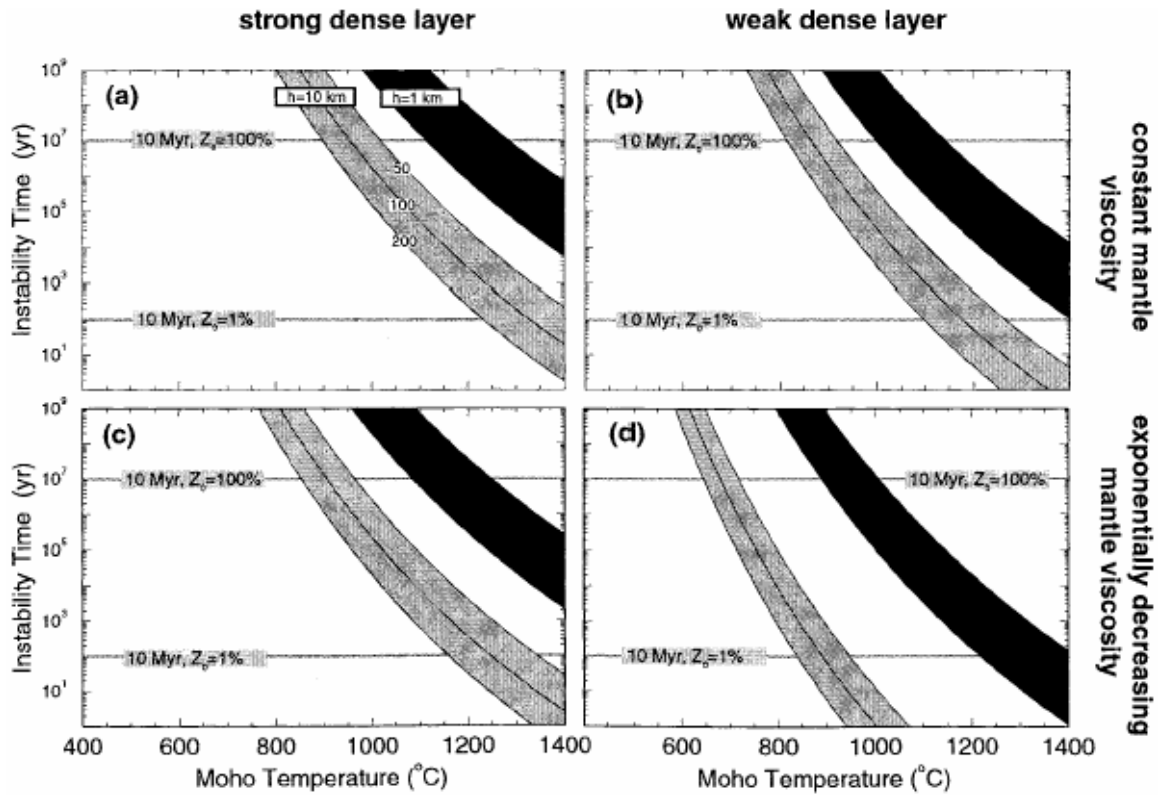
Instability time for various layer thicknesses, viscosity ratios and viscosity profiles. 1 and 10 km thick dense layers with $\Delta\rho = 50$, 100, and 200 kg/m^3. Upper panels constant mantle viscosity, lower panels exponentially decreasing viscosity; left panels for equal viscosities in dense layer and asthenosphere; right layers for dense layer with 1% of the viscosity of the asthenosphere (Jull & Kelemen, 2001)
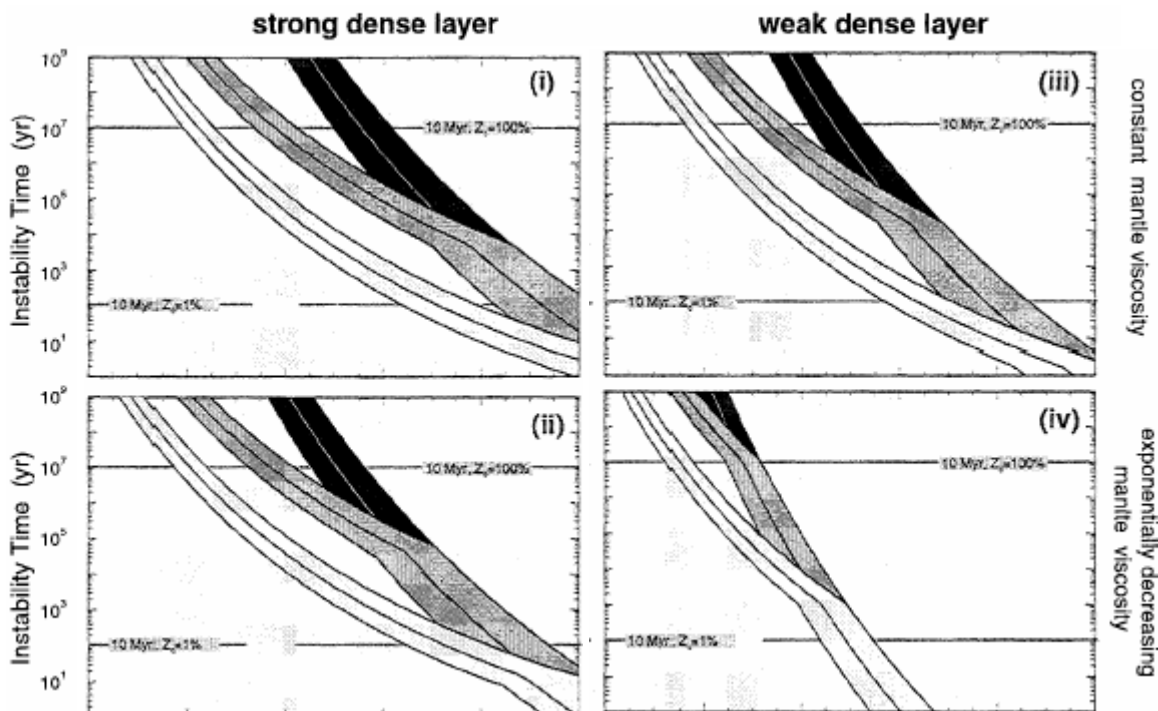
| 400 | 600 | 800 | 1000 | 1200 | 1400 | | 600 | 800 | 1000 | 1200 | 1400 |

Moho Temperature (°C)   Moho Temperature (°C)

Same for coincident horizontal strain rates of $10–14$ s^{-1} (white), $10–18$ s^{-1} (grey) and zero (black) and a layer thickness of 10 km (Jull & Kelemen, 2001)

Shear-Wave Polarization and Olivine Fabrics
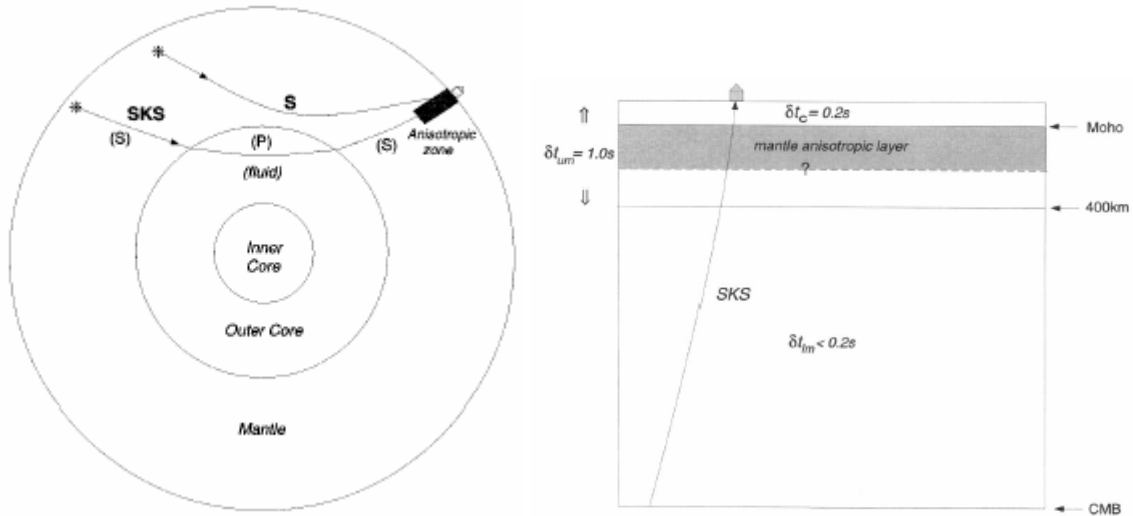
(Silver, 1996)

(after Luc Mehl)

(Park & Levin, 2002)

GPS velocities (Schmid et al., 2001)

shear wave splitting (Schmid et al., 2001)
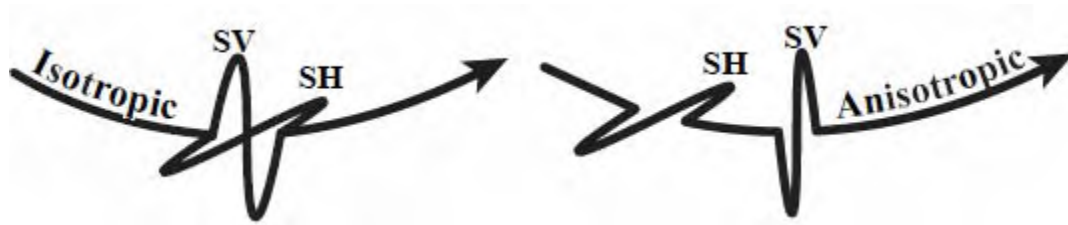
fast directions turn parallel to Tonga arc axis (Smith et al., 2001)
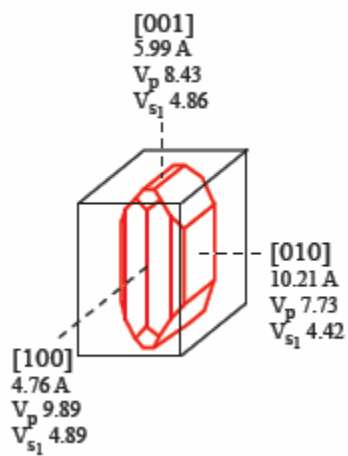
olivine wave speeds (after Luc Mehl)
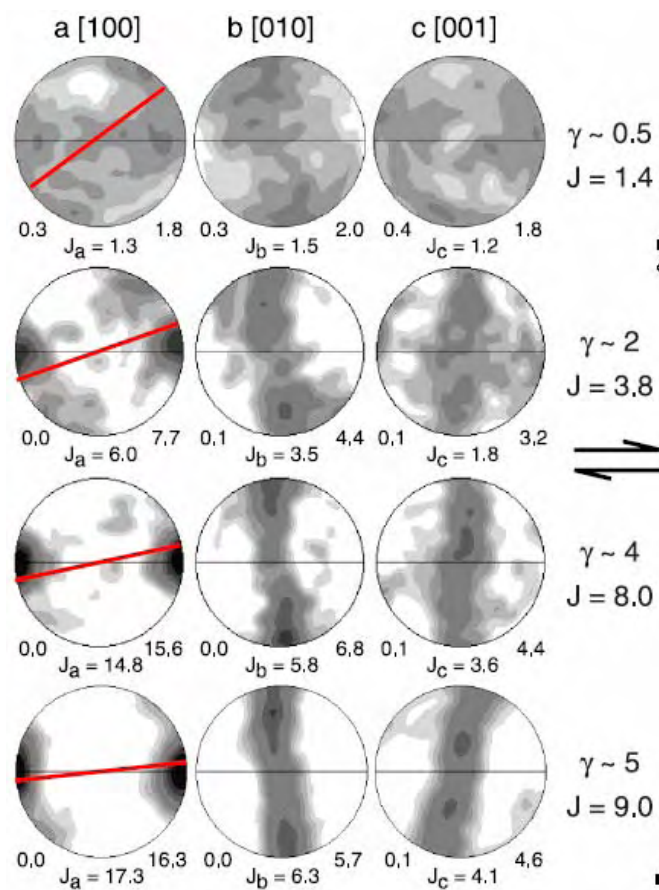
reminder that olivine axes track the shear direction, even for small strains (Bystricky et al., 2001)
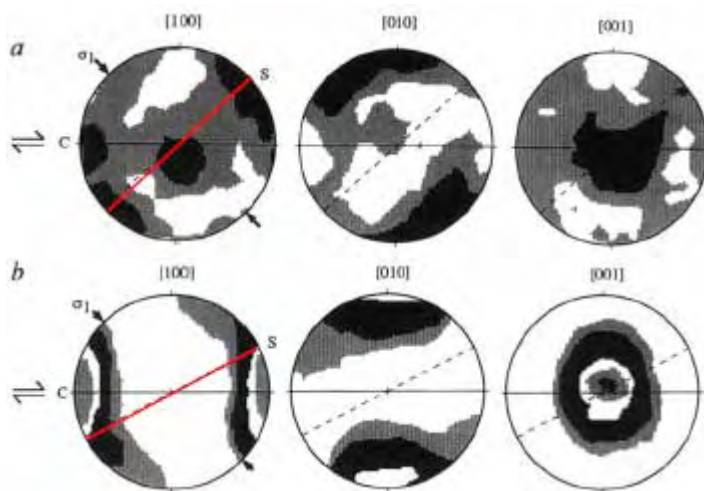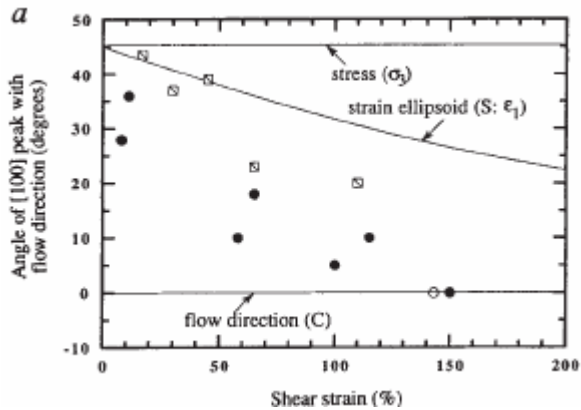
At small strains, [100] and [010] are close to the finite strain axes, whereas at strains >50% they are closer to the flow direction. This is a function of recrystallization, such that strain may not be the right way to compare this to the mantle. Note that [001] is invariant regardless of strain magnitude (Zhang & Karato, 1995)
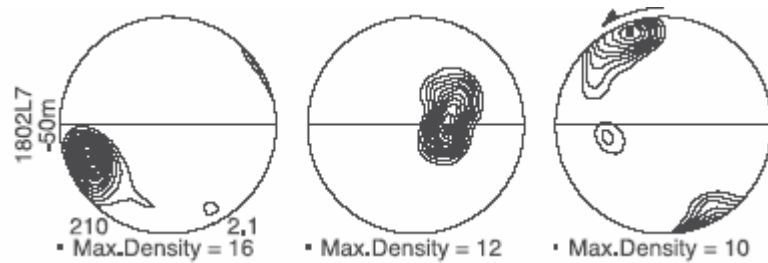
measured olivine LPO (Mehl et al., 2003)
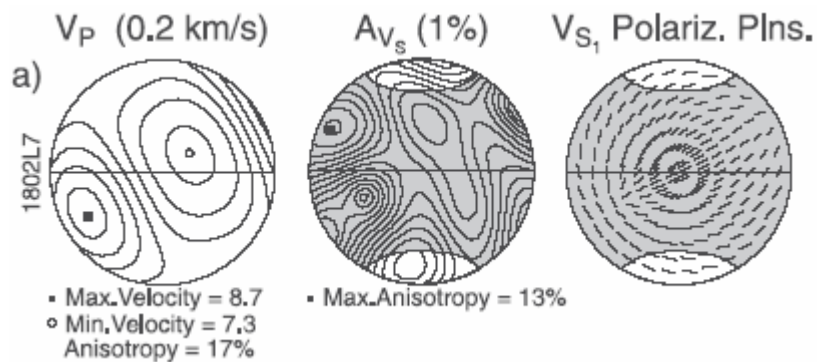
calculated P-wave anisotropy, S-wave anisotropy, and polarization directions; white circles indicates shear-wave window (Mehl et al., 2003)
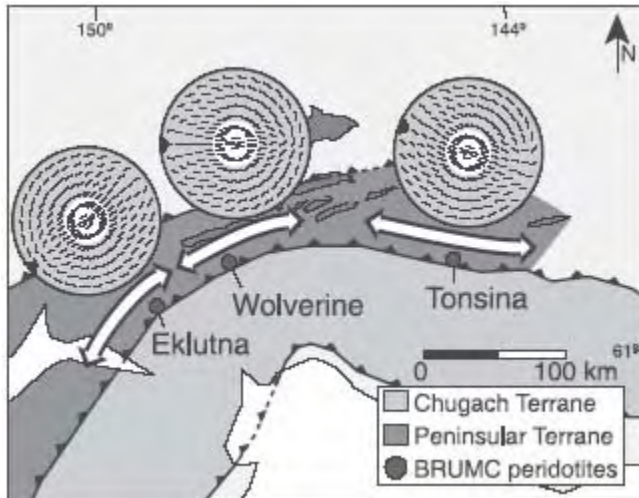
shear-wave polarization planes are parallel to axis of Talkeetna Arc (Mehl et al., 2003)
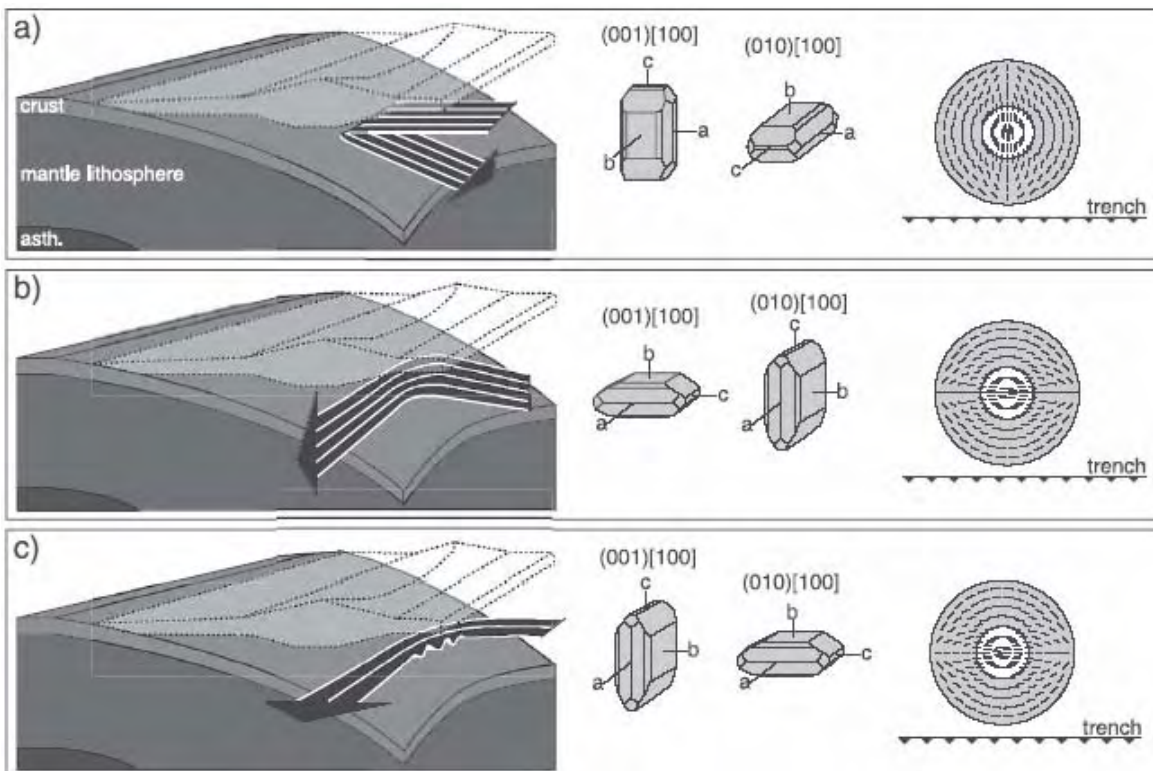
without information about active slip system, anisotropy measurements are equivocal (Mehl et al., 2003)
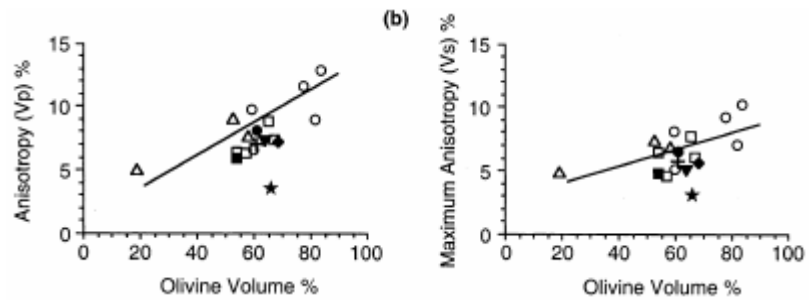
anisotropy also depends on proportion of olivine (Saruwatari et al., 2001)

Late-Breaking News
Effect of H₂O on the Strength of Calcite
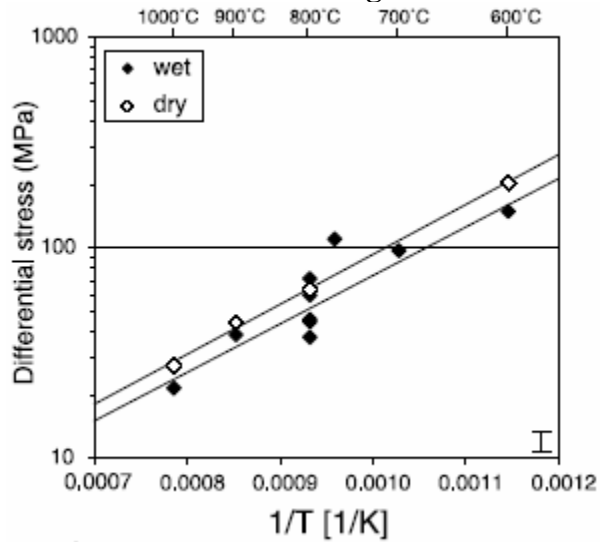
Addition of H₂O has little effect on strength of marble (De Bresser et al., 2004).
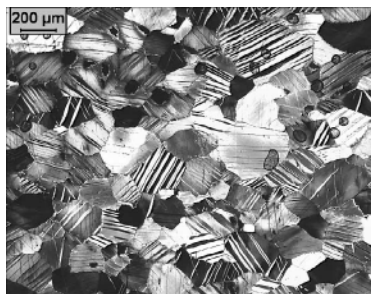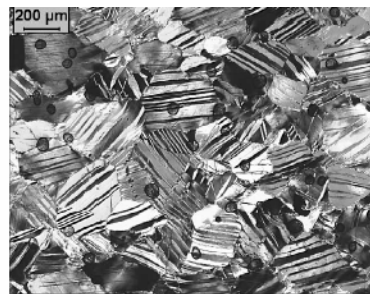
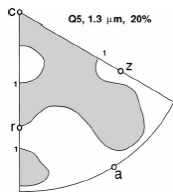600°C - Dry   600°C - Wet
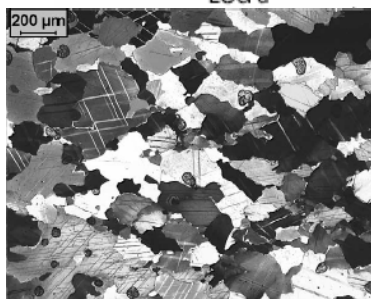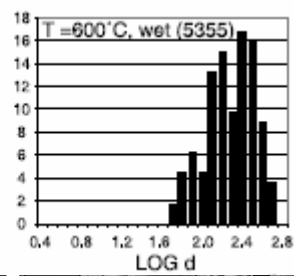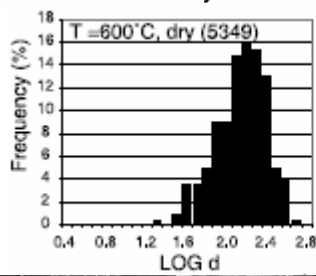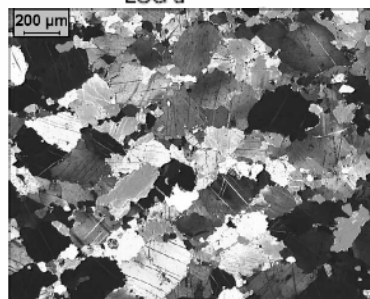
1000°C - Dry   1000°C - Wet
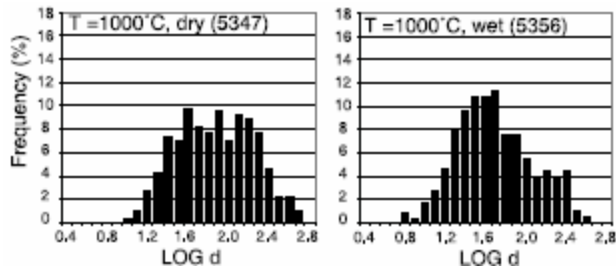
Addition of H₂O has little effect on texture of marble (De Bresser et al., 2004).

Diffusion Creep in Quartzite
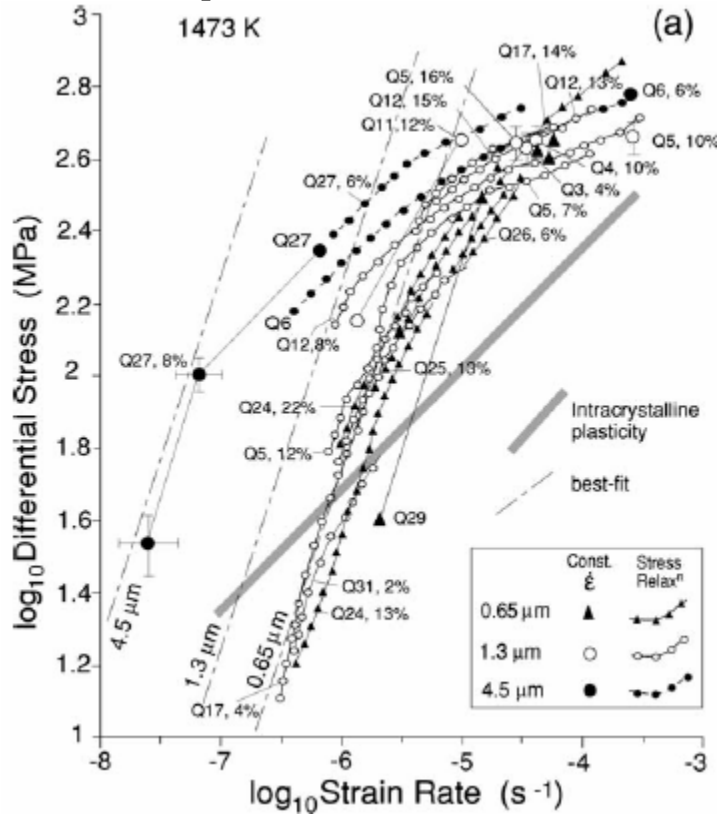
Experiments on sintered quartz at 1200°C show dislocation creep at $>10^{-6}$ s^{-1} (gray line) and diffusion creep at slower strain rates (dashed lines). The diffusion creep can be fit with

$$\dot{e} = 10^{-0.4 \pm 2.1} \sigma^{1.0 \pm 0.14} \exp\left(-\frac{220 \pm 55 kJ / mol}{RT}\right) d^{2.0 \pm 0.75}$$

fine-grained rocks show no LPO.
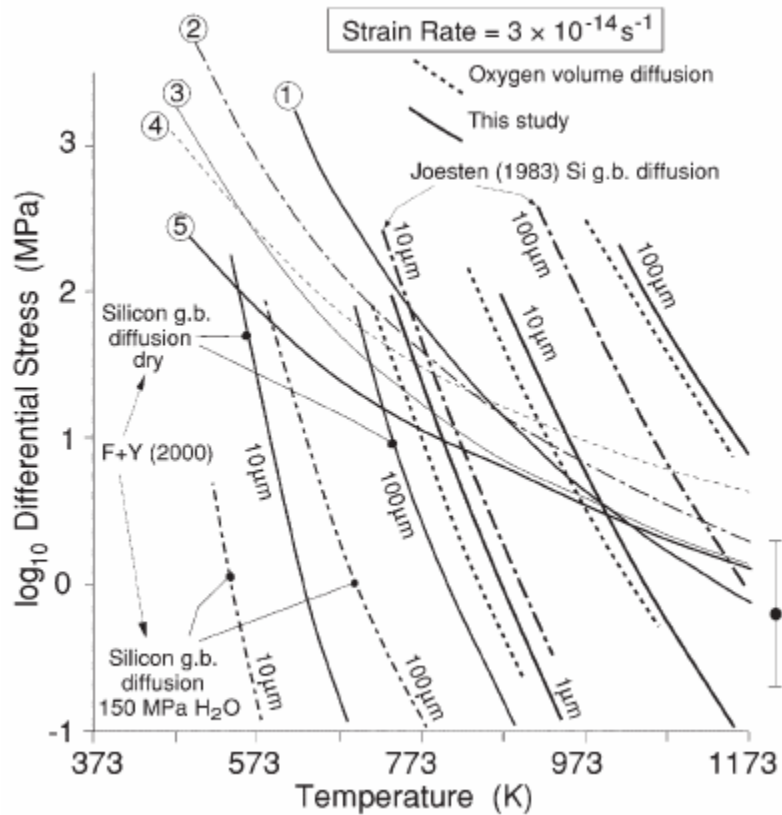
Extrapolation suggests GSS creep in quartz should only be important at >500 °C and <1 µm (Rutter & Brodie, 2004). (1,2,3,4,5 various dislocation creep laws; solid lines from this study).

The Importance of Grain-Size Variation: Calcite

Existing flow laws predict that calcite mylonites should be in the GSS creep field, but microstructural observations indicate that they deformed under GSI conditions.
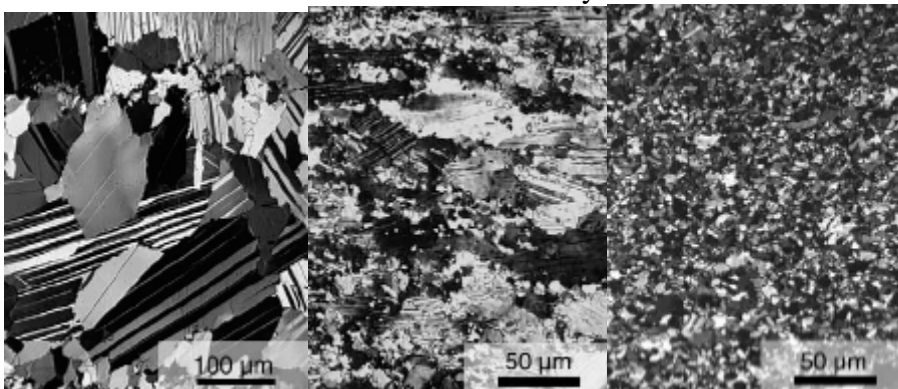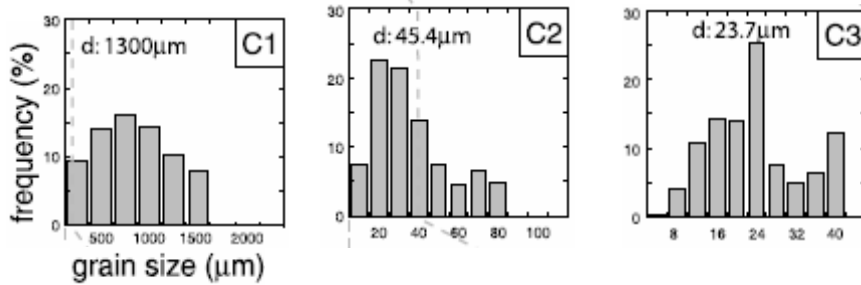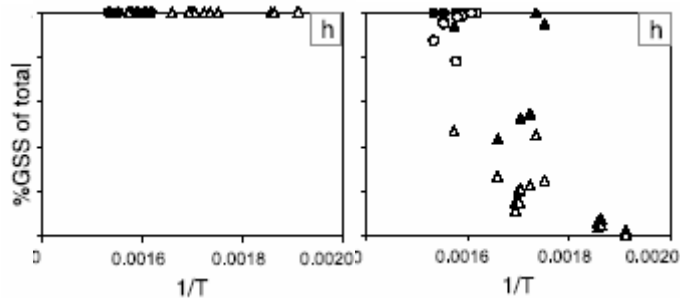
Calcite mylonites in the Swiss Alps deformed at 10^{-12} s^{-1} and 250–380°C (Herwegh et al., 2005). Grain-size reduction proceeded via comminution, SGR recrystallization and GBM recrystallization.
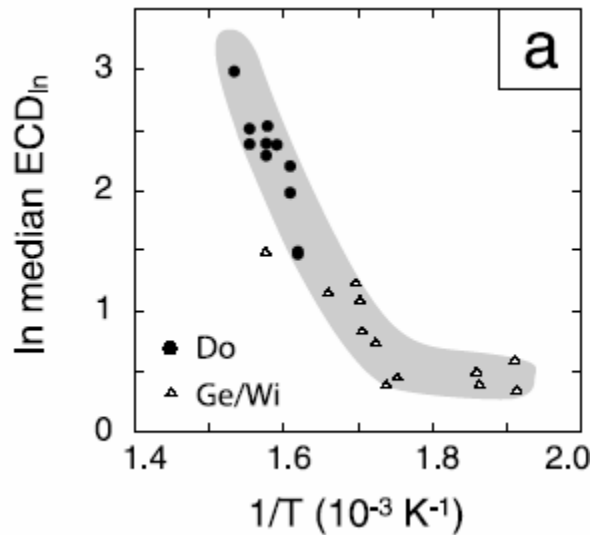
Grain size varies as a function of temperature at different localities within the mylonites.

The relative influences of GSS and GSI creep can be predicted using the cross-slip controlled creep equation of de Bresser et al. (2002) and the diffusion creep equation of Walker et al. (1990) or Herwegh et al. (2003). If only mean grain sizes are considered (left), flow laws suggest deformation entirely by GSS creep, whereas if the range of grain sizes is considered (right), flow laws suggest a mix of GSI and GSS creep (Herwegh et al., 2005).

The Importance of Grain-Size Variation: Olivine
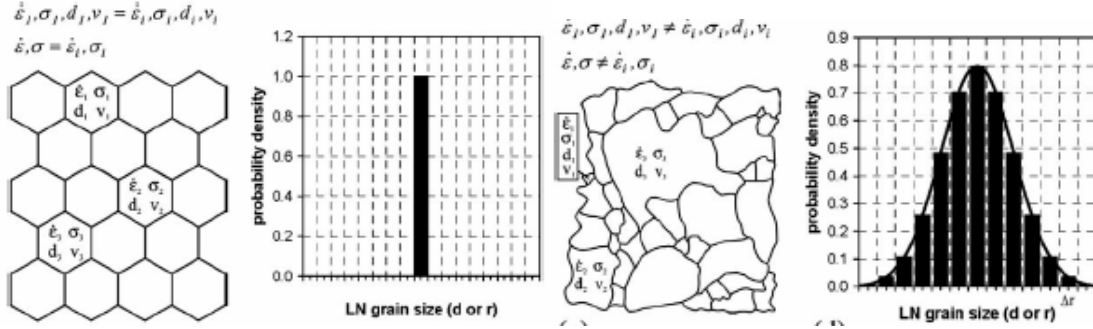
Important to consider real grain size distribution in rocks (Ter Heege et al., 2004).

Combine dislocation creep

$$\dot{e} = \frac{A_{disl} b D_{disl} \mu}{kT} \left(\frac{\sigma}{\mu} \right)^n$$

and diffusion creep

$$\dot{e} = \frac{A_{diff} b D_{diff} \mu}{kT} \left(\frac{b}{d} \right)^m \left(\frac{\sigma}{\mu} \right)$$

flow laws to get

$$\dot{e} = \frac{A_{diff} b D_{diff} \mu}{kT} \left(\frac{b}{d} \right)^m \left(\frac{\sigma}{\mu} \right) + \frac{A_{disl} b D_{disl} \mu}{kT} \left(\frac{\sigma}{\mu} \right)^n$$

Assume a log-normal distribution of grain sizes. Either assume same stress in all grains such that strain rates varies:

$$\dot{e} = \frac{A_{diff} b D_{diff} \mu}{kT} \left(\frac{b}{\exp[(3-0.5m)\Phi^2]d_{median}} \right)^m \left(\frac{\sigma}{\mu} \right) + \frac{A_{disl} b D_{disl} \mu}{kT} \left(\frac{\sigma}{\mu} \right)^n$$

or same strain rate in all grains such that stress varies:

$$\dot{e} = \left\{ \left[\frac{A_{diff} b D_{diff} \mu}{kT} \left(\frac{b}{\exp[(3+0.5m)\Phi^2]d_{median}} \right)^m \left(\frac{\sigma}{\mu} \right) \right] + \left[\frac{A_{disl} b D_{disl} \mu}{kT} \left(\frac{\sigma}{\mu} \right)^n \right] \right\} \left\{ \frac{1}{1-F} \right\}$$

where

$$F = \exp(\alpha + \beta \bar{\sigma}^{*0.5} \ln(\bar{\sigma}^*) + \gamma \ln(\bar{\sigma}^*)^2$$

and

$$\bar{\sigma}^* = \frac{\sigma}{\left(\frac{A_{diff} D_{diff}}{A_{disl} D_{disl}} \right)^{\frac{1}{n-1}} \left(\frac{b}{\exp[(3+0.5m)\Phi^2]d_{median}} \right)^{\frac{m}{n-1}}}$$

and α, β, and γ follow a table such as

Standard deviation	Expression $\alpha = (a + be^{-n})^{-1}$	Expression $\beta = a + bn$	Expression $\gamma = (a + b/n^2)^{-1}$
0.1	a = −0.335	a = 1.13082	a = 0.2339
	b = 0.4619	b = −0.5664	b = −19.96
0.2	a = −0.581	a = 0.6056	a = 0.1760
	b = 1.203	b = −0.3515	b = −25.93
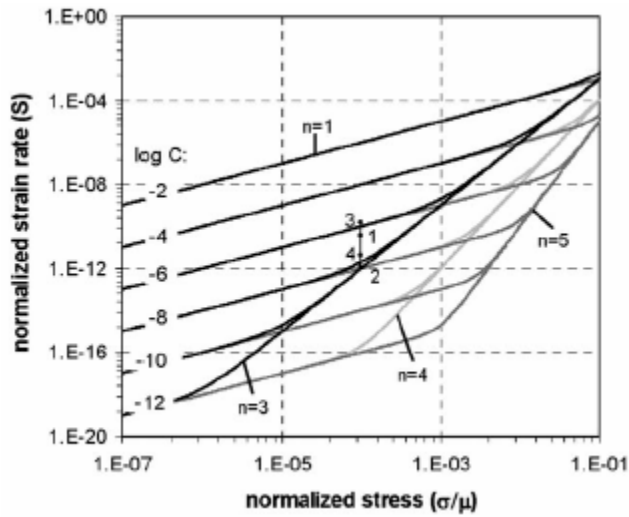
The deformation mechanism map obtained using a single grain size (for n = 3,4,5) and contoured in $C = \dot{e}_{diff} \Big/ \dot{e}_{disl}$ differs considerably from
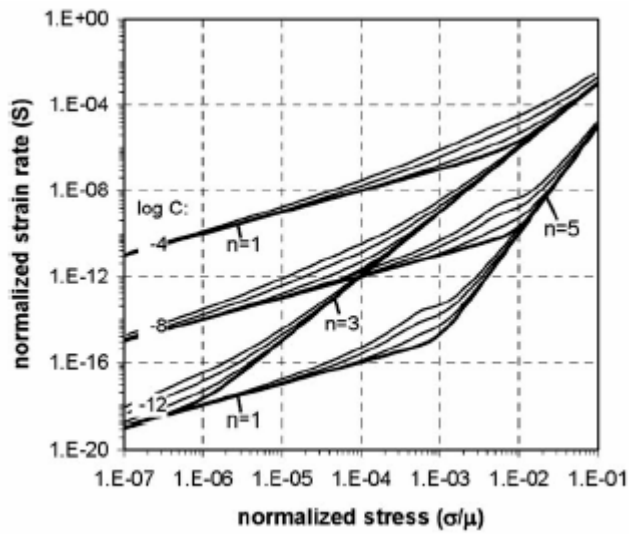

the deformation mechanism map obtained using distributed grain size (thin lines are constant strain-rate model; thick lines are constant-stress model) (Ter Heege et al., 2004).
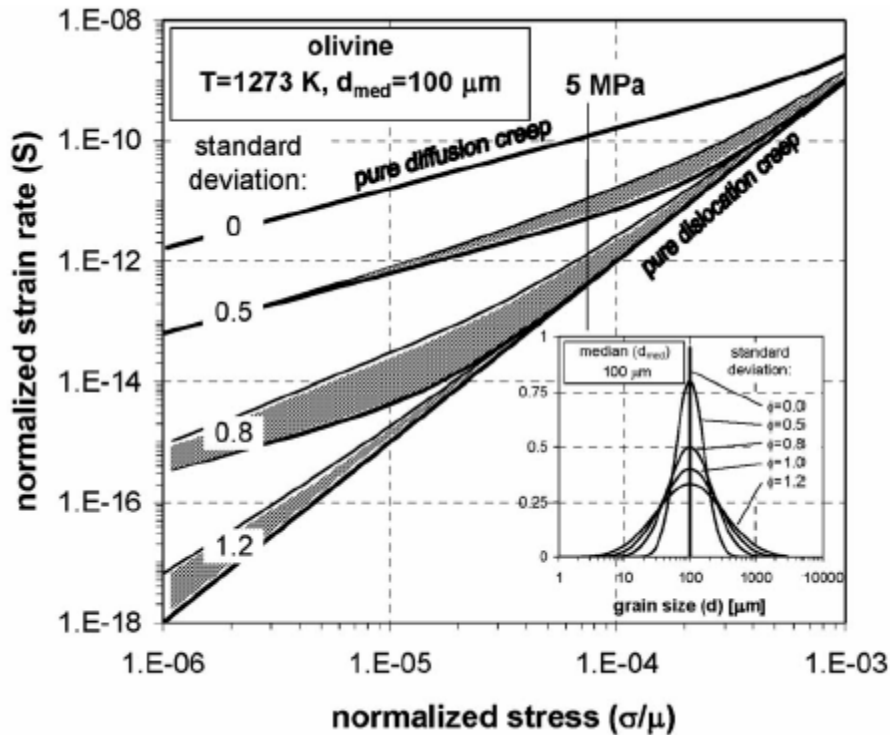
If there is a range of grain sizes rather than a single grain size (inset), this leads to a range of behaviors from pure diffusion creep ($\phi = 0$) to pure dislocation creep ($\phi = 1.2$) (Ter Heege et al., 2004).

H$_2$O-Induced Olivine Slip (Type "B"; Katayama et al., 2004) [001](010)
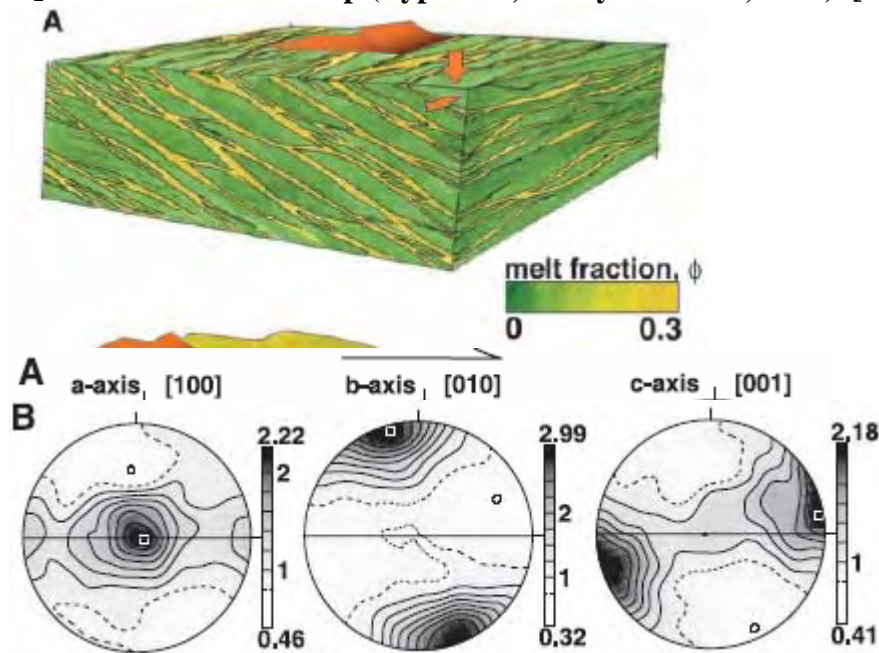
Olivine deformed in the presence of 8% melt shows the formation of melt-rich "C' " lenses and a type "B" LPO. Normally a type "B" LPO would indicate [001](010) slip, but TEM shows dislocations with b = [100] not [001] (Holtzman et al., 2003). Moreover, the

high H_2O activity and high stress that Jung & Karato (2001) suggested are necessary to produce a type "B" LPO are not present in the Holtzman et al. (2003) experiments. Holtzman et al. (2003) suggest that deformation is partitioned such that melt-free zones undergo orthogonal extension.
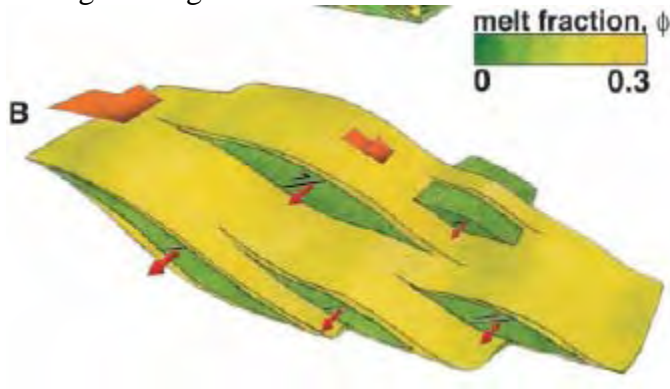
Clinopyroxene Lattice Preferred Orientations
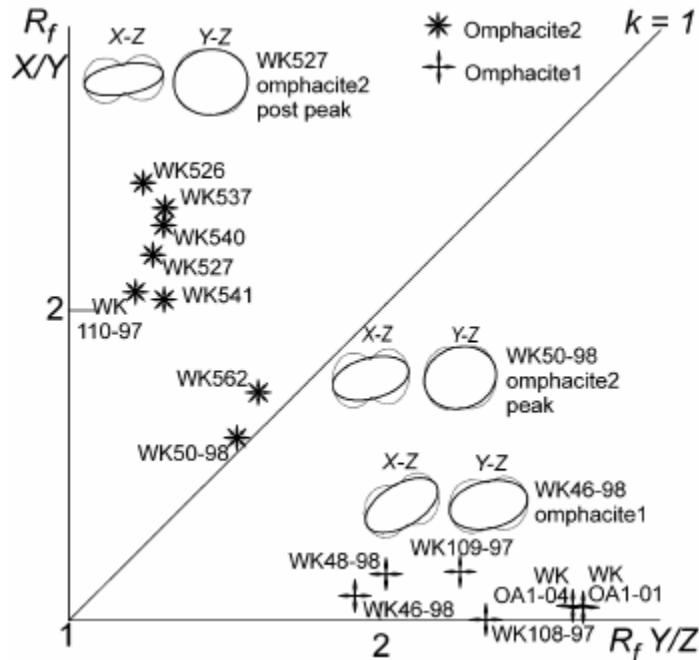
eclogites from the Tauern Window have textures indicating flattening to constrictional strains (Kurz, 2005)
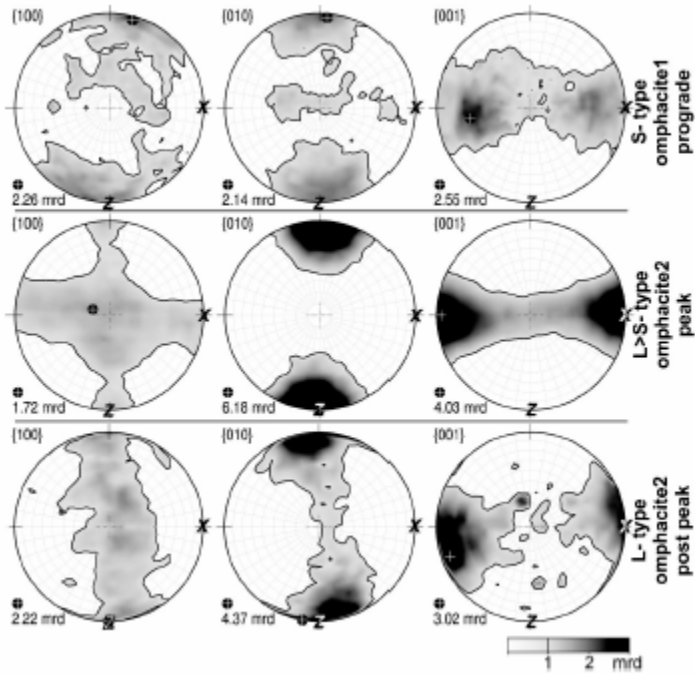
The LPO's are "compatible with this", indicating [001](100) slip (Kurz, 2005). Actually, the top row is barely statistically significant.

Effect of a Second Phase: Quartz
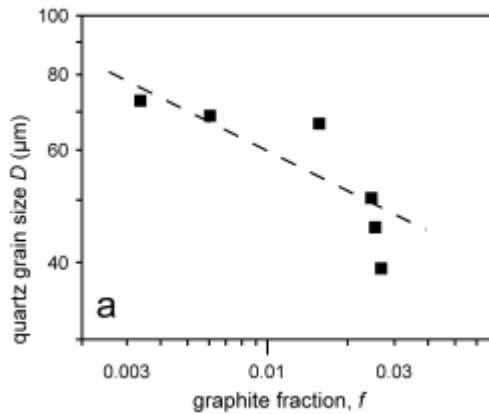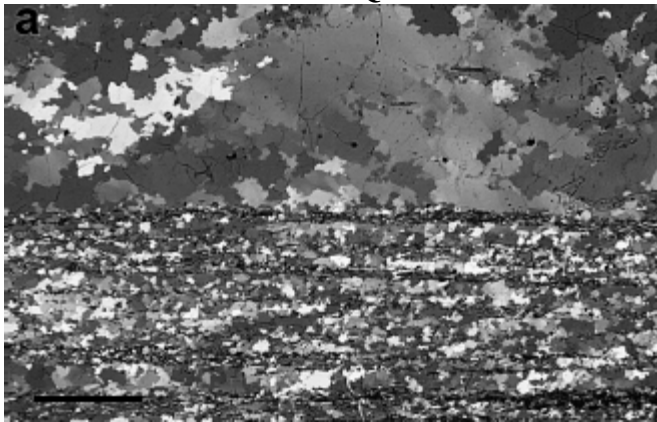
Quartz pinned by graphite (Krabbendam et al., 2003).
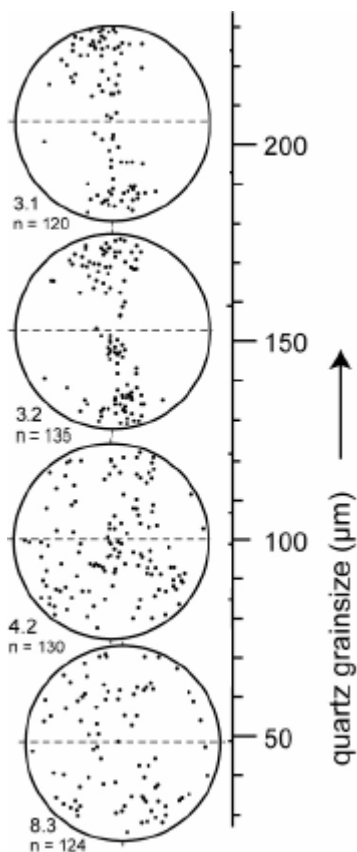
LPO affected by second phase (Krabbendam et al., 2003).
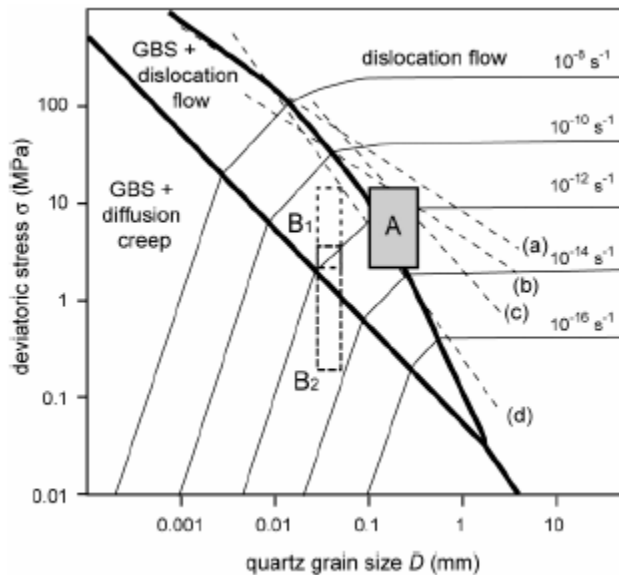
Conditions for (A) graphite-free layers and (B) graphite-rich layers (Krabbendam et al., 2003).
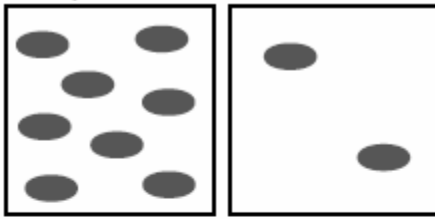
Effect of a Second Phase: Calcite
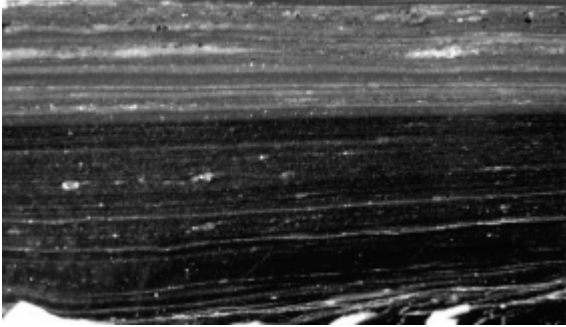
marble with varying proportions of phyllosilicates (Herwegh & Berger, 2004). The Zener parameter is

$$Z = \frac{d_p}{f_p}$$

where d_p is the grain size of the second-phase particles and f_p is the volume fraction of the second-phase particles.
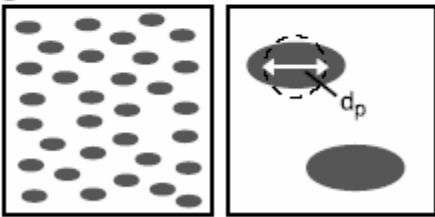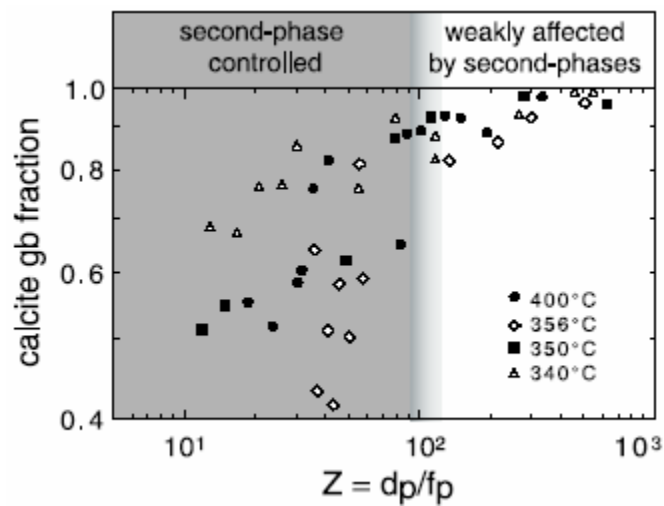

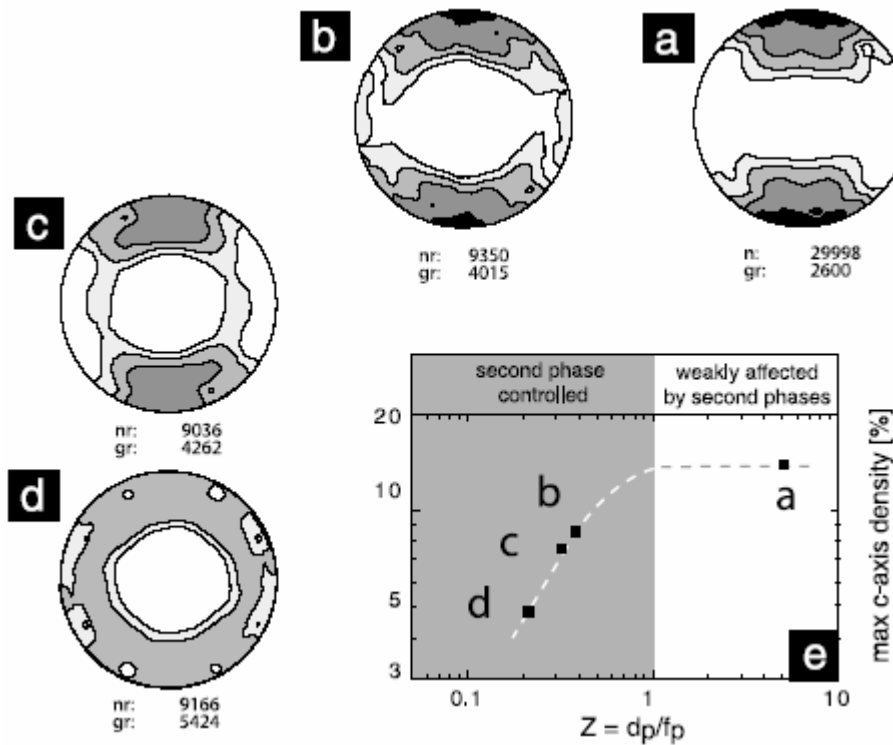Zener parameter (Herwegh & Berger, 2004).
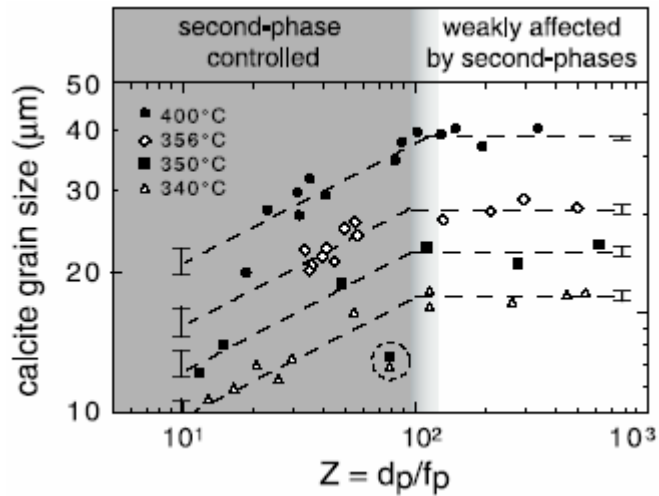
Pinning of calcite grain size is most effective at small Z and ineffective for $Z \geq 100$ (Herwegh & Berger, 2004).
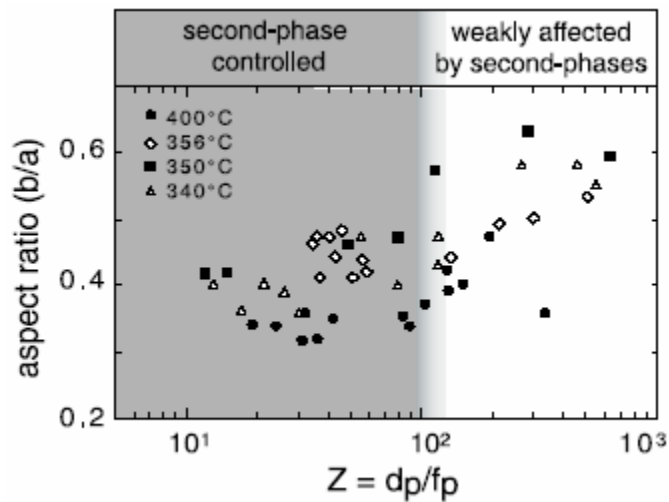
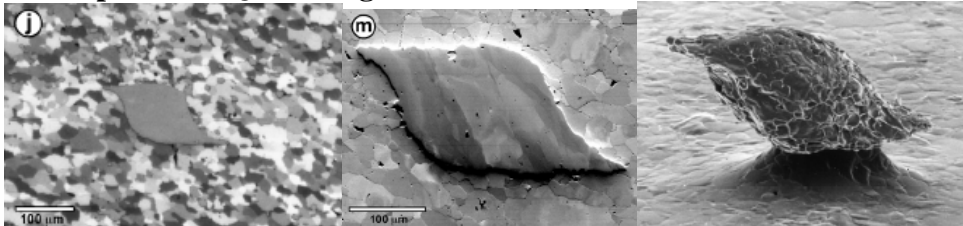Calcite grains are more inequant at small Z (Herwegh & Berger, 2004).

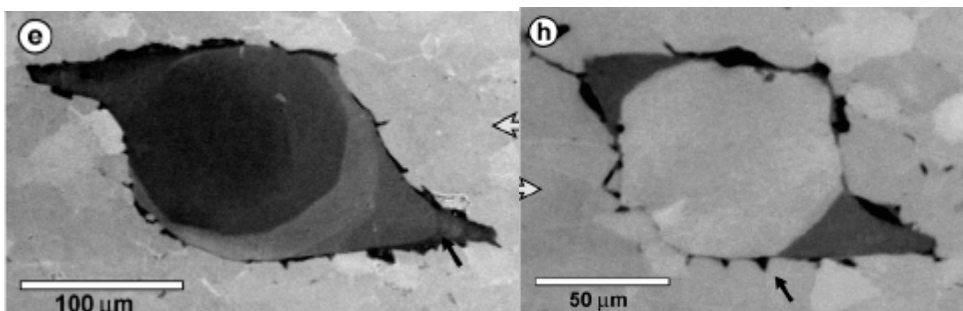The proportion of calcite–calcite grains in contact decreases with Z (Herwegh & Berger, 2004).

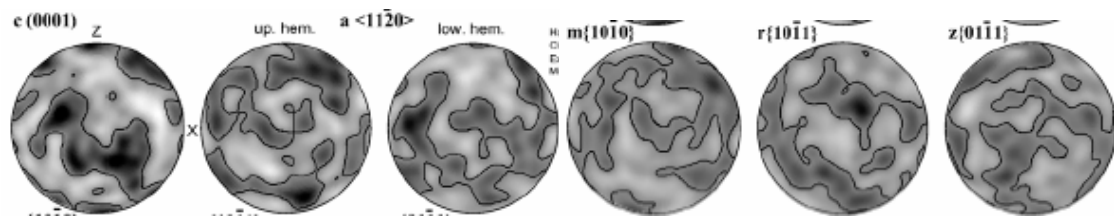LPO is strongly modified at low Z (Herwegh & Berger, 2004).

Development of Quartz Sigma Clasts in Marble

Single quartz grains in marble are sigma clasts (Bestmann et al., 2004).

CL images show absence of dislocation creep (Bestmann et al., 2004).

LPO indicate no dislocation creep (Bestmann et al., 2004).